



JRC CONFERENCE AND WORKSHOP REPORTS

Proceedings of the 23rd Transport and Air Pollution (TAP) conference – Part II

*15th-17th May 2019,
Thessaloniki, Greece*

Editors:
Mamarikas, Sokratis
Ntziachristos, Leonidas
Karamountzou, Georgia
Fontaras, Georgios

2020

This publication is a Conference and Workshop report by the Joint Research Centre (JRC), the European Commission's science and knowledge service. It aims to provide evidence-based scientific support to the European policymaking process. The scientific output expressed does not imply a policy position of the European Commission. Neither the European Commission nor any person acting on behalf of the Commission is responsible for the use that might be made of this publication. For information on the methodology and quality underlying the data used in this publication for which the source is neither Eurostat nor other Commission services, users should contact the referenced source. The designations employed and the presentation of material on the maps do not imply the expression of any opinion whatsoever on the part of the European Union concerning the legal status of any country, territory, city or area or of its authorities, or concerning the delimitation of its frontiers or boundaries.

Contact information

Name: Georgios FONTARAS

Address: European Commission, Joint Research Centre, Via Enrico Fermi, 2749, I - 21027 Ispra (VA) Italy

Email: Georgios.FONTARAS@ec.europa.eu

Tel.: +39 0332 786425

EU Science Hub

<https://ec.europa.eu/jrc>

JRC117559

EUR 30140 EN

PDF ISBN 978-92-76-17329-8 ISSN 1831-9424 doi:10.2760/978944

Luxembourg: Publications Office of the European Union, 2020

© European Union, 2020

The reuse policy of the European Commission is implemented by the Commission Decision 2011/833/EU of 12 December 2011 on the reuse of Commission documents (OJ L 330, 14.12.2011, p. 39). Except otherwise noted, the reuse of this document is authorised under the Creative Commons Attribution 4.0 International (CC BY 4.0) licence (<https://creativecommons.org/licenses/by/4.0/>). This means that reuse is allowed provided appropriate credit is given and any changes are indicated. For any use or reproduction of photos or other material that is not owned by the EU, permission must be sought directly from the copyright holders.

All content © European Union, 2020

How to cite this report: *Proceedings of the 23rd Transport and Air Pollution (TAP) conference – Part II*, EUR 30140 EN, Publications Office of the European Union, Luxembourg, 2020, ISBN 978-92-76-17329-8, doi:10.2760/978944, JRC117559.

Contents

2.5 Road transport management and emissions estimation	355
2.5.1 Microscale Vehicle Emission Modelling in Hong Kong.....	356
2.5.2 Vehicle velocity and air pollution: challenges on the speed limit reduction to 80 km/h in France	369
2.5.3 Network performance under different departure time strategies from traffic and emission perspective.....	375
2.5.4 Impacts of urban forms on road transport emissions and air quality	382
2.5.5 Mobility Scenarios in the Milan area: a modelling assessment of Air Quality	
389	
2.5.6 Scenarios for proposed updated Low Emission Zone in Denmark - impacts to emissions and air quality in Copenhagen	400
2.6 Alternative fuels, new powertrains	410
2.6.1 Real Driving Emissions of Passenger Cars – Examples of Testing and Evaluating	411
2.6.2 Charecterization of sub-23 nm particles and their measure for PFI/DI SI engines fueled with gasoline, ethanol and blend	425
2.6.3 Comprehensive Emission Characterisation of Exhaust from Alternative Fuelled Cars.....	435
2.6.4 Air Quality Impacts from Ethanol-blended Gasoline Deployment in China's Beijing-Tianjin-Hebei Region	446
2.6.5 Comparison of On-road Gaseous Emissions of a Best Seller Passenger Car with Different Powertrains: Diesel vs Gasoline vs Compressed Natural Gas	453
2.6.6 Comparative investigation on particulate and gaseous emissions from a pre-Euro 6 diesel LCVs fleet fuelled with different second-generation biodiesel blends	
462	
2.6.7 A Novel Technology of High-Pressure Thermochemical Recuperation for Efficiency Increase and Emissions Mitigation	474
2.6.8 Analysis of Pollutant Emissions of three Plug-in Hybrid Electric Vehicles ..	482
2.6.9 Simulation-based assessment of the CO ₂ emissions reduction potential from the implementation of mild-hybrid architectures on passenger cars to support the development of CO2MPAS.....	496
2.6.10 Main Diesel, Petrol or electric vehicles: what choice for improving urban air quality? A simulation plate-form and case study.	508
2.6.11 Electric Vehicles in the Republic of Croatia – Market Development, Usage and Outlook	521
2.7 Remote sensing of vehicle emissions	532
2.7.1 Finding NO _x -cheaters on the spot with Remote Sensing Devices	533
2.7.2 A Novel Method for Comparing Passenger Car Fleets and Identifying High-Chance Gross Emitting Vehicles using Kerbside Remote Sensing Data	546
2.7.3 NO _x RDE measurements with Plume Chasing - Validation, detection of high emitters and manipulated SCR systems	556

2.7.4 Multi-instrument enhancement of remote sensing on-road vehicle emissions measurements	565
2.7.5 NO _x emissions from Euro 5 and Euro 6 light-duty diesel vehicles as measured by remote sensing, PEMS and in legislative laboratory test cycles	575
2.7.6 Study on the durability of UK diesel and petrol passenger car emission control systems utilising remote sensing data.....	582
2.8 Particulate Matter	589
2.8.1 Vertical profiles of lung deposited surface area concentration of particulate matter measured with a drone in a street canyon	590
2.8.2 How much Tyre Wear (Microplastic) is Effectively Contributing to PM10? Insights from Automated SEM/EDX Single Particle Analysis	594
2.8.3 Numerical study of particle dispersion emitted from train brakes in underground station.....	602
2.9 Special Session on H2020 projects.....	613
2.9.1 The PEMS4Nano project: measuring engine emissions below 23nm	614
2.9.2 Particle Reduced, Efficient Gasoline Engines: A Second Year Report on the PaREGEn Project.....	646
2.9.3 GPF model-based optimization methodologies supporting RDE conformity	656
2.9.4 Particle emissions measurements on CNG vehicle focusing on, sub-23nm	666
2.10 New sensors and techniques	678
2.10.1 Development and test of a new device collecting at source airborne particles issued from rolling stocks brakes systems.....	679
2.10.2 REAL-e: Robust and affordable IoT solution for market surveillance	691
2.10.3 Development of a Low-Cost Quartz-Enhanced Photoacoustic Spectroscopy Nitrogen Dioxide Sensor Network for Air Pollution Measurements.....	703
2.10.4 Making sense of variability in real-world vehicles emissions.....	708
2.10.5 Ultrafine particle dispersion in the wake of a squarecak vehicle model.....	725

2.5 Road transport management and emissions estimation

This section includes papers presented in the context of the “Road transport management and emissions estimation” session of the TAP conference. Table 6 provides an overview of these papers, as they are listed in the following sub-sections.

Table 6. Titles and authors of “Road transport management and emissions estimation” papers

	Paper Title	Authors
2.5.1	Microscale Vehicle emission modelling in Hong Kong	C.K.L. Wong, T.S. Lo, H.L.A. Wong, K.L. Lam, H. C. Frey, R. Smit, S. Hausberger, K. Weller and L. Ntziachristos
2.5.2	Vehicle velocity and air pollution: challenges on the speed limit reduction to 80 km/h in France	M. Long-Fournel, V. Buttignol and C. Eyssartier
2.5.3	Network performance under different departure time strategies from traffic and emission perspective: a global sensitivity analysis	D. Lejri, G. Meynet and L. Leclercq
2.5.4	Impacts of urban forms on road transport emissions and air quality	A. Elessa Etuman and I. Coll
2.5.5	Mobility scenarios in the Milan city centre: a modelling assessment of air quality	V. Agresti, P. Giani, G. Pirovano, G. Lonati and N. Pepe
2.5.6	Scenarios for proposed updated Low Emission Zone in Denmark - impacts to emissions and air quality in Copenhagen	S.S. Jensen, M. Winther, M. Ketzel and T. Ellermann

2.5.1 Microscale Vehicle Emission Modelling in Hong Kong

C.K.L. Wong¹, T.S. Lo¹, H.L.A. Wong¹, K.L. Lam¹, H. C. Frey², R. Smit³, S. Hausberger⁴, K. Weller⁴, L. Ntziachristos

¹ Mobile Source Group, Hong Kong Environmental Protection Department, Hong Kong SAR Government, China, carolw@epd.gov.hk

² Department of Civil, Construction and Environmental Engineering, North Carolina State University, Raleigh, North Carolina, 27695-7908, United States

³ Centre of Transport Strategy, University of Queensland, Brisbane, Australia

⁴ Institute of Internal Combustion Engines and Thermodynamics, Graz University of Technology, Ineffeldgasse 19, 8010 Graz, Austria

⁵ Department of Mechanical Engineering, Aristotle University of Thessaloniki, Thessaloníki, Greece

Introduction

A vehicle emission model is a mathematical tool to estimate vehicular emissions according to vehicle fleet composition, activities and ambient conditions. Their applications include compilation of vehicle emission inventory, evaluating the environmental impact for various projects, and estimating the effectiveness of various emission reduction control policies. Most of the popular vehicle emission models, e.g., COPERT developed for EUJRC (COPERT, <https://www.emisia.com/utilities/copert/>), MOVES (MOVES, <https://www.epa.gov/moves>) developed by USEPA and EMFAC (EMFAC, <https://www.arb.ca.gov/emfac/>) developed by CARB are macroscale or mesoscale. That is, the temporal resolution is at most hourly and the spatial resolution is in area level.

Real-world application of vehicle emission models, however, is often in microscale. For example, in metropolis such as Hong Kong, the road segments are often of the scale around 200 m. The average distance of the road segments between junctions in the urban area is about 50 m. To correctly model the vehicle emissions, one has to consider much more details of the driving situations. The characteristics of stop-and-go driving, frequency of hard accelerations and road gradient may have significant impact to the emissions. These impacts, however, may have been largely ignored or averaged in the macroscale/mesoscale model. Microscale vehicle emission model would be more useful in these applications.

In this study, we strive at developing a microscale vehicle emission model. The targeting application is a short road segment in Hong Kong. We shall consider 3 models, namely Passenger car and Heavy duty Emission Model (PHEM), P Δ P and Modal and Peak Model (MAPM), in this study. These models differ considerably in the modelling methodology. 1) PHEM, (Hausberger, 2016), (Luz, 2014), (Hausberger, 2012), (Hausberger, 2003), employs engine map to predict the second-by-second emissions. The model has been used to generate the vehicles emission factors in the HBEFA (HBEFA, <http://www.hbefa.net/e/index.html>). 2) P Δ P is a microscale vehicle emission model used in Australia for light duty and heavy duty vehicles vehicles (Smit, 2013; 2014; Smit et al., 2017). The model involves multivariate regression of the emission to numerous and optimised variables. The model is mainly statistically based on power and its derivative. 3) MAPM uses power binning as the core methodology similar to MOVES. The fundamental variables for the prediction are the binned vehicle speed and vehicle specific power (VSP) for light duty vehicles and scaled traction power (STP) for heavy duty vehicles). Mappings from these variables to the emissions are then created for the prediction. This binning method has been mainly used for meso/macro-scale emission modelling in US, but its applicability could be extended to microscale if more details are added.

The targeting application area is streets in Hong Kong. The spatial resolution is around 200m, and the temporal resolution is about 10 seconds. The aforementioned three models are developed/calibrated for the Hong Kong specific situation. Real-world vehicle emission measurement data using Portable Emissions Measurement System (PEMS) are used for the model development and validation. Data from a total of 18 vehicles including double deck buses, coaches and taxis are used for model development and another 3 vehicles for model validation.

In this paper, we shall present in details: the methodology used, development of the three models and their validation results.

Measurement Methodology

PEMS data from 18 vehicles are used for the model development as follows:

Table 1. Vehicles used for the model development.

Vehicle Class	Fuel	Euro Standard	GVW	Vehicle Brand	No. of Vehicles
Double deck bus	Diesel	Euro V	24 t	ALEXANDER DENNIS	5
Coach	Diesel	Euro V	16 – 17 t	MAN	1
				DAEWOO	3
				VOLVO	1
				SCANIA	3
Taxi	LPG	Euro 5	< 3 t	TOYOTA	5

The testing procedure of PEMS follows the most stringent testing requirements stipulated in ISO 16183, US CFR 1065 Subpart J and PEMS requirements in Euro VI regulation. Zero checking/calibrations, audit checking and span checking/calibration of the gaseous analysers were performed every hour, 3 hours and twice a day, respectively. The PEMS tests were conducted in real-world driving. The drivers are professional drivers of the same type of vehicles. There are two types of measurements; 1) the testing vehicle follows the vehicles of the same type to simulate their driving characteristics; 2) the testing vehicle is driven on a pre-determined route which includes both urban and highway driving. For heavy duty vehicles, the payload would be 50-60% of the maximum, whereas the payload would be the weight of PEMS and its accessories which are >50% of the maximum for the light duty vehicles. 2-3 fuel samples from the fuel tank were analysed for each vehicle to ensure no abnormality in the fuel specification.

The analysers being used for CO₂, CO, NO, NO₂ and THC measurements are SEMTECH-DS and AVL GAS PEMS. For SCR vehicles, N₂O, CH₄, NH₃ & various HC species were also measured by A&D portable FTIR. Exhaust flow meter was used to measure the exhaust flow rate and the exhaust flow temperature. A speedometer was attached to the wheel of the vehicle to record the vehicle speed. A weather probe was installed at the top of the vehicle to record the ambient temperature and relative humidity. An engine speed sensor is used to record the engine speed of the vehicle. GPS with dead reckoning is used to record the position of the vehicle. Its result is combined with the measurement from barometer, and the survey data from the Lands Department to estimate the road gradient of the testing vehicle. The data frequency of all these measurement is 1Hz. The example installation of PEMS is shown in Figure 1.

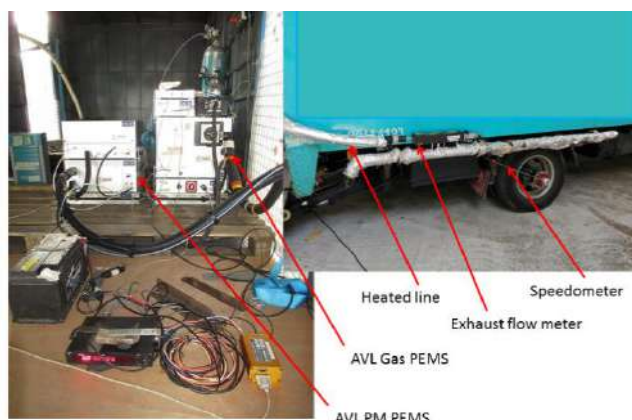


Figure 1: Example PEMS set-up for a heavy duty truck

PHEM

Model Development

The modelling methodology in PHEM is depicted in Figure 2. The heart of the model is the engine map (emissions vs. engine power and engine speed). To build the engine map using the PEMS data, the engine speed data from the engine speed sensors are used. The engine speed and the CO₂ emissions are used to determine the engine power through a generic CO₂ engine map.

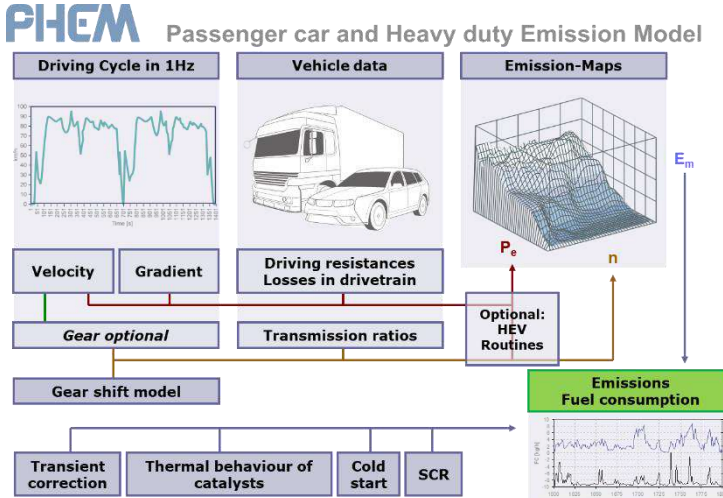


Figure 2: Schematic presentation of the methodology used in PHEM

The emission predictions from the engine maps can also be corrected by transient correction functions (Hausberger, 2016), (Luz, 2014), (Hausberger, 2012), (Hausberger, 2003). Due to time constraints, for the Hong Kong data set no transient correction was applied yet in PHEM.

For building the engine map, data from two road tests with at least 4,000 seconds for each vehicle are used for modelling. For this data set instantaneous engine speed and emission signals were accurately time aligned, which is a prerequisite for correct engine emission maps.

The rest of the data are used for the calibration. For calibration, the simulated and measured 100 second averaged emission results for every component are plotted over the 100 second averaged power values. Then linear equations are fitted for the simulated and the measured emissions. The difference between the two lines is added to the values in the emission map simply as function of the engine power value of the map point.

The SCR and the cold start corrections cannot be done in this study because no temperature upstream of SCR data is available from the measurements to set up the model.

PHEM Light, a simplified version of PHEM designed to be integrated into traffic models (e.g. SUMO), is also used. Characteristic emission lines (emission vs normalized engine power) are used instead of engine maps in PHEM Light. The model is independent of engine speed. No details on transmissions of the vehicle and gear shift model are needed. The transient corrections are not applied, but the model calibration is adjusted by the characteristic emission line generated by the rest of the PEMS data.

Model Application

Engine speed is estimated by a gear shift model of PHEM. Power is estimated by the second-by-second vehicle speed and road gradient (Hausberger, 2016), (Luz, 2014), (Hausberger, 2012), (Hausberger, 2003):

$$P = P_R + P_L + P_a + P_s + P_{\text{auxiliaries}},$$

where P_R is the power to overcome rolling resistance in [W], P_L is the power to overcome air resistance in [W], P_a is the acceleration power in [W], P_s is the power to overcome the road gradient in [W], $P_{\text{Auxiliaries}}$ is the power consumption of auxiliaries in [W].

$P\Delta P$

The model is designed to simulate the impacts of changing traffic and operational conditions, as well as a wide range of traffic measures, on air pollution and greenhouse gas emission levels *at fleet level* (Smit, 2013). These include, for instance different degrees of congestion, tunnel emissions, signals versus roundabouts, signal settings, eco-driving and dynamic speed limits.

Central to the $P\Delta P$ is the estimation of vehicle power (P) and the change of power (ΔP). The following on-road instantaneous power is estimated with algorithms (Smit R., 2014) from the European ARTEMIS project (Rexeis et al., 2005) were adopted for the $P\Delta P$ model:

- power required to overcome aerodynamic resistance
- power required to overcome tyre rolling resistance
- power required to overcome drive train/transmission resistance
- power required to overcome inertial resistance
- power required to overcome gravitational resistance
- power required to run auxiliaries

The power and the change of power are the explanatory variables. For power, both positive and negative engine powers and their transformations (log or square-root) are used. For the change of power, i) power difference: $\Delta P(\tau)_t = P_t - P_{t-\tau}$; ii) power oscillation: $\Delta P(\tau)_t = |P_t - P_{t-1}| + \dots + |P_{t-\tau+1} - P_{t-\tau}|$ and iii) normalised power oscillation: $\Delta P(\tau)_t^* = \Delta P(\tau)_t / \Delta x(\tau)_t$ are used.

The preceding time period τ covered by $\Delta P(\tau)_t^*$ is variable, and takes the values of $\tau = 3, 6, 9, 12, 15, 30$ and 60 seconds. Note that the last variable $\Delta P(\tau)_t^*$ (kW/m) represents the $\Delta P(\tau)_t^*$ variable normalised for distance over preceding time period τ .

In addition, the temperature of the exhaust is an important factor affecting the emissions especially for the taxis equipped with three way catalyst and vehicles equipped with SCR. The after-treatment device functions properly only when the temperature is above the light-off temperature, and emission control efficiency changes sharply around this temperature, which could be roughly described as a reverse logistic function $e_t = \beta_0 + \frac{\beta_1}{(1 + \beta_2 e^{T(\tau)t - T^*})} + \varepsilon$, where e_t is pollutant emission rate at $t = t$ (g/s), $T(\tau)t$ is average exhaust temperature over the last τ seconds at time t ($^{\circ}\text{C}$) and T^* is light-off exhaust temperature ($^{\circ}\text{C}$).

To linearize the effect of the exhaust temperature, the modelling team considers the transformation:

$$F_t = \left(b_0 + \frac{b_1}{(1 + \exp^{T(\tau)t - T^*})} \right) / (b_0 + b_1) \quad \text{if } b_1 > 0$$

$$F_t = \left(b_0 + \frac{b_1}{(1 + \exp^{T(\tau)t - T^*})} \right) / b_0 \quad \text{if } b_1 \leq 0$$

A method is required to estimate temperature as a function of variables for which input data are available. The model, $T_t = \beta_0 + \beta_1 \ln(1 + W(\Delta t)_t^+) + \beta_2 \ln(1 + W(\tau)_t^+) + \varepsilon$, is used to predict instantaneous exhaust temperature T_t as function of work. $W(\Delta t)_t^+$ is the accumulated positive

work at time = t since the engine start and $W(\tau)_t^+$ is accumulated positive work over a period of τ seconds before time = t . Figure 3 shows two examples of the exhaust temperature predictions versus observed values.

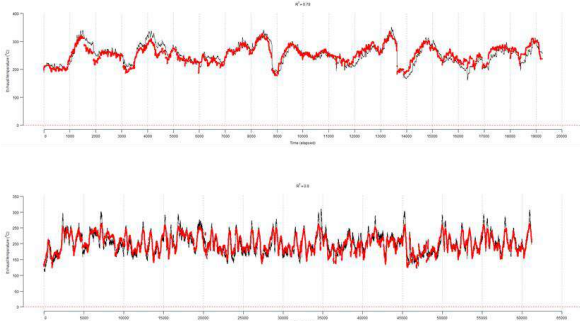


Figure 3: Time-series plots of temperature predictions for the coaches. Red dots: the exhaust temperature prediction; Black line: the measurement values after the tailpipe.

$P\Delta P$ backcasts driving behaviour which computes accumulated work, temperature and other model variables, such as delta power since $t = 0$ (engine start).

Various $P\Delta P$ model structures are possible with different levels of complexity and different expressions/definitions of power, delta power and temperature. For instance, the following structures could be used:

$$e_t = \beta_0 + \beta_1 P_t^+ + \varepsilon,$$

$$e_t = \beta_0 + \beta_1 P_t^+ + \beta_2 \Delta P(\tau)_t^* + \beta_3 P_t^2 + \beta_4 T(\tau)_t' + \varepsilon, \text{ or}$$

$$e_t = \beta_0 + \beta_1 \ln(1 + P_t^+) + \beta_2 P_t^2 + \beta_3 T(\tau)_t' + \beta_4 P_t \Delta P(\tau)_t + \beta_5 P_t T_t + \varepsilon.$$

The best model structure is identified as possessing using i) Mallow's C_p criterion (minimized C_p value, with $C_p \leq p$ and low p value); ii) 'Variance inflation factors' (VIFs) are calculated to check for significant multicollinearity; and iii) 'Constancy of error variance' (CEV) was created to check for homoscedasticity.

Modal and Peak Models

MAPM is a model similar to MOVES (MOVES, <https://www.epa.gov/moves>) developed by U.S. EPA. The modelling team modified i) the definition of operating modes in MOVES to better represent Hong Kong driving situations, and ii) added two new modes, peak and fuel cut-off modes, to improve the prediction of emission peak and fuel cut-off driving. In this section, the modelling methodology is described.

It was demonstrated that vehicle energy use and emissions (EU&E) are proportional to vehicle specific power (VSP) (Frey et al., 2002) (Jimenez-Palacios, 1999). Emission rates of different pollutants have different relationships with VSP (Frey et al., 2010). In MOVES, VSP is defined as power over vehicle mass for light duty vehicles and Scaled Tractive Power (STP) for heavy duty vehicles power over scaling factor (f_{scale}).

MOVES cannot be directly applied to Hong Kong because 1) maximum speed limit for heavy duty vehicles in Hong Kong is 70 kph and so most of the MOVES Operating Modes in high speed are not applicable in Hong Kong; and 2) the model may "average out" some of the high frequency variability in specially low and high emissions that cannot be directly explained by speed, acceleration, grade, VSP, STP, or other parameters derived from these.

To tackle the issue 1) above, the modelling team tried to re-define the Operating modes such that each mode has sufficient data samples and CO₂ emissions for different modes are significantly different. To achieve this target, the modelling team has tried different definitions of operating modes to the best model.

To tackle the issue 2) above, the modelling team devised two additional modes: the fuel cut-off mode and the peak mode for predicting the specially low and high emissions, respectively. To build those modes, CO₂ emission analysis by CART tree was used. In the CART analysis, the lagged VSP, i.e., VSP from 1 second ago, 2 seconds ago, etc., are also considered for modelling the possible "history" or "lag" effect of the emission.

MAPM for Taxi

Here we give an example to develop the model for taxis, the methodology of the developing the model for coaches and double deck buses are similar.

After a few iterations, the definition of the operating modes is proposed for taxi (Table 2). This definition has narrower speed range than MOVES. Braking is defined as being a deceleration of 3 km/h/s, or 1 km/h continuously for three seconds. Idle is defined as speed of 0 kph and acceleration of 0 kph/s.

Table 2: MAPM for an Average Hong Kong LPG Taxi Based on 20 kph Speed Ranges with Fuel Cut-Off and Peak Modes: Mode Definition, Time in Mode, Emission Rates and Total Emissions by Mode for CO₂, CO, HC, NO, and NO₂ (N= 401,251). (speed in kph)

HK Modes		Time		CO ₂			CO			HC			NO			NO ₂			Exhaust Temperature (°C)	
Speed	VSP	HK Mode	Secs	Percent	Ave (g/s)	Total (g)	Percent of Total	Ave (g/s)	Total (g)	Percent of Total	Ave (g/s)	Total (g)	Percent of Total	Ave (g/s)	Total (g)	Percent of Total	Ave (g/s)	Total (g)	Percent of Total	
Fuel cut-off	-3	27939	7.0%	0.90	25092	2.6%	0.001	36	2.4%	4.80E-05	1.34	1.8%	1.93E-04	5.38	2.8%	1.10E-05	0.31	4.2%	182	
-1	-2	27484	6.8%	1.19	32819	3.4%	0.002	42	2.8%	6.32E-05	1.74	2.4%	2.32E-04	6.38	3.3%	1.24E-05	0.34	4.7%	160	
0	-1	84651	21.1%	1.09	92537	9.6%	0.001	64	4.3%	7.32E-05	6.19	8.4%	3.95E-05	3.34	1.7%	5.36E-06	0.45	6.3%	144	
0-20	<0	0	15597	3.9%	1.22	19066	2.0%	0.001	20	1.3%	8.84E-05	1.38	1.9%	2.01E-04	3.14	1.6%	1.00E-05	0.16	2.2%	150
0-20	0-3	1	23004	5.7%	1.56	35811	3.7%	0.002	48	3.2%	1.96E-04	4.51	6.1%	3.22E-04	7.41	3.8%	1.16E-05	0.27	3.7%	151
0-20	3-6	2	8169	2.0%	2.75	22437	2.3%	0.004	35	2.3%	4.32E-04	5.53	4.8%	5.42E-04	4.43	2.3%	1.62E-05	0.13	1.8%	157
0-20	>6	3	3938	1.0%	3.77	14845	1.5%	0.006	22	1.5%	5.90E-04	2.32	3.1%	6.28E-04	2.47	1.3%	2.02E-05	0.08	1.1%	162
20-40	<0	20	18307	4.6%	1.64	29987	3.1%	0.002	36	2.4%	1.22E-04	2.24	3.0%	4.06E-04	7.44	3.8%	2.01E-05	0.37	5.1%	161
20-40	0-3	21	15406	3.8%	2.21	34100	3.5%	0.003	44	2.9%	1.96E-04	3.02	4.1%	7.69E-04	11.84	6.1%	3.46E-05	0.53	7.4%	164
20-40	3-6	22	13788	3.4%	3.03	41762	4.3%	0.004	53	3.6%	2.84E-04	3.91	5.5%	8.69E-04	11.98	6.2%	3.19E-05	0.44	6.1%	168
20-40	6-9	23	10997	2.7%	3.98	43792	4.5%	0.006	62	4.1%	4.55E-04	5.00	6.8%	8.02E-04	8.82	4.5%	2.76E-05	0.30	4.2%	174
20-40	9-12	24	6924	1.7%	4.94	34190	3.5%	0.007	50	3.3%	5.66E-04	3.92	5.3%	1.01E-03	6.99	3.6%	3.10E-05	0.21	3.0%	180
20-40	12-15	25	2984	0.7%	5.86	17501	1.8%	0.007	21	1.4%	6.08E-04	1.82	2.5%	1.19E-03	3.54	1.8%	3.54E-05	0.11	1.5%	184
20-40	>15	26	972	0.2%	7.08	6882	0.7%	0.010	10	0.7%	7.97E-04	0.78	1.1%	2.02E-03	1.96	1.0%	4.52E-05	0.04	0.6%	193
40-60	<0	40	13488	3.4%	1.93	25973	2.7%	0.003	35	2.4%	1.04E-04	1.40	1.9%	4.42E-04	5.97	3.1%	2.02E-05	0.27	3.8%	182
40-60	0-3	41	12210	3.0%	2.32	28269	2.9%	0.003	38	2.5%	1.24E-04	1.51	2.0%	5.91E-04	7.22	3.7%	2.44E-05	0.30	4.1%	186
40-60	3-6	42	13190	3.3%	3.02	39808	4.1%	0.004	54	3.6%	1.70E-04	2.24	3.0%	7.40E-04	9.77	5.0%	2.89E-05	0.38	5.3%	188
40-60	6-9	43	10903	2.7%	3.91	42637	4.4%	0.006	64	4.3%	2.48E-04	2.70	3.7%	7.21E-04	7.86	4.0%	2.70E-05	0.29	4.1%	192
40-60	9-12	44	8272	2.1%	4.92	40670	4.2%	0.008	64	4.2%	3.46E-04	2.86	3.9%	8.32E-04	6.88	3.5%	2.58E-05	0.21	2.9%	204
40-60	12-15	45	4597	1.1%	5.83	26812	2.8%	0.008	37	2.5%	3.75E-04	1.73	2.3%	1.02E-03	4.69	2.4%	3.10E-05	0.14	2.0%	207
40-60	>15	46	2520	0.6%	7.15	18009	1.9%	0.012	31	2.1%	5.31E-04	1.34	1.8%	1.73E-03	4.36	2.2%	3.91E-05	0.10	1.4%	207
>60	<0	60	10234	2.6%	2.35	24083	2.5%	0.005	52	3.5%	1.36E-04	1.39	1.9%	5.06E-04	5.17	2.7%	1.73E-05	0.18	2.4%	210
>60	0-3	61	10236	2.6%	2.55	26090	2.7%	0.005	46	3.1%	1.18E-04	1.20	1.6%	7.47E-04	7.65	3.9%	2.33E-05	0.24	3.3%	206
>60	3-6	62	14351	3.6%	3.05	43780	4.5%	0.005	71	4.8%	1.39E-04	1.99	2.7%	8.21E-04	11.78	6.0%	2.41E-05	0.35	4.8%	207
>60	6-9	63	14888	3.7%	3.74	55631	5.8%	0.006	96	6.4%	2.04E-04	3.03	4.1%	7.61E-04	11.32	5.8%	2.42E-05	0.36	5.0%	210
>60	9-12	64	12003	3.0%	4.58	54934	5.7%	0.010	116	7.7%	2.99E-04	3.59	4.9%	7.63E-04	9.15	4.7%	2.32E-05	0.28	3.8%	218
>60	12-15	65	7729	1.9%	5.43	41954	4.3%	0.012	92	6.1%	3.71E-04	2.87	3.9%	9.59E-04	7.41	3.8%	2.47E-05	0.19	2.6%	227
>60	15-18	66	3468	0.9%	6.18	21434	2.2%	0.016	55	3.7%	4.45E-04	1.54	2.1%	1.16E-03	4.01	2.1%	2.84E-05	0.10	1.4%	233
>60	18-21	67	1293	0.3%	6.82	8823	0.9%	0.020	26	1.7%	5.26E-04	0.68	0.9%	1.37E-03	1.77	0.9%	3.06E-05	0.04	0.5%	243
>60	>21	68	734	0.2%	7.97	5847	0.6%	0.043	32	2.1%	9.43E-04	0.69	0.9%	2.09E-03	1.54	0.8%	2.98E-05	0.02	0.3%	247
Peak		99	974	0.2%	10.54	10267	1.1%	0.046	45	3.0%	1.39E-03	1.36	1.8%	3.17E-03	3.09	1.6%	5.26E-05	0.05	0.7%	233

Fuel Cut-off Mode Development

CART analysis is used to identify conditions in which the fuel use rate of the measured data is lower than the lowest modal average rate. The CART tree is shown in Figure 4. In the figure, VSP_Lx represents the value of VSP in the previous x seconds. The fuel cut-off mode is defined as the lowest CO₂ emission leaf node (in red circle).

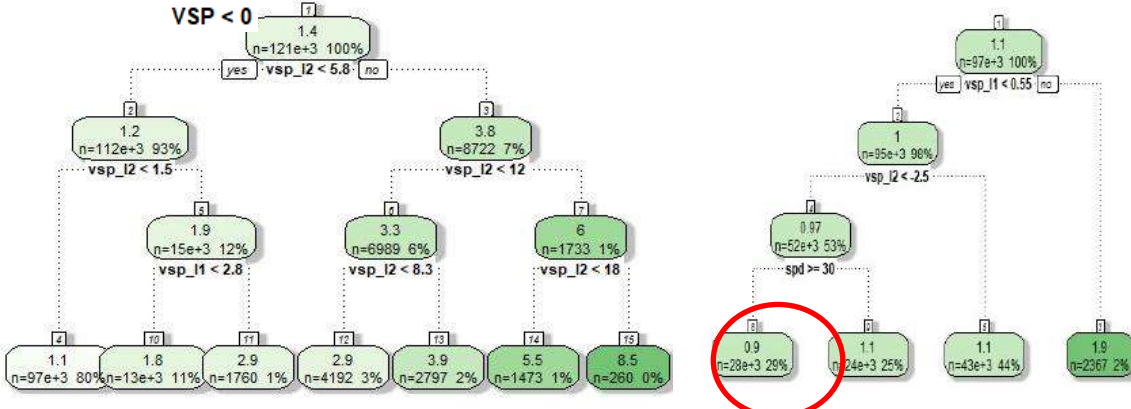


Figure 4: CART Regression Tree analysis for LPG Taxi Data for the definition of the fuel cut-off mode. Fuel cut-off mode is defined as the tree node in the red circle.

When CART-derived rule is applied to detect fuel cut-off in the measured data, it correctly predicts CO₂ emission rates that are less than the idle modal average rate for 22,102 data points. It also correctly identifies that 285,055 data points do not have fuel cut-off. It predicts, incorrectly, that 5,837 data points are fuel cut-off when they really are not (false positives), and it predicts that 88,257 data points are not fuel cut-off when they really are (false negatives).

Peak Mode Development

The peak mode is defined by another CART tree analysis (Figure 5). The peak is defined as VSP_L1>19, VSP_L2>19 and speed <85 km/h. Based on the simplified rule, the mean CO₂ emission rate is 10.23 g/sec from a total sample size of 1183, which is substantially higher than the highest modal average rate of 8.62 g/sec. This rule leads to 827 true positives and only 356 false positives, while it has 397,348 true negatives and 2,719 false negatives.

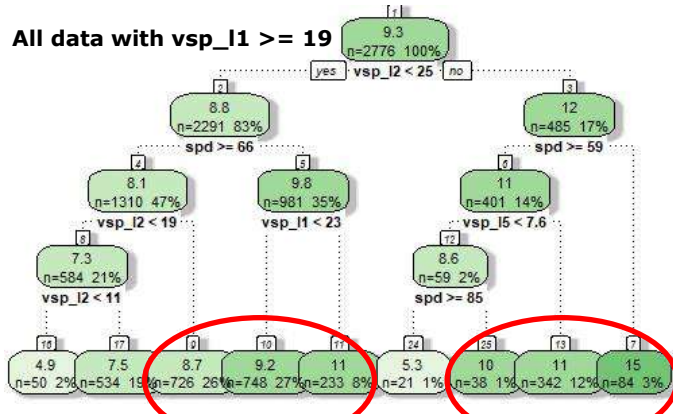


Figure 5: CART Regression Tree analysis for LPG Taxi Data for the definition of the peak mode. The rule for the peak mode is simplified as $VSP_L1 \geq 19$, $VSP_L2 \geq 19$ and speed < 85 (The CO₂ emissions are higher than 8.7 g/s)

Final MAPM for Taxi

The modal average emission rates for the final MAPM for LPG Taxis are shown in Figure 6. The modal average CO₂ emission rate clearly increases monotonically with positive VSP in each speed range. The CO emission rates are highest at high VSP in the two highest speed ranges. The HC emission rates are typically increasing monotonically with VSP in each speed range. The highest NO emission rate are observed at mode 26, 46 and 68, which is the highest range of VSP at the each speed range. The trend in NO₂ emission rates is somewhat counter-intuitive, in that it seems to either decrease with increasing positive VSP or to not have much of a trend with respect to VSP.

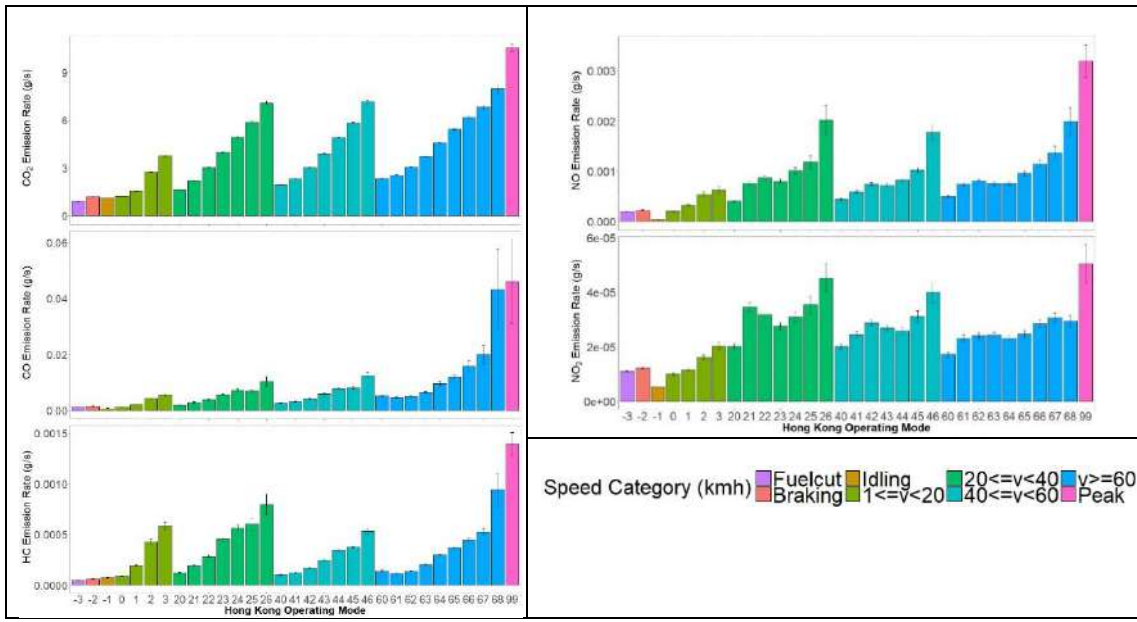


Figure 6: Modal average emission rates, with 95 percent confidence intervals on the mean, for the Modal and Peak Model for an Average Hong Kong LPG Taxi (N= 401,251)

Model Validation

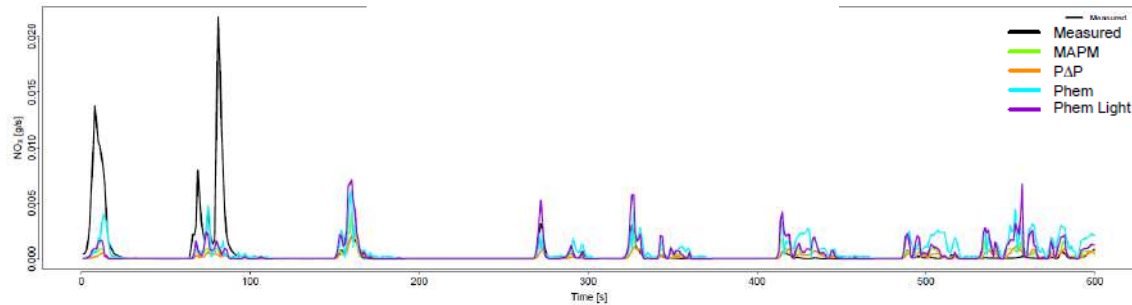
The models' predictions are validated by two PEMS datasets after the model development (Table 3), Dataset A and Dataset B.

For dataset A: while the vehicles of the validation data are included in the model development, the dataset itself is not. For dataset B: the vehicles are not included in the modelling. The NOx emissions of these 3 vehicles are close to the average emissions of the vehicles in that particular class.

Table 3: Datasets for model validation

Dataset A	Dataset B
PEMS data for 3 road networks for all the vehicles in the Modelling Dataset, each lasting for 10 minutes	PEMS data for 3 road networks for all the following vehicles which are not in the Modelling Dataset, each lasting for 10 minutes: <ul style="list-style-type: none"> ● 1 Euro 5 LPG taxi ● 1 Euro V diesel coach of 15-24 tonnes ● 1 Euro V diesel double deck bus of about 24 tonnes

Figures 7-9 show the exemplified time series of the predictions and the measurement for NOx. It is observed that the predictions for double deck buses and coaches are better than those of taxis. There seems no significant difference between the prediction for dataset A and B. All models could predict the locations of the emission peaks quite accurately. However, none of the model could estimate the amplitude of the peak correctly, especially for taxis.



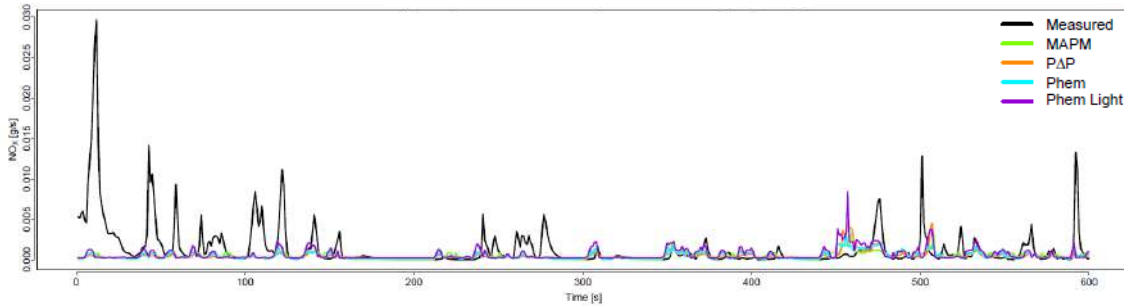


Figure 7: Time plot comparison of measured NO_x emission rate (g/sec) for taxi. Above: validation of dataset A, and bottom: validation of dataset B.

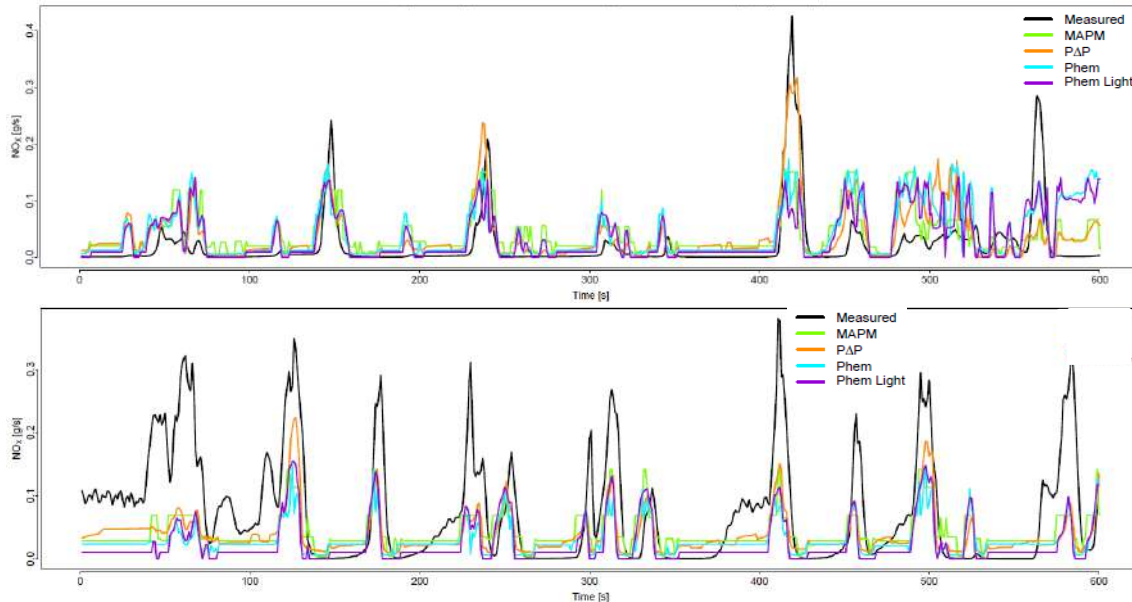


Figure 8: Time plot comparison of measured NO_x emission rate (g/sec) for bus. Above: validation of dataset A, and bottom: validation of dataset B.

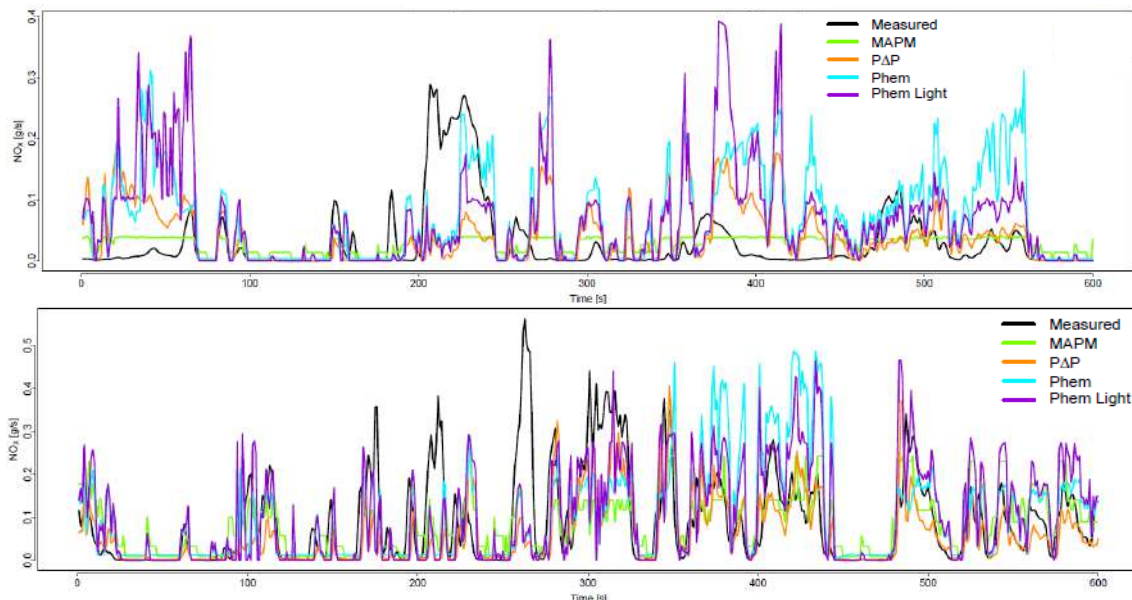


Figure 9: Time plot comparison of measured NO_x emission rate (g/sec) for coach. Above: validation of dataset A, and bottom: validation of dataset B.

To further quantify the errors, three statistical metrics are used. Firstly, Mean absolute error (MAE) (Hyndman and Koehler, 2006; Makridakis et al. 1998) is used to quantify the errors in second-by-second level.

$$MAE = \frac{1}{n} \sum_{i=1}^n |e_i|$$

where $e_i = y_i - \hat{y}_i$.

To eliminate scale dependency, we employ MAEm which was defined as the ratio [%] of the MAE to the respective average observed emission rate (g/s) in each case

$$MAEm = 100 * \frac{MAE}{\bar{y}}$$

The ideal value for both MAE and MAEm is 0. To quantify the error of the whole trip, Total emissions error (TEE)

$$TEE = 100 * \frac{\sum_{i=1}^n \hat{y}_i - \sum_{i=1}^n y_i}{\sum_{i=1}^n y_i}$$

is computed as a measure of the accuracy in predicting the total sum of emissions based on one-step-forecasts. The ideal value for TEE is 0. Pearson's r (R) (Bennett et al., 2013) is a measure of the linear correlation between the predicted and the observed values.

$$R = \frac{\sum_{i=1}^n (y_i - \bar{y})(\hat{y}_i - \bar{\hat{y}})}{\sqrt{\sum_{i=1}^n (y_i - \bar{y})^2} \sqrt{\sum_{i=1}^n (\hat{y}_i - \bar{\hat{y}})^2}}$$

Pearson's R is insensitive to systematic overestimation/underestimation of the observed values. The ideal value for R in our case is 1.

All the statistical metrics above were calculated in 10-second time steps, i.e., the 10-second average emission was predicted and compared. And the values were then averaged over all vehicles in the vehicle class. The results are shown in table 4-5. The accuracies for CO₂ for all models are good, no matter in 10-second level (MAEm), and 30-minute level (TEE). Also, the prediction correlated very well with the measurement as indicated in the value of R. There is no significant difference between the results in dataset A and B, meaning that the models are no over-specified for the modelling dataset.

Table 4: Validation results of CO₂ for different vehicle classes and models

CO ₂	Metric	Model	Dataset A			Dataset B		
			Bus	Coach	Taxi	Bus	Coach	Taxi
MAEm	MAPM		20%	24%	15%	21%	23%	21%
	PΔP		19%	20%	12%	21%	19%	16%
	PHEM		20%	22%	15%	23%	21%	20%
	PHEM Light		29%	21%	16%	42%	21%	22%
TEE	MAPM		5%	7%	2%	4%	6%	1%
	PΔP		6%	5%	2%	9%	7%	1%
	PHEM		6%	9%	6%	7%	2%	1%
	PHEM Light		13%	7%	3%	26%	3%	14%
R	MAPM		94%	93%	94%	92%	92%	88%
	PΔP		95%	95%	96%	93%	92%	92%
	PHEM		93%	94%	94%	91%	91%	89%
	PHEM Light		95%	94%	93%	92%	92%	90%

Table 5: Validation results of NOx for different vehicle classes and models

	Metric	Model	Dataset A			Dataset B		
			Bus	Coach	Taxi	Bus	Coach	Taxi
MAEm	MAPM	83%	61%	132%	67%	47%	90%	
		PΔP	82%	59%	123%	56%	51%	92%
	PHEM	106%	67%	223%	71%	54%	93%	
		PHEM Light	94%	68%	188%	72%	44%	101%
NOx	TEE	MAPM	19%	13%	53%	27%	15%	38%
		PΔP	14%	15%	26%	32%	43%	43%
	PHEM	38%	25%	153%	47%	25%	38%	
		PHEM Light	35%	22%	112%	56%	15%	22%
R	MAPM	58%	67%	41%	64%	74%	9%	
		PΔP	49%	70%	24%	72%	76%	1%
	PHEM	42%	62%	30%	60%	72%	3%	
		PHEM Light	40%	60%	35%	61%	80%	0%

Compared to CO₂ results, the NOx results are much worse. Regarding the 10-second level evaluation, the best predictions are for the Coach in which the MAEm is about 60% for all models. For buses and taxis, the values of MAEm rise to 82%-106% and 123%-223% for dataset A and 56%-72% and 90%-101% for dataset B. Roughly speaking, the MAPM and PΔP models perform better than PHEM and PHEM Light. Interestingly, the accuracy for dataset B is better than dataset A.

For the 30-minute evaluation, still the MAPM and PΔP models perform better than PHEM and PHEM Light. Especially for Taxi, the values of TEE of PHEM and PHEM Light could be double of that of MAPM and PΔP. The performance of PΔP drops when the evaluation data switches from dataset A to dataset B. It may mean that the model has some degree of over-specifying to the modelling dataset.

For the results of Pearson's correlation R, all models are basically the same, with MAPM and PΔP slightly better. However, the performances of all models are considerably better for buses and coaches, especially in dataset B.

The performance of the models for other pollutants CO, THC, NO, NO₂ and PM are more or less similar to NOx. If we weigh the importance of different vehicle classes by their share in total emissions of 2016 vehicle emission inventory in Hong Kong, and the pollutants by table 6 (Roughly representing their importance in the environment impacts in Hong Kong). The weighted averaged of all the statistical metrics are given in Table 7.

Table 6: Importance weighting of different pollutants by class

Weights	FBDD	NFB	Taxi
NO	27.3%	9.5%	3.2%
NO ₂	17.1%	5.9%	2.0%
NOx	0.0%	0.0%	0.0%
CO	1.9%	0.3%	2.7%
CO ₂	2.4%	0.5%	2.1%
THC	3.1%	0.5%	1.4%
PM ₁₀	16.6%	3.4%	0.0%

Table 7: Averaged statistical metrics of all models

Model	Dataset A			Dataset B		
	MAEm	TEE	R	MAEm	TEE	R
MAPM	75%	22%	62%	69%	27%	60%
PΔP	85%	29%	50%	70%	36%	61%
PHEM	93%	37%	49%	82%	49%	54%
PHEM Light	82%	35%	50%	77%	43%	54%

The overall statistics indicate that the MAPM and PΔP models perform slightly better than PHEM and PHEM light in this validation exercise.

Discussion and Conclusion

This paper discusses the development/calibration of microscale models from the PEMS data in Hong Kong. Three models PHEM, PΔP and MAPM are involved in this study for the vehicle classes: double deck bus, coach and taxi. The models developed/calibrated were validated by independent datasets. The results indicate that the accuracy of all models are approximately the same, with MAPM and PΔP slightly better. The evaluation of 30-minute level resolution is better than that of the 10-second level. Also, the predictions for bus and coach are better than that for taxi.

One should note that besides accuracy, many aspects of the model are important. For example:

- The computational speed,
- Easiness to use,
- Whether the required input data are available, and
- Whether model parameters are easy to update or calibrate

are important factors affecting whether the model is suitable for the users. However, these factors are not considered in this study.

Acknowledgements

We thank Alberto Ayala, Robert Sawyer and Alex Wai for their review and discussion.

References

- Bennett N.D., Croke B.F.W., Guariso G., Guillaume J.H.A., Hamilton S.H., Jakeman A.J., Andreassian V. (2013). Characterising performance of environmental models, *Environmental Modelling & Software*, 40, 1–20.
- COPERT, <https://www.emisia.com/utilities/copert/>
- EMFAC, <https://www.arb.ca.gov/emfac/>
- Frey H.C., Unal A., Chen J., Li S., Xuan C.(2002), Methodology for Developing Modal Emission Rates for EPA's Multi-Scale Motor Vehicle and Equipment Emission Estimation System, *EPA420-R-02-027, Prepared by North Carolina State University for the Office of Transportation and Air Quality, U.S. Environmental Protection Agency, Ann Arbor, MI, October 2002*
- Frey, H.C., Zhang K., Roushail N.M.(2010), Vehicle-Specific Emissions Modeling Based Upon On-Road Measurements, *Environmental Science and Technology*, 44(9):3594-3600.
- Hausberger S, (2003). Simulation of Real World Vehicle Exhaust Emissions; *VKM-THD Mitteilungen; Heft/Volumen 82; Verlag der Technischen Universität*; ISBN 3-901351-74-4; Graz 2003.
- Hausberger S., Rexeis M., Kies A., Schulte L., Verbeek R. et. al. (2012). Reduction and Testing of Greenhouse Gas Emissions from Heavy Duty Vehicles. *LOT 2; Development and testing of a certification procedure for CO₂ emissions and fuel consumption of HDV;DG CLIMA Contract N 070307/2009/548300/SER/C3*; Graz 2012
- Hausberger S., Rexeis M., Kies A., Weller K., Siberholz G. (2016). Future HD vehicle requirements due to legislation and effects on CO₂ and air quality, *3 INTERNATIONALER MOTORENKONGRESS 2016 ANTRIEBSTECHNIK 1M FAHRZEUG*, Baden Baden; 2016
- HBEFA, <http://www.hbefa.net/e/index.html>
- Hyndman R.J., Koehler A.B.(2006). Another look at measures of forecast accuracy. *International Journal of Forecasting*, 22(4), 679–688.
- Jimenez-Palacios (1999), J. L. Ph.D. Dissertation, *Massachusetts Institute of Technology*: Cambridge, MA, 1999.
- Luz R., Rexeis M., Hausberger S., Schulte L., Hammer J., Steven H., Verbeek R. et. al. (2014). Development and validation of a methodology for monitoring and certification of greenhouse gas emissions from heavy duty vehicles through vehicle simulation, *Final report, Service contract CLIMA.C.2/SER/2012/0004*; Report No. | 07/14/Rex EM-1 2012/08 699 from 15.05.2014
- Makridakis S.G., Wheelwright S.C., & Hyndman R.J. (1998). *Forecasting: methods and applications* (3rd ed). New York: John Wiley & Sons.
- MOVES, <https://www.epa.gov/moves>
- Rexeis M., Hausberger S., Riemersma I., Tartakovskiy L., Zvirin Y., Van Poppel M., Cornelis E., (2005). ARTEMIS - Assessment and Reliability of Transport Emission Models and Inventory Systems, *WP400 - Heavy Duty Vehicle Emissions*, DGTRN Contract 1999-RD.10429.
- Smit R.,(2013). Development and performance of a new vehicle emissions and fuel consumption software (PΔP) with a high resolution in time and space, *Atmospheric Pollution Research*, 4, 336-345.
- Smit R., 2014. PΔP: A simulationtable tool for vehicle emissions and fuel consumption software with a high resolution in time and space, *Vehicle Technology Engineer*, SAE Australasia, July 2014, 17-21.
- Smit, R., Kingston, P., Wainwright, D., Tooker, R. (2017). A tunnel study to validate motor vehicle emission prediction software in Australia, *Atmospheric Environment*, 151, 188-199.

2.5.2 Vehicle velocity and air pollution: challenges on the speed limit reduction to 80 km/h in France

M. Long-Fournel¹, V. Buttignol¹, C. Eyssartier²

marlene.long@cerema.fr

¹ Department of Transportation, Cerema, Aix en Provence, 13593, France

² Department of Transportation security, Cerema, Nantes, 44262, France

Introduction

Pollutant emissions from the road transport sector are generated by several types of sources: vehicles in road traffic (exhaust, leaks, tyre wear, brakes, corrosion), road abrasion, road equipment wear (slides, traffic signs, etc.). The energy consumption and pollutant emissions of road vehicles depend on (CITEPA, 2004): (i) vehicle features ("fleet" data): vehicle type (passenger car, light commercial vehicle, heavy goods vehicle, powered two-wheelers), engine and fuel (petrol, diesel, etc.), equipment, age, etc., (ii) conditions of use ("traffic" data): annual distance travelled, average length of a journey, networks used (which partly determine traffic speeds), weather conditions, vehicle maintenance, driving behaviour, etc.

Many pollutants emitted by the road transport sector may cause damages at different scales of time and space. Some pollutants have global impacts such as greenhouse gases (CO₂ and HFC especially) which contribute to global warming, while some pollutants have local and regional impacts on the environment and health (NOx, PM, benzene, etc.).

On pollutants with a global impact, according to the CITEPA (June 2015 report), in 2013, the share of greenhouse gases emissions due to the road transport sector represents more than 25% of total greenhouse gases emissions in France, i.e. nearly 125 Mteq CO₂. Unlike France's greenhouse gases emissions, which fell by about 11% over the period 1990-2013, transport sector emissions increased by 12% due to traffic growth (+32% between 1990 and 2003, +1.4% between 2003 and 2013). However, since 2015, road traffic has been increasing at a much higher rate than its annual average since 2011 (+2.5% in 2015 and 2016).

On pollutants with local or regional impacts, epidemiological studies (French Institute for Public Health Surveillance, 2013) show a relationship between distance from major roads or atmospheric concentrations of specific pollutants emitted by vehicles, and different health effects (asthma, disorders of lung function, heart diseases, etc.). According to the CITEPA (June 2015 report), in 2013, the share of main road pollutants represents 58% for NO_x, 13% and 16% for PM₁₀ and PM_{2.5}. When close to the road traffic, average annual concentrations are twice as high for NO₂ as for urban background, 1.2 times for PM₁₀ and PM_{2.5}. According to the regional air quality monitoring association AirParif, for nitrogen dioxide, the influence distance is more than 100 metres for major roads with traffic between 100,000 and 200,000 vehicles per day, between 50 and 100 metres for smaller roads (30,000 vehicles per day). At the same time, large urban areas (with more than 250,000 inhabitants) and, to a lesser extent, medium size urban areas (50,000 to 250,000 inhabitants), have concentration levels higher than the allowed values, mainly at measuring stations located near road traffic.

As part of the International Climate Conference (COP 21) held in Paris at the end of 2015, France committed itself to reducing greenhouse gases emissions in transport by 29% over the period 2015-2028. On the other hand, in February 2017, France received a warning from the European Commission for exceeding nitrogen dioxide air quality standards and insufficient action plans for 13 zones or urban areas; in May 2018, the European Commission announced their decision to refer the matter to the European Court of Justice.

To achieve these objectives, several actions to reduce greenhouse gases and nitrogen dioxide emissions are planned, such as changing individual behaviour (choice of transport mode, compliance with speed limits, way of driving, etc.).

The reduction of vehicle velocity should impact air quality thanks to some improvement to traffic flow conditions. The speed limit reduction measure (90 to 80 km/h) introduced by the French Prime Minister in January 2018 is part of a set of measures to reduce the number of people killed or seriously injured in road accidents. The change is implemented for a trial period from 1st July 2018 to 1st July 2020. As the ex-post impact assessment includes environmental and socio-economic aspects, this paper focuses on the methodology for assessing the impact of the reduction in vehicle velocity on air pollution, socio-economic effects and user's perception.

Background

Concerning greenhouse gases, a literature review by the French Environment & Energy Management Agency (2014) shows that, for a speed limit reduction from 90 km/h to 70 km/h (Chanut et al., 2012), CO₂ emissions estimated with macroscopic calculation methods – using emission laws according to a variable representative of the driving mode: speed for aggregate models like COPERT (COmputer Programme to calculate Emissions from Road Transport), traffic conditions for semi-aggregated models like ARTEMIS (Assessment and Reliability of Transport Emission Models and Inventory Systems) – increase from 2 to 4% while emissions estimated with microscopic methods – using traffic conditions usually derived from traffic modelling, taking not only an aggregated variable but a large number of parameters – decrease by 4%.

Concerning local and regional pollutants, many studies showed speed limits on roads and highways may reduce pollutant emissions and/ or concentrations. Especially if the new speed limit is not below 80 km/h, emissions or concentrations on all pollutants generally decrease (French Environment & Energy Management Agency, 2014). The speed limitation effects to 80 km/h in the Barcelona Metropolitan area (reducing speed limit up to 40 km/h) assessed with the modified modelling system show improvements in air quality levels; a reduction up to 5.7% according to pollutants over the area affected by the new speed limit (Gonçalvez et al., 2008). The comparison between free-flowing traffic (100 km/h) and an 80 km/h strict enforcement in Amsterdam and Rotterdam showed that emission reductions, estimated by air quality monitoring and traffic dynamics approaches, were in the range of 5–20% PM₁₀ and 20–30% NO_x (Heukens et al., 2010).

Methodology

The assessment of the societal effects of reducing speed limit to 80 km/h discussed in this paper should identify impacts in terms of environment, socio-economics effects and social acceptability based on qualitative and, where possible, quantitative analysis.

The environmental assessment examines the impact of the measure on air pollution considering greenhouse gases emission with an impact on climate change, but also local and regional pollutants emission with a health impact. If recent and representative air quality data exist for some road networks, an analysis of air quality measurements before implementation of the speed limit reduction will be performed; these data will have to be supplemented by new measurement campaigns after implementation of the speed limit reduction in order to compare results. Another way is modelling air pollutant emissions before and after the implementation of speed limit reduction. In this way, the impact of speed limit reduction will be estimated, for selected representative roads, based on the knowledge of factors that affect emissions of air pollutants from a vehicle. This modelling will be performed with the COPCETE tool for calculating pollutant emissions from road traffic according to the COPERT IV methodology and including the 1990–2030 French fleet from The French Institute of Science and Technology for Transport, Development and Networks (IFSTTAR). The COPCETE tool was developed by Cerema (previously CETE: technical centre for equipment) for internal use within the French Ministry of Ecology; based on the same methods and equations as the COPERT and Impact-Ademe software. It will take into account different factors like traffic volume and fleet characteristics, road network features, emission factors, speed profiles to estimate actual traffic speeds.

The socio-economic impact assessment is performed from the observation of benefits and losses for communities: killed and injured people, travel times losses and environmental externalities. The French frame reference for evaluating transport projects is the reference for our approach. The reference values of the French guide give a monetary valuation of the socio-economic impacts (such as time value, statistical value of human life, value of the CO₂ ton) and complement the qualitative and quantitative analysis of the effects. The socio-economic impact assessment follows the guidelines of proportionality and progressiveness, as required by the government instruction (2014) for the assessment of transport projects in France. The speed limit reduction measure is considered as a transport network modification. The methodology is based on a selection of 298 routes throughout France, representing commuting journeys. The collection of data is carried out on nearly 7,751 kilometers. More specifically, the study encompasses the travel time savings and losses by road users as well as the traffic flow conditions (API Gmaps, Floating Car Data, measurement campaigns). The various consequences of road accidents are grasped through the evolution of the number of killed and injured people, and accident rates on the secondary road network. The characterization of the time lost by road users is expressed in seconds per kilometre.

The social acceptability assessment examines the changes of the acceptability/ acceptance of this measure for 2 years. Several survey-waves of questionnaire will be disseminated from 2018 to 2020. In April 2018, a questionnaire was administrated before implementation of the measure to 5,310 respondents representative of the French population. For next waves, around 3,000 respondents should be considered. The chosen criteria for studying the acceptability/ acceptance of the measure are those usually studied for evaluating the acceptability of a road safety policy: attitude, efficiency, reliability, fairness, impact, etc. In the first wave, only a few items were introduced in the questionnaire about air pollution: one about the impact of the measure on reducing air pollution and another about the reason for having the intention to abide by the new speed limit. About this last question, one proposal was about the intent to pollute less. For the next waves, more items will be introduced on this aspect that deserve to be carefully studied. One question was about the impact of the measure on the travel time of a usual travel. To measure this item, the respondents had to choose between several proposals, from a reduction of time travel to an increase that could be over 20 minutes.

Results and discussion

The expected results from the environmental impact assessment should be compared to the regional air quality monitoring association Atmo Auvergne-Rhône-Alpes estimates. They expected: (i) a decrease in exhaust emissions, the extent of which depended on the traffic share of heavy goods vehicles (for which the speed limit is unchanged); (ii) larger decreases observed for nitrogen dioxide and particulate matter PM_{2.5} emissions down to minus 7% for the lowest traffic shares of heavy goods vehicles; (iii) decreases not exceeding 3% for CO₂ emissions (figure below).

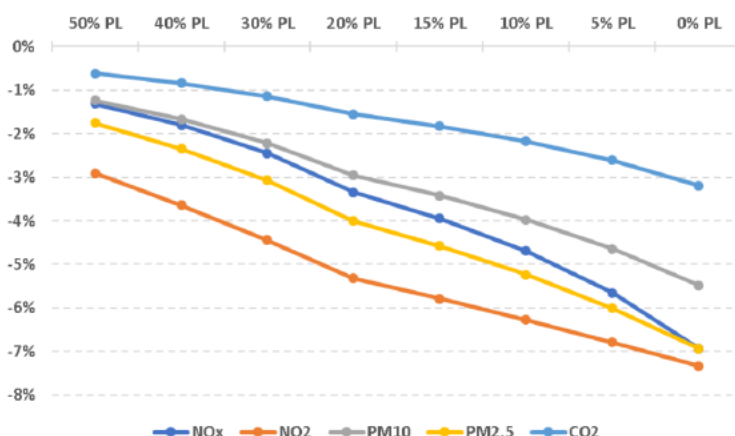


Figure 1: Evolution of emissions induced by the speed limit reduction for the main pollutants and greenhouse gases, according to the traffic share of heavy goods vehicles (source: Atmo Auvergne-Rhône Alpes, 2018).

The Google Maps results for travel times changes, 3-months after implementation of the speed limit reduction (1st July 2018), show over all 298 routes an average loss of travel time of less than one second per kilometre on a pendulum journey (average daily lost time in weeks) for users of the routes covered by the measure. The number of routes with average daily journey time savings of more than 1 second per kilometre is generally higher in September 2018 than in July 2018, but is still very limited (13% of all routes). Few routes show a time loss (i.e. extension of travel time) higher than 2 seconds per kilometre (12% of all routes). However, disparities are observed between routes: for 34% of the routes, users save up to 5 seconds per kilometre between June and September 2018, and for 37% of the routes, the increase in travel time is of less than 1 second per kilometre. This trend needs to be further explored over longer periods of analysis.

The results for social acceptability assessment, before the implementation of the measure, are presented here for the first survey-wave. They concern: (i) the perceived reduction of pollutants emissions; (ii) the perceived travel time change. (i) Reducing the emission of pollutants: when we consider the impact of the measure, the environmental factor, reducing the emission of pollutants ($\beta=0.005$; $t=0.75$; $p=0.45$) does not have any impact on the acceptability of the measure, something that differs from factors about increasing road safety (reducing the number of fatal road accidents, etc.). In any case, the impact of the measure is a main element of the acceptability of the measure, as it explained 60% of the variance of acceptability of the measure ($R^2 \text{ adj}= 0.60$; $F(16 ; 950)=382.5$, $p=0.0000$). When we focus on the item "reducing the emission of pollutants", all four categories of respondents ("totally against", "fairly against", "fairly in favour" and "totally in favour of the measure") differ statistically from one another. However, the more the respondents have a positive attitude about the measure, the more they think that the measure will have a positive impact on reducing air pollution (an a four-points scale, M ("totally against")=1.80; M("fairly against") =2.22; M ("fairly in favour the measure")=2.72; M ("totally in favour of the measure")=2.98).

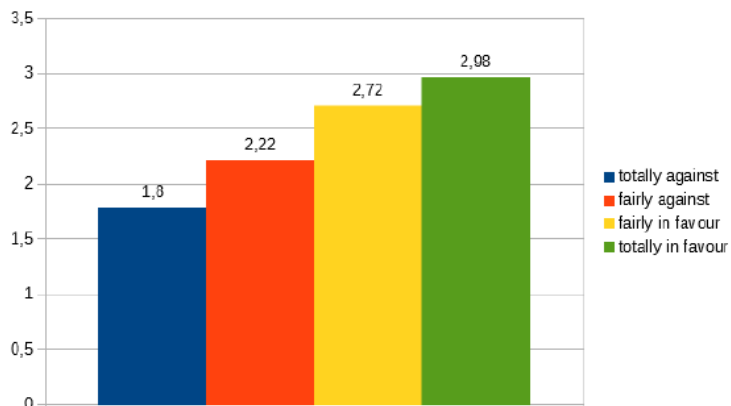


Figure 2: Reducing air pollution according to the level of acceptability of the measure.

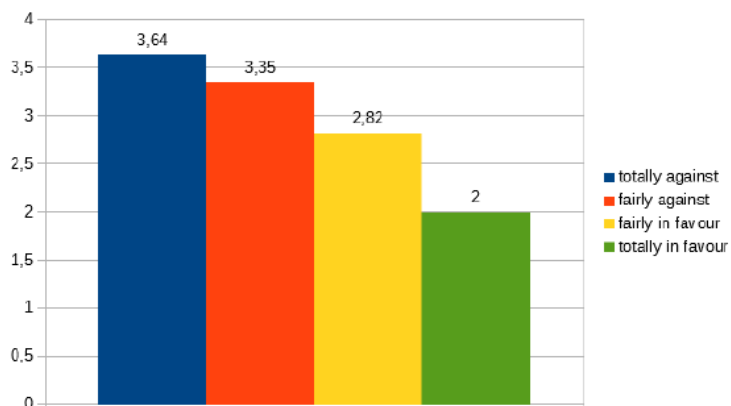


Figure 3: Perceived time travel according to the level of acceptability of the measure.

Concerning the reasons for abiding by the new speed limit, reducing air pollution is the reason quoted by only 4.5% of the respondents (N=163/3576) who declare having the intention to respect the measure "all the time" and "most often". The main reason is the habit to respect traffic rules (59.7%, N=2136/3576). (ii) Travel time: an increase of travel time is one of the argument most often quoted in the media against the measure. The results show that there is a relationship between the acceptability of the measure and the perceived travel time. The more the respondents are in favour of the measure, the more they think that there will be no impact on their travel time; and the more they are against the measure, the more they think that they could lose between 5 and 10 minutes on their usual travel. The respondents estimate the length of their usual travel between 20 and 30 km whatever the level of the acceptability of the measure.

Discussion and perspectives

The results of the scientific research and the methodology implemented suggest that the speed limit reduction from 90 to 80 km/h will have a positive impact on air quality but a limited impact on the increase of travel times. Anyway, the environmental factors seem to have a small or no impact on the acceptability of the measure. Respondents, especially opponents to the measure, also overestimate the time lost on a typical journey as they estimate it at about one minute per kilometre, which is much higher than the first data collected in terms of estimated travel time where time loss was in average less than one second per kilometre. Considering the speed limit reduction from 90 to 80 km/h, a loss of time of five minutes would correspond to a daily journey of 300 kilometres! This outcome is not surprising as the communication focuses on the impact on road safety; the main objective of the measure is to reduce serious accidents on the concerned network.

As mentioned in the methodological section, environmental issues were not the main objective of the acceptability component of this first wave of survey. Therefore, the collected information is limited so far. The impact of the measure on air quality and people's health will be further developed in future waves of surveys; this will allow a more detailed assessment of the relevance or lack of interest of this dimension on acceptability.

For travel times assessment, the Google Maps database compiled here is not intended to cover the entire French road network concerned by the measure. Google Maps data are not vehicle Floating Car Data (FCD) tracks. They are the estimated travel time of the Google algorithm at a given time. The Google Maps data series shows a large dispersion, which makes the average less meaningful. Nevertheless, the methodology used makes it possible to study the evolution of travel time "before/ after" implementation of the measure, and to estimate the time lost overall with a large panel of routes concerned by the measure and located all over the French territory. The present analysis allows us to give a trend. However, it should be noted that the duration of the reporting period should be extended for both the "before" and "after" periods. Indeed, this would allow to reduce punctual factors (works, accidents, weather) or seasonal factors (tourist traffic) that could significantly modify travel times on the different selected routes.

Acknowledgements

This work is supported by the French Ministry of Transport and the French Ministry of Interior.

References

- ATMO Auvergne-Rhône-Alpes, (2018). Abaissement de la vitesse à 80 km/h et impact sur les émissions polluantes.
- Chanut, S. & Chevallier, E. Recherche Transport Sécurité (2012). 28: 1. <https://doi.org/10.1007/s13547-011-0018-4>, Estimation des impacts atmosphériques des projets de gestion de trafic: de l'application des modèles théoriques sur des cas concrets.
- Interprofessional Technical Centre for Studies on Air Pollution (CITEPA), (2004). Calcul des émissions dans l'air, Principes méthodologiques généraux.
- French Environment & Energy Management Agency (ADEME), (2014). Impact des limitations de vitesse sur la qualité de l'air, le climat, l'énergie et le bruit, Synthèse d'étude.

French Institute for Public Health Surveillance, (2013). Bulletin épidémiologique hebdomadaire, Numéro thématique – Épidémiologie et pollution atmosphérique urbaine: l'observation au service de l'action, n°1-2, janvier 2013.

French Ministry of Ecological and Solidarity Transition, DGITM (2014). Instruction du Gouvernement du 16 juin 2014 relative à l'évaluation des projets de transport. 5 p.

Gonçalves M., Jimenez-Guerrero P., Lopez E., Baldasano J.M. (2008) Air quality models sensitivity to on-road traffic speed representation: Effects on air quality of 80 km/h speed limit in the Barcelona Metropolitan area, *Atmospheric Environment* 42, 8389–8402.

Keuken M.P., Jonkers S., Wilminck I.R., Wesseling J. (2010) Reduced NOx and PM10 emissions on urban motorways in The Netherlands by 80 km/h speed management, *Science of Total Environment* 408, 2517-2526.

2.5.3 Network performance under different departure time strategies from traffic and emission perspective

D.Lejri¹, G.Meynet¹ and L.Leclercq¹

¹ Univ. Lyon, ENTPE, IFSTTAR, LICIT, F-69518 Vaulx-En-Velin, France

1. Introduction

Effects of road traffic on climate change and health are now well established. As mobility needs are constantly increasing, policy decision-makers are looking for solutions to reduce greenhouse gases and pollutant emissions in large cities. Various traffic management measures can be considered. One of the possible strategies is based on changing users' departure time. Indeed, spreading users over time can potentially calm traffic, reduce peak congestion and related emissions.

Previous studies (Djukic, 2017) (Duruisseau, 2018) already performed sensitivity analysis to measure the urban-scale network performances to parameters related to dynamic loadings. (Djukic, 2017) focuses on dynamic Origin Destination (OD) demand estimation. (Duruisseau, 2018) highlights the influence of parameters tuning OD matrix, routing alternatives, and paths flow distribution on network performance. Results notably reveal that the demand level is the most decisive parameter. (Chen, 2017) implemented a global sensitivity analysis to explore the sensitivity of traffic-related emissions.

This current work focuses on the impact of changes in departure times on traffic conditions and related emissions. The baseline scenario has been implemented in a traffic microsimulator that provides a detailed overview of the traffic conditions. Computation times being significant and irreducible, a large-scale network modelling approach, based on the Macroscopic Fundamental Diagram (MFD) theory, has been first considered. These relationships are effective tools for describing large urban areas. The theoretical foundation of these modelling approaches has been established in Daganzo (2007) and Geroliminis and Daganzo (2007). This first study should reveal trends in order to see how the variations in the model inputs (departure time) induce variations in the model outputs (network performance and road traffic emissions). The related objective is to identify changes in departure times that optimize the network performance and minimize fuel consumption and pollutant emissions evaluated thanks to Copert model (Ntziachristos et al., 2009).

This paper is organised as follows: section 2 describes the case study and compare the microscopic and macroscopic traffic modelling approaches, section 3 details the departure time changes design, and section 4 presents the results analyses.

2. Case study

The case study is the Lyon63V¹ network, a 15 km² urban area divided into 75 sub-areas. The supply specification covers the various transportation modes: light, heavy vehicles, and public transport (metro, tram and bus). The demand specifications are defined dynamically on morning peak hour (6:30 – 11:00), for each vehicle category and each OD. Traffic demand is composed of internal flow (within the area) and transit flow (exchange at the area boundaries). The baseline scenario has been constructed with the same demand time evolution for each of the 6969 OD pairs, which corresponds to the departure time profile P3 (Fig.3). This baseline demand profile has been calibrated on loop detectors measurements.

The traffic microsimulation was implemented in the Symuvia platform². Vehicle movements at the microscopic scale are governed by a set of rules, including car-following modelling (Leclercq, 2007a, 2007b), lane-changes (Laval and Leclercq, 2008) and specific movements at intersections (Chevallier and Leclercq, 2007). The platform also copes with the cohabitation on the network of vehicles with different kinematics, including passenger cars, buses and heavy-duty vehicles.

¹ 3rd and 6th districts of Lyon and Villeurbanne

² <http://www.licit-lyon.eu/themes/realisations/plateformes/symuvia/>

Routing choices are governed by a dynamic traffic assignment model (Symumaster), which guides each user in the network on the route that minimizes its travel time to its initially assigned destination, taking into account all transportation modes. User distribution on the multi-modal paths is determined every 30 minutes.

The time evolution of traffic conditions during the simulation is monitored through mean speed v , production p and accumulation n , for the overall network and each period $\Delta T = 3\text{min}$.

$$p = \frac{\text{Total Travel Distance}}{\Delta T}$$

$$n = \frac{\text{Total Travel Time}}{\Delta T}$$

$$v = \frac{P}{n}$$

From these variables, it is possible to fit quadratic MFD curves (Fig.1).

A crucial point concerns the representation of vehicle trip length within the reservoir (Leclercq et al., 2015). A formulation of the single-reservoir dynamics, which copes with variable trip lengths, has been proposed in (Mariotte et al., 2017). The numerical resolution method is event-based: the variables are updated each time a vehicle enters or exits the reservoir.

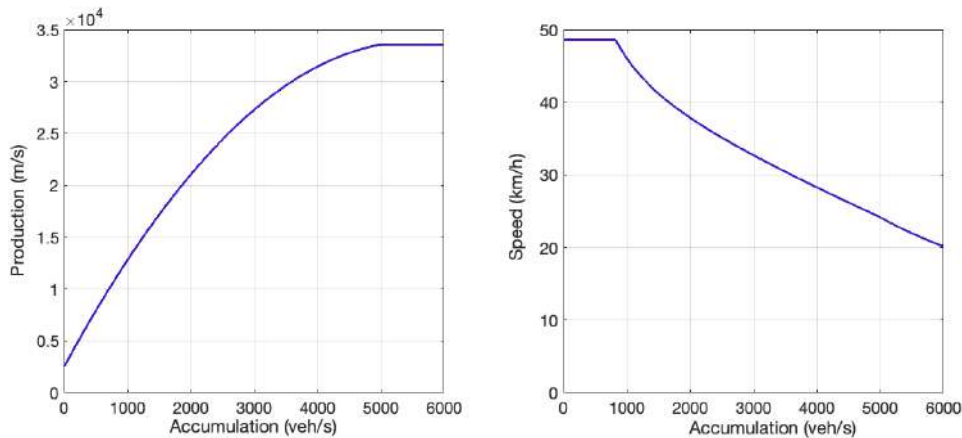


Figure 1 : Lyon63V network MFD curves

Vehicles are considered individually and characterized by their departure time and their individual trip length. This information is provided by the baseline microsimulation. The Trip-Based (TB) model is based on strong hypotheses: (i) the individual trip lengths are unchanged and (ii) at each time step, the traffic conditions are governed by a uniform mean speed. There is no longer any notion of space. Once entering the reservoir, vehicles are travelling respecting the MFD speed function until they accomplish their travel distance.

The time step of this simulation is variable, since it is related to an event: a vehicle enters or exits the reservoir. The results are aggregated in 3-minute periods to compare them with the results of

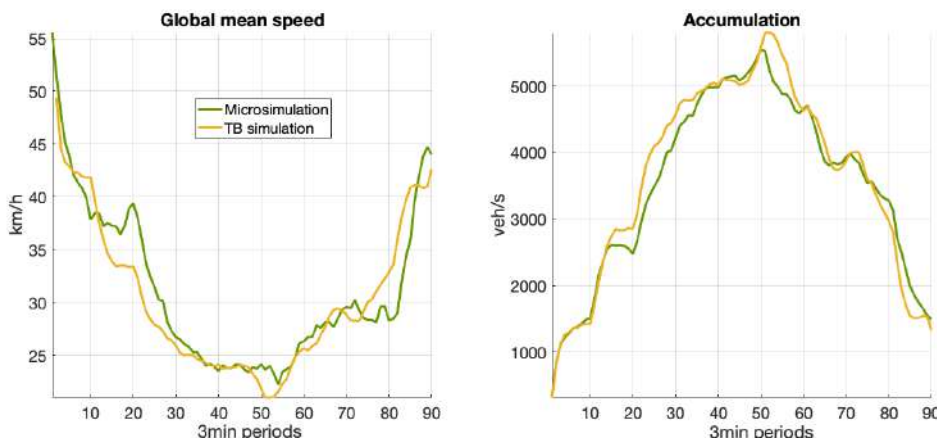


Figure 2 Traffic modelling comparison: mean speed and accumulation evolution for both microsimulation and tip-based model.

the baseline microsimulation (Fig.2). There is a good agreement between aggregated traffic indicators obtained thanks to a complete microsimulation and a trip-based modelling.

This macroscopic model can be used to assess the impact of changes in departure times. This approach does not fully investigate the effects of departure time variations, because it considers that users keep the same mode and route regardless of their departure time. However, it can be assumed that these effects are of a second order and that trends can be identified with this macroscopic approach.

3. Experiment design

a. Departure time changes

This section presents the way departure time changes were performed. There are six demand profiles under investigation, in order to explore different possible departure time choices (Fig.3). Two profiles are representing earlier departure time (Profile 1 and 2), whereas two others are representing later departure time (Profile 5 and 6). The two last are the baseline profile (Profile 3) and a more uniform profile (Profile 4).

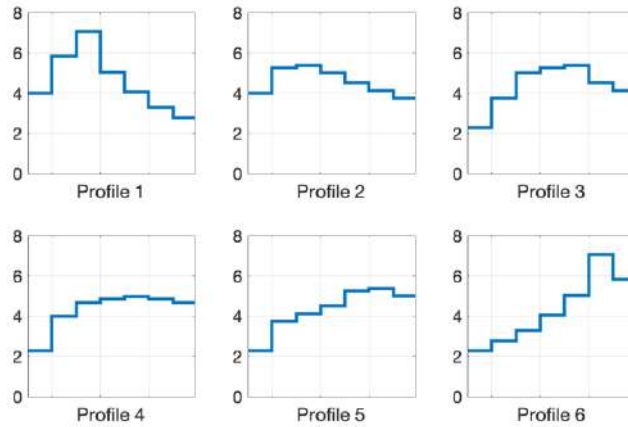


Figure 3 Six demand profiles applied to OD groups expressed as a percentage of the total daily demand for each 30min period during the morning peak

These six profiles, reflecting departure time changes, are applied to each OD. Given the large number of ODs, we decided to gather them together and to apply the profiles to each OD group. The OD clustering was carried out on the basis of available data describing on the one hand attractiveness of each network area in terms of employment (destination-oriented strategy) and on the other hand residential location (origin-oriented strategy). Indeed, what defines the departure time is mainly the time at which the commuter must arrive at his workplace and the time at which the commuter has to meet obligations near his home (drop the children off at school for instance). These two strategies were decomposed into either a geographically continuous (S_1 and S_3) or discontinuous (S_2 and S_4) implementation of the demand profiles, to handle more varied cases. The various groups and sub-groups are ensured to be equivalent in terms of demand. This results in four strategies for changing departure times, depicted in Fig.4.

Table 1: Total trip length (km) per group and strategy

Strategy	Group 1	Group 2	Group 3	Group 4	Group 5
S_1	79131	107404	90680	125822	-
S_2	81701	126768	75862	118706	-
S_3	68658	119978	95270	96060	61647
S_4	114418	122805	123110	81279	-

The total travel distance is a key variable in emissions assessment. The macroscopic simulation framework assumes that this quantity is invariant as the TB model has no spatial dimension. The total travel distance of the baseline simulation is estimated at 403037 km for the entire network and is described per group and strategy in Table 1.

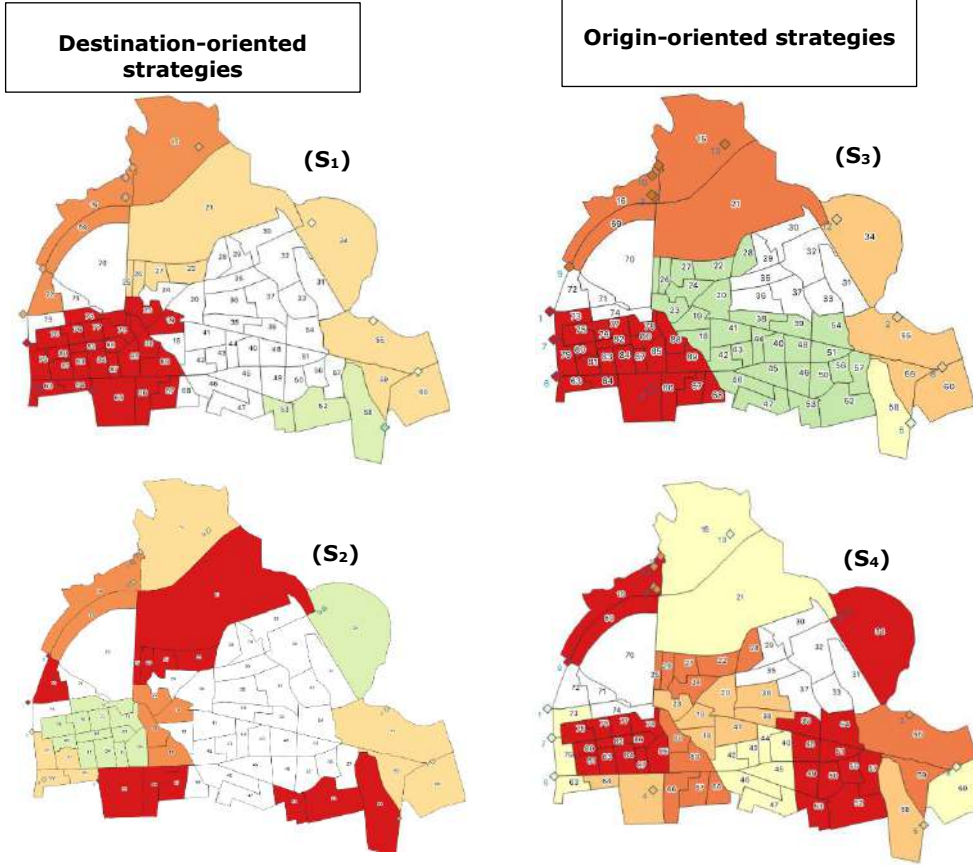


Figure 4: Four strategies for OD clustering: S₁, S₂ and S₄ are composed of 4 groups either geographically compact or fragmented and S₃ is composed of 5 compact groups. White areas are not concerned by departure time changes.

This experimental design (six profiles, four strategies) requires 11664 simulations to be run, which is still too time consuming. To reduce drastically the computation time, we will focus on a 20% Latin hypercube sampling, which means 2340 simulations.

b. Trip-Based model outputs

The simulation results are analysed in terms of global traffic variables. The key aggregate traffic indicators are the global mean speed V and the total travel time TTT for the overall network and the total morning peak hour. Two additional indicators were used to characterize the variability of the mean speed over time periods: the minimum mean speed and the standard deviation of mean speed (Fig.5).

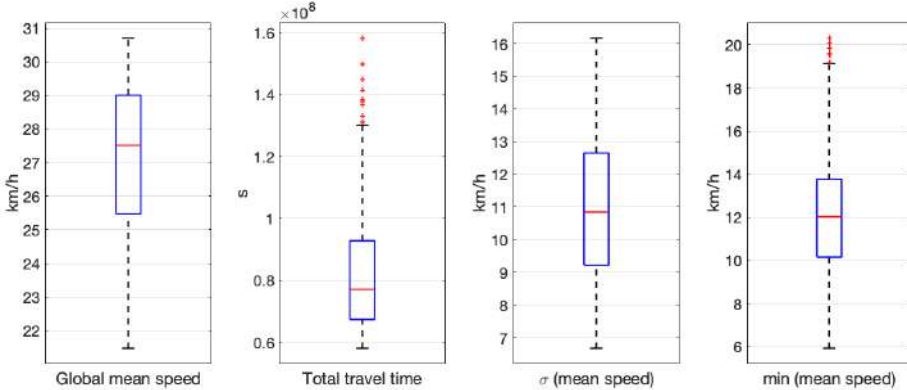


Figure 5 Traffic indicators variation over 2340 simulations

The related fuel consumption and NOx emissions are then estimated for each 3min periods and the overall network, thanks to Copert 5 emission factors (FE_{fc} and FE_{nox}), considering an urban French fleet composition (Ifsttar, 2013).

$$E_{fc} = \sum_t \delta_t FE_{fc} (v_t) \quad E_{nox} = \sum_t \delta_t FE_{nox} (v_t)$$

$$E_{fc}^{max} = \max(\delta_t FE_{fc} (v_t)) \quad E_{nox}^{max} = \max(\delta_t FE_{nox} (v_t))$$

with $t = 1..90$ time periods.

These indicators (Fig.6) will allow assessing the scenarios with the greatest effect on global and peak emissions.

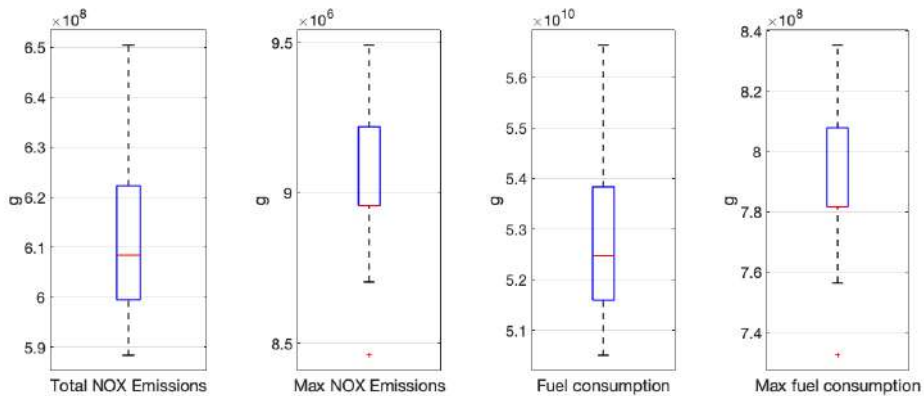


Figure 6 Emission indicators variation over 2340 simulations

4. Results

This section is devoted to the Trip-Based results analyses. The objective is to search among the 2340 simulations performed, for simulations that improve traffic conditions and minimize related emissions.

On one hand, the 10 best simulations that meet the following traffic criteria were identified: maximize global mean speed, minimize total travel time, mean speed standard deviation and minimum speed. On the other hand, the 10 best simulations that meet emission criteria were identified: minimize E_{nox} , E_{fc} and also the corresponding maximum values. All these simulations are part of strategy S_3 , which means that origin-oriented strategy seems to induce the best effects. This result illustrates that it is possible to improve the network performance by managing departure times.

These two sets include four common simulations that have been studied in detail. Fig.7 highlights the way the latter improve traffic conditions. However, the effects on emissions are modest. The macroscopic approach predicts a reduction of -1.9% for the total fuel consumption and -3.3% for the most emitting period. For NOx emissions, the trends are similar, the reduction is assessed around -1.7% for total NOx emissions et -3.0% for the most emitting period.

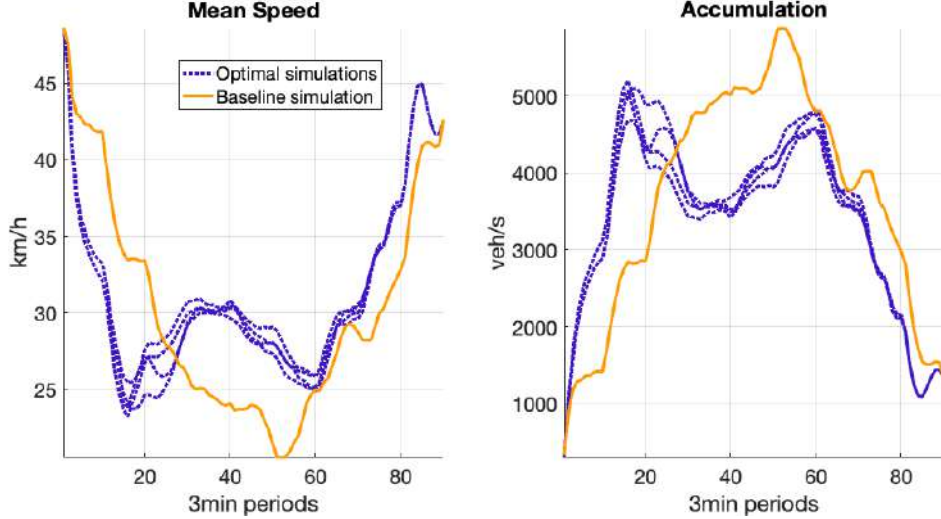


Figure 7 Reduction of peak congestion due to departure time changes

Profile demand distribution for those four simulations are exhibited in Table 2. It can be seen that profile 6 (delayed departure) is the most commonly used. Contrasting profiles (early and delayed departure) are assigned to groups 1 and 5 while groups 2 to 4 remain mainly on more spread profiles (3 and 4). This allocation induces a distribution of balanced and equivalent distances travelled for these optimal simulations. Only the simulation #1880 differs slightly, since the delayed departures (profile 5 and 6) are more represented (assigned to 3 groups instead of 2)

Table 2: Profile distribution for the four optimal TB simulations regarding traffic and emissions indicators

ID simulation	Group 1	Group 2	Group 3	Group 4	Group5
630	6	4	6	3	1
1716	2	4	4	6	6
1850	2	6	3	3	6
1880	6	3	6	5	1

5. Conclusion

This current work focuses on departure time impact. This initial analysis showed that changing the departure time can lead to improved network performance and reduced modestly related emissions. The proposed approach is based on MFD simulation, which allows a large number of simulations to be performed in a reasonable time. The results indicate that the S₃ strategy makes it possible to optimize overall results, but also to reduce peaks in terms of traffic and emissions. S₃ is the origin-oriented strategy, which suggests that in Lyon, it would be more effective to target users by their place of residence, rather than by their place of work. We can also suppose that this strategy is more effective because it is more flexible with these 5 groups, compared to 4 for the other strategies.

However, these analyses need to be further developed. Several perspectives are considered. It is possible to perform all simulations with the MFD approach in order to validate that these simulations are optimal and that S₃ is the best strategy.

On the other hand, it is planned to compare these results with microscopic simulations on the 20% Latin hypercube sample. For the latter, the expected simulation times are about 1000 days,

which can be reduced by parallel calculation. It would be interesting to compare the results with a more precise traffic simulation, which integrates the effects of dynamic reassignment of users (changes in distances travelled, in mode choices, etc.) and allows congestion phenomena to be located.

Acknowledgements

This study has received funding from the European Research Council (ERC) under the European Union's Horizon 2020 research and innovation program (grant agreement No 646592 – MAGnUM project).

References

- Chen, R., Aguiléra, V., Mallet, V., Cohn, F. Poulet, D., Brocheton, F. (2017). *Journal of Earth Sciences and Geotechnical Engineering*. 7. 151-173.
- Chevallier, E., Leclercq, L., (2007). A macroscopic theory for unsignalized intersections, *Transp. Res. Part B Methodol.* 41, 1139–1150. <https://doi.org/10.1016/j.trb.2007.05.003>
- Daganzo, C. F., Jan. (2007). Urban gridlock: Macroscopic modeling and mitigation approaches. *Transportation Research Part B: Methodological*, 41 (1), 49–62.
- Djukic, T., Breen, M., Masip, D., Perarnau, J., Budin, J., (2017). Marginal effects evaluation with respect to changes in OD demand for dynamic OD demand estimation. *International Conference on Intelligent Transport Systems in Theory and Practice, Mobil.TUM*. pp. 4–5.
- Duruisseaux, C., Leclercq, L. (2018) A Global Sensitivity Analysis of Dynamic Loading and Route Selection Parameters on Network Performances *Journal of Advanced Transportation*, Volume 2018, Article ID 8414069, <https://doi.org/10.1155/2018/8414069>.
- Geroliminis, N., Daganzo, C. F. (2007). Macroscopic modeling of traffic in cities. In: *Transportation Research Board 86th Annual Meeting*, 07-0413, Washington DC.
- Laval, J.A., Leclercq, L. (2008). Microscopic modeling of the relaxation phenomenon using a macroscopic lane-changing model, *Transp. Res. Part B Methodol.* 42, 511–522, <https://doi.org/10.1016/j.trb.2007.10.004>
- Leclercq, L. (2007a). Hybrid approaches to the solutions of the “Lighthill-Whitham-Richards” model, *Transp. Res. Part B Methodol.* 41, 701–709, <https://doi.org/10.1016/j.trb.2006.11.004>
- Leclercq, L. (2007b). Bounded acceleration close to fixed and moving bottlenecks, *Transp. Res. Part B Methodol.* 41, 309–319, <https://doi.org/10.1016/j.trb.2006.05.001>
- Leclercq, L., Parzani, C., Knoop, V. L., Amourette, J., Hoogendoorn, S. P. (2015). Macroscopic traffic dynamics with heterogeneous route patterns, *Transportation Research Part C: Emerging Technologies* 55, 292–307.
- Mariotte G., Leclercq L., Laval J.A. (2017). Macroscopic urban dynamics: Analytical and numerical comparisons of existing models, *Transportation Research Part B: Methodological*, 101, 245-267, <https://doi.org/10.1016/j.trb.2017.04.002>.
- Ntziachristos, L., Gkatzoflias, D., Kouridis, C. (2009). COPERT: A European Road Transport Emission Inventory Model, *Inf. Technol. Environ. Eng*, <https://doi.org/10.1007/978-3-540-88351-7>

2.5.4 Impacts of urban forms on road transport emissions and air quality

A. Elessa Etuman¹, I. Coll¹

¹ Laboratoire Interuniversitaire des Systèmes Atmosphériques (LISA), UMR CNRS 7583, Université Paris Est Créteil et Université Paris Diderot, Institut Pierre Simon Laplace (IPSL), Créteil, France

Abstract

This modeling study aims to analyze air quality and to define the key drivers of the distribution and the intensity of air pollutants and greenhouse gases emissions, for a set of urban planning scenarios. In particular, the impacts of various urban forms on road transport emissions and air quality is investigated through a numerical modeling approach. For this purpose, we have used an innovative modeling chain centered on the OLYMPUS tool, which generates pollutant emissions from the mobility and energy consumption practices of a population, on a given territory. In the end, the CHIMERE mesoscale chemistry-transport model is used for the simulation of atmospheric pollutants concentrations.

Introduction

Urban policies aim to maintain or even improve the quality of the urban environment by regulating the urbanization of the natural land or by controlling the development of urban transport infrastructures. Urban planning impacts many components such as housing, urban economy and the transportation of goods and people. All these aspects have in turn an impact on air quality. Given the health issues related to exposure to pollutants, it is therefore necessary to consider urban planning as a potential lever for air quality. However, currently in France, urban planning is only conceived in the framework of decarbonization policies, and is not evaluated on the basis of air quality indicators. The idea is that dense cities would be more sustainable as they would favor the soft modes of transport and lead to a reduction in energy consumption and in the emission of carbon compounds, which would be beneficial for both climate and air quality issues. The question is, therefore, how much can be expected in the medium term from an evolution of the urban environment towards dense urban forms? While all the signals tend to confirm that we are not investing heavily in emission reduction technologies - energy-efficient engines, vehicles operating on principles other than combustion - and that we are not conducting radical changes in our energy consumption practices, one has to think of the possibility of an important forcing by the urban form, which would make it possible to reduce the transport demand and the motorized modal share in urban mobility. The concepts of a sustainable urban growth and an optimized city density remain however open questions and the envisaged dense urban models are widely debated, in particular due to the propensity for these dense cities to create confined spaces where pollutants accumulate. We propose here to address the nature of the impact of urban forms on primary pollutant emissions from fossil fuel combustion, through the simulation of transport demand deriving from the practices of individuals living in a given urban environment.

To this end, we have tested the sensitivity of the OLYMPUS emission platform to various urban morphologies. The urban form indeed strongly impacts the location of services, employment and households, and plays a crucial role in the individual motorized trips, and subsequently on the population's exposure to the pollutants resulting from these trips. In its last report, the IPCC [Seto K. C. et al., 2014](#) sets out 4 variables key characteristic of the urban form that are:

- Urban fabric density
- Degree of diversity of the land use
- Connectivity
- Accessibility

In this study, we used the total emissions from motorized trip which accounts for both the total kilometers traveled in the city and the conditions for this travel (that is, congestion and kilometers driven in cold start regime). The objectives of the present work are the implementation of

scenarios of contrasting urban shapes and fabrics, and the study of their impacts on pollutant emissions.

In the literature, [Borrego et al., 2006](#); [Manins et al., 1998](#) has focused on these issues by setting up modeling chains that link transport and land-use models to air quality modules. The interest of our approach is the use of the OLYMPUS platform which allows to quantify at the individual scale the impacts of different urban forms on the air quality.

Methodology and Results

The results presented below come from the OLYMPUS-CHIMERE modeling chain. OLYMPUS is an activity-based emission model relying on a synthetic population of agents having socio-demographic attributes. For each simulated agent, the model generates its energy consumption practices and the agenda of its daily mobility. Using the road network features and the fleet composition, OLYMPUS make it possible to derive the spatial and temporal properties of anthropogenic pollutant emissions ([Elessa Etuman and Coll, 2018](#)). The simulated emissions are then used as input in the CHIMERE model, a classic chemistry-transport model (CTM) that provides the composition of the atmosphere at an hourly time step in the simulated domain by solving the mass conservation equation over time for all pollutants, which takes into account their emissions and reactivity, and the dynamics of the atmosphere ([Maillet et al., 2016](#)).

The urban forms can be characterized by their compact or sprawl, grouped or dispersed, continuous or discontinuous, self-organized or spontaneous features. Compact and sprawl cities are the most common forms of resulting from urban growth. The other structures are generally derived from these two forms. In order to answer the questions about the environmental leverage that can be expected from alternative urban forms, we have designed 4 city scenarios based on the variation of the 4 above-mentioned parameters, which are particularly distinguished by the density, accessibility, mixity and connectivity of the urban fabric:

- **REF**, a reference based on Paris megacity
- **COMPACT**, a monocentric city
- **SPRAWL**, a spread city
- **CORRIDOR**, a corridor town
- **STARS**, a polycentric city

The COMPACT scenario simulates a megacity with very high accessibility, connectivity, density and urban mix. Conversely, the SPRAWL scenario represents an extended and sparsely populated city, where accessibility, connectivity, combination and density are very moderate. The CORRIDOR scenario is an interesting theoretical approach of a connected city according to a limited number of major transport axes. Finally, STARS scenario offers the possibility of considering a mobility radically different from that governed by the attractiveness of a single center. It illustrates the situation of large cities that have allowed the emergence of new urban centers capable of exercising a strong attractiveness on populations and having developed their own interconnections.

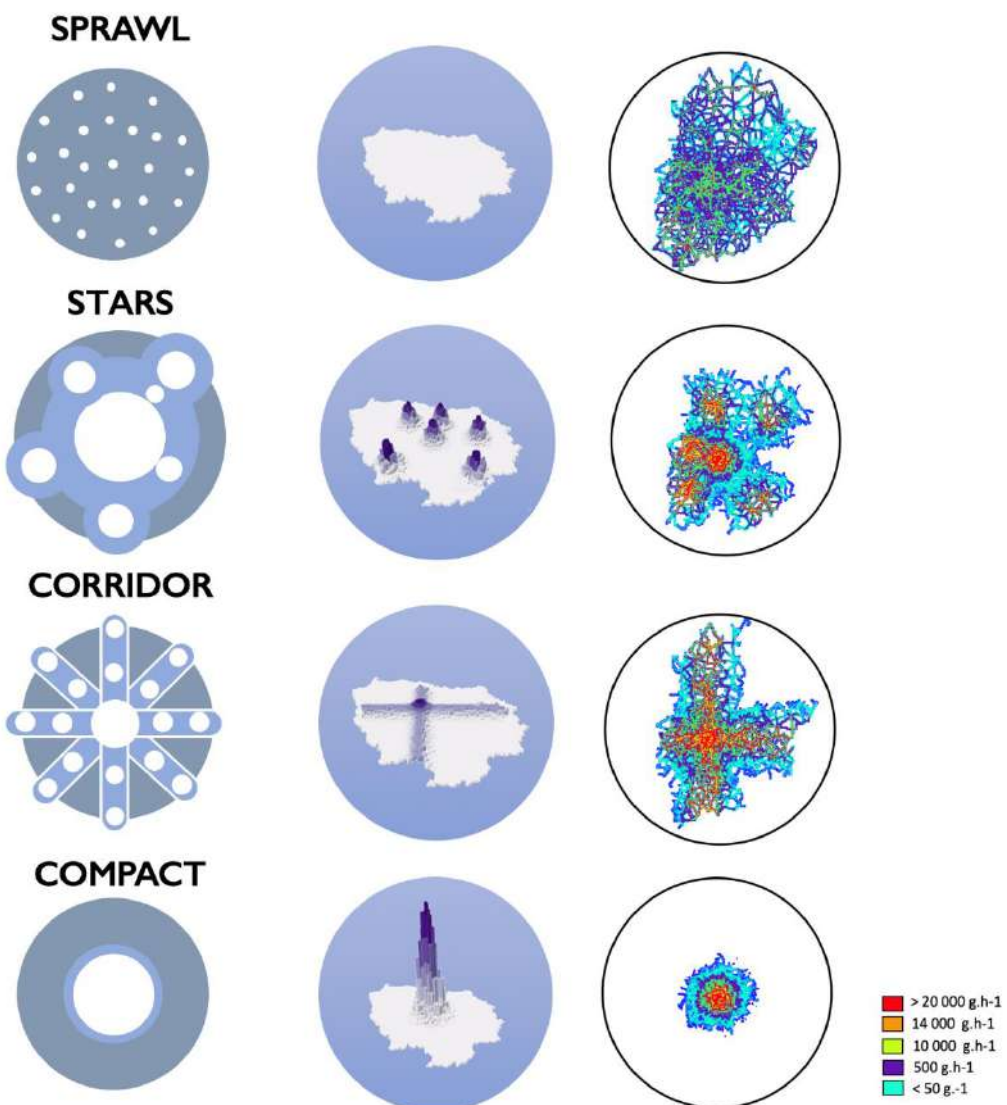


Figure 1. Schematic representation of the urban form scenarios, the household's density and mapping of daily NO₂ emissions from the OLYMPUS model.

The generation of the synthetic population in the different scenarios of this study is based on the number of households per district. In the COMPACT and CORRIDOR scenarios, the distribution of households is centered on Paris, while in the STARS scenario, it is distributed around 5 poles including the Paris municipality. In the SPRAWL scenario, the density of households by district is homogeneous throughout the territory, but as the size of this area for household allocation decreases towards the center, there remains a slight effect of central densification, which is anyway realistic. The maximum values of household density per km² in the different scenarios are as follows:

- 135,841 households/km² (**COMPACT**)
- 23,378 households/km² (**CORRIDOR**)
- 39,824 households/km² (**STARS**)
- 3,846 households/km² (**SPRAWL**)

The average density of households in the city center is about 10,000 households / km². The variation of the total population according to the scenarios does not exceed 0,2%, with a total number of households of 4,999,989 persons for the COMPACT scenario. The age distribution of populations is essentially the same in the 4 scenarios with a slight difference of 0.4% for the population aged 15 to 30 in the STARS and CORRIDOR scenarios compared to the COMPACT and SPRAWL scenarios. This difference is mainly due to the variation in the number of households in each scenario.

The first thing we observe is a slight decline in the demand for public transit in each of the situations, mainly in favor of the soft travel modes over short distances. However, the mobility associated with private cars does not change much in the COMPACT scenario, given the 25% penalty applied to the generalized cost of transportation. It appears that the model is not very sensitive to the penalties of motorized mobility, and particularly not to the potential impacts of traffic congestion on transport times. The tendency to a disutility of public transport is explained here by the reduction in distances traveled because of compactness urban, which reinforces the interest of soft modes. In the SPRAWL scenario, the model manages to capture a slight over-utility of the car and walking in favor of public transit. This is mainly due to the penalty of public transport, less effective in this situation. The results of the STARS scenario are identical on this point to those of the CORRIDOR scenario. Here as in COMPACT, the reduction of distances traveled is related to the densification of urban centers. But another hypothesis is the poor accessibility to the public transport network, which is initially limited in the suburbs.

The variability of the utility of the modes of transport thus appears to have very little impact on the average modal choice of populations. Modal choice modeling can be questioned, which is quite rigid and does not propose in these situations a breaking point compared to the current situation. It will therefore be interesting to vary over a wider range the usefulness of the car, to set up parking constraints and to consider feedback on the impact of congestion on modal choices, in future developments of OLYMPUS. It will be then particularly interesting to study the sensitivity of modal choices to transport costs, and to identify the value for which there is a break in the simulated behaviors.

Despite these moderate changes, we have to consider that the length and duration of trips change from one scenario to another, which has a great impact on emissions. Furthermore, building heating also strongly depends on housing distribution and type and is strongly impacted by the urban form and density.

Scenario	Walk	Public Transport	Car
COMPACT	4%	-3%	-1%
CORRIDOR	3%	-3%	0%
SPRAWL	2%	-3%	1%
STARS	3%	-3%	0%
REF			

Table 1. Relative difference in the modal choice by scenario, with respect to the reference situation

Air pollutant emissions from the residential sector are dependent on population density, as they are proportional in some respects to energy demand. In terms of annual emissions budget, the COMPACT scenario is the least emitter with almost -50% of fine particle emissions than the reference situation, which is highly significant. The difference in particle emissions is due to the reduction in the energy demand but also by the smaller number of individual dwellings in the scenario, which are the largest contributors to wood combustion (huge source of fine particulate matter). The SPRAWL scenario is the most emitting scenario in terms of nitrogen oxides, particulates and carbon monoxide. The CORRIDOR and STARS scenarios are similar in terms of pollutant emissions. They question environmental issues, since they are more emitters of polluting gases than the reference situation (+15% approximately) but less emitters (-20% approximately) of particles. This is because of the specific distribution of energies (gases and wood mainly) for heating between the suburbs and Paris.

	COMPACT	CORRIDOR	SPRAWL	STARS	REF
NOx	-20%	+18%	+30%	+20%	-
PM10	-58%	-19%	-7%	-19%	-
PM2.5	-59%	-21%	-8%	-20%	-
CO	-40%	+15%	+33%	+16%	-

Table 2. Relative difference of annual emissions from building energy demand by scenario according to the reference situation

The mobile emissions of the different scenarios are presented in figure 1. Here we can see the main road transport axes as well as the preferred directions for travel. Table 3 summarizes the main differences simulated between the scenarios and the baseline situation. We can see that the SPRAWL scenario differs from the other scenarios in terms of total emissions, and that due to its geography, the entire transport network is used - unlike other scenarios. The compact city scenario is the least emitting of all scenarios from the point of view of road traffic, and according to this configuration of OLYMPUS. It shows an increase in emissions compared to the current situation, but is approximately twice lower than observed in the other scenarios. In this scenario where a low modal shift is observed, the occupation of roadways is greater than in the other scenarios and has a strong impact on road speeds. Ultimately, road emissions which become more important at low speeds. The scenario CORRIDOR and the scenario STARS are substantially identical in terms of air pollutant emissions. And their performance is pretty close to that of the best configuration, SPRAWL. There is a slight difference in NMVOC emissions that can be explained by shorter trips in these scenarios. The main variable that impacts emissions here is the number of kilometers driven which is larger in the spread city situation than in the compact city situation with an average of 5.02 km/trip versus 4.70 km/trip.

	COMPACT	CORRIDOR	SPRAWL	STARS	REF
NOx	+8%	+14%	+17%	+14%	-
CO2	+9%	+15%	+18%	+15%	-
COV	+9%	+12%	+13%	+13%	-
PM	+7%	+15%	+18%	+15%	-

Table 3. Relative difference in road transport annual emissions by scenario according to baseline situation

In terms of air quality assessment, the pollutant emissions from the OLYMPUS model have been implemented in the CHIMERE transport chemistry model. We have conducted a simulation for a duration of 1 month on the Île-de-France domain for the 4 different scenarios. Figure 2 shows the boxplots of the simulated NO₂ concentrations. We note here that the average concentration values are quite similar for all the scenarios but the distribution of the concentration values differs notably according to the scenarios, with STARS and CORRIDOR scenarios which have greater maxima. This has to be compared with the distribution of the population for exposure assessment, which will be done in a second phase of this study.

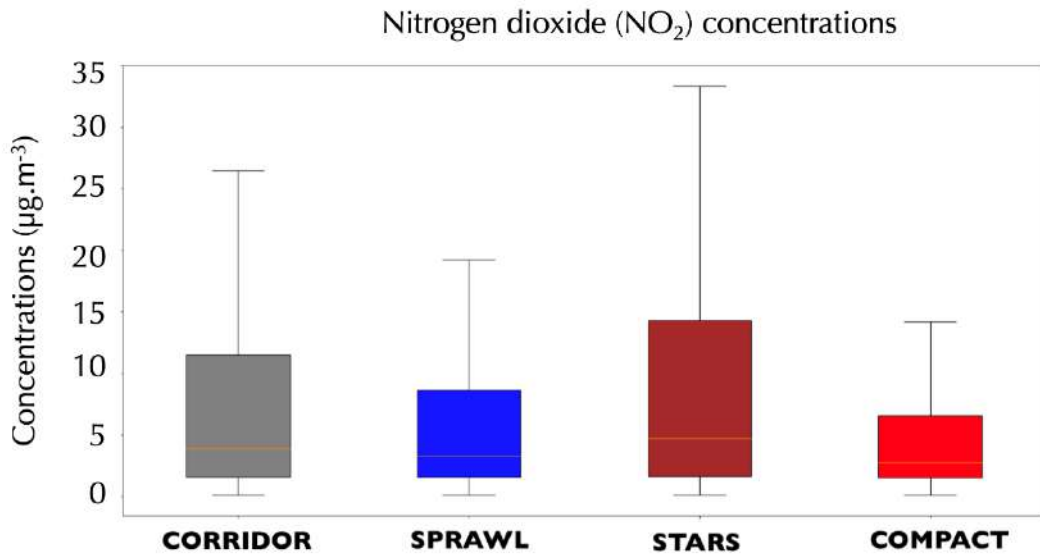


Figure 2. Boxplots of NO_2 concentrations from the different urban forms scenarios

Conclusions

This modeling exercise allowed us to test the impacts of the city morphology on energy consumption and on the emissions accounting for air quality. Our results first confirm what has been found in other studies, namely that urban density plays a key role in emissions distribution, whether in terms of surface or linear emissions, because it is strongly correlated with the urban fabric density. However, we show that density is not the only parameter controlling emissions. Accessibility, connectivity and land mix also play a key role in the variability of the emissions and have been considered in specific scenarios. In the simulations presented, it should be remembered that emissions from sectors other than the combustion of transport and the residential and commercial sectors are not spatialized according to population density, but are derived from the reference situation for Paris (based on the local emissions inventory). This redistribution of emissions could have an impact on pollutant concentrations and, ultimately, exposure of populations under different scenarios. It mainly concerns industrial activity.

We note, in terms of mobility, that the model is not very sensitive to variations in the utility of public transport but also of the car. The generalized cost of modeled transport in the various scenarios is surely quite rigid in the model, which may explain these small variations in the modal choice. However, this poses many questions. First of all, is this effect an effect of the model, or is reality also a system where car utility and public transport utility do little alter practices? What resistance does the use of the private vehicle actually offer? In any case, how much should urban parameters be modified to sufficiently modify the utility of travel modes in order to change practices? New academic scenarios offering a modification of the usefulness of certain modes could be carried out, in order to see when the system switches in favor of a mode other than the car, and in which urban form this phenomenon is the easiest to bring. These elements could serve as a guide for the design of new cities, but also for the evolution of existing cities.

Acknowledgements

This work was performed using HPC resources from GENCI-CCRT (grant 2017-t2015017232). This work also received support from the French National Agency for Research (ANR-14-CE22-0013) and the Île-de-France region (DIM R2DS). We also acknowledge AIRPARIF and the LABEX Urban Futures.

References

- Borrego, C., Martins, H., Tchepel, O., Salmim, L., Monteiro, A., Miranda, A.I., 2006. How urban structure can affect city sustainability from an air quality perspective. Environ. Model. Softw. 21, 461–467. <https://doi.org/10.1016/j.envsoft.2004.07.009>
- Elessa Etuman, A., Coll, I., 2018. OLYMPUS v1 . 0 : development of an integrated air pollutant and GHG urban emissions model – methodology and calibration over greater Paris 5085–5111.
- Mailler, S., Menut, L., Khvorostyanov, D., Valari, M., Couvidat, F., Siour, G., Turquety, S., Briant, R., Tuccella, P., Bessagnet, B., Colette, A., Létinois, L., Meleux, F., 2016. CHIMERE-2016: From urban to hemispheric chemistry-transport modeling. Geosci. Model Dev. Discuss. 0, 1–41. <https://doi.org/10.5194/gmd-2016-196>
- Manins, P.C., Cope, M.E., Hurley, P.J., Newton, P.W., Smith, N.C., Marquez, L.O., 1998. The impact of urban development on air quality and energy use. Proc. 14th Int. Clean Air Environ. Conf. Melb. 331–336.
- Seto K. C., S. Dhakal, Bigio, A., Blanco, H., Delgado, G.C., Dewar, D., Huang, L., Inaba, A., Kansal, A., Lwasa, S., McMahon, J.E., Müller, D.B., Murakami, J., Nagendra, H., Ramaswami, A., 2014. Human Settlements, Infrastructure and Spatial Planning., in: Climate Change 2014: Mitigation of Climate Change. Contribution of Working Group III to the Fifth Assessment Report of the Intergovernmental Panel on Climate Change. pp. 923–1000. <https://doi.org/10.1017/CBO9781107415416.018>

2.5.5 Mobility Scenarios in the Milan area: a modelling assessment of Air Quality

V. Agresti^{1*}, P. Giani^{1, #}, G. Pirovano¹, G. Lonati², N. Pepe^{1, §}

¹ Sustainable Development and Energy Sources Department, RSE Spa, via Rubattino 54 - 20134 Milano, Italy

² Department of Civil and Environmental Engineering, Politecnico di Milano - 20133 Milano, Italy

now at: Department of Civil and Environmental Engineering and Earth Sciences, University of Notre Dame, Notre Dame, IN, USA

§ now at: ARIANET S.R.L., Via Giacomo Gilino 9 – 20128 Milano, Italy

Corresponding author: Valentina Agresti, E-mail: valentina.agresti@rse-web.it, via Rubattino 54, 20134, Milano, Italy.

Abstract

The purpose of this study is the estimation of possible environmental benefits deriving from the achievement of sustainability targets linked to mobility policies and consequently the human health impact. The focus is on the private road transport segment and the object of this study is the metropolitan city of Milan. At a first stage, the emissions of pollutants associated to road traffic, such as NO_x, and PM_{2.5}, are estimated in case of implementation of mobility policies and compared to a base case. This analysis is based on the variation of vehicle kilometres travelled (VKT) by different fuelled vehicles, assuming zero exhaust emissions associated to electric vehicles. Afterwards the impact on urban air quality due to road traffic is estimated, thanks to a WRF-CAMx modelling system. Following the impact pathway approach, a local scale health impact assessment is finally performed to quantify the actual benefits that might derive from such changes in air quality. Two mobility scenarios with different levels of incisiveness are analysed in this work: a *Fleet electrification only Scenario* and a *Fleet Electrification + Mobility Policy Scenario*. The former considers the introduction of 20% of pure electric vehicles (BEV) in the car fleet and the same amount of vehicles fuelled with LPG and methane, the remaining 60% being conventional. This mobility scenario leads to a slight reduction of PM_{2.5} and an abatement of 17% of NO₂ annual mean concentration. However to get a more significant lowering of the atmospheric pollutants further actions are needed such as the enhancement of shared cars, more effectiveness of private vehicles, strengthening of public transport, including infrastructural interventions. In fact most promising results are associated with the second scenario. The decrease in PM_{2.5} and NO₂ annual mean concentrations under this scenario entails a consistent reduction in the health burden associated to air pollution exposure: 118 premature deaths (1329 years of life lost) and 244 days of hospitalization due to cardiovascular and respiratory diseases would be avoided annually.

Introduction

This study aims to estimate the effects of a partial car fleet electrification on the mitigation of air pollution in a metropolitan context. The attempt here is also to assess the impact of such scenario in terms of human exposure to air pollution. The case test refers to the city of Milan and its surroundings where the harmful pollutants concentration limit values, imposed by the law, are often exceeded.

Air pollution is a major environmental risk to health (WHO, 2013) particularly in urbanized areas, where most part of European population live. It also has considerable economic impacts, cutting lives short, increasing medical costs and reducing productivity through working days lost across the economy. Europe's most serious pollutants in terms of harm to human health are fine particulate matter (PM_{2.5}), NO₂ and ground-level O₃ (EEA, 2018).

In urban areas on-road transport is one of the main sources of atmospheric pollutant emissions and passenger transport is the most critical segment. For a receptor placed in the city centre of Milan, Pepe et al., 2019 estimate that road traffic, residential heating by biomass, and long range transport are responsible for 73% of PM_{2.5} annual average concentration. The transport sector yields the principal contribution (28%), with half contribution due to cars, 8% and 5% respectively due to heavy and light duty vehicles, and 1% due to mopeds and motorcycles. For NO₂ they find that road transport is, by far, the most impacting source, with a 72% share: 60% of NO₂

concentration derives from heavy duty (31%) and passengers cars (29%) emissions, 11% from light duty vehicles, and about 1% from mopeds and motorcycles (Pepe, et al., 2019). These estimates are obtained thanks to the source apportionment (SA) algorithm implemented in CAMx model (PSAT, Yarwood et al., 2004) and provide a comprehensive picture of the actual role of the different sources, thus representing a good starting point for further development of emission reduction strategies (Pepe et al, 2019). Among the strategies designed to reduce on road traffic emissions and their impact on air quality, fleet electrification is one of the most promising one. It comprises a wide spectrum of technological options that range from the early-stages hybrid vehicles to pure electric battery vehicles (BEV) that are entirely propelled by stored electricity with no direct exhaust emissions. Electric vehicles are particularly suitable to improve air quality in urban areas, where short distance trips at low speeds are prevalent (Soret, et al., 2014). Furthermore, higher potential benefits of reducing atmospheric emissions are found in highly populated areas (Ayalon, et al., 2013).

In this work the impact of a partial car fleet electrification on air pollution levels in a metropolitan context are estimated by means of air quality modelling. Additionally, the impact of the car fleet change is also assessed in terms of population exposure to air pollution and related adverse health effects. The modelling study is focused on Milan, the major metropolitan area of the Po Valley, a well-known European hot-spot for many air pollutants (Perrino et al., 2014). Surrounded by the Alps to the North and North-West and by the Apennines to the South, the Po Valley experiences poor circulation of air masses (Caserini et al., 2017). In addition, the occurrence of frequent and prolonged wind calm periods and atmospheric stability conditions, especially during the coldest months, favors the accumulation of locally-emitted pollutants as well as the development of high pollution episodes at regional scale, so that regulatory air quality limits are often exceeded. The work is focused on NO₂ and PM_{2.5}: besides being the most important pollutants associated to road transport and regulated by European air quality standards, they are suitable for a metropolitan scale study. On the contrary, the analysis of O₃ atmospheric concentration variation requires wider spatial scales.

In the following section 2 the set-up of WRF-CAMx modelling system, upon which the present work is based, is described together with the health impact assessment tool. The methodology developed to transpose mobility scenarios into passenger cars emission scenarios is then reported. This crucial step leads to the estimation of the effects of mobility policies on air quality, the main results being reported in section 3. Finally the expected impact on human health, resulting from the reduction of ambient PM_{2.5} concentration for the two mobility scenarios considered, is discussed.

Methods

Modelling system

Air quality modelling simulations were performed through WRF (Weather Research and Forecasting meteorological model, Skamarock et al., 2008) and CAMx (Comprehensive Air Quality Model with Extensions, ENVIRON, 2016) for the entire 2010 calendar year.

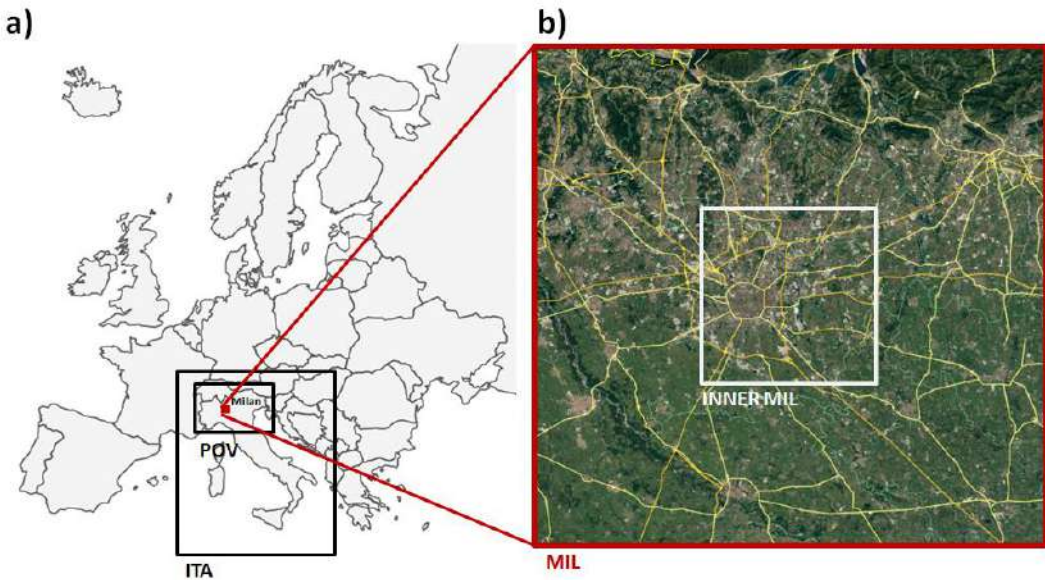


Figure 1: (a) WRF-CAMx domains of simulations: ITA and POV. (b) POV nested MIL domain (1.7 km of horizontal resolution) and the area of study (INNER MIL).

WRF model setup

WRF model (version 3.4.1) simulations were performed on four computational domains: a European domain and the three nested domains (ITA, POV and MIL) shown in Figure 1. The biggest domain has an European extent ($3870 \times 4140 \text{ km}^2$) and a horizontal resolution of 45 km. The first nested domain (ITA) covers the Italian peninsula ($1350 \times 1530 \text{ km}^2$) at 15 km of horizontal resolution; the second nested domain (POV) covers the Po Valley ($600 \times 420 \text{ km}^2$), and the last domain (MIL) covers Milan metropolitan area, spanning over the city of Milan and its surroundings ($85 \times 85 \text{ km}^2$). The horizontal resolution of POV and MIL domain are respectively 5 km and 1.7 km. All the domains are solved by 30 vertical levels, from about 25 m up to more than 15 km from ground level. This configuration of WRF model is forced on its open boundaries with ECMWF analysis fields at 0.5×0.5 degrees of resolution, both at the ground level and at different pressure levels. Further details on WRF set-up are given in Pepe et al., 2006.

CAMx model setup

In this work the simulation of dispersion phenomena and chemical processes is entrusted to CAMx model (version 6.3) that estimated concentration fields over the three innermost domains of WRF: ITA, POV and MIL (Figure 1). CAMx configuration shares the same horizontal resolution of WRF, with a slightly reduced grid dimensions in order to remove boundary effects. Conversely, the vertical grid is defined collapsing the first 21 WRF levels into 14 layers even though the layers up to 1 km above the ground level are kept at the same height.

Homogeneous gas phase reactions of nitrogen compounds and organic species are reproduced through CB05 mechanism (Yarwood et al., 2005). The aerosol scheme is based on two static modes (coarse and fine). Secondary inorganic compounds evolution is described by thermodynamic algorithm ISORROPIA (Nenes et al. 1998), while SOAP (ENVIRON, 2011) is used to describe secondary organic aerosol formation. Input emission fields were derived from emission inventory data at different spatial scale resolution: EMEP (European Monitoring and Evaluation Programme), available over a regular grid of $50 \times 50 \text{ km}^2$, ISPRA (Italian national inventory data), which provides province-scale emission data, INEMAR, which provides emission data at municipality resolution over the POV and MIL domain (INEMAR – ARPA Lombardia, 2015). Each emission inventory was processed using SMOKE model (version 3.5) (Sparse Matrix Operator for Kernel Emissions model, UNC, 2013) that allows the conversion of emission

inventory data to the both spatial and temporal resolution needed by the air quality model. Additional details on CAMx configuration are available in Pepe et al., 2016.

Health impact assessment

The impact on human health of different air quality scenarios on human health can be calculated by combining gridded changes in PM_{2.5} concentration fields, municipality-level population data and baseline incidence rates. Following the well-established European Environment Agency methodology (De Leeuw et al., 2016), a log-linear model has been used to derive the health impact function, which results in the following equation:

$$I_{ijk} = P_{ij} \cdot r_{ijk} \left(1 - \frac{1}{e^{\beta_k \Delta C_{ij}}} \right) \quad (1)$$

Where I_{ijk} is the impact on health endpoint k (e.g. avoided mortality) due to change in PM_{2.5} concentration ΔC_{ij} in the grid cell (i, j) , P_{ij} is the population in grid cell (i, j) , β_k is a parameter which accounts for the sensitivity of impact on health endpoint k on a concentration change ΔC_{ij} and r_{ijk} is the baseline incidence rate of endpoint k in cell (i, j) . In this work only two health endpoints have been taken into account (i.e. $k = \{1,2\}$), namely hospital admissions and premature deaths, as they are classified as reliable by the most up-to-date European literature on PM_{2.5} health impact assessments (WHO, 2013). The value of parameter β_k is directly linked to the relative risk (RR_k), which is defined in the log-linear model as:

$$RR_k = \frac{r_{k,BC}}{r_{k,SC}} = e^{\beta_k \Delta C} \quad (2)$$

Where $r_{k,BC}$ stand for the baseline incidence rate whereas $r_{k,SC}$ is the incidence rate under a defined scenario. As RR_k values and their 95% confidence interval for different health endpoints k have been estimated during the European HRAPIE project (WHO, 2013) for a 10 µg m⁻³ change in PM_{2.5}, β_k can be simply computed as:

$$\beta_k = \frac{\ln(RR_k)}{10} \quad (3)$$

The total impact for the endpoint k is finally the sum of I_{ijk} over each grid cell (i, j) .

It should be noted that for premature deaths, ΔC_{ij} in Equation (1) is expressed in terms of the change in the annual average PM_{2.5} concentration, as premature mortality is supposed to be an effect of a long-term exposure; on the other hand, for hospital admissions ΔC_{ij} is expressed as the change in daily mean PM_{2.5} concentration (being the result of a short-term exposure), and Equation (1) is solved for each day of the year. We assume, coherently with WHO, 2013, that premature mortality affects only 30+ adults whereas hospital admissions are related to all ages. Following WHO 2013, in this work we use a value of RR per 10 µg/m³ equal to 1.062 (1.040–1.083, 95% confidence interval) for premature mortality and equal to 1.0190 (1.0017–1.0166) and 1.0091 (0.9982–1.0402) for hospital admissions due to respiratory and cardiovascular diseases respectively.

Population and sanitary data have been collected from different sources. We used age-specific and municipality-level population and baseline incidence rates from the Italian National Institution of Statistics (ISTAT) for year 2010, which have been re-gridded onto the air quality modelling grid. The national average number of hospital admissions (2010), due to both respiratory and cardiovascular diseases, was instead recovered from the “European Hospital Morbidity Database”, which provides endpoint-specific data at a national level for each European country. Finally, RR_k values are taken from the results of HRAPIE project (WHO, 2013).

Base case and scenarios

Mobility scenarios

One base case and two mobility scenarios have been analysed. The base case refers to fleet composition and vehicle kilometres travelled (VKT) data for year 2010. The first scenario (*Scenario A - Fleet Electrification*) considers a car fleet composed by a share of 20% of Battery Electric Vehicles (BEV), a share of 20% of LPG and NGV cars, fuelled with both natural and liquefied petroleum gas, with the remainder 60% of the fleet being conventional cars. The second scenario (*Scenario B - Fleet Electrification + Mobility Policies*) considers the same car fleet composition of *Scenario A*, but assumes an overall transition toward a more sustainable mobility. More precisely, *Scenario B* supposes some political strategies designed in order to discourage the use of private cars in favour of bikes and the car pooling and by the extension of the restricted traffic zones. Moreover this scenario supposes the strengthening of public transport infrastructures. Basically the two scenarios differ from the base case (2010) by a different distribution of vehicle kilometres travelled (VKT) by three categories of cars. We assume that the changes imposed by the scenarios have immediate effects, so that the technological evolution of vehicles (e.g., Euro classes distribution) is neglected. More details on both scenarios can be found in Borgarello et al., 2016.

VKT gridded data are provided on a subdomain of the MIL domain (INNER-MIL in Figure 1b). These data have the same horizontal resolution of CAMx grid, i.e. 1.7 km. INNER MIL domain includes the city of Milan and 54 surrounding municipalities, 46 of them belonging to the area of Milan and the remaining 8 to the Monza and Brianza province. For the grid cells of INNER MIL domain, VKT data are provided with a hourly time step for a typical day traffic profile, with one peak during the morning and one peak during the afternoon and an overall traffic damping during the night.

VKT data refer to three macro classes of vehicles:

- Petrol and diesel cars, to whom we refer as *Conventional Vehicles (CV)*
- LPG and NGV cars, to whom we refer as *(LN)*
- BEV, to whom we refer as *Electric Vehicles (EV)*

According to car register data for the INNER-MIL domain in 2010 (ACI Automobile Club Italia 2010), CV class had a 65%-35% split between petrol and diesel cars, whilst LN class had a 84%-16% split between LPG and NGV cars. BEV were limited to very few vehicles in 2010 fleet.

A similar distribution of the car fleet characterizes the Monza and Brianza province. In this study we suppose that the share of electric vehicles are all BEV, neglecting plug-in electric cars.

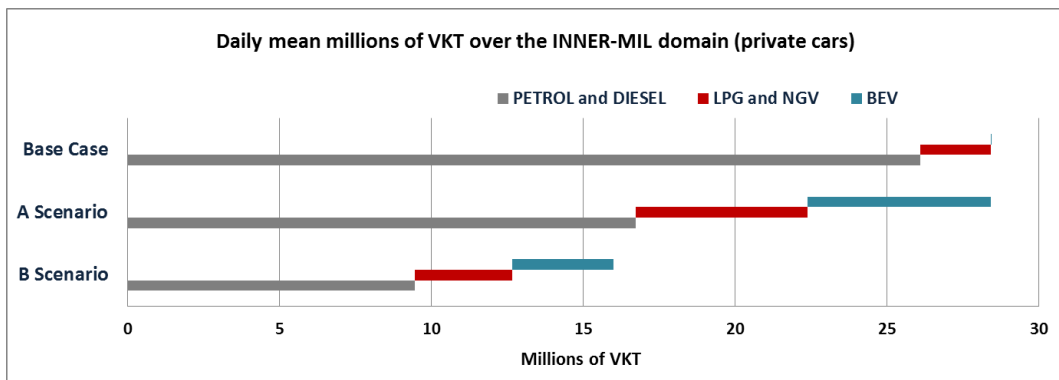


Figure 2: Daily mean millions of VKT averaged over the INNER-MIL domain for the classes of vehicles: CV, LN and EV, according to the Base case, A and B Scenarios.

Figure 2 provides the overview of the characteristics of the base case and of the two scenarios in terms of daily mean VKT by vehicle class. Almost all the vehicles are conventional in the base case (92%) where BEV vehicles are negligible. The two mobility scenarios introduce a drastic change to the distribution of the car fleet, with the total amount of VKT unchanged for *A Scenario*

and reduced by 44% for *B scenario*, because of the replacement of private cars by other transport solutions.

Emission scenarios

Assessing the impact of mobility scenarios on air quality with a chemical and transport model, requires an intermediate and crucial step i.e., the careful rescaling of private road transport base case emission field in the area of study. For this purpose we use VKT data in order to calculate emission rescaling coefficients and emission factors (EF) as multiplicative weights. NO, NO₂, CO, NH₃, NMVOC, SO₂ rescaling coefficients are estimated according to equation 4, while for PM₁₀ equation 5 is used. Both coefficients are estimated for each grid cell of the domain (*i,j*) - where VKT data are available - and for each hour of the day (*t*). We distinguish two coefficients *C_gs* and *C_PM* respectively for gaseous species and PM, in order to take account for PM₁₀ non-exhaust emissions, such as brake, tire and road wear that characterize also EV cars.

$$C_{gs,i,j,t} = \frac{\{\sum_n(VKT \times EF)_n\}_{sc}}{\{\sum_n(VKT \times EF)_n\}_{bc}} \quad (4)$$

$$C_{PM,i,j,t} = \frac{\{\sum_n(VKT \times EF)_n + \sum_m VKT_{BEV} \times (EF)_m\}_{sc}}{\{\sum_n(VKT \times EF)_n\}_{bc}} \quad (5)$$

For gaseous species the coefficient *C_gs* is calculated as the ratio between the weighted sum of the VKTs in a scenario with respect to the base case. As weighting coefficient a mean EF, representative of each vehicle macro class *n*, is used (Figure 3). For *C_gs* we assume EV as zero exhaust-emissions. For what concerns *C_PM* we consider an additional term in equation 5, taking account also brake wear, tyre and road abrasion associated to EV (*m* index) (Ntziachristos et al., 2009). EF are provided by COPERT database (COPERT 2010, Gkatzoflias et al., 2010) and they are averaged for each class of vehicles, according to the car fleet composition in 2010 in the metropolitan area of Milan. Even though recent studies suggest higher road and tyre emissions for EV respect to CV, due to the greater weight of the vehicle, here we suppose the same order of magnitude. Conversely we suppose that non-exhaust emission fraction associated to brake wear of an EV corresponds to 20% of a CV one (Del Duce et al., 2016).

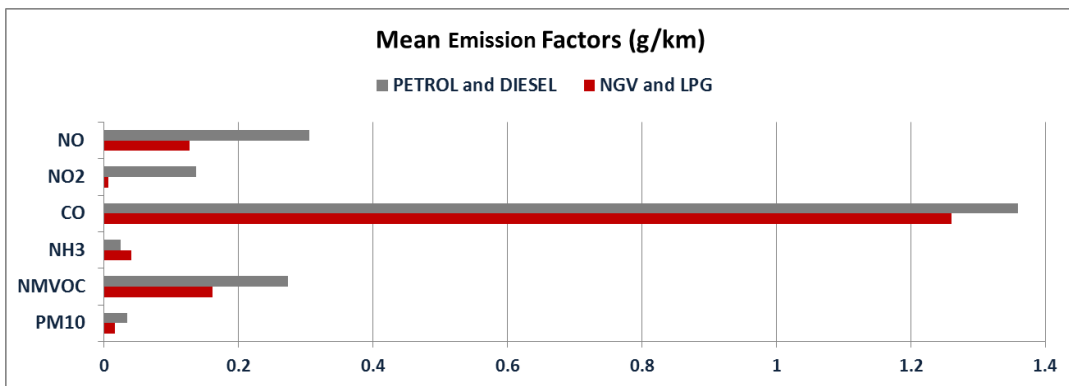


Figure 3: NO, NO₂, CO, NH₃, NMVOC and PM₁₀ mean EF (g/km) (COPERT, 2010) employed in Equations 4 and 5. SO₂ coefficients are omitted because of the lower order of magnitude.

Daily mean rescaling coefficients, averaged over all cells of the INNER-MIL domain, are listed in Table 1. In general the overall effect of the *A scenario* is a reduction of 20% - 35% of private cars

emission segment while the *B scenario* entails more than a halving of the base case passenger car emissions. This is mostly due to the shift of vehicles kilometres travelled by private cars toward the public transport.

Table 1: Daily mean NO, NO₂, CO, NH₃, SO₂, NMVOC and PM₁₀ emission rescaling coefficients.

Emission Rescaling Coefficients		
	A scenario	B scenario
NO	0.72	0.46
NO ₂	0.65	0.42
CO	0.77	0.49
NH ₃	0.81	0.52
SO ₂	0.64	0.41
NMVOC	0.71	0.45
PM ₁₀	0.76	0.49

Finally, emission fields for *Scenarios A* and *B* are obtained, for each hour of the day, multiplying the base case emission field by a reduction matrix (composed by all the rescaling emission coefficients), over all the INNER-MIL domain. Other emission sources (e.g., the ones associated to industrial plants, residential and commercial heating with biomass, light duty and heavy duty vehicles) are unchanged respect to the base case, so the overall emission field suitable for CAMx model is obtained by the sum of all the emission macro-sectors.

It is worth mentioning that in this study the possible impact on air quality due to a possible increase in the emissions of the energy production sector has been neglected, due to their minor impact on air quality at regional scale (Balzarini et al., 2012).

Results

Mobility scenarios impact on air quality

The effects of sustainable mobility scenarios on air quality are estimated by the comparison of the scenario simulated concentrations with the base case ones. Figure 4a shows the yearly mean concentration of NO₂ simulated by WRF-CAMx modelling system for the base case in the MIL domain (year 2010). NO₂ concentration peaks are reached at the most urbanized areas of MIL domain, the yearly mean concentration ranging between 15 and 20 ppbV in the INNER-MIL portion of MIL domain. Figure 4b and 4c show the fields of the absolute concentration difference between the simulated scenarios and the base case. The effects of mobility policies are important in the INNER-MIL domain, where the partial electrification of the car fleet entails a reduction of about 17% of NO₂ yearly mean atmospheric concentration. This result is amplified in the case of *Scenario B*, which additionally implies an overall reduction of vehicle kilometres travelled by passenger cars, hence leading to a 30% abatement of the NO₂ concentration with respect to the base case.

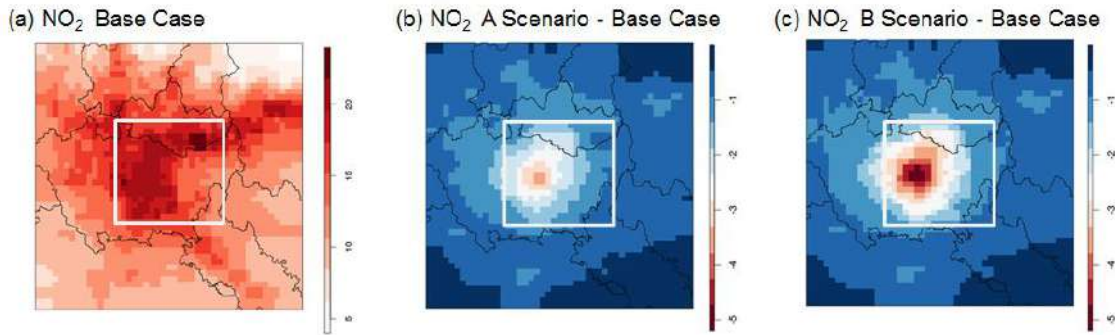


Figure 4: (a) Yearly mean NO₂ concentration (ppbV) for the base case in the MIL domain. (b) Absolute difference between A Scenario and the base case and (c) B Scenario and the base case. White box corresponds to INNER-MIL domain.

The exposure to fine PM reduces the life expectancy of the population, especially in polluted cities, so the estimation of mobility scenarios impacts on PM_{2.5} atmospheric concentration is of primary importance. Figure 5a shows the base case concentration of PM_{2.5} in the MIL domain, calculated with WRF-CAMx. Here the urban footprint of PM_{2.5} is less evident than NO₂ since fine PM is more subject to transport and diffusion processes related to formation timescales of its secondary component. In the INNER-MIL part of the domain the yearly mean concentration of PM_{2.5} is about 17 $\mu\text{g m}^{-3}$ while the reduction of PM_{2.5} due to the mobility scenarios is about 4% and 8.5% respectively for the A and B scenarios (Figure 5b and 5c). Fleet electrification has a limited impact on PM_{2.5} concentration. This is partially due to the fact that non-exhaust emissions (resuspension and brake, tyre and road abrasion) cannot be reduced by the variation of the composition of the car fleet.

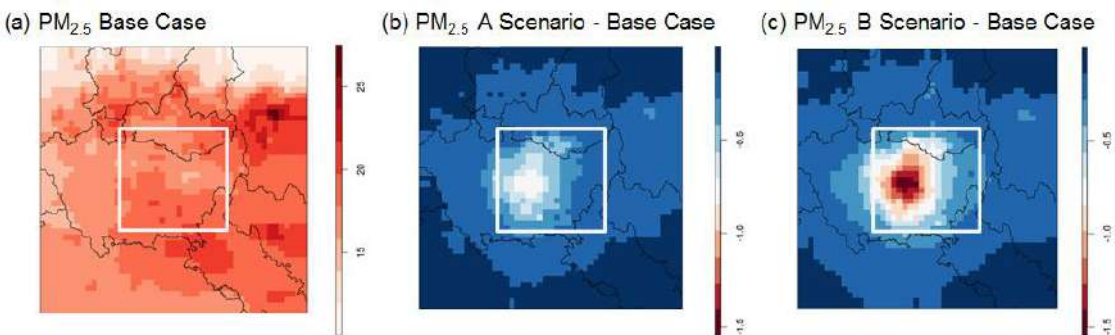


Figure 5: (a) Yearly mean PM_{2.5} concentration ($\mu\text{g m}^{-3}$) for the Base case in the MIL domain. (b) Absolute difference between A scenario and the base case and (c) B scenario and the Base case. White box corresponds to INNER-MIL domain.

Mobility scenarios impact on human health

Differences in PM_{2.5} concentration fields presented in the previous section entail a non-negligible impact on human health. On annual basis, the total amount of avoided premature deaths, achievable in the two different scenarios, is equal to 113±19 and 182±31 (mean ± standard deviation), respectively for the A and B scenarios (Table 2). The difference between the two scenarios can be ascribed to the impact of other mobility policies, which account for 69 avoided premature deaths (37.9% of the total). On top of that, 50±25 hospitalizations due to respiratory and cardiovascular diseases would be avoided annually in the A Scenario and 32 more would be avoided when including also the mobility policies (B Scenario), as summarized in Table 2. The uncertainty associated to our health impact calculations derives from the uncertainty in the relative risk estimation given by the HRAPIE project (WHO2013).

Table 2: Effects on human health due to the abatement of $\text{PM}_{2.5}$ ($\mu\text{g m}^{-3}$) respect to the base case, due to the A and B Scenarios. All the numbers refer to avoided effects.

	A Scenario	B Scenario
Avoided premature deaths	113 ± 19	182 ± 31
Avoided hospitalizations	50 ± 25	82 ± 42

The fine resolution modelling allowed assessing the spatial distribution of such avoided impacts, which is far from being uniform across the domain. As clear from Figure 6, positive impacts are mostly concentrated in the highly populated area of Milan, which is the middle of the MIL domain. This is related to the combined effect of the higher degree of $\text{PM}_{2.5}$ reduction in the city of Milan (Figure 5) and the higher population exposure (i.e., population density is greater in the city of Milan and it decreases in the city hinterland). In order to better quantify such spatial pattern, we computed the average avoided premature deaths per unit of area, both in the city of Milan and in the rest of the domain. We found that, under the B scenario, 0.609 deaths/ km^2 are avoided in the city of Milan whereas only 0.013 deaths/ km^2 could be avoided, on average, in the hinterland of Milan.

This finding implies that the most polluted areas (i.e. densely populated urban areas) would benefit the most from the two mobility scenarios, highlighting the importance of mobility policies in addressing current human health concerns in urban areas.

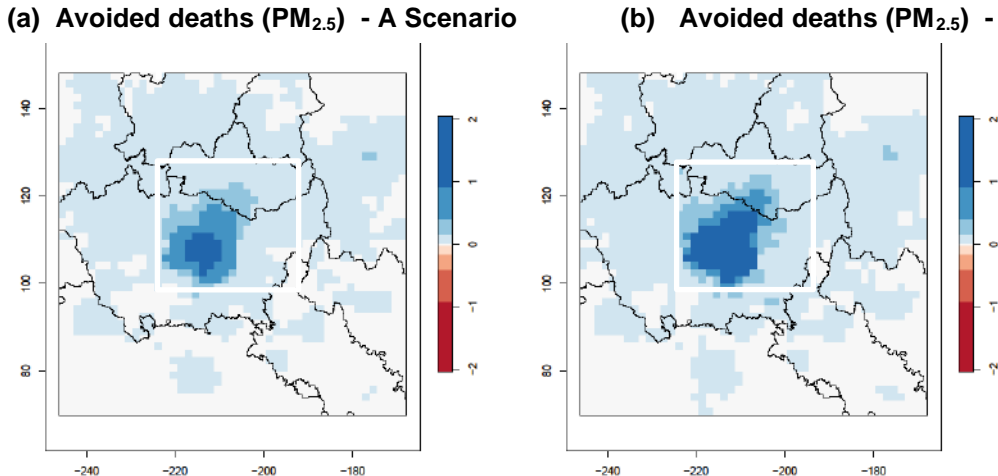


Figure 6: Estimated premature deaths avoided thanks to the abatement of the $\text{PM}_{2.5}$ ($\mu\text{g m}^{-3}$) resulting from the application of the A scenario (a) and the B scenario (b). The differences are calculated respect to the base case. White box corresponds to INNER-MIL domain.

Conclusions

The transition toward a more sustainable mobility is becoming increasingly more achievable thanks to the spread of electric and low carbon vehicles. Dedicated mobility policies can accelerate this trend. In this work the focus is on the private road transport sector, being amongst the main contributors to the poor air quality in urban areas. Particularly potential emission and air quality impacts of partial fleet electrification in the city of Milan and its surroundings are analysed. This area, which is located in the North-Western section of the Po Valley, is known for critical episodes of urban pollution. The air quality assessment has been performed with the WRF-CAMx modelling system and a novel tool has been developed and applied, over the INNER-MIL domain, to estimate the health impact associated with different policies.

Two fleet electrification scenarios (with 20% of vehicle kilometres travelled by BEV), have been defined and compared to a base case, where the *Scenario A* is an electrification-only scenario and the *Scenario B* takes account also of sustainable mobility policies. Hereinafter we provide average estimates of scenarios impacts, over all the INNER-MIL domain, even though both scenarios are most incisive in the city centre of Milan in terms of emissions, air quality and health impact. Both scenarios entail more than a halving of the base case passenger car emissions, the reduction being respectively of 58% for NO₂ and 51% for PM_{2.5}. The overall result in terms of pollutant atmospheric concentration abatement is less incisive, since other emission macro categories have an important weight. As expected the *B scenario* is more incisive than *A scenario* in terms of both emissions and air quality, since the effect of mobility policies is an overall decrease of vehicle kilometres travelled by passenger cars. In particular the more ambitious scenario (*B*) entails a 30% abatement of the NO₂ yearly mean concentration with respect to the base case in the INNER-MIL domain, while it has a limited impact on PM_{2.5} (a lowering of 8.5%). This is partially due to the fact that non-exhaust cannot be reduced by the variation of the composition of the car fleet.

We conclude that fleet electrification presents potential air quality benefits even though the reductions achieved are insufficient to ensure proper air quality levels, especially for PM. Nevertheless we estimate non-negligible effects of *B scenario* on human health, due to the abatement of PM_{2.5} concentration: 180 premature deaths are avoided in the area of Milan.

In order to reach greater benefits other management measures should involve all vehicle categories (two-wheelers, heavy-duty vehicles, buses and light-duty vehicles) not only passenger cars and further reductions should be considered also for other emission sources. Finally the WRF-CAMx modelling system, used to estimate the scenarios yearly mean concentration pollutant variations, is a suitable tool for the management and assessment of urban air quality, as well as the health impact assessment tool.

Acknowledgments

This work has been financed by the Research Fund for the Italian Electrical System in compliance with the Decree of Minister of Economic Development April 16, 2018.

References

- ACI Automobile Club Italia 2010, <http://www.aci.it/laci/studi-e-ricerche/dati-e-statistiche/autoritratto/autoritratto-2010.html>
- Ayalon O., Flicstein B., and Shtibelman A. (2013). Benefits of reducing air emissions: replacing conventional with electric passenger vehicles, *Journal of Environmental Protection* 4.10, 1035.
- Balzarini, A., G. Pirovano, G.M. Riva, A. Toppetti (2012). Modelling the impact of plug-in electric vehicles (phev/pev) on emissions and air quality over Italy. Proceedings of Abstracts 8th International Conference on Air Quality Science and Application, Greece; ed. Vikas Singh, Heather Price, John G. Bartzis, Ranjeet S Sokhi, ISBN/ISSN: 978-1-907396-80-9.
- Bedogni M. and Pirovano G. (2011). Source apportionment technique: inorganic aerosol transformation processes in the Milan area. *International Journal of Environment and Pollution*, 47, 167-183.
- Borgarello M., Viani S., Cavicchioli C., Caruso C., Tripodi G., Soresinetti S. (2016). Area Metropolitana milanese: mobilità ed efficienza energetica, RSE, Ricerca di Sistema, 17001221.
- Caserini, S., Giani, P., Cacciamani, C., Ozgen, S., & Lonati, G. (2017). Influence of climate change on the frequency of daytime temperature inversions and stagnation events in the Po Valley: historical trend and future projections, *Atmospheric Research*, 184, 15-23.
- COPERT 2010 – The EU standard vehicle emissions calculator, <https://www.emisia.com/utilities/copert-data/>
- Del Duce A., Gauch M., Althaus H.J. (2016). Electric passenger car transport and passenger car life cycle inventories in ecoinvent version 3, *The International Journal of Life Cycle Assessment* 21.9, 1314-1326.
- De Leeuw F, Horálek J. (2016). Quantifying the health impacts of ambient air pollution: methodology and input data.

- ECMWF European Centre for Medium-Range Weather Forecasts, <https://www.ecmwf.int/en/research/projects/ensembles/data-archiving>
- EEA, 2018. Air Quality in Europe - 2018 report. European Environmental Agency, ISBN 978-92-9213-989-6, No 12/2018.
- EMEP European Monitoring and Evaluation Programme, <http://www.ceip.at/emission-data-webdab/emissions-used-in-emep-models/>
- ENVIRON, 2016. CAMx (Comprehensive Air Quality Model with extensions) User's Guide Version 6.3. ENVIRON International Corporation, Novato, CA.
- Gkatzoflias D., Kouridis C., Mellios G., Ntziachristos L. (2010). COPERT 4 v7 (https://www.emisia.com/wp-content/uploads/files/docs/COPERT_v4.7.1.pdf)
- INEMAR, Inventario Emissioni in Atmosfera: emissioni in Regione Lombardia nell'anno 2012 - revisione pubblica. ARPA Lombardia Settore Monitoraggi Ambientali.
- INERIS, 2006. Documentation of the Chemistry-transport Model CHIMERE [version V200606A]. Available at: <http://euler.lmd.polytechnique.fr/chimere/>.
- ISPRA, Italian national inventory data, <http://www.sinanet.isprambiente.it/it/sia-ispra/inventaria/disaggregazione-dellinventario-nazionale-2010>.
- ISTAT Italian National Institution of Statistic, <http://dati.istat.it/>.
- Nenes, A., Pandis, S. N., & Pilinis, C. (1998). ISORROPIA: A new thermodynamic equilibrium model for multiphase multicomponent inorganic aerosols, *Aquatic geochemistry*, 4(1), 123-152.
- Ntziachristos L. and Boulter P. (2009). EMEP/EEA air pollutant emissions inventory guidebook 2009: Road vehicle tyre and brake wear, Road surface wear." Copenhagen, European Environment Agency.
- Pepe, N., Pirovano, G., Lonati, G., Balzarini, A., Toppetti, A., Riva, G. M., Bedogni, M. (2016). Development and application of a high resolution hybrid modelling system for the evaluation of urban air quality. *Atmospheric environment*, 141, 297-311.
- Pepe, N., Pirovano, G., Balzarini, A., Toppetti, A., Riva, G. M., Amato, F., & Lonati, G. (2019). Enhanced CAMx source apportionment analysis at an urban receptor in Milan based on source categories and emission regions, *Atmospheric Environment*: X, 100020.
- Pernigotti D., Thunis P., Cuvelier C., Georgieva E., Gsella A., De Meij A., Pirovano G., Balzarini A., Riva G.M., Carnevale C., Pisoni E., Volta M., Bessagnet B., Kerschbaumer A., Viaene P., De Ridder K., Nyiri A., Wind P. (2013). POMI: a model inter-comparison exercise over the Po Valley." *Air Quality, Atmosphere & Health*, 6.4, 701-715.
- Perrino C., Catrambone M., Dalla Torre S., Rantica E., Sargolini T., Canepari, S. (2014). Seasonal variation in the chemical composition of particulate matter: a case study in the Po Valley. Part I: macro-components and mass closure. *Environmental Science and Pollution Res.*, 21, 3999-4009.
- Pirovano G., Colombi C., Balzarini A., Riva G.M., Gianelle V., Lonati G. (2015). PM_{2.5} source apportionment in Lombardy (Italy): comparison of receptor and chemistry-transport modelling results. *Atmospheric Environment*, 106, 56-70.
- Skamarock W. C., Klemp J. B., Dudhia J., Gill D.O., Barker D. M., Duda M. G., Powers J. G. (2008). A description of the advanced research WRF version 3, NCAR Technical Note. National Center for Atmospheric Research, Boulder, Colorado, USA.
- Soret A., Guevara M., Baldasano J.M. (2014) The potential impacts of electric vehicles on air quality in the urban areas of Barcelona and Madrid (Spain). *Atmospheric environment*, 99, 51-63.
- UNC, 2013. SMOKE v3.5 User's manual. (https://www.cmascenter.org/smoke/documentation/3.5.1/manual_smokev351.pdf.)
- World Health Organization (WHO, 2013). Health Risk of air pollution in Europe – HRAPIE project. Recommendations for concentration-response function for cost-benefit analysis of particulate matter, ozone and nitrogen dioxide." WHO Regional Office for Europe.
- World Health Organization (WHO, 2016). Ambient air pollution: A global assessment of exposure and burden of disease, Geneva, Switzerland, ISBN 9789241511353 (<http://wwwwho.int>).
- Yarwood G., Morris R.E., Wilson G.M. (2004). Particulate matter source apportionment technology (PSAT) in the CAMx photochemical grid model. In: Proceedings of the 27th NATO/CCMS International Technical Meeting on Air Pollution Modeling and Application. Springer Verlag.
- Yarwood G., Rao S., Yocke M., Whitten G. (2005). Updates to the carbon bond chemical mechanism: CB05 final report to the US EPA. RT-0400675.

2.5.6 Scenarios for proposed updated Low Emission Zone in Denmark - impacts to emissions and air quality in Copenhagen

S.S. Jensen, M. Winther, M. Ketzel, Ellermann, T.

Aarhus University, Department of Environmental Science, Roskilde, Denmark

Corresponding author: ssj@envs.au.dk

1. Introduction

A number of European countries have implemented Low Emission Zones as a policy measure to reduce emissions from road transport, to improve air quality and to reduce the health burden of air pollution in cities (www.urbanaccessregulations.eu). A Low Emission Zone (LEZ) is a limited geographic area with special emission requirements typically based on banning vehicles with older Euro emission standards. LEZs are typical urban areas characterized by a combination of relatively high density of emissions and population.

In Denmark, LEZs were implemented in the four largest cities in a two-stage process in 2008 and 2010. Trucks and buses above 3.5 tons have to comply with at least the Euro IV emission standard or have to be retrofitted with a diesel particle filter (DPF). The LEZs were implemented through national legislation that allowed the four largest cities to establish the LEZs. The cities include Copenhagen, Aarhus, Odense and Aalborg. A comprehensive evaluation program has previously been conducted to assess the impacts to emissions and air quality based on a combination of air quality measurements, dispersion modelling and registration of vehicle number plates (Jensen et al., 2011). Due to the renewal of the vehicle fleet almost all heavy-duty vehicles comply to the requirements in 2018 and hence the present LEZ has no or marginal remaining impact on emissions.

The Ministry of Environment and Food of Denmark initiated a study during first half of 2018 on different scenarios for updating the LEZs in Denmark. Aarhus University carried out the study (Jensen et al., 2018a). This paper describes the scenarios, the methodology of the impact assessment, and the results of the scenarios on emissions and air quality with focus on Copenhagen.

2. Methodology

2.1 Scenarios

The Ministry of Environment and Food of Denmark defined five scenarios as shown in table 1. Green indicates that the vehicle category is allowed to enter the LEZ and red indicates it is not allowed to enter. However, there are some exemptions if retrofitted with DPF, and for scenario C-E for trucks and buses if retrofitted with DPF and SCR (Selective Catalytic Reduction for NO_x reduction).

The scenarios are different concerning the vehicle types they include and the Euro vehicle emission classes required to enter the LEZ. All scenarios focus only on diesel vehicles and exempt petrol vehicles for regulation. All scenarios assume 2022 as implementation year to allow for new legislation to be passed in parliament and a longer grace period to implement the LEZs.

Scenario A and B includes requirements to all vehicle categories: passenger cars, vans and heavy-duty vehicles. The difference between the two scenarios is that scenario A only requires Euro 5 whereas scenario B requires Euro 6.

Scenario C is the only scenario that only has requirements for heavy-duty vehicles.

Scenario D and E also have requirements for vans apart from requirements for heavy-duty vehicles. The only difference between scenario D and E is that scenario D only requires Euro 5 for vans whereas scenario E requires Euro 6.

Overall, scenario B is the most stringent scenarios and Scenario C is the least stringent.

Table 1 Emission requirements in 5 scenarios for updated Low Emission Zones

Fuel	Vehicle type	Euro class	A	B	C	D	E
			2022	2022	2022	2022	2022
Diesel	Passenger car	Euro <=4	Red	Red			
Diesel	Passenger car	Euro 5		Red			
Diesel	Passenger car	Euro 6					
Petrol	Passenger car	Euro <=6					
Diesel	Van	Euro <=3	Red	Red		Red	Red
Diesel	Van	Euro 4	Red	Red			
Diesel	Van	Euro 5		Red			Red
Diesel	Van	Euro 6					
Petrol	Van	Euro <=6					
Diesel	Truck and bus	Euro <=IV	Red	Red		Red	Red
Diesel	Truck and bus	Euro V		Red	Red	Red	Red
Diesel	Truck and bus	Euro VI					

Green indicates allowed to enter LEZ and red not. Vehicles in red category may enter if retrofitted with DPF, and for scenario C-E for trucks and buses if retrofitted with DPF and SCR (Selective Catalytic Reduction).

2.2 Overall methodology

In previous studies of the impact of the existing LEZ dispersion models were used to calculate the impact on air quality for street concentrations, urban background concentrations and regional concentrations (Jensen et al., 2011). This is a relatively resource-demanding approach due to the establishment of the required input data.

A simpler yet scientifically sound approach was applied in this study due to time and financial constraints. This approach uses the street contribution from traffic to concentrations for 2017 in a specific street as the starting point derived from the Danish Air Quality Monitoring Programme in Denmark. The street considered is one of the busiest streets in Copenhagen, H.C. Andersen Boulevard that has a vehicle distribution that is typical for streets in Copenhagen. The concentration contribution from traffic is the difference between the urban background concentration measured at the roof of H.C. Ørsted Institute and the street concentration measured at H.C. Andersen Boulevard. This is called the street contribution or the street increment. To allocate the street contribution to the different vehicle categories the emission module of the Operational Street Pollution Model (OSPM) was used (Berkowicz 2000; Kakosimos et al., 2011; Ketzel et al., 2012). OSPM is used to model air quality at approx. 100 streets in Copenhagen every year as a supplement to measurements at fixed monitor stations (Ellermann et al. 2018).

The street contribution from 2017 is scaled with the emission reduction between 2017 and 2022 to estimate the reduction in concentrations in 2022 due to emission reduction. The emission reduction of the five scenarios are based on emission factors (g/km) in 2017 and 2022 derived from the Danish national emission inventory for the different vehicle categories (Winther, 2018). The impact of the scenarios on the air quality of NO₂, PM_{2.5} and PM₁₀ has been calculated for H.C. Andersen Boulevard for 2022.

2.3 Vehicle emission factors

Emission factors (g/km) have been derived from the Danish national emission inventory for the different vehicle categories and subdivided into fuel type (diesel/petrol) and Euro emission standards for 2017 and 2022. Emission data originates from the European road traffic COPERT 5 emission model and traffic and vehicle fleet data are provided by the Technical University of

Denmark (Transport DTU) and is based on annual data from Statistics Denmark's vehicle registry and the Danish Road Directorate (Winther, 2018). Emission and traffic data are subdivided into highway, main road and urban driving, and urban driving has been chosen to reflect city conditions.

Emissions include health-related pollutants: NO_x (nitrogen oxides), particle exhaust, and non-exhaust (road wear, tyre wear, brake wear) for PM_{2.5} and PM₁₀, respectively the mass of particles under 2.5 micrometre and 10 micrometre in diameter. Additionally, emission factors are established for total PM_{2.5} (exhaust and non-exhaust of PM_{2.5}) and total PM₁₀ (exhaust and non-exhaust of PM₁₀).

2.4 Vehicle distribution at H.C. Andersen Boulevard

Annual Average Daily Traffic (AADT) is 55,500 at H.C. Andersen Boulevard and the vehicle distribution in 2017 is shown in table 2.

Table 2 Vehicle distribution at H.C. Andersen Boulevard in 2017 (%)

Passenger car	Taxi	Vans	Truck < 32t	Truck > 32t	Bus	Total
76.6	5.03	15.05	1.01	0.90	1.41	100

In the emission model buses are subdivided into urban buses and coaches. Previous assessments have shown that there is approx. 50% urban buses and approx. 50% coaches at H.C. Andersen Boulevard, which differs somewhat from the average of 98 streets in Copenhagen, where the distribution was approx. 80% buses and 20% coaches (Jensen et al., 2016). However, the distribution between buses and coaches plays no role in the assessment of the scenarios, since the same LEZ requirements apply to all types of buses. In addition, taxis are assumed to be passenger cars in the calculations. Due to other Danish regulation, taxis are required to meet the Euro 6 emission standard. Hence, emissions for taxis will be overestimated in the applied approach. However, the influence is modest since there are relatively few taxis in relation to passenger cars. Diesel passenger cars account for approx. 44% of distance travelled in km of all passenger cars and gasoline passenger cars 56%. For vans approx. 96% of distance travelled are on diesel and 4% on gasoline. Heavy-duty vehicles are all diesel vehicles.

2.5 Assumptions of implementation of LEZ requirements

The assumptions of the LEZ requirements have been implemented in the following way for the different scenarios. In scenario A, at least Euro 5 is a requirement for diesel-powered passenger cars, vans and heavy-duty vehicles in 2022, except for vehicles with a retrofitted DPF. The degree of retrofitting is very difficult to predict, but is expected to be very small since retrofitting is expensive on vehicles with a relatively short remaining lifetime. Therefore, it has been assumed that all vehicles prior to Euro 5, are replaced by Euro 5 and 6 vehicles in the relative distribution of their distance travelled in km in 2022. The same principle applies for the other scenarios.

2.6 Air quality estimation

In the present assessment we have estimated the street contribution of the different vehicle categories at H.C. Andersen Boulevard in 2017 according to their emissions calculated by OSPM. The street contribution is based on street measurements at H.C. Andersen Boulevard minus urban background concentrations measured at the urban background monitor station of H.C. Ørsted Institute. The impact of the scenarios on the air quality of NO₂, PM_{2.5} and PM₁₀ has also been calculated for H.C. Andersen Boulevard for 2022. The street contribution from traffic for 2017 is scaled with the emission reduction for the different vehicle categories between 2017 and 2022 to estimate the reduction in concentrations due to emission reduction.

The contribution of the different vehicle categories to concentrations at H.C. Andersen Boulevard in 2017 is shown in Figure 1 (NO_x and NO₂) and Figure 2 (PM_{2.5} and PM₁₀), and the supporting data is given in table 3.

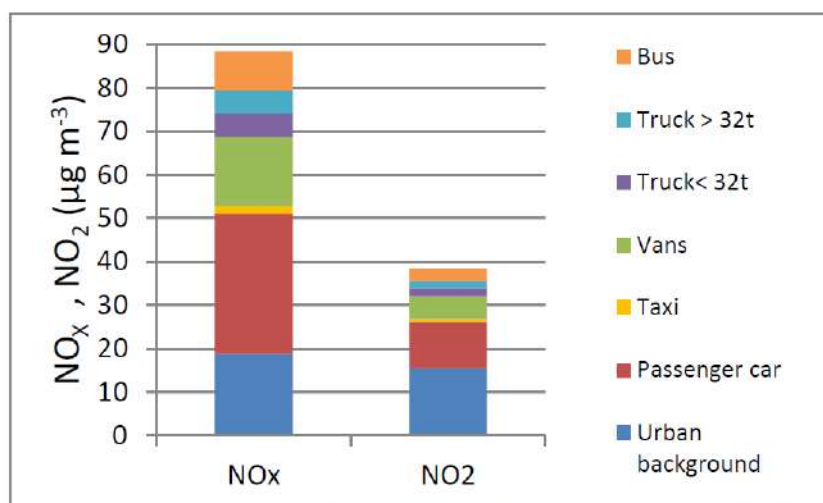


Figure 1. Source apportionment of NO_x and NO₂ at H.C. Andersen Boulevard in 2017.

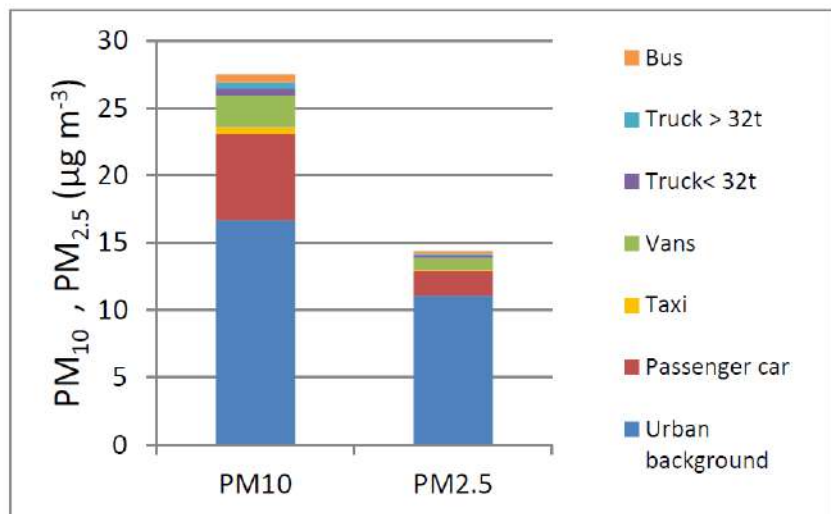


Figure 2. Source apportionment of PM₁₀ and PM_{2.5} at H.C. Andersen Boulevard in 2017.

Table 3. Concentration contributions ($\mu\text{g}/\text{m}^3$) at H.C. Andersen Boulevard based on source apportionment for 2017. Street conc. = total measured street concentration, Street contrib. = Street conc. minus Urban background

$\mu\text{g}/\text{m}^3$	Risø ¹		HCO ²			Truck < 32t	Truck > 32t	Street conc.	Street contrib.	
	Reg. backg.	Urb. backg.	Pass. car	Taxi	Van					
NO _x	8.0	18.8	32.3	1.8	15.9	5.5	5.3	8.8	88	69.6
NO ₂	6.8	15.5	10.7	0.6	5.2	1.8	1.8	2.9	38	23.0
PM ₁₀	14.4	16.7	6.3	0.5	2.4	0.5	0.5	0.6	28	10.8
PM _{2.5}	9.4	11.1	1.8	0.1	0.9	0.1	0.1	0.2	14	3.3
PM ₁₀ -non-exhaust			5.8	0.5	1.8	0.4	0.4	0.5		9.5
PM _{2.5} -non-exhaust			1.4	0.1	0.4	0.1	0.1	0.1		2.0
PM-exhaust			0.4	0.0	0.5	0.1	0.1	0.1		1.3

¹Regional background to Copenhagen. ² HCO is roof of H.C. Ørsted Institute in Copenhagen.

The street contribution is relatively large for NO_x and NO₂. For NO₂ it is 23 µg/m³ out of the street concentration of 38 µg/m³.

The street contribution is relatively small for particles as the background concentration of particles is large. For PM_{2.5} the street contribution is only 3.3 µg/m³ out of the street concentration of 14 µg/m³. The share of the street contribution is larger for PM₁₀ as non-exhaust plays a large role for PM₁₀ compared to PM_{2.5}.

For the street contribution of NO_x and NO₂ passenger cars are the largest source followed by vans and heavy-duty vehicles.

For the street contribution of PM₁₀ and PM_{2.5} passenger cars are also the largest source followed by vans whereas heavy-duty vehicles contribute relatively little since a relatively large share of these are Euro 6 in 2017.

The contribution of particle exhaust to the street contribution in 2017 is approx. 1.3 µg/m³. Therefore, if all particle exhaust was removed, the concentration of PM_{2.5} as well as PM₁₀ would decrease 1.3 µg/m³. This is a relatively small decrease in relation to the street concentrations of PM_{2.5} and PM₁₀ that are 14 µg/m³ and 28 µg/m³, respectively. In this context, it is clear that non-exhaust for particles make up a very large part of the concentration of PM_{2.5} and PM₁₀. Although the particle exhaust do not constitute a large proportion of the street concentration, it will still have a relatively large impact on health effects to reduce particulate emissions, as there is a strong dose-response between particulate matter and health effects, and because the direct emitted particles (EC) per mass have a greater health impact than particles formed in the atmosphere (secondary PM_{2.5}).

3. Results and discussion

3.1 Impacts of LEZ on emissions

The emission reduction for the different scenarios are shown in table 4 as the percentage change in relation to 2017.

Table 4. Percentage change in emissions for 5 scenarios in 2022 in relation to baseline in 2017 (%).

Scenario	NO _x	PM exhaust	PM _{2.5} Non-exhaust	PM ₁₀ Non-exhaust	PM _{2.5}	PM ₁₀ Total
					Total	
Baseline 2017	0	0	0	0	0	0
Baseline 2022	-32	-59	0	0	-31	-22
Scenarie A	-35	-83	0	0	-44	-31
Scenarie B	-46	-85	0	0	-45	-32
Scenarie C	-35	-60	0	0	-32	-23
Scenarie D	-36	-69	0	0	-37	-26
Scenarie E	-40	-69	0	0	-37	-26

There is a substantial emission reduction in the baseline scenario from 2017 to 2022. This reduction is due to continuous renewal of the vehicle fleet where new vehicles meeting Euro 6 replace older vehicles with higher emissions. The LEZ scenarios further reduce emissions as the reduction is the combined effect of the baseline development and the effect of the LEZs. The baseline scenario plays a larger role in reduction of emissions than the additional effect of the LEZs. Scenario B has the largest emission reductions as it regulates all vehicle categories whereas scenario C has the least emission reduction as it only regulates heavy-duty vehicles. The reductions are based on the assumption that Euro 6 meets expectations in emission reduction as defined in the COPERT 5 model.

The emission reduction for the different scenarios are shown in table 5 as the percentage change in relation to 2022, that is, the isolated effect of the LEZ in 2022 in relation to the baseline in 2022.

Table 5. Percentage change in emissions for 5 scenarios in 2022 in relation to baseline in 2022 (%).

Scenario	NO _x	PM		PM _{2.5} Non-exhaust	PM ₁₀ Non-exhaust	PM _{2.5} Total	PM ₁₀ Total
		Exhaust	Non-exhaust				
Baseline 2022	0	0	0	0	0	0	0
Scenario A	-4	-59	0	0	0	-19	-12
Scenario B	-21	-64	0	0	0	-20	-13
Scenario C	-5	-4	0	0	0	-1	-1
Scenario D	-5	-25	0	0	0	-8	-5
Scenario E	-11	-25	0	0	0	-8	-5

Table 6 shows how the total emission reduction in a scenario is distributed among the different vehicle categories. This table summarizes the distribution up to 100%. For example, diesel passenger cars in Scenario (A) contributes 60.6% of the total emission reduction of PM exhaust, vans 35.5%, and heavy-duty vehicles only 4%. To support the understanding of the results the percentage distribution of distance travelled in km of the different vehicle categories is also shown.

Table 6 Percentage distribution on vehicle categories of the total emission reduction in the scenarios for H.C Andersen Boulevard in relation to 2022 (%)

Scenarie A	2022	Distance travelled (km) (%)	NOx (%)	PM exhaust (%)	PM2.5 total (%)	PM10 total (%)
Diesel	Passenger car	39.3	36.0	60.6	60.6	60.6
Benzin	Passenger car	42.3	0.0	0.0	0.0	0.0
Diesel	Van	14.7	6.3	35.3	35.3	35.3
Benzin	Van	0.3	0.0	0.0	0.0	0.0
Diesel	Truck < 32t	1.0	9.6	0.6	0.6	0.6
Diesel	Truck > 32t	0.9	4.3	0.2	0.2	0.2
Diesel	Urban bus	0.7	12.3	0.5	0.5	0.5
Diesel	Coach	0.7	31.3	2.7	2.7	2.7
Total		100.0	100.0	100.0	100.0	100.0
Scenarie B	2022	Distance travelled (km) (%)	NOx (%)	PM exhaust (%)	PM2.5 total (%)	PM10 total (%)
Diesel	Passenger car	39.3	47.7	60.9	60.9	60.9
Benzin	Passenger car	42.3	0.0	0.0	0.0	0.0
Diesel	Van	14.7	28.8	32.9	32.9	32.9
Benzin	Van	0.3	0.0	0.0	0.0	0.0
Diesel	Truck < 32t	1.0	5.1	1.2	1.2	1.2
Diesel	Truck > 32t	0.9	2.4	0.6	0.6	0.6
Diesel	Urban bus	0.7	5.9	1.2	1.2	1.2
Diesel	Coach	0.7	10.0	3.2	3.2	3.2
Total		100.0	100	100	100	100
Scenarie C	2022	Distance travelled (km) (%)	NOx (%)	PM exhaust (%)	PM2.5 total (%)	PM10 total (%)
Diesel	Passenger car	39.3	0.0	0.0	0.0	0.0
Benzin	Passenger car	42.3	0.0	0.0	0.0	0.0
Diesel	Van	14.7	0.0	0.0	0.0	0.0
Benzin	Van	0.3	0.0	0.0	0.0	0.0
Diesel	Truck < 32t	1.0	21.9	19.6	19.6	19.6
Diesel	Truck > 32t	0.9	10.3	9.4	9.4	9.4
Diesel	Urban bus	0.7	25.3	19.2	19.2	19.2
Diesel	Coach	0.7	42.5	51.7	51.7	51.7
Total		100.0	100.0	100.0	100.0	100.0
Scenarie D	2022	Distance travelled (km) (%)	NOx (%)	PM exhaust (%)	PM2.5 total (%)	PM10 total (%)
Diesel	Passenger car	39.3	0.0	0.0	0.0	0.0
Benzin	Passenger car	42.3	0.0	0.0	0.0	0.0
Diesel	Van	14.7	4.6	84.2	84.2	84.2
Benzin	Van	0.3	0.0	0.0	0.0	0.0
Diesel	Truck < 32t	1.0	20.9	3.1	3.1	3.1
Diesel	Truck > 32t	0.9	9.9	1.5	1.5	1.5
Diesel	Urban bus	0.7	24.2	3.0	3.0	3.0
Diesel	Coach	0.7	40.5	8.2	8.2	8.2
Total		100.0	100.0	100.0	100.0	100.0
Scenarie E	2022	Distance travelled (km) (%)	NOx (%)	PM exhaust (%)	PM2.5 total (%)	PM10 total (%)
Diesel	Passenger car	39.3	0.0	0.0	0.0	0.0
Benzin	Passenger car	42.3	0.0	0.0	0.0	0.0
Diesel	Van	14.7	55.1	84.2	84.2	84.2
Benzin	Van	0.3	0.0	0.0	0.0	0.0
Diesel	Truck < 32t	1.0	9.8	3.1	3.1	3.1
Diesel	Truck > 32t	0.9	4.6	1.5	1.5	1.5
Diesel	Urban bus	0.7	11.4	3.0	3.0	3.0
Diesel	Coach	0.7	19.0	8.2	8.2	8.2
Total		100.0	100.0	100.0	100.0	100.0

3.2 Impacts of LEZ on air quality

In table 7, an estimate is shown of the street contribution at H.C. Andersen Boulevard in 2017 and 2022 in the baseline, as well as for the five LEZ scenarios in 2022. The street contribution in 2022 for the baseline and the five scenarios in 2022 are for each of these calculated by scaling the street contribution for 2017 with the reduction in emissions from the baseline year 2017 to 2022.

Table 7. Estimate of street contribution for H.C. Andersen Boulevard in the baseline of 2017 and 2022 and for the LEZ scenarios in 2022 ($\mu\text{g}/\text{m}^3$)

Scenario	NO _x	NO ₂	PM ₁₀	PM _{2.5}	PM ₁₀	PM _{2.5}	PM
	Total	Total	Non-exhaust	Non-exhaust	Exhaust		
Baseline 2017	69.6	23.0	10.8	3.3	9.5	2.0	1.3
Baseline 2022	47.4	15.6	10.0	2.5	9.5	2.0	0.5
Scenario A	45.5	15.1	9.7	2.2	9.5	2.0	0.2
Scenario B	37.3	12.3	9.7	2.2	9.5	2.0	0.2
Scenario C	45.0	14.9	10.0	2.5	9.5	2.0	0.5
Scenario D	44.9	14.8	9.9	2.4	9.5	2.0	0.4
Scenario E	42.1	13.9	9.9	2.4	9.5	2.0	0.4

In table 8, the reduction in the street contribution in relation to the baseline concentration in 2022 is shown. Thus, the figures indicate how many micrograms per cubic meter the different LEZs will decrease concentrations in relation to the baseline in 2022. For example, the most stringent scenario (B) will reduce NO₂ by 3.3 $\mu\text{g}/\text{m}^3$ and PM_{2.5} and PM₁₀ by 0.35 $\mu\text{g}/\text{m}^3$.

Table 8. Reduction in street contribution in relation to baseline in 2022 ($\mu\text{g}/\text{m}^3$).

Scenario	NO _x	NO ₂	PM ₁₀	PM _{2.5}	PM ₁₀	PM _{2.5}	PM
	Total	Total	Non-exhaust	Non-exhaust	Exhaust		
Scenario A	1.8	0.6	0.32	0.32	0.0	0.0	0.32
Scenario B	10.1	3.3	0.35	0.35	0.0	0.0	0.35
Scenario C	2.4	0.8	0.021	0.021	0.0	0.0	0.021
Scenario D	2.5	0.8	0.14	0.14	0.0	0.0	0.14
Scenario E	5.3	1.7	0.14	0.14	0.0	0.0	0.14

The street concentration will decrease due to the development in the baseline as well as the additional effect of the LEZ. However, urban background concentrations are also expected to decrease from 2017 to 2022 due to emission regulation, and will further reduce street concentrations in 2022. A study has modelled the expected reduction in concentrations from 2014 to 2025 for urban background concentrations over the Capital Region of Copenhagen (Jensen et al., 2018b). From 2014 to 2025, urban background concentrations are expected to decrease 27% for NO₂, 13% for PM_{2.5} and 17% for PM₁₀ due to expected emission reductions in Europe. Ozone concentrations are expected to increase slightly by approx. 4%. Since the above study covers a 10 year period, roughly half of these changes can be expected during 2017 to 2022. Concentrations of ozone in Denmark are increasing as a result of the reduction of NO_x emissions leading to less NO to consume ozone in formation of NO₂. This development will lead to lower urban background concentrations of NO₂ and PM in 2022 and hence lower street concentrations beyond the reductions of the LEZs.

The LEZ will further reduce urban background concentration in Copenhagen due to vehicle emission reduction within the LEZ as well as gains outside the LEZ. However, previous estimates based on evaluation of the existing LEZ (Jensen et al., 2011) indicates that urban background concentration only to a limited extent will be reduced because of LEZ. The reason is that the

urban background concentration within the LEZ also is influenced by emissions from other sources than traffic within the LEZ, as well as emissions from the rest of Denmark and abroad.

In 2015 and 2016, 300 urban buses in Greater Copenhagen were retrofitted with SCRT (combined SCR and DPF) that also affected H.C. Andersen Boulevard. SCRT reduces the emission of NO_x and the particle exhaust. The effect for H.C. Andersen Boulevard has been calculated to 1.3 µg/m³ for the concentration of NO₂ and 0.02 µg/m³ for the concentrations of particles in 2015 (Jensen et al., 2016). This effect is not taken into account for the assessment of the LEZ in 2022.

The method used to estimate the impact of LEZ to air quality is simplified compared to calculations with air quality models because it assumes a linear relationship between emission and concentration. For NO₂, this is an oversimplification, as photochemical reactions of NO and NO₂ from traffic with ozone are non-linear. Furthermore, the development in the direct emission of NO₂ (share of NO_x) has not been taken into account as only the development in NO_x emissions from 2017 and to 2022 have been estimated, and the share of direct NO₂ emission will vary over time as it varies between the different categories of vehicles, fuel types and Euro classes. Furthermore, the method does not take into account changes in the background concentration in the future. That is why the method may be characterised as an approximation method for assessment of the reduction in concentrations.

New national legislation on LEZs is required to make changes to the existing LEZ. In October 2018, the Danish government proposed updated LEZ to be implemented in stages leading to requirements for Euro 6 for vans in 2025 and Euro VI for trucks and buses in 2022. These requirements are very close to scenario E, and hence impacts are comparable to scenario E. The proposal has been during a public hearing that ended in January 2019. As of February 2019, new legislation has not yet been passed in Parliament.

4. Conclusion

In Denmark, the existing LEZ was fully implemented in the four largest cities in 2010 requiring trucks and buses to comply with at least the Euro IV emission standard or be retrofitted with DPF. Due to the renewal of the vehicle fleet almost all heavy-duty vehicles comply to the requirements in 2018 and hence the present LEZ has no or marginal remaining impact on emissions. The Ministry of Environment and Food of Denmark conducted a study carried out by Aarhus University during first half of 2018 on five different scenarios for updating the LEZs in Denmark. The scenarios are different concerning the vehicle types they include and the Euro vehicle emission classes required to enter the LEZ. All scenarios focus only on diesel vehicles and exempt petrol vehicles for regulation and require either Euro 5 or Euro 6 in 2022.

A simple yet scientifically sound approach with some limitations was applied to estimate the impact of the LEZs on air quality in 2022. The approach uses the street contribution from traffic (street increment) for 2017 for a busy street in Copenhagen. The street contribution is the difference between the street concentration and urban background concentration derived from measurements from the Danish Air Quality Monitoring Programme. To allocate the street contribution to the different vehicle categories the emission module of the Operational Street Pollution Model (OSPM) was used. The street contribution from 2017 is then scaled with the emission reduction between 2017 and 2022 to estimate the reduction in concentrations in 2022 due to emission reduction. The emission reduction of the five scenarios is based on emission factors (g/km) in 2017 and 2022 for the different vehicle categories derived from the Danish national emission inventory.

There is a substantial emission reduction of NO_x, PM_{2.5} and PM₁₀ in the baseline scenario from 2017 to 2022 due to continuous renewal of the vehicle fleet. The LEZ scenarios further reduce emissions as the reduction is the combined effect of the baseline development and the effect of the LEZs. The baseline scenario plays a larger role in reduction of emissions than the additional effect of the LEZs.

The most effective scenario with the largest emission reductions is scenario (B) that requires Euro 6 for all passenger cars, vans and heavy-duty vehicles whereas the least effective scenario is scenario (C) that only requires Euro 6 for heavy-duty vehicles.

The most effective scenario (B) will reduce NO₂ by approx. 3.3 µg/m³ and PM_{2.5} and PM₁₀ by 0.35 µg/m³ whereas the least effective scenarios will reduce NO₂ by 0.6 and PM_{2.5} and PM₁₀ by 0.14 µg/m³.

Acknowledgements

The Ministry of Environment and Food of Denmark funded the study.

References

- Berkowicz, R. 2000b. [OSPM - A parameterised street pollution model](#). Environmental Monitoring and Assessment, Volume 65, Issue 1/2, pp. 323-331.
- Ellermann T., Nygaard J., Nøjgaard J.K., Nordstrøm C., Brandt J., Christensen J., Ketzel M., Massling, A., Bossi R. & Jensen S.S. 2018. The Danish Air Quality Monitoring Programme. Annual Summary for 2017. Aarhus University, DCE – Danish Centre for Environment and Energy, *Scientific Report from DCE* No. 281. <http://dce2.au.dk/pub/SR281.pdf>
- Jensen, S.S., Ketzel, M., Nøjgaard, J. K. & Becker, T. (2011) What are the Impacts on Air Quality of Low Emission Zones in Denmark? http://www.trafikdage.dk/td/papers/papers11/31_SteenSolvangJensen.pdf; Trafikdage på Aalborg Universitet, 22.-23. august 2011. Annual Transport Conference at Aalborg University. Peer-reviewed. ISSN 1603-9696.
- Jensen, S.S., Ketzel, M., Ellermann, T., Winther, M., (2016): Air Quality Impact Assessment of Retrofitting of SCRT on 300 Urban Busses in Greater Copenhagen. Aarhus University, DCE – Danish Centre for Environment and Energy, 32 p. – Scientific Report No. 192. <http://dce2.au.dk/pub/SR192.pdf>. In Danish with English summary.
- Jensen S.S., Winther M., Ketzel M., Ellermann T. (2018a): Impact assessment of 5 scenarios for more stringent Low Emission Zones. 44 p. In Danish. http://dce.au.dk/fileadmin/dce.au.dk/Udgivelser/Notater_2018/Scenarier_for_miljoezoner_til_MFVM_v9.pdf
- Jensen, S.S., Brandt, J., Christensen, J.H., Geels, C., Ketzel, M., Plejdrup, M. S., Nielsen, O.-K. (2018b): Mapping of the health and environmental Effects of air Pollution in the Capital Region of Denmark, Aarhus University, DCE – Danish Centre for Environment and Energy, 127 p. – Science rapport No. 254. In Danish with English summary. <http://dce2.au.dk/pub/SR254.pdf>
- Kakosimos, K.E., Hertel O., Ketzel M., Berkowicz R. (2011): "Operational Street Pollution Model (OSPM) - a review of performed validation studies, and future prospects", Environmental Chemistry, 7, 485-503.(doi-Link).
- Ketzel, M., Jensen, S.S., Brandt, J., Ellermann, T., Olesen, H.R., Berkowicz, R., Hertel, O. (2012): Evaluation of the Street Pollution Model OSPM for Measurements at 12 Streets Stations Using a Newly Developed and Freely Available Evaluation Tool. J Civil Environ Eng, S1:004.(doi-Link)
- Winther, M. 2018: Danish emission inventories for road transport and other mobile sources. Inventories until the year 2016. Aarhus University, DCE – Danish Centre for Environment and Energy, 127pp. Scientific Report from DCE – Danish Centre for Environment and Energy No. 277. <http://dce2.au.dk/pub/SR277.pdf>.

2.6 Alternative fuels, new powertrains

This section includes papers presented in the context of the “Alternative fuels, new powertrains” sessions of the TAP conference. Table 7 provides an overview of these papers, as they are listed in the following sub-sections.

Table 7. Titles and authors of “Alternative fuels, new powertrains” papers

	Paper Title	Authors
2.6.1	Real Driving Emissions of Passenger Cars – Examples of Testing and Evaluating	D. Engelmann, J. Czerwinski, Y. Zimmerli, P. Comte and P. Bonsack
2.6.2	Characterization of sub-23 nm particles and their measure for PFI/DI SI engines fuelled with gasoline, ethanol and blend	F. Catapano, S. Di Iorio and B.M. Vaglieco
2.6.3	Comprehensive emission characterisation of exhaust from alternative fuelled cars	P. Aakko-Saksa, P. Koponen, J. Laurikko, N.-O. Nylund, P. Karjalainen, T. Rönkkö and H. Timonen
2.6.4	Air Quality Impacts from Ethanol-blended Gasoline Deployment in China’s Beijing-Tianjin-Hebei Region	X. Liang, Y. Wu and J. Hao
2.6.5	Comparison of on-road gaseous emissions of a best seller passenger car with different powertrains: diesel vs gasoline vs compressed natural gas	V. Valverde, P. and P. Bonnel
2.6.6	Comparative investigation on particulate and gaseous emissions from a pre-Euro 6 diesel LCVs fleet fuelled with different second-generation biodiesel blends	T. Rossi, S. Casadei and M. Siviero
2.6.7	A Novel Technology of High-Pressure Thermochemical Recuperation for Efficiency Increase and Emissions Mitigation	L. Tartakovsky, A. Eyal, A. Thawko and H. Yadav
2.6.8	Analysis of Pollutant Emissions of three Plug-in Hybrid Electric Vehicles	S.I. Ehrenberger, F. Philipps and M. Konrad
2.6.9	Simulation-based assessment of the CO2 emissions reduction potential from the implementation of mild-hybrid architectures on passenger cars to support the development of CO2MPAS	S. Doulgeris, A. Tansini, A. Dimaratos, G. Fontaras and Z. Samaras
2.6.10	Main Diesel, Petrol or electric vehicles: what choice for improving urban air quality? A simulation plate-form and case study	M. André, K. Sartelet, S. Moukthar, J.M. André and M. Redaelli
2.6.11	Electric Vehicles in the Republic of Croatia – Market Development, Usage and Outlook	P. Ilinčić, G. Šagi, M. Pečet and Z. Lulić

2.6.1 Real Driving Emissions of Passenger Cars – Examples of Testing and Evaluating

D. Engelmann¹, J. Czerwinski^{1}, Y. Zimmerli¹, P. Comte¹ and P. Bonsack²*

¹ University of Applied Sciences, 2500 Biel-Bienne, Laboratory of Applied Science, jan.czerwinski@bfh.ch

² Federal Office for the Environment (FOEN), Air Pollution Control and Chemicals Division, CH 3003 Bern, Switzerland

Abstract

Since September 2017, testing of real driving emissions (RDE) with portable emission measuring system (PEMS) in an appropriate road circuit became an obligatory element of new type approval of passenger cars. Toxic exhaust emissions and their control still remain one of the major problems faced by road transport.

In several projects the Laboratory for Exhaust Emissions Control (AFHB) of the Berne University of Applied Sciences (BFH) performed comparisons on passenger cars with different PEMS's on chassis dynamometer and on road, considering the quality and the correlations of results. Particle number measuring systems (PN PEMS) were also included in the tests.

The present paper informs about influences of E85 on RDE on two flex-fuel-vehicles, shows influence of payload for a heavy car with trailer and presents RDE of a HEV in different operating modes. This combined look on different vehicle technologies allows the comparisons of these technologies, but first of all it gives information about the potentials and limits of the used measuring procedures and tools.

The most important conclusions are:

E0 & E85

- The use of E85 fuel is advantageous for emission reduction: with E85 there is reduction of NO_x and PN for both investigated vehicles in all driving conditions.
- Both vehicles attain similar levels of emissions at the end of RDE cycle, while the dispersion of results for each vehicle/fuel variant is much larger than on the chassis dynamometer (in WLTC).

Payload/trailer

- Higher payload increases the cumulated emissions of CO, HC, NO_x and PN.

HEV

- The investigated hybrid vehicle confirmed a very efficient and intelligent control of energy management, of engine parametrization, as well as very low emission values.

Introduction

Testing of Real Driving Emissions (RDE) became since 2017, an element of legal homologation procedure for passenger cars WLTP (Worldwide Harmonized Light-Duty Vehicles Test Procedure), [1, 2, 3]. This new procedure will enforce for new cars (introduced to the market since September 2017), that there will be no intentional discrepancy between the emissions and fuel consumption values obtained in the homologation tests and in real application, [4, 5].

Unlike previous vehicle emission tests, parameters such as engine load and vehicle speed are no longer defined by a fixed pattern, but are largely determined by the traffic situation, driver behavior and the course of the route during the RDE test. [6, 7, 8].

There are new requirements and challenges for all market participants: the industry has to adapt the R&D processes of engines, [9, 10, 11]; the measuring technics, including PN PEMS are continuously improved and developed, [12, 13] and the official testing laboratories and organizations perform intense research activities in order to increase the knowledge, the experience and to adapt the testing capacities to the new requirements, [4, 5, 7, 8, 14].

In this interesting dynamic situation of progress AFHB performs several test & research projects or working packages. Some of the recent results are presented in this paper.

Several countries have objectives to substitute a part of the energy of traffic by ethanol as the renewable energy source and some manufactures introduced the FFV (Flex-Fuel Vehicles) variants and published extensive information about their R&D and performances: GM / Saab [15, 16]; Toyota [17]; VW [18]. In the present work, RDE with different fuels and vehicle technologies were investigated offering some new interesting insights in the results, as well as in the testing methodology.

Test installation

Chassis dynamometer test cell

Parts of the tests were performed on the 4WD-chassis dynamometer of AFHB (Laboratory for Exhaust Emission Control of the Bern University of Applied Sciences, Biel, CH).

The stationary system for regulated exhaust gas emissions is considered as reference. This equipment fulfills the requirements of the Swiss and European exhaust gas legislation. The regulated gaseous components are measured with exhaust gas measuring system Horiba MEXA-7200; CO, CO₂ ... infrared analysers (IR); HC_{FID} ... flame ionization detector for total hydrocarbons; CH₄FID ... flame ionization detector with catalyst for only CH₄; NO/NO_x ... chemiluminescence analyzer (CLA).

The dilution ratio DF in the CVS-dilution tunnel is variable and can be controlled by means of the CO₂-analysis.

The measurements of summary particle counts in the size range 23-1000nm were performed with the CPC TSI 3790 (according to PMP).

For the exhaust gas sampling and conditioning a ViPR system (ViPR...volatile particle remover) from Matter Aerosol was used. This system contains:

- Primary dilution - MD19 tunable rotating disk diluter (Matter Eng. MD19-2E)
- Secondary dilution – dilution of the primary diluted and thermally conditioned sample gas on the outlet of evaporative tube.
- Thermoconditioner (TC) - sample heating at 300°C.

GAS PEMS and PN PEMS

An information about the used Horiba Gas PEMS and about the gas measuring installation of the chassis dynamometer is given in Table 1.

As PN PEMS for Real Driving Emissions two systems were used and compared:

- NanoMet3 from TESTO (NM3). This analyzer works on diffusion charging (DC) principle, has an integrated sample conditioning system, as described above for chassis dynamometer and it indicates the solid particle number concentration and geometric mean diameter in the size range 10-700 nm. NM3 was used for the tests with Ethanol blend fuels.
- Horiba OBS-ONE PN measurement system (OBS-PN). This analyzer works on the condensation particles counter (CPC) principle, has an integrated sample conditioning system (double dilution and catalytic stripper ViPR, 350°C) and it indicates the summary PN concentrations in the size range 23 to approximately 1000 nm. This system was used in the tests with increased payload and with hybrid vehicle.

Both systems present several advantages like compactness, robustness, fast on-line response and both are recognized for legal testing purposes.

Table 1. Overview of used measuring systems.

	HORIBA MEXA 7200	HORIBA OBS ONE
	4x4 chassis dyno CVS	PEMS ^① wet
CO	NDIR	heated NDIR
CO ₂	NDIR	heated NDIR
NO _x	CLD	CLD
NO	CLD	CLD
NO ₂	calculated	calculated
O ₂	-	-
HC	FID	-
PN	not measured	-
OBD logger	-	yes
GPS logger	-	yes
ambient (p, T, H)	yes	yes
EFM	-	pitot tube

OBS - one H₂O monitored to compensate the H₂O interference on CO and CO₂ sample cell heated to 60°C

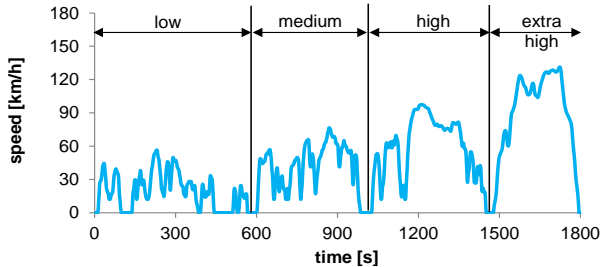


Figure 1: WLTC driving cycle

Test procedures

Driving cycles on chassis dynamometer

The vehicles were tested on a chassis dynamometer in the dynamic driving cycle WLTC, Fig. 1.

For the research with different fuels important objective was to always keep the same procedure of changing the fuel quality. The fuel change was performed at the day preceding the tests. The fuel tank was emptied and filled with the new fuel. Than the vehicle was pushed on the chassis dynamometer, cold-started and driven in one WLTC as conditioning. Than the vehicle stayed on the chassis dyno until the next test-day.

The braking resistances were set according to legal prescriptions (table values ECER83); they were not increased i.e. responded to the horizontal road.

On road testing

In order to reach the validity according to the actual requirements several road tests were performed. Finally, the used valid road circuit was always the same with approximately 1.5h duration and parts of urban, rural and highway roads. Fig. 2 represents an example of a road trip from the PN PEMS test program.

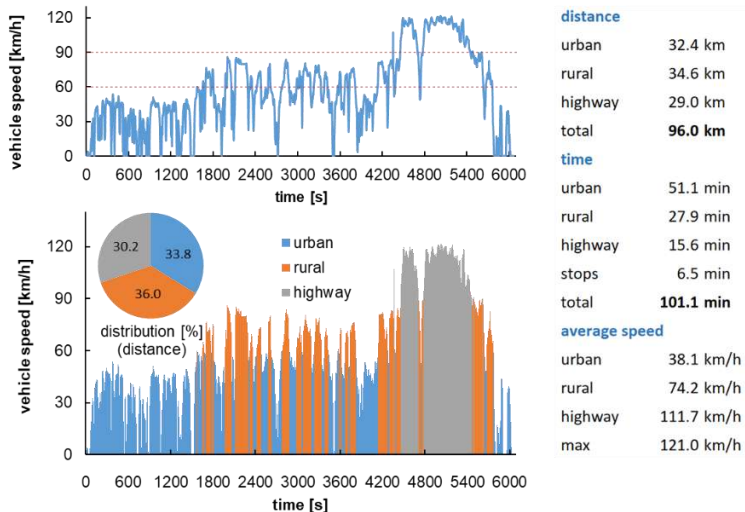


Figure 2: AFHB, road trip for RDE

Test vehicles and fuels

The tests with Ethanol blend fuels were performed with two Euro 5 flex fuel vehicles: Volvo V60 (GDI) and Audi A4 TFSI (GDI). Both vehicles were equipped with PEMS and tested on-road with E0 & E85. Fig. 3 shows the vehicles in laboratory and Table 2 gives the most important data.

Table 2: Data of tested vehicles

Vehicles	Volvo V60 T4F FFV gasoline (V1)	Audi A4 2.0 TFSI FFV gasoline (V2)	DODGE RAM 2500 HDV Diesel (V3)	Toyota Prius III gasoline (V4)
Number and arrangement of cylinder	4 in line	4 in line	6 / in line	Engine gasoline 1.8L DACT 16-valve with multipoint injection of 98 hp, naturally aspirated, variocam-Atkinson
Displacement cm ³	1596	1984	6.690	Electric engine of 80 hp
Power kW	132 @ 5700 rpm	132@4000 rpm	260@2800 rpm	Total power: 136 hp
Torque Nm	240 @ 1600 rpm	320@1500 rpm	1085@1600 rpm	Max. torque: 142 Nm
Injection type	Direct Injection (DI)	Direct Injection (DI)	Direct Injection (DI)	-
Curb weight kg	1554	1570	3690	Curb weight: 1500 kg
Gross vehicle weight kg	2110	2065	4200	-
Drive wheel	Front-wheel drive	Front-wheel drive	Four-wheel drive	-
Gearbox	a6	m6	a6	Gearbox: continuously variable transmission
First registration	2012	2010	2015	-
Exhaust	EURO 5a	Euro 5	Cal. LEV III/EGR, DPF, SCR	Anti-pollution standard : Euro 5b, 3WC, EGR

The tests with increased payload (with a trailer) were performed with a Dodge Ram 2500 Diesel and for the tests of a hybrid vehicle a Toyota Prius III (gasoline) was used. Fig. 4 represents these vehicles and Table 2 summarizes their most important data.

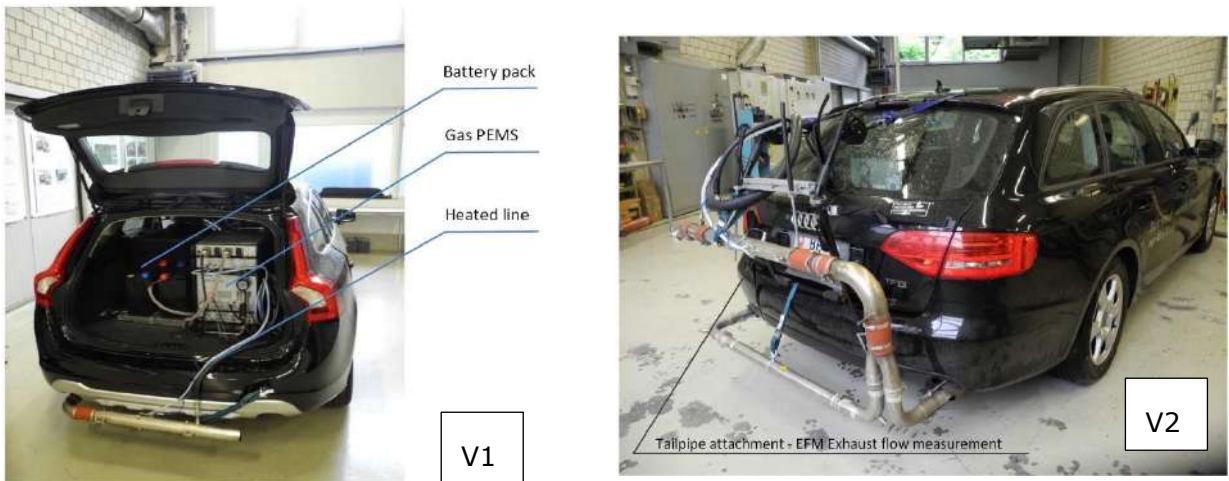


Figure 3: Tested vehicles (FFV) equipped with PEMS

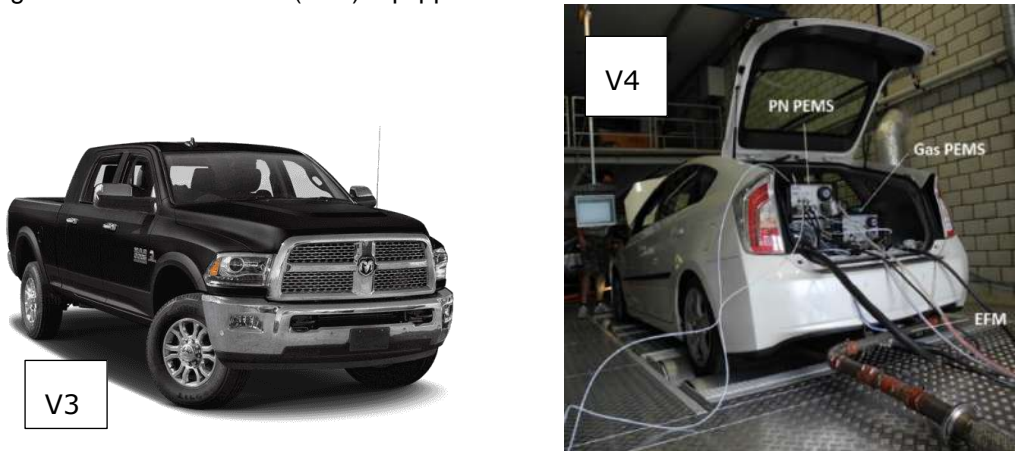


Figure 4: Tested vehicles V3 and V4 equipped with PEMS

Fuels

The gasoline used was from the Swiss market, RON 95, according to SN EN228. For the tests a charge of fuel was purchased to keep always the unchanged chemistry.

As a further variants of fuels E10 and E85 were used. These are respectively blends with: 90% v gasoline and 10% v Ethanol, or with 15% v gasoline and 85% v Ethanol. The blend fuels were prepared on the basis of E85 purchased on the Swiss market.

Table 3 summarizes the most important parameters of the fuels.

Table 3: Parameters of used fuels

		Gasoline	Ethanol C ₂ H ₅ OH	E10	E85
density 15°C	[g/cm ³]	0.737	0.789	0.742	0.781
stoichiometric air/fuel ratio	[-]	14.6	9.0	14.0	9.8
lower calorific value	[MJ/kg]	43.0	26.8	41.3	28.9
boiling point	[°C]	30-200	78.5		
research octane nbr.	[-]	95	110		
latent heat of evaporation	[kJ/kg]	420	900		
Oxygen content	[%m]	<5	34.8		

For the Diesel vehicle (V3) a Swiss market Diesel fuel, according to SN EN590 was used.

Results and discussions

Ethanol blend fuels

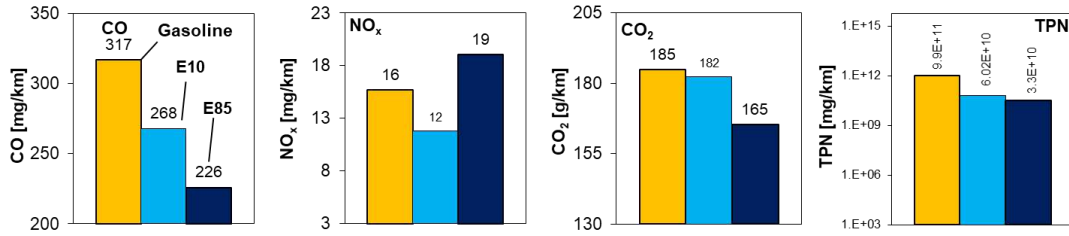


Figure 5: Emissions in WLTC warm, with gasoline E10 & E85 V1: Volvo V60 T4F, 3WC

Fig. 5 represents the comparisons of average emission values from the operation with gasoline, E10 and E85 in WLTC warm. These results are averages of 2 cycles. The warm-up procedure was always by means of a preliminary cold started WLTC.

The particle counts emissions are generally significantly reduced with Exx (more than 1 order of magnitude).

CO-emissions are clearly reduced with increasing Exx-content. For NO_x no regular tendencies with E10 & E85 are visible. Nevertheless, this is strongly dependent on the electronic control of this FFV and the indicated differences of few [ppm] can also be an effect of emitting dispersion.

With each vehicle three RDE tests were performed with E0 and E85. Figures 6, 7, 8 and 9 show the cumulated results of NO_x, PN, CO₂ and CO. The tendencies are similar as in WLTC:

- E85 instead of E0 reduces significantly NO_x-emission; there is a certain dispersion of results, but this tendency is clearer than in WLTC and it is similar for both vehicles,
- PN is strongly reduced with E85 for both vehicles, which confirms the previous experiences on chassis dynamometer with vehicle V1,
- E85: CO₂ is only slightly reduced with V1 and more clearly with V2,
- E85: CO is not reduced with V1 but clearly reduced with V2 – it can be remarked that the acceleration events, very often in the last high-speed part of the cycle, can significantly contribute to the increase of cumulated emission.

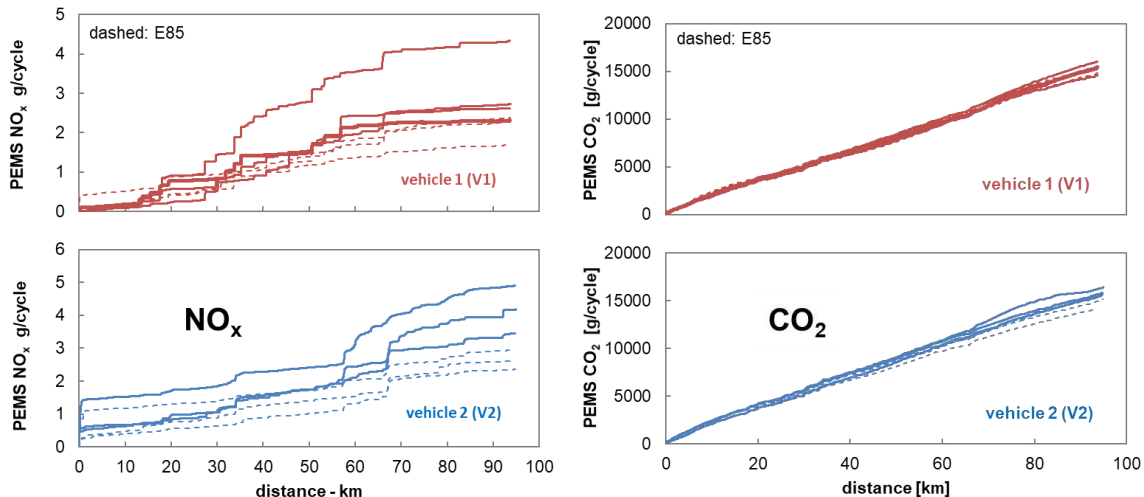


Figure 6: NO_x - Emissions during RDE with E0 and E85; Volvo V60 Flexfuel (V1); Audi A4 Flexfuel (V2)

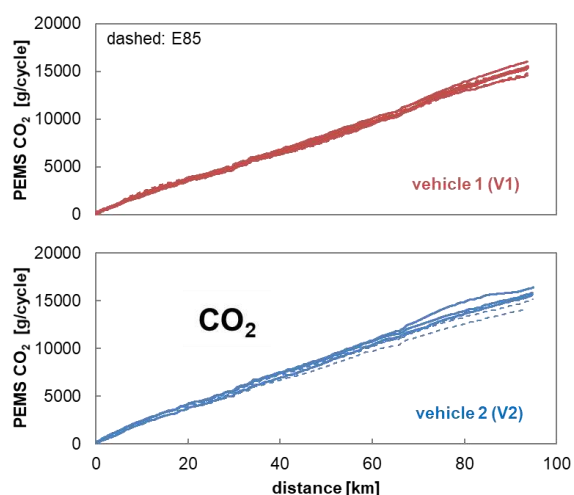


Figure 8: CO₂ – Emissions during RDE with E0 and E85; Volvo (V1); Audi (V2)

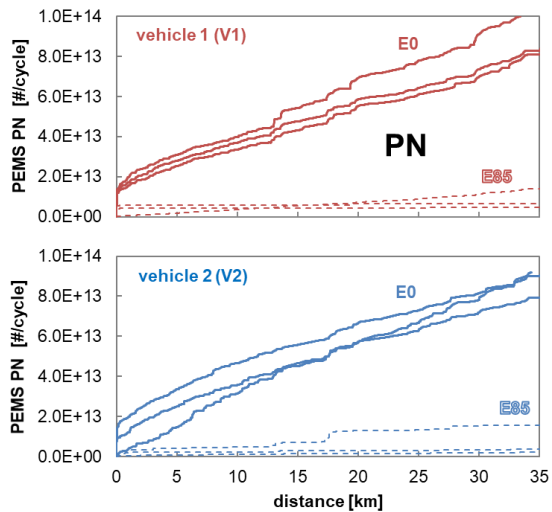


Figure 7: PN – Emissions during RDE urban part with E0 and E85; Volvo (V1); Audi (V2)

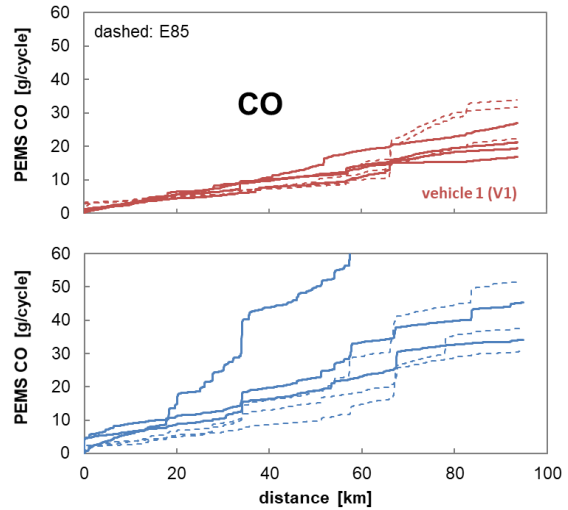


Figure 9: CO – Emissions during RDE with E0 and E85; Volvo (V1); Audi (V2)

Emissions with different payload

This part of tests was performed on the vehicle V3; Dodge Ram 2500 Diesel. In Switzerland, this vehicle is registered as a HDV since its total weight is higher than 3500 kg. The on-road testing of this vehicle for RDE is carried out, according to the procedures and on the test circuit for LDV's. This vehicle is strongly motorized with the weight/power ratio 15-30 kg/kW, comparing to usual HDV's (30t) with 40-90 kg/kW.

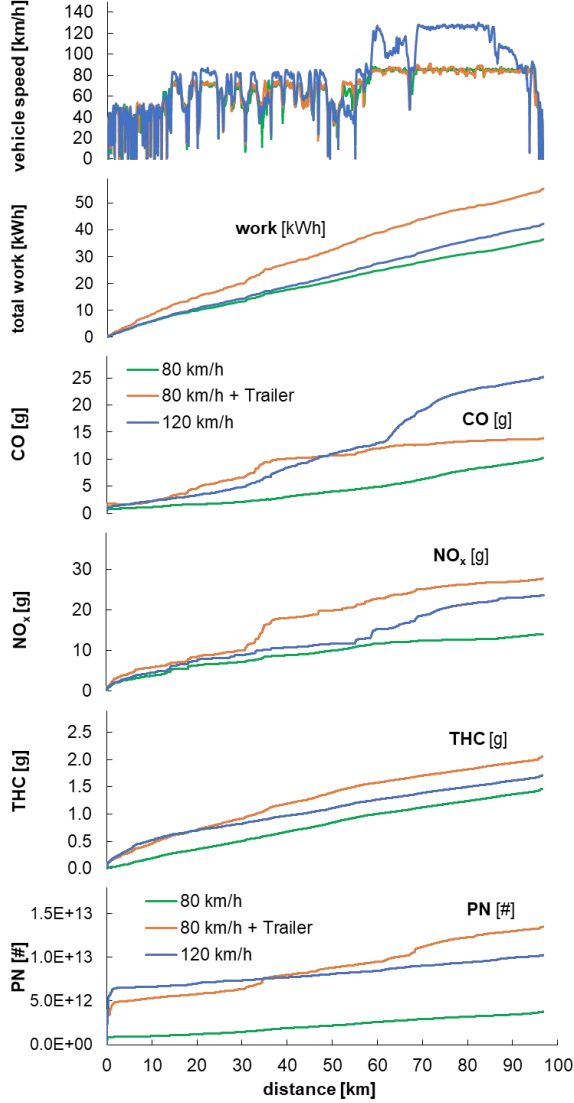


Figure 10: Influences of maximal speed and payload on real driving emissions, Dodge Ram, (V3)

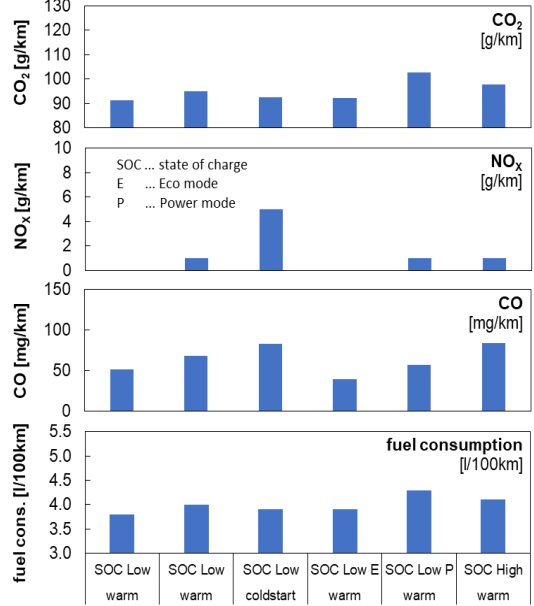


Figure 11: Integral emissions measured with PEMS in the RDE – Tests, Toyota Prius III, (V4)

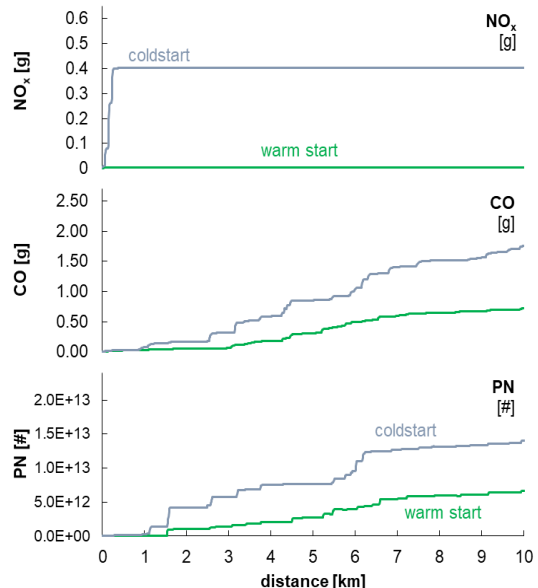


Figure 12: RDE in urban part cold / warm cumulated emissions in the RDE - Tests, Toyota Prius III, (V4)

One of the validity criteria of the windows, the MAW evaluating method for HDV's, is that the windows with average power bigger than 10% (since 2018) of a maximum engine power are recognized as valid and are considered for the calculation (according to the EU-regulation Nbr. 582/2011, Annex II). In the case of this highly motorized vehicle, only a little part of windows arrives to average power > 10%, so the NO_x emissions would be very much underestimated or even zero in some cases. It results, that this vehicle does not adapt to the HDV-regulation either.

In Fig. 10 are given the comparisons of total work of engine operating collectives and of cumulated emissions for three cases:

1. driving on the RDE circuit with maximum speed of 80 km/h
2. driving on the RDE circuit with maximum speed of 80 km/h + a trailer with 3.5t
3. driving on the RDE circuit with maximum speed of 120 km/h

The cold start (summer) was included in the tests and results. It can be summarized for the changes of the operating conditions: higher maximum speed or higher payload, that both of them increase the cumulated emissions of CO, HC, NO_x and PN.

RDE of A HEV

This section presents some results obtained with HEV Toyota Prius III (Euro 5), V4 on chassis dynamometer and on-road. This vehicle offers to the driver the choice between different modes of driving behaviour: "Normal", "Power" or "ECO" and also a limited possibility of electric driving "EV" or battery charging "B". This working package compares the emissions with different state of charge (SOC) of the batteries pack and with different driving modes. It also gives some insights in the control of strategies (EGR, throttle) of this vehicle.

Fig. 11 shows the results of some performed RDE-tests. Regarding the cycles with "SOC_{low}, warm start" a good repeatability of results can be stated.

Influence of SOC

The state of charge (SOC) of the batteries pack of this vehicle is indicated by the OBD. Depending on temperature of batteries and different other parameters the SOC is maintained by the system between approximately 40% and 80%.

The lowest SOC can be caused by driving the vehicle in electric (E) mode up to the point when the engine is started. The highest SOC can be obtained by motoring the vehicle on the chassis dynamometer (CD). After performing the driving cycles, the final SOC results in the range of about 60%. With higher SOC the probability of electric driving and the frequency of engine switch off/on increase. The effect of this is visible in WLTC (not represented here), where the test with "SOC_{high}" indicates lower CO₂ and lower fuel consumption. The emission of CO is tendentially higher than the average of cycles with "SOC_{low}". Nevertheless, the differences are small, and they are in the dispersion range of the repeated cycles with "SOC_{low}". In RDE-tests (Fig. 14), there is no tendency of lower fuel consumption with "SOC_{high}", this, because the higher SOC influences mostly the urban driving, which represents only a part of the RDE cycle. CO-values with "SOC_{high}" are similar to the values with "SOC_{low} cold start" and they are at the upper limit of the dispersion range.

The emissions of NO_x and CO are for this vehicle very low, so the indicated differences can be regarded as insignificant.

Further tendencies

It can be remarked, Fig. 12, that the cold start is the mayor reason for the increased NO_x-emissions (still the absolute values of NO_x are very low). The cumulated values of all measured toxic compounds (NO_x, CO and PN) were increased with the cold start. The CO-emissions with cold start are on the upper limit of the dispersion range of all cycles. The use of driving mode "Power" (+P) shows the tendency of higher fuel consumption, but the emissions are in the usual dispersion range of all cycles. Driving in mode "Economy" (+E) does not cause any particular differences. Finally, it can be said that this tested vehicle has very low emissions and fuel consumption and that these values are only slightly influenced by different modes, such as SOC, Power, Economy and cold start.

EGR and NO_x- control

The strategy of Toyota uses the EGR as an important measure to reduce NO_x-emissions in addition to the 3WC-technology and use of variocam-Atkinson-cycle. The EGR-valve is electrically driven, which enables a quick and precise control.

Fig. 13 shows the functionality of EGR-valve opening in the initial phase of the RDE-test with cold start.

Several parameters, like: vehicle speed, engine speed, coolant temperature, catalyst temperature, battery SOC, load factor, EGR control and Lambda are registered from the engine ECU.

During the warm-up (first 1.2 km) EGR stays closed. After that it is controlled according to the events with running engine and with higher engine load, with lean operation. The lean Lambda-excursions, when the 3WC cannot reduce NO_x, result from engine switching off/on. The engine speed zero-value indicates, that the engine is switched-off quite often.

The engine switching strategy, sometimes lean engine operation and EGR offer very low fuel consumption and low, near-to-zero NO_x-emissions.

The openings of EGR-valve coincide in most cases with the peaks of CO & PN.

The analysis of vehicle stops, and engine stops revealed that the vehicle stops, in the urban part of RDE-test, are in the range between 10% and 15% of the total cycle time and the engine works between 39% and 59% of the total cycle time. In the operating mode "Power", there is the highest portion of the "engine on time".

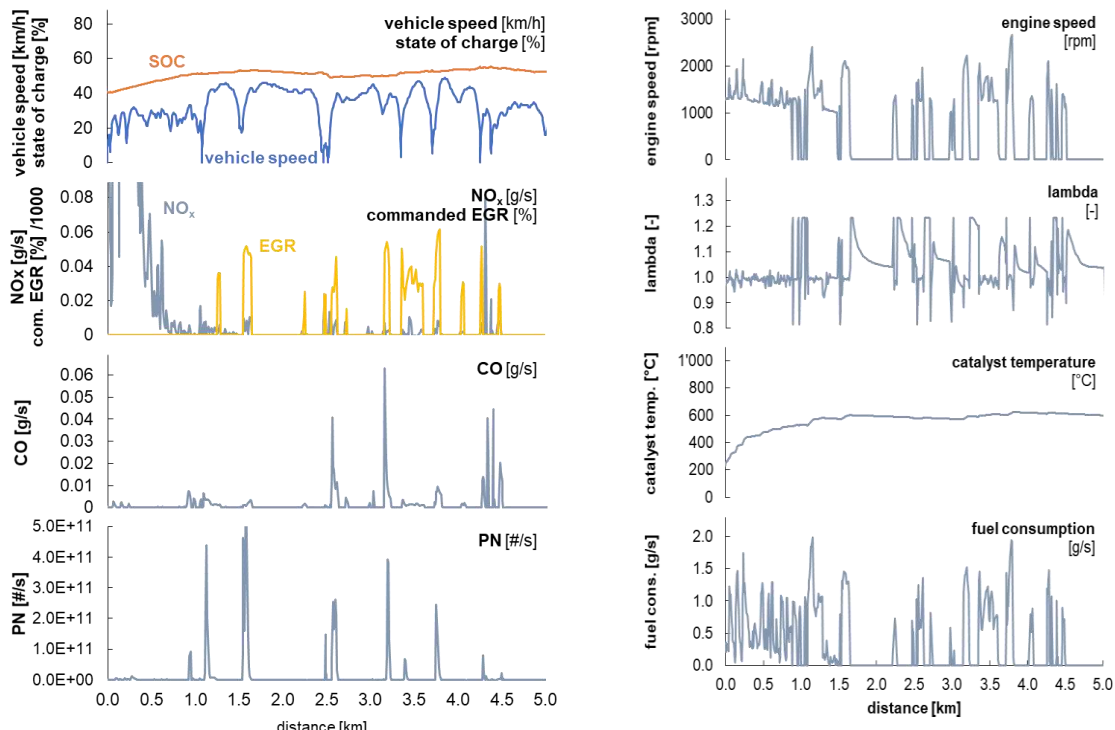


Figure 13a: Influence of EGR on NO_x, CO & PN; example RDE cold, (no 11), urban part, Toyota Prius III, (V4)

Figure 13b: ECU engine operating parameters in the RDE cycle cold, (no 11), urban part, Toyota Prius III, (V4)

Positions of accelerator vs. throttle

Fig. 14 shows the correlations of throttle positions and accelerator positions for different modes of vehicle operation. These values are extracted from the OBD. It can be commented that in the mode "Eco", more accelerator pedal action is necessary to obtain a certain opening of the throttle valve. Inversely, in the mode "Power", the throttle opening reacts more sensibly on the accelerator

positions. It can be concluded that this way of throttle control underlines or supports the subjective attitude of the driver.

Battery pack charging

Tests of battery pack charging were performed by means of motoring the vehicle on chassis dynamometer.

Two tests were driven in mode "D" (normal driving) and one test in mode "B" (braking, battery charging).

Fig. 15 represents the used speed profile, the resulting engine speeds and SOC. In mode "B", the charging progress is much quicker, and the engine speed is strongly increased to promote the charging. In mode "D", the battery charging is slower and when SOC attains c.a.50% the engine is stopped and due to the motoring (by CD) the SOC continues to increase slowly.

By the attempts of discharging the battery pack on CD, it was observed that at SOC around 40% the engine is automatically started to recharge the batteries and attaining nearly SOC 50% the engine switch-off and the electric driving are again enabled.

The SOC of this vehicle can vary between 40% and 80%.

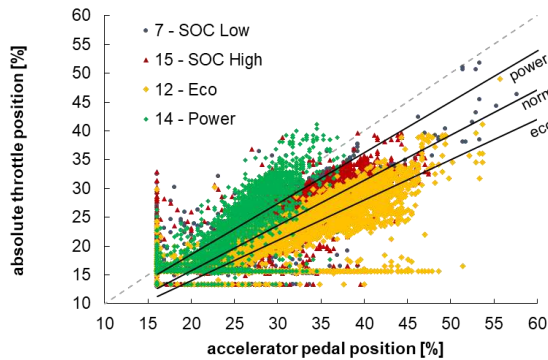


Figure 14: Distribution of throttle vs. accelerator positions in different driving modes, (no 7, 12, 14, 15), Toyota Prius III, (V4)

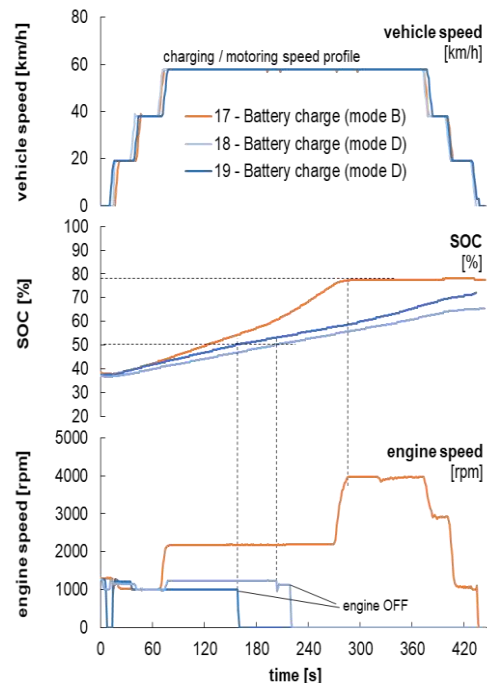


Figure 15: Attempts of battery charging in modes "B" (Brake) and "D" (Drive), chassis dynamometer in motored mode, Toyota Prius III, (V4)

Conclusions

Following conclusions can be mentioned:

E0 & E85

- The use of E85 fuel is advantageous for emission reduction: with E85 there is reduction of NO_x and PN for both investigated vehicles in all driving conditions.
- The volumetric fuel consumption with E85 is generally higher, due to the lower heat value of this fuel.
- Both vehicles attain similar levels of emissions at the end of RDE cycle, while the dispersion of results for each vehicle/fuel variant is much larger than on the chassis dynamometer (in WLTC).

Payload/trailer

Higher maximum speed, or higher payload increase the cumulated emissions of CO, HC, NO_x and PN.

HEV

- There is a good repeatability of results obtained with PEMS on the chassis dynamometer and on-road.
- Depending on temperature of batteries and different other parameters the SOC is maintained by the system between approximately 40% and 80%.
- The tested vehicle has very low emissions and fuel consumption and these values are only slightly influenced by different modes, such as SOC, Power, Economy and cold start.
- There are: higher CO- and NO_x-emissions at cold start and higher fuel consumption in the driving mode "Power".
- A rapidly controlled EGR is an important measure to reduce NO_x-emissions in addition to the 3WC-technology and variocam-Atkinson-cycle.
- The engine switching strategy, sometimes lean engine operation and EGR offer very low fuel consumption and low, near-to-zero NO_x-emissions.
- The openings of EGR-valve cause often CO- and PN-peaks.
- In the real world driving on the RDE-circuit the engine works between 39% and 59% of the total cycle time, with the highest share in driving mode "Power".
- In the driving modes "Power" or "Economy", there are different control strategies of throttle position versus accelerator position, which support the wish of the driver.
- The maximal charging of the battery pack, up to SOC ~80%, is possible only in the operating mode "B".

Acknowledgement

The authors express gratitude to the Swiss Federal Offices for Environment (BAFU) and for Roads (ASTRA) for the financial support of these activities.

References

- [1] *Official Journal of the European Union: Commission regulation (EU) 2016, 427 of 10 March 2016, amending regulation (EC) No 692/2008.*
- [2] *Commission regulation (EC) no 2008, 692 of 18 July 2008 implementing and amending Regulation (EC) No 715/2007 of the European Parliament and of the Council on type-approval of motor vehicles with respect to emissions from light passenger and commercial vehicles (Euro 5 and Euro 6) and on access to vehicle repair and maintenance information*
Available at: <http://eur-lex.europa.eu/legal-content/en/ALL/?uri=CELEX:32008R0692>
- [3] *Draft of the Annex IIIa: Verifying Real Driving Emissions amending Regulation (EC) No 692/2008 as regards emissions from light passenger and commercial vehicles (Euro 6).*
- [4] HOFACKER, A. Abgasnorm und Wirklichkeit Eine Annäherung. Springer: *MTZ-Motortechnische Zeitschrift*, January 2015, **76**(2), 8-13.
- [5] VLACHOS, T. G., BONNEL, P., WEISS, M. Die Bewertung des Abgasverhaltens von Fahrzeugen im realen Fahrbetrieb – Eine Herausforderung für die europäische Emissionsgesetzgebung. *36. Internationales Wiener MotorenSymposium*, 2015.
- [6] GERSTENBERG, J., SCHYR, CH., STERZING-OPPEL, S., TRENKLE, D. RDE Engineering via Engine-in-the-loop Test-bench. *MTZ worldwide* 2017 **78**(6), 16-23.
- [7] CZERWINSKI, J., ZIMMERLI, Y., COMTE, P., BÜTLER, TH. Experiences and Results with different PEMS. *TAP Paper, International Transport and Air Pollution Conference*, May 24th-26th, 2016, Lyon, France.
- [8] CZERWINSKI, J., ZIMMERLI, Y., COMTE, P., CACHON, L., RICCOBONO, F. Potentials of the portable emission measuring systems (PN PEMS) to control real driving emissions (RDE). *38. International Vienna Motor Symposium*, 27-28 April 2017, *VDI Fortschritt-Bericht Reihe 12*, Nr. 802, Vol. 2.
- [9] MASCHMEYER, H., BEIDL, C. RDE Homologation – Herausforderungen, Lösungen und Chancen. *MTZ* 2016, **77** (10), 84-91

- [10] ZELLBECK, H., WALTER, R., STIEGLER, M., ROß, T. RDE – Der reale Fahrbetrieb auf dem hochdynamischen Motorenprüfstand. *MTZ* 2015 **76** (2), 42-47
- [11] RÖTTGER, D., PÉREZ-GUZMÁN, E., VIGILD, CH., DE SMET, F. Feature Function Development for RDE in Diesel Engines. *MTZ* 2017 **78** (3), 46-51
- [12] SCHRÖDER, M., BALTES, N., DANZER, J. Impact of RDE Legislation on Test-bed Measurements. *MTZ worldwide* 2017 **78** (6), 28-35.
- [13] GIECHASKIEL B., RICCOBONO, F., BONNEL, P. Feasibility study on the extension of the Real Driving Emissions (RDE) procedure to Particle Number (PN). *European Commission, Joint Research Centre*, ISBN: 978-92-79-51003-8, ISSN: 1831-9424, DOI: 10.2790/74218
- [14] ANDERSON, J., MAY, J., FAVRE, C., BOSTEELS, D. et al. On-Road and Chassis Dynamometer Evaluations of Emissions from Two Euro 6 Diesel Vehicles. *SAE Technical Paper 2014-01-2826*. SAE Detroit, April 2014.
- [15] BERGSTRÖM, K., MELIN, S.-A., JONES, C. The New ECOTEC Turbo BioPower Engine from GM powertrain – Utilizing the Power of Nature's resources. 28. *Internationales Wiener Motoren-Symposium* 2007, **2**, 47.
- [16] BERGSTRÖM, K., NORDIN, H., KÖNIGSTEIN, A., MARRIOTT, C., WILES, M. ABC – Alcohol Based Combustion Engines – Challenges and Opportunities. 16. *Aachener Kolloquium Fahrzeug- und Motorentechnik* 2007, **2**, 1031.
- [17] KAWAI, T., TSUNOOKA, T., CHIBA, F., UDA, H., SONODA, Y. Effect of High Concentration Ethanol on SI Engine Cold Startability and Emissions. 16. *Aachener Kolloquium Fahrzeug- und Motorentechnik* 2007, **2**, 1075.
- [18] HADLER, J., SZENGEL, R., MIDDENDORF, H., SPERLING, H., GRÖER, H-G., TILCHNER, L. Der 1.4l 118kW TSI für E85 Betrieb – die Erweiterung der verbrauchsgünstigen Ottomotorenlinie von Volkswagen. 32. *Internationales Wiener MotorenSymposium* 2011, **1**, 263.

Abbreviations

AFHB	Abgasprüfstelle FH Biel, CH	LFE	laminar flow element
ASTRA	Amt für Strassen (CH)	MAW	moving averaging windows
BAFU	Bundesamt für Umwelt, (Swiss EPA)	MFS	mass flow sensor
CD	chassis dynamometer	NM3	NanoMet3
CLA	chemiluminescence analyser	NO	nitrogen monoxide
CLD	chemiluminescence detector	NO ₂	nitrogen dioxide
CPC	condensation particle counter	N ₂ O	nitrous oxide
CVS	constant volume sampling	NO _x	nitric oxides
c/w	cold/warm	OBD	on-board diagnostics
DC	diffusion charging	OBS-ONE	Horiba Gas PEMS
DF	dilution factor	OBS-PN	Horiba PN PEMS
DI	Direct Injection	OP	operating point
E0	gasoline (zero Ethanol)	PEMS	portable emission measuring systems
E85	85% vol. Ethanol	PF	Pitot flow meter
EC	European Commission	PMP	EC Particle Measuring Program
ECE	Economic Commission Europe	PN	particle number
ECU	electronic control unit	PN-PEMS	PEMS with PN measuring device
EFM	exhaust flow meter	RDE	real driving emissions
EGR	exhaust gas recirculation	SOC	state of charge
EMROAD	RDE emissions evaluation program	TP	tailpipe
GDI	gasoline direct injection	TWC	three way catalyst
GMD	geometric mean diameter	V1-V4	vehicle 1 – vehicle 4
HC	unburned hydrocarbons	ViPR	nanoparticle sample preparation with volatile particles remover
HD	heavy duty	WLTC	worldwide harmonized light duty test cycle
HDV	heavy duty vehicle		
HEV	hybrid electric vehicle		
INT	integral average values		
LDV	light duty vehicle		

WLTP worldwide harmonized light
duty test procedure
3WC three way cata

2.6.2 Characterization of sub-23 nm particles and their measure for PFI/DI SI engines fueled with gasoline, ethanol and blend

Catapano Francesco, Di Iorio Silvana, Vaglieco Bianca Maria

Istituto Motori CNR, P.O.Box 80125, Naples, Italy, s.diiorio@im.cnr.it.

Abstract

Particulate matter (PM) pollution in urban area is mainly due to internal combustion engines. PM are linked to hazardous health effects, and it is more dangerous as smaller are the particle size. The current emissions legislation introduced a number limitation only for particle larger than 23 nm. The sampling procedure as indicated by the PMP aims, in fact, to remove volatile particles smaller than 23 nm. There are many evidence on emissions of sub-23 nm particles. The nature of these particles is not well understood and their measurement is very sensitive to dilution conditions. A comprehensive characterization of their nature can help to define a well-consolidated procedure for their measurement.

In this paper the effect of the sampling conditions on the emissions of sub-23 nm particles was analyzed. The investigation was performed on a small displacement PFI/DI SI engines fueled with gasoline, ethanol and blend of ethanol and gasoline. Particle size distribution and number concentration were measured on-line with an EEPS and an advanced DMA.

Introduction

Great attention is being paid to electric and fuel-cell vehicles because of the growing concerns on the severe adverse effects of the particle emissions on human being health (Morakinyo, 2016). Nevertheless, the internal combustion engines (ICE) will play a dominant role in the powertrain vehicles for the next years although Diesel and Gasoline Direct Injection (GDI) engines are the main source of ultra-fine particle emissions in the urban area. Until some years ago, Diesel engines mainly contributed to the particulate matter pollution in the urban area. The introduction of Diesel Particulate Filters (DPF) allows the reduction of the particle emissions, both in term of mass and number. During the regeneration of the filters a large number of ultra-fine particles were emitted (Beatrice, 2012, Rodríguez-Fernandez, 2017). Nowadays, GDI engines play a relevant role in particle emissions as well. The introduction of the direct injection (DI) in the spark ignition (SI) engines from one side allows the improvement of the fuel saving and the engine performance but worsens the particle emissions with respect the port fuel injection (PFI) SI engines because of the less time for fuel evaporation and mixing and because of the fuel impingement (Fang, 2017, Longfei, 2017). In comparison with Diesel engines equipped with DPF, GDI engines emit more ultrafine particles (Chen, 2017, Fatouraie, 2015). Several solutions are underway to reduce particle emissions, and one of these is the use of the oxygenated biofuels because of their contribution to reducing the fossil fuel dependence as well as the pollutant and CO₂ emissions. For the SI engines ethanol is the most promising alternative fuel (Cooney, 2009, Schifter, 2011) because of the higher octane number and the higher heat of vaporization compared to gasoline. Anyway, typically emit a larger number of particles smaller than 100 nm (Szybist, 2011, Catapano, 2014).

Several studies have pointed out that health effect of particle emissions on human health is strongly related to particle number. For this reason, a particle number (PN) emission limit of $6 \times 10^{11} \text{ #/km}$ was introduced (UNECE, 2010) for particles larger than 23 nm emitted from Diesel and GDI engines. The measurement of the particle number is more sensitive than the measurement of the mass. The exhaust is in fact a complex mixture of soot particles, and semi-volatile heavy hydrocarbons that can nucleate or adsorbing/condensing on the existing carbonaceous particles as temperature is lowered (Kittelson, 1998). A procedure for the particle number particles was defined by the PMP protocol (Andersson, 2007), there were concerns whether the methodology applied to diesel engines could be applied to gasoline engines and other technologies (Giechaskiel, 2017). Moreover, the PMP was developed for the measurement of solid particles larger than 23 nm in order to exclude volatile nucleation mode improving the repeatability and reproducibility of the method to levels acceptable for legislative purposes (Martini, 2009). Several researches evidenced a large presence of solid nucleation mode of particles smaller than 23 nm

from internal combustion in Diesel, SI Port fuel injection GPFI and GDI (Khalek, 2009, Ntziachristos, 2013, Karjalainen, 2014) engines. The emissions of sub-23 nm particles can be more harmful to human health than bigger particles as they have higher deposition efficiency in the respiratory system and can translocate to other areas such as the brain (Oberdorster, 2004, Li, 2017). Their nature is not fully clear (Kittelson, 1998) and their measure can be biased by the sampling conditions (Khalek, 2007, Burtscher, 2005). For this reason, appropriate sampling and measurement procedure should be developed

The necessity to further investigation on sub-23 nm particles leads to the promotion of European project focused on the development of instruments that can measure particle smaller than 23 nm and a procedure for their measurement. The procedure for the measurements of the number defined by PMP aims to measure only the solid particles define as the particles that survive at a Volatile Particle Remover (VPR). The procedure consists on the use of two dilution stages, a heated one and cold one, and an evaporation tube between them. The aim is to reduce the particle concentration enough with the first dilution so that re-nucleation after the evaporation tube is improbable (Zheng, 2012). In order to properly define a measurement procedure for particle number emissions of the internal combustion engines it has to be better characterize the effect of the sampling parameters on the sub-23 nm particles.

This paper aims to characterize the sub-23 nm particle nature by means the analysis of the effect of the temperature of sampling, dilution and evaporation chamber. The investigation was performed on small displacement SI DI/PFI engines fueled with gasoline, ethanol and a blend of 25%v/v of ethanol in gasoline. The tests were carried out at full load and 2000 and 4000 rpm. The investigated engine operating conditions are representative of the European homologation urban driving cycle. Particle emissions were measured by means of a smokemeter, to measure the particle concentration, and an Engine Exhaust Particle Sizer (EEPS), for the measurement of number and size in the range from 5.6 to 560 nm. An advanced HM-DMA was used to measure the particle in the size range from 1 up to 23 nm. The tests were carried out at two sampling conditions, Cold and Hot in order to estimate the presence of Volatile Organic Fraction (VOF).

Experimental Apparatus and Procedures

Engine

The investigation was carried out on a 4-stroke single cylinder SI engine equipped with the cylinder head of a naturally aspirated GDI engine. The engine head has four valves and a centrally located spark plug. A six-hole injector is located between the intake valves. A PFI injector was located in the intake duct. A quartz pressure transducer is flush-mounted in the region between intake and exhaust valves. Engine specifications are listed in Table 1.

Table 1: Engine specifications.

Cylinder volume	250
Bore (mm)	72
Stroke (mm)	60
Compression ratio	11.5
Max power (kW)	16 @ 8000 rpm
Max torque (Nm)	20 @ 5500 rpm

The gasoline mass flow was measured by means of an oval gear meter operating in the range from 0.005 to 1.75 l/min. A linear lambda sensor Bosch LSU 4.9 installed at the exhaust was used to measure the air fuel ratio. A programmable electronic control unit (PECU) allowed the management of the injection timing as well as the ignition timing. The injection-duration (DOI) was properly adjusted by a closed loop control on the lambda value to obtain a stoichiometric equivalence ratio. The engine was equipped with a three way catalyst (TWC). The in-cylinder pressure was measured by means of a quartz pressure transducer flush-mounted in the region between the intake and exhaust valves. The engine was fueled with commercial European Gasoline, Ethanol and a blend of 25%v/v of Ethanol in gasoline (E25). The fuel chemical and physical properties are listed in Table 2.

Table 2: Chemical and physical properties of gasoline and ethanol.

Fuel property	Gasoline	Ethanol
Carbon (mass%)	86.12	52.2
Hydrogen (mass%)	13.25	13.1
Oxygen (mass%)	0.63	34.7
Aromatic content (%v/v)	35	-
Density @15 °C (kg/l)	0.751	0.79
Viscosity at 20 °C (mPa s)	0.39	1.19
LHV (MJ/l)	32	21.1
Stoichiometric air/fuel	14.7	9

Engine operating conditions

The engine was run at two engine speeds, 2000 and 4000 rpm, chosen as representative of the typical driving conditions. The duration of injection was properly modified for each fuel to have a stoichiometric condition. The timing of injection and the start of spark was properly set to have a stable and optimized combustion. All the experiments were performed at steady state conditions. To ensure a proper operation and a reliable response of the exhaust gas analyzers, the engine was first “warmed up” until the coolant and lubricating temperatures had stabilized at 80 and 90°C, respectively. The data were recorded after about 120 s that the engine conditions were stabilized. Tests were repeated three times in order to take into account the engine variability as well as to have a good statistics of the measurements. The in cylinder pressure and heat release were obtained on an individual cycle basis and averaged over 500 consecutive cycles.

Emissions measurement systems

A smoke meter (AVL 415S) was used for measuring the filter smoke number (FSN) which was converted in mass concentration through an empirical relation. Particle number concentration and size were measured in the range from 5.6 to 560 nm by means of a TSI® engine exhaust particle sizer (EEPS). For particle number measure the exhaust was sampled and diluted by means of the Dekati® engine exhaust diluter (DEED), a Particle Measurement Program (PMP)-compliant engine exhaust conditioning system. The dilution ratio was fixed at 1:79. A 1.5 m heated line was used for the sampling of the engine exhaust in order to avoid the condensation of the combustion water. This system allows the measurement of the solid particles defined by the PMP as particles that can survive after passing through an evaporation tube (ET) that has a wall temperature of 300–400 °C. An advanced Half-Mini DMA (HM-DMA) was used to classify particles with high resolution from 1 nm up to 30 nm by measuring the ions current (de la Mora, 2017). This device is capable of high classification efficiency at sample temperatures approaching 200 °C. A Dekati® single diluter was used for the sampling and the dilution of the exhaust before entering the HM-DMA. The dilution ratio was 1:10. A 1.5 m heated line was used for the sampling of the engine exhaust in order to avoid the condensation of the combustion water.

Methodology

The effect of sampling conditions was characterized by changing the temperature of the 1st dilution (T_{DR1}) and of the evaporation chamber (TEC) in case of DEED. It was investigated two sampling condition:

For number concentration measurement:

Cold: T_{DR1} and TEC set at 50°C; Hot: T_{DR1} 150°C and TEC 400 °C.

For ions current measurements:

Cold: T_{DR} set at 50°C; Hot: T_{DR} set at 150°C.

The volatile fraction (αVOF) was estimated as the percentage difference of the actual sub-23nm particle number measured from EEPS and ions current measured by HMDMA for Hot and Cold with respect to Hot conditions:

$$\alpha\text{VOF} (\%) = (\text{N10-23(Cold)} - \text{N10-23(Hot)}) / \text{N10-23(Hot)} * 100$$

Results and Discussion

The effect of ethanol, a widely used biofuel in SI engines, on sub-23 nm particle emission was studied in a small displacement SI engine, equipped with both PFI and DI injection systems. Engine was fueled with pure ethanol and a blend of 25%v/v of ethanol in gasoline.

In Figure 1 the sub-23 nm particle number concentration measured in DI and PFI SI engines fueled with Gasoline, Ethanol and E25 was shown.

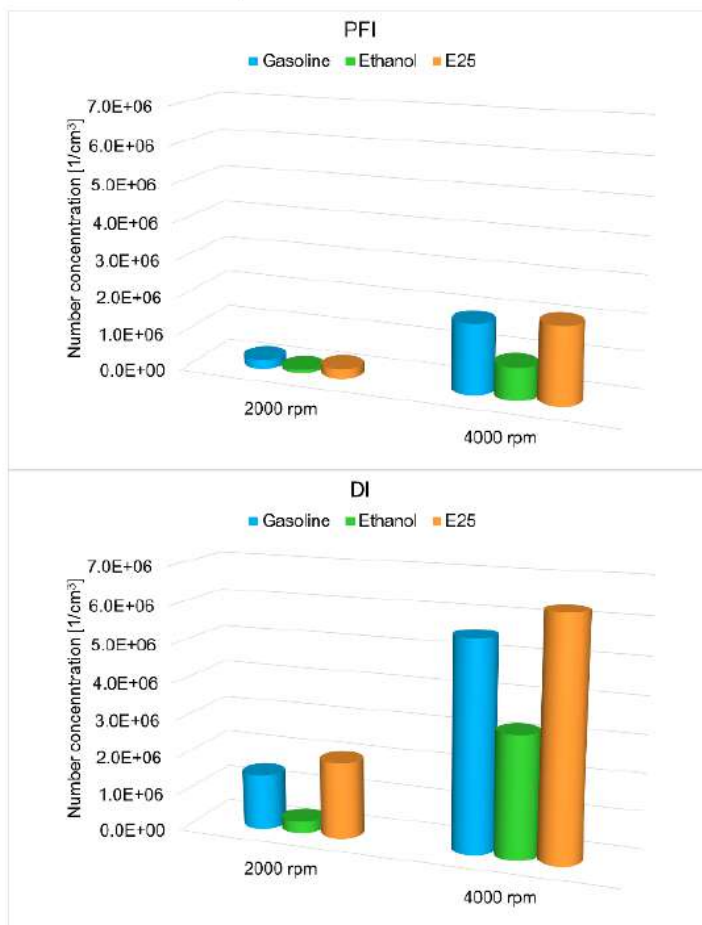


Figure 1: Number concentration of sub-23 nm particles emitted in PFI and DI configuration for Gasoline, Ethanol, E25 fueling at 2000 and 4000 rpm.

The sub-23nm particle emission was strongly influenced by the injection configuration, the operating condition and fuels as well.

For each engine speed and fuel, sub-23 nm particle emission is larger for DI configuration. This is well known and ascribable to the different combustion evolution (Catapano, 2014). In DI mode the less time for fuel evaporation and for air/fuel mixing as well as the large wall impingement result in to the presence of liquid fuel and large rich zone where particle formation is strongly enhanced. In GPFI configuration, fuel being injected in the intake duct has more time for gasoline evaporation and mixing. In this case, particles are formed in small rich zone localized across the intake valves where despite the high temperature fuel does not evaporate completely and burns in a diffusive way, pool fire (Catapano, 2014).

For all fuels and injection configurations sub-23 nm particle emissions increases with speed. Higher the engine speed faster the combustion process. In case of the DI configuration particle number increase is more evident as the effect of the less time for fuel evaporation and mixing is coupled with the worsening of the fuel impingement (Catapano, 2014).

Regarding the fuel effect, a decrease of sub-23nm particles for ethanol fueling in both DI and PFI configurations can be observed. Ethanol evaporates more easily providing lower presence of liquid fuel and rich zone. Moreover, the lower aromatic content and higher presence of oxygen acts reducing the soot precursor formation. The larger oxygen content from one side enables a more complete combustion even in fuel-rich regions of the combustion chamber and from another side enhances the oxidation of formed soot. When ethanol was blended with gasoline the sub-23 nm particle emission increases with respect to ethanol fueling. If compared with gasoline is not observed a linear trend. The sub-23 nm particles in DI mode are larger with respect to Gasoline. The addition of gasoline significantly affects the evaporation of the Ethanol. Ethanol forms an almost azeotropic mixture with the lighter compounds of gasoline hydrocarbons (Balabin, 2007). The evaporation of lighter compounds of gasoline is strongly enhanced by ethanol addition, and the residual fuel will mainly contain heavier and highly sooting hydrocarbons that burn in a colder environment extremely favorable for the formation of soot particles.

The effect of the sampling parameters on the measurements of the sub-23 nm particles was investigated for all the tested fuels in PFI and DI configuration at 2000 rpm and 4000 rpm. The tests were performed in Hot sampling condition: 1st dilution at 150°C, evaporation chamber at 400°C, in this case the PMP guidelines were accomplished, and in Cold sampling condition: 1st dilution and evaporation chamber at 50°C, in this case the system is not PMP compliant.

The particle mass concentration (PM (mg/m³)) measured for each fuel in PFI and DI configurations at low and high engine speeds was listed in Table 3.

Table 3: PM measured for Gasoline, Ethanol and E25 in PFI and DI configurations at 2000 and 4000 rpm.

Test case	2000 rpm		4000 rpm	
	Hot	Cold	Hot	Cold
GPFI	0.07	0.07	0.78	0.81
E25PFI	0.02	0.01	0.14	0.18
EPFI	0.03	0.04	0.35	0.30
GDI	1.52	1.52	3.42	3.27
E25DI	11.48	12.5	0.94	1.18
EDI	0.26	0.23	0.06	0.06

The difference between the particle mass measured in Hot and Cold conditions are negligible meanwhile all the differences observed in the PSDF can be ascribed to the effect of the temperature of the sampling.

In Figure 2 the PSDF in the size range 10-23 nm measured in DI configuration at low and high engine speeds were depicted for all tested fuels.

For each engine configuration whatever the fuel the PSDF behavior is not influenced by the sampling condition. The sub-23 nm particle number increases for the sampling at low temperature except for GDI at high speed. In this case the PSDF is shifted towards larger diameter and the effect of the sampling condition is more evident for the particles larger than 23 nm.

In Figure 3 the PSDF in the size range 10-23 nm measured in PFI configuration at low and high engine speed for all tested fuels were depicted.

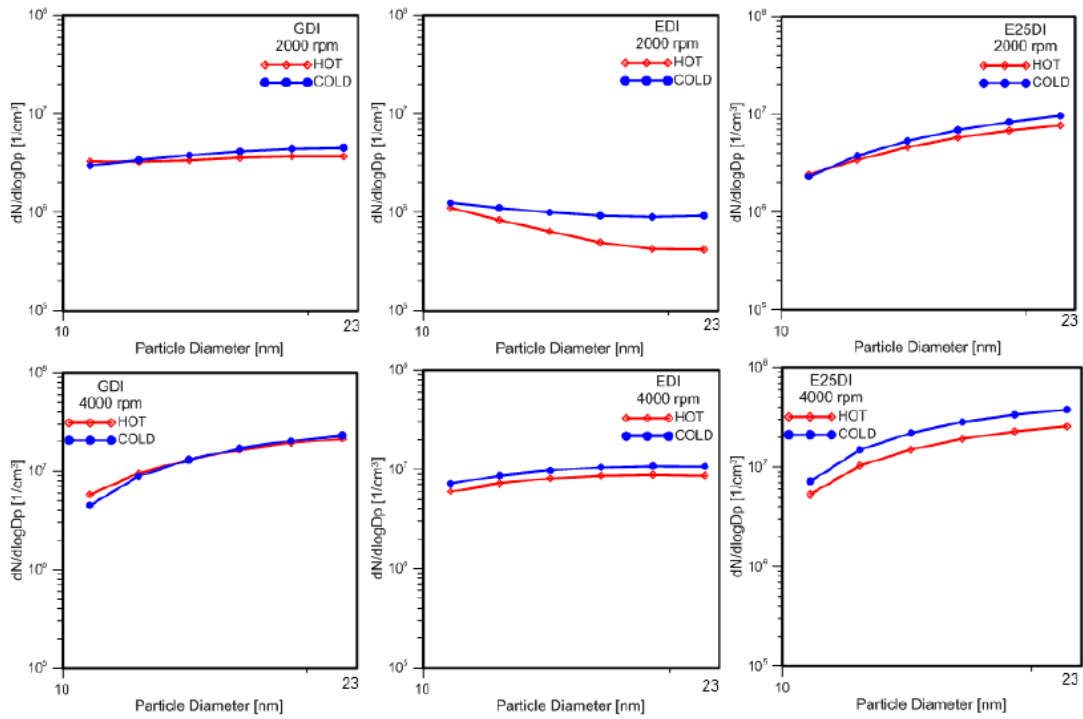


Figure 2: PSDF in 10-23 nm size rage measured in Hot and Cold sampling condition in DI configuration for Gasoline, Ethanol, E25 fueling at 2000 and 4000 rpm.

As for DI configuration also in this case the sub-23 nm particle number increases for the sampling at low temperature and the effect on the size distribution is negligible. For 2000 rpm the Noise Signal Ratio is too high especially for E25, as evidenced by the necessity to lower of around one order of magnitude the value of the y-axis, and is quite difficult to distinguish the effect of temperature.

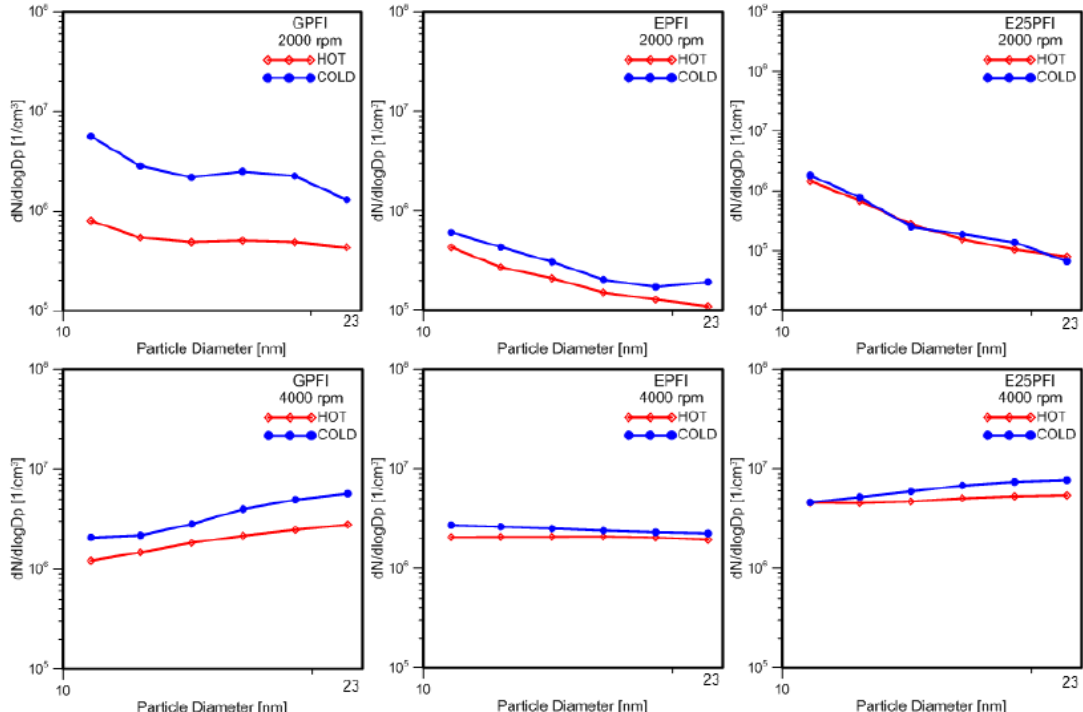


Figure 3: PSDF in 10-23 nm size rage measured in Hot and Cold sampling condition in PFI configuration for Gasoline, Ethanol, E25 fueling at 2000 and 4000 rpm.

In Figure 4 was illustrated the percentage variation of sub-23 nm particle number for DI and PFI configuration at low and high engine speed for all the tested fuels.

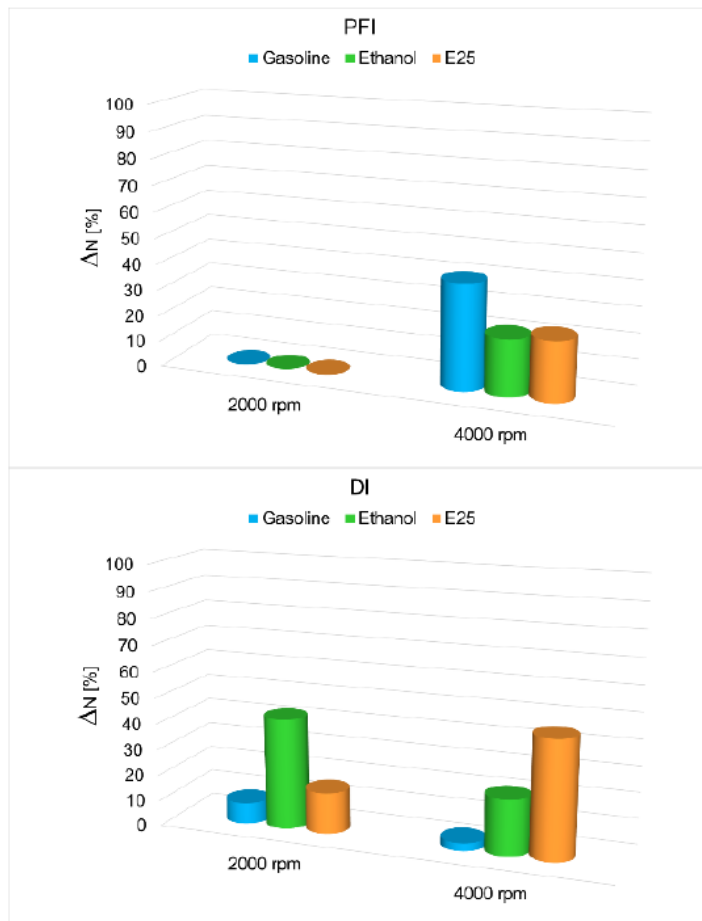


Figure 4: ΔN of the sub-23nm particle emissions as evaluated from particle number concentration in PFI and DI configurations and Gasoline, Ethanol and E25 fueling at 2000 and 4000 rpm

The volatile fraction of the sub-23nm particle emissions was evaluated as percentage difference of the actual sub-23nm particle number for Hot and Cold with respect to Hot. For PFI at 2000 rpm the Noise Signal Ratio is too high, for this reason it was not considered in the analysis of the evaluation of the volatile fraction. For PFI the higher volatile fraction was evaluated for Gasoline. On the contrary, for DI, Gasoline shows the lower volatile content with respect to Ethanol and E25 whatever the engine speed. It has to be taken in to account the different PSDF. Particle emitted from GDI are larger so the volatile component likely condensed on the particle more than nucleate. The effect of the temperature on sub-23 nm particles is less evident in this case. Anyway, a different trend is observed according to the engine speed for the biofuel and blend. At low engine speed, the volatile content is larger for Ethanol, at high engine speed, instead the volatile content is larger for E25. This can be due to the different evaporation condition of the fuels. At low engine speed the evaporation of ethanol is worsen because of the low temperature typical of this engine point; when blended with gasoline the ethanol evaporation was enhanced resulting in a lower presence of volatile. On the contrary, at high engine speed the ethanol evaporates easier while the blend evaporation is worsen as previously described.

The volatile fraction of sub-23nm particles was evaluated by the variations of the ions current measured by the HMDMA, Figure 5.

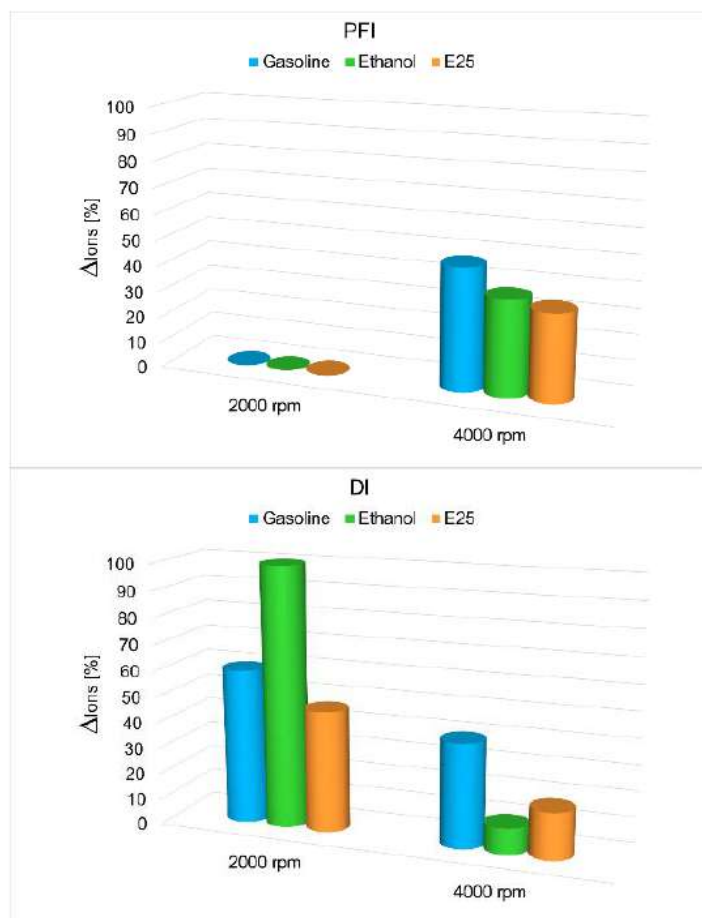


Figure 5: ΔI_{ions} of the sub-23nm particle emissions as evaluated from ions current in PFI and DI configurations and Gasoline, Ethanol and E25 fueling at 2000 and 4000 rpm

HM-DMA shows similar results of EEPS except for the DI at 4000 rpm where a decrease in the volatile nature of the sub-23 nm particles when ethanol is used was observed.

The different results can be ascribable to the differences in the measurements principle as well as to the different sampling system. The presence of an evaporation chamber in the system used for number measure can create some artefacts, especially during cold operation. For this reason the use of only one dilution step can be more robust for the measure of the sub-23 nm particles.

Conclusions

The sub-23 nm particle nature was characterized by means of the analysis of the effect of the temperature of sampling. The investigation was performed on small displacement SI DI/PFI engines fueled with gasoline, ethanol and a blend of 25%v/v of ethanol in gasoline.

The sub-23 nm particle emissions are dependent on engine configuration and fuel. Larger particles are emitted from DI engines. A different result is observed when pure ethanol and the blend was used. In particular, in DI configuration the particles emitted from E25 are larger than those emitted from gasoline. This result is ascribable to the worsening of the evaporation of the heavier compound of gasoline.

The analysis of the effect of the temperature of the dilution and eventually of the evaporation chamber evidenced the strong influence of the sampling conditions on the measurement of the sub-23nm particles highlighting the necessity to a definition of a proper measurement protocol for the sub-23 nm particles.

Acknowledgment

This work is part of SUREAL-23 project that has received funding from the European Union's Horizon 2020 research and innovation programme under grant agreement No 724136. The authors are thankful to the project partners E. Papaioannou, D. Zarvalis, P. Baltzopoulou, D. Zamora, Juan Carlos del Castillo Rafael Delgado Ballesteros. The authors are grateful to Mr. Carlo Rossi and Mr. Bruno Sgammato for the support in the experimental activities carried out.

References

- Andersson, J., Giechaskiel, B., Munoz-Bueno, R., and Dilara, P. (2007). Particle measurement programme (PMP): Lightduty inter-laboratory correlation exercise (ILCE LD)-Final report (EUR 22775 EN) GRPE-54-08-Rev.1, <http://www.unece.org/trans/main/wp29/wp29wgs/wp29grpe/grpeinf54.html>
- Balabin R M, Syntaev R Z, and Karpov S A. (2007). Quantitative Measurement of Ethanol Distribution over Fractions of Ethanol-Gasoline Fuel. *Energy & Fuels* 21,2460-2465.
- Beatrice. C., Di Iorio, S., Guido, C., Napolitano, P., (2012). Detailed characterization of particulate emissions of an automotive catalyzed DPF using actual regeneration strategies, *Exp. Therm. Fluid Sci.* 39 45-53.
- Burtscher, H. (2005). Physical characterization of particulate emissions from diesel engines: a review. *Journal of Aerosol Science*, 36, 896–932.
- Catapano, F., Di Iorio, S., Sementa, P., and Vaglieco, B., (2014). Characterization of Ethanol-Gasoline Blends Combustion processes and Particle Emissions in a GDI/PFI Small Engine, SAE Technical Paper 2014-01-1382, doi:10.4271/2014-01-1382.
- Chen, L.; Liang, Z.; Zhang, X.; Shuai, S. (2017). Characterizing particulate matter emissions from GDI and PFI vehicles under transient and cold start conditions. *Fuel*, 189, 131–140.
- Cooney, C.P., Worm, Y.J., Naber, J.D., (2009). Combustion characterization in an internal combustion engine with ethanol-gasoline blended fuels varying compression ratios and ignition timing, *Energy Fuels*:2319–24, 2009.
- de la Mora JF, (2017). Expanded flow rate range of high-resolution nanoDMAs via improved sample flow injection at the aerosol inlet slit, *Journal of Aerosol Science*, Vol.113, 265-275.
- Fang, Ti., Wang, L, Wang Z. (2017). Particulate Matter Emissions from Gasoline Direct Injection Engines: Research Review, 10.3969/j.issn.1674-8484.2017.03.002.
- Fatouraie, M.; Wooldridge, M.S.; Petersen, B.R.; Wooldridge, S.T. (2015). Effects of Ethanol on In-Cylinder and Exhaust Gas Particulate Emissions of a Gasoline Direct Injection Spark Ignition Engine. *Energy Fuel*, 29, 3399–3412.
- Giechaskiel, B., Vanhanen, J., Väkevä M., Martini G., (2017). Investigation of vehicle exhaust sub-23 nm particle emissions, *Aerosol Science and Technology*, 51:5, 626–641, DOI: 10.1080/02786826.2017.1286291
- Karjalainen, P., Pirjola, L., Heikkilä, J., Lahde, T., Tzamkiosis, T., Ntziachristos, L., Keskinen, J., and Ronkko, T. (2014). Exhaust particles of modern gasoline vehicles: A laboratory and an on-road study. *Atmos. Environ.*, 97:262–270.
- Khalek, I. (2007). Sampling System for Solid and Volatile Exhaust Particle Size, Number, and Mass Emissions. SAE Technical Paper 2007-01-0307. doi:10.4271/2007-01-0307.
- Khalek, I., Bouger, T., and Jetter, J. (2010). Particle Emissions from a 2009 Gasoline Direct Injection Engine Using Different Commercially Available Fuels. *SAE Int. J. Fuels Lubr.*, 3 (2):623–637, doi:10.4271/2010-01-2117
- Kittelson, D., (1998). Engines and Nanoparticles: A Review, *J. Aerosol Sci.* 29, 575-588.
- Li, Y.; Lane, K.; Corlin, L.; Patton, A.; Durant, J.; Thanikachalam, M.; Woodin, M.; Wang, M.; Brugge, D. (2017). Association of long-term near-highway exposure to ultrafine particles with cardiovascular diseases, diabetes and hypertension. *Int. J. Environ. Res. Public Health*, 14, 461.
- Longfei C., Zhirong L., Xin Z. Shijin S., (2017). Characterizing particulate matter emissions from GDI and PFI vehicles under transient and cold start conditions, *Fuel* 189 131–140.
- Martini, G., Giechaskiel, B., Dilara, P.(2009). Future European emission standards for vehicles: the importance of the UN-ECE particle measurement programme. *Biomarkers*, 14, 29–33.
- Morakinyo, O.; Mokgobu, M.; Mukhola, M.; Hunter, R. (2016). Health outcomes of exposure to biological and chemical components of inhalable and respirable particulate matter. *Int. J. Environ. Res. Public Health*, 13, 592.

- Ntziachristos, L., Amanatidis, S., Samaras, Z., Giechaskiel, B., and Bergmann, A. (2013). Use of a Catalytic Stripper as an Alternative to the Original PMP Measurement Protocol. *SAE Int. J. Fuels Lubr.*, 6(2):532–541. doi:10.4271/2013-01-1563
- Oberdorster, G., Sharp, Z., Atudorei, V., Elder, A., Gelein, R., Kreyling, W., and Cox, C. (2004). Translocation of Inhaled Ultrafine Particles to the Brain. *Inhal Toxicol.*, 16(6–7):437–45.
- Rodríguez-Fernandez, J., Lapuerta, M., Sanchez-Valdepenas, J., (2017). Regeneration of diesel particulate filters: Effect of renewable fuels, *Renewable Energy* 104 30–39.
- Schifter, L., Diaz, R., Rodriguez, J.P., Gómez, Gonzalez, U., (2011). Combustion and emissions behavior for ethanol–gasoline blends in a single cylinder engine, *Fuel* 90 3586–3592.
- Szybist, J., Youngquist, A., Barone, T., Storey, J., Moore, W., Foster, M., and Confer, K. (2011). Ethanol Blends and Engine Operating Strategy Effects on Light-Duty Spark-Ignition Engine Particle Emissions. *Energy Fuels*, 25 (11):4977–4985.
- UNECE. (2010). Uniform Provisions Concerning the Approval of Vehicles with Regard to the Emission of Pollutants According to Engine Fuel Requirements (83).
- Zheng, Z., Durbin, T., Karavalakis, G., Johnson, K., Chaudhary, A., Cocker, D., III; Herner, J., Robertson, W., Huai, T., Ayala, A., Kittelson, D., and Jung, H. (2012). Nature of Sub-23 nm Particles in the Solid Particle Measurement Method: A Real Time Data Perspective. *Aerosol Sci. Technol.*, 46 (7):886–896. doi: 10.1080/02786826.2012.679167.

2.6.3 Comprehensive Emission Characterisation of Exhaust from Alternative Fuelled Cars

P. Aakko-Saksa^{1*}, P. Koponen¹, J. Laurikko¹ N.-O. Nylund¹, P. Karjalainen², T. Rönkkö² and H. Timonen³

¹ VTT Technical Research Centre of Finland, VTT Espoo, Finland, paivi.aakko-saksa@vtt.fi

² Tampere University, Tampere, 33101, Finland

² Finnish Meteorological Institute, Helsinki, 00560, Finland

Keywords: alternative fuels, cars, emissions, unregulated, aldehydes, PM, mutagenicity, oxidative potential

Introduction

New renewable and alternative fuels are introduced in the transport sector, and also engine and exhaust aftertreatment technologies develop. Valid and comparable data is needed both on the direct and indirect effects of these new technologies to enable wide-ranging decision-making to increase competitiveness of the best low-emission technologies and to avoid investment in the harmful technologies that could lead to new emission-related problems. In this respect, real-time measurements are increasingly important to monitor (both gaseous and particle) emissions during transient driving and after cold-starts, when the emission level is typically at the highest.

Regulated emissions (carbon monoxide, total hydrocarbons, nitrogen oxides, particulate matter, particle number emissions) from new cars have been studied more extensively than unregulated emissions. Furthermore, emissions may be elevated emissions at certain driving conditions, e.g. during cold-starts. For example Saliba et al. (Saliba et al., 2017) observed that emissions during cold-starts dominated emissions from the gasoline cars certified to most stringent emission regulation in the California. Suarez-Bertoá and Astorga (Suarez-Bertoá and Astorga, 2018) found challenges with Euro 6 cars in meeting the emission limits at cold ambient temperatures. Yang et al. (Yang et al., 2015) observed that 73 Euro 6 diesel cars tested met the legislative limits, however, emission factors rose dramatically over the more realistic driving cycle. Triantafyllopoulos et al. (Triantafyllopoulos et al., 2018) found potential of exhaust aftertreatment devices to effectively reduce NO_x emissions from a typical Euro 6 diesel vehicle under real driving conditions.

For alternative fuels and new engine and exhaust aftertreatment technologies, exhaust composition can be different from that for the traditional technologies. Toxicity, mutagenicity, and carcinogenicity of exhaust can also vary. However, emission results for new cars using alternative fuels are scarce, and particularly as concerns unregulated emissions. The goal here was to investigate comprehensively emissions from Euro 5 and Euro 6 cars. Exhaust emission characterization included regulated emissions, individual hydrocarbons (e.g. methane and aromatic compounds), carbonyls (e.g. formaldehyde and acetaldehyde) and nitrogen containing species (e.g. nitrogen dioxide, nitrous oxide and ammonia), based on real-time measurements or extractive sampling combined with several analytical principles. Additionally, semivolatile organic compound (SVOC) and particulate matter (PM) were collected and analysed for e.g. polycyclic aromatic hydrocarbons (PAHs), mutagenicity (Ames test) and oxidative potential. Main focus was given on the results obtained at -7 °C temperature to indicate potential risks related to real-driving conditions, where emission control devices are not necessarily performing optimally. Emissions obtained at normal temperature (+23 °C) as well as results from the older cars are shown in Appendix 1. The Euro 2 diesel car was tested as a reference in the same measurement campaign as the Euro 6 cars to achieve comparable results without uncertainties related to possible changes in laboratory procedures and methods over the years. Advanced engine and exhaust aftertreatment technologies clean up exhaust emissions from cars substantially, however, there are still differences between technologies adapted for alternative fuels.

Experimental procedures

The cars tested included Euro 5 and Euro 6 passenger cars using gasoline, diesel, E85, E100 and CNG fuels. European driving cycle (NEDC) according to the UN ECE R83 was used in the tests. Cars were tested mainly at -7 °C, and selectively at +23 °C. More details of testing procedure, cars and fuels are found in the reports cited in Table 1.

Table 1: Cars tested.

Emission class	Car	Fuel	Temperature (°C)	Reference
Euro 5	MPFI	E10	+23, -7	(Roslund <i>et al.</i> , 2014)
Euro 5	MPFI Hybrid	E10	+23, -7	"
Euro 5	DISI 1	E10	+23, -7	"
Euro 5	DISI 2	E10	+23, -7	"
Euro 5	FFV 1	E10, E85	+23, -7	"
Euro 5	FFV 2	E10, E85	+23, -7	"
Euro 5	Diesel 1	Diesel	+23, -7	"
Euro 5	Diesel 2	Diesel	+23, -7	"
Euro 5	Diesel 3	Diesel	+23, -7	"
Euro 6	DISI	E10	-7	(Aakko-Saksa, Roslund and Koponen, 2017)
Euro 6	FFV	E85	-7	"
Euro 6	Diesel	Diesel	-7	"
Euro 6	NGV	CNG	-7	"
Euro 2	Diesel	Diesel	-7	"
Euro 5	FFV-DISI	E85, E100	+23, -7	(Aakko-Saksa <i>et al.</i> , 2014)
Euro 4	FFV-MPI	E85, E100	+23, -7	"
Euro 2	Diesel	Diesel	+23, +5, -7	(Aakko and Nylund, 2003)
Euro 2	Diesel (IDI)	Diesel	+23, +5, -7	"
Euro 3	MPI	E0	+23, +5, -7	"
Euro 3	DISI	E0	+23, +5, -7	"
Euro 3	FFV	E85	+23, +5, -7	"
Euro 2	NGV	CNG	+23, +5, -7	"
Euro 3	LPG	LPG	+23, +5, -7	"

MPFI = multi point fuel injection; DISI = direct injection spark ignited; IDI = indirect injection; FFV = flexible fuel vehicle; NGV = Natural gas vehicle; CNG = Compressed natural gas; LPG = liquefied petroleum

Equipment used in the measurement of carbon monoxide (CO), total hydrocarbons (HC), and nitrogen oxide (NO_x) emissions conforms to the specifications of the UN ECE R83. Regulated HC emission measured with flame ionisation detector (FID) detects all carbon-containing compounds, also oxygenates (Sandström-Dahl, Erlandsson and Gåsste, 2010). Although response factors are not adjusted, the FID results represent rather a sum of volatile organic compounds (VOCs) than hydrocarbons in the exhaust gas, and thus called VOC emission hereinafter. In the calculation, the VOC density of 0.619 g/dm³ was used, except 0.923 g/dm³ for the FFV/E85 (EC regulation 692/2008).

A number of gaseous compounds, e.g. ethanol, ammonia (NH₃) and nitrous oxide (N₂O) were measured on-line at one-second intervals using Fourier Transformation Infra-Red (FTIR) equipment (Gasmet Cr-2000). Aldehydes were collected from the CVS diluted exhaust gas using 2,4-dinitrophenylhydrazine (DNPH) cartridges. The DNPH derivatives were extracted with acetonitrile and analysed using HPLC technology (Agilent 1260, UV detector, Nova-Pak C18 column). Aldehydes analysed are formaldehyde, acetaldehyde and nine other carbonyl compounds. C1-C8 hydrocarbons were analysed by the gas chromatograph (HP 5890 Series II, Al2O₃, KCl/PLOT column, FID-detector, an external standard method) from the diluted exhaust gas fed from the same Tedlar bags as used for the measurement of the regulated emissions. HCs analysed are methane, ethane, ethene, propane, propene, acetylene, isobutene, 1,3-butadiene, and BTEX aromatics (benzene, toluene, ethyl benzene and m-, p-, and o-xylenes).

Standard PM sampling system with filter holders with diameter of 47 mm was used for samplings for anions (sulphates, nitrates), elemental carbon (EC), organic carbon (OC) and SVOC. For anion sampling, Pallflex® TX-40 were used and capillary electrophoresis for analyses (based on the SAEJ1936 and IP 416 guidelines). For EC/OC, Munktell MK 360 quartz filters had been heated in an oven at 700 °C for 1 hour and stabilized prior sample collection. EC/OC was evaluated using thermal-optical analysis (TOA) by Sunset 4L analyser. SVOC fraction was collected using Empore SDB-XC disks placed instead of standard back-up filters in the PM sampler (primary filters TX-40).

High-capacity collection system (in-house, see (Kokko *et al.*, 2000)) was used for the PM sampling for PAH, Ames and DTT analyses. The system included a dilution tunnel (Ø 265 mm), a sample probe (Ø 80 mm), two filter holders in parallel (Ø 142 mm), a blower (Siemens ELMO-G), a flow meter

(Bronkhorst) and a controller (Stafsjö). The sample flow can be controlled to obtain appropriate masses of particles. Here the flow was from 200 to 1500 L/min depending on car measured, and two Fluoropore 3.0 µm FSLW Ø 142 mm filters were used in parallel. After weighing (a Sartorius SE2-F microbalance) the filters were wrapped in aluminum foil and stored in freezer to protect them from light, and to avoid changes that could affect the mutagenicity results from the samples. At MetropoliLab, 24 individual PAH compounds were analysed from the Fluoropore filters and Empore disks according to ISO 16000-6:2011, EN 14662-4:2005 analysis method. The filters and disks were extracted with toluene in ultrasonic bath. For biological tests by Biosafe Biological Safety Solutions Ltd, fluoropore filters and Empore disks were extracted at NabLabs laboratories and VTT Expert Services by Soxhlet extraction (16 h, low level light) using dichloromethane, after which the solvent was changed into 1 mL DMSO for microAmes samples. Ames and microAmes Salmonella typhimurium reverse mutation test with and without metabolic activation (rat liver fraction S9) was used with Salmonella typhimurium strain TA98. DMSO was used as solvent control. 4-nitroquinoline 1-oxide (4-NQO) and 2-amino anthracene were used as positive control without and with S-9 mix, respectively. Role of nitro-PAH-type compounds can be studied using tester strains TA98 and the nitroreductase-deficient TA98NR in parallel. Oxidative potential tests with the DTT assay was performed according to Charrier & Anastasio (2012) except that 200 µM DTT in Chelex treated 0.10 M phosphate buffer (77.8 mM NaH₂PO₄ and 22.2 mM KHPO₄) was used and OD 412 nm measurements were performed after 5, 10, 15, and 20 minutes.

Non-volatile (solid) particle number emission (PN) was measured by the procedure in compliance with the Euro 6 emission regulation (EU No 133/2014). The butanol Condensation Particle Counter (bCPC) used was Airmodus A23 (23 nm to 2.5 µm).

Results and discussion

Nitrogen containing emission species

Expectedly, the NO_x and nitrogen dioxide (NO₂) emissions were the highest for the diesel cars regardless of their Euro class. NO_x emission consists mainly of NO, which is formed in combustion process from nitrogen and oxygen of intake air, particularly in the presence of excess air of diesel engines. At -7 °C, the NO_x emissions for Euro 2 and 5 diesel cars were substantially high. Euro 2 diesel cars had no NO_x reduction technologies, which explains their high NO_x emissions. High NO_x emissions for Euro 5 cars at -7 °C demonstrated vulnerability of their NO_x reduction technologies. Besides high NO_x emissions at low test temperature, Euro 5 diesel cars had substantial NO_x emissions at +23 °C (3 cars +23 °C: 190; 180 and 440 mg/km; note Euro 5b limit 180 mg/km). Euro 6 diesel car had high NO_x emissions at -7 °C (460 mg/km) particularly when considering the Euro 6 limit at +23 °C is for diesel cars (80 mg/km, for gasoline cars 60 mg/km). However, NO_x emission level of the Euro 6 diesel car was much lower than that of the Euro 5 diesel cars. The lowest NO_x emission (16 mg/km) was observed for the Euro 6 FFV/E85 car. NO₂ emissions were the highest for the Euro 5 and 6 diesel cars of all the cars tested.

Nitrous oxide (N₂O) emission was high for diesel cars, while ammonia (NH₃) emission was high for the three-way catalyst (TWC) equipped spark-ignition (SI) cars (Fig. 1). Formation of NO₂, N₂O and NH₃ are not typically related to combustion of fuel in engine, whereas they are induced by the catalyst chemistry in the exhaust aftertreatment systems (see e.g. (Mejía-Centeno, Martínez-Hernández and Fuentes, 2007) (Aakko-Saksa *et al.*, 2014)) and NH₃ also by the urea-based NO_x reduction system (selective catalytic reduction, SCR). N₂O emissions for the Euro 2, 5 and 6 diesel cars varied from 10 to 16 mg/km. For the Euro 6 SI cars, N₂O emissions were between 0.1 and 0.5 mg/km, and for Euro 5 SI cars slightly higher. N₂O is a strong greenhouse gas with CO₂ equivalence factor of 298. In the US, tailpipe N₂O emission limit is 10 mg/mile (www.dieselnet.com 5.7.2016), which was exceeded by the diesel cars tested here. However, measurement methodology here was different from that used in the US. The highest ammonia emissions were measured for SI cars, and the lowest emissions for diesel cars (e.g. 0.4 mg/km for Euro 6 diesel). Ammonia emission for Euro 6 gasoline car and for FFV/E85 was 2-3 mg/km, and for NGV/CNG car 6 mg/km. Atmospheric ammonia originates mainly from agricultural sources.

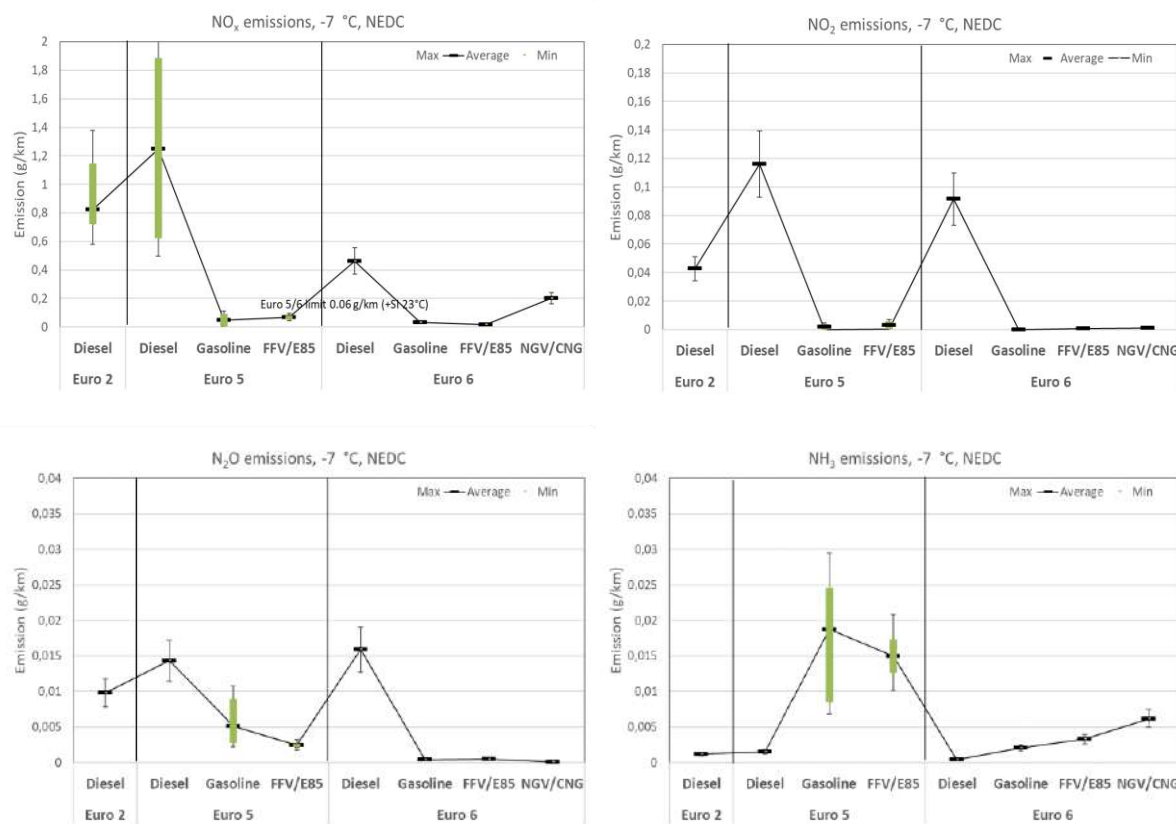


Figure 1: NO_x , NO_2 , N_2O and NH_3 emissions. NEDC at -7 °C.

Carbon monoxide and volatile organic compounds

The highest VOC and CO emissions at -7 °C were found for the gasoline fuelled SI cars and FFV/E85 (e.g. VOC 0.48 g/km and CO 2.7 g/km for Euro 6) (Fig 2). CO emissions of all cars were below the Euro 6 limits at +23 °C, but increased substantially for SI cars when moving from normal to low test temperature. Control of VOC and CO emissions seemed to be particularly challenging for FFV/E85 and Euro 5 gasoline cars. The VOC and CO emissions were very low for diesel cars and for NGV/CNG even at -7 °C.

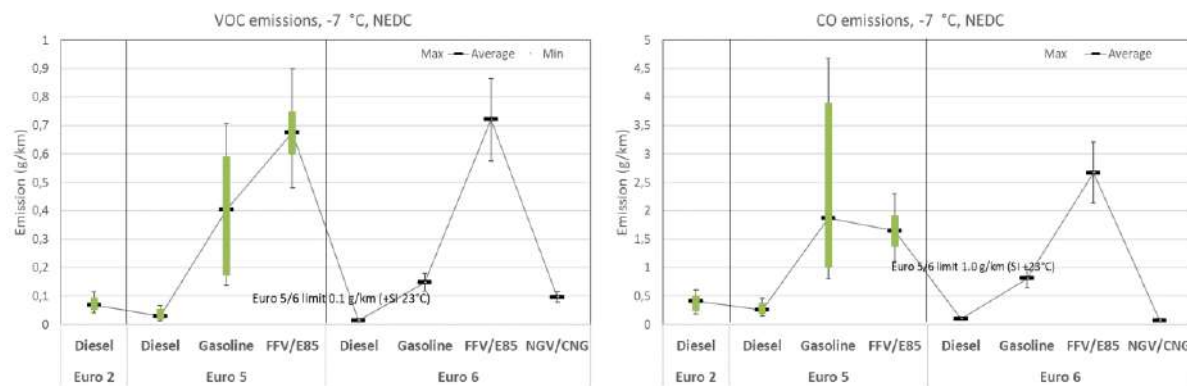


Figure 2: VOC and CO emissions, NEDC at -7 °C.

Results of the individual C1–C8 hydrocarbons and carbonyl compounds reveal dominating species in the VOC group of exhaust (Figs. 3–5).

Methane emission was the highest for NGV/CNG and FFV/E85 cars amongst cars studied. For the FFV/E85, VOC emissions composed mostly of methane and ethene. Sum of these emissions was higher

for FFV/E85 than for other SI cars, e.g. for Euro 6 FFV/E85 methane emission was 56 mg/km and ethene emission 40 mg/km. Methane is a greenhouse gas with a CO₂ equivalence factor of 28. In the US, tailpipe methane emission limit is 30 mg/mile (www.dieselnet.com 5.7.2016), which was exceeded by NGV/CNG and FFV/E85 cars tested here.

For the gasoline fuelled SI cars, the aromatic BTEX compounds were dominating VOCs both at +23°C and at -7 °C. Presence of aromatic compounds in the exhaust gas depends on the amount of aromatic compounds in fuel. BTEX emissions for SI cars increased at low test temperature, e.g. for Euro 5 car BTEX emissions increased from 17.8 to 141 mg/km when moving from +23 °C to -7 °C test temperature. For Euro 6 gasoline car, the highest BTEX emission observed was 41 mg/km. Both Euro 6 CNG and diesel cars had very low BTEX emissions (0.3-0.4 mg/km), one tenth of those for gasoline cars. For diesel cars, C1-C8 hydrocarbon emissions were low when compared with the SI cars at -7 °C, whereas at +23 °C differences in C1-C8 emissions between cars were rather small.

Emission level of 1,3-butadiene was very low for all the cars tested, e.g. in maximum 1.9 mg/km for Euro 5 cars at -7 °C.

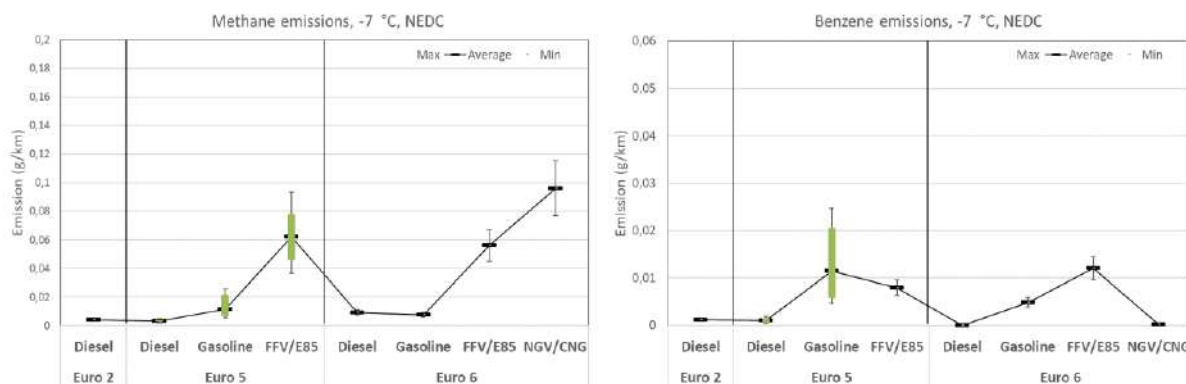


Figure 3: Methane and benzene emissions analysed for Euro 2 diesel and Euro 6 cars. NEDC at -7 °C.

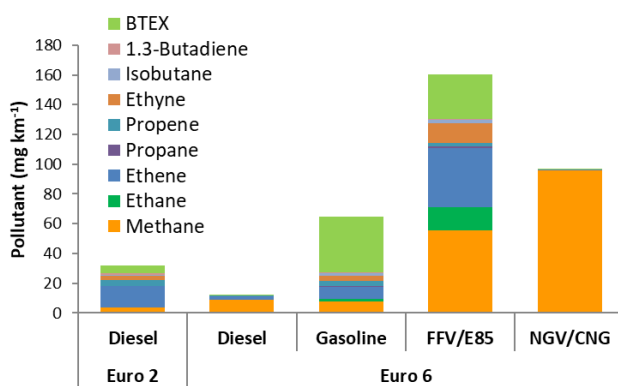


Figure 4: Individual C1-C8 emissions analysed for Euro 2 diesel and Euro 6 cars. NEDC at -7 °C.

Formaldehyde and acetaldehyde were dominating carbonyl compounds in the exhaust. In some cases, also benzaldehyde and crotonaldehyde emissions were notable at -7 °C.

The aldehyde (particularly formaldehyde) emissions were the highest for the Euro 2 diesel car, while the lowest for the Euro 6 diesel car having diesel particulate filter (DPF). The formaldehyde emission for Euro 2 diesel car was even as high as 18 mg/km, and high also for the Euro 5 diesel cars (higher than for the SI cars tested), while formaldehyde emission from Euro 6 diesel car was extremely low (0.3 mg/km). Aldehyde emissions were low for the gasoline cars at +23 °C, though they increased when moving to -7 °C. An exception was the MPFI hybrid that had low aldehyde emissions at both temperatures. Low aldehyde emissions were detected also for NGV/CNG car.

Formaldehyde emissions for Euro 6 FFV/E85 car were low, whereas slightly elevated for Euro 5 FFV/E85 cars. A known hurdle for the FFV/E85 cars are high acetaldehyde and ethanol emissions, which increased also here as the test temperature decreased (e.g. from 8.0 mg/km to 52.6 mg/km for a Euro 5 FFV/E85). Even for Euro 6 FFV/E85 car, high acetaldehyde emission was detected for (24.6 mg/km), significantly higher than that for other Euro 6 cars.

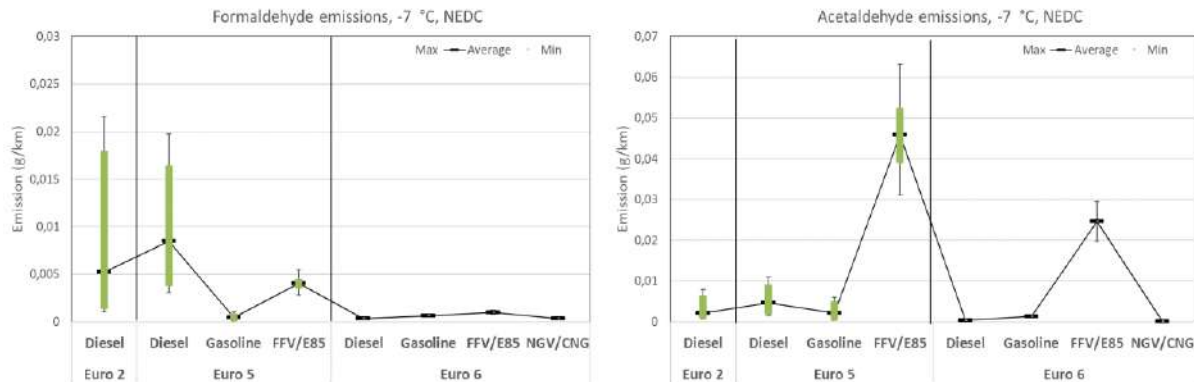


Figure 5: Formaldehyde and acetaldehyde emissions, NEDC at -7 °C.

High ethanol emission was detected for FFV/E85 cars, especially at -7 °C, for example 533 mg/km Euro 6 FFV/E85. Additionally, ETBE emissions were elevated (11 mg/km). Gasoline car using E10 fuel had ethanol emissions of 6 mg/km, and ETBE emissions were below the detection limit. Acetic acid emissions were observed for Euro 2 diesel (21 mg/km) and Euro 6 diesel cars (2 mg/km). Ethanol, ETBE and acetic acid were not measured for other cars.

SVOC, PM, EC, OC, anions and PN emissions

The PM emission measurements from cars are standardised and widely studied, while SVOC emissions from cars are not well-known. SVOCs are compounds that are sufficiently volatile to be in vapor form at the temperature of engine-out exhaust, but condensable under atmospheric conditions. Most SVOC molecules have at least 14 carbon atoms and boiling points from 240 to 400 °C. SVOCs may contain, besides other compounds, for example harmful PAHs, dioxins and nitro-PAHs (US EPA 40 CFR 1065.1103–1111). Phase partitioning of SVOC compounds vary depending on their concentration and saturation pressure, the other constituents of exhaust gas and sampling parameters. This will lead to differences in the SVOC results depending on the collection principles selected. In these measurements, SVOCs were collected using Empore disks from the diluted exhaust gas after PM filters (more details in Aakko-Saksa et al. 2014).

Results indicate higher SVOC emissions than the PM emissions for all cars tested (Fig. 6). Surprisingly, very high SVOC emission was observed for Euro 6 diesel car. Unfortunately, more detailed analysis of the chemical composition of the SVOC sample was not be conducted (except PAH analyses presented later). Back-up filter of PM sampling method captures some SVOCs, however, in-depth research would be needed to understand which compounds are captured with different sampling methods.

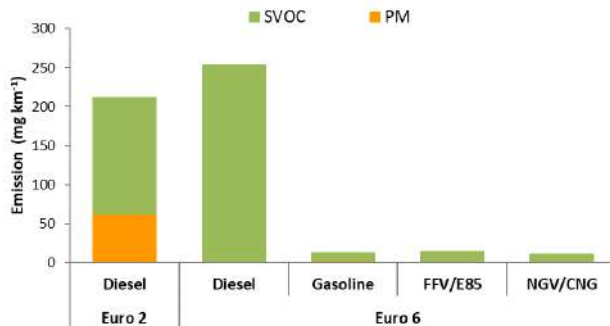


Figure 6: PM and SVOC emissions for Euro 2 diesel car and Euro 6 cars. NEDC at -7 °C.

The highest PM emission (63 mg/km) was measured for Euro 2 diesel car (without DPF, Fig. 7). For all Euro 5 cars, PM emissions at +23 °C were below the Euro 5/6 limit (5 mg/km), while DISI car had PM emission of 7.3 mg/km at -7 °C. For Euro 5 cars, the highest PM emissions were observed for three SI cars using E10 gasoline at +23 °C and at -7 °C. PM emission level was low for FFVs using E85 fuel, i.e. 2.8 mg/km at -7 °C, but elevated when using E10 fuel (14 mg/km). Low PM emissions for FFV/E85 were reported also by Timonen et al. (Timonen et al., 2017). The lowest PM emission (0.48 mg/km) was measured for Euro 6 CNG car.

Composition of PM emissions (EC, OC and anions) are rarely studied. Here we found that for diesel car, share of EC of total PM was 50-60% and OC 30-40% (total carbon 90-98% of PM). For E10 fuelled SI car, EC was 50% and OC 50%, while for FFV/E85, EC was 5% and OC 31%. PM emission contained very low amounts of anions. Sulphate and nitrate emissions were low even for the Euro 2 diesel car, both at level of 0.125 mg/km, and lower for Euro 6 diesel car (nitrate emission 0.053 mg/km). Anion emissions for gasoline, FFV/E85 and NGV/E85 were below the detection limit.

Particle number (non-volatile >23 nm) emission was the highest for the Euro 2 diesel car ($1.28E+14$ #/km), while the lowest for the Euro 6 diesel car having DPF ($5.62E+09$ #/km) and for NGV/CNG ($6.63E+10$ #/km). The respective PN emission observed for Euro 6 gasoline car ($7.63E+11$ #/km) and FFV/E85 ($7.49E+11$ #/km) were close to the Euro 6 limit at +23 °C ($6.0E+11$ #/km; until 09/2017 for DISI $6.0E+12$ #/km).

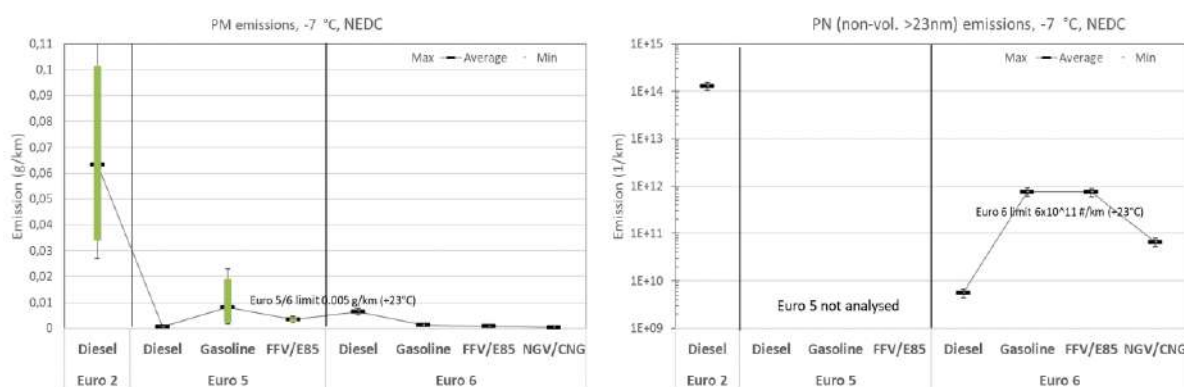


Figure 7: PM and PN emissions, NEDC at -7 °C.

PAH emissions, oxidative potential and Ames tests

Emissions of 7 priority PAHs were present mainly in PM phase (Fig. 8), while a wider set of priority PAHs, so called EPA 16 PAHs, were present mainly in SVOC phase (Fig. 9). Euro 2 diesel car, and Euro 6 FFV/E85 and gasoline cars had the highest priority PAH emissions in SVOC phase, while Euro 6 NGV/CNG and diesel cars had the smallest level of PAHs in SVOC-phase. PAH emissions from SVOC phase were not analysed for Euro 5 cars.

The Euro 6 NGV/CNG and modern diesel cars were the lowest emitters of 7 PAHs in PM phase, while the highest emitters were the Euro 5 gasoline cars. Euro 6 NGV/CNG and diesel cars had hardly detectable emissions of priority 7 PAHs. For all the Euro 5 cars tested, sum of 7 PAHs in PM emission considerably increased when moving from +23 to -7 °C. The sum of 7 PAHs in PM emission at +23 °C for SI cars were 0.1–1.3 µg/km, while 4.5–43 µg/km at -7 °C excluding MPFI hybrid (0.5 µg/km). Priority 7 PAH emissions in PM for the new diesel cars were below 0.10 µg/km for combined sample from the tests at +23 and -7 °C. Priority 7 PAH emissions were lower for the FFV cars when using E85 than when using gasoline.

From 7 priority PAHs, the most dominant were benzo(a)pyrene, benz(a)anthracene, benzo(b)fluoranthene and indeno[1,2,3-cd]pyrene. For gasoline car and FFV/E85, the highest priority PAH emission was found for benzo(ghi)perylene (1.0 µg/km). Benzo(a)pyrene emissions were higher for Euro 2 diesel (0.8 µg/km), gasoline (0.5 µg/km) and for FFV/E85 (0.4 µg/km) than for Euro 6 diesel (0.006 µg/km). From lighter PAHs analysed, the Euro 2 diesel had phenanthrene as the main PAH compound in PM (9.5 µg/km), and the next were pyrene (5.8 µg/km) and fluoranthene (5.7 µg/km).

The oxidative potential was indicatively the highest for the Euro 2 diesel car, both for PM and SVOC phases considered (Fig. 9). Additionally, Euro 6 diesel car showed potentially harmful SVOC emission in this respect. The next highest oxidative potentials were observed for SVOC from Euro 6 gasoline and FFV/E85 cars. Oxidative potential for NGV/CNG car was very low. For other cars than NGV/CNG and Euro 2 diesel, the oxidative potentials of SVOC was higher than that of PM.

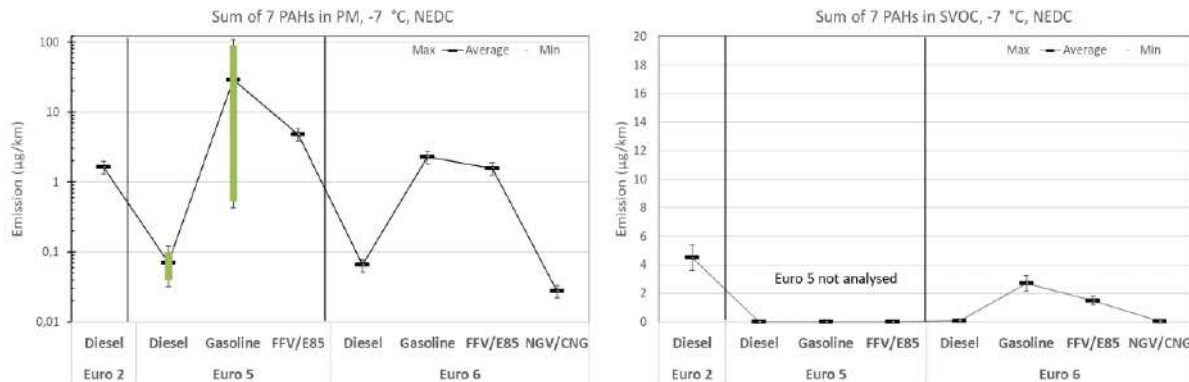


Figure 8: PAH emissions, NEDC at -7 °C.

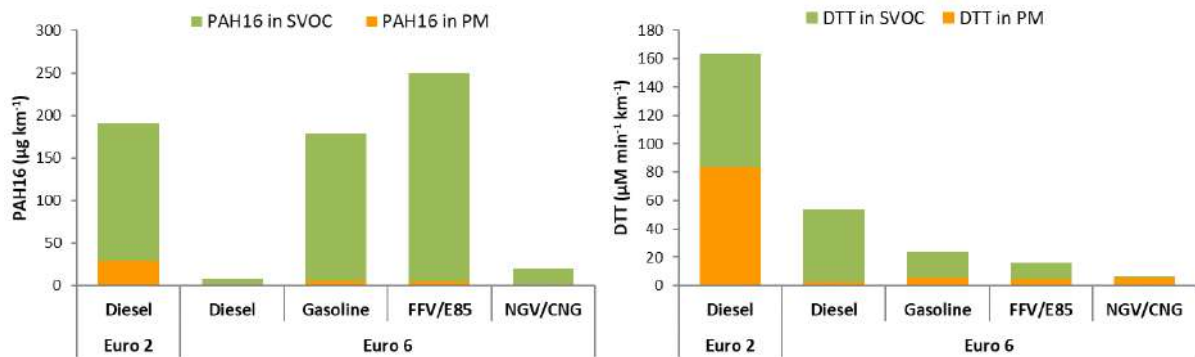


Figure 9: Sum of 16 PAHs and oxidative potential (DTT assay) associated in PM and in SVOC. Euro 2 diesel car and Euro 6 cars. NEDC at -7 °C.

In the Ames test, all the PM samples were mutagenic, while the SVOC samples only from diesel cars were mutagenic when tested for indirect mutagenicity (i.e. after metabolic activation, +S9 mix, induced e.g. by PAHs). Euro 2 diesel car was not tested for mutagenicity in these studies. Earlier tests in the same laboratory showed for Euro 3 cars mutagenicity results below 10 krev/km (TA98-S9) (Rantanen *et al.*, 2005), while for Euro 0 cars over 100 krev/km (Kokko *et al.*, 2000). However, comparisons between project is difficult as Ames test is regarded rather qualitative than quantitative. Indirect mutagenicity was very low for Euro 5 diesel cars (below 2 krev/km) due to low PM emission (per km) despite of very high specific mutagenicity (rev/mg). The highest PM emission associated indirect mutagenicity was exhibited by gasoline fuelled DISI cars, which is largely attributable to the high PM emissions (per km) by these cars. FFV/E85 indicated low amount of mutagens. The lowest mutagenicity was observed for NGV/CNG car. A few samples were studied also with TA98 strain without metabolic activation and with the TA98NR (-S9 mix) to study role of direct acting mutagens and specifically, nitro-PAHs³. Results indicated that the role of indirect-acting mutagens is substantial when compared to direct-acting mutagens. Nitro-PAHs seemed not to be present in the PM from DISI and FFV cars, except possibly for one FFV car (TA98: 19 krev/km vs. TA98NR: 4.8 krev/km).

³ Mutagenicity in TA98 but not in TA98NR indicates presence of nitro-PAHs (direct-acting mutagens).

Conclusions

Emissions from Euro 5 and 6 cars using traditional and alternative/renewable fuels were studied comprehensively in challenging testing conditions, at cold ambient temperatures. Differences in exhaust emissions were observed between cars using conventional and alternative fuels, as well as between cars representing different emission classes.

- For diesel cars, NO_x, NO₂ and N₂O emissions were elevated indicating need for further control of these emission components. Formaldehyde emission was low for Euro 6 diesel cars, however, substantial for older diesel cars.
- Exhaust emissions from NGV/CNG were generally low. However, methane emissions from these cars were elevated and deserve further attention.
- For FFV/E85, the PM emissions were low, whereas acetaldehyde and methane emissions were elevated. Furthermore, emission performance was worse when using conventional gasoline in FFVs than in cars designed for gasoline only.
- Non-volatile PN emissions were higher than desired for many of the cars tested.
- SVOC emissions and related PAHs need further research, particularly as regards observations made for the Euro 6 diesel car.

All in all, emission performance improved significantly when moving from Euro 5 to Euro 6 cars, although some advances are still needed. The engine-out exhaust emissions from cars seems not to have decreased, except potentially for hybrid cars, and thus correct operation of the emission control technologies is increasingly important. Some emissions components are still higher than desired in challenging testing conditions (e.g. methane emission for NGV/CNG and NO₂/N₂O for diesel). Additionally, some new observations need attention, specifically, SVOC emission from a Euro 6 diesel car was surprisingly high, and its composition and effects on human health and environment are unknown. Generally, emission performance of Euro 6 cars was promising in this study, although we note that a few cars studied are not a representative sample of the wide spectrum of technologies introduced to meet the most stringent emission legislation.

Acknowledgements

The measurements belong to the BioPilot (40223/13) and EFFICARUSE projects in Finland, and to within two projects of the Advanced Motor Fuels (AMF, www.iea-amf.org), which is one of the International Energy Agency's (IEA) transportation related Technology Collaboration Programmes. IEA AMF projects were Annex 44 "Unregulated Pollutants Emissions of Vehicles Fuelled with Alcohol Alternative Fuels" and Annex 22 "Particulate Emissions at Moderate and Cold Temperatures Using Different Fuels". The financial support from Business Finland and from industrial partners is gratefully acknowledged. Authors are deeply grateful to all persons involved in the measurements, particularly to Hannu Vesala, Timo Murtonen, Tommi Hangasmaa and former VTT's employees Piritta Roslund and Reijo Mikkola.

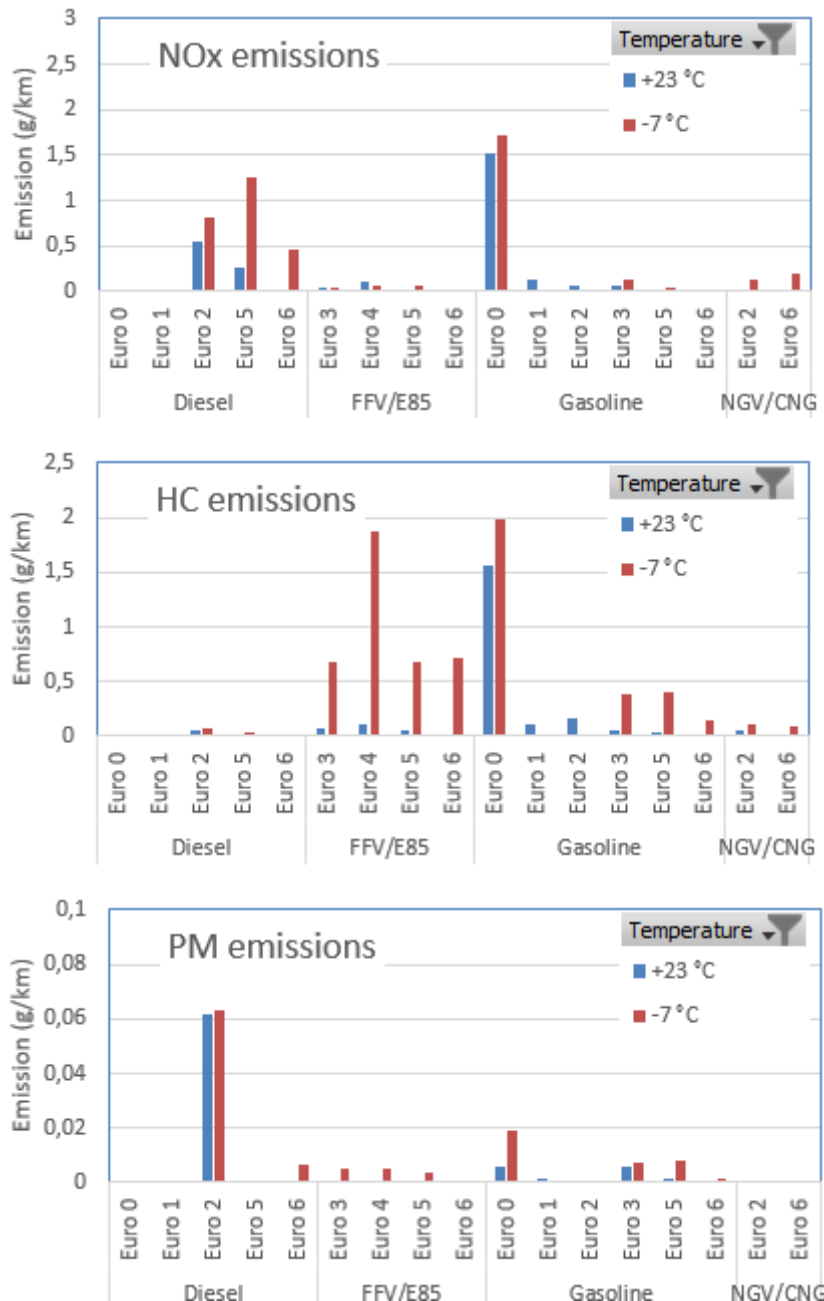
References

- Aakko-Saksa, P. et al. (2014) 'Research on Unregulated Pollutants Emissions of Vehicles Fuelled with Alcohol Alternative Fuels – VTT 's contribution to the IEA-AMF Annex 44 (VTT-R-03970-14)', p. 35.
- Aakko-Saksa, P., Roslund, P. and Koponen, P. (2017) 'Development and validation of comprehensive emission measurement methods for alternative fuels at VTT (VTT-R-04494-16)', pp. 1–104.
- Aakko, P. and Nylund, N.-O. (2003) 'Particle emissions at moderate and cold temperatures using different fuels', *SAE Technical Papers*. doi: 10.4271/2003-01-3285.
- Kokko, J. et al. (2000) 'Reduced particulate emissions with reformulated gasoline', *SAE Technical Papers*. doi: 10.4271/2000-01-2017.
- Mejía-Centeno, I., Martínez-Hernández, A. and Fuentes, G. A. (2007) 'Effect of low-sulfur fuels upon NH₃and N₂O emission during operation of commercial three-way catalytic converters', *Topics in Catalysis*, 42–43(1–4), pp. 381–385. doi: 10.1007/s11244-007-0210-2.
- Rantanen, L. et al. (2005) 'NExBTL - Biodiesel Fuel of the Second Generation'. doi: 10.4271/2005-01-3771.

- Roslund, P. et al. (2014) 'Unregulated emissions from Euro 5 emission level cars (VTT-R-04308-14)'.
- Saliba, G. et al. (2017) 'Comparison of Gasoline Direct-Injection (GDI) and Port Fuel Injection (PFI) Vehicle Emissions: Emission Certification Standards, Cold-Start, Secondary Organic Aerosol Formation Potential, and Potential Climate Impacts', *Environmental Science and Technology*. doi: 10.1021/acs.est.6b06509.
- Sandström-Dahl, C., Erlandsson, L. and Gässte, J. (2010) 'Measurement Methodologies for Hydrocarbons , Ethanol and Aldehyde Emissions from Ethanol Fuelled Vehicles', *Measurement*, pp. 1–20. doi: 10.4271/2010-01-1557.
- Suarez-Bertoa, R. and Astorga, C. (2018) 'Impact of cold temperature on Euro 6 passenger car emissions', *Environmental Pollution*. Elsevier Ltd, 234, pp. 318–329. doi: 10.1016/j.envpol.2017.10.096.
- Timonen, H. et al. (2017) 'Influence of fuel ethanol content on primary emissions and secondary aerosol formation potential for a modern flex-fuel gasoline vehicle', *Atmospheric Chemistry and Physics*, 17(8). doi: 10.5194/acp-17-5311-2017.
- Triantafyllopoulos, G. et al. (2018) 'Experimental assessment of the potential to decrease diesel NOxemissions beyond minimum requirements for Euro 6 Real Drive Emissions (RDE) compliance', *Science of the Total Environment*. Elsevier B.V., 618(x), pp. 1400–1407. doi: 10.1016/j.scitotenv.2017.09.274.
- Yang, L. et al. (2015) 'Experimental Assessment of NOx Emissions from 73 Euro 6 Diesel Passenger Cars', *Environmental Science and Technology*, 49(24), pp. 14409–14415. doi: 10.1021/acs.est.5b04242.

APPENDIX 1.

As a background, the results including some earlier projects here show that in some respect older diesel cars were rather insensitive towards test temperature when compared with the SI cars equipped with three-way catalyst (TWC), whereas this does not necessarily apply to Euro 5 and 6 cars.



2.6.4 Air Quality Impacts from Ethanol-blended Gasoline Deployment in China's Beijing-Tianjin-Hebei Region

Xinyu Liang¹; Ye Wu¹; Jiming Hao¹

¹ School of Environment, Tsinghua University, Beijing, China

Abstract

As a potential gateway to reducing oil dependency and improve regional air quality, applying ethanol gasoline has been booming in recent years. This study selects Beijing-Tianjin-Hebei region in China to investigate whether the deployment of ethanol gasoline can improve future air quality. The Community Multiscale Air Quality (CMAQ) model enhanced by the two-dimensional volatility basis set module (2D-VBS) is applied to simulate the temporally and spatially changes in concentrations of PM_{2.5} and other pollutants' concentrations by future ethanol gasoline deployment scenarios. Results show that using ethanol gasoline (Scenario E2 and E3) can reduce average PM_{2.5} concentrations by up to 0.5 µg m⁻³ in 2030. The reduction is more significant under Scenario E3. However, using ethanol gasoline could increase ozone concentration, and the increasing ratio is below 2%. Under Scenario E3, the increasing is slighter. The increasing trend is also found in ambient NO₂ concentrations (<1%), and the increasing is more significant in the traffic-dense urban areas, like Beijing and Shijiazhuang city. Our results indicate that ethanol-blended gasoline deployment could effectively reduce PM_{2.5} concentraion and increasing NO₂ and ozone concentration, although the increasing is negligible.

1. Introduction

With the rapid growth of vehicle ownership in China, the fuel consumption for vehicles is increasing rapidly. According to statistics from the National Bureau of Statistics, China imported about 282 million tons of oil in 2013, 2.3 times that of 2004, and its dependence on foreign countries exceeded 60%. It is predicted that China's dependence on foreign oil will exceed 60% in 2020, and the International Energy Agency estimates that China's dependence on foreign oil will increase to 75% in 2030. Therefore, selecting reasonable and efficient clean fuel production technologies and alternative energy sources is very important.

Ethanol gasoline is an alternative energy source that combines fuel ethanol and ordinary gasoline, which are processed from grain or various plant fibers. According to China's national standards, the current ethanol gasoline is made up of 90% ordinary gasoline and 10% fuel ethanol. With the development of modern automobile and engine technology, the impact of alcohol replacement components on the emissions, economic and dynamic performance of engines and after-treatment systems needs to be studied in a targeted manner, through the relevant motor vehicle emission tests. And on this basis, vehicle emission inventories are developed and air quality impacts are simulated to quantify the environmental effects of deploying ethanol gasoline.

This study selects Beijing-Tianjin-Hebei region (BTH region) to quantitatively evaluate the environmental benefits of ethanol gasoline. BTH region is one of the regions with the most serious air pollution in China. At the same time, some cities in Hebei Province in BTH region have already popularized the use of ethanol gasoline. Therefore, choosing BTH region as a typical representative region, and analyzing the environmental benefits of ethanol gasoline promotion in this region, is representative and practical.

2. Methods

2.1 Definition scenarios of ethanol-gasoline blends deployment

This study is based on vehicle tests finished by our colleagues. The results of tests are presented in an unpublished paper. This study involves three types of gasoline, E2, E3, and E4. E2 and E3 are both ethanol gasoline, but there is differences about organic content between them. E2 has lower aromatic content (<20%), and E3 has lower olefin content (<10%). E4 is the widely used commodity gasoline.

Considering the actual situation and the research purpose of this study, the extreme scenarios of ethanol gasoline promotion are adopted (i.e., 100% gasoline vehicles are replaced by E2 and E3 gasoline), which can maximize the environmental impacts.

2.2 Emission inventories

As an essential input of air quality model, the detailed multi-sector spatio-temporal emission inventory has been developed. For all emission sectors except for on-road transportation (including power plants, industrial sectors, residential sectors, and agriculture activities), the emission inventory reported by Zhao et al., 2018 and Cai et al., 2018 are used as the baseline year (2015) and future year (2030). For on-road transportation, emission inventories reported by Wu et al., 2017 are applied. The emission inventoried include major air pollutants (e.g., NO_x, SO₂, primary PM_{2.5}, NH₃, and non-methane volatile organic compounds (NMVOC)).

The emission reductions under Scenarios E2 and E3 compared with Scenario base are calculated based on functions below.

$$E = E_1 + E_2 \quad (2-1)$$

$$E_1 = \sum_i P_i \times EF_i \times VKT_i \times 10^{-6} \quad (2-2)$$

$$E_2 = (EF_1 \times \frac{VKT}{V} + EF_2 \times 365) \times P \times 10^{-6} \quad (2-3)$$

$$\text{For NMVOC} \quad \Delta E\% = \frac{E_1 \times \theta \times \varepsilon + E_2 \times \varepsilon'}{E} \quad (2-4)$$

$$\text{For other pollutants} \quad \Delta E\% = \frac{E_1 \times \theta \times \varepsilon}{E} \quad (2-5)$$

In (2-1), E is emissions of on-road transportation sector, and E1 and E2 represent is the exhaust emissions and HC evaporative emissions, respectively. Except HC, the source of other pollutants is only exhaust emissions. In (2-2), EF_i is the emission factors of the i-type vehicle (the three-level classification of vehicles), grams/km. P is i-type vehicle population. VKT_i is the average annual mileage of vehicles of type i, kilometers per vehicle per year. In (2-3), EF₁ is the evaporative emission coefficient of vehicles during driving, grams/hour. V is the average running speed of vehicles, kilometers/hour. EF₂ is the comprehensive emission factors during the parking period. The coefficient mainly includes the emission coefficient during hot dip, day and infiltration, grams per day. Activity data, VKT data and emission factor of vehicles are derived from the China Urban Vehicle Emission Factor Model (EMBEV-CHINA) developed by Tsinghua University. In (2-4) and (2-5), θ indicates the proportion of gasoline vehicle emissions. ε indicates the proportion of changes in ethanol gasoline emission factors, and ε' indicates the proportion of changes in evaporation HC emission factors.

To develop the temporal inventory, time allocation files are applied. The hourly emissions allocations from the on-road transportation sector are estimated based on the diurnal fluctuations in traffic activity and average speeds for typical city (Beijing) in BTH region. Coupled with the spatial requirement by the grid-based air quality modeling, emissions from on-road are distributed based on the spatial density of traffic networks and the activity split within the urban areas for high-polluting freight trucks. Power plant emissions are explicitly calculated as large point sources according to power unit technology and location information. emissions from industrial and residential activities are distributed to the county-level based on economic quantity (i.e., gross domestic production, GDP) and further allocated to grid cells based on the spatial distribution of the resident population.

2.3. Air quality modeling

The Community Multiscale Air Quality (CMAQ) model (version 5.0.1) is applied to simulate the air pollutant concentrations under various fleet electrification scenarios. 2D-VBS simulation technology was incorporated into the CMAQ v5.0.1 model to improve the SOA simulation. The default SOA mechanisms applied by the CMAQ model have been criticized due to the large underestimation of SOA concentrations. As transportation is the important source of NO_x and VOC emissions, applying default mechanisms would significantly affect the evaluation results of air quality impacts from fleet electrification. The Weather Research and Forecasting (WRF) model is used to generate the meteorological conditions, and meteorological data from 2010 are applied as input for future scenarios. The modeling domain includes a coarse grid setup covering most of China and part of East Asia with a $36 \times 36 \text{ km}^2$ resolution, a medium grid setup covering East China with a $12 \times 12 \text{ km}^2$ resolution, and a fine grid setup over BTH region with a $4 \times 4 \text{ km}^2$ resolution. Fourteen vertical layers are defined in the modeling system for all grid setups. Detailed configurations of the CMAQ and WRF models are summarized in Table 1.

Table 1: Configurations of the CMAQ and WRF models in this study

WRF v3.7	CMAQ (v5.0.1) /2D-VBS
Planetary boundary layer: Mellor-Yamada-Janjic	Gas-phase chemistry scheme: SAPRC99
Microphysics: WSM3	Aerosol module: AERO6
Cumulus scheme: Grell-Devenyi ensemble	SOA module: 2D-VBS
Land surface layer: Noah	Horizontal advection scheme: Hyamo
Long/Short wave radiation: RRTM	Vertical advection scheme: Vwrf
	Horizontal diffusion scheme: Eddy diffusivity theory
	Vertical diffusion scheme: Acm2
	Dry deposition velocity: M3dry

3. Preliminary Results

3.1. Emission changes from Ethanol-gasoline Blends Deployment

The emission change ratio of the major primary pollutants (i.e., NO_x, PM_{2.5}, VOC, BC and OC) for the transportation sector in 2030 under Scenario E2 and E3 are presented in Fig.1, respectively. The decreasing primary PM_{2.5} and key components (BC, OC) can be observed under two scenarios. PM_{2.5} emission is calculated to reduce by 12% under Scenario E2 in BTH region. The decreasing ratio under Scenario E3 can reach to 16% in BTH region. In the region, the reduction benefit is maximized in Beijing because the contribution of gasoline vehicles among total vehicle fleets is the highest.

For NO_x, the emission is tested to increase when applying ethanol-gasoline. The increasing ratio among total fleets in 2030 is calculated to be 1-3% under two scenarios. The change trend of other precursor for SOA, i.e., VOC, is the opposite under two scenarios due to the change in evaporation emissions. 8-9% emission would be increased under Scenario E2 while 3% would be reduced under Scenario E3.

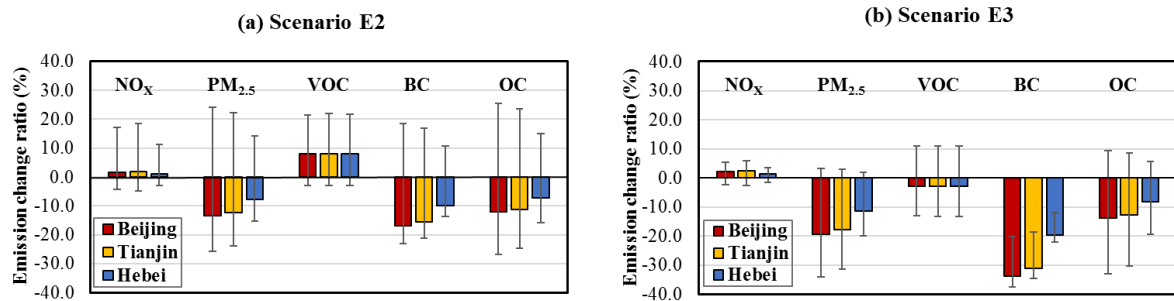


Fig. 1 Emission change ratio under Scenario E2 and E3 in BTH region

3.2. PM_{2.5}

Fig.2 presents the simulation results about PM_{2.5} concentration. The monthly average concentrations of PM_{2.5} under Scenario Base are simulated to be 38.4 ± 36.8 , $19.4 \pm 12.3 \mu\text{g m}^{-3}$ in January and August, respectively. The concentrations of PM_{2.5} show high values which exceed the annual-average limit of the National Ambient Air Quality Standard (NAAQS) ($35 \mu\text{g m}^{-3}$) across much of the Southeastern BTH region (e.g., Tianjin, several cities with heavy industries in Hebei province like Tangshan, Shijiazhuang and Xingtai).

The adoption of dedicated ethanol gasoline (both E2 and E3) vehicles causes decreases in monthly average PM_{2.5} concentrations in January and August except slight increase in some areas of BTH region in January under Scenario E2. The absolute change in monthly average concentrations of PM_{2.5} was simulated to be below $0.5 \mu\text{g m}^{-3}$ in both region and city level. Under Scenario E2, the change in monthly average PM_{2.5} concentration is slight in January ($\pm 0.1 \mu\text{g m}^{-3}$) in BTH region. In August, significant decreases were predicted to occur across urban areas of Beijing (about $0.2 \pm 0.1 \mu\text{g m}^{-3}$), Tianjin and several cities in Hebei province (i.e., Tangshan, Langfang, and Shijiazhuang). The similar spatial distribution of changes in PM_{2.5} concentrations can be observed in the Scenario E3. Larger PM_{2.5} reductions for Scenario E3 are restricted to a few (dark blue) areas in Fig. 2, mostly in Beijing (about $0.3 \pm 0.2 \mu\text{g m}^{-3}$), Tianjin, Tangshan and south Hebei (about $0.4 \pm 0.2 \mu\text{g m}^{-3}$) of BTH region.

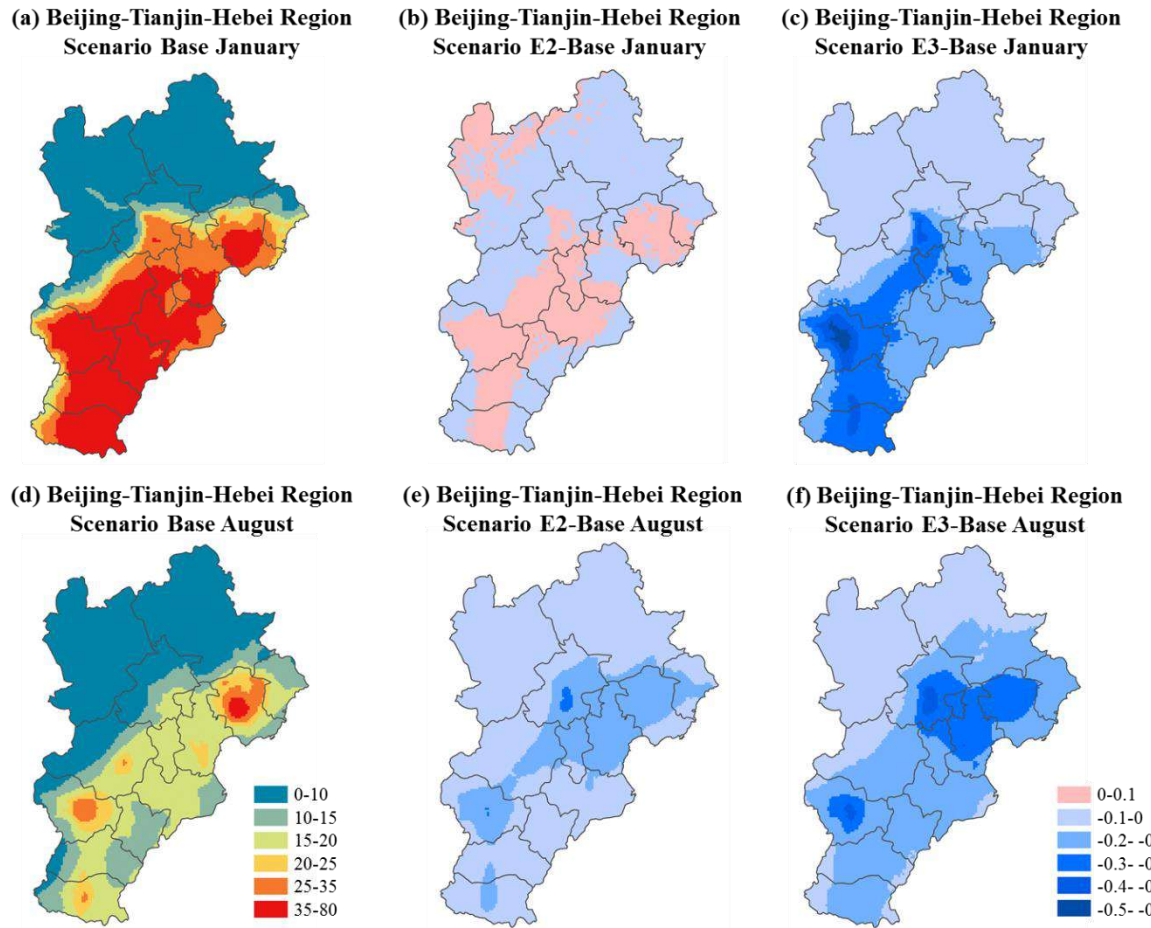


Fig. 2 Annual average PM_{2.5} concentration under Scenario base and concentration changes under two ethanol scenario in BTH region.

3.3. Ozone

Deploying ethanol-gasoline blends with low aromatics content (Scenario E2) is simulated to increase ozone concentration by 0.2-0.5 ppb (0.3-0.9%) in both months (shown in Fig.3). In this study, the indicator for ozone concentration is the daily average 8h-peak concentration of ozone. Greater increase is observed to occur in areas where ozone concentrations were relatively high in January. However, considering that the ozone concentration is lower than the national limit (75 ppb) under the Scenario base and the ethanol gasoline E2 promotion has the relatively low impact (<1%) on the ozone concentration, the negative impact brought by E2 gasoline can be ignored. Under Scenario E3, the impact is slighter compared with that under Scenario E2, with the change of ozone concentration below 0.2 ppb (<0.3%). In January, decreases were achieved whereas increases in ozone were estimated to occur in the north areas of BTH region. In August, the decrease was observed in areas where the ozone concentration was relatively high (e.g., Beijing, Tianjin, Shijiazhuang of BTH region).

The varied situation about ozone concentration changes can be attributed to the ozone formation characteristic which will be influenced by VOC and NO_x emission. NO_x emission increase show non-linear change in ozone concentration (Sillman et al, 2002). In January, due to the characteristic of VOC-sensitive areas, ozone concentration would decrease while in August, NO_x emission increase leads to the increase of ozone concentration. However, the changes in ozone concentration should also consider the changes of VOC emission. Under Scenario E2, VOC emission increase leads to the increase in ozone concentration, while ozone concentration would reduce under Scenario E2 due to the decrease of VOC emission. Generally speaking, the ozone concentration change can be attributed to the combine effect of VOC and NO_x.

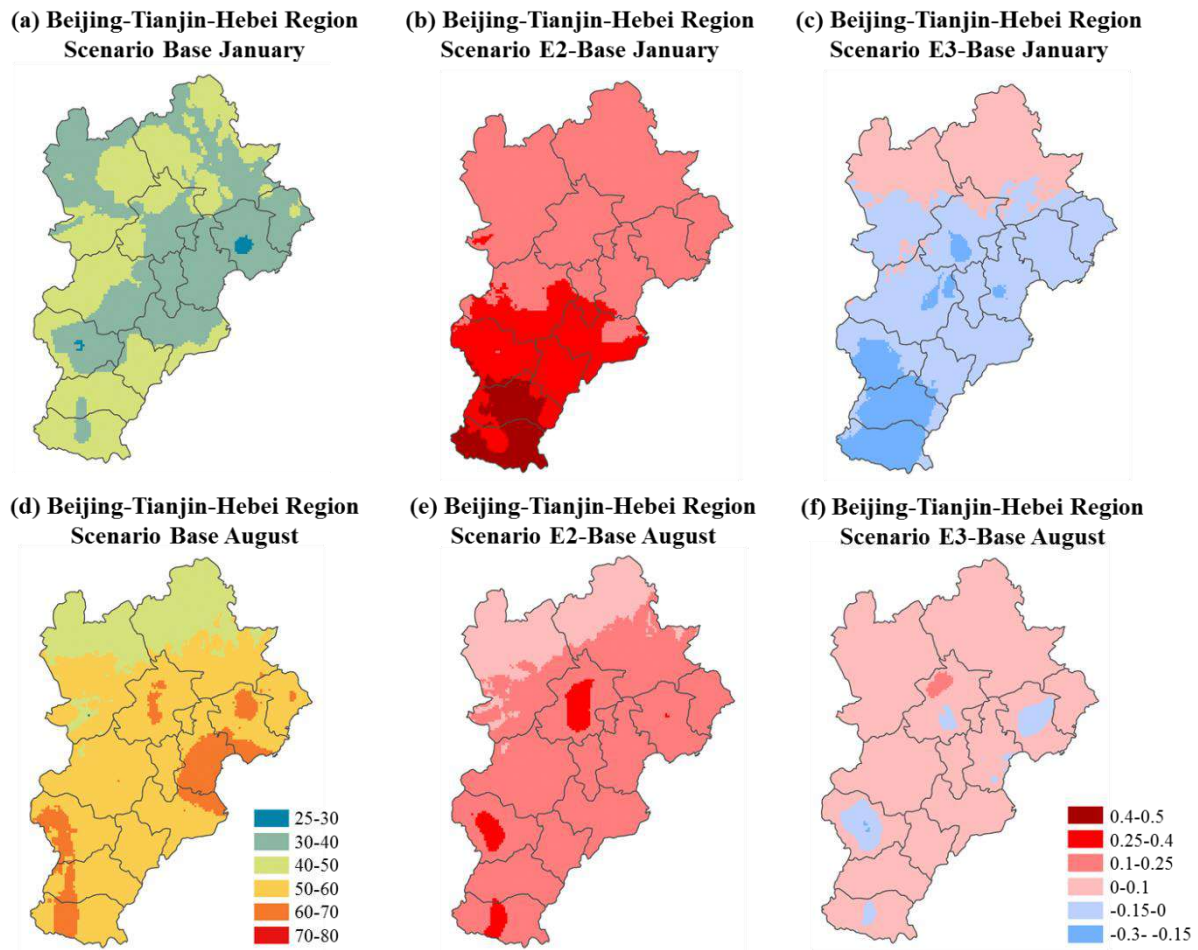


Fig. 3 Annual average of daily 8h-peak Ozone concentration and concentration changes

3.4. NO₂

Fig.4 shows that, ethanol-gasoline blends deployment results in significant increase in NO₂ emission. In BTH region, the monthly average NO₂ concentration will increase by 0.14 ± 0.17 ($0.4\%\pm0.3\%$), 0.12 ± 0.12 ($0.6\%\pm0.2\%$), 0.22 ± 0.15 ($0.7\%\pm0.3\%$), 0.16 ± 0.14 ($0.9\%\pm0.3\%$) $\mu\text{g m}^{-3}$ in January and August under Scenario E2 and E3, respectively. The spatial distributions of NO₂ concentration change show that greater increase occurs in traffic dense areas, like Beijing and the peripheral areas. Results show that, $0.4\text{-}0.5 \mu\text{g m}^{-3}$ ($0.7\%\text{-}1.5\%$) increase would be achieved in Beijing. However, the negative impacts caused by ethanol-gasoline blends are mostly below 1%.

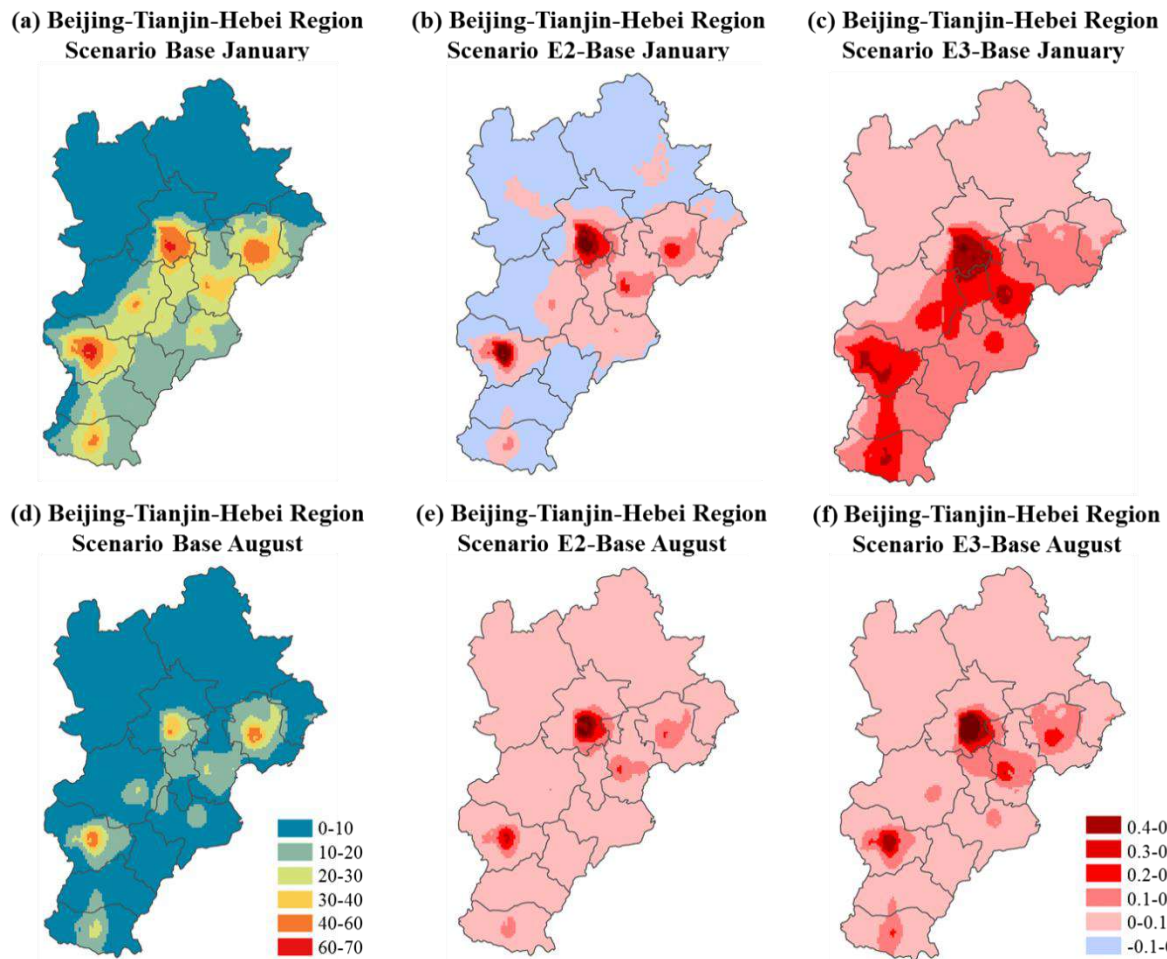


Fig. 4 Annual average NO₂ concentration under Scenario base and concentration changes

References

- Zhao B., et al (2018) Change in household fuels dominates the decrease in PM_{2.5} exposure and premature mortality in China in 2005-2015 *Proceedings of the National Academy of Sciences* 115(49): 12401-12406.
- Cai S.Y., et al. (2018) Impact of air pollution control policies on future PM_{2.5} concentrations and their source contributions in China. *Journal of Environmental Management* 227: 124-133.
- Wu, Y., et al. (2017) On-road vehicle emissions and their control in China: A review and outlook, *Sci. Total Environ.* 574: 332-349.
- Sillman S. and D. He (2002) Some theoretical results concerning O₃-NO_x-VOC chemistry and NO_x-VOC indicators. *Journal of Geophysical Research* 107(26):1-15.

2.6.5 Comparison of On-road Gaseous Emissions of a Best Seller Passenger Car with Different Powertrains: Diesel vs Gasoline vs Compressed Natural Gas

V. Valverde^{1}, P. and P. Bonnel¹*

¹ European Commission, Joint Research Centre (JRC), Ispra, Italy, victor.valverde-morales@ec.europa.eu

Introduction

Air pollution has been recognized by the World Health Organization as the single largest environmental risk to health worldwide (WHO, 2016). In the European Union (EU), exposure to unhealthy levels of Nitrogen dioxide (NO_2), Ozone (O_3), and fine particles (PM2.5) in the air causes 76 000, 16 400, and 391 000 premature deaths per year, respectively (EEA, 2018). In addition to its health effects, air pollution also results in considerable impacts on the environment (eutrophication, acid rain) and the economy through increase of healthcare costs, reduced growth of crops, reduced visibility, etc. (OECD, 2016).

Road transport is a major source of primary pollutants and greenhouse gases. In fact, in the EU 39% percent of the Nitrogen oxides emissions (NO_x), 20% of Carbon monoxide (CO), 9% of volatile organic compounds (VOCs), 11% of PM2.5, and 20% of greenhouse gases were emitted by road transport in 2016 (EEA, 2018). Secondary particles and O_3 are formed in the atmosphere by the oxidation of VOCs and its chemical reactions with NO_x and CO.

Despite a general improvement in air quality and a reduction in emissions over the last decade (EEA, 2018) curbing emissions of air pollutants and greenhouse gases from road transport are still among the EU top priorities. In order to secure low tailpipe emissions of light duty vehicles under real life operation, the EU has developed the Real Driving Emissions (RDE) regulation (EU 2017/1151 and its amendments) which is applicable for all new sold vehicles since September 2018. RDE regulation is based on the principle of measuring the environmental performance of vehicles under real traffic operation by means of Portable Emissions Measurement Systems (PEMS). Vehicles tested under the RDE regulation need not-to-exceed (NTE) certain NO_x and Particle Number (PN) limits over a route that complies with a series of testing boundaries (ambient temperature between -7 °C and 35 °C, maximum altitude of 1 300 m.a.s.l., test duration between 90 and 120 minutes, at least 16 km driven on urban, rural and motorway conditions, etc.). RDE regulation foresees that vehicles need to comply with the NTE limits at type-approval (i.e., before entering the market) but also during their normal life (up to a mileage of 100 000 km or five years, whichever occurs first). In order to meet the environmental requirements of the RDE and the WLTP (the novel laboratory test protocol) as well as stringent Carbon dioxide (CO_2) fleet-averaged targets, the automotive industry is being pushed to introduce into the market fuel efficient vehicles that generate low emissions under a widespread conditions of use.

The RDE regulation fosters transparency by making available to the general public the emission results of RDE tests performed at type approval. In addition, during the phasing-in of the RDE regulation, a monitoring system was put in place. During the monitoring period, no NTE limits applied but vehicle manufacturers had the obligation to make the emission results of their type-approval RDE tests public. The objective of the work is twofold:

- to provide an overview of the on-road gaseous emissions of a best seller, B-segment passenger car with different powertrains and after-treatment technologies making use of data collected during the monitoring period;
- to evaluate the potential of using on-road measurements to assess the environmental performance of the considered technologies when tested within the RDE boundaries with relatively narrow ranges of variability of testing conditions.

Experimental

The considered fleet was composed of four vehicles of the same make, model, and model year (2018 Volkswagen Polo) with four different powertrains: diesel, gasoline with direct injection (GDI), gasoline with port fuel injection (PFI), and compressed natural gas (CNG). All vehicles had manual transmission with five gears, were front-wheel drive and mounted tyres of the same dimension (185/65R15) during the tests. Also, the vehicles had similar engine power and capacity (Table 1) and operated a start-stop

system. Gasoline vehicles and the CNG one were equipped with a three way catalyst (TWC) whereas the diesel after treatment system combined a lean NO_x-trap (LNT), and a Selective Catalytic Reduction catalyst (SCR) on top of an Exhaust Gas Recirculation system (EGR), a Diesel Oxidation Catalyst (DOC) and a Diesel Particle Filter (DPF). It must be stressed that the four vehicles were type approved according to the Euro6b/c requirements (e.g. including the NEDC procedure) and that no NTE limit applied to the RDE tests performed. The WLTC CO₂ reported in Table 1, used to assess the normality of the test according to RDE regulation, was obtained from a WLTP test which did not necessarily fully match with the final WLTP procedure.

Table 1: Vehicles characteristics

Fuel type	Emission standard	Engine power [kW]	Engine capacity [cc]	Test mass [kg]	Mileage [km]	WLTC CO ₂ [g/km]	After-treatment systems
Diesel	Euro 6c	59	1600	1686	11 000	116.8	EGR+DOC+DPF +SCR+LNT
Gasoline – GDI	Euro 6b	66	999	1429	10 000	124.9	TWC
Gasoline – PFI	Euro 6b	55	999	1304	12 000	130.0	TWC
CNG	Euro 6b	66	999	1429	10 000	93.8	TWC

All on-road tests were driven in Wolfsburg (Germany) between March and July 2017 under the supervision of TÜV Nord which is a German technical service. Vehicles were instrumented with a Maha-AIP gas PEMS which measure CO and CO₂ concentrations using a Non-Dispersive Infrared detector (NDIR), NO using a chemiluminiscence detector (CLD), and NO₂ using photoacoustic spectroscopy (PAS). The exhaust mass flow was measured using a Pitot tube-based Maha-AIP exhaust mass flowmeter of 2 inch-diameter (1.5 inch on the gasoline vehicles). Zero and span checks were performed before and after all tests to verify the drifts of the analysers which complied well with the regulation requirements. PEMS validation tests against standard laboratory equipment as defined in the RDE Regulation were performed on each test by TÜV Nord. The outcomes of the validation tests, reported within the data exchange files, are analysed to assess the quality of the data measured on the road.

Two tests, one with cold engine and one with hot engine, were performed for each vehicle (only cold on the PFI) using the same route (on the PFI and the CNG some variants were used). The main test characteristics are described in Table 2. The ambient temperature and altitude conditions were moderate for all tests: average temperature ranging 14 °C to 21 °C, and maximum altitude 176 m.a.s.l. No overall excess or absence of driving dynamics was verified on any of the considered tests according to the calculation procedures of Appendix 7a of the RDE regulation (95th percentile of the product of vehicle speed per positive acceleration, and Relative Positive Acceleration, respectively) and a significant spread of the v*a_pos95 was observed among tests in particular for the urban, and motorway sections (Figure 1).

On-road emissions values discussed in the results section correspond to 'raw' values, i.e. without applying any correction during the post-processing. In addition, emissions over the cold start period (when available) are discussed. Cold start is defined in the RDE regulation as the period from the test start (first ignition of the engine) until the engine coolant temperature reaches 70 °C or until it runs cumulatively for five minutes, whichever occurs before. The same definition is applied in this work to calculate emissions during the cold start.

Table 2: Tests characteristics

Fuel type	Engine coolant temp. at test start [°C]	Test date (year 2017)	Average ambient temp. [°C]	Average RH [%]	Cumulative elevation gain [m/100 km]	Total distance [km] U/R/M share (%)
Diesel	Cold (26)	July 20	21	76	360	91 (42/31/27)
Diesel	Hot (90)	July 24	20	53	360	91 (40/32/28)
Gasoline – GDI	Cold (25)	June 28	21	61	360	91 (39/32/29)
Gasoline – GDI	Hot (50)	June 28	20	84	360	91 (39/32/29)
Gasoline – PFI	Cold (24)	March 30	14	80	470	91 (42/31/27)
CNG	Cold (25)	July 13	16	59	360	99 (40/33/27)
CNG	Hot (73)	July 13	18	50	360	99 (38/37/25)

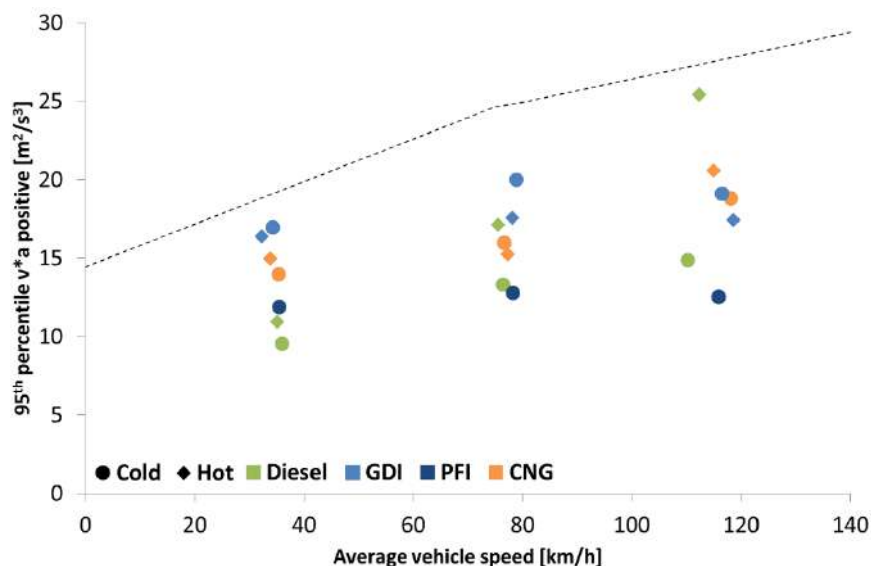


Figure 1: 95th percentile of the product of vehicle speed per positive acceleration [m²/s³] per RDE test, vehicle, and trip section.

Results

Overview of validation tests

The PEMS validation tests performed on all vehicles show that the deviation between the PEMS and standard laboratory equipment were within the permissible tolerances defined in the RDE regulation for all pollutants (Table 3). However, it is important to notice that the PEMS measured roughly 10% lower CO emission on the diesel and the gasoline vehicles, and 35% lower on the CNG than the laboratory. The CO₂ measured with the PEMS was 8.5% and approximately 3% lower than what was reported by the laboratory on the diesel vehicle, and on the PFI and the CNG, respectively. Finally, PEMS measured 9 mg/km lower NO_x on the diesel vehicle and roughly 1.5 mg/km lower NO_x on the other powertrains than the laboratory equipment. It is therefore very likely that, on the road, the emissions are slightly larger than those measured by the PEMS for all three pollutants.

Table 3: Results of PEMS validation tests on the chassis dynamometer

Fuel type	Permissible CO tolerances	Actual CO deviation from lab [mg/km; %]	Permissible CO ₂ tolerances	Actual CO ₂ deviation from lab [g/km; %]	Permissible NOx tolerances	Actual NOx deviation from lab [mg/km; %]
Diesel		-15.2; 12.6%		-10.3; 8.5%		-8.9; 37.4%
Gasoline – GDI	150 mg/km or 15% of lab	-10.9; 9.7%	10 g/km or 10% of lab reference,	0.2; 0.1%	15 mg/km or 15% of lab reference,	-1.5; 11.3%
Gasoline – PFI	reference, whichever is larger	-67.7; 12.2%	whichever is larger	-5.0; -3.8%	whichever is larger	-1.6; 12.9%
CNG		-35.6; 31.3%		-2.3; -2.3%		-1.0; 6.3%

On-road emissions assessment

The on-road emissions performance of the four vehicles is discussed considering the results of the cold and hot tests, first for NO_x and the NO₂ fraction, then for CO and CO₂.

The gasoline vehicles had the lowest NO_x emissions of all the powertrains with the GDI exhibiting the minimum emissions value on the total trip (< 6.5 mg/km) as well as on the urban and rural sections (Figure 2). Emissions on cold and hot tests were very similar (Figure 2). The PFI NO_x emissions on the total trip (7.8 mg/km) were similar to the ones from the GDI considering that the PFI-cold test was conducted with 6 °C colder ambient temperatures, on a route with a slightly higher cumulative positive elevation gain than the one of the GDI. The CNG vehicle had also low NO_x emissions overall (< 15 mg/km) with up to 4 times more emissions on the urban section than over the rural and motorway ones. It is noteworthy that on the urban section of the hot test, the CNG emitted one third more emission than on the cold test even if the cold test was driven on a 2 °C colder day with similar dynamicity (Figure 1). The diesel vehicle had a NO_x emission of 18 mg/km and 24 mg/km on the cold and hot tests, respectively. Urban NO_x emissions were twice as high as the total trip ones and up to 25 times higher than on the motorway. In fact, the diesel vehicle reached the lowest NO_x emissions on the motorway of the four powertrains (1.5 mg/km). Similarly to the CNG, the diesel vehicle had urban NO_x emission 20% higher on the hot test than on the cold one. The lowest NO_x emission on the cold start corresponded to the GDI (71 mg/km) which emitted approximately 7 times more during the cold start than during the whole urban section (Table 4). The largest NO_x emission on the cold start was measured in the diesel (123 mg/km) approximately 3 times higher than the emission over the urban section. In terms of NO_x mass, the cold start contributed to roughly 37% of mass emitted during the urban section on the diesel vehicle, the GDI and the CNG (approximately 54% on the PFI).

Considering all powertrains and tests, the average shares of NO_x emissions were 97% of NO and 3% of NO₂. The NO₂/NO_x fraction was lower on the PFI and the CNG (2%) than on the diesel vehicle (5%) and the GDI (6%, Figure 3). The NO₂ emission on the total trip ranged from 0.1 mg/km (PFI) to 0.7 mg/km (diesel vehicle). It is noticeable that on the diesel vehicle, the NO₂/NO_x fraction on the urban section was five times higher on the cold-started test than on the hot-started one with an NO₂ emission of 2 mg/km. The maximum NO₂/NO_x fraction (20%) was found on the motorway during the hot test on the diesel vehicle when NO_x emissions were very low (1.5 mg/km of which 0.3 mg/km of NO₂). During the cold start (5 minutes or time to reach an engine coolant temperature of 70 °C, whichever occurs first) the NO₂/NO_x fraction was lower than during the corresponding urban section for all powertrains with a maximum share of 1% for the GDI (Table 4).

Table 4: Cold start characteristics and emissions

Fuel type	Duration [s]	Coolant T. at cold start end [°C]	Distance [km]	Average speed [km/h]	Stop time [s]	NOx [mg/km]	NO ₂ /NOx [%]	CO [mg/km]	CO ₂ [g/km]
Diesel	300	68	2.29	27.5	39	123	0.4	347	181
Gasoline – GDI	164	70	1.12	24.6	42	71	1.0	112 1	249
Gasoline – PFI	207	70	1.54	26.9	43	87	0.2	292 9	191
CNG	201	70	1.61	28.8	43	114	0.2	0	143

The lowest CO emissions of the fleet corresponded to the diesel vehicle on the hot test (10 mg/km, Figure 4). On the cold test, the diesel vehicle yielded the same emission values over the rural and motorway sections whereas on the urban, emissions were 3.4 times higher than on the hot test associated to cold start emissions (31 mg/km vs 9 mg/km). In fact, CO emissions for the cold start of the diesel vehicle reached 347 mg/km which is one order of magnitude higher than the emissions over the urban section. In any case, emissions on the cold test on the road were at least 25 times lower than the type approval limit for diesels on Type I (500 mg/km). The CNG vehicle also reached low CO emissions on the road totaling 72 mg/km and 60 mg/km on the cold and hot tests, respectively. On the CNG, CO emissions increased with the engine load being more than two times higher on the motorway than on the city. CO emissions measured during the cold start on the CNG cold test were 0 mg/km (Table 4). On the cold test, the GDI emitted twice as much CO on the city than the CNG (with up to 1.1 g/km on the cold start) but it was cleaner on the rural and motorway bins. The highest CO emissions corresponded to the PFI vehicle which averaged 400 mg/km over the complete route. Emissions were particularly high on the motorway under high load conditions that reached 830 mg/km. Also, the CO emissions from the PFI in the urban section were 3.8 times higher than the GDI, and up to 10 times higher than the diesel. PFI CO emissions on the cold start reached 2.9 g/km, one order of magnitude higher than what was measured on the diesel vehicle.

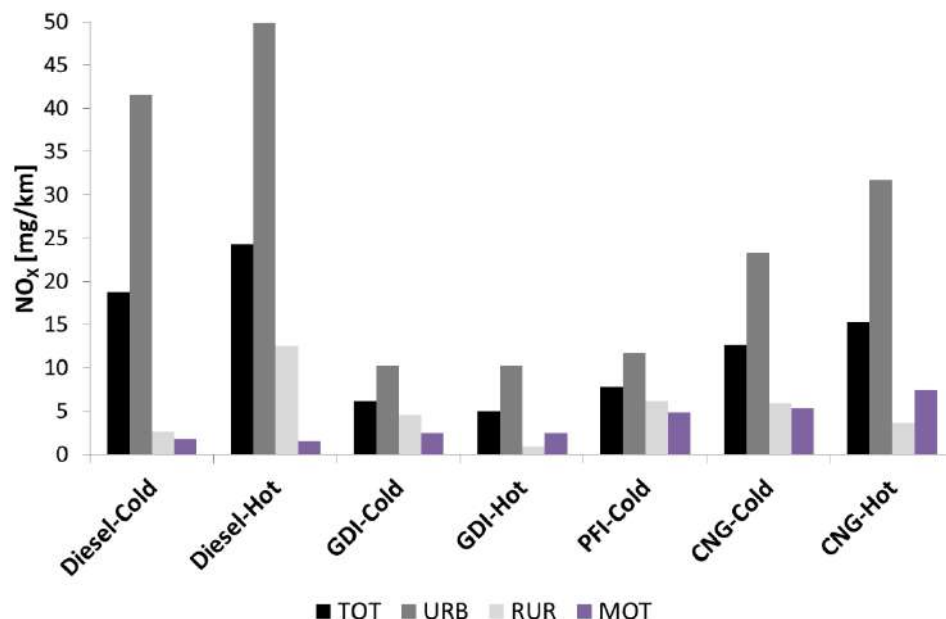


Figure 2: Comparison of raw NO_x emissions of each test over total, urban, rural, and motorway sections.

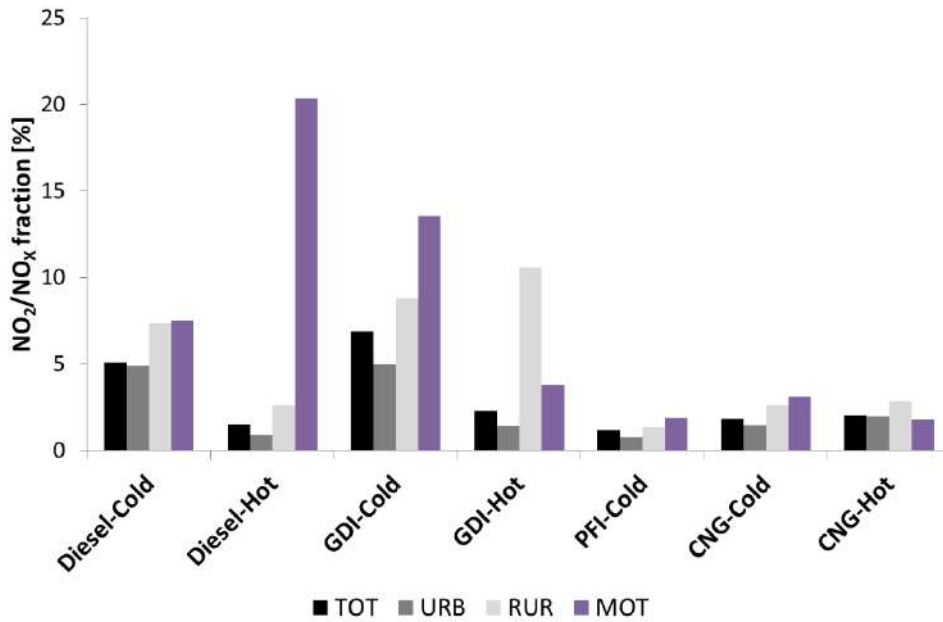


Figure 3: Comparison of the NO₂/NO_x fraction of each test over total, urban, rural, and motorway sections.

The CNG had the best CO₂ performance under cold conditions with CO₂ emissions approximately 100 g/km and 115 g/km for total and urban sections, respectively (Figure 6). The diesel and the PFI followed with roughly 115 g/km and 139 g/km, and 118 g/km and 127 g/km, respectively on total and urban sections. The GDI had the highest CO₂ emissions of all the four powertrains with emission on the total and urban sections totaling 132 g/km and 157 g/km on the cold test. On the CNG and the diesel vehicle, the CO₂ emission on the tests performed with a hot engine were lower on the urban section as compared to the respective cold tests pointing to contribution of the cold start emissions at test start. Over the cold start, CO₂ emissions of the GDI (249 g/km) were 1.3, 1.4 and 1.7 higher than on the PFI, the diesel and the CNG cars, respectively.

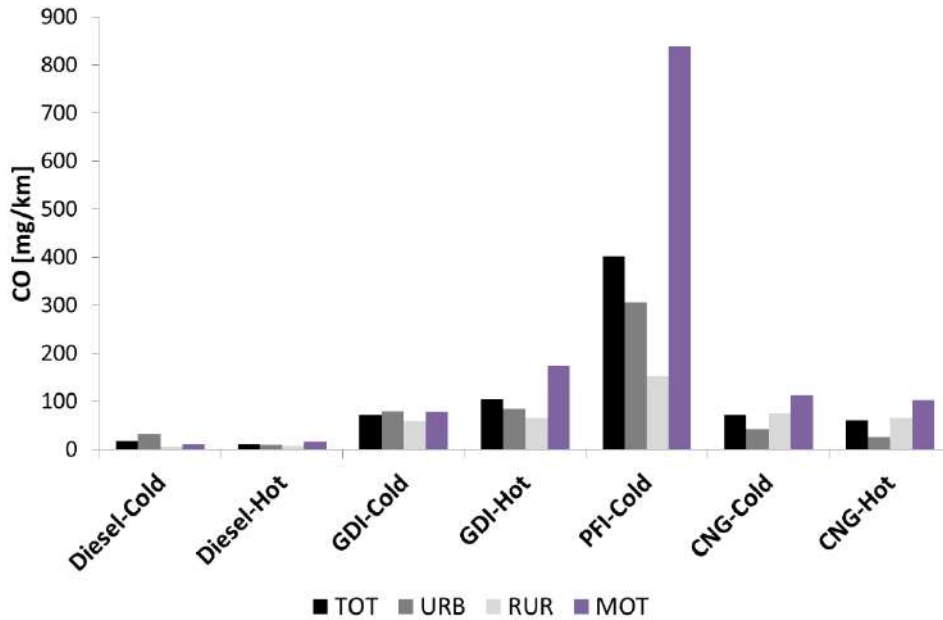


Figure 4: Comparison of raw CO emissions of each test over total, urban, rural, and motorway sections.

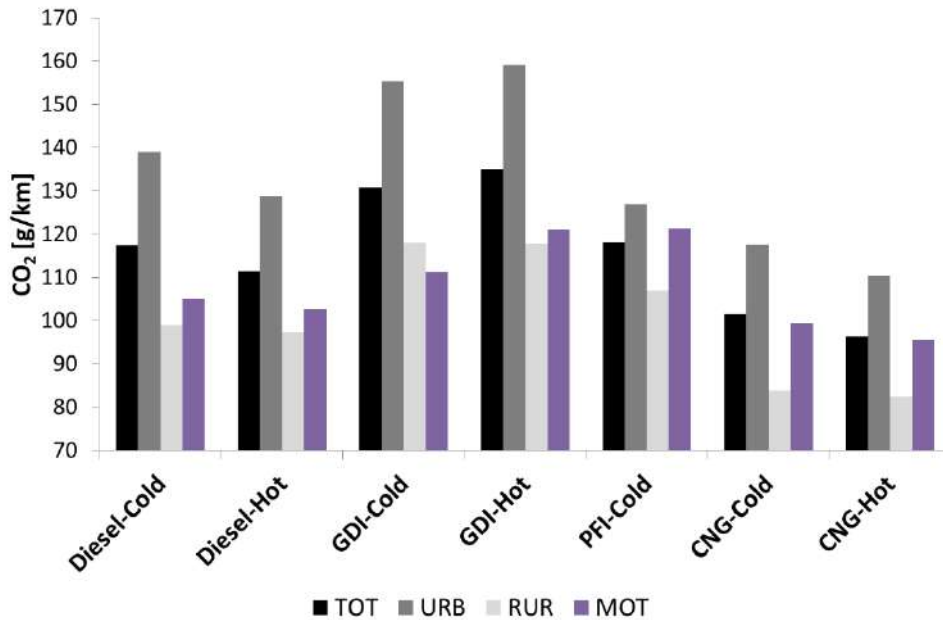


Figure 5: Comparison of raw CO₂ emissions of each test over total, urban, rural, and motorway sections.

Discussion

Despite the fact that they were approved prior to the RDE requirements, all vehicles comply well with the RDE NTE limit for NO_x applied for Euro 6d-TEMP vehicles (168 mg/km for diesel, 126 mg/km for gasolines and CNG). In fact, since emissions for all powertrains on the complete trip as well as in all sections are below 50 mg/km the vehicles would also comply with the NTE that is applicable for Euro 6d vehicles (114.4 mg/km for the diesel and 85.8 mg/km for the others). The diesel vehicle emits close to zero NO_x emissions on the motorway showing good NO_x abatement performance of the SCR catalyst on a warm vehicle and under high engine load conditions. In the city, before reaching the light off temperature of the SCR, NO_x emissions are well reduced by the LNT and the EGR and reach 240 mg/km. In any case, on-road NO_x emissions of the diesel vehicle are one order of magnitude lower than those reported in the literature for Euro 6b diesels (O'Driscoll et al., 2018) proving that modern diesel vehicles can operate on low NO_x on a wide range of driving conditions.

It is noticeable that despite the fact that the Diesel, the GDI and the CNG had a similar contribution of the cold start to their NO_x mass emission on the urban section, the diesel and the CNG exhibited ~20% higher emissions on the hot test as compared to the cold one, whereas the opposite occurred for the GDI. This might be related to the fact that for the Diesel and the CNG the hot test was driven slightly more dynamically than the cold one (and reverse for GDI). On the urban section of tests performed on the diesel vehicle, the NO₂/NO_x fraction was five times higher on the cold-started test than on the hot-started one with a direct NO₂ emission of 2 mg/km. This is a relevant point for air quality since most of the cold starts take place inside the cities.

CO emissions are well controlled by the diesel vehicle, the CNG and the GDI vehicle with emission values far from the regulatory limits on the chassis dyno. However, the PFI (and in second instance, the GDI) shows very high CO emissions on the motorway under high load operation which could be related to a change in the stoichiometry as suggested by other authors (Weiss et al., 2011). This potential change in the operation of the TWC could also determine high emission of hydrocarbons (as reported by Luján et al., 2019).

Due to the variability of the testing conditions (different ambient temperature, dynamicity, traffic conditions, etc.) the CO₂ measurements with PEMS according to the RDE procedure are not suitable to compare CO₂ emission performance of different vehicles. However, based on the few tests performed with each vehicle it is possible to say from a qualitative point of view that the CNG tended to emit less CO₂ than the diesel vehicle and the PFI, and that the GDI had the highest CO₂ emissions overall. The CNG and the diesel showed similar CO₂ emission on the road as compared to the CO₂ emissions

measured over the WLTC, whereas the GDI had higher emission on the road than in the chassis dyno. However, the uncertainty of the PEMS measurement on the CNG is higher than for the other vehicles and therefore it is difficult to generalise the findings of the study. Also the fact that the GDI was tested in more dynamic conditions than the others could explain partially its higher CO₂ emissions. In any case, on-road results are in good agreement with the powertrain review by Khan et al. (2015).

Each powertrain presents strengths and weaknesses in terms of emissions as compared to the others. The gasoline engines, both GDI and PFI performed well for what regards NOx but they proved to have significant emissions of CO in the motorway, in comparison to the other technologies. The CNG outperformed the other powertrains for CO₂ but NOx emissions in the city (though low) were twice as important as those measured on the gasolines. Finally, the diesel, which mounts state-of-the art after-treatment technologies performed excellently in terms of CO but its urban NOx emissions were still 4 times higher than those of the gasoline vehicles. DPFs, which are widespread mounted on diesel vehicles, can cope well with particle emissions whereas GDIs, PFIs, and CNGs have been found to emit larger PN emission on the road and in the laboratory than diesel vehicles with DPFs (He et al., 2018; Giechaskiel et al., 2019). Therefore, when considering overall tailpipe emissions (gases and particles) and CO₂ emissions, modern diesel vehicles seem to be in a good technical position to exhibit a good environmental performance in the coming years.

Several conclusions can be drawn from this research for what regards the use on-road measurements to assess the environmental performance of vehicles:

- i) The RDE regulation foster openness and transparency by making publicly available the results of any test done at type approval. This will certainly contribute rebuilding public trust in the way vehicle emissions are measured, assessed, and reported.
- ii) The technical requirements imposed for the PEMS instruments and their calibration by the RDE regulation help guaranteeing the quality of the emissions data acquired during a test.
- iii) Data measured during RDE tests are comprehensive. Beyond checking the compliance with the NTE limits, the data are very useful to assess emissions performance of various technologies under a wide range of operating conditions (e.g., emissions at cold start, at idling, at high engine load, during acceleration, etc.).
- iv) However, emissions performance of a vehicle cannot be robustly assessed solely on the measurements done over a single RDE test: emissions may be dramatically different under other testing conditions within the RDE boundaries
- v) Due to the multi-pollutant nature of air pollution, providing a fair and complete assessment of the environmental performance remains challenging even when comparing on-road emissions obtained from similar vehicles and testing conditions.
- vi) From the consumer's point of view, it remains difficult to purchase a vehicle with low tailpipe emissions even when RDE data is available.
- vii) A rating system for environmental performance of tailpipe emissions that would consider at least all regulated pollutants measured on the road could be a solution to integrate in a single figure the overall pollutant emissions performance. Such a system should consider the diversity of testing conditions when providing rates for individual vehicle models (e.g., a model with 0.5*NTE over three largely different testing conditions should be better rated than another model with 0.4*NTE tested only once).

References

- EEA, European Environmental Agency (2018). *Air quality in Europe – 2018 report*, 83 pp.
- Giechaskiel, B., Lahde, T., Drossinos, Y. (2019). Regulating particle number measurements from the tailpipe of light-duty vehicles: The next step? *Environmental Research*, 172, 1-9.
- He, L., Hu, J., Zhang, S., Wu, Y., Zhu, R., Zu, L., Bao, X., Lai, Y., Su, S. (2018). The impact from the direct injection and multi-port fuel injection technologies for gasoline vehicles on solid particle number and black carbon emissions, *Applied Energy*, 226, 819-826.
- Khan, M., Yasmin, T., Shakoor, A. (2015). International Experience with compressed natural gas (CNG) as environmental friendly fuel, *Energy Syst.* 6, 507-531
- Luján, J.M., Bermúdez, V., Dolz, V., Monsalve-Serrano, J. (2018). An assessment of the real-world driving gaseous emissions from a Euro 6 light-duty diesel vehicle using a portable emissions measurement system (PEMS), *Atmospheric Environment*, 174, 112-121.
- OCED, Organisation for Economic Co-operation and Development (2016). *The Economic Consequences of Outdoor Air Pollution*, OECD Publishing, Paris, 120 pp.
- O'Driscoll, R., Stettler, M.E.J., Molden, N., Oxley, T., ApSimon, H.M. (2018). Real world CO₂ and NOx emissions from 149 Euro 5 and 6 diesel, gasoline and hybrid passenger cars, *Sci. Total Environ.* 621, 282-290.
- Weiss, M., Bonnel, P., Hummel, R., Provenza, A., Manfredi, U. (2011). On-Road Emissions of Light-Duty Vehicles in Europe, *Environ. Sci. Technol.*, 45, 8575-8581.
- WHO, World Health Organisation (2016). *Ambient air pollution: a global assessment of exposure and burden of disease*, 131 pp.

2.6.6 Comparative investigation on particulate and gaseous emissions from a pre-Euro 6 diesel LCVs fleet fuelled with different second-generation biodiesel blends

T. Rossi, S. Casadei and M. Siviero*

*Innovhub - Stazioni Sperimentali per l'Industria, Fuels Department – Via G. Galilei 1 – At
20097 San Donato Milanese, Milano - Italy*

*Keywords: second-generation biodiesel, particulate, LCVs emissions
Presenting author email: tommaso.rossi@mi.camcom.it*

Abstract

This study, named “Biagio”, is focused on second-generation biodiesel, obtained from transesterification of palm fatty acid distillate (PFAD) and of used cooking oil (UCO), blended with EN590 diesel, to verify the effects on particulate and gaseous exhaust emissions from a LCVs testing fleet. The experimental blends were used to fuel one Euro 3, one Euro 4 (both without DPF) and one Euro 5b LCV that were tested driving on a chassis dynamometer a cycle composed of a cold-start NEDC followed by a hot-start Artemis Urban. Regarding vehicles without DPF, by increasing the content of biodiesel, statistically significant reductions were ascertained especially, but not only, for the soot fraction and for the total particle number emissions. Euro 5 vehicle showed lower differences than the other two LCVs about particulate emissions, due to DPF efficiency hiding the effect of the biodiesel fraction. A focus on formaldehyde emission pointed out that this species progressively decreased as the content of PFAD biodiesel increased, but this trend was not detected for UCO biodiesel. Biagio study confirms the effectiveness of second-generation biodiesel blends in reducing the environmental impact of exhaust emissions from pre-Euro 6 diesel LCVs.

Introduction

The current growing concern surrounding the use of fossil fuels related to global climate change and environmental degradation have forced governments, policymakers and researchers to look for alternative energy sources. The production of biodiesel from renewable sources is widely considered to be one of the most sustainable alternatives to fossil fuels and a viable means for environmental and economic sustainability (Alam et al., 2015). Second-generation liquid biofuels are generally produced by two fundamentally different approaches i.e. biological or thermochemical processing, from agricultural lignocellulosic biomass, which are either non-edible residues of food crop production or non-edible whole plant biomass (e.g. grasses or trees specifically grown for production of energy). The main advantage of the production of second-generation biofuels from non-edible feedstocks is that it limits the direct food production versus fuel competition associated with first-generation biofuels.

European Union Directive 2018/2001 on the promotion of the use of energy from renewable sources, entered into force in December 2018, sets a binding Union target for the overall share of energy from renewable sources in the Union's gross final consumption of energy in 2030, and establishes sustainability and greenhouse gas emissions saving criteria for biofuels, bioliquids and biomass fuels. In order to optimize and define the use of renewable energy in the transport sector, each Member State shall set an obligation on fuel suppliers to ensure that the share of renewable energy within the final consumption of energy in the transport sector will reach at least 14% by 2030 (minimum share) in accordance with an indicative trajectory set by the Member State itself. Within the minimum share, the contribution of advanced biofuels and biogas produced from the feedstock listed in Part A of Annex IX of the Directive as a share of final consumption of energy in the transport sector shall be at least 0,2% in 2022, at least 1% in 2025 and at least 3,5% in 2030. The share of biofuels and biogas produced from the feedstock listed in Part B of Annex IX shall be limited to 1,7% of the energy content of transport fuels supplied for consumption or use onto the market. Member States may, where justified and approved by the Commission, modify that limit, taking into account the availability of feedstock. Both Part A and Part B feedstocks for the production of biogas for transport and advanced biofuels can be considered to be twice their energy content: palm oil mill effluent (POME) is reported in Part A, UCO in Part B. Nowadays it is unclear and debated whether PFAD can be considered as a feedstock compatible with point (d) of Part A: *Biomass fraction of industrial waste not fit for use in the food or feed chain, including material from retail and wholesale and the agro-food and fish and aquaculture industry, and excluding feedstocks listed in part B of this Annex.*

Advanced biofuels and other biofuels and biogas produced from feedstock listed in Annex IX of the Directive, renewable liquid, gaseous transport fuels of non-biological origin and renewable electricity in the transport sector can contribute to reduce carbon emissions, stimulating the decarbonisation of the Union transport sector in a cost-effective manner, and improving, *inter alia*, energy diversification in the transport sector while promoting innovation, growth and jobs in the Union economy and reducing reliance on energy imports. The obligation on Member States to require fuel suppliers to ensure a minimum share of advanced biofuels and certain biogases, is intended to encourage continuous development of advanced fuels, including biofuels and the Directive also promotes improvements in the greenhouse gas performance of the fuels supplied to meet it.

Biodiesels used within Biagio project were obtained from transesterification of PFAD and of UCO, both of which can be considered second-generation obtained by waste products. In the transesterification process, the added alcohol (commonly methanol) can be deprotonated with a base to make it a stronger nucleophile; the reaction has no other inputs than the triglyceride and the alcohol. Under normal conditions, this reaction will proceed either exceedingly slowly or not at all, so heat, as well as catalysts (acid and/or base) are used to speed the reaction as showed in Figure 1 (Font De Mora et al., 2015). UCO, showed below as an example, is initially filtered and decanted in order to separate solid particles and water. Once refined, the oil is sent to the transesterification plant following the process described in Figure 1 which also includes energy sources and any other substances needed at each step.

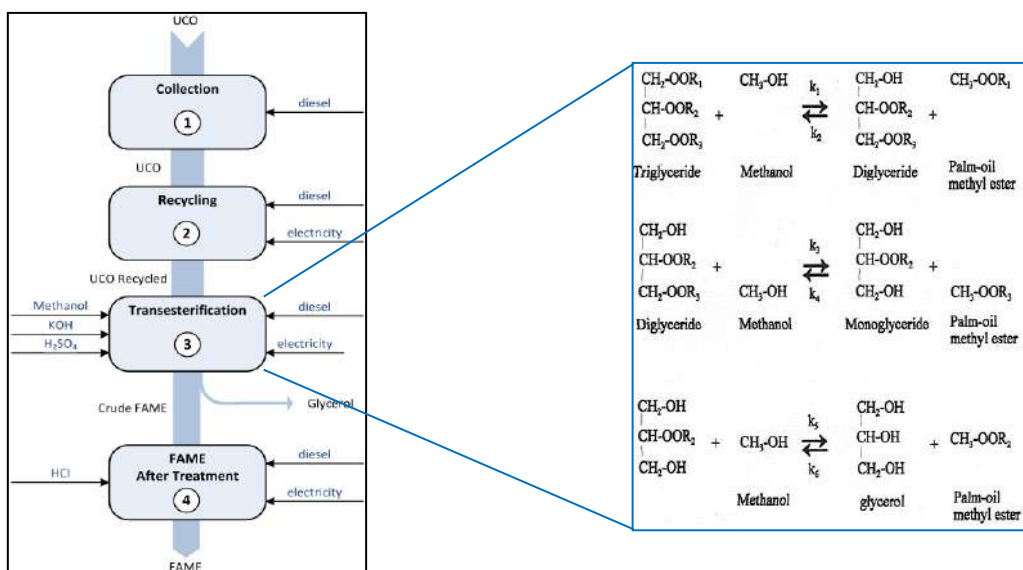


Figure 1: UCO biodiesel from feedstock to FAME, including the energy inputs for each step (on the left), and focus on transesterification chemical process (on the right).

UCOs produced in the EU are considered non-hazardous wastes according to the Consolidated European Waste Catalogue. They are classified as municipal wastes (household waste and similar commercial, industrial and institutional wastes), including separately-collected fractions, under the code 20 01 25 (edible oils and fats). The wrong disposal of UCO and PFAD can have important negative effects on the environment: if the waste is not eliminated by waste water treatment plants, it can produce a negative effect on the capacity of the auto-regeneration of rivers, fauna and flora and can increase the population of jelly fish on coastlines, as reported by Font De Mora et al..

Therefore, the use of UCO and PFAD biodiesels in diesel blends can be a valid solution also taking into account its potential ecological risk, especially in those countries where waste water treatment plants are not well developed yet.

Another alternative for waste UCO is the development of enzymatic biodiesel production, as reported by Cesarini S. et al., (2015) who describe that, by using liquid lipase Callera Trans L in a particulate form and in association with other enzymes, numerous benefits can be achieved, such as cost reduction and therefore much better efficiency for production at industrial scale. After European Commission's mandates to European Committee for Standardisation for the development of technical standards for biodiesel/diesel blends above 7% V/V, EN 16734:2016 and EN 16709:2015 have been approved and published to respectively specify requirements and test methods for marketed and delivered automotive B10 diesel fuel and B20/B30 diesel fuel (*i.e.* diesel fuel containing up to 10,0% V/V, 20,0% V/V, 30%

V/V Fatty Acid Methyl Ester). At the time of Biagio project implementation, B10 and B30 technical standards were under discussion and definition, but it was clear that these blends would have been soon introduced onto the European market, which is the main reason why B10 and B30 have been chosen as experimental blends to be investigated compared to an EN 590 B7 reference blend.

As of today, pre-Euro 6 diesel LCVs are widely used in Italy, as showed in Figure 2, which reports the Euro category percentages of circulating LCV Italian fleet in 2014 (Automobile Club Italia, 2014) and in 2017 (Automobile Club Italia, 2018). In 2017, around 4 million LCVs were circulating in Italy and only 7% were diesel Euro 6 (introduced in September 2014).

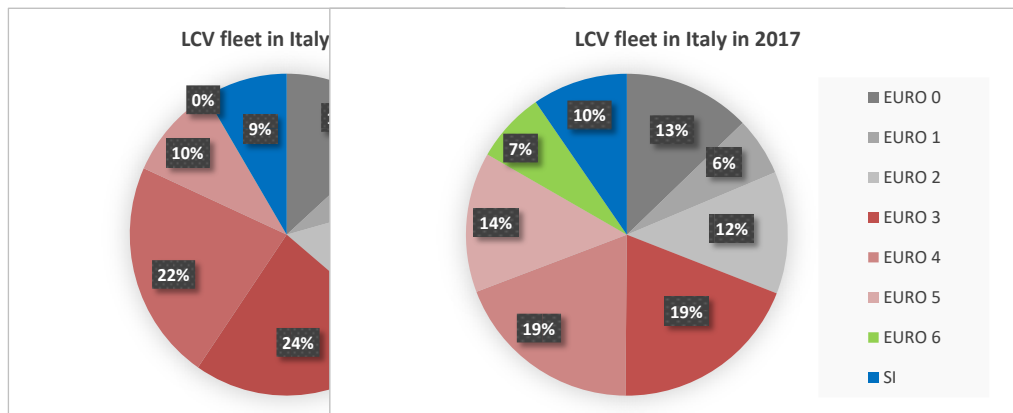


Figure 2: circulating LCV Italian fleet in 2014 on the left and in 2017 on the right, divided by Euro homologation categories for diesel vehicles. SI stands for Spark Ignition LCV whereas all other percentages concern CI ones.

Materials and methods

PFAD and UCO biodiesel pure blends were purchased and analysed according to EN 14214 to verify their compliance with the standard. In order to make the testing biodiesels more stable over the storage period, an antioxidant (tert-Butylhydroquinone TBHQ, 70 - mg/kg) was added to the biodiesels. Since the tanks containing biodiesels were stored into an unheated building over the winter period, both biodiesels solidified and it was necessary to heat the tanks to liquefy the products. Then B10 and B30 (10% V/V and 30% V/V respectively biodiesel in EN590 diesel blends) testing blends were prepared with both UCO and PFAD biodiesels mixing them with B0 EN590 diesel. With the same B0 EN590 diesel a B7 blend with RME (Rapeseed Oil Methyl Ester) was prepared to be used as a reference fuel for the B10 and B30 tests. All testing fuels (biodiesels, B0, B7, B10 and B30 blends) were generally found to be compliant with standards, except for Water content and Oxydation stability at 110 °C, detected for the UCO biodiesel after over one year storage period: however these parameters did not influence fuel consumption and exhaust emission detected results. B10 and B30 were characterized according to EN590 since EN 16734:2016 and EN 16709:2015 not yet approved at the time of testing.

The testing fleet used for the Biagio project has been chosen to represent the Italian diesel LCV circulating fleet at the moment of testing (last tests performed early 2016), and it included a Euro 3 Fiat Doblo 1.9 JTD (hereafter named “Euro 3”), a Euro 4 Fiat Scudo 2.0 Mjet Cargo 120 (“Euro 4”) and a Euro 5 Fiat Doblo 2.0 Mjet Cargo (“Euro 5”), the latter was the only one equipped with a diesel particulate filter (DPF). At the time of testing, Euro 3 had accumulated 180.000 km, Euro 4 47.000 km and Euro 5 6.500 km. Euro 3 was regularly maintained and passed all periodical inspections, Euro 4 and Euro 5 were obtained for rent. No modifications of engine maps or aftertreatments have been performed to reduce emissions or fuel consumption correspondingly to fuelling by biodiesel blends.

Within the Biagio project, the three testing vehicles were chosen in order to cover more than 50% of the real LCV Italian circulating fleet, as Figure 2 shows.

Each vehicle was fuelled with 10% and 30% V/V UCO and PFAD biodiesel/diesel blends except for Euro 3, about which h RME and PFAD biodiesel blends were no longer available, in order to detect the correspondent emissions values to be compared to the emissions detected fuelling LCVs with reference fuels. For each vehicle and for each fuelling, before detecting exhaust emissions, tank and engine supply system were conditioned by driving over several NEDCs on the chassis dynamometer.

The testing vehicles have been installed on the chassis dyno and tested over their cold-start homologation cycle (NEDC), followed by a hot-start Artemis Urban cycle (André M., 2004), as showed in Figure 2. The hot-start cycle has been chosen because it well represents the typical urban driving style of these vehicles, often used for last mile deliveries.

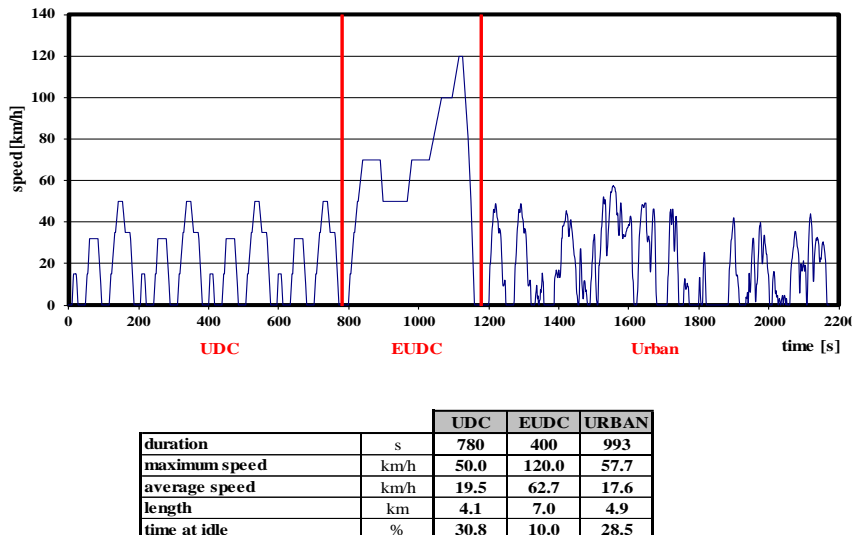


Figure 3: NEDC (UDC+EUDC) + Artemis Urban driving cycles sequence and their characteristics.

Vehicles' stability, temperature and humidity conditions were checked before beginning the testing phase and over each phase and the chassis dynamometer calibration (coast down), according to Regulation UN/ECE N. 83, was performed for every vehicle.

The equipment used to execute the test program is represented in Figure 4 within the sampling scheme of Innovhub-SSI Automotive Emission Laboratory (LEA) and it is described as follows:

- Chassis dynamometer system (BOSCH) with electrical simulation of inertia and braking (API-COM);
- Driver-aid (AVL305);
- Constant Volume Sampler (CVS) with dilution tunnel (API-COM);
- Exhaust measuring system: two NDIR analyzers for CO and CO₂, one HCLD for NO/NO_x and one HFID for THC and CH₄ (AMAI60 AVL);
- Automated system for test execution and data acquisition (AVLi4L);
- Speed controlled vehicle cooling fan;
- Total particulate matter (TPM) collected on Pallflex T60A20 membranes and measured by a 10⁻⁷ g precision balance;
- Total particle number (PN) [#/km] with a Dekati Deed and a TSI CPC (PMP compliant system able to count particles whose diameter is within 0.023 ÷ 2.5 µm), following the PMP protocol [Regulation n. 83];
- Dekati ELPI (Electrical Low Pressure Impactor) used to measure airborne particle number in the aerodynamic diameter range of 0.007÷10 µm;
- AVL MSS (Micro Soot Sensor) used to measure PM soot fraction [mg/m³];
- NI-USB 9211 module to detect engine oil and exhaust gas temperatures;
- HPLC (High-Pressure Liquid Chromatography) for measuring main Aldehydes compounds sampled through DNPH cartridges following EPA N. TO-11 A (Method TO-11A, 1999).

In order to compare the total particle number values from ELPI with those detected with the PMP compliant system, the first two ELPI measuring ranges were not considered for total particle calculations. Therefore, the 0.031÷10 µm measuring window was consider for ELPI total particle number.

All the gas analyzers have been calibrated (zero and span checks) before each test sampling with certified gas cylinders.

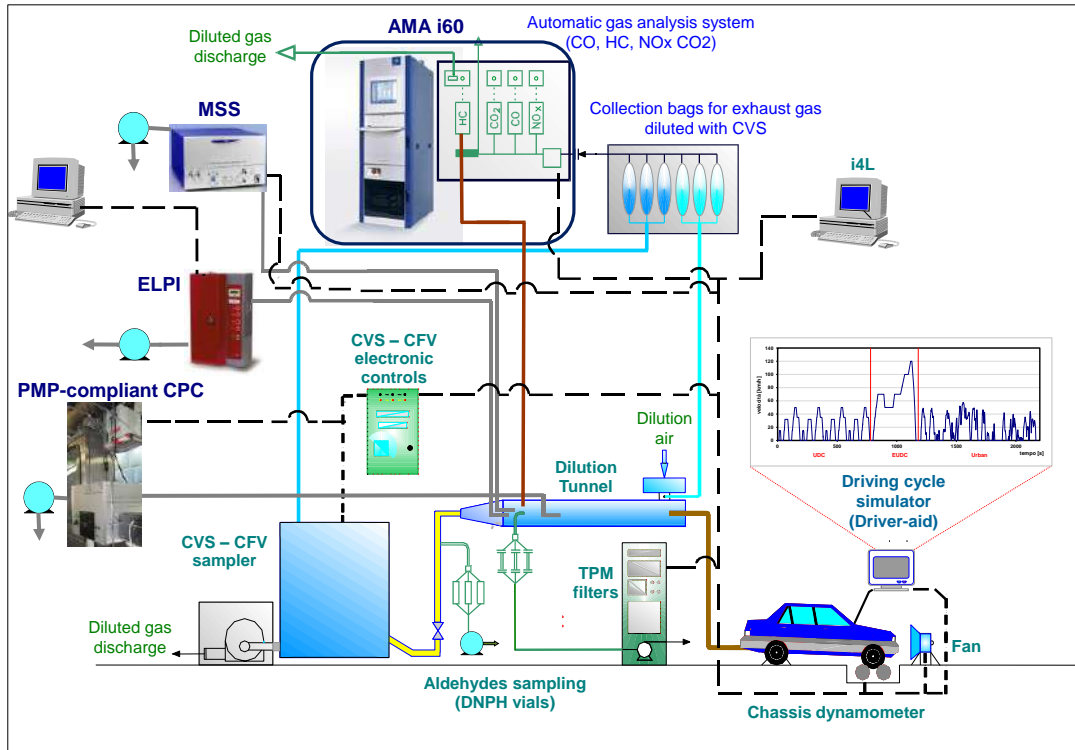


Figure 4: Innovhub-SSI's Automotive Emission Laboratory (LEA) equipment scheme.

All emission data have been processed by checking results' repeatability (at least 3 repeatable tests for each vehicle and fuelling) and finally by applying the Student's t-test to determine whether the differences detected on emissions, attributed to the use of different fuels, were statistically significant or not. The degrees of freedom have been calculated by the 95% confidence interval.

Results and discussion

1. Regulated and gaseous emissions

Regulated emission values from all tested vehicles are reported in Table 1. Although Euro 3 passed all periodical inspections (during which just CO and PM are detected in the exhaust), CO emission did not meet its EU emission standard: a slight decrease towards the limit was detected with UCO B30 blend fuelling. For Euro 4 the NO_x limit was not compliant with both reference and B30 blends, which favoured high HC+NO_x levels, with the limit for UCO fuelling slightly exceeded. All regulated gaseous emissions were compliant with standards for Euro 5, except for PN emissions, being slightly above the limit for any used fuelling.

Table 1: Regulated emission values: comparison with limits.

Euro 3				
	NEDC	B0	UCO_B30	Euro 3 emission standards
CO	g/km	1.97	1.80	0.80
HC + NOx	g/km	0.57	0.59	0.72
NOx	g/km	0.48	0.50	0.65
PM	g/km	0.010	0.010	0.07

Euro 4				
	NEDC	B7	UCO_B30	PFAD_B30
				Euro 4 emission standards
CO	g/km	0.40	0.39	0.29
HC + NOx	g/km	0.381	0.398	0.378
NOx	g/km	0.339	0.351	0.347
PM	g/km	0.012	0.011	0.011

Euro 5				
	NEDC	B7	UCO_B30	PFAD_B30
				Euro 5b emission standards
CO	g/km	0.11	0.11	0.07
HC + NOx	g/km	0.191	0.197	0.190
NOx	g/km	0.162	0.168	0.171
PM	g/km	0.0015	0.0014	0.0013
PN_PMP Compliant	#/km	7.17E+11	6.94E+11	7.22E+11
				6.00E+11

For all vehicles tested with the experimental blends, comparing the regulated gaseous emission values over the entire homologation cycle no statistically significant differences related to the use of different fuel blends were observed. NO_x emissions also slight increase noticeably in Table 1, occurring on average for all vehicles, but not statistically validated.

Regarding gaseous emissions and fuel consumption, with increasing the content of biodiesel a few statistically validated results over NEDC phases were found. For Euro 3 an around 5% increase of NO_x and HC+NO_x values with UCO B30 blend, over the EUDC phase, were the only results to be statistically significant, however not confirmed by tests with the other two vehicles fuelled with UCO blends. Regarding the slight increase in NO_x emission with increasing the biodiesel content, this work tends to confirm what has been reported in literature (Cheung et al., 2015; Nanta Gopal et al., 2014).

The use of PFAD blends produced more interesting results about THC emissions over UDC phase, leading to a decrease by 24% for Euro 4 and by 38% for Euro 5 with B30 blend, as showed in Figure 5, these reductions were confirmed to be statistically significant.

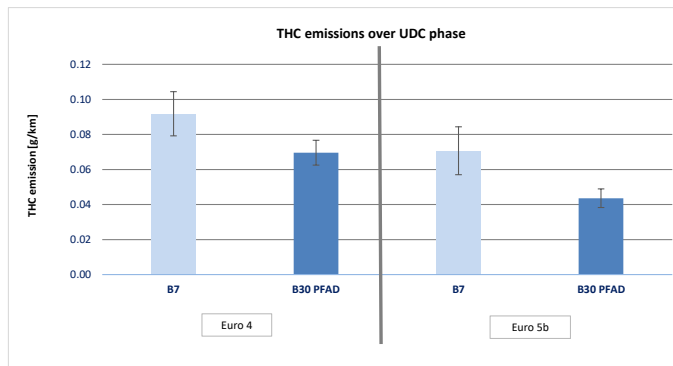


Figure 5: THC emission over UDC phase for Euro 4 and Euro 5: B7 vs B30 PFAD blend.

Regarding fuel consumption, considering all testing, B10 and B30 second-generation biodiesel blends, statistically significant increases were detected only with UCO B30 blend over EUDC: by 5.6% for Euro 3 and by 7.1% for Euro 5. Regarding Euro 3, only one statistically significant increase was detected in fuel consumption over NEDC (by 4.9%). Lower heating values, to analyze fuel energy demand, were determined only for PFAD and UCO pure products and B30 blends and the volumetric energy content showed no significant differences comparing both pure products and B30 blends.

2. Main Aldehyde emissions

Emission of aldehyde compounds from the testing fleet was determined as well. The highest emission values were detected over the UDC phase (due to the cold start with the vehicles' oxidation catalyst not

yet at its operating temperature), which were on average one order of magnitude higher than those from hot phases. Formaldehyde, Acetaldehyde and Propionaldehyde were the most emitted species among the aldehydes detected. Euro 3 showed no correlation but the vehicle was only fuelled with UCO blends. Euro 4 and 5 showed interesting results when fuelled with PFAD blends since a gradual decrease of Formaldehyde was noticed as the PFAD percentage increased. Figure 6 represents aldehyde compound exhaust emissions measured over UDC from Euro 4, for which the most important reductions were detected (by around 30% on average, comparing B7 with B30 PFAD blend).

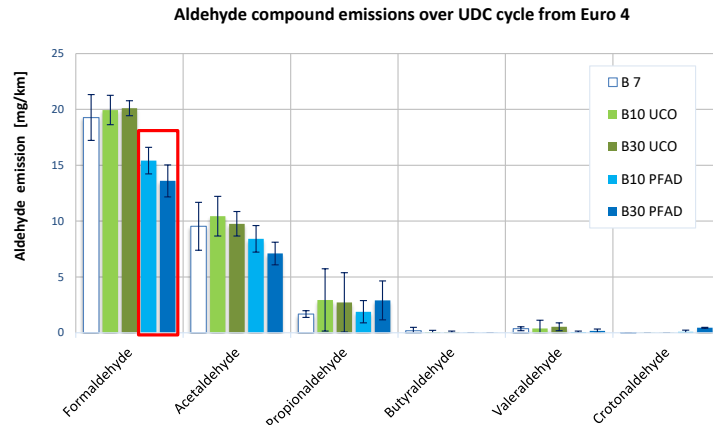


Figure 6: Most significant aldehyde compound exhaust emissions detected from Euro 4 correspondingly to different experimental fuelling.

3. Particulate emissions

The most interesting results within Biagio experimental study came up when particulate emissions were taken into account. Among the results of performed tests, it is worth pointing out the effect of the addition of the biodiesel on emissions under cold start conditions (Urban Driving Cycle) and under real world driving conditions (Artemis Urban) since these are widely considered critical for exhaust emissions affecting air quality and for human beings' pollutants exposure and their health effects.

Table 2 PM, soot, total particles (PN_ELPI) and solid particles (PN_PMP Compliant) exhaust emissions detected from LCVs testing fleet over UDC and Artemis Urban with reference and B30 blends (top PFAD, down UCO)

PFAD		Euro 3				Euro 4				Euro 5							
UDC		Not carried out				B7	B30	Δ, %	t-test	B7	B30	Δ, %	t-test				
PM	mg/km					15.30	13.56	-11.4	NO	1.87	2.54	35.9	NO				
PM soot	mg/km					10.18	9.54	-6.4	NO	0.09	0.08	-6.1	NO				
PN_ELPI	#/km					1.02E+15	8.65E+14	-14.8	YES	6.12E+12	7.09E+12	15.9	YES				
PN_PMP Compliant	#/km					3.45E+12	3.79E+12	9.7	NO	3.30E+11	3.57E+11	8.4	NO				
Artemis URBAN						15.78	14.89	-5.7	NO	2.32	4.18	80.7	NO				
PM	mg/km					14.76	12.65	-14.3	YES	0.21	0.18	-12.8	NO				
PM soot	mg/km					9.75E+14	7.21E+14	-26.0	YES	8.48E+12	8.59E+12	1.3	NO				
PN_ELPI	#/km					4.21E+12	4.39E+12	4.2	NO	6.63E+11	6.38E+11	-3.7	NO				
PN_PMP Compliant																	
UCO		Euro 3				Euro 4				Euro 5							
UDC		B0	B30	Δ, %	t-test	B7	B30	Δ, %	t-test	B7	B30	Δ, %	t-test				
PM	mg/km	16.81	16.12	-4.1	NO	15.30	13.07	-14.6	NO	1.87	2.61	39.3	NO				
PM soot	mg/km	24.68	19.56	-20.8	YES	10.18	8.47	-16.8	YES	0.09	0.09	9.6	NO				
PN_ELPI	#/km	4.24E+13	4.16E+13	-2.1	NO	1.02E+15	8.79E+14	-13.5	YES	6.12E+12	9.74E+12	59.2	NO				
PN_PMP Compliant	#/km	6.71E+13	7.36E+13	9.7	NO	3.45E+12	3.25E+12	-5.9	NO	3.30E+11	4.42E+11	34.1	NO				
Artemis URBAN																	
PM	mg/km	15.99	13.32	-16.7	YES	15.78	11.10	-29.7	YES	2.32	3.81	64.5	NO				
PM soot	mg/km	26.92	18.42	-31.6	YES	14.76	11.20	-24.1	YES	0.21	0.12	-39.4	NO				
PN_ELPI	#/km	3.83E+13	3.33E+13	-13.1	YES	9.75E+14	7.88E+14	-19.1	YES	8.48E+12	8.34E+12	-1.7	NO				
PN_PMP Compliant	#/km	6.15E+13	5.12E+13	-16.7	YES	4.21E+12	4.17E+12	-0.9	NO	6.63E+11	5.22E+11	-21.3	YES				

Table 2 shows the values of particulate emissions and compares results of every testing vehicle fuelled with B0/B7 and B30 biodiesel blends. The detected percentage difference (named "Δ, %") is then reported, highlighting in green the decrease and in orange the increase of each emitted species; the results of Student's t-test (named "t-test") are showed in tables too, highlighting in yellow the statistically

significant results. The comparison between reference blends and B10 blends is not here reported because the differences were not found to be statistically significant like those detected with B30 blends.

For Euro 5 DPF regenerations occurred during testing and corresponding exhaust emission values were not considered; the vehicle was then reconditioned by driving a series of NEDC until the DPF maximum efficiency was definitely reached and detected by particles measurement.

For diesel LCVs, particulate matter ("PM") and, from Euro 5 standard forward, solid particles determined following PMP procedure ("PN_PMP compliant") are regulated by exhaust emission limits. Particulate emission, collected on filters according to UN ECE Regulation N. 83, evidenced different results, on Euro 3 and Euro 4 on one hand, and Euro 5 on the other. LCVs without DPF showed a decrease of PM emission as the biodiesel percentages increased and statistically significant emission differences between reference and B30 UCO blends were found over the Artemis Urban phase with reductions by 16.7% and by 29.7% for Euro 3 and Euro 4, respectively. With increasing the biodiesel percentage in Euro 5, PM apparently increased, but these values were not statistically significant, certainly due to low emission values measured as the DPF efficiently reduced this emission species.

Regarding solid PN emissions detected with the PMP compliant system, statistically significant differences due to different fuels were detected with UCO B30 blends on Artemis Urban cycle with reductions for Euro 3 (by 16.7%) and for Euro 5 (by 21.3%).

In addition to PM and PN_PMP compliant, the unregulated soot fraction of PM ("PM soot") and particle number within the $0.031\text{--}10 \mu\text{m}$ aerodynamic diameter determined with ELPI ("PN_ELPI") were investigated by comparing the LCVs exhaust emissions associated to the different experimental blends.

The only statistically significant differences regarding PM soot were detected for B30 blends compared to reference blends. These were all reductions: for Euro 3 by 20.8% and by 31.6% with UCO B30 over UDC and Artemis Urban respectively, for Euro 4 by 14.3% with PFAD B30 fuelling over Artemis Urban, by 16.8% and by 24.1% with UCO B30 respectively over UDC and Artemis Urban. Statistically significant reductions by around 30% were also detected over EUDC for vehicles without DPF with both PFAD (used only for Euro 4) and UCO B30 blend.

Just as measured with the Micro Soot Sensor, with the ELPI very similar results were observed considering the PN emission detected over each phase. For LCVs without DPF all statistical significant differences detected for this parameter were reductions: for Euro 3 by 13.1% with B30 UCO over Artemis Urban cycle, for Euro 4 with B30 PFAD by 14.8% over UDC and by 26.0% over Artemis Urban, with B30 UCO by 13.5% over UDC and by 19.1% over Artemis Urban. Noticeably for Euro 4 statistically significant reductions of PN_ELPI exhaust emissions compared to B7 reference blend were detected also for UDC on both UCO (7.7%) and PFAD (5.9%) B10 blends and also for EUDC on UCO (23.1%) and PFAD (30.3%) B30 blends and PFAD (13.4%) B10 blend. However it should be taken into account that since ELPI was found to measure in over-range mode during the testing with Euro 3, PN_ELPI absolute values for this vehicle should be considered as not completely reliable.

For Euro 5 vehicle, due to DPF role already described for PM, no statistically validated decreasing of particulate emission was detected with ELPI. On the opposite, using the PFAD blends, statistically significant increases for PN_ELPI exhaust emissions were detected over EUDC (17%) and Artemis Urban (20.3%) with B10, over UDC (15.9%) and EUDC (9.3%) with B30, in contrast to values obtained with other two testing vehicles. Since this counterintuitive and apparently contradictory behavior that has not been reflected in literature (total particle number increase with PFAD biodiesel blends and B10 exhaust emissions higher than B30 ones) occurred, in order to verify Euro 5 to be stable over the testing period a closure test, using B7 blend, was in the end carried out. Results finally obtained, compared to those obtained over B7 initial tests, were generally higher about particulates and NO_x and lower about CO₂. A bad stability of Euro 5 was then proved, which obligates being careful in interpreting its particulate exhaust emission data also considering the role of DPF and the PN_PMP compliant exhaust emission level measured above the limit, also with B7 reference blend. However Carbone R. et al. (2016), conclude that the addition of FAME in diesel fuel decreases the engine-out PM emissions and therefore DPF regeneration frequency.

In Figure 7 the decrease of PM soot fraction detected over the urban cycles for LCVs without DPF can be easily pointed out.

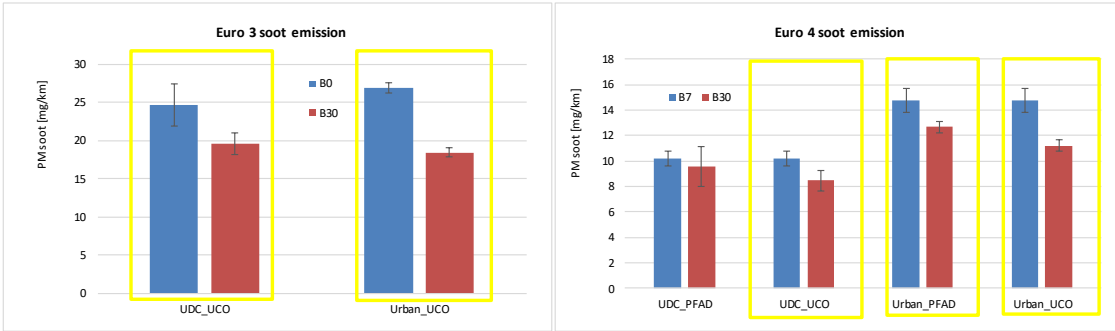


Figure 7: Euro 3 and Euro 4 PM soot emissions on urban cycles with different blends. Evidenced in yellow the differences validated as statistically significant.

Due to most interesting and statistically validated differences observed in Euro 3 and Euro 4, a focus on particle distribution detected by ELPI within the range $0.007\text{--}10 \mu\text{m}$ aerodynamic diameter was performed, being the dimension of particles, together with their chemical composition, an important physical parameter to evaluate their potential health effect on human beings. Reported particle distributions refer to values detected over Artemis Urban, being this one a demanding laboratory cycle and effectively mimicking real driving speed and acceleration profiles and conditions in a urban context, often characterized by frequent discontinuities and stop&go.

As already pointed out previously, Euro 3 showed a statistically significant reduction of PN_ELPI exhaust emission by 13.1% within the $0.031\text{--}10 \mu\text{m}$ range with UCO B30 blend compared to B0 for Artemis Urban. In Figure 8 it can be noticed that this reduction can be correlated mainly to coarser particles about which, for average aerodynamic diameters within the range $0.027\text{--}6 \mu\text{m}$, reductions up to nearly 50% can be observed corresponding to some distribution points. Focusing on nanoparticles (i.e. in Figure 8, particles with average D_p $<0.027 \mu\text{m}$) in fact an increase compared to both B0 and B10 can be noticed, respectively by around 25% and 15%.

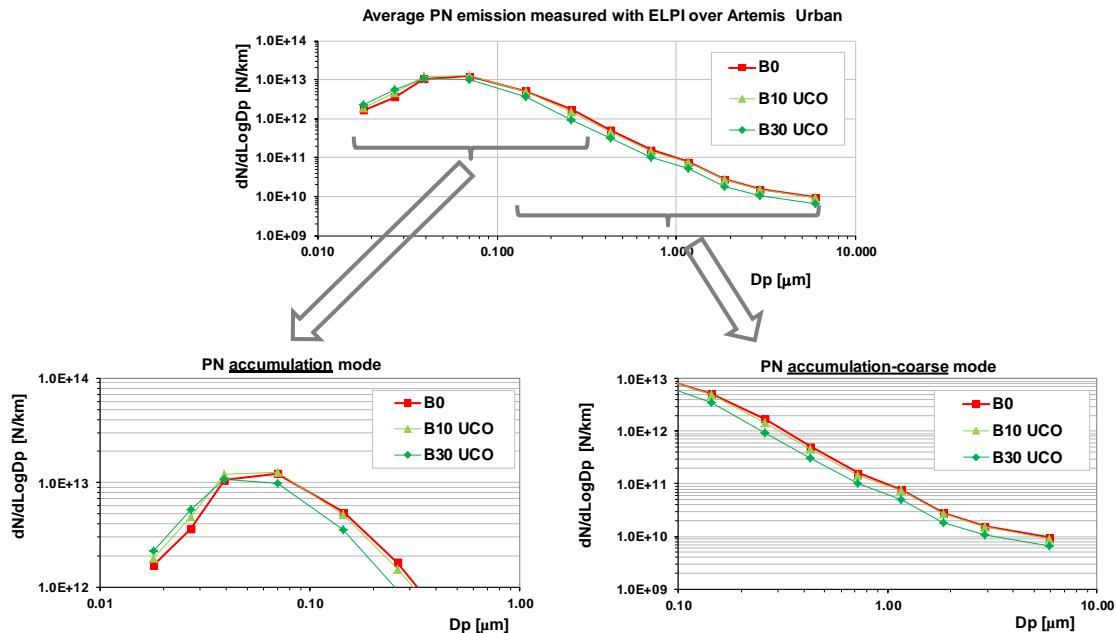


Figure 8: Particles distribution detected by ELPI ($0.007\text{--}10 \mu\text{m}$ aerodynamic diameter) in the exhaust of Euro 3 fed with B0 vs UCO B10 and B30 blends.

As already reported above, Euro 4 also showed a statistically significant reduction of PN_ELPI exhaust emission within the $0.031\text{--}10 \mu\text{m}$ range, by 26% with PFAD B30 and by 19.1% with UCO B30 blend. Considering all blends compared to B7 reference one, it was noticed a general reduction of PN_ELPI exhaust emission on all sizes, except for one size for UCO B10 (around 70 nm) and several sizes for PFAD B10.

Considering all B10-B30 blends, the most evident reduction coincides with the emission peak detected around 40 nm average D_{pi} , the maximum reference diameter by which the nanoparticles are often identified, close to the typical accumulation mode of diesel exhaust particles (Kittelson, 1998). Regarding this fraction of great toxicological interest, here identified by the sum of the number of particles detected through the first 3 stages of ELPI, there were reductions compared to the B7 by 12% for UCO B10, by 18% for UCO B30, by 13% for PFAD B10 and by 25% for PFAD B30. The most important percentage reduction (by 42.1%) was detected at 40 nm average D_{pi} in correspondence to PFAD B30 compared to B7 reference one.

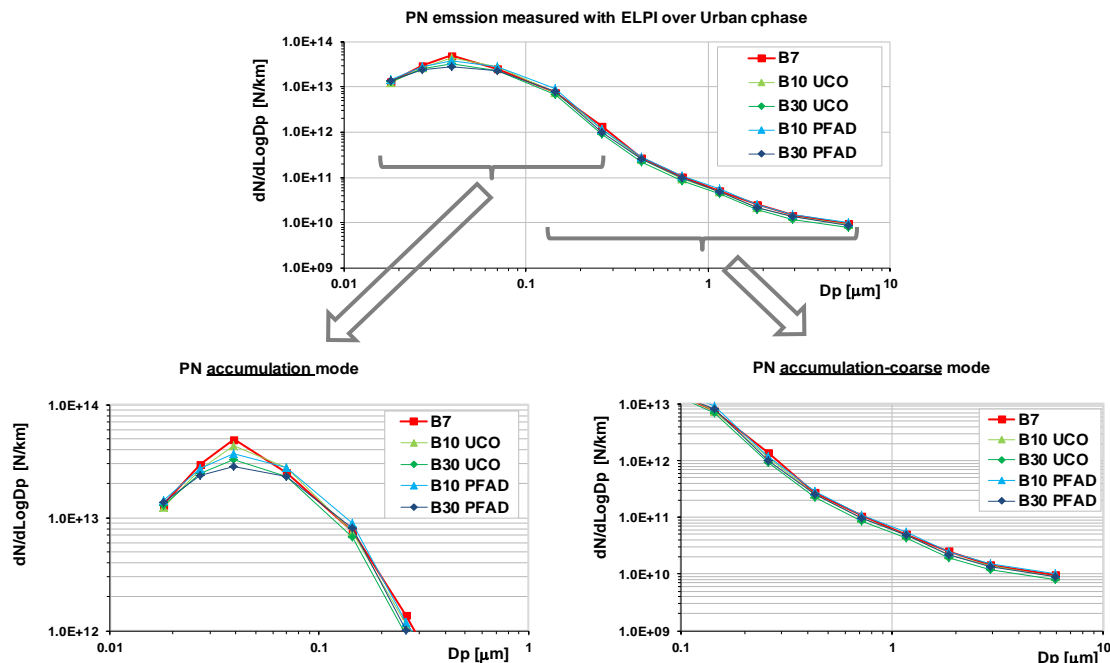


Figure 9: Particles distribution detected by ELPI (0.007÷10 μm aerodynamic diameter) in the exhaust of Euro 4 fuelled with B7 vs UCO/PFAD B10 and B30 blends.

Despite the differences between Euro 3 and Euro 4 PN_ELPI distributions previously discussed, comparing modal trends of PN_ELPI (in the range 0.007÷10 μm aerodynamic diameter) associated with reference and both UCO and PFAD B10-B30 blends, both LCVs without DPF show the highest reductions mainly corresponding with the cold-start phase accelerations of UDC and Artemis Urban cycle, with reductions increasing correspondingly to the increase of second generation biodiesel content blended with diesel.

These results can be considered as quite in agreement with literature (Lapuerta et al., 2008; Shah et al., 2014; Shahira et al., 2015), confirming that the tested biodiesels can play an important role as fuels useful for exhaust PM and PN reduction.

Conclusions

According to most recent data provided by Automobile Club Italia, in Italy in 2017 more than 80% of the LCVs circulating fleet was composed of pre-Euro 6 vehicles. Since among some developing countries this percentage might be even greater, much attention should be payed to their impact on air quality and to their contribution to transport greenhouse gas emissions, possibly with an LCA approach. Since in the debate about the European Union Directive 2018/2001 it is still uncertain whether PFAD can be included in Part A of Annex IX of the Directive, this study could be considered of interest about it.

Within the Biagio project, a LCV testing fleet was chosen to be representative of the real circulating one at the time of testing. It was composed of one Euro 3, one Euro 4 (both without DPF) and one Euro 5 vehicle which were fuelled with PFAD and UCO B10 and B30 second-generation biodiesel blends. This study's aim was to detect gaseous and particulate exhaust emissions and to be compared with those obtained by fuelling the same vehicles with B0 or B7 reference blends. Pure UCO and PFAD biodiesel turned out to be difficultly stored because of their tendency to solidify.

Regarding gaseous emissions and fuel consumption, with increasing the content of biodiesel very few statistically significant results were found: for Euro 3 vehicle around 5% increase of NO_x, HC+NO_x and fuel consumption values with UCO B30 blend, over the EUDC phase, while in UDC phase the use of PFAD B30 blend determined a decrease by 24% for Euro 4 and by 38% for Euro 5. For the latter a 7.1% increase in fuel consumption over EUDC phase was detected with UCO B30. Regarding Aldehydes, in cold start cycle as the content of PFAD biodiesel increased Formaldehyde emission progressively decreased up to 30% with B30, this trend not detected with UCO biodiesel.

Regarding particulate exhaust emissions measurement on Euro 3 and Euro 4, with increasing biodiesel blends progressive statistically significant reductions of regulated PM and of PM soot fraction were detected in comparison to standard fuel: for PM by 16.7% and by 29.7% respectively for Euro 3 and Euro 4 B30 UCO blends were found over the Artemis Urban, for PM soot for both PFAD and UCO B30 blends reductions between 14.3% and 31.6% for both vehicles in all cycles.

Particle number exhaust emission was statistically significantly reduced, too: PN PMP compliant by 16.7% for Euro 3 and by 21.3% for Euro 5 with UCO B30 blends over Artemis Urban, for PN ELPI (total particles with D_p 0.031÷10 µm) reductions for Euro 3 and Euro 4 respectively up to 13.1% (with UCO B30) over Artemis Urban and up to 30.3% (with PFAD B30) over EUDC. A focus on particle distributions for LCVs without DPF showed a general decrease in fine particles mainly corresponding with the cold-start acceleration phases of UDC and Artemis Urban cycle, different effects regarding accumulation mode and nanoparticles for Euro 3 and Euro 4, which is in agreement with literature.

An investigation on DPF role over the tested Euro 5 particles exhaust emissions has been developed and here reported.

Even though a more considerable testing activity would be required to confirm some of these results (i.e. a more numerous testing fleet, PAHs and other unregulated species detected), Biagio study give confirmations to the effectiveness of UCO and PFAD second-generation biodiesel blends in reducing the environmental impact of exhaust emissions from pre-Euro 6 diesel LCVs particularly in a urban context (where cold starts, stop&go drive style and human beings pollutants exposure are significant), stressing the potential usefulness of this fuelling where older LCVs diesel circulating fleets are large and cannot be easily and quickly replaced to improve air quality.

Acknowledgements

Many thanks to the colleagues of Innovhub SSI Paolo Bondioli, Davide Faedo and Gabriele Migliavacca and to Andrea Carrassi (Assitol) for their precious support provided within both the testing and the paper writing phases.

References

- Adaileh Wail M. and AlQdah Khaled S. (2012). Performance of Diesel Engine Fuelled by a Biodiesel Extracted From A Waste Cocking Oil. *Energy Procedia*, vol 18, pp 1317 – 1334.
- Automobile Club Italia. *Autoritratto* 2017, June 2015. www.aci.it.
- Automobile Club Italia. *Autoritratto* 2017, June 2018. www.aci.it.
- Alam F., Mobin S., Chowdhury H. (2015). Third generation biofuel from Algae. *Procedia Engineering*, Vol 105, pp 763-768.
- André M. (2004). The ARTEMIS European driving cycles for measuring car pollutant emissions. *Science of the Total Environment*, Volume 334–335, 2004, 73–84.
- Carbone R., Cardenas Almena M.D., Clark R., Fittavolini C., Gunter G., Jansen L., Lehto K., Kar K., Kraft H., Krebes L., Pellegrini L., Williams R (2016). Impact of FAME Content on the Regeneration Frequency of Diesel Particulate Filters (DPFs). CONCAWE, Report no. 14/16.
- Cheung C.S., Man X.J., Fong K.W., Tsang O.K. (2015). Effect of waste cooking oil biodiesel on the emissions of a diesel engine. *Energy Procedia*. Vol 66, pp 93 – 96.
- COMMISSION DECISION of 3 May 2000 replacing Decision 94/3/EC establishing a list of wastes pursuant to Article 1(a) of Council Directive 75/442/EEC on waste and Council Decision 94/904/EC establishing a list of hazardous waste pursuant to Article 1(4) of Council Directive 91/689/EEC on hazardous waste.
- COMMISSION REGULATION (EC) No 692/2008 of 18 July 2008 implementing and amending Regulation (EC) No 715/2007 of the European Parliament and of the Council on type-approval of motor vehicles with respect to

emissions from light passenger and commercial vehicles (Euro 5 and Euro 6) and on access to vehicle repair and maintenance information.

DIRECTIVE (EU) 2018/2001 OF THE EUROPEAN PARLIAMENT AND OF THE COUNCIL of 11 December 2018 on the promotion of the use of energy from renewable sources (recast).

De Filippo A., C. Ciaravino C., Millo F., Vezza D., Fino D., Russo N., Vlachos T. (2011). Particle Number, Size and Mass Emissions of Different Biodiesel Blends Versus ULSD from a Small Displacement Automotive Diesel Engine. *SAE Technical Paper* N. 2011-01-0633.

EN590 Automotive fuels - Diesel - Requirements and test methods.

EN14214 Liquid petroleum products - Fatty acid methyl esters (FAME) for use in diesel engines and heating applications - Requirements and test methods.

EN16709 Automotive fuels - High FAME diesel fuel (B20 and B30) - Requirements and test methods.

EN16734 Automotive fuels - Automotive B10 diesel fuel - Requirements and test methods.

EPA Method TO, "Method TO-11A: Compendium of Methods for the Determination of Toxic Organic Compounds in Ambient Air Second Edition Compendium Method TO-11A Determination of Formaldehyde in Ambient Air Using Adsorbent Cartridge Followed by High Performance Liquid Chromat," Environ. Prot., no. January, 1999.

Font de Mora E., Torres C. and Valero A. (2015). Thermo-economic Analysis of Biodiesel Production from Used Cooking Oils. *Sustainability*. Vol 7, pp 6321-6335.

Kittelson D. B. (1998). Engines and Nanoparticulates: a Review. *J. Aerosol Sci.*, 29, N. 56, p.575.

Lapuerta M., Rodríguez-Fernández J., Agudelo J. R. (2008). Diesel particulate emissions from used cooking oil biodiesel. *Bioresource Technology*. Vol 99, pp 731-740.

LIFE Programme. Ecobus (2012). Collecting Used Cooking Oils to Their Recycling as Biofuel for Diesel Engines; Technical Report; European Commission.

Macor A., Avella F., Faedo D. (2011). Effects of 30% v/v biodiesel/diesel fuel blend on regulated and unregulated pollutant emissions from diesel engines. *Applied Energy* 88, 4989– 5001.

Nanta Gopal K, Pal A., Sharma S., Samanchi C., Sathyaranayanan K., Elango T. (2014). Investigation of emissions and combustion characteristics of a CI engine fueled with waste cooking oil methyl ester and diesel blends. *Alexandria Engineering Journal*. Vol 53, pp 281-287.

Poonam S. N., Anoop S. (2011). Production of liquid biofuels from renewable resources. *Progress in Energy and Combustion Science*, Vol 37, pp 52-68.

Rose K. D., Samaras Z., Jansen L., Clark R., Elliott N., Fontaras G., Zemroch P. J., Hall D., Almena M.D.C., Higham C., Kalogirou M. (2010) Impact of Biodiesel Blends on Fuel Consumption and Emissions in Euro 4 Compliant Vehicles. *SAE Technical Paper* N. 2010-01-1484.

Shah A. N., Yun-shan G., Shah F. H., Mughal H. U., Rahman Z. u., Naveed A. (2014). Effect of biodiesel on particulate numbers and composition emitted from turbocharged diesel engine. *Int. J. Environ. Sci. Technol.* Vol 11, pp 385–394.

Shahira V.K., Jawaharb C.P., Sureshc P.R. (2015). Comparative study of diesel and biodiesel on CI engine with emphasis to emissions—A review. *Renewable and Sustainable Energy Reviews*. Vol 45, pp 686-697.

UN ECE Regulation N. 83 – “Uniform provisions concerning the approval of vehicles with regard to the emission of pollutants according to engine fuel requirements – Revision 4, 26 April 2011.

Zahan K. A., Kano M. (2018). Biodiesel production from palm oil, its by-products, and mill effluent: a review. *Energies* 2018, 11, 2132.

2.6.7 A Novel Technology of High-Pressure Thermochemical Recuperation for Efficiency Increase and Emissions Mitigation

L. Tartakovsky^{1,2*}, A. Eyal¹, A. Thawko² and H. Yadav¹

¹ Faculty of Mechanical Engineering, Technion – Israel Institute of Technology, Technion City, Haifa 3200003, Israel, tartak@technion.ac.il

² Nancy and Stephen Grand Technion Energy Program, Technion – Israel Institute of Technology, Technion City, Haifa 3200003, Israel

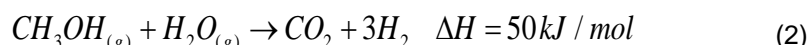
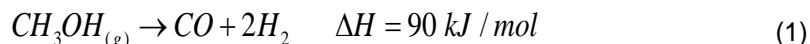
Introduction

The climate change challenges make necessary a continuous effort toward reduction of global environmental pollution and fossil oil consumption. Transportation is responsible for a significant share of the energy consumption worldwide. Thus, to decrease oil dependency, meet GHG emission and air quality targets, overall energy consumption and emissions of road vehicles must be substantially reduced (Tartakovsky et al., 2012).

Autonomous transport technology is intensively developed nowadays (Saykin et al., 2016; Saykin et al., 2017; Barry et al., 2018). It has a potential of energy efficiency and driving safety improvement, commuting time and traffic reduction, significant parking space saving, among other. There is a believe that the autonomous vehicle technology will promote deployment of electric vehicles. However, experts showed that the additional computing and data processing hardware and sensors needed by fully autonomous vehicles will require significant amounts of additional energy and a tremendous investment in infrastructure (Kalghatgi, 2018). This, together with energy consumption of air conditioning and heating systems, will make impractical applying a pure electric drive for autonomous vehicles propulsion. A more viable option for autonomous driving would be a hybrid or plug-in hybrid, not a battery electric vehicle (Thomas, 2017). Understanding this fact, with mentioned above global challenges, emphasizes an utmost importance of internal combustion engine (ICE) efficiency improvement for both human-driven and autonomous vehicle technologies.

Ethanol and methanol are widely investigated as alternative fuels since they have low carbon content (Al-Baghdadi, 2000; Wang et al., 2016; Nguyen and Verhelst, 2017). Methanol has an advantage because it can be produced from both fossil and renewable sources such as natural gas, coal, biomass, and renewable energy-derived hydrogen (electrofuel). Methanol is also an excellent primary fuel for ICEs with TCR because of its low reforming temperature (250 – 300 C). Thus, we employed methanol as a primary fuel for a propulsion system with waste heat recovery (WHR) through High-Pressure Thermochemical Recuperation (HP-TCR).

TCR has two main advantages over other WHR methods. It increases the fuel lower heating value due to sustaining endothermic fuel reforming reactions — Eq. 1 – 2 (Poran et al., 2018), and enables onboard production of a hydrogen-rich reformate with its subsequent combustion. The latter results in wider flammability limits, increased burning velocity and higher knock resistance (Verhelst and Wallner, 2009). Hence, ICE efficiency improvement is achieved not only due to the WHR but also because of lean-burn operating possibilities, combustion that better approximates the most efficient Otto cycle and the possibility of increasing the engine compression ratio (Tartakovsky and Sheintuch, 2018).



TCR for ICE applications was investigated in the past and a possibility of up to 40% brake thermal efficiency (BTE) improvement compared to the gasoline counterparts was demonstrated. However, a number of major drawbacks were identified. The main problems that were reported include catalyst deactivation, system's start-up and transient behaviour, uncontrolled combustion and a maximal power loss due to reduced volumetric efficiency (Pettersson and Sjostrom, 1991). The latter is a result of supplying gaseous reformate into the intake system that reduces the partial pressure of the air in the intake manifold, and the absence of an evaporative cooling effect compared to the case of a liquid fuel port injection.

HP-TCR description

We suggested a novel concept of a direct-injection ICE with HP-TCR – Fig. 1 (Tartakovsky et al., 2015; Poran and Tartakovsky, 2015; Poran and Tartakovsky, 2017a; Poran and Tartakovsky, 2017b). Direct injection of the reforming products allows prevention of the uncontrolled combustion and the power loss problems. We showed that performing the reforming reactions at high pressure is essential to enable direct injection of the reformat. Otherwise, a significant fraction of the engine power would be required to compress the reformat prior to its injection (Poran and Tartakovsky, 2015). The cold start and transient behaviour problems can be resolved by integrating the HP-TCR system into a hybrid-electric propulsion scheme and/or keeping a small on-board pressurized vessel with reformat for start-up or injection of some of the primary fuel with a port fuel injector (Tartakovsky et al., 2011).

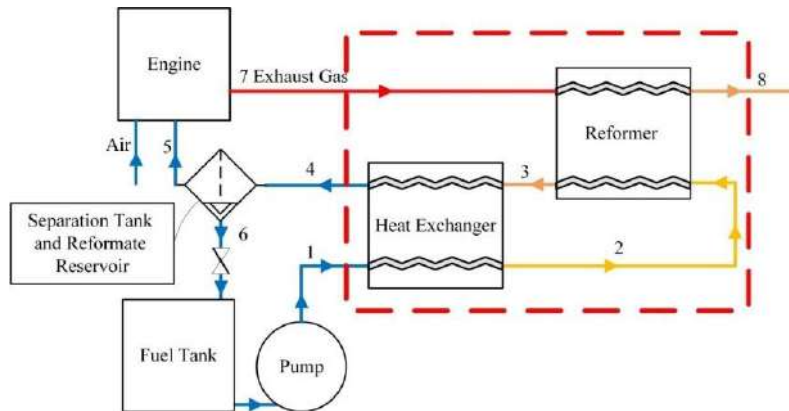


Figure 1: Schematic layout of the High-Pressure TCR system (Poran and Tartakovsky, 2017b). 1 – methanol and water mix (1:1 molar ratio) at high pressure; 2 – preheated methanol and water mix; 3 – hot reforming products with residues of unreformed methanol and water; 4 – cooled reforming products with condensed unreformed methanol and water; 5 – cooled gaseous reformat; 6 – condensed unreformed methanol and water; 7 – hot exhaust gas; 8 – cooled exhaust gas.

As a first experimental step, a DI ICE fueled with artificially prepared MSR products (0.25 CO₂ and 0.75 H₂ mole fractions) from the compressed gas cylinder was developed and investigated. It showed 18%-39% increase in indicated efficiency and reduction of 73-94%, 90-96%, 85-97%, 10-25% in NO_x, CO, HC and CO₂ emissions, respectively, compared with a baseline gasoline single cylinder engine with carburettor in a wide power range (Poran and Tartakovsky, 2017a). Further investigation showed an importance of reformat injection strategy and especially end-of-injection event on engine efficiency and pollutant emissions (Poran and Tartakovsky, 2017b). To improve energy utilization, the primary fuel pre-heating by a hot reformat was suggested (Poran and Tartakovsky, 2017b). An importance of this approach as an efficient method of exergy destruction minimization was confirmed later by (Chuahy and Kokjohn, 2017).

Further, the previously developed DI engine was coupled with a high-pressure methanol steam-reforming reactor to form the first ever working prototype of a DI ICE with HP-TCR system.

Methodology

The experimental setup was based on a single-cylinder carburetor gasoline-fed SI engine (baseline configuration) converted to operate with direct injection of gaseous reformat. Fig. 2 (Poran et al., 2018) shows the experimental setup scheme.

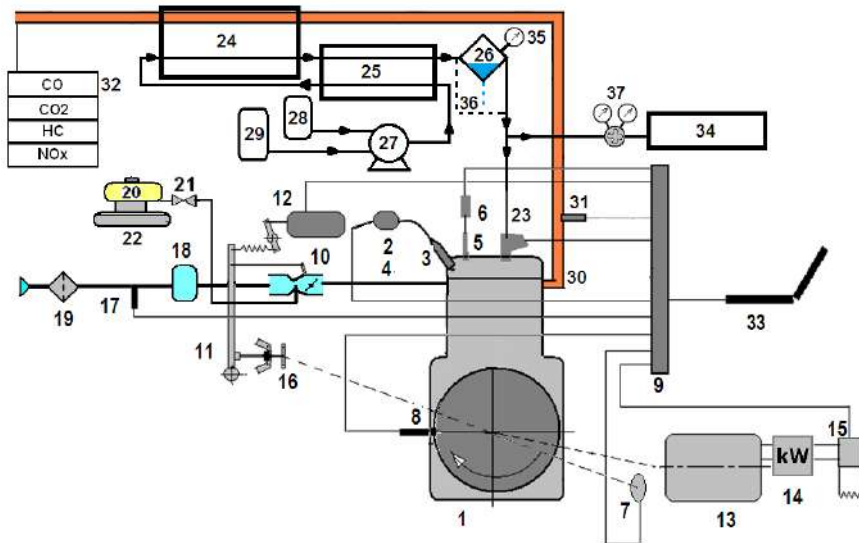


Figure 2: Schematic layout of the experimental setup (Poran et al., 2018). 1 - Robin EY20-3 single cylinder ICE; 2 - ignition coil; 3 - spark plug; 4 - air intake system; 5 - pressure transducer; 6 - charge amplifier; 7 - crankshaft encoder; 8 – top dead center proximity sensor; 9 - ECU and data acquisitor; 10 – throttle; 11 – centrifugal speed governor; 12 – linear actuator; 13 – generator; 14 – power gauge 15 –proportional controller; 16 – crankshaft driven gear of the engine speed governor; 17 – air flow meter; 18 – pressure wave damper; 19 – air filter; 20 – gasoline tank; 21 – valve; 22 – electronic scales; 23 - DI gas injector; 24 – reformer; 25 – heat exchanger; 26 – liquid separation tank and reformate reservoir; 27 – fuel pump; 28 – methanol tank; 29 – water tank; 30 – exhaust line; 31 – O₂ sensor; 32 – exhaust gas analyzers; 33 – computer; 34 – gas chromatograph; 35 – pressure gauge; 36 – liquid separation tank bypass; 37 – pressure regulator.

As seen from Fig.2, from the heat exchanger, the preheated methanol-water mixture entered an in-house developed reformer (24). A detailed description of the reformer design can be found in (Poran et al., 2018). The catalyst tubes were filled with a commercial G-66 CuO/ZnO catalyst (cylindrical pellets of 3mm diameter and length), courtesy of Clariant. From the reformer, the hot reformat was conveyed to the heat exchanger (25) to cool down and preheat the methanol-water mixture delivered by the pump (27).

Reformat composition was measured by Agilent 490 micro gas chromatograph (GC) equipped with 1m COX and 10m PPU columns through a pressure regulator (37) and two thermal conductivity detectors (TCD). CO₂ and CO concentrations were measured from a dried exhaust gas sample line with a California Analytical Instrument (CAI) 600 series NDIR analyser. NO_x concentration was measured from the same sampling line using a Thermal Converter 501x and NO_x chemiluminiscent analyser 200EH from Teledyne Instruments. Total hydrocarbons (HC) were measured through a heated sample line with a CAI 600 series FID HC analyser. A detailed description of the measuring system and uncertainties analysis can be found in (Poran and Tartakovsky, 2017a; Poran et al., 2018). We used an in-house-developed direct reformat injector. The injector was developed based on a commercial Magneti Marelli IHP072 gasoline DI injector modified to enable higher volumetric flow rates necessary for gaseous reformat injection. Further details on the injector and its installation in the engine head can be found in (Tartakovsky et al., 2015; Poran and Tartakovsky, 2017b).

A performance of the ICE with HP-TCR was investigated at steady-state regimes. The operating regimes (various loads at constant engine speed and wide-open-throttle – WOT) were chosen based on the previous engine running experience (Poran and Tartakovsky, 2017a; Poran and Tartakovsky, 2017b). The measured data were processed as explained in (Poran et al., 2018).

Results and Discussion

It is known that the engine operating mode and the employed method of waste heat recovery affect the reforming temperature. The measured gaseous reforming products composition for the reformer hot side temperature of 615K is shown in Fig. 3.

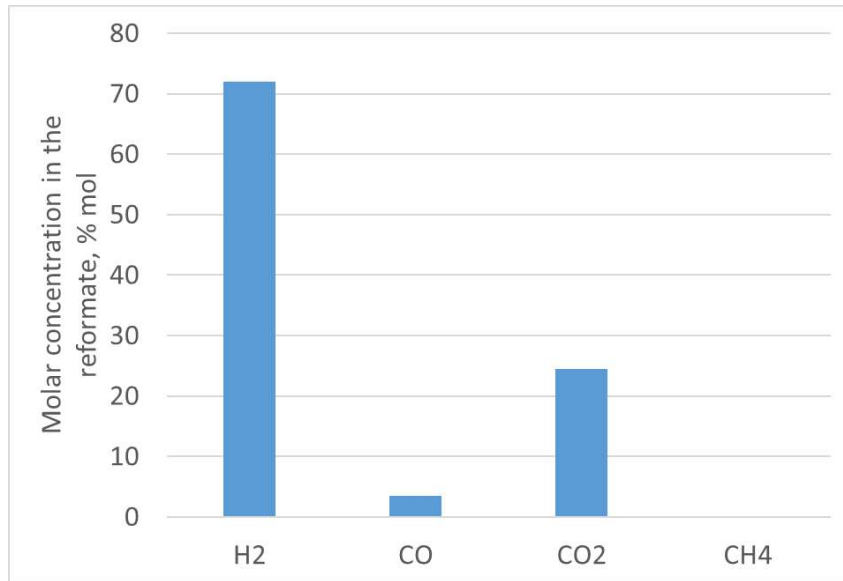


Figure 3: The measured methanol reformate composition (water excluded). Reformer hot side temperature – 615K.

As demonstrated by Poran et al. in the theoretical study (Poran et al., 2014), a higher CO fraction and respectively lower CO₂ and H₂ fractions in the reformat are expected with the reforming temperature increase, due to the reverse water gas shift reaction. The presence of methane is not expected at steam-to-methanol ratio of unity (Choi and Stenger, 2002). Indeed, methane occurrence (in very small fractions) was observed only at the excessively high reforming temperature exceeded the planned temperature range of 573–623K (Poran et al., 2018). The high reforming temperature also resulted in higher than expected CO fraction. Notably, higher CO and CH₄ fractions are advantageous for ICE with TCR since more waste heat is recovered and reformat with higher molar energy density is produced. The latter allows more flexibility in direct reformat injection (Poran and Tartakovsky, 2015). It is important to underline that the measured H₂ content in the reformat was $\geq 65\%$ mol. at all investigated regimes and thus made possible exploiting the great advantages of H₂ combustion. When the reforming temperature was in the expected range (573–623K), H₂ content in the reformat was very close to the theoretical 75% of the methanol steam reforming (MSR) reaction (Fig. 3).

In the considered TCR configuration (hot reformat is cooled before injection while preheating methanol-water mixture), this fuel-water mixture starts evaporating in the heat exchanger, and hence enters the cold side of the reformer at its evaporation temperature (T_{ev}). Thus, the exhaust gas outlet temperature (down-bounded by the temperature at the cold side of the reformer - Fig. 1) is actually bounded by the mixture evaporation temperature: $T_8 \geq T_2 = T_{ev}$. The experimental results demonstrated that indeed the temperature at the cold side of the reformer is very close to published methanol-water mixture evaporation temperatures (Teutenberg et al., 2009). Considering this fact, the control strategies can be employed (depending on engine operation regime) to improve waste heat recovery and primary fuel conversion. For example, it is possible to increase exhaust gas energy utilization by arranging the primary fuel flow (pt. 1 in Fig. 1) in such a way that a part of the fuel flows through the heat exchanger as in Fig. 1, and the rest is preheated in an additional heat exchanger by the exhaust gases leaving the reformer at temperature T_8 . This complicates the system, but allows more waste heat recovery by cooling the exhaust gas below T_{ev} . A possibility to increase methanol conversion by injecting the hot reformat to the engine without cooling it in the HE could be considered as well for some operating modes. This would increase exhaust gas temperature at the reformer inlet, prevent methanol condensation and allow achieving lower temperatures at the reformer outlet (because MWM would enter the reformer at ambient temperature). The negative aspects of this approach, like some increase in the compression work and elevated heat losses should be taken into account. When the available waste energy is not enough to sustain endothermic fuel reforming reactions, a separate injection of some unreformed methanol may be considered. This would increase the HE effectiveness, the reformer temperatures and would finally lead to a higher usage of the reformed fuel compared to the case when the MWM just circulates in the system. An analysis of the suggested ways to improve waste heat recovery and conversion was out of the scope of this work.

The relatively high content of CO in the reformate together with the incomplete methanol conversion implies that the reformer suffers from diffusion limitation and possibly from unequal flow in its tubes. The latter results in elevated CO formation in the tubes with lower space velocity and higher residence time, as well as in reduced conversion in the tubes with higher space velocity and lower residence time. The performance of the high-pressure reforming system coupled with the previously studied DI-ICE was investigated and is discussed below.

Emissions and efficiency measurements of ICE with HP-TCR system were compared with baseline gasoline engine and performance of the same engine fed with artificially prepared MSR products from compressed gas cylinders. The experimental results of the engine performance improvement in comparison with a baseline gasoline-fed counterpart are shown in Fig. 4.

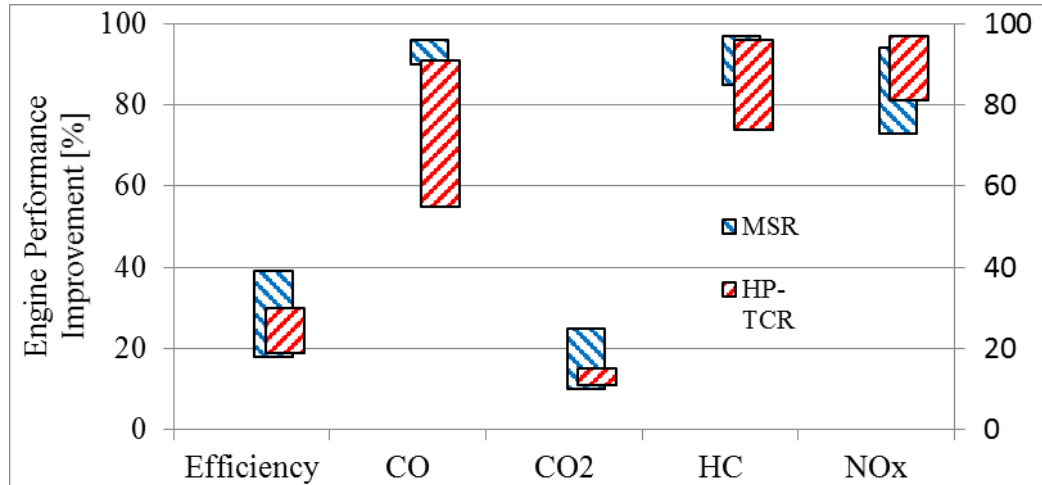


Figure 4: Engine performance improvement range over gasoline of artificially prepared MSR fuel and HP-TCR system.

As expected, the engine CO emissions with HP-TCR are much lower compared to the gasoline counterpart and lie in the same range with the artificial MSR. At the lowest investigated load, CO emissions increased significantly due to drops of condensed unreformed methanol that occasionally entered the cylinder through the injector and resulted in rich-mixture combustion. These methanol drops also caused increased HC emissions (Fig. 4).

The occasional intrusion of methanol drops to the combustion chamber roughly doubled or tripled the HC emissions compared to the case of artificial MSR products where lubricant was the only source of HC emissions. In the case of complete conversion (highest load), the HC emissions remained the same as for artificial MSR products. This means that by further improvement of the high-pressure reforming system in one of the ways discussed in (Poran et al., 2018), CO and HC emissions of DI-ICE with HP-TCR can be significantly reduced. For NO_x, unlike the CO and HC emission cases, the HP-TCR system showed even better results than those of the artificial MSR (Fig. 4).

The low NO_x emissions of artificial MSR products and HP-TCR system are due to the lean-burn ability of the hydrogen-rich reformate and the CO₂ presence in methanol steam reforming products. The latter is a diluent gas and when injected into the cylinder as a part of the reformate fuel it reduces the combustion temperatures. In the case of HP-TCR, the NO_x emissions are even lower than with artificial MSR due to the presence of water in the injected reformate that further reduces the combustion temperatures and hence the NO_x formation.

Also in the case of CO₂ emissions, the HP-TCR showed significant improvement over gasoline case compared to artificial MSR products (Fig. 4). Notably, some of the measured reduction in specific CO₂ emissions (~7%) originates from using a low carbon intensity primary fuel – methanol as compared to gasoline, while the rest comes from the improvement in fuel conversion efficiency.

HP-TCR shows great improvement in terms of efficiency compared to gasoline. Despite the fact that some of the efficiency enhancement should be related to retrofitting the gasoline carburettor engine with a DI injector, the major improvement comes from the waste heat recovery, lean burn benefits and the

improved reformate combustion properties. For HP-TCR the achieved efficiency gain is slightly lower compared to artificial MSR products, especially at low load. There is less energy in the exhaust gases with engine load reduction, which reduces the reforming system performance (lower conversion and lower HE effectiveness) and subsequently adversely affects the ICE with HP-TCR performance. As mentioned previously, lower conversion resulted in the sporadic intrusion of unreformed condensed methanol drops into the cylinder, which led to worsened combustion quality and a subsequent efficiency reduction. The results achieved with engine feeding by the artificial MSR products may serve as a reference case to show how much improvement may be achieved by improving the reforming system. The range of improvement over gasoline achieved with HP-TCR system and compared with artificial MSR is summarized in Table 1.

Table 1: Engine performance improvement range of artificial MSR, and HP-TCR over gasoline.

	Engine performance improvement range	
	MSR	HP-TCR
Efficiency	18-39	19-30
CO	90-96	55-91
CO ₂	10-25	11-15
HC	85-97	74-96
NOx	73-94	81-97

As seen from Fig. 4 and Table 1, although the system is not optimized yet, it shows a significant improvement over the gasoline reference case with 19%-30% increase in indicated efficiency and reduction in NO_x, CO, HC and CO₂ emissions by up to 97, 91, 96 and 15 percent, respectively. The results obtained for ICE fed with artificially prepared MSR reformate show even higher performance improvement that may be achieved. Note that the percentage efficiency improvement (19–30%) over ICE feeding with gasoline is higher than the reduction in CO₂ emissions (11–15%) because of carbon redistribution from CO and HC emissions to CO₂ (note that engine-out emissions are considered in this work). When ICE is fed with gasoline, the carbon supplied with the fuel is emitted as CO₂, CO, and HC. Whereas, for ICE with HP-TCR, CO and HC emissions are mitigated by up to 91% and 96%, respectively. Hence, the majority of carbon introduced with the fuel into the ICE is emitted as CO₂, thereby resulting in a lower reduction of CO₂ emissions relative to efficiency improvement.

Summary and Conclusions

A need in substantial efficiency improvement of propulsion systems together with mitigation of their GHG and target pollutant emissions, as well as in use of renewable alternatives to fossil oil fuels were the main reasons that lead to the reported study.

This work reports the experimental study results of a novel approach - an internal combustion engine with High-Pressure Thermochemical Recuperation. The system employs methanol - a low-carbon-intensity alternative liquid primary fuel (enables convenient gasoline-like vehicle fuelling), however the ICE burns hydrogen-rich methanol steam reforming products as a standalone fuel. The suggested concept allows eliminating the major drawbacks of the known TCR methods, like engine power loss and abnormal combustion. The experimental results discussed in the reported study of DI ICE with HP-TCR system is a significant step forward, because the developed system is the first ever working prototype of ICE with HP- TCR which was investigated for the first time.

Although the system is not optimized, it demonstrates a significant performance improvement over the reference case of a gasoline-fed single cylinder carburettor engine with 19%-30% increase in indicated efficiency and reduction in NO_x, CO, HC and CO₂ emissions by up to 97, 91, 96 and 15 percent, respectively. The results of engine feeding with artificially prepared MSR products show the further improvement potential that may be achieved.

The achieved performance of ICE with HP-TCR shows a good prospect to continue the research towards an automotive-scale system development.

Despite the achieved significant gain in efficiency and emissions mitigation, the obtained results clearly show that HP-TCR system performance can be further improved. The reformer reaction rate is too slow and its speeding-up may allow reduction of the reformer size together with the increase of methanol

conversion. For this purpose, reducing the catalyst pellet size in the reformer or applying a coated reformer type is suggested.

It is shown that reforming pressure reduction can enable better exhaust gas energy extraction. The pressure reduction can be achieved by increasing the injector flow area. Among other performance improvement options, further heat exchanger effectiveness increase, splitting the methanol-water mixture flow (where part of the mixture is preheated by the hot reformate and another part – by the exhaust gas) and injecting the reformate directly after the reformer at low-load regimes are mentioned.

Acknowledgements

The authors gratefully acknowledge the financial support of the Israel Science Foundation (grant 2054/17); Israel Ministry of Energy (grant 215-11-025); Israel Innovation Authority (grant 63352), the Council for Higher Education (CHE) - Planning and Budgeting Committee (PBC), and the Grand Technion Energy Program.

References

- Al-Baghdadi M.A.R.S. (2000), Performance study of a four-stroke spark ignition engine working with both of hydrogen and ethyl alcohol as supplementary fuel. *International Journal of Hydrogen Energy* 25(10): 1005-1009.
- Barry A. J., Florence P. R., Tedrake R. (2018), High-speed autonomous obstacle avoidance with pushbroom stereo. *Journal of Field Robotics* 35, 52-68.
- Choi Y., Stenger H. G. (2002). Fuel cell grade hydrogen from methanol on a commercial Cu/ZnO/Al₂O₃ catalyst. *Applied Catalysis B: Environmental*, 38(4), 259-269.
- Chuahy F.D.F., Kokjohn S.L. (2017), High efficiency dual-fuel combustion through thermochemical recovery and diesel reforming. *Applied Energy* 195, 503–522.
- Kalghatgi G. (2018), Is it really the end of internal combustion engines and petroleum in transport? *Applied Energy*, 225, 965-974.
- Nguyen D. K., Verhelst, S. (2017), Computational Study of the Laminar Reaction Front Properties of Diluted Methanol–Air Flames Enriched by the Fuel Reforming Product. *Energy & Fuels*, 31(9), 9991-10002.
- Pettersson L., Sjostrom K. (1991), Decomposed Methanol as a Fuel—A review. *Combustion Science and Technology* 80(4-6), 265-303.
- Poran A., Artoul M., Sheintuch M., Tartakovsky L. (2014), Modeling internal combustion engine with thermochemical recuperation of the waste heat by methanol steam reforming. *SAE International Journal of Engines*, 7, 234-242.
- Poran A., Tartakovsky L. (2015), Energy efficiency of a direct-injection internal combustion engine with high-pressure methanol steam reforming. *Energy* 88, 506-514.
- Poran A., Tartakovsky L. (2017a), Performance and emissions of a direct injection internal combustion engine devised for joint operation with a high-pressure thermochemical recuperation system. *Energy* 124, 214-226.
- Poran A., Tartakovsky L. (2017b), Influence of methanol reformate injection strategy on performance, available exhaust gas enthalpy and emissions of a direct-injection spark ignition engine. *International Journal of Hydrogen Energy* 42(23), 15652-15668.
- Poran A., Thawko A., Eyal A., Tartakovsky L. (2018), Direct injection internal combustion engine with high-pressure thermochemical recuperation - experimental study of the first prototype. *International Journal of Hydrogen Energy* 43: 11969-11980.
- Saykin A. M., Buznikov S. E., Endachev D. V., Karpukhin K. E., Terenchenko A. S. (2017), Development of Russian Driverless Electric Vehicle. *International Journal of Mechanical Engineering and Technology* 8(12), 955–965.
- Saykin A., Buznikov S., Karpukhin K. (2016), The Analysis of Technical Vision Problems Typical for Driverless Vehicles. *Research Journal of Pharmaceutical, Biological and Chemical Sciences* 7, 2053-2059.
- Tartakovsky L., Baibikov V., Gutman M., Mosyak A., Veinblat M. (2011), Performance analysis of SI engine fueled by ethanol steam reforming products. *SAE Technical Paper* 2011-01-1992.
- Tartakovsky L., Gutman M., Mosyak A. (2012), Energy efficiency of road vehicles – trends and challenges. Chapter 3 in the Edited Collection. In: Cavalcanti Emmanuel F. Santos, Barbosa Marcos Ribeiro, editors. *Energy Efficiency: Methods, limitations and challenges*. Nova Science Publishers; 2012. p.63 – 90.

Tartakovsky L., Amiel R., Baibikov V., Fleischman R., Gutman M., Poran A., Veinblat M. (2015), SI Engine with Direct Injection of Methanol Reforming Products – First Experimental Results. SAE Technical Paper 2015-32-0712.

Tartakovsky L., Sheintuch M. (2018), Fuel reforming in internal combustion engines. Progress in Energy and Combustion Science, 67, 88-114.

Teutenberg T., Wagner P., Gmehling J. (2009), High-temperature liquid chromatography. Part I. Determination of the vapour pressures of binary solvent mixtures—Implications for liquid chromatographic separations. Journal of Chromatography A, 1216(37), 6471-6480.

Thomas C. (2017), Overcoming the ‘CO₂ penalty’ of autonomous vehicles. SAE High-Efficiency Engines Symposium, Detroit, USA.

Verhelst S., Wallner T. (2009), Hydrogen-fueled internal combustion engines. Progress in Energy & Combustion Science 35: 490-527.

Wang X., Ge Y., Zhang C., Tan J., Hao L., Liu J., Gong H. (2016), Effects of engine misfire on regulated, unregulated emissions from a methanol-fueled vehicle and its ozone forming potential. Applied Energy 177: 187-195.

2.6.8 Analysis of Pollutant Emissions of three Plug-in Hybrid Electric Vehicles

S.I. Ehrenberger¹, F. Philipps¹ and M. Konrad¹

¹ Institute of Vehicle Concepts, German Aerospace Center, Stuttgart, 70569, Germany,
simone.ehrenberger@dlr.de

Abstract

In order to evaluate real-world energy consumption and tail-pipe emissions of current PHEVs, we tested three PHEVs in different driving conditions. We consider measurements of emissions at different ambient temperatures and for different operating conditions of the vehicles. The results show that the battery state-of-charge (SOC) determines the absolute CO₂ emissions, as the CO₂ emissions decrease with higher electric shares. However, this does not apply for other pollutants like NO_x and particles as discussed in this paper. Furthermore, the results show that the cold start emissions have a high influence on the average emissions of the driving cycle at low ambient temperatures. Generally, the average pollutant emissions are less related to the speed or road category than in case of CO₂.

Keywords: plug-in hybrid vehicle, direct emissions, energy consumption, RDE test, dynamometer test

1. Introduction

In the past years, more and more passenger cars with alternative drive-trains have entered the market throughout Europe. Though their overall share in the car stock is still low, the need of lowering emissions of road transport and especially individual motorized mobility is broadly recognized. One of the main trends of the future vehicle markets is electrification, and plug-in hybrid electric vehicles (PHEVs) are seen as one important option for further reducing energy consumption and emissions of passenger car transport. Like purely battery electric vehicles, PHEVs can be charged from the electric grid. Thus, such power-trains can bring the benefits of an increasing share of renewable electric energy into the transport sector. Previous studies which analysed dynamometer tests with standard driving cycles have shown a certain potential of direct energy and emission savings during vehicle operation compared to conventional vehicles (Fontaras et al., 2008; Alvarez and Weilenmann, 2012, Suarez-Bertoa and Astorga, 2016). Nonetheless, the tests have further shown that lower ambient temperatures might lead to significantly higher emissions. For some pollutants analysed, the emissions measured have been in the range of conventional gasoline vehicles (Suarez-Bertoa and Astorga, 2016). Furthermore, recent tests applying the world harmonized light-duty test procedure (WLTP) with EURO6 compliant PHEVs have shown that these vehicles can emit similar or even higher amounts of pollutants as conventional gasoline or diesel vehicles (Suarez-Bertoa et al., 2019). Few results for on-road emission measurements have been published so far (Demuyck et al., 2018; Graver et al., 2011). They conclude that PHEV emissions in restart occasions of the internal combustion engine (ICE) are difficult to predict quantitatively, but are crucial for assessing the overall emission performance of this vehicle type.

In order to evaluate real-world energy consumption and tail-pipe emissions of current PHEVs in different driving modes, we tested three PHEVs in different driving conditions. We considered measurements of emissions and energy consumption at different ambient temperatures and for different operating conditions of the vehicles. In order to analyse possible systematic deviations, the vehicles were equipped with sensors and measurement technology and measurements on the test bench were compared with on-road measurements.

In this paper, we will compare the results of real-driving emission (RDE) tests with the results of the standard worldwide harmonized light duty vehicle test cycle (WLTC) tested on the dynamometer. The main focus of our analysis is on carbon dioxide (CO₂), carbon monoxide (CO), nitrogen oxides (NO_x) and particle (PN) emissions.

2. Methodology and Experimental Set-up

2.1 Vehicle Test Cycles

EU legislation has been gradually tightening up emission requirements. Until September 2017, certification took place via the NEDC (New European Driving Cycle) on the chassis dynamometer. Due to several shortcomings, the NEDC has been replaced by the WLTC (Worldwide harmonized Light vehicles Test Cycle) which is based on real driving data. The WLTC is characterized by both a higher maximum speed of 130 km/h instead of 120 km/h and more dynamic acceleration (Figure 1) (European

Commission, 2017). Additionally, the weight of optional vehicle equipment is taken into account, the idling events within the cycle have been reduced, and the total cycle time is extended from 20 to 30 minutes. Overall, the WLTC cycle is supposed to be closer to the real driving behaviour of most users than the NEDC driving cycle.

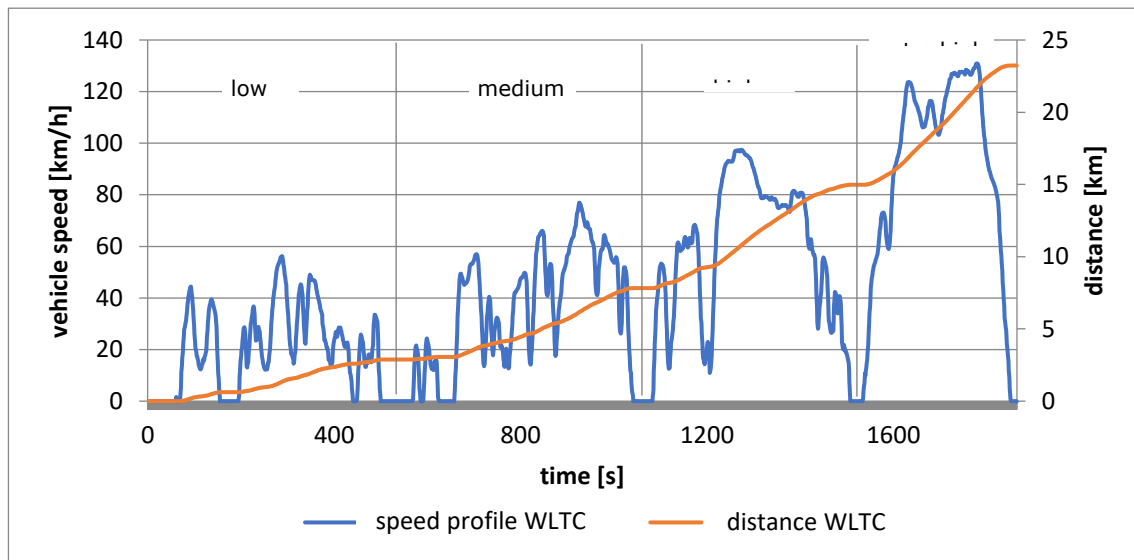


Figure 1: Speed profile of the Worldwide Harmonized Light Vehicle Test Cycle (WLTC) (data according to speed profile as described in (European Commission, 2017))

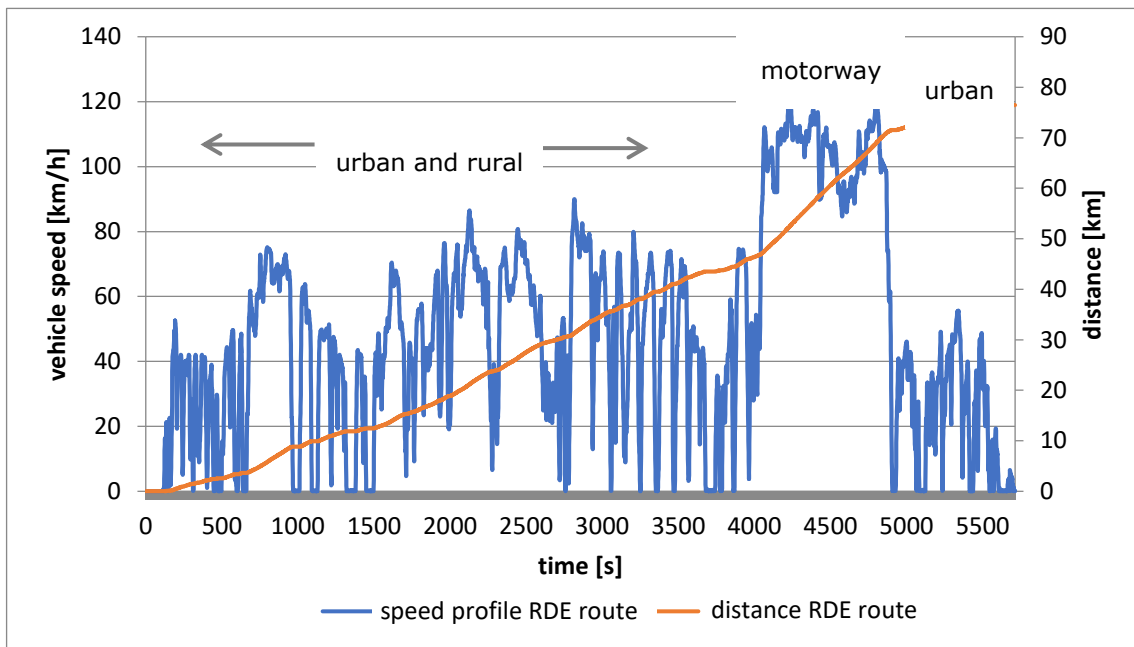


Figure 2: Exemplary speed profile of the chosen RDE route

Apart from the WLTP (Worldwide harmonized Light vehicles Test Procedure) standard type approval process, in which the vehicles pass through the WLTC (Worldwide harmonized Light Duty Test Cycle) standard cycle on the chassis dynamometer, RDE (Real Driving Emissions) tests have been mandatory since September 2017. In order to carry out standard-compliant RDE trips, a route in the Stuttgart area in Germany has been determined which meets the requirements described in the standard. This includes both the percentage share of approx. 33% each into the traffic situations "urban" (< 60 km/h), "rural" (60-90 km/h) and "motorway" (> 90 km/h) as well as the total test time (90-120 min), stopping times, cumulated gradients, accelerations and speed requirements (European Commission, 2016). Additionally, the cumulated positive gradient is lower than 1200 m/100 km. The driving profile of the

chosen RDE route is not only significantly longer over time, but also more dynamic than the speed profiles of the standard cycles. The motorway part of the RDE route is typically travelled at a speed between 100-130 km/h. The length of the selected RDE cycle is about 78 km and consists of urban, rural and motorway sections. The average driving time is 95 minutes.

2.2 Technical Characteristics of Test Vehicles

Three representative PHEVs have been selected for our evaluation. PHEV 1 with the lowest power, but the largest battery capacity and therefore the largest electrical range of 50 km, represents a compact class vehicle. PHEV 2 stands for the segment of the sportive mid-size vehicles. It has an electric range of 40 km with a system power of 185 kW. PHEV 3 is a 4-door limousine representing the upper midsize class with the highest system power and the lowest battery capacity. The technical data of the vehicles are listed in detail in Table 1.

Table 1: Technical data of the tested vehicles

	PHEV 1	PHEV 2	PHEV 3
Power of ICE [kW]	110	135	155
Power of e-motor [kW]	75	65	60
Overall system power [kW]	150	185	215
Battery capacity [kWh]	8.7	7.6	6.4
Electric range (NEDC) [km]	50	40	30
Electric energy consumption (NEDC) [kWh/100km]	11.4	11.0	11.0
Fuel consumption (NEDC) [l/100km]	1.5	1.9	2.1
CO ₂ emissions (NEDC) [g/km]	35	44	48

2.3 Test Procedure

PHEVs offer a variety of available driving modes. Additionally to the modes affecting driving dynamics, different choices of hybrid driving are possible. Depending on the battery's state of charge (SOC) and on the driver's preference, the vehicle can be driven in the charge depletion (CD), charge sustaining (CD), battery hold or battery charge mode. These hybrid driving modes differ basically in their operating strategy with regard to the use of electric motor and combustion engine. Overall, a multitude of possibilities and combinations of the different test parameters of real drives, test bench drives and driving modes is possible. Since not all variations can be covered with the resources available in our project, a selection of varying parameters is inevitable. On the one hand, this is necessary in order to carry out standard-compliant and reproducible measurements. On the other hand, this ensures a uniform approach to the tests, even if each vehicle has different operating modes and the vehicles may differ in the default modes. Although choosing the battery charge mode would result in highest fuel consumption and CO₂ emissions, we did not consider this mode to represent a common use case for a PHEV in practice. The driving modes for the three vehicles are chosen as follows:

- Eco-max: Maximum electric driving in electric mode with 100% SOC of the battery at the start of the test drive (mode with highest electric energy consumption)
- Comfort-hybrid, hybrid mode with 100% SOC of the battery at the beginning of the trip
- Comfort-hybrid, hybrid mode with 0% SOC of the battery at the beginning of the trip
- Sport mode with 0% SOC of the battery at the beginning of the trip (mode with highest dynamics and highest fuel consumption)

For standard-compliant measurements on the dynamometer, the reference temperature is 23°C. The temperatures of the RDE tests cover a range from approx. 5°C to 28°C. With regard to the use of auxiliary consumers, e.g. air conditioning, we assume that the air conditioning is switched on and set to 22°C for the RDE tests, as this corresponds to our understanding of normal behaviour of the user. In the standard cycles the auxiliary consumers are switched off, as required by the WLTP standard. For comparison purposes, the vehicles are additionally tested in the NEDC cycle at warm and cold temperatures.

Different modes have been chosen varying the vehicle dynamic behaviour and the SOC at the beginning of the test to analyse patterns in emission range and to identify key issues which determine the absolute amount of emitted substances. In order to compare emissions at different ambient temperatures, WLTC tests at 23 °C and -7 °C have been performed for all PHEVs. All on-road and dynamometer tests we performed are cold start tests. Both the RDE and the dynamometer tests are evaluated according to the emissions in different road categories. These values represent the average mass of emissions – or number in case of particles - per kilometre for urban, rural and highway driving.

2.4 Test Equipment

The vehicles have been equipped with sensors in order to obtain data of the electrical, thermal and fuel characteristics as well as emission data during RDE and dynamometer driving (Figure 2). Additionally, the internal measured values of the vehicles were logged via the on-board diagnostics (OBD) interface. For emission and particle measurement, a mobile PEMS exhaust gas analysis system is used. The device includes the gas measurement technology for CO, CO₂, NO and NO₂, a particle counter for solid particles, a GPS module as well as an integrated control and operating software. The gas analysers which are installed in the PEMS are a chemiluminescence detector (CLD), a photoacoustic sensor (PAS) and a non-dispersive infrared sensor (NDIR). The chemiluminescence detector is used to determine the NO concentration in the exhaust gas. The NO₂ concentration is determined by the photoacoustic sensor and the CO and CO₂ concentrations in the exhaust gas are measured by the non-dispersive infrared sensor. The emissions are measured in ppm (parts per million) as mass fraction in the exhaust gas. Particle measurement at the PEMS is performed with a condensation particle counter (CPC). An exhaust gas mass flow meter (EFM), a weather station for determining air humidity and ambient temperature and a GPS system are connected to the PEMS via interfaces. To perform emission and consumption measurements in accordance with standards for the WLTC, a four-wheel dynamometer with air conditioning and exhaust gas analysis at the DLR Institute of Vehicle Concepts is used.

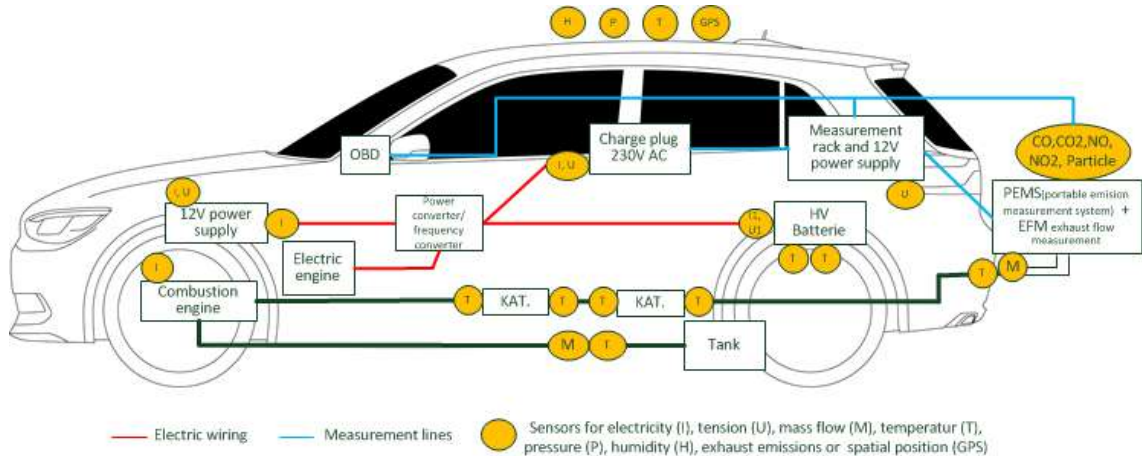


Figure 3: Schematic overview of main sensors and PEMS in test vehicles for RDE and dynamometer tests

2.5 Data Handling

In order to analyze the collected data, the individual measurement files of the various measuring instruments are merged using a self-programmed script for data post-processing. The PEMS measurement is synchronized with the data from the vehicle measurement technology. A engine speed correction is then carried out for each measurement. If the engine speed is zero, i.e. if the combustion engine is not active, the emission concentrations are also calculated as zero. The same correction is carried out with the exhaust mass flow.

The emissions are analyzed with regard to the speed distribution. For RDE drives, a distinction is made between "urban", "rural" and "motorway". If the speed of the vehicle \leq is 60 km/h, the emissions emitted are assigned to the "urban" classification. An allocation to "rural" takes place at speeds of \geq 60 km/h and \leq 90 km/h. At speeds $>$ 90 km/h, the route section is assigned to the "highway" section. The WLTC is divided into "low", "medium", "high" and "extra high". In order to ensure comparability with the RDE tests, the "low" and "medium" areas are combined as "urban". The parts "high" and "extra high" are assigned accordingly to "rural" and "highway".

Since RDE drives do not take place in a defined and preconditioned test bench environment, there are differences between different vehicles, drivers and environmental conditions such as temperature and traffic volume. Two methods are used in type approval to compensate for such external influences. On the one hand there is the EMROAD method developed by the Joint Research Centre (JRC) of the European Commission, on the other hand there is the CLEAR method implemented by Graz University of Technology. EMROAD uses the "Moving Averaging Window" approach. The length of each window is based on the amount of CO₂ emitted during a WLTC. A window is defined as half of the accumulated CO₂ of a WLTC. The emissions of a window are calculated from the accumulated mass over the length of the window. The result is an average emission in g/km for each window [3]. The evaluation tool CLEAR is based on the "Power Binning Method". The pollutant emissions are divided into power classes according to their power at the wheels of the test vehicle and weighted according to a target frequency distribution of the power requirement [3]. Since, on the one hand, there were no specifications for the normalization of emissions for PHEVs at the time the project was carried out and, on the other hand, the actual ranges of the real emissions are in focus of our analysis, these evaluation approaches are not presented in this paper.

3. Results and Discussions

3.1 RDE Emissions

The single measurement results of the real driving tests are evaluated with regard to their emission profile. Figure 4 shows the RDE measurements of the PHEV 1. A distinction is made between the different driving modes and the state of charge of the battery. The green and red curves are measurements where the battery was fully charged when the test started. The blue and purple curves are measurements with start - SOC = 0%. In addition, a distinction is made between the individual driving modes. Since the RDE drives are not reproducible in the speed profile, the curves are not on top of each other. The measurements are nevertheless comparable, since the basic speed profile of the test route remains the same for each trip. In case of PHEV 1, the vehicle manages to complete about half of the RDE measurement distance purely electric, when the battery is fully charged. This is more than for PHEV2 and PHEV3, mainly due to the larger battery capacity, but also because of the lower empty weight (see Table 1). CO₂ emissions increase continuously after the combustion engine is started (Figure 4). In sections with high speeds, fuel consumption and thus the generation of CO₂ increase disproportionately. CO₂ emissions are about twice as high in the eco-mode test with full battery at start compared to the hybrid or sports mode test with empty battery at start, as the RDE section driven by the combustion engine has rather high speeds. As long as the vehicle drives purely electric, i.e. the engine speed is zero, no emissions are produced. Since no combustion takes place, the exhaust section and thus the catalyst remain cold. If the combustion engine then starts because of a low SOC, the raw emissions meet a cold catalyst. At low temperatures in the catalytic converter, the chemical reactions cannot take place optimally and therefore the conversion rate is low. As a result, emissions increase sharply (see green lines in Figure 4). The CO emissions show that the catalytic converter is correspondingly cold when the combustion engine is started. If this start takes place at high speeds, CO emissions increase disproportionately. For this reason, CO emissions are around 210 mg/km. This is high compared to the test in the hybrid mode with full battery at start, where engine and exhaust components are continuously warming up (CO = 80 mg/km). RDE measurements with a full battery at test start partly exceed those with an empty battery at test start. But overall, CO and NO_x remain below the allowed limits.

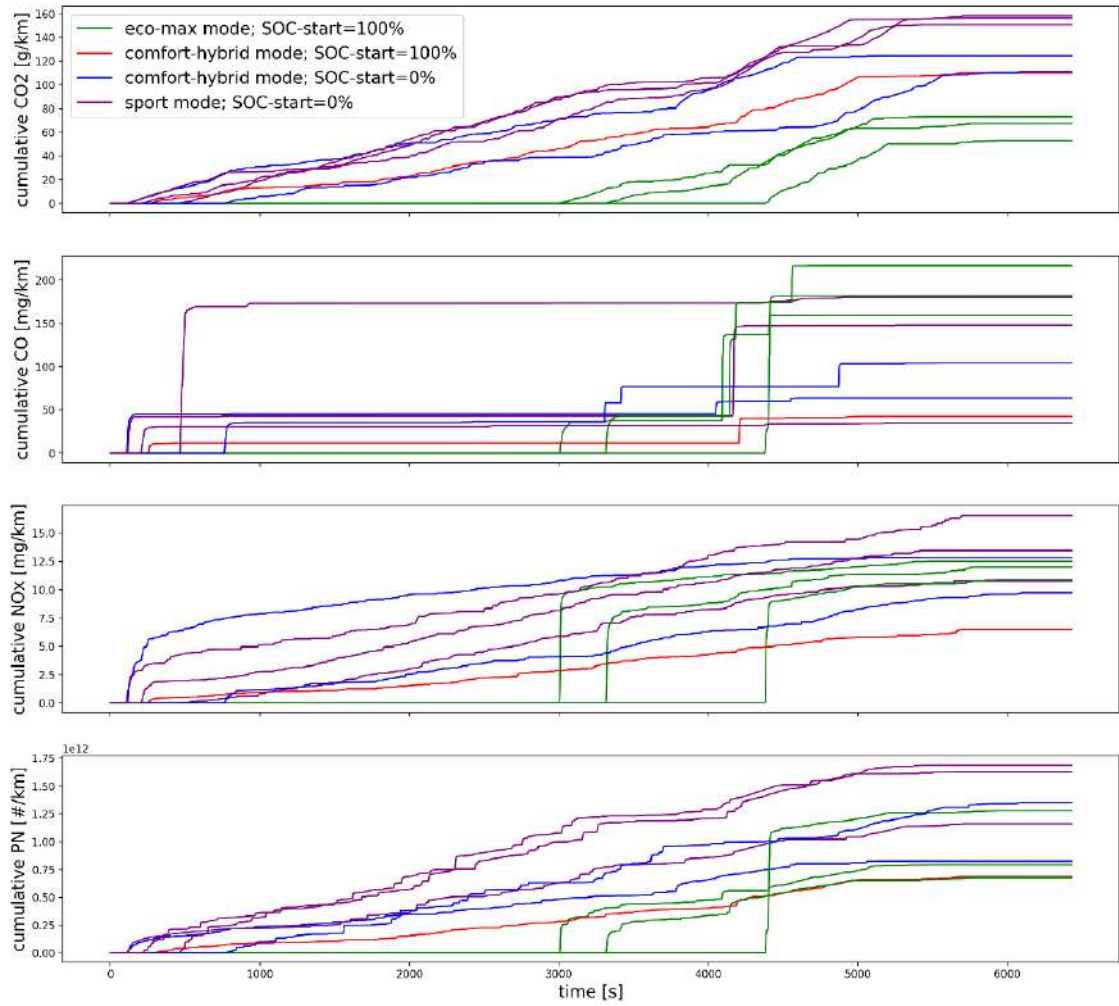


Figure 4: Accumulated CO₂, CO, NO_x and PN emissions and speed profile for RDE measurements of PHEV 1

In the case of the RDE-compliant measurements of the PHEV 2 in the driving modes described above (Figure 5), similar patterns can be seen as in the case of the PHEV 1. Despite different stopping times and driving dynamics on the RDE route, the tests with the same vehicle mode settings are relatively reproducible in terms of CO₂ emissions. In contrast to the PHEV 1, the difference between driving with the maximum electrical component and hybrid mode with a fully charged battery is hardly noticeable in terms of the electrically driven distance and CO₂ emissions for PHEV 2. Both the electric driving components and the absolute CO₂ emissions are almost identical. Likewise, the CO₂ emissions of the hybrid mode with 0 % SOC are only about 20 g CO₂/km higher than those of the mode with 100 % SOC at the start of the test, since a considerable part of the second half of the distance is covered electrically. On the entire RDE route, this measurement thus compensates for the high energy requirement and the associated high CO₂ emissions of the first half of the route with a high recuperation rate for the urban and rural sections of the trip and a high share of electric driving in the motorway section.

In the RDE tests which start with a full battery, CO and particle emissions show a significant increase due to repeated cold engine starts, which take place at high power requirements. Overall, the total emissions in both RDE journeys with a full battery are in the range of journeys with a far lower proportion of electric driving. The measurements of the other two vehicles show a similar behavior, especially with regard to the sudden increase of particle number, NO_x and CO emissions after longer electric driving phases. As with PHEV 1, pollutant emissions, in contrast to CO₂ emissions, do not depend on the proportion of electric driving in the test drives.

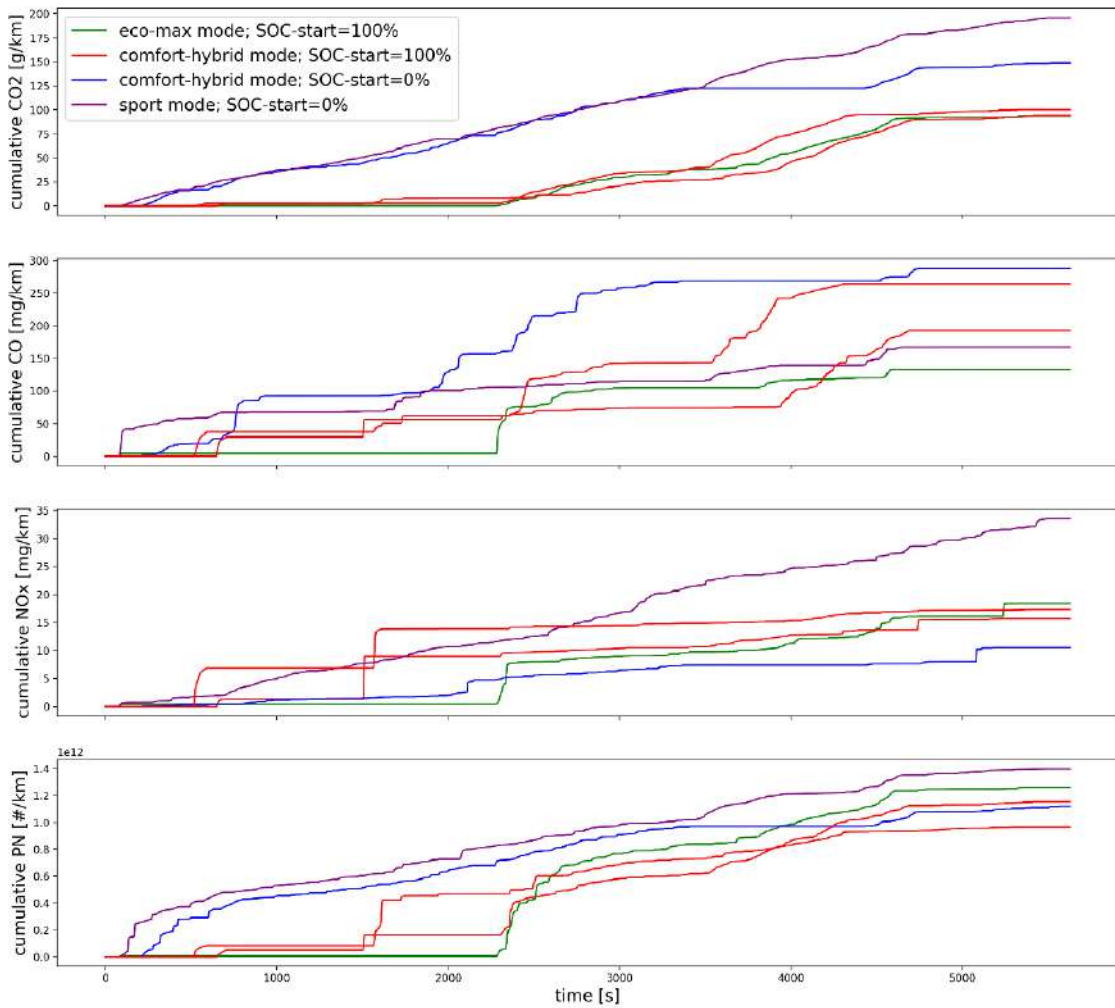


Figure 5: Accumulated CO₂, CO, NO_x and PN emissions and speed profile for RDE measurements of PHEV 2

The effect of the engine and cat cold start during vehicle operation is also clearly visible in the test results of PHEV 3 (Figure 6). As an extreme, the hybrid mode test with full battery at start emits more than 50% of the total CO emissions within one incident at around 2000 s. As the measurement progresses, CO emissions rise continuously as the catalytic converter reaches its working temperature. The development of CO emissions is probably due to engine operation with slightly rich mixture formation. NO_x emissions also show very striking peaks at the start of the combustion engine. Furthermore, the test in sports mode has the lowest particle emissions. Most particles are emitted at low engine temperatures after starting the engine. If the load or vehicle speed at engine start is high, many particles are emitted. This is the case when testing in eco mode. In the course of the further measurement, the particle emissions increase evenly and only slightly in all tests.

Particularly interesting is the final value of the emitted CO₂ emissions. This is approximately 100 g/km for all measurements with a fully charged battery at test start. In the more dynamic sports mode, more fuel is consumed and CO₂ emissions increase to about 280 g/km. The hybridisation of the vehicle and usage of the battery capacity has a positive effect in terms of CO₂ emissions and fuel consumption.

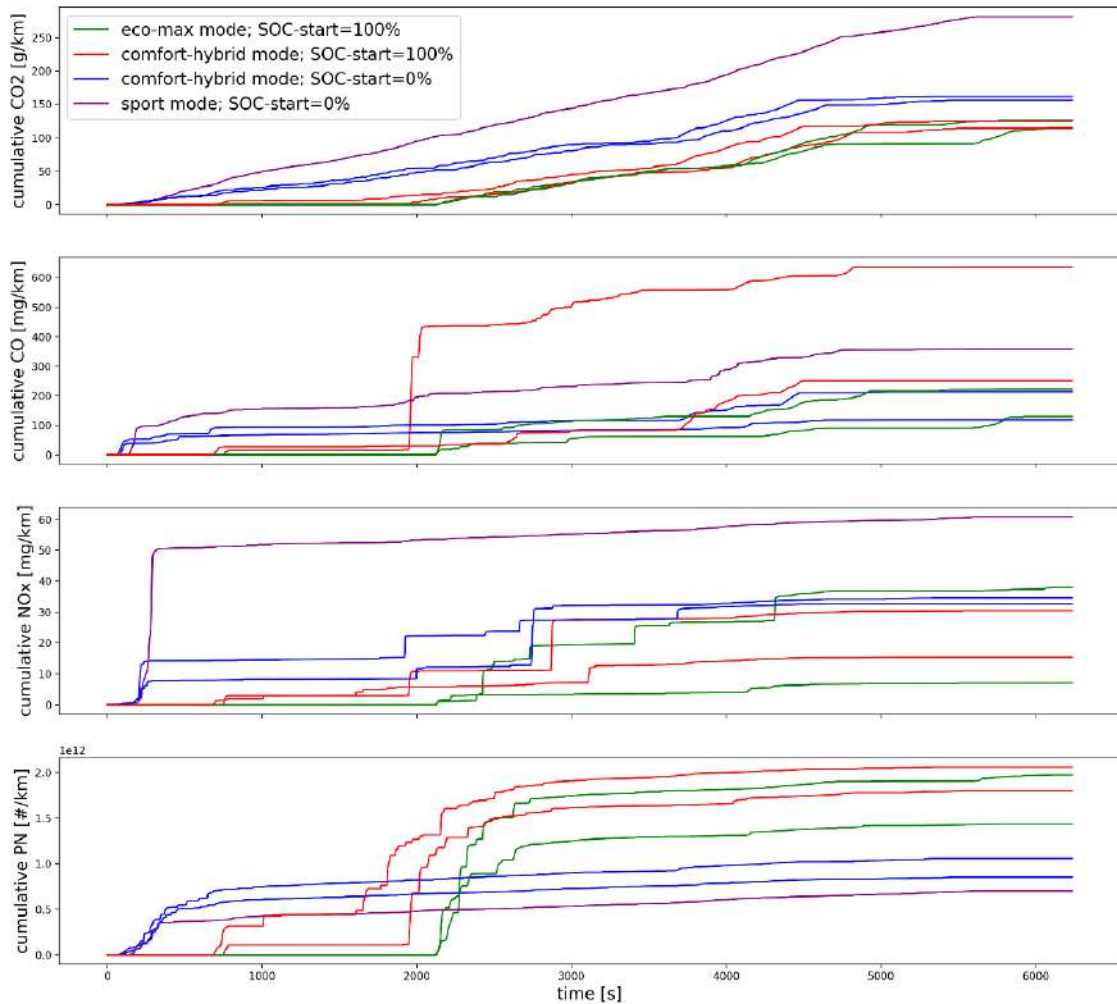


Figure 6: Accumulated CO_2 , CO , NO_x and PN emissions and speed profile for RDE measurements of PHEV 3

3.2 Comparison of RDE and WLTC tests

In case of RDE tests, the three road type categories are classified according to the speeds driven, and in the case of WLTC tests according to the cycle sections. Firstly, it becomes apparent that, under the given conditions, the emissions of the RDE measurements are in part far above the values of the type approval. The official NEDC approval value for the PHEV 1 is 36 g/km. This value is exceeded with every RDE measurement, because of the length of the trip. The CO_2 emissions during the measurements on the dynamometer fall below this value, if the battery is fully charged at test start. The motorway section, shown in Figure 7 as a green triangle, has a strong influence on the overall high CO_2 emissions. Mainly in the tests with a full battery at test start, the values are relatively low, but the motorway section worsens the overall result in terms of CO_2 enormously. Due to the high electrical range, the WLTC test can be carried out completely electrically and thus without local emissions in the respective first cycle. The CO emission factors are shown in the second graph. The CO limit value is adhered to in the RDE and WLTC tests shown here. Only a NEDC test at an ambient temperature of -7°C clearly exceeds the limit value, as the combustion engine was started at high speeds. With regard to NO_x emission factors, most measurements do not exceed the limit value. Since this vehicle has a gasoline engine, this observation is not surprising. Only the second WLTC at low temperature clearly exceeds the current limit value. This is mainly due to the motorway section. The limit value is also frequently exceeded for particulate emissions. A particulate filter, as already present in many newer vehicles, would significantly reduce particulate emissions.

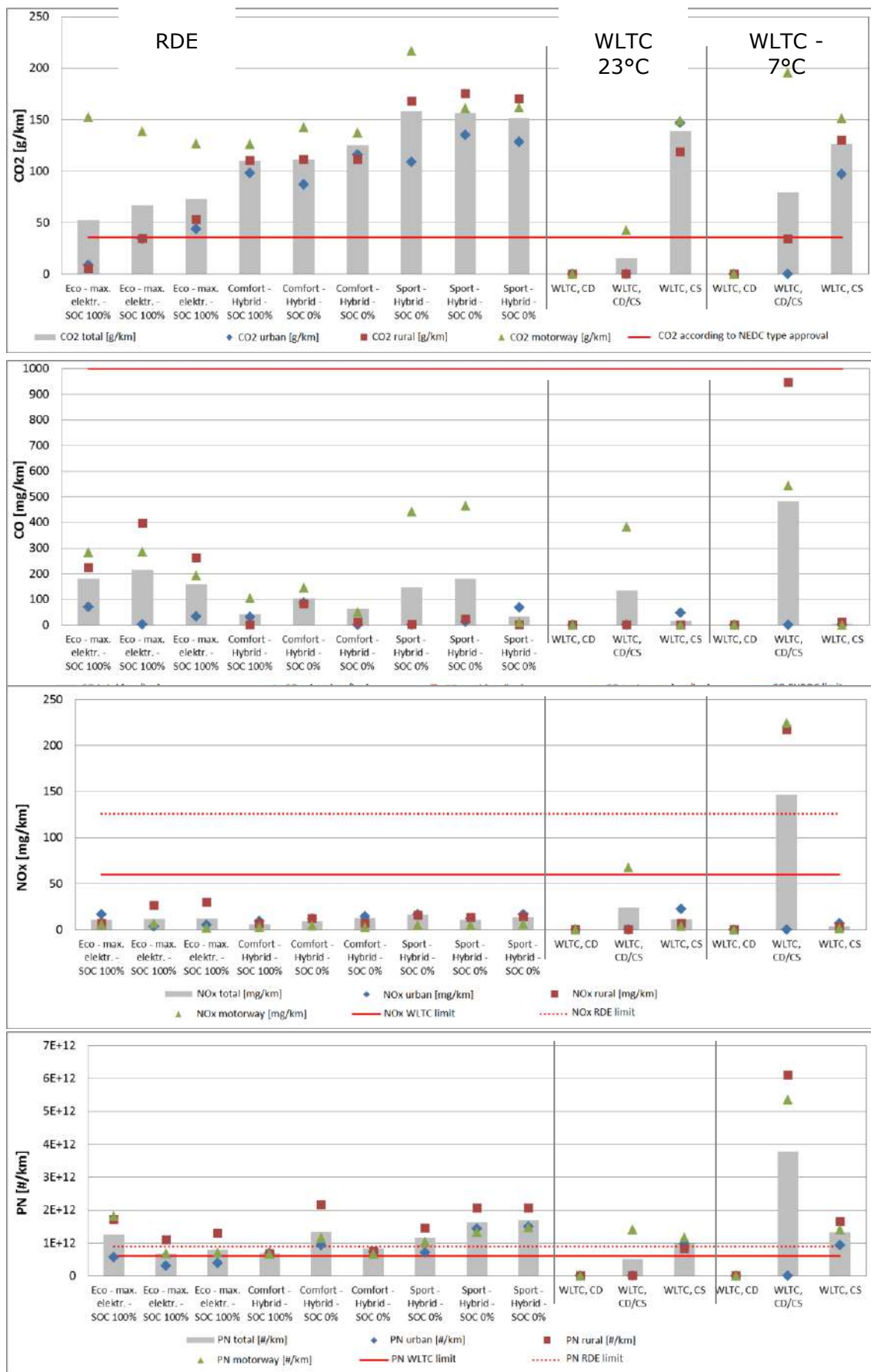
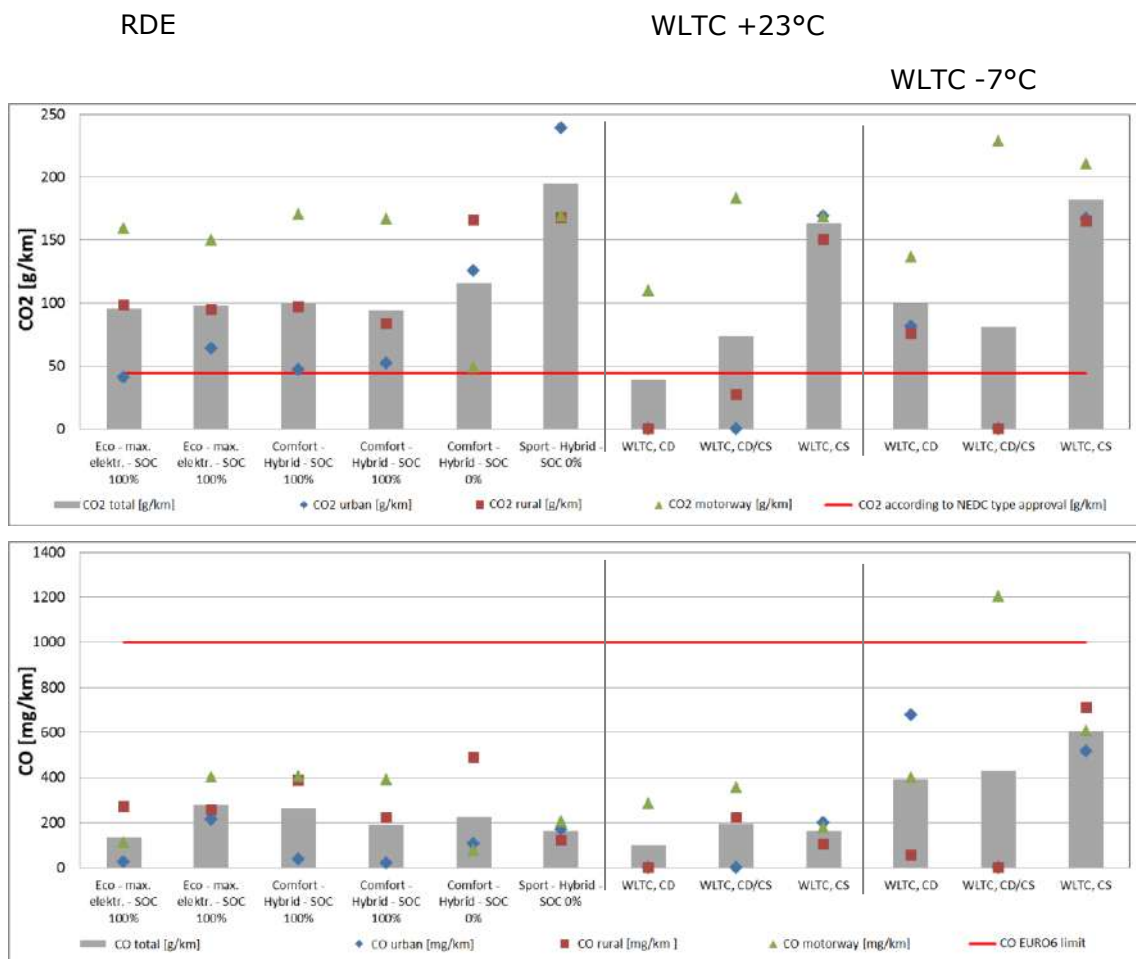


Figure 7: Comparison of CO₂ and pollutant emissions of the RDE and WLTC tests of PHEV 1

Figure 8 shows such average CO₂ emissions in g/km for the PHEV 2. It can be seen that the CO₂ emissions in the RDE test are significantly higher in the sports mode and when the battery is initially empty. It is also clear that, regardless of road type or driving mode, there is a direct correlation between electric driving performance and CO₂ emissions and fuel consumption, which decrease continuously with increasing electrical content.

The other pollutant emissions shown in Figure 8 show that the absolute values for measurements at -7°C are in some cases significantly higher than those at moderate temperatures. The test in the sports mode is also no longer outstanding. If the today valid RDE limit values are taken as a reference, the vehicle complies with the CO and NO_x values, but in some tests exceeds them in the case of particulates. It should be noted that the vehicle generally complies with the limit values applicable at the time of type approval. In contrast to CO₂ emissions, there is no direct linear relationship between the proportion of electric driving and the amount of pollutant emissions. Although the highest values were measured with a low electrical content and -7°C, only a 100% electrical content shows a clear correlation. Otherwise, the average pollutant emissions are relatively similarly distributed regardless of driving mode and electrical content.



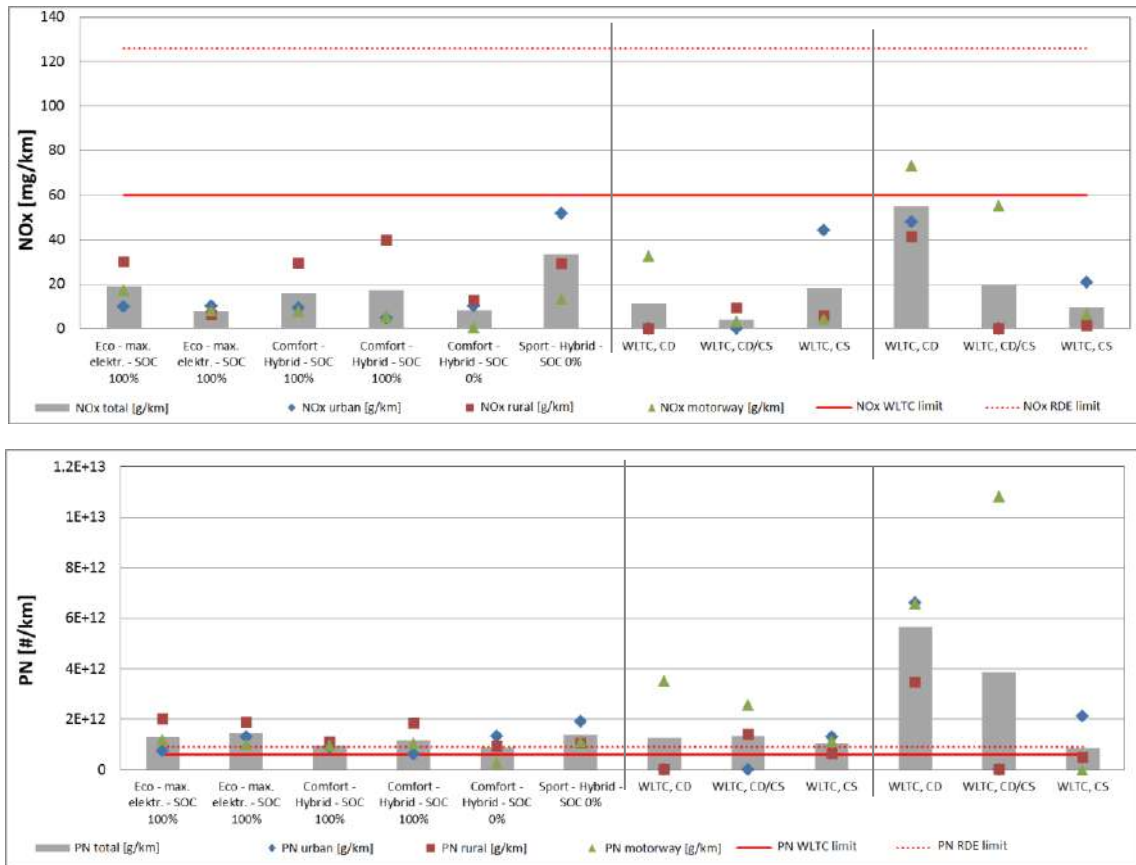


Figure 8: Comparison of CO₂ and pollutant emissions of the RDE and WLTC tests of PHEV 2

Figure 9 shows the emissions of the PHEV 3 with the respective limit values. As expected, measurements started with a full battery result in lower CO₂ emissions. It makes virtually no difference whether the driving mode hybrid or eco is selected. The test with sports driving mode clearly exceeds the type approval value. The situation is similar in the tests on the dynamometer. The comparison at different temperatures is also interesting. CO₂ emissions are higher at -7°C ambient temperature than at 23°C ambient temperature. This difference is particularly visible with the WLTC. If the measured CO₂ emissions are compared with the official NEDC value in Table 1, it becomes clear that this value cannot be met in real driving conditions. According to official approval measurements, PHEV 3 emits only 48 g/km.

Regarding the CO emission factors, the difference caused by the battery SOC at test start is not visible. For the RDE tests, the CO emission factors are all at the lower level and comply with the limit value. Only one outlier can be observed. This is due to the very poor result in the "rural" section of the respective test. In the "hybrid - SOC 100%" test, the combustion engine starts in a very unfavorable acceleration phase. This produces CO and the cold catalyst is unable to convert it. Overall, the limit value is also adhered to in this test. The CO limit value is also usually met during the test bench measurements. All RDE tests also comply with the NO_x RDE limit value. With regard to particulate emissions, it can be stated that most measurements are above the limit value. The RDE tests started with a fully charged battery show higher particulate emissions than test drives with start-SOC = 0%. The measurements on the dynamometer show a correlation between ambient temperature and emitted particles. Tests with an ambient temperature of -7°C show more particle emissions than tests with an ambient temperature of 23°C.

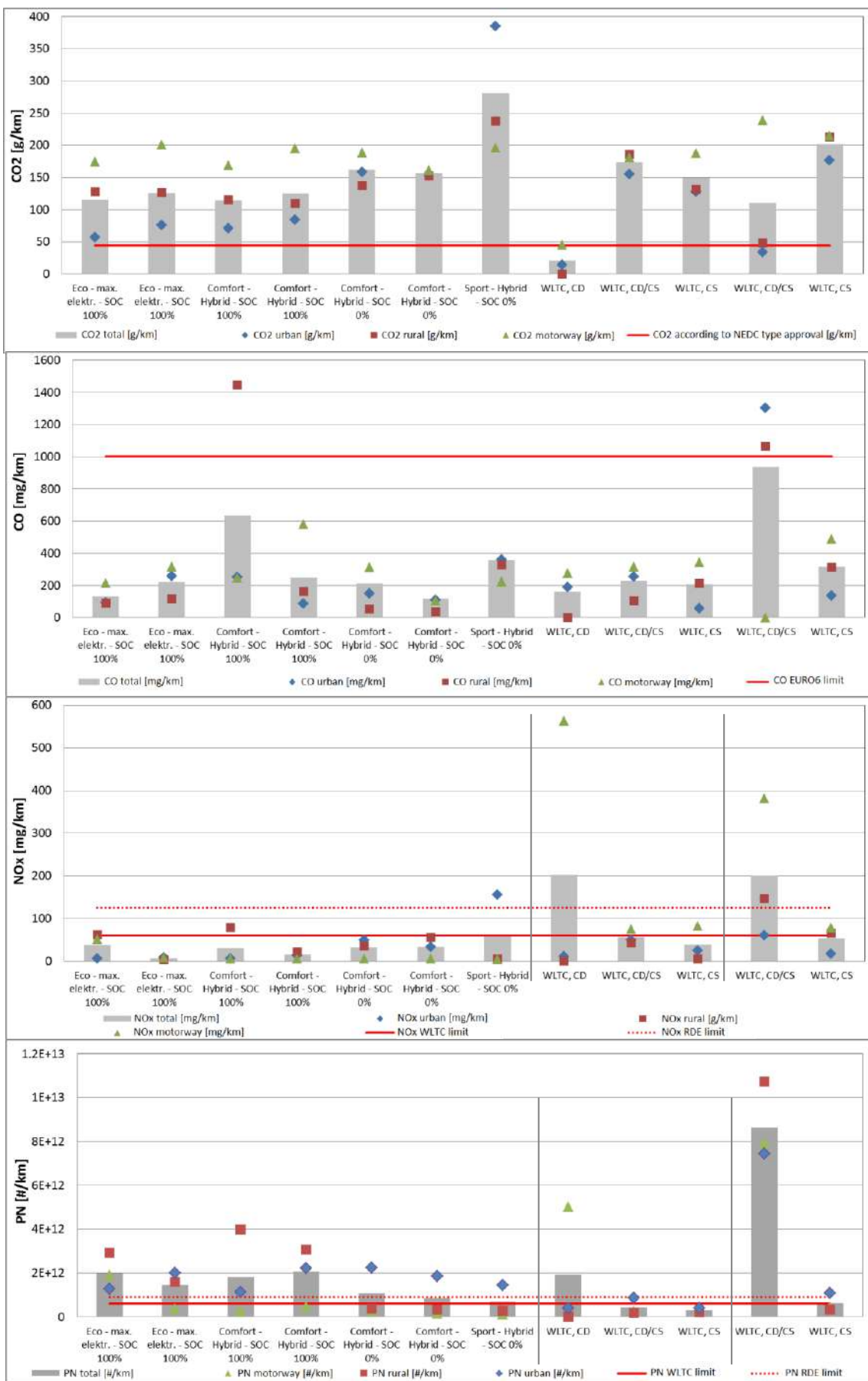


Figure 9: Comparison of CO₂ and pollutant emissions of the RDE and WLTC tests of PHEV 3

4. Conclusions

The main objective of the study is to answer the question of how hybrid vehicles behave in the real driving test, mainly with regard to CO₂, CO, NO_x, and particulate emissions. The challenge in answering the question is to cope with the great complexity of the legislation on the one hand, which changed over the course of the project, and the comparability with regard to the reproducibility of test drives on the road.

The measured particulate emissions are within the limits at the time of vehicle registration (reference value was NEDC, Euro 6), the currently applicable lower Euro 6 d temp limits are frequently exceeded due to the lack of a particulate filter. NO_x emissions in some situations exceed the WLTC limits (Euro 6d), mainly when the combustion engine is switched on or off at low temperatures (-7°C) and high loads (motorway) despite the battery being fully charged when driving.

The tests presented in this study show that CO₂ emissions correlate directly with the driving mode and battery SOC of the PHEV. For all vehicles, hybridization is advantageous in terms of lower CO₂ emissions in both RDE and WLTP tests, although different strategies of hybrid driving behaviour and the resulting fuel saving potentials can be observed. However, there is no such correlation for CO, NO_x and particulate emissions. For these pollutants, the concentration in the exhaust gas stream and the absolute emissions depend on the driving conditions in which the combustion engine starts. If the combustion engine starts at high load and high speed, emissions increase considerably. This effect increases when the PHEV is operated at low ambient temperatures as similarly described in Suarez-Bertoá et al. (2019). Due to the low catalyst temperature, CO and NO_x are not reduced in such cases. For example, with PHEV 2 at an ambient temperature of -7°C, the test shows a different operating strategy and emission formation than the measurements at moderate temperatures. The electric driving part cannot compensate these high emissions within the tested cycles in all cases.

Various technical measures are possible to address these problems. In addition to the introduction of particulate filters for gasoline vehicles (see also Demuyck et al., 2018), the operating strategy of the PHEVs plays a major role. High cold start emissions could be avoided, for example, by adjusting the load distribution between the internal combustion engine and the electric motor during the cold start phase or by electrically preheating the catalytic converter system. It will not be possible to cover all eventualities, if the restart processes of the combustion engine require preheating of the cooling circuit or catalytic converter.

In general, the emission measurements in real driving distances show a higher variance compared to test bench tests. In the case of PHEVs, this effect is increased due to the different choice of driving modes, different charging behaviour of the users, the required electric mileage and the hybrid driving strategy of the vehicle, as it leads to engine cold starts during electric driving (even with high engine loads). In addition, the ambient temperature influences the electric range and cold starts emissions (see also Alvarez and Weilenmann, 2012). When the outside temperature is low, the electric range decreases due to the reduced energy content of the battery. The variance of these parameters makes it difficult to estimate the emission benefits of PHEVs.

Furthermore, the standard-compliant RDE measurements cannot fully reflect the advantages of the PHEV and are not representative of (intended) PHEV user profiles. Additional data on the actual use of PHEV are required to assess the potential benefits and further technical measures are required to exploit the full potential of emission reduction of this vehicle type.

Likewise, the actual influences of different ambient temperatures, as they prevail in winter or summer in Europe, on the energetic percentage distribution between electric drive and high-voltage auxiliary consumers have not yet been examined in detail. An electrical range that may be greatly reduced by the auxiliary consumers inevitably leads to an increase in the energy consumption and CO₂ emissions of the vehicle.

Acknowledgements

This work was supported by the German Federal Ministry for the Environment, Nature Conservation, Building and Nuclear Safety (BMUB) in the frame of the project InitiativE-BW under contract 16EM2064-1. We further thank our colleague Dr. Michael Schier for his comments on the evaluation of the vehicle tests.

References

- Alvarez, R., Weilenmann,M., 2012. Effect of low ambient temperature on fuel consumption and pollutant and CO₂ emissions of hybrid electric vehicles in real-world conditions. *Fuel*, 97, 119-124, <https://doi.org/10.1016/j.fuel.2012.01.022>.
- Demuynck, J., Favre, C., Bosteels, D., 2018. Real Driving Emissions from a Gasoline Plug-in Hybrid Vehicle with and without a Gasoline Particulate Filter. Presented at the proceedings of the 10th AVL International Gas and Particulate Emissions Forum, Ludwigsburg, Germany.
- European Commission, 2017. Commission Regulation (EU) 2017/1154 of 7 June 2017 amending Regulation (EU) 2017/1151 supplementing Regulation (EC) No 715/2007 of the European Parliament and of the Council on type-approval of motor vehicles with respect to emissions from light passenger and commercial vehicles (Euro 5 and Euro 6) and on access to vehicle repair and maintenance information, amending Directive 2007/46/EC of the European Parliament and of the Council, Commission Regulation (EC) No 692/2008 and Commission Regulation (EU) No 1230/2012 and repealing Regulation (EC) No 692/2008 and Directive 2007/46/EC of the European Parliament and of the Council as regards real-driving emissions from light passenger and commercial vehicles (Euro 6).
- European Commission, 2016. Regulation (EU) 2016/427 amending Regulation (EC) No 692/2008 as regards emissions from light passenger and commercial vehicles (Euro 6).
- Fontaras, G., Pistikopoulos, P., Samaras, Z., 2008. Experimental evaluation of hybrid vehicle fuel economy and pollutant emissions over real-world simulation driving cycles. *Atmospheric Environment* 42, 4023–4035. <https://doi.org/10.1016/j.atmosenv.2008.01.053>
- Graver, B.M., Frey, H.C., Choi, H.-W., 2011. In-use measurement of activity, energy use, and emissions of a plug-in hybrid electric vehicle. *Environmental Science and Technology* 45, 9044–9051. <https://doi.org/10.1021/es201165d>
- Suarez-Bertoa, R., Astorga, C., 2016. Unregulated emissions from light-duty hybrid electric vehicles. *Atmospheric Environment* 136, 134–143. <https://doi.org/10.1016/j.atmosenv.2016.04.021>
- Suarez-Bertoa, R., Pavlovic, J., Trentadue, G., Otura-Garcia, M., Tansini, A., Ciuffo, B., Astorga, C., 2019. Effect of Low Ambient Temperature on Emissions and Electric Range of Plug-In Hybrid Electric Vehicles. *ACS Omega* 4, 3159–3168. <https://doi.org/10.1021/acsomega.8b02459>

2.6.9 Simulation-based assessment of the CO₂ emissions reduction potential from the implementation of mild-hybrid architectures on passenger cars to support the development of CO2MPAS

S.Doulgeris¹, A.Tansini², A. Dimaratos¹, G.Fontaras² and Z.Samaras^{1*}

¹ Laboratory of Applied Thermodynamics, Department of Mechanical Engineering, Aristotle University of Thessaloniki, 54124, Greece, *Corresponding author: zisis@auth.gr

² European Commission Joint Research Centre, Via E. Fermi 2749, Ispra, Italy

Introduction

Electrification of vehicle powertrains becomes more and more popular and market penetration of hybrid electric and pure electric vehicles increased rapidly over the last five years. This is indicated from the data of new registrations in Europe reported from ACEA, EEA and ICCT, Figure 1. On top of this, projections for 2030 vehicle fleet composition show that market share for electric vehicles (EVs), hybrid electric vehicles (HEVs) and plug-in hybrid electric vehicles (PHEVs) will range between 8%-26%, 20%-25% and 10%-12% respectively (Tsokolis et.al, 2017) and (Powell et.al, 2018). Thus, the introduction of electrified vehicles is proved to be one of the key measures towards the reduction of fuel consumption and tailpipe CO₂ emissions from passenger cars in order to meet 2020 and 2025 CO₂ target of 95 g/km and 68-78 g/km respectively (ICCT, 2016).

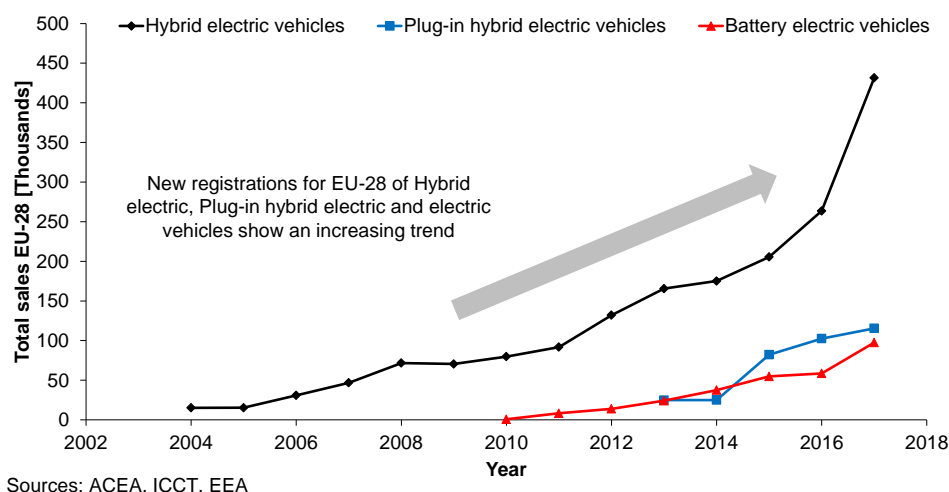


Figure 1: Total sales of hybrid, plug-in hybrid and electric vehicles for EU-28

Fuel consumption and CO₂ emissions reduction potential from hybridisation ranges from 3.5% to 30%, depending on the level of electrification of the vehicle's powertrain and the selected layout. The different hybrid powertrain configurations are classified into four major categories according to the level of electrification:

- the micro-hybrids: vehicles with conventional powertrain equipped with Start&Stop (S&S) technology and brake energy recuperation system (BERS), a very common technology since almost all new registered vehicles over the last years include S&S as standard equipment, providing a reduction on CO₂ emissions of 2.5–4.8% and 1.2–2.6% in NEDC and WLTP respectively (Dimaratos et al., 2016)
- the mild-hybrids: vehicles equipped with an electric machine that works as a motor, a generator and a starter integrated in a conventional powertrain, a configuration that is lately introduced from car manufacturers and offers a higher reduction potential of CO₂ emissions compared to micro-hybrid vehicles
- the full-hybrids: vehicles that are equipped with one or more electric machines that are able to propel the vehicle and generate electric power to recharge the battery, combined with an internal combustion engine (ICE) and with a battery pack that supplies energy for a limited

pure electric range. The CO₂ reduction potential is achieved via the extensive use of the electric energy and the implemented energy management strategy

- the plug-in hybrids: vehicles that usually have the same powertrain layout as the full-hybrids, but equipped with a battery which allows driving for an extended electric range, of approximately 20-50 km, providing the ability to go on pure electric mode (zero tailpipe emissions) especially when driving in urban areas. After the depletion of the battery, the vehicle operates in a similar way to a full-hybrid vehicle.

Vehicles with mild-hybrid powertrains provide a cost-effective solution for the improvement of CO₂ emissions performance of passenger cars, since they combine the benefits of hybridisation with lower implementation cost. The main advantage of a mild-hybrid system is the adoption of a single, compact electric machine (EM) that is used as a booster motor, a starter and a generator. This EM may work in parallel to the engine, providing additional power for propulsion, be switched to generator mode for battery charging during ICE propulsion, or even recuperate energy during deceleration. Given the aforementioned benefits combined with a relatively simple and cheap 48V electric system, mild-hybrid powertrains are expected to become more and more attractive for the market.

Simulation is a powerful tool that can support the design of hybrid systems, since it provides the flexibility to investigate with high accuracy different layouts and variations of components specifications in a cost- and time-effective way while minimising the experimental effort. Thus, the aim of this study is to develop a simulation methodology for 48V mild-hybrid vehicle technology, based on the topology descriptions found in literature and to present a simulation approach that is developed and implemented on top of validated simulation models of conventional vehicles. The electric system of the model is modified to comply with the 48V architecture and the relevant components are added (battery and EM). The study is focused particularly on the development of the simulation approach of 48V mild-hybrid, equipped with a belt-driven starter generator (BSG), as this is the most common configuration applied to passenger cars. Based on the developed simulation model, this study also aims to present the potential improvement on CO₂ emissions performance under type approval (NEDC and WLTP) cycles. Finally, the outcome of this study will serve as a basis for the introduction of a generic simulation approach for mild-hybrid vehicles in CO2MPAS (CO₂ Model for PAssenger and commercial vehicles Simulation), the simulation tool adopted from the European Commission (EC) for the correlation between WLTP and NEDC CO₂ emissions at vehicles type-approval (EU Regulation 443/2009, 510/2011, 2017/1152 and 2017/1153).

Mild-hybrid architecture

Mild-hybrid vehicles can be considered as the evolution of micro-hybrid configurations, but with higher potential in CO₂ emissions reduction. Although in literature a variety of mild-hybrid layouts can be found, the core of such configuration is based on a 48V electrical system with an EM that operates as a motor and generator. A scheme of the possible mild-hybrid configurations can be found in Figure 2.

Schaeffler proposed a mild-hybrid configuration with an EM mounted on the powered axle (Smetana et al., 2014). A 48V battery powers the EM which is able to provide a maximum power output of 12kW. This EM is able to provide sufficient torque to run the vehicle in fully electric at a low speed range of 0-20 km/h. Additionally, the EM is used as a generator to recuperate energy during deceleration and to shift the operating point of the ICE to a more efficient area of the engine map. The CO₂ emissions reduction potential that can be achieved with this system is 9% in the NEDC, taking as reference a conventional vehicle equipped with Start&Stop technology.

A mild-hybrid system for vehicles is also developed and introduced by Delphi. This system combines two electrical circuits, one with a conventional 12V battery that powers all devices working on 12V nominal voltage and one with a 48V battery that is used to provide power to the electric motor and the electric supercharger. For this layout, the EM replaces the conventional alternator and is responsible of starting the engine, providing torque to move the vehicle and charging the two batteries. The operation of this system is handled through a Hybrid controller, which defines when the thermal engine starts, when the EM is propelling the vehicle or when it works as a generator recharging the battery. The system described, offers a 25% increase of the low-end torque and an improvement of 10-15% in fuel consumption. A similar powertrain with a 48V mild-hybrid configuration based on a BSG powered by a lithium-ion battery is also presented by Audi, where the BSG replaces the conventional alternator and acts via a belt directly to the engine's crankshaft. With S&S function working up to 22 km/h, such

configuration can lead to a 0.7 l/100km reduction of fuel consumption. Finally, Continental propose a 48V mild-hybrid powertrain (Romanato et al., 2018) based on a BSG, mechanically connected to engine's crankshaft. The BSG is used, as for the previous solutions, for torque assist leading to fuel consumption reduction, but is also used to increase the load of the ICE, shifting the operating point to a more efficient area of the map for battery charging. The system is combined also with an electric compressor and electrically heated oxidation catalyst.

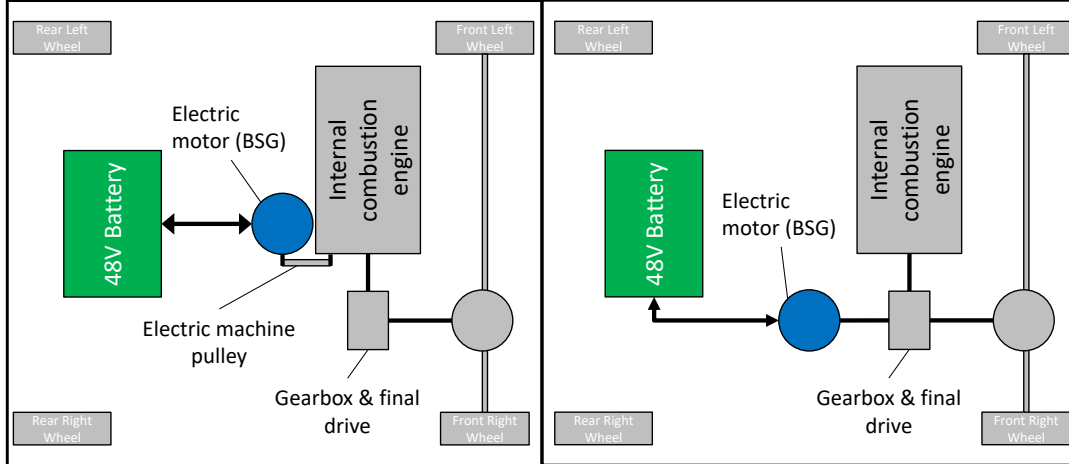


Figure 2: Mild-hybrid vehicle basic topology P0 (left) and P2 (right)

Development of the mild-hybrid vehicle simulation model

The basis for the implementation of the mild-hybrid architecture is a set of vehicle simulation models that were developed in AVL CRUISE (AVL, 2018) simulation platform and validated with experimental data in the context of WLTP/NEDC correlation exercise (Tsokolis et al., 2015). For the purpose of this study, two different vehicle simulation models are selected, diesel- and a gasoline-powered one, specifications of which are included in Table 1. These models were modified from their original micro-hybrid architecture to a BSG (acting directly on the engine's crankshaft) 48V mild-hybrid layout.

Table 1: Specifications of the vehicles considered for this study

Vehicle	Engine Type	Displacement [cc]	Max. Power [kW]	Max. Torque [Nm]	Transmission	Curb mass [kg]
SUV	Diesel	1995	120	380	MT, 6 gears	1465
D segment	Gasoline	1798	125	318	MT, 6 gears	1450

Consequently, modifications to the vehicle model topology were necessary. The electric system of the models is modified and converted from 12V to 48V circuit. For simplicity reasons, the 12V electric circuit was not considered as being part of the powertrain but it has been implemented as an equivalent power demand from the 48V battery. The battery was converted to 48V nominal voltage and the generator was replaced with an EM acting on the engine power shaft. The constant electric consumer and the starter Ohmic resistances (which simulate electric power consumption from auxiliaries and the starter respectively) were adjusted in order to keep the same overall energy consumption, after the change of nominal voltage of the system. In addition, the control strategy of the mild-hybrid system was implemented by means of user-defined functions. The layout of the mild-hybrid vehicle simulation model is presented in Figure 3. It consists of the main mechanical and electrical powertrain components along with the relevant control modules. All the necessary data such as engine specifications, characteristic curves, consumption maps or efficiency maps are used as input for the respective components. In addition, test mass and road load coefficients are provided as the vehicle's driving resistance. In the same figure, the 48V electric circuit and the developed controller are highlighted.

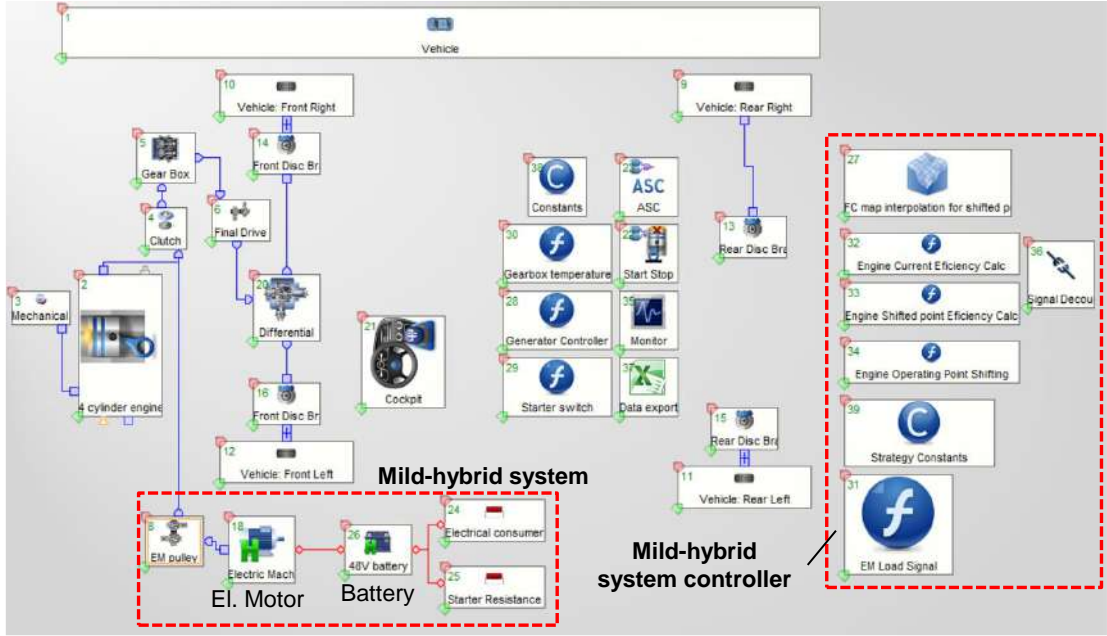


Figure 3: Vehicle simulation model layout

Typical specifications of the mild-hybrid configurations can be found in Table 2. The values reported in this table have been used as the default specifications for the development of the simulation model considered by this study.

Table 2: Specifications of mild-hybrid system components

Component	Parameter	Value
Battery	Nominal Voltage [V]	48
	Maximum capacity [Ah]	10-20
Electric machine	Maximum Power [kW]	10-14
Strategy	Velocity threshold [km/h]	12-22

Implementation of the control strategy

The main target of the study is to develop a generic control module, which will be applicable to vehicles with a mild-hybrid powertrain. For this purpose, a controller that regulates the operation strategy of such system is developed and implemented in the simulation model, as illustrated in Figure 3. This control module performs a real-time evaluation of the energy flow, based on the driving conditions and the hybrid powertrain state in order to switch the vehicle's operating mode, actuating the most appropriate strategy. Additionally, this controller is responsible for the calculation of the EM and ICE load in each possible working mode and for every instant of the simulation.

For the selected approach, four different operating modes are identified: EM torque assist, battery charging, engine operating point shift with battery charging and regenerative braking. These operating modes along with the selection logic for each mode and the decision tree of the control module are presented in Figure 4. The selection between the different states of the system is determined based on the driver's power demand, the instantaneous battery state of charge (SOC) and the pre-defined SOC limit, which is the basic criterion upon which the decision is made. It is important to state that a hysteresis that acts around the SOC limit is implemented in order to prevent frequent switches of the controller between charge and discharge operations.

During hybrid mode there are two possible modes selected according to the driving conditions. When driver's power demand is lower than the available power of the EM and vehicle speed is below the selected velocity limit, the controller selects electric propulsion mode. This means that only the EM

propels the vehicle, whereas the thermal engine is off. Although such mode is included in the control module, it was not used for the current study. When the previous condition is not fulfilled and vehicle acceleration demand is higher than the selected threshold, ICE and EM operate in parallel (EM torque assist mode). In contrast to discharge mode, the EM operates as a generator during regenerative braking and charge mode. The first is activated during vehicle deceleration and the second when battery SOC is lower than the predefined SOC limit, or the EM is used to shift the operating point of the ICE to a more efficient area of the map. The additional EM load can be set to a constant value or calculated in order to bring the ICE to the optimal point. A scheme of the aforementioned strategy is illustrated in Figure 5.

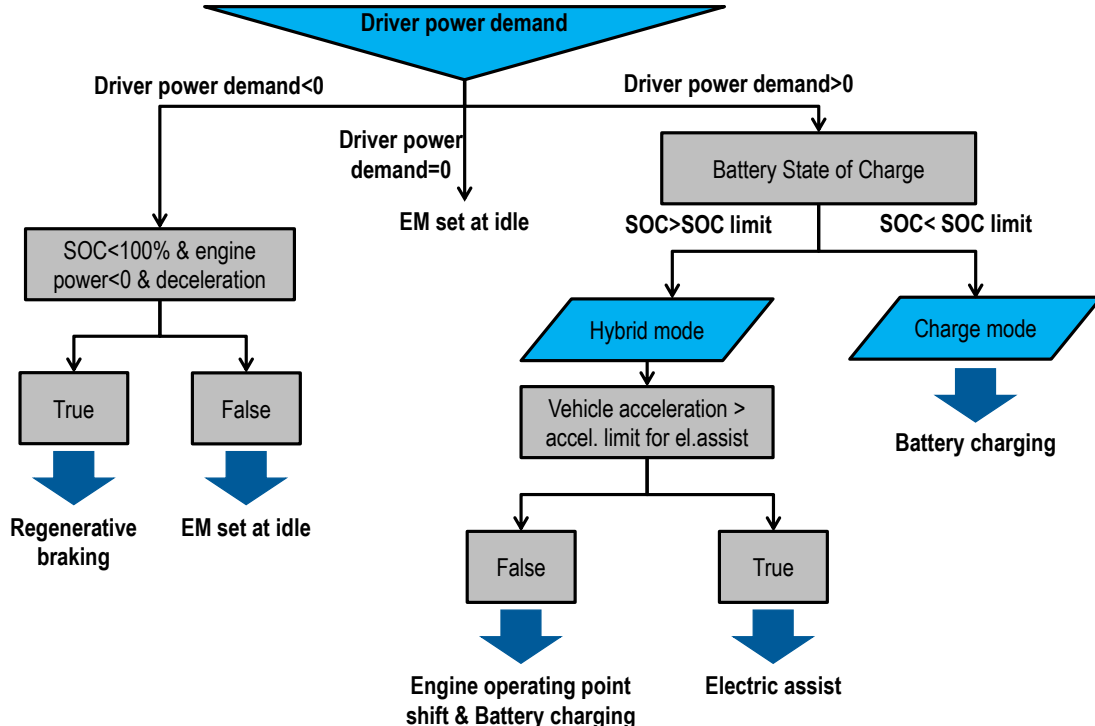


Figure 4: Mild-hybrid control logic diagram

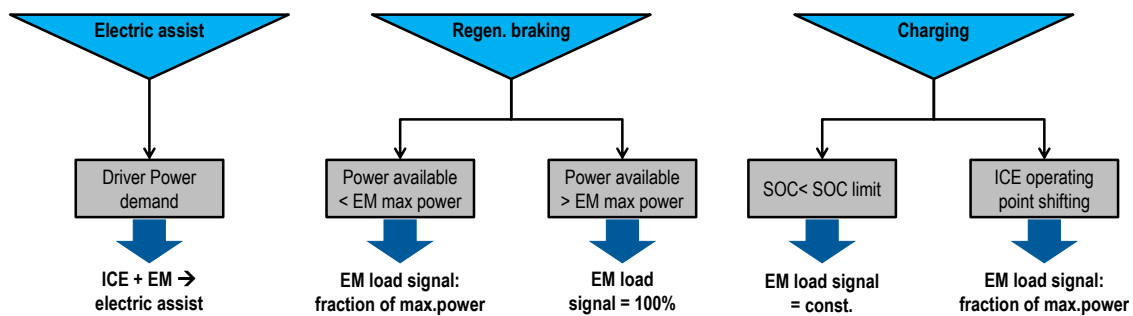


Figure 5: Electric machine load signal calculation

Figure 6 shows the instantaneous data for battery state of charge and electric motor load for WLTP, where the different modes of the system are highlighted. Torque assist from the electric motor can be identified with the positive values of the load signal with the respective drop of the battery SOC. In contrast, during battery charging, regenerative braking or ICE operating point shift, EM load signal takes negative values and an increase of battery SOC is observed.

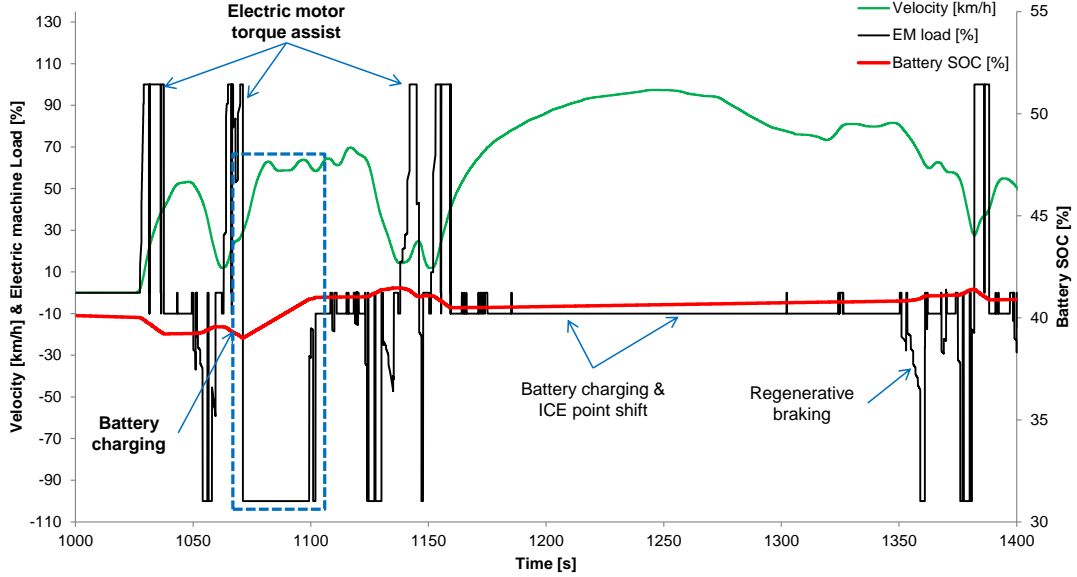


Figure 6: Instantaneous battery state of charge and electric machine load over WLTP

An important aspect of the control logic is the battery charging when no electric torque assist or regenerative braking is selected. To that aim the EM operates as a generator during pure ICE propulsion, shifting the operating point of the thermal engine towards the optimal operating area of the engine map. With this operation, battery starts to be re-charged when SOC reaches a lower threshold up to a specific higher limit, so that a long term oscillation of battery SOC is implemented and battery usage is not limited to a small operating window around the SOC lower threshold. As a result, battery SOC varies between a specific operating window that is beneficial for both fuel consumption and the life of the battery. This operation is illustrated in Figure 7 where battery SOC over the WLTP and NEDC is presented. Based on such operation, it is possible to optimize the selection between battery charge and discharge in order to keep energy balance close to zero along with a fuel consumption benefit. As it can be seen, for the developed simulation approach a zero energy balance during a WLTP is achieved, as initial and final battery SOC is almost the same ($\Delta\text{SOC}=-0.67\%$). In case that zero energy balance of the battery is not achieved within a cycle, an algebraic correction is considered. Two or three simulations are executed using different levels of initial battery SOC (high, low and medium) and a linear regression for CO_2 emissions versus cumulative battery power is applied. With the derived linear function, CO_2 emissions for zero energy balance are calculated. As a result the evaluation of the CO_2 emissions performance for the mild-hybrid simulation models is compliant also with the regulation suggestions.

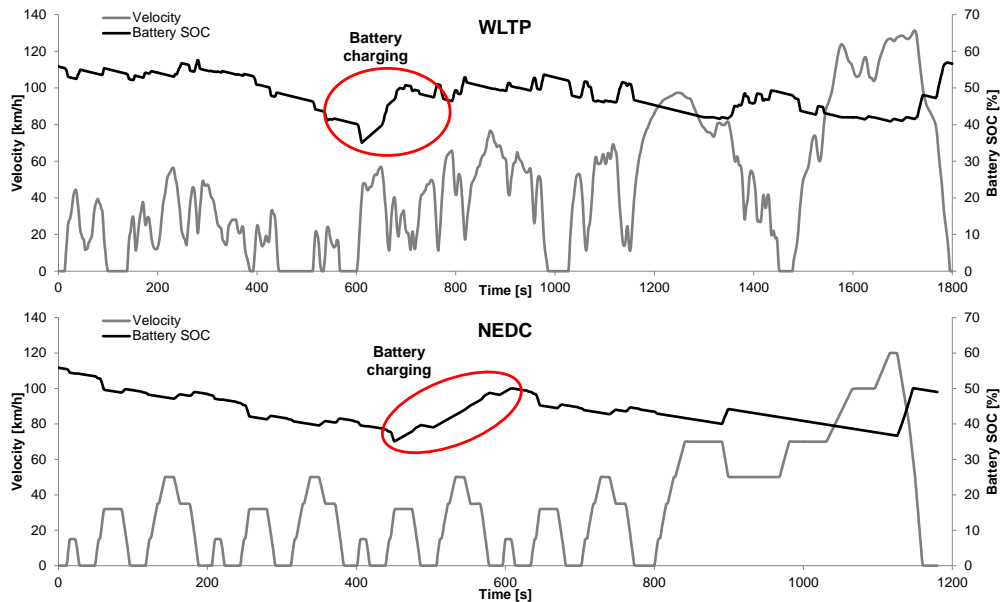


Figure 7: Instantaneous battery state of charge during WLTP and NEDC

Simulation-based support for CO2MPAS development

The introduction of the WLTP for light-duty vehicles type-approval raised the necessity for a legal basis that explained how to deal with the CO₂ emissions targets under the new procedure. These targets were defined in the framework of Europe 2020 strategy, a set of binding legislation for ensuring the compliance with the climate and energy targets for the year 2020, and were tailored on the NEDC CO₂ emissions baseline. The CO2MPAS simulation tool has been developed to equally preserve the stringency of the CO₂ emissions targets, by processing the data from experimental measurements obtained at vehicles' type-approval under the WLTP and evaluating the equivalent CO₂ emissions that these vehicles would have under the NEDC procedure. CO2MPAS is constantly kept under development in order to follow the evolution of the automotive market, ensuring that new technologies that express a fuel saving potential when tested under the WLTC are appropriately captured. Technologies as variable compression ratio, cylinders deactivation, hybrid powertrains and others are being studied and implemented in the tool. In this sense, simulation plays a very important since it allows to:

- get insight on the way new technologies interact at vehicle level, how they can be controlled and the fuel saving potential they can express
- produce data out of simulation, either of existing or non-existing vehicles, to test the capabilities of CO2MPAS to reproduce vehicle behavior and explore limits

The development team of CO2MPAS is working on the introduction of hybrid electric powertrains in the tool, and 48V systems are already being studied for the implementation. To this aim, experimental data from existing vehicles are being collected, analysed and used for CO2MPAS simulations. It is important to consider that, for a successful implementation, multiple configurations and control strategies have to be tested to be sure that the tool is able to replicate them, with the challenge of conceiving solutions that might appear in the market in the near future. Through simulation, it is possible to explore many different solutions for hybrid powertrains with no experimental effort and in a time- and cost-effective way. In this sense, the CRUISE simulation environment presented in this work will be used to produce cases with a modified powertrain layout, different component sizing and control strategies, or to understand the impact of the same hybrid powertrain on a vehicle with different specifications. The simulated data of these virtual vehicles will be used to calibrate the CO2MPAS model and test the capabilities of capturing the CO₂ emissions, providing in this way a very valuable support for the development of the tool.

CO₂ emissions reduction potential

With the given configuration and the simulation models considered for this study, CO₂ emissions over type approval cycles, NEDC and WLTP, are calculated. Since a mild-hybrid powertrain involves significantly electric propulsion, an evaluation of the battery use need to be considered and a correction due to battery energy balance is applied. Figure 8 presents the CO₂ emissions and the cumulative battery energy simulation results for both vehicles used for this study for high, medium and low initial battery SOC. A linear regression is used to calculate the corrected CO₂ emissions results. The correction is applied according to EU Regulation 2017/1151 regarding vehicles with hybrid electric powertrains. The corrected CO₂ emissions value presented in this graph corresponds to zero energy balance of the battery (neither battery depletion nor recharging). Given the applied correction, the estimated improvement on CO₂ emissions performance over these cycles is illustrated in Figure 9 for the SUV diesel and the D segment gasoline vehicle. The reduction potential for WLTP is calculated approximately 4% for both the vehicles considered for the study. Since this study is considered as a preliminary development of a mild-hybrid simulation model the reduction rate may not be considered as the optimal. An optimisation of the system may lead to the selection of different operational parameters and an improved fuel consumption performance.

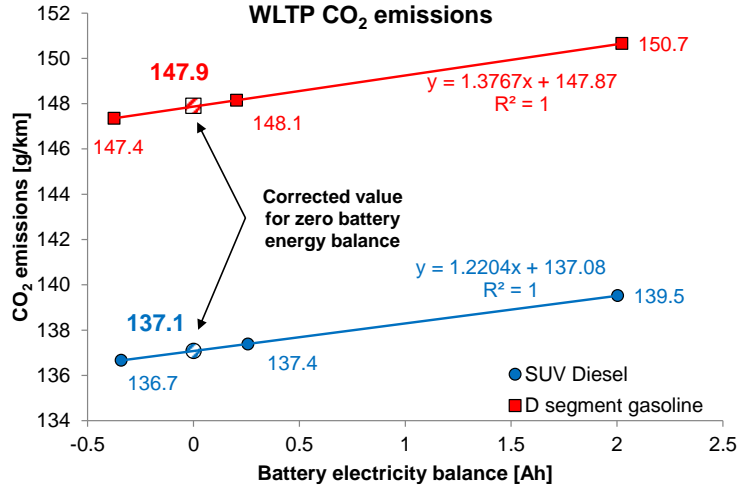


Figure 8: CO₂ emissions versus battery's integrated current over WLTP (simulation results for high, medium and low initial SOC)

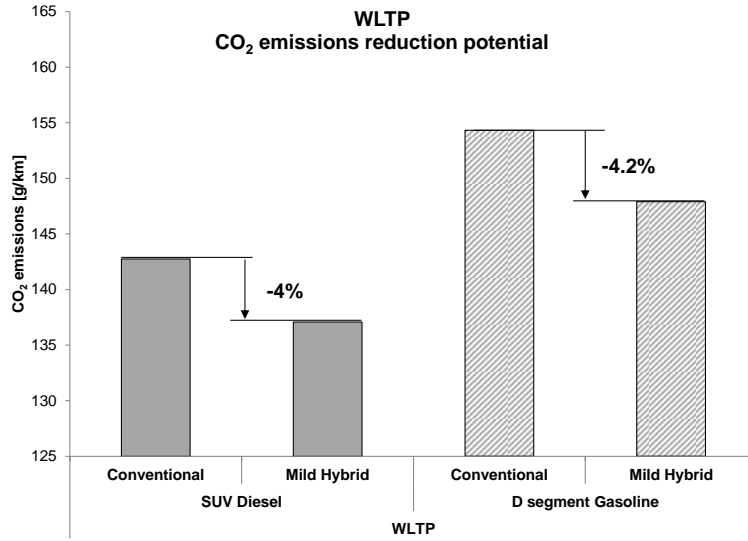


Figure 9: Reduction of CO₂ emissions results over WLTP for both vehicles used in this study

In contrast to WLTP, CO₂ reduction is not achieved for NEDC as it can be seen in Figure 10 and fuel consumption for both vehicles is higher for the mild-hybrid configuration as it is presented Figure 11. This can be partially explained from the driving dynamics of NEDC and the energy that can be recuperated. The methodology developed, strongly depends on the exploitation of energy recuperation during braking, operation that returns more benefits for the WLTP due to its more transient nature. On the contrary, the energy that can be recuperated from the less frequent decelerations of the NEDC is not sufficient to recharge the battery leading the system to an extended charging phase, highlighted in Figure 7. In addition, the developed controller was optimised in order to get fuel savings over WLTP. Thus, the selection of the operating points defined by the controller is not appropriate for the NEDC, leading to slightly higher CO₂ emissions, compared to the micro-hybrid architectures. As a result, for the follow-up of this work, a controller that performs an optimization of the operating condition will be implemented in order to achieve a reduction on CO₂ emissions for all possible driving cycles.

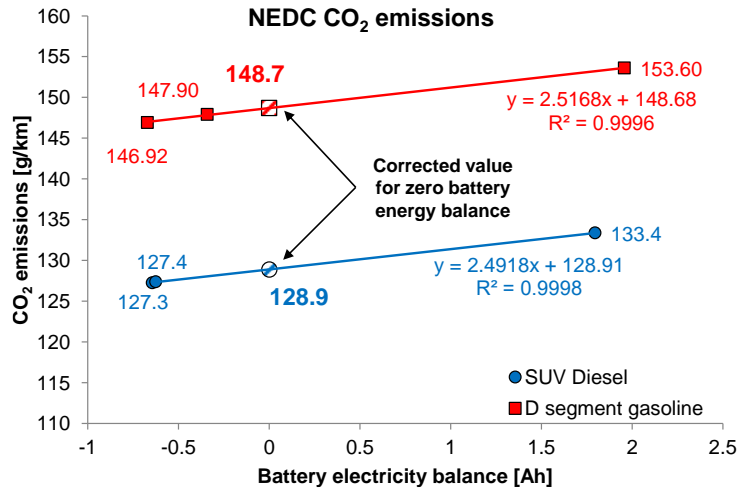


Figure 10: CO₂ emissions versus battery's integrated current over NEDC (simulation results for high, medium and low initial SOC)

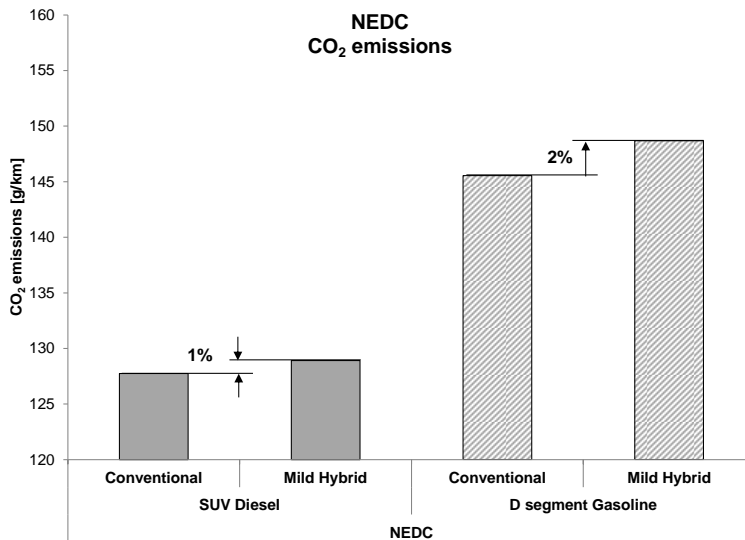


Figure 11: CO₂ emissions results over NEDC for both vehicles used in this study compared to the conventional powertrain layout

Conclusions and future actions

The aim of the study was to develop a simulation approach for mild-hybrids and identify a set of parameters in order to achieve a CO₂ emissions reduction for the selected vehicles. To this aim, the simulation models of two conventional vehicles were modified from micro to mild-hybrid layout and a simulation methodology was developed. Fuel consumption reduction from the modification to mild-hybrid powertrain is calculated approximately 4% over WLTP for an SUV diesel and a D segment gasoline vehicle. In contrast to WLTP, no benefit in the CO₂ emissions performance is observed for NEDC. For both vehicles the same control module was used, thus a higher reduction rate can be achieved after a further optimisation of the approach for each individual vehicle. In addition an extended S&S operation, that was not used for the current approach, with a pure electric range for low velocity (e.g. up to 10 km/h) may lead to further savings in CO₂ emissions for both EU type approval cycles, especially for the NEDC. In order to increase the accuracy of the results a more detailed simulation of the drivetrain efficiency such as BSG belt losses should be considered.

The mild-hybrid simulation approach was developed in a way to make it as generic as possible, and it can be used as the base for the development of the simulation model of an actual mild-hybrid vehicle.

All parameters that regulate the operation of the control module, such as acceleration and SOC thresholds, are not vehicle specific. As a result the developed simulation approach can be easily parametrized and can be tailored to any vehicle. Validation of the model against experimental data may lead to modifications in respect to the experimental data and the specifications of the vehicle, in order to increase the accuracy of the simulation results.

As following steps, a vehicle specific multi-variable analysis and optimisation of the mild-hybrid system may be conducted in order to identify the optimal strategy of such powertrain and achieve a better CO₂ emission performance. Additionally, this study may be enhanced with the development of a P2 mild-hybrid powertrain layout simulation model and a comparison between the two different mild-hybrid layouts (P0 and P2).

Abbreviations

ACEA	European Automobile Manufacturers' Association
BERS	Brake Energy Recuperation System
BSG	Belt-driven Starter Generator
CO ₂	Carbon Dioxide
CO2MPAS	CO ₂ Model for PAssenger and commercial vehicles Simulation
EC	European Commission
EEA	European Environment Agency
EM	Electric Machine
EU	European Union
EV	Electric Vehicle
HEV	Hybrid Electric Vehicle
ICCT	International Council on Clean Transportation
ICE	Internal Combustion Engine
NEDC	New European Driving Cycle
PHEV	Plug-in Hybrid Electric Vehicle
S&S	Start & Stop
SOC	State Of Charge
SUV	Sport Utility Vehicle
WLTP	World-wide harmonized Light vehicles Test Procedure

Acknowledgements

We acknowledge support of this work by the project "DEVELOPMENT OF THE RESEARCH INFRASTRUCTURE "CENTRE OF EXCELLENCE FOR FUTURE VEHICLE ENVIRONMENTAL PERFORMANCE"-FuVEP" (MIS 5002370) which is implemented under the Action "Reinforcement of the Research and Innovation Infrastructure", funded by the Operational Programme "Competitiveness, Entrepreneurship and Innovation" (NSRF 2014-2020) and co-financed by Greece and the European Union (European Regional Development Fund).



References

- A. Dimaratos, D. Tsokolis, G. Fontaras, S. Tsiakkakis, B. Ciuffo, Z. Samaras, (2016). Comparative Evaluation of the Effect of Various Technologies on Light-duty Vehicle CO₂ Emissions over NEDC and WLTP, 6th Transport Research Arena April 18-21, 2016, Transportation Research Procedia. Elsevier B.V., 14, pp. 3169–3178. doi: 10.1016/j.trpro.2016.05.257.
- Audi MediaCenter, <https://www.audi-mediacenter.com/en/press-releases/upgrade-in-the-business-class-the-new-audi-a6-sedan-9883> [accessed February 2019]
- AVL, 2018. AVL Cruise - Vehicle System and Driveline Analysis, <https://www.avl.com/cruise>; [accessed on January 2018].
- D. Tsokolis, S. Tsiakkakis, G. Triantafyllopoulos, A. Kontses, Z. Toumasatos, G. Fontaras, A. Dimaratos, B. Ciuffo, J. Pavlovic, A. Marotta, Z. Samaras (2015). Development of a Template Model and Simulation Approach for Quantifying the Effect of WLTP Introduction on Light-Duty Vehicle CO₂ Emissions and Fuel Consumption. SAE Technical Paper 2015-24-2391.
- D. Tsokolis, Z. Samos, S. Doulgeris, A. Dimaratos, L. Ntziachristos and Z. Samaras (2017). Estimating the European Passenger Car Fleet Composition and CO₂ Emissions for 2030, 22th International Transport and Air Pollution Conference (TAP), 15-16 November 2017, Zurich, Switzerland
- Delphi Technologies, <https://www.delphi.com/innovations/48-volt-mild-hybrid> [accessed February 2019]
- European Commission (2009). Regulation (EC) No 443/2009 of the European Parliament and of the Council, of 23 April 2009. Setting emission performance standards for new passenger cars as part of the Community's integrated approach to reduce CO₂ emissions from light-duty vehicles, Official Journal of the European Union.
- European Commission (2011). Regulation EU No 510/2011 of the European Parliament and of the Council of 11 May 2011. Setting emission performance standards for new light commercial vehicles as part of the Union's integrated approach to reduce CO₂ emissions from light-duty vehicles, Official Journal of the European Union.
- European Commission (2017). COMMISSION IMPLEMENTING REGULATION (EU) 2017/1151 of 1 June 2017. Supplementing Regulation (EC) No 715/2007 of the European Parliament and of the Council on type-approval of motor vehicles with respect to emissions from light passenger and commercial vehicles (Euro 5 and Euro 6) and on access to vehicle repair and maintenance information, amending Directive 2007/46/EC of the European Parliament and of the Council, Commission Regulation (EC) No 692/2008 and Commission Regulation (EU) No 1230/2012 and repealing Commission Regulation (EC) No 692/2008, Official Journal of the European Union.
- European Commission (2017). COMMISSION IMPLEMENTING REGULATION (EU) 2017/1152 of 2 June 2017. Setting out a methodology for determining the correlation parameters necessary for reflecting the change in the regulatory test procedure with regard to light commercial vehicles and amending Implementing Regulation (EU) No 293/2012, Official Journal of the European Union.
- European Commission (2017). COMMISSION IMPLEMENTING REGULATION (EU) 2017/1153 of 2 June 2017. Setting out a methodology for determining the correlation parameters necessary for reflecting the change in the regulatory test procedure and amending Regulation (EU) No 1014/2010, Official Journal of the European Union.
- European Commission. 2020 climate and energy package. Available online at http://ec.europa.eu/clima/policies/strategies/2020/index_en.htm
- F. Kuhnle, (2015). 48V – Past, presence, future – An essay on a possible 48V development direction, 3rd International Conference Automotive 48V Power Supply Systems, 23 November 2015, Dusseldorf, Germany.

- ICCT, "2020-2030 CO₂ standards for new cars and light-commercial vehicles in the European Union", 11/2016
- N. Powell, N. Hill, J. Bates, N. Bottrell, M. Biedka, B. White, T. Pine, S. Carter, J. Patterson , S. Yucel (2018). Impact Analysis of Mass EV Adoption and Low Carbon Intensity Fuels Scenarios, CONCAWE 2018
- R. Romanato, F. Acquaviva, F. Duma, R. Fuso, et al. (2018). 48 V Hybrid System Technologies to Develop the Most Efficient and Cleanest Diesel, SAE Technical Paper 2018-37-0011, 2018, doi:10.4271/2018-37-0011
- T. Smetana (2014). Modular electric axle drive in a 48-volt on-board electric system, Solving the Powertrain Puzzle, Schaeffler Technologies GmbH, 10th Schaeffler Symposium April 3/4, 2014
- W. Engang, C. Banister (2017). Modelling and control of hybrid electric vehicles (A comprehensive review), Renewable and Sustainable Energy Reviews 74 (2017) 1210–1239

2.6.10 Main Diesel, Petrol or electric vehicles: what choice for improving urban air quality? A simulation plate-form and case study.

M. André¹, K. Sartelet², S. Moukhtar³, J.M. André⁴, M. Redaelli⁵

¹ IFSTTAR, Bron, 69675, France, michel.andre@ifsttar.fr

² CEREA, ENPC-ParisTech, University of Paris-Est, 77455 - Marne-la-Vallée, France

³ Airparif, 75004 - Paris, France

⁴ CITEPA, 75010 - Paris, France

⁵ ANSES, 94701 - Maisons-Alfort, France

Introduction

Air pollution is a major concern in most European cities and road traffic is often considered as one of the main causes even if other sectors can contribute significantly. Development and promotion of vehicle technologies and traffic restrictions (e.g. Low Emissions Zones) are levers frequently considered for improving air quality, although their actual effectiveness is rarely established. Amongst the issues in France, there are several questions regarding Diesel cars, their evolution and the actual efficiency of particulate filter and NOx depolluting systems, their possible progressive substitution by petrol cars, or even their ban from city centres, the promotion of electric vehicles and alternative motorisations.

As part of a larger study on the health effects from ambient particulate matter, the ANSES (French Agency for Food, Environmental and Occupational Health & Safety) was asked to investigate the evolution of air pollution as a function of different scenarios of evolution of the road traffic, and the impact of the vehicle technologies. A working group with several research laboratories and institutions undertook thus a large state-of-the-art of the emissions and of the atmospheric concentrations of the pollutants in France, their retrospective and prospective evolution, the specific contribution from the road traffic and from other sources, identifying also lacks of knowledges (André et al., 2019). In this framework, a simulation study over France and Île-de-France was conducted for analysing the prospective evolution of emissions and concentrations under different assumptions regarding the vehicle technologies. Methodological aspects and results for the simulations on the Île-de-France region are discussed here.

Case study

The Île-de-France region is the most populated region of France (12 million inhabitants in 2014, 19% of the national population), with a density of 1 000 inh./km². Paris covers a little less than 1% of the area of Île-de-France but more than 20% of its population (2,3 million inh.). The intra-A86 zone (delimited by the A86 motorway also called the second ring road, see Fig. 1) accounts for approximately 3% of the area (including Paris) and 41% of the Île-de-France population. Thus, the intra-A86 area is a dense urban and highly populated area.

The main sources of anthropogenic pollutant emissions in Île-de-France are the road traffic (56% of NOx, 28% of PM₁₀), the residential (of which wood burning) and tertiary sectors (18 % of NOx, 26 % of PM₁₀), and agriculture (18 % of PM₁₀). Due to a slight decrease of the road traffic in Île-de-France and to a strong reduction of its exhaust pollutant emissions (around -60% of PM₁₀, -48% of NOx over the period 2000-2012), the pollutant concentrations have also decreased by about -25% for PM₁₀ and PM_{2,5} (annual mean concentrations), and by about -45% near the roads. Despite these improvements, exceedances of European regulatory standards and exceedances of air quality guidelines (PM₁₀, NO₂, O₃) are still observed, as well as high pollution episodes.

The Île-de-France Region is used here as a case study for analyzing the evolution of pollutants emissions and atmospheric concentrations under different scenarios with varying vehicle technologies. One scenario also includes a reduction of the traffic volume.

Method, tools

The approach consists in simulating pollutant emissions and atmospheric concentrations, under different scenarios with different composition of the vehicle fleet. These scenarios correspond to different technological options (policies in favour of clean diesel engines, of Petrol cars, etc.).

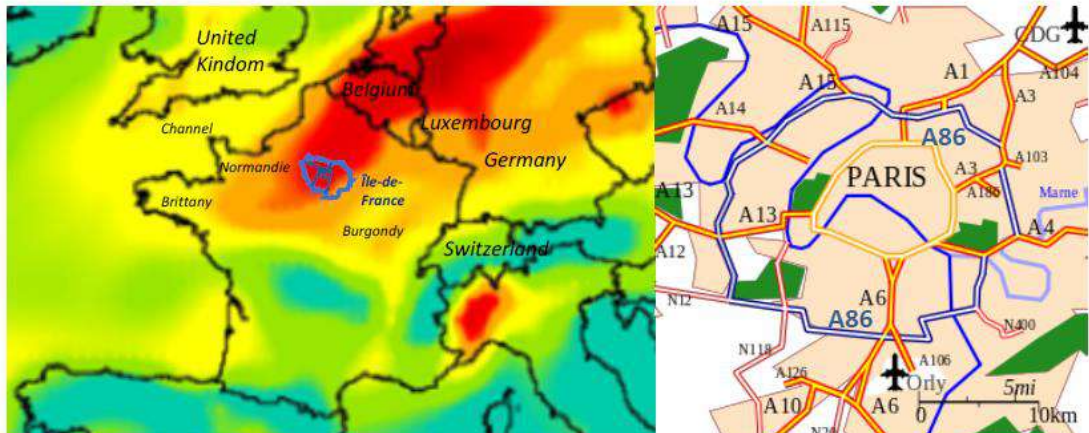


Figure 1: The Île-de-France Region during a PM₁₀ pollution episode in March 2015 (source Prevair <http://www2.prevair.org>, left); main roads and A86 motorway (in blue) delimiting the intra-A86 area (right)

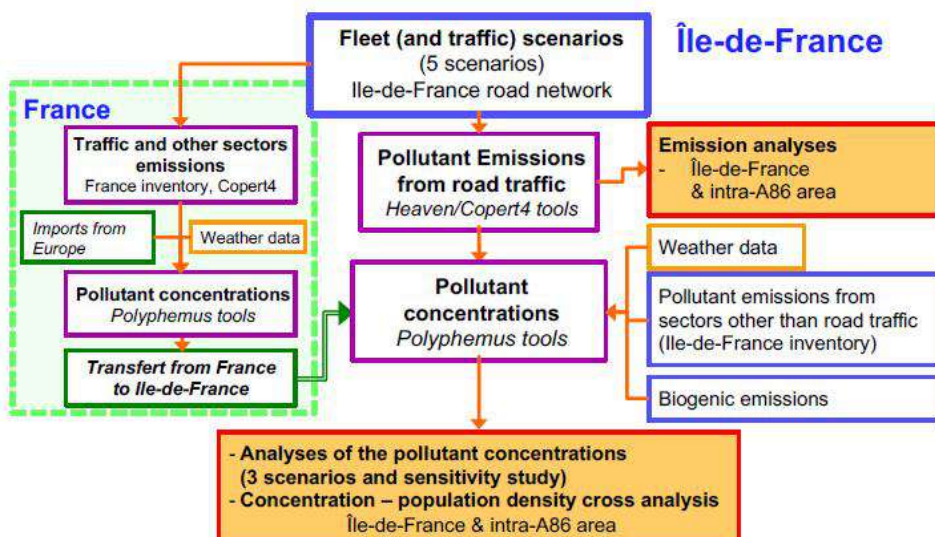


Figure 2: Block diagram of the simulations of pollutant emissions and atmospheric concentrations

The overall analysis of air quality requires an estimation of the pollutant emissions from all activity sectors, as well as natural emissions and imports of pollution from neighbouring areas, and the modelling of the transport and physico-chemical transformations of pollutants in the atmosphere, which depends on contextual conditions such as the chemical regime of the atmosphere.

Three nested domains are thus considered for the simulation: the Europe, the metropolitan France and the Île-de-France region (for the outcome of the present case study) (Fig. 2). Pollutant emissions from road traffic are computed according to the scenarios for France and Île-de-France, while emissions from the other sectors are derived from the national and regional inventories and are invariant. Weather conditions are also kept constant. Concentrations are simulated successively over 3 nested domains (Europe, France and Île-de-France) to estimate the boundary conditions and transfers between the domains.

The following sections describe the platform used for simulating pollutants emissions and concentrations. The selection of the examined pollutants was based on their relevance with the particulate pollution (particulate fractions, precursor gases), with the traffic-related air pollution and with air quality issues. For emission, the following pollutants were estimated: PM₁₀, PM_{2,5}, PM_{1,0}, Particles Number (PN), Black Carbon (BC), Organic Matter (OM), nitrogen oxides (NOx) and nitrogen dioxide (NO₂), Volatile Organic Compounds (VOC), ammonia (NH₃) carbon monoxide (CO) and carbon dioxide (CO₂). Amongst the outputs of the air-quality model,

Secondary pollutants such as ozone (O_3) and some particulate precursors are formed in the gas phase by degradation of NOx and VOCs, depending on their respective concentrations (chemical regime of the atmosphere).

Particles consist of a complex mixture of dust, black carbon (BC), inorganic compounds (sodium, sulphate, ammonium, nitrate, chloride) and organic compounds (OM). Their sizes vary from a few nanometres to several micrometres. The inorganic and organic compounds of particles are largely secondary. OM precursors are volatile organic compounds of biogenic (isoprene, monoterpenes, sesquiterpenes) or anthropogenic (aromatics, intermediate and semi volatile organic compounds) origins. A detailed set-up of the model used in this study may be found in Sartelet et al. (2018) and André et al. (2019).

Model input data

Land-use data were obtained from the "Global Land Cover" and Corine bases. Meteorological input data were derived from ECMWF (European Center for Medium Range Weather Forecasts) reanalyses for the simulations over Europe and France, and from the WRF model (*Weather Research and Forecasting*) version 3.6 (Skamarock, 2008) for the simulations over Île-de-France (Kim et al., 2013). Marine salt emissions relied on Jaeglé et al. (2011) parameterization, while biogenic emissions are estimated using the Model of Emissions of Gases and Aerosols from Nature - MEGAN (Guenther et al., 2006).

The initial and boundary conditions of the Europe simulations were based on the global model MOZART-4 and the meteorological fields of the NASA GMAO GEOS-5 model. The concentrations simulated for Europe served as initial and limit conditions for the simulations on France, which themselves served as initial and boundary conditions for Île-de-France. The air quality simulations were carried out with 14 vertical levels: from 0 to 30 meters, 60, 100, 150 m, and up to 12 km. The horizontal resolution is 50x50 km² for Europe and France, 1x1 km² for Île-de-France.

Emission speciation

A detailed speciation of pollutant emissions (e.g. NOx into NO, NO₂ and HONO, VOCs, particle mass PM into elemental carbon EC, OM) was needed for the simulations. The NOx, VOCs and particles speciations were modified for each of the scenarios, in order to take into account the specificities of the vehicle fleet, as these speciations depend on engine (for example, petrol vehicles tend to emit more aromatic compounds than diesel, while diesel vehicles tend to emit more NO₂). VOCs speciation were derived from (Theloke and Friedrich, 2007), NOx and particles speciation from EMEP guidelines (Ntziachristos et al., 2013).

Secondary organic aerosols (SOA) depends particularly on VOCs and ISVOCs (intermediate and semi-volatile) organic compounds, whose composition varies with the engine (diesel, petrol) and the emission control systems (DPF). ISVOCs are however poorly known although they contribute significantly to the formation of organic particles. Gas-phase ISVOCs were estimated by multiplying by 1.5 the emissions of the primary organic compounds (Kim et al., 2016). An alternative approach using a SVOC / NMHC ratio was also tested in a sensitivity study (Sartelet et al., 2018).

Scenarios assumptions and simulation conditions

The year 2014 was chosen as a reference, while scenarios were built-up for 2025. An evaluation of the modelled concentrations for 2014 by comparisons to measurements was presented in Sartelet et al. (2018) and André et al. (2019).

For France and Île-de-France, road traffic emissions changed with the vehicle fleet scenarios, while most assumptions and input data were kept invariant between the scenarios, to study the impact of technological options. These invariants were notably: weather conditions (2014), land cover, biogenic emissions and emissions from sectors other than traffic, populations and their geographical distribution, total traffic volume (except for one scenario with a traffic reduction) and its spatial and temporal distribution and share between the vehicle categories, traffic conditions and more generally, mobility behaviour and socio-economic context.

The geographical distribution of the simulated pollution was also cross-referenced with the spatial distribution of the populations approximated by their place of residence in order to assess the impact of the scenarios on the population exposure.

Fleet scenarios and data

The vehicle fleet evolution was estimated using a model which simulates a realistic fleet renewal (introduction of new vehicles and withdrawal of old ones, André et al. 2016), under different assumptions regarding technological choices. The reference fleet compositions (Île-de-France and France) were those observed for the current years (2013-2014). The scenarios and evolution of fleets were considered for the 2025 horizon. The scenarios were thus designed as followed:

- 1-REF: the actual vehicle fleet compositions in France (2013) and Île-de-France (2014).
- 2-DPF: this "business-as-usual" scenario corresponds to the expected evolution up to 2025, inducing a generalization of Diesel Particulate Filters, and a high share of vehicles complying with recent emissions regulations Euro5 and 6. The balance between the engines (petrol, diesel, electric) and between the categories and sizes of vehicles is unchanged.
- 3-Petrol: this scenario supposes a marked decline of Diesel engines in favour of petrol for light vehicles (inversion of the Diesel/Petrol share), by a steady decline in sales of Diesel (from 60% to 5% in 2025), with the same regulatory evolution as for the DPF scenario.
- 4-Elec: this scenario adds a marked promotion of electric vehicles on the urban road network, for all vehicles. Sales reach 40% of pass. cars and 60% of light commercial vehicles in 2025. All Euro 3 and earlier trucks and buses, and all motorized two-wheelers under 250cc are also converted in electric. The vehicle fleet of the DPF scenario is used in rural and on motorway,
- 5-Air: this scenario combines the fleet composition of the 4-Elec scenario and a reduction of traffic in the intra-A86 densely populated area by about 17%. The vehicle fleet of the DPF scenario is used outside that area.

The three first scenarios were simulated in pollutant emissions and concentrations over France and Île-de-France. The two last ones were simulated only in emissions over Île-de-France:

Results

Fleet compositions

The average fleet composition of Île-de-France is estimated by weighting the fleets typical of urban, rural, Boulevard Périphérique (ring road around Paris) and highway. Light vehicles (passenger cars and light commercial vehicles) account for a very high proportion of traffic (86%), followed by motorized two-wheelers (8%). Lorries account for only 5% and buses / coaches less than 1% (Table 1). The DPF scenario doubles the equipment of diesel light vehicles with particulate filters and renews almost the entire fleet to the Euro 5 and 6 regulations (from 40 to 80%); the Petrol scenario reverses the Diesel/Petrol ratio from 73-27% to 43-56% (light vehicles). This important change requires a greater renewal of the fleet, which broadly amplifies the evolution towards Euro 5 and 6 regulations (from 39 to 91%); on the other hand, the fleet of light diesel vehicles is less renewing and aging.

The scenario promoting electric vehicles leads to a lower turnover of conventional vehicles (diesel and gasoline) and thus to lower rates of vehicles complying with the most recent regulations and of Diesel equipped with DPF. The 5-Air scenario applies only in Intra-A86 and results in a lower number of electric vehicles over Île-de-France, but in a higher share in Intra-A86 cumulated with a traffic reduction, which can give it a "local" efficiency.

Fig. 3 gives the average light vehicles composition for Île-de-France. The share of Euro 5 and 6 regulations (including electric vehicles) increased from 39% in the reference scenario to 80-90% in the "prospective" scenarios. Diesel light vehicles decreased from 73% to 43% in the Petrol scenario, 58% in the 4-Elec, 68% with the 5-Air scenario (50% in the intra-A86 area). About 80% of diesel light vehicles were equipped with DPF in the different prospective scenarios, against 42% in the reference. Electric vehicles represented 11% in the 4-Elec scenario in Île-de-France, and reached 16% in the intra-A86 area with the 5-Air scenario.

Table 1: Average fleet composition for the scenarios in Île-de-France (main evolution in Bold)

In % of veh x km, for the different scenarios						
Vehicles	Categories	1-REF	2-DPF	3-Petrol	4-Elec	5-Air (with traffic reduc)
Light duty vehicles (passenger cars and vans)	Diesel (incl. hybrids)	73	73	43	58	68
	% with DPF	42	80	83	78	79
	Petrol (incl. hybrids)	27	26	56	31	28
	Electric	0,4	0,4	0,6	10,9	3,7
	% Euro 5 and 6	39	79	91	81	80
	% of total traffic of which Pass. Cars	86	86	86	86	84
Lorries	Electric	71	71	71	71	69
	Diesel	99	99	99	97	98
	Electric	0,1	0,1	0,1	2,3	0,9
	% Euro 5 and 6	43	83	83	85	84
Urban bus and coaches	Electric	-	-	-	15	6
	Diesel	99	99	99	99	99
	% Euro 5 and 6	49	90	90	97	92
	% of total traffic	0,7	0,7	0,7	0,7	0,8
Motorized two-wheelers	Petrol	100	100	100	59	80
	Electric	0,0	0,0	0,0	42	18
	% Euro 5 and 6	0,0	54	54	54	54
	% of total traffic	7,8	7,8	7,8	7,8	9,4

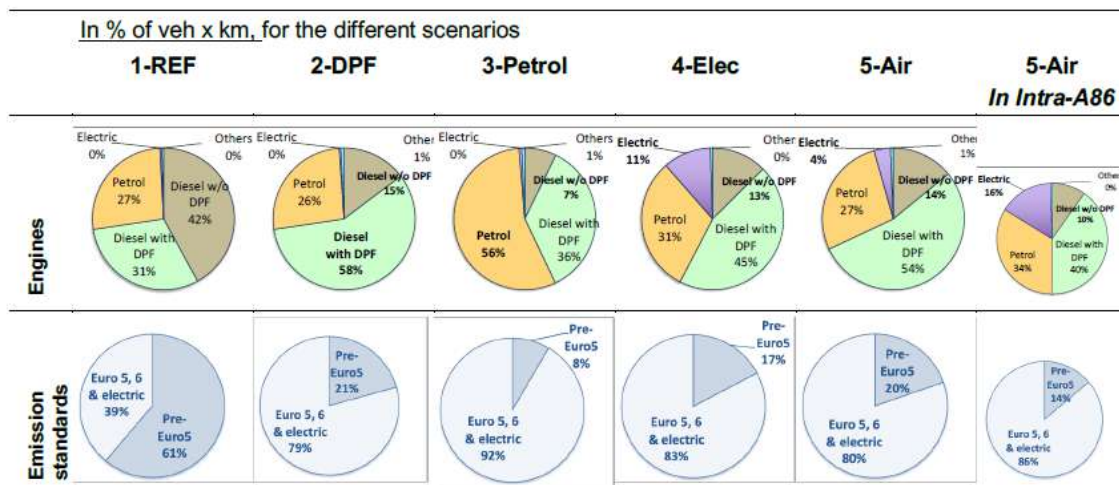


Figure 3: Light vehicles fleet composition in the Île-de-France region and intra-A86 area, as regards motorisation and emission standards

Pollutant emissions

Overall, road traffic contributes significantly to nitrogen oxide emissions (58% and 78% of total NOx and NO₂ in Île-de-France, Tab. 2), as well as BC (54%), less to particulate PM₁₀ and PM_{2,5} (20-25%), and non-methane NMVOCs (11%), but significantly to the intermediate and semi-volatile compounds ISVOC (37%).

Passenger cars represent 71% of the traffic and contribute to 58% of CO₂ emissions, 44% of NMVOCs, 46% of NOx, and 42% to 46% of particles (Tab. 3). Light commercial vehicles (vans less than 3.5 tons) account for 16% of traffic and emit 19% of CO₂, 17% of NOx. They contribute more strongly to particulate emissions (36-40%). Motorized two-wheelers account for around 8% of traffic, but contribute very significantly to VOC (45% of the total). Their contribution to other

pollutants is rather limited. Heavy vehicles (lorries, buses and coaches) account for only 6% of traffic, but contribute significantly to emissions of CO₂ (20%), NOx (36%), NO₂ (18%) and particulates (12-16%).

Table 2: Total pollutant emissions (per year) in Île-de-France and traffic contribution in the reference situation (scenario 1-REF)

Total emissions (in tons)	NOx	NO ₂	NH ₃	NMCOV	PM ₁₀	PM _{2.5}	BC
All sectors	78490	13682	5713	82253	19038	12200	2037
Road traffic	45216	10622	508	8631	3769	2993	1096
<i>In % of total</i>	57,6	77,6	8,9	10,5	19,8	24,5	53,8

Table 3: Distribution of road traffic and pollutant emissions as regards vehicles categories in the reference situation (scenario 1-REF)

Vehicles	Traffic	Combustion & evaporation (VOC)		Combustion and abrasion		
	CO ₂	NMVOC	NOx	PM ₁₀	PM _{2.5}	BC
Passenger cars	70,8 %	57,6 %	43,8 %	45,9 %	42,8 %	45,3 %
Light duty vehicles	15,5 %	18,6 %	5,5 %	17,1 %	40,0 %	35,9 %
Two-wheelers	7,8 %	3,6 %	45,2 %	1,3 %	3,3 %	3,3 %
Lorries	5,3 %	15,0 %	3,5 %	24,2 %	10,7 %	12,3 %
Busses / coaches	0,7 %	5,2 %	1,9 %	11,6 %	3,2 %	3,1 %
Total	5,46 x 10 ⁴ vehxkm	1,13 x 10 ⁷ tons	8,64 x 10 ³	4,39 x 10 ⁴	2,93 x 10 ³	3,62 x 10 ³ 1,09 x 10 ³

In the reference, 69% of traffic is made by diesel vehicles (light and heavy), which emit 75% of CO₂, 92% of NOx, 96 to 98% of particulate. Gasoline traffic (25% of CO₂) emits mainly NMVOCS and NH₃ (86 and 87%) and contributes marginally to particulate (2 to 4%) and NOx (8%).

With regard to emission regulations, 68% of the reference traffic is carried by Euro 4 and earlier vehicles, which produce 69 to 96% of the emissions of the different pollutants. Euro 5 and 6 technologies (V and VI for heavy vehicles) represent 31% of total traffic and contribute much less to emissions (8% of VOCs, 16% of NH₃, 4 to 6% of particulate pollutants), except for NOx (29%).

Among Diesel passenger cars and light commercial vehicles, those equipped with particulate filters cover 28% of the distances traveled, but only contribute 1 to 2% of particulate emissions and 5% of NH₃ emissions. However, they are responsible for 30% of NOx emissions.

Evolution of the traffic emissions with the technology scenarios

The DPF scenario, which is almost a business-as-usual progression from Diesel with particulate filters, resulted in very sharp reductions in combustion particulate emissions (-60% BC, Tab. 4), while larger particles were less reduced (30-40%) due to the wear and abrasion contribution. With the regulatory evolution and renewal of vehicles, the emissions of gaseous pollutants also decrease: by 10% for CO₂, 30% for VOCs, 50% for nitrogen oxides and 36% for NH₃.

The Petrol scenario accentuated reductions in NOx (-60%) and combustion particles (-74%), but led to a lower reduction of VOCs (-12%) and NH₃ (17%). The 4-Elec scenario (promotion of electric vehicles in urban) has a clear CO₂ advantage (-19% vs -10%). NOx and NH₃ reductions are also very high (-60 and -37%). Particle emission reductions are slightly higher than those of the DPF scenario, but lower than those the Petrol scenario.

The 5-Air scenario (combining promotion of electric vehicles and reduction of traffic in Intra-A86) does not offer a significant advantage over the Petrol and Elec scenarios at the Île-de-France scale. However, the emission reductions are markedly increased in the intra-A86 perimeter (-71% for NOx instead of -58% in Île-de-France, -75% for BC, -57% for PM_{2.5}). This scenario, which includes restriction on a given perimeter, therefore has a definite advantage over the most urbanized intra-A86 territory, which also concerns a significant proportion of the population.

Technological scenarios are compared in Tab.5. The Petrol scenario led to an increase of 15% of VOC emissions and 30% of NH₃, while it brings a further reduction of PM from -10 to -30%.

These differences are quite similar in intra-86 and throughout the Île-de-France. The reduction of particulate emissions is more limited with the Elec scenario (but it is more marked in intra-A86). This scenario brings a net profit of VOC (-25%) and CO₂. Finally, the 5-Air scenario brings the strongest benefits in intra-A86: -34% of BC, -38% of nitrogen oxide and about -20% of VOCs, highlighting the benefit of reduced traffic in densely populated areas.

Table 4: Evolution of traffic volume and pollutant emissions in Île-de-France with the scenarios

Variations in %	Traffic	Combustion & evaporation (VOC)		Combustion and abrasion			
Vehicles		CO ₂	NMVOC	NOx	PM ₁₀	PM _{2,5}	BC
1-Reference	1	1	1	1	1	1	1
For the whole Île-de-France Region							
2-DPF, high share of DPF	0,0	-10	-30	-53	-33	-43	-62
3-Petrol, decl of Diesel light veh.	0,0	-9	-12	-62	-40	-52	-74
4-Elec, promo. of electric veh.	0,0	-19	-42	-62	-36	-47	-66
5- Air, traffic reduction	-3,9	-17	-39	-58	-37	-47	-65
In the highly populated intra-A86 area							
5- Air, traffic reduction	-14,5	-34	-47	-71	-47%	-57	-75

Table 5: Comparison of the technological scenarios (traffic and emissions) in Île-de-France

Variations in %	Traffic	Combustion & evaporation (VOC)		Combustion and abrasion			
Vehicles		CO ₂	NMVOC	NOx	PM ₁₀	PM _{2,5}	BC
2-DPF, high share of DPF	1	1	1	1	1	1	1
For the whole Île-de-France Region							
3-Petrol, decl of Diesel light veh.	0,0	1	15	-19	-11	-16	-31
4-Elec, promo. of electric veh.	0,0	-10	-25	-18	-5	-7	-11
5- Air, traffic reduction	-3,9	-7	-6	-10	-6	-7	-8
In the highly populated intra-A86 area							
5- Air, traffic reduction	-14,5	-26	-19	-38	-24	-27	-34

Vehicle fleet renewal effect

It was noted that the fleet compositions differed both in terms of technologies (Diesel, petrol, etc.) and their proportions in traffic, but also by the renewal induced by the evolution from the reference to the scenarios in 2025. So, the Petrol scenario led to a higher turnover of the fleet and a higher proportion of Euro 5 and Euro 6 vehicles. The differences in emissions included thus a renewal effect, which can be separated from the technology effect, by adjusting the emissions estimation according to similar Euro distributions (Tab. 6).

For NOx, the benefit is mainly linked due to the change from Diesel to Petrol engines, while the renewal effect is contradictory between Diesel (NOx increase) and petrol (NOx decrease) vehicles. The reduction of combustion VOCs between DPF and Petrol scenarios is driven by the accelerated renewal of the Petrol vehicles, which induce an increase of the evaporative (and total) VOCs emission. For particulates, the benefit of the Petrol engines is around 55 and 70% of the total effect, the remaining benefit being due to the accelerated renewal.

Evolution of the total emissions with the technology scenarios

The reductions of the total emissions (all sectors) through the scenarios are however more limited than the reduction of the road traffic emissions, due to their respective share. The most significant reductions concern NOx (-35 to -40%) and NO₂ (-47 to -54%), and BC (-36 to -42%) compared to the reference situation. Reduction of particulate emissions are lower (-15 % for PM_{2,5}, -20 to -23 % for OM, less than 5% for PM₁₀).

Table 6: Respective contribution due to the Diesel to Petrol change, and to the accelerated fleet renewal due to the transition from a limited to a large share of Petrol light vehicles in the fleet

Difference (in%) of emission (combustion or total) between scenarios 3-Petrol and 2-DPF							
(All vehicles - Île-de-France)	NOx	VOCs Comb.	VOCs Total	PM _{2,5} Comb.	PM _{2,5} Total	BC Comb.	BC Total
Total difference	-19,8	-12,4	+15,2	-32,7	-15,8	-40,4	-31,3
Contribution due to the Euro structure change due to the vehicle renewal							
- Light vehicles - Diesel	+11,4	-0,9	-0,7	-9,1	-3,1	-18,2	-13,3
- Light vehicles - Petrol	-4,5	-17,2	-10,1	-0,1	+0,1	-0,1	-0,0
Vehicle renewal total effect	+6,9	-18,1	-10,8	-9,1	-3,0	-18,3	-13,3
Net effect due to the Diesel-Petrol change	-25,7	+5,8	+26,0	-23,5	-12,8	-22,1	-18,0

Evolution of the pollutant concentrations

- Spatial distribution and evolution of the concentrations*

Figure 4 shows the annual average concentrations of ozone, PM_{2,5}, BC, and of secondary inorganic and organic aerosols over Île-de-France in the reference simulation, as well as the relative differences between the 1-DPF scenario and the reference.

In the reference, O₃ concentrations are lower in Paris and along the roads than on the rest of the Île-de-France. Indeed, O₃ is titrated by the high concentrations of NOx in Paris and along the roads. On the opposite, the average PM_{2,5} concentrations (and other primary particulate compounds) are higher in Paris than in the rest of Île-de-France. BC is an inert compound and emitted mainly by road traffic. The highest concentrations are therefore observed in Paris and along the roads with concentrations between 0 and 2 µg / m³, while concentrations are less than 0.4 µg / m³ over most of Île-de-France. However, these are concentrations averaged annually and on meshes, and thus they are much lower than those measured at roadside.

Inorganics aerosols are secondary pollutants formed mainly by the condensation of nitric acid and ammonia (NH₃) in Île-de-France (in other regions, sulfates may be predominant). Their concentration is relatively uniform over Île-de-France, with levels higher than 6 µg/m³. Organics aerosols are also largely secondary pollutants. Their concentrations are greater than 2 µg/m³ throughout Île-de-France. Higher concentrations are observed in Paris due to anthropogenic emissions of VOCs and ISVOC, as well as near the Fontainebleau Forest (South-West), the Chevreuse High Valley Nature Park (South-East) and the Regional Park of Oise (North of Île-de-France). In the vicinity of these forests, organic matter is formed by the oxidation of biogenic VOCs emitted by forests. The oxidized compounds partition on the particles (i.e. they share between the gas phase and the particulate phase).

Compared to the reference situation (i.e. year 2014), all scenarios lead to quite similar evolution due to the large reduction of emissions. We discuss thus here only the difference between the 2-DPF scenario and the 1-Reference. We will compare 2-DPF and 3-Petrol later.

The DPF scenario, which mainly induces a decrease in NOx emissions, leads to a slight decrease in O₃ over the majority of Île-de-France, where the chemical regime is rather limited in NOx. However, the O₃ increases significantly (up to 27% annual average) in Paris and along the roads, where the regime is rather limited in VOC. These increases in O₃ are not a real problem because they occur in areas of low average concentrations. This nevertheless indicates that the DPF scenario also leads to an increase in oxidants in Paris and along the roads, which leads to an increased production of secondary aerosols.

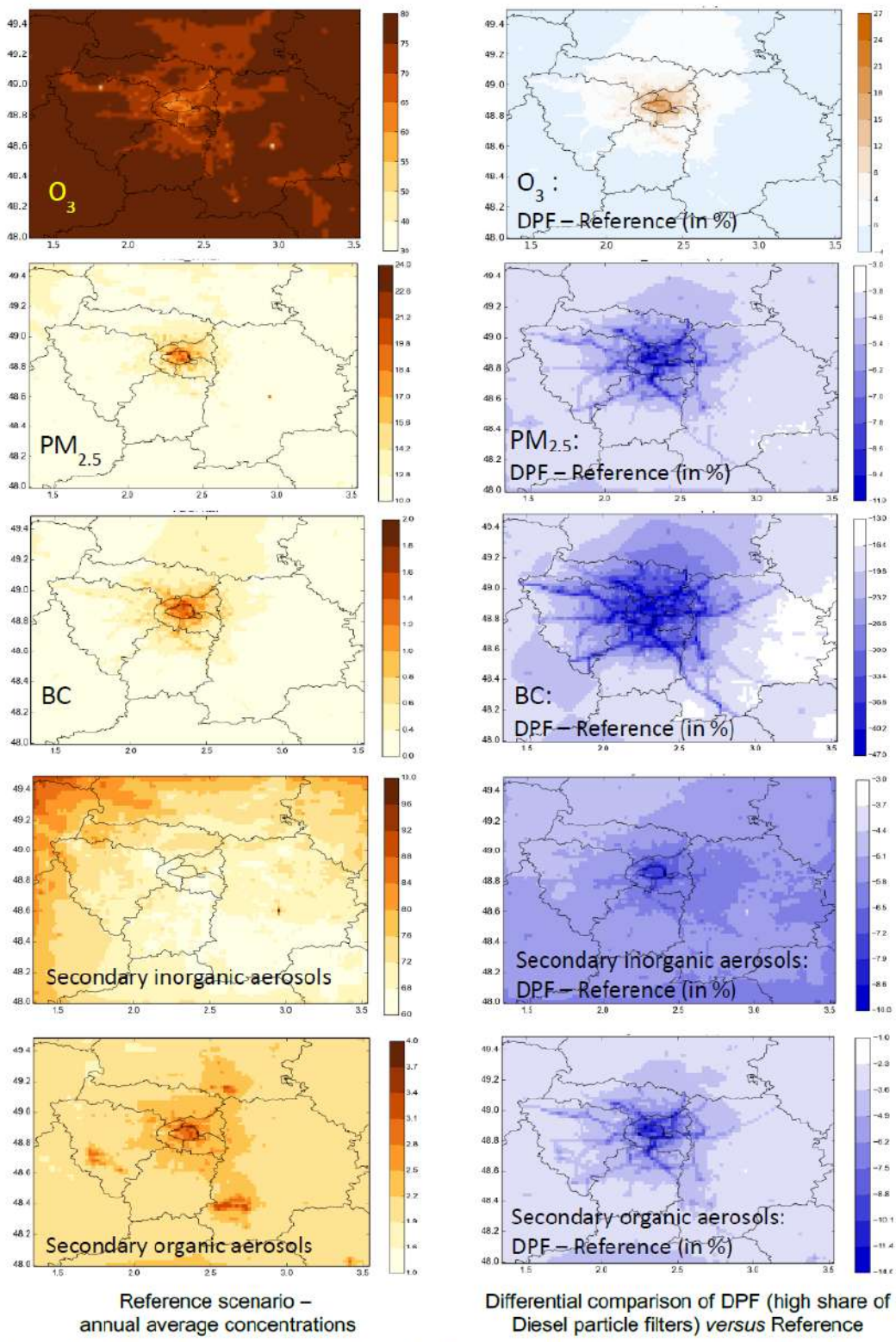


Figure 4: Annual average concentrations of pollutants for the reference situation (left) and impact of the DPF scenario (right)

For $\text{PM}_{2.5}$, the highest differences between the DPF scenario and the baseline simulation are observed along major highways as well as in Paris. Across the Île-de-France, $\text{PM}_{2.5}$ concentrations decrease from 3% to 12%. A strong reduction of BC concentrations (up to -47%) is also observed.

The DPF scenario induces a reduction of inorganic concentrations between 3 and 10%, due to the decrease in NOx emissions, and thus of the concentrations of nitric acid. The sharpest decline is in Paris. The reduction along the roads is less visible than for $\text{PM}_{2.5}$.

The DPF scenario leads also to a reduction in organic concentrations in Paris, along roads, but also near forests and nature parks. The decrease is due to the diminution of ISVOC emissions along the roads, and to the decrease of oxidants (due to the NOx emissions reduction) in the vicinity of the forests.

Compared to the 2-DPF scenario (see Fig. 5), the 3-Petrol scenario induces a slightly larger increase of O_3 concentrations in Paris (+ 3%) due to a further reduction of NOx emission whilst VOC are limited. On the opposite, the 3-Petrol scenario reduces more the particulate compounds than the 2-DPF scenario.

Thus, the Petrol scenario leads to a further reduction of concentrations of $\text{PM}_{2.5}$, by 1 to 2% in Île-de-France, more marked along the roads around Paris. Additional reductions of BC concentrations are also observed, reaching up to 17% along the roads.

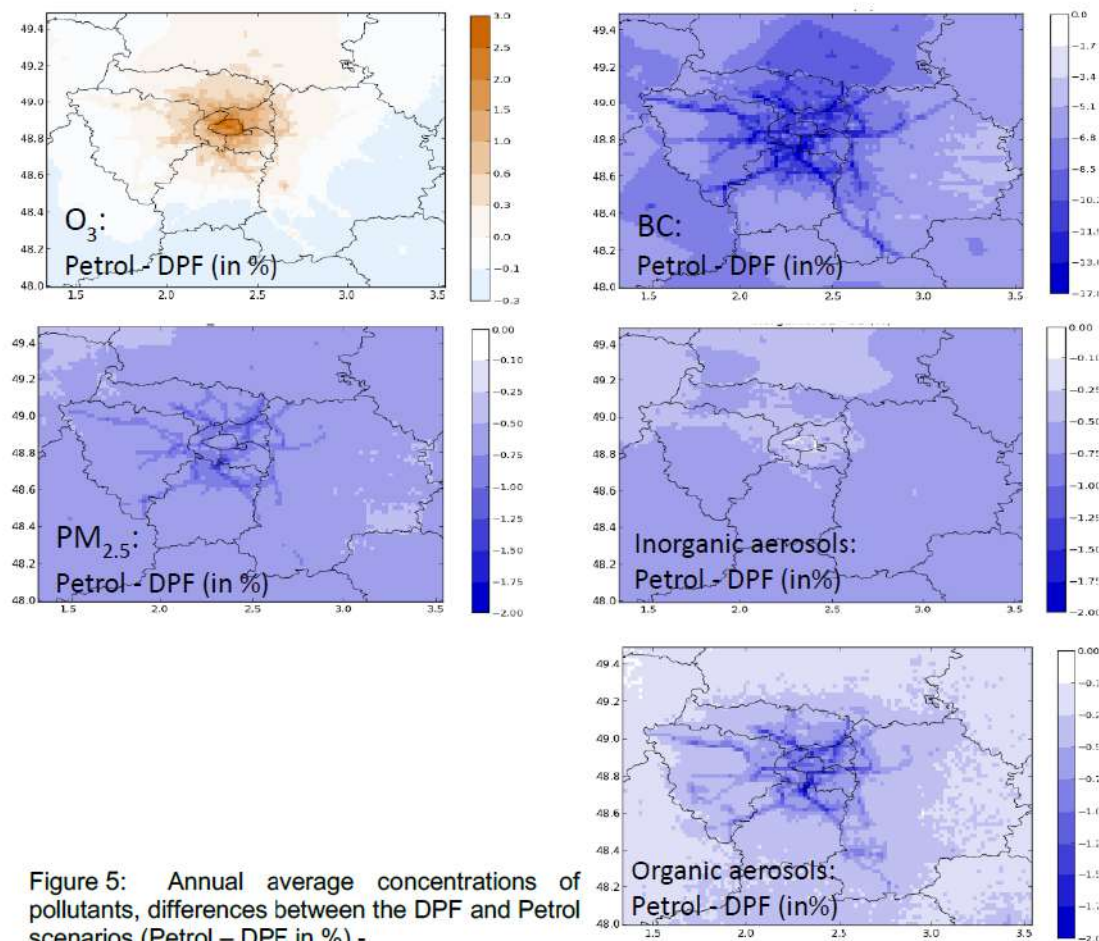


Figure 5: Annual average concentrations of pollutants, differences between the DPF and Petrol scenarios (Petrol - DPF in %) -

A drop of a few percent more for inorganic concentrations is due to the greater decrease in NO₂ emissions in this Petrol scenario, compared to the DPF scenario. This decrease is slightly lower

in Paris and along the Boulevard Périphérique (ring road), because the oxidants are higher in the Petrol scenario.

The Petrol scenario causes a further decrease in organic concentrations (up to -1.5%, especially along the roads), due to a larger decline in emissions from organic aerosol precursors ISVOC. This decline is however more limited in Paris where this scenario induces an increase in oxidants.

- *Concentrations statistics*

For the reference simulation over Île-de-France, Table 7 shows the average annual concentrations ($\mu\text{g}/\text{m}^3$) for each of pollutants as well as their standard deviation (spatial variation of the annual concentrations). The standard deviation is large for NO_2 and BC because they are local pollutants mainly emitted by traffic. It is smaller for O_3 and inorganic particles because they are secondary pollutants forming away from emission sources.

We have also defined a threshold or limit (P98, i.e. the percentile 98% of the average values in the Reference situation) to count the number of temporal events for which daily concentration values are higher than this limit, and to assess the evolution of this number of exceedances through the scenarios. This P98 threshold is thus a theoretical short-term concentration limit (it does not correspond to the recommended or authorized limits for health), but it enables however to assess events corresponding to high levels of pollution, for each of the pollutants.

Table 7: Statistics of the pollutant concentrations (average concentrations and number of values exceeding the P98 threshold) for the different scenarios compared to the reference

	PM _{2,5}	PM ₁₀	PM ₁₀ inorganic	PM ₁₀ organic	BC	NO ₂	O ₃
1-Reference							
Average concentration ($\mu\text{g}/\text{m}^3$)	12,3	13,1	7,0	2,2	0,4	6,7	75,5
Standard deviation (spatial variations)	1,1	1,4	0,3	0,2	0,2	5,3	2,9
P98 threshold (i.e 2% of val. exceeding)	27,9	29,9	16,5	6,0	1,3	35,5	126,3
2- DPF scenario (generalisation of Diesel DPF) – compared to 1-Reference							
Variation of average concentration (%)	-5,0	-4,8	-5,7	-4,1	-26,8	-40,5	0,6
Variation of the number of values exceeding the P98 threshold (%)	-10,5	-11,2	-16,9	-12,2	-73,0	-84,6	-7,4
3- Petrol scenario (strong decline of Diesel for the light vehicles) – compared to 1-Reference							
Variation of average concentration (%)	-5,6	-5,3	-6,2	-4,5	-32,6	-40,8	0,6
Variation of the number of values exceeding the P98 threshold (%)	-11,8	-11,6	-21,2	-14,2	-77,9	-85,0	-12,4

Except for O_3 (for which an increase of 0.6% is recorded), the average concentrations decrease for each of the scenarios compared to the reference situation. The greatest differences are observed for NO_2 (-41%), BC (-27% for 2-DPF, -33% for 3-Petrol). For particulate matter (PM_{2,5}, PM₁₀) and secondary particulate matter (inorganic, organic), the decrease in mean annual concentrations is lower (between -4% and -6% for the DPF scenario; -4.5 to -6.2% for the Petrol scenario).

Although the average concentration of O_3 increases, the high concentrations, i.e. the occurrences of exceeding the threshold P98, decrease (by 7% for the 2-DPF, and 12% for 3-Petrol scenario).

For NO_2 and BC, the decrease of the occurrence of high concentrations is much stronger. It reaches -85% for NO_2 and -73% for BC with the DPF scenario. The reduction is slightly higher with the Petrol scenario (resp. -95% and 78%). Finally, for particulate matter, similarly to that was observed for the average value, the reduction of exceedance events is more limited. It remains however at a good level: from -11% to -17% for the DPF scenario, -12 to -21% for the Petrol scenario.

A first conclusion is that the scenarios reduce more strongly the occurrences of exceedance of short-term thresholds (estimated here through P98), than the annual average concentrations, and that is true for all pollutants.

The second conclusion concerns the comparison of the DPF and Petrol scenarios. Although the statistics are quite close, we observe a slight advantage for the Petrol scenario, the differences with the reference situation being always greater than those observed with the DPF scenario.

The increase in annual O₃ is slightly higher in the Petrol scenario, but the high concentrations are more reduced. Indeed, the O₃ increase mainly concerns Paris and its periphery (where the chemical regime is limited in VOC) due to higher VOC emissions by the Petrol scenario. However, the higher concentrations mainly concern the areas outside Paris (NOx limited chemical regime), where the Petrol scenario is more favourable due to lower NOx emissions.

For BC (inert pollutant) the concentrations are also more reduced by the Petrol scenario due to stronger reduction of the BC emissions.

For organic and inorganic secondary aerosols, The Petrol scenario leads also to slightly larger decreases of the concentrations. For organics the high concentrations along the roads and in Paris decrease more than with the DPF scenario, although the concentrations of O₃ and oxidants are there higher. This is due to lower emissions of intermediate semi-volatile species ISVOC, which are supposed to be proportional to the emissions of organic particles (OM), these last ones being lower with the Petrol scenario. The same conclusions hold when simulations were performed by estimating ISVOC emissions from VOC emissions rather than OM emissions (Sartelet et al. 2018).

For inorganics, the advantage of the Petrol scenario is due to lower NOx emissions and concentrations, inducing a decrease of nitric acid (HNO₃) concentrations. As far as inorganics in Ile-de-France are mainly composed of ammonium nitrate whose formation is limited by HNO₃ concentrations (Sartelet et al., 2007), the decrease of NOx and thus of HNO₃ concentrations induces a reduction of inorganic concentrations.

Conclusions

Simulations of pollutant emissions and concentrations over the Île-de-France region and under different technological scenarios demonstrate a strong decrease of road traffic emissions by 2025 (-30 to -60% according to the different pollutants), due to the generalization of particulates filters on Diesel vehicles and to the large renewal of the vehicles fleet towards the most recent regulations (Euro5 and 6) (DPF scenario). A scenario favoring Petrol engine would induce a stronger renewal of the fleet and reduce more particles and NOx emissions, but less VOC and NH₃ compared to the business-as-usual DPF scenario, which see the quasi generalization of DPF at this time horizon.

Both DPF and Petrol scenarios led to lower annual average concentrations compared to the reference, especially for NO₂ (-54 to -60%) and BC (-47% to -56%), and reduce more strongly the number of high concentrations events. For other compounds (PM_{2.5}, secondary pollutants), reductions were more limited due to the influence of the other sectors and atmospheric chemistry. Ozone concentrations may even increase in some urban locations and periods, but remain low in these cases.

The differences between the scenarios themselves are smaller. For PM emissions and concentrations, the Petrol scenario is slightly more favorable than the DPF one, for all pollutants. Differences are marked for primary particles from traffic (BC) and less for secondary compounds (PM_{2.5}, organic and inorganic fractions). The difference is also marked for NO₂. The Petrol scenario advantage is mainly due to lower emissions (-80% of PM_{2.5}, -60% of BC), partially linked to the accelerated fleet renewal with the Petrol scenario (higher share of Euro 5 & 6).

A voluntary scenario combining the promotion of electric vehicles and a traffic reduction in the densely populated urban area Intra-A86 would bring supplementary benefits for all emissions in that area (-34% for BC, -20 to -44% for gaseous pollutants). Although concentrations were not simulated for that scenario, a definite advantage would be expected, due to the combination of vehicles technologies and traffic reduction for the most urbanized territory, which also concerns a significant proportion of the population.

Acknowledgements

This study received a financial support from the French Agency for Food, Environmental and Occupational Health & Safety (Anses) through Grant 2016-CRD-04 and is part of the work done by the Anses working group on ambient particulate matter (chemical composition and road traffic emissions) whose members are André M., André J.M., Baeza-Squiban A., Blanchard M., Charron A., Gagnepain L., Garçon G., Honoré C. (from May to December 2016), Jacquemin B., Moukhtar S., Mullot J.U. and Sartelet K. The analyses, interpretations and conclusions in the present study are those of the authors and do not necessarily reflect those of the mentioned institutions

References

- Airparif (2016). Inventaire régional des émissions en Île-de-France. Année de référence 2012. Eléments synthétiques. http://www.airparif.fr/_pdf/publications/inventaire-emissions-idf-2012-150121.pdf
- André M., Carteret M., Pasquier A. (2016). Traffic and vehicle fleet statistics for the calculation of air pollutant emissions from road transports in France; *In: André M. (Ed.) Res. for Innov. Transp. Sets, Vol. 1: Energy and Environment.* ISTE Wiley. 417-433.
- André M., Redaelli M., André J.M., Charron A., Gagnepain L., Honoré C., Moukhtar S., Sartelet K., Brasseur A., Léger C. (2019). Impact sur la pollution atmosphérique des technologies et de la composition du parc de véhicules automobiles circulant en France. Part B (*in French*). Saisine n°2014-SA-0156. Expertise report, ANSES Maisons-Alfort (France). 280p.
- CITEPA (2016a). Inventaire des émissions de polluants atmosphériques en France métropolitaine, format CEE-NU (March 2016 edition)
- CITEPA (2016b). Rapport OMINEA – 13^{ème} Ed (methodology of the French inventory of pollutant emissions).
- EEA (2013). EMEP/EEA – Air Pollutant Emission Inventory Guidebook – Technical report N° 12/2013 - 1.A.3.b Road transport <https://www.eea.europa.eu/publications/>
- Guenther, A., Karl, T., Harley, P., Wiedinmyer, C., Palmer, P. et Geron, C. (2006). Estimates of global terrestrial isoprene emissions using MEGAN (Model of Emissions of Gases and Aerosols from Nature). *Atmos. Chem. Phys.*, 6:3181–3210.
- Jaeglé, L., Quinn, P.K., Bates, T.S., Alexander, B., and Lin, J. (2011). Global distribution of sea salt aerosols: new constraints from in situ and 5 remote sensing observations, *Atmos. Chem. Phys.*, 11, 3137–3157.
- Kim Y. K., Sartelet, J.-C. Raut and P. Chazette (2013). Evaluation of the WRF/urban model over Greater Paris. *Boundary-Layer Meteorology*, 2013, 149, 105–132.
- Kim Y., Sartelet K., Seigneur C., Charron A., Besombes J.-L., Jaffrezo J.-L., Marchand N., Polo L. (2016). Effect of measurement protocol on organic aerosol measurements of exhaust emissions from gasoline and diesel vehicles *Atmos. Env.*, 140, 176-187.
- Mallet, V., Quélo, D., Sportisse, B., Ahmed de Biasi, M., Debry, É., Korsakissok, I., Wu, L., Roustan, Y., Sartelet, K., Tombette,M. et Foudhil, H. (2007). Technical Note: The air quality modeling system Polyphemus. *Atmos. Chem. Phys.*, 7(20):5479–5487.
- Ntziachristos L., Samaras, Z., Kouridis C., Hassel D., Mellios G., McCrae I., Hickman J., Zierock K.-H., Keller M., Rexeis M., Andre M., Winther M., Pastramas N., Gorissen N., Boulter P., Katsis P., Jourard,R., Rijkeboer R., Geivanidis S., Hausberger S. (2013). Exhaust emissions from road transport, EMEP Guidebook 2014.
- Sartelet, K., Debry, É., Fahey, K., Roustan, Y., Tombette, M. et Sportisse, B. (2007). Simulation of aerosols and gas-phase species over Europe with the Polyphemus system: Part I Model-to-data comparison for 2001. *Atmos. Env.*, 41:6116–6131.
- Sartelet K., S. Zhu, S. Moukhtar, M. André, J.M. André, V. Gros, O. Favez, A. Brasseur, M. Redaelli (2018). Emission of intermediate, semi and low volatile organic compounds from traffic and their impact on secondary organic aerosol concentrations over Greater Paris, *Atmos. Env.*, 180: 126-137
- Skamarock W., J. Klemp, J. Dudhia, D. Gill, D. Barker, M. Duda, X. Huang, W. Wang and J. Powers (2008). A description of the advanced research WRF version 3, NCAR Techn. Note, NCAR/TN-475+STR, 8, p. 123.
- Theloke J. et Friedrich R. (2007), Compilation of database on the composition of anthropogenic VOC emissions for atmospheric modeling in Europe, *Atmos. Env.*, 41, 19, 4148-4160.
- Tomassini M. (coord.) (2003) Healthier Environment through Abatement of Vehicle Emission and Noise, EC project IST-1999-112444, Final Report. 61p.

2.6.11 Electric Vehicles in the Republic of Croatia – Market Development, Usage and Outlook

P. Ilinčić¹, G. Šagić¹, G. Pejić² and Z. Lulić^{1*}

¹ Department of IC Engines and Transportation Systems, Faculty of Mechanical Engineering and Naval Architecture, University of Zagreb, Ivana Lučića 5, 10002, Zagreb, Croatia

² Centre for Vehicles of Croatia, Capraška 6, 10000 Zagreb, Croatia

Introduction

In 2016, the transport sector (including international aviation and maritime emissions) was responsible for 27% of total greenhouse gas emissions in the European Union. Of these emissions, road transport was responsible for almost 72%, where passenger cars contributed 44%, while 19% came from heavy-duty vehicles. According to the adopted EU targets, in the road transport sector by 2030, greenhouse gas emissions must be reduced by 30% compared to 2005 (European Council, 2014), (Mock, 2016). To reduce emissions from road transport by such a significant rate, shift to low-emission mobility is inevitable. With the Directive 2014/94/EU on the deployment of alternative fuel infrastructure (European Commission, 2014), one of the European Union strategies towards that goal is electrification of the road transport sector. Electric vehicles are considered as a most promising solution for the reduction of GHG emissions from the road transport sector, why many countries are taking actions and promoting the sale of electric vehicles and shaping fleets towards electric vehicles (Kwon et al., 2018). Reduction of transport GHG emissions with electric vehicles is greatly influenced by the power generation mix, in the Republic of Croatia, this should not be a problem because in 2016 renewable sources accounted for 66% of overall electricity generation what result whit CO₂ emission intensity of 210 g CO₂/kWh (EEA, 2019). To follow the goals of European Union in the Republic of Croatia, Ministry of Environmental and Nature Protection (MENP) prepared the *Transportation emissions reduction programme for the period 2013 – 2020.*, which envisages measures to reduce the emissions from transport and to achieve the goal of a 10% share of renewable energy sources in all modes of transport. Financial and operational implementation of the program was carried out through the Environmental Protection and Energy Efficiency Fund (EPEEF) which was founded in 2004.

Promotion of clean transport in the Republic of Croatia

Measures to reduce emissions from the transport sector and promote energy efficiency are implemented through the Environmental Protection and Energy Efficiency Fund 3 main objectives: incentives for electric and hybrid vehicles, eco-driving training and other measures for energy efficiency in traffic. In the initial period, the EPEEF was dealing with environmental issues like wild waste dumps (landfills), while promotion of energy efficient, clean transport began in 2008 with several small actions. Significant activities started in 2009, with incentives for the purchase of "green" trucks (Euro 5 and EEV trucks).

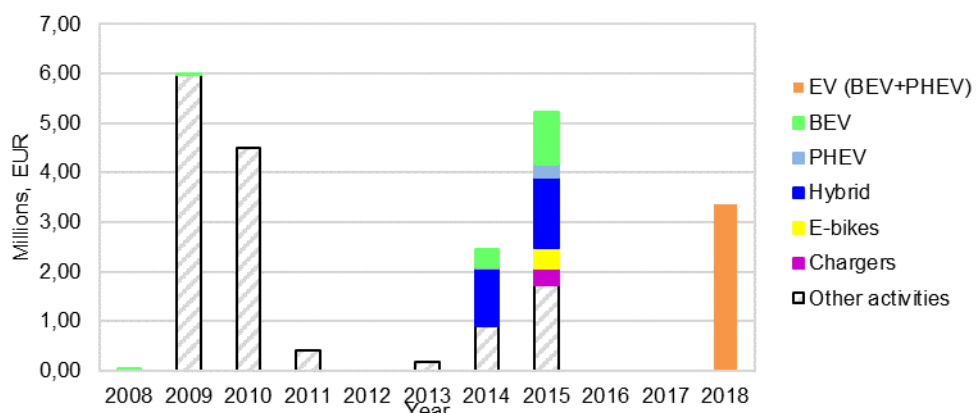


Figure 1: Incentives for energy efficient clean transport.

Activities related to electric and hybrid vehicles started a few years later, in 2014 as shown in Figure 1. In that year, 2014, EPEEF opened a public call for incentives for the purchase of hybrid and electric vehicles in which 379 hybrid electric vehicles (HEV), 53 battery electric vehicles (BEV) and 8 plug-in

hybrid electric vehicles (PHEV) were co-financed. In 2015, public calls for electric vehicles incentives were open in February and September. In both calls, EPEEF has co-financed purchase of electric vehicles for individuals (citizens) and companies in the total amount of about 2.7 million Euros (EPEEF, 2015). In the next two years, 2016 and 2017, activates supporting clean transport were temporarily stopped. They were resumed back in 2018 when the public call for co-financing purchase of electric vehicles for individuals in the amount of 1.6 million Euros and public call for co-financing purchase of electric vehicles for companies in the amount of about 1.73 million Euros (EPEEF, 2018). Unfortunately for 2018, there were no officially published data on how many vehicles of which type were co-financed in total, which is why the data for that year in Figure 1 were given for all-electric vehicles, regardless of their technology. Unlike the previous years, when hybrid vehicles were also financed, in calls in 2018, it was decided that only PHEVs and BEVs will be co-financed. Interestingly, call for this set of incentives for individuals (citizens) in 2018 was open and closed at the same day, because all available funds allocated for this call have been used (EPEEF, 2018).

Electric vehicles in the Republic of Croatia

All vehicles registered in the Republic of Croatia are mandatory to pass periodical technical inspection. All procedures related to technical inspections of vehicles and renewals of vehicle registration certificates are carried out by company Centre for Vehicles of Croatia under the authorisation of the Ministry of the Interior of the Republic of Croatia. All data used in this research were taken from the official vehicle database of Centre for Vehicles of Croatia.

First battery electric vehicle in the Republic of Croatia was registered in 2007, a self-made conversion of conventional internal combustion engine powered vehicle to fully electric vehicle. From that time, in the period of almost 12 years, a number of electric vehicles (battery electric vehicles, plug-in hybrid electric vehicles) of different ECE categories have grown up to about 1500 vehicles registered until March 2019. Vehicle categories and their numbers are shown in Figure 2.

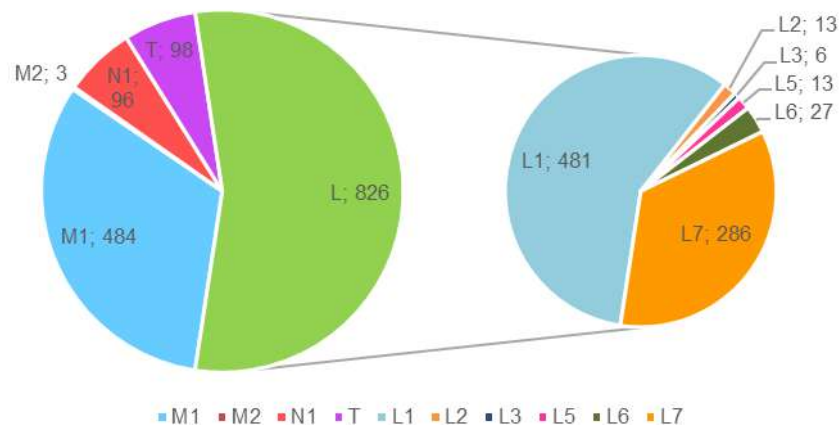


Figure 2: Number of electric vehicles by category in 2019 in Croatia.

From the given, it can be concluded that most of the electric vehicles in the Republic of Croatia are two-wheelers and quads followed by passenger cars (M1 category) mainly due to the incentive policy as it will be explained in detail later. Like with the passenger cars, about 100 electric vans (N1 category) are also a consequence of the incentives given by EPEEF in 2015 (EPEEF, 2015).

Considering two major categories, M1 and L, a number of electric vehicles over a 10-year period, from 2008 to 2018, is shown in Figure 3. Like the first electric vehicle registered in the Republic of Croatia, from 2007, all-electric vehicles were a self-made conversion of conventional vehicles until 2011, when first production electric vehicle was sold and registered.

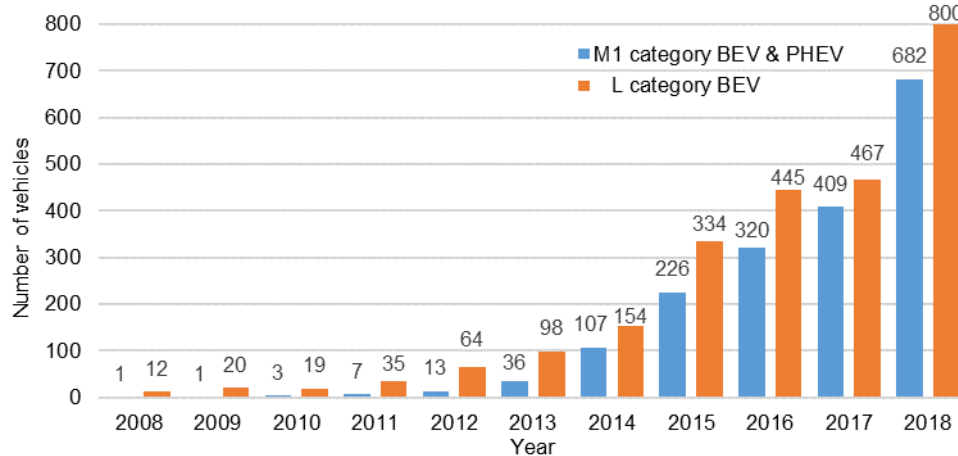


Figure 3: Number of registered EV by the vehicle category (M1, L) from 2008 to 2018.

With 452 battery electric passenger cars and 230 PHEV passenger cars, a total number of electrically-chargeable vehicles of M1 category rises to 682, which makes a market share of EV passenger cars in overall fleet only 0.04%. Such a market share is in line with the European Automobile Manufacturers Association study made in June 2018 where affordability was stated as a major barrier to penetration of electric vehicles to passenger cars fleet in EU countries. In the countries with a GDP below 18,000 €, the market share of ECVs is practically 0% (European Automobile Manufacturers Association, 2018). Similar was concluded in the JRC study where it was stated that electric vehicles are considered as quite expensive and importantly that the purchase price is the most important factor for people when buying a new car. Other negative reasons influencing the buyer's decision and avoiding buying an electric vehicle are relatively short range and lack of recharging infrastructure (Gómez Vilchez et al., 2017).

Besides the price of the vehicle, high EV market penetration depends on their acceptance by both consumers and businesses (Wallis and Lane, 2013) Ownership structure (privately owned vs company owned) of electric vehicles (BEV and PHEV) of category M1 in the Republic of Croatia over the 10-year period is shown in Figure 4, on the left side battery electric vehicles and PHEV on the right side. Data for PHEVs are given for period after 2013, because after July 2013 plug-in hybrids are introduced as a separate category of hybrid vehicles in the official vehicle database managed by Vehicle Centre of Croatia. As mentioned before, in the first three years (2008 to 2010) all battery electric passenger cars were self-made conversion, and all were privately owned. In the years 2011 and 2012, ownership structure begins to change, since companies dealing with the production of vehicles and electricity production introduced electric passenger cars to the market which served as technology demonstrators. If we neglect those 5 years, it is clear, that 60% of battery electric passenger cars are company owned. Same can be concluded for the PHEVs. The reason for such distribution is primarily of economic nature and the fact that the price of the electric vehicle is way too high for most of the Croatian citizens.

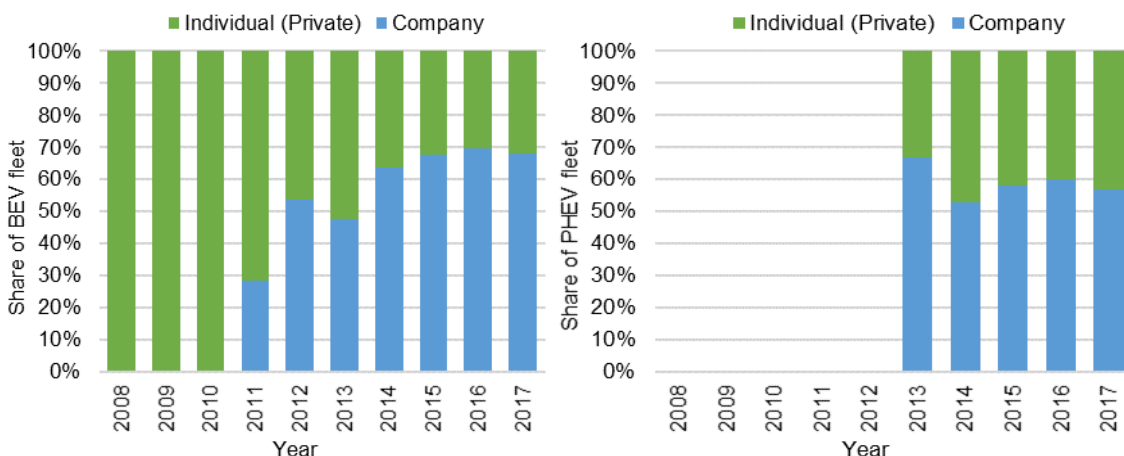


Figure 4: Ownership share of the BEV (left) and PHEV (right) fleet.

Well-marked influence of electric vehicle price on purchasing opportunities can be seen when analysing newly registered passenger cars, bikes and quads in the Republic of Croatia over the years as given in Figure 5. Strong growths in sales are recorded in the years 2014, 2015 when incentives for new purchased EVs were given. After that, in the next two years (2016 and 2017) incentives were stopped and drop in the sale was automatically seen. A significant increase in sales of EVs was also recorded in 2018 when it was decided to revive the EV market after years without incentives. The same trend, even more obvious, is seen in the number of L category vehicles new registrations. In 2015, a number of new registrations were 3 times higher than the year before and even more extreme in 2018, when a number of new registrations went up 15 times, mostly due to the relatively high incentives.

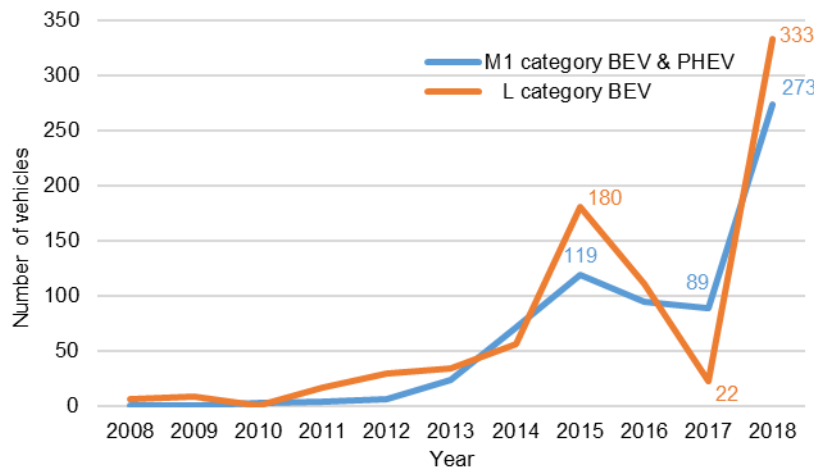


Figure 5: Number of new registered EV by category (M1, L) from 2008 to 2018.

Diffusion of electric vehicles and influence on GHG reduction in the Republic of Croatia

After a review of the electric vehicle fleet in the Republic of Croatia, scenarios about EV influence and capabilities to enable the fulfilment of EU's goals of reducing CO₂ emissions by 50% by 2030 are discussed. Electric vehicle (EV) diffusion in the Croatian vehicle fleet will play an important role in meeting this goal. All considerations were made on the passenger car fleet (category M1), and the results were then applied to the entire fleet of road motor vehicles. For the observed period, from 2007 to 2017, with the precise, comprehensive data available, the share of M1 vehicles in the entire fleet of road vehicles is extremely stable, with a slight tendency to decline from 76% to 75%. According to European Environment Agency greenhouse gas - data viewer (EEA, 2018) in the EU-28, a very strong ratio of 60% between the passenger cars CO₂ fleet emissions and the total emissions of all greenhouse gases (GHGs) of the entire fleet of road vehicles in the period from 2005 to 2016 can be seen in Figure 6. The same ratio was applied in the estimation of emissions from road transport in the Republic of Croatia.

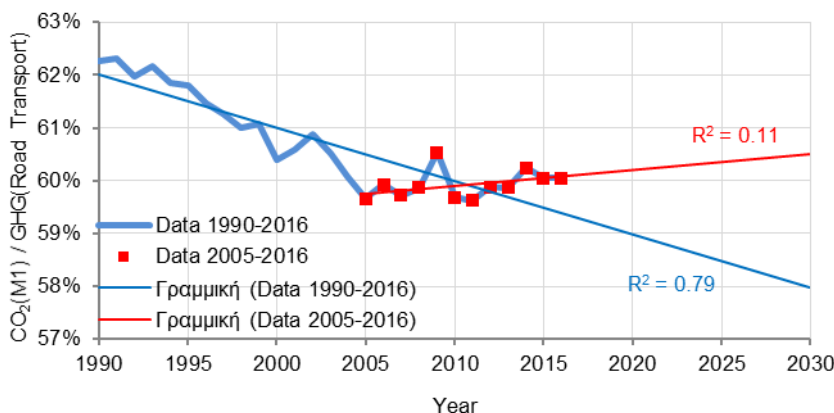


Figure 6: The ratio of CO₂ emission of passenger cars and total GHG emissions of road transport emissions (expressed as CO₂ equivalent) in the EU-28.

All data relevant for emission calculation with Tier 3 method were taken from the vehicle database of Centre for Vehicles of Croatia (CVH), where data recorded during a periodical technical inspection from 2007 onwards are stored. Mileage of each vehicle is also recorded, which enables the calculation of annual mileage. All calculations were made in COPERT 5 software. GHG emissions from road transport in Croatia, in the reference year 2005, according to the National Inventory Report 2018 (NIR, 2018), are calculated using the Tier 1 method and amount to 5,314 Mt CO₂e. Since this report lacks data from 2006 to 2009, data from three other official sources are taken for the comparison: Energy in Croatia - Annual Energy Report 2010, 2014 and 2016. Additionally, passenger cars (M1 category) fleet emissions calculated in COPERT 5, (Rešetar et al., 2017) and (Rešetar et al., 2018) were used to calculate overall emission from the road transport sector in the Republic of Croatia. Results in Figure 7 have shown that the discrepancies in the data from government official documents (NIR and Energy in Croatia) are negligible. However, concerning the result obtained by much more accurate Tier 3 method (COPERT 5), GHG emissions in 2005 had to be at least 32% higher. Such a low value will completely prevent Croatia from achieving a reduction of 30% by 2030.

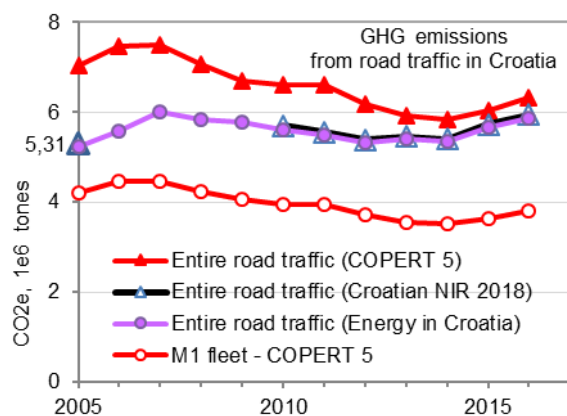


Figure 7: GHG emissions from the road transport sector in the Republic of Croatia.

Analysis of Croatian passenger cars fleet (M1 category) found that there are very strong trends in changes in gasoline and diesel cars share (Figure 8) and if effective incentive measures for purchase of hybrid and electric vehicles will not be provided, the situation with road transport emissions will not change at all and targets for 2030 will not be reached.

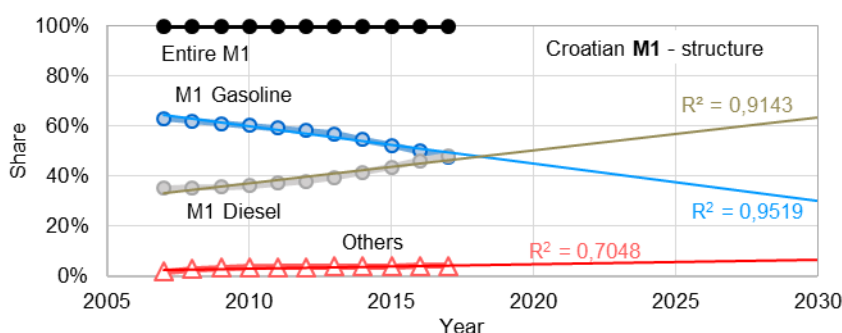


Figure 8: Shares of vehicles in the fleet, by type of fuel, and linear trends up to 2030.

Likewise, there are strong trends in changes in CO₂ emission factors for passenger cars fleet (M1 category) like shown in Figure 9. The correlation coefficient for M1 hybrid vehicles does not have a particularly high value ($r = 0.61$, $R^2 = 0.37$), mainly due to the small number of vehicles. In such a case, relatively small dissipation results in relatively large oscillations of the emission factor. With the increasing number of vehicles, it is expected that the emission factor trendline for hybrids will stabilise which will lead to a higher correlation coefficient. Penetration of new powertrain systems in the road transport sector is only possible by appropriate shaping of vehicle structure that annually enters the fleet, i.e. new and used vehicles registered for the first time in the country. Both diagrams show that incentives for the purchase of hybrid and electric vehicles (mentioned before), from 2009 to 2015, had no impact on changing the fleet structure nor reducing average emission factors.

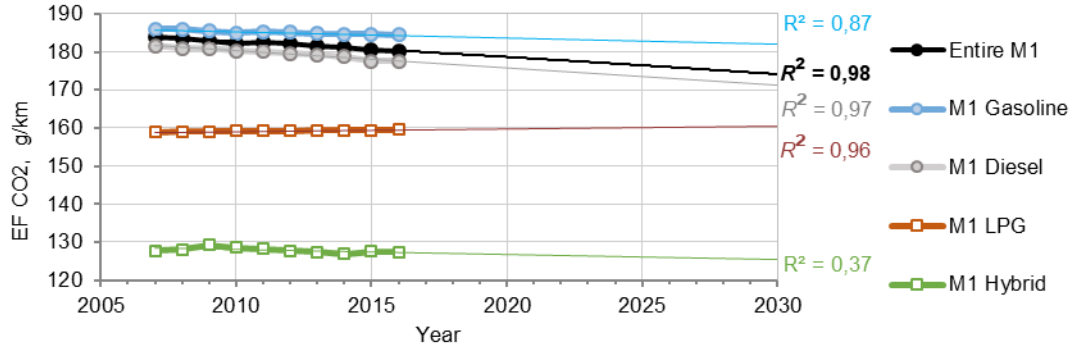


Figure 9: Average passenger car (M1) fleet emission factors: data to 2016 and linear trends up to 2030.

Forecasts of Croatian passenger cars fleet relevant parameters

To address the challenges Croatia will face in meeting the emission reduction target by 2030, the diffusion of hybrid electric and battery electric vehicle in the vehicle fleet by 2030 has been modelled. For diffusion modelling, relationships between the total fleet number of vehicles N_j in the observed year j , number of the vehicles registered for the first time $N_j^{1\text{st IN}}$ and the number of out-of-service vehicles N_j^{OUT} should be established. These variables are interlinked with the expression:

$$N_j = N_{j-1} + N_j^{1\text{st IN}} - N_j^{\text{OUT}} \quad (1)$$

Equation (1) shows that, with the predicted number of vehicles in the fleet N_j , only one variable can be predicted: either the number of first-time registered vehicles $N_j^{1\text{st IN}}$ or the number of out-of-service vehicles N_j^{OUT} . From this apparently trivial insight, different fleet renewal rates arise ($N_j^{1\text{st IN}}/N_j$). Therefore, in the scenarios considered in 2030 share of vehicles registered for the first time $N_j^{1\text{st IN}}$, compared to the total fleet number of vehicles N_j would be 6.23% at slow renewal rate, 11.5% at medium renewal rate and 19.0% at the fastest renewal rate of passenger cars (M1 category) fleet. A forecast example of a number of vehicles registered for the first time using a regression function and ARIMA model is shown in Figure 10.

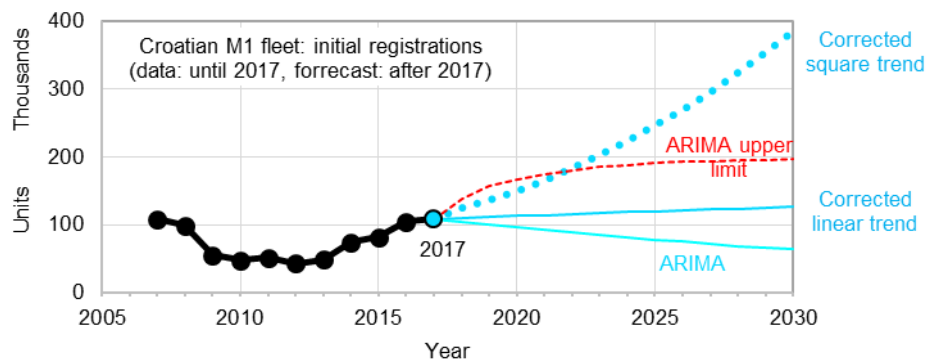


Figure 10: Forecast of a number of vehicles registered for the first time using a regression function and ARIMA model.

Diffusion of hybrid electric and battery electric vehicles in the area of first-time registered vehicles was modelled using the S-curve theory. Research history of the diffusion of innovation and new technologies on the market was described in 1962 in the first edition of his book (Rogers, 1983) while (Meade and Islam, 1988) identified 29 different models suitable for predicting the diffusion of new technologies. Very good and detailed reviews of S-models were also provided by Oh (Oh, 1988), Radas (Radas, 2005),

Kucharavy and De Guio (Kucharavy and De Guio, 2011), and the effects of incentive policies have been demonstrated by Mercure et al. (Mercure et al., 2014).

In this paper, two S-curve models (Figure 11) were used: a symmetric logistic model and Bass's model, which were mathematically well described by Sokele (Sokele, 2008).

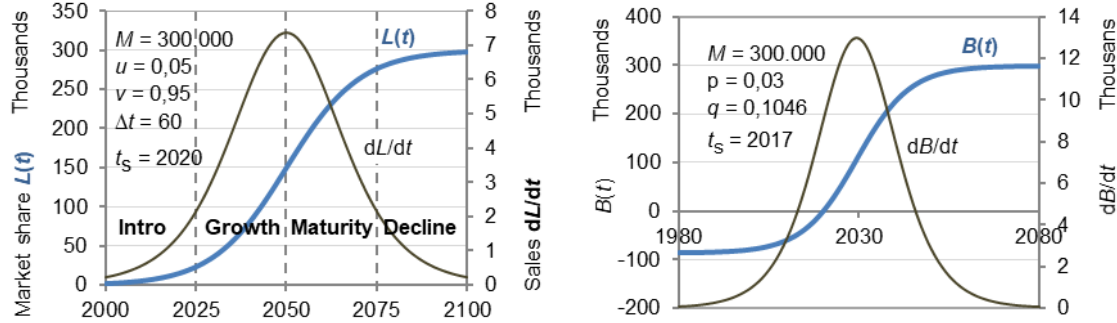


Figure 11: S-curve models: symmetric logistic (left) and Bass's model (right). Examples show the diffusion of a new product into the markets of the same capacity M , with different initial years t_s .

Number of vehicles in the passenger cars (M1 category) fleet and average annual mileage by 2030 were forecasted with the ARIMA (p,d,q) method, Linden et al. (2003), Box et al. (2008), Armstrong (2002), Hyndman and Athanasopoulos (Internet 2018), Zaiontz (Internet 2018). For the identification of (p,d,q) parameters, correlation coefficients of autocorrelation (ACF) and partial autocorrelation (PACF) were applied, SPSS (1999), Minitab (Internet 2018). Their analysis, as well as analysis of the results forecasted by twelve different ARIMA models, it was concluded that for these time series best-suited model was ARIMA $(p,q,d = 1,1,0)$.

Forecasts (Figure 12) have shown that in the probable future an increase in the number of vehicles should be expected, with the simultaneous decline in the annual average mileage. This apparently pessimistic forecast can be explained by the fact that the number of households having two or more vehicles is growing, like in the example, in the case of a rural area with poor public transport where one can travel only by personal car. Their annual mileage is slightly over the minimum mileage necessary for everyday travel from home to workplace and back.

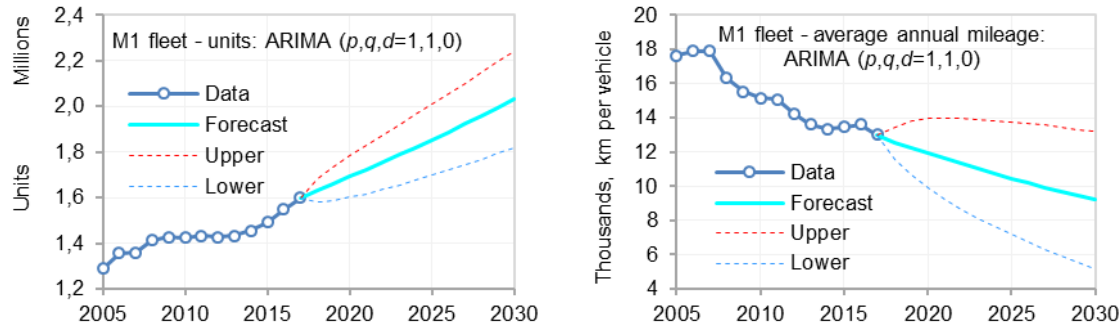


Figure 12: ARIMA forecasts: number of vehicles (left) and average annual mileage (right).

Scenario analysis and discussion

Considering emission factors diagram in Figure 9, larger emission reduction in the future can only be achieved with a significant increase in the share of hybrid electric and especially battery electric vehicles in the Croatian fleet, whose numbers are currently negligible.

Therefore, it is crucial to evaluate possible diffusion limits of these new technologies in the road transport sector in Croatia. As a basis for this evaluation, Bloomberg assessment, shown in Figure 13, was used.

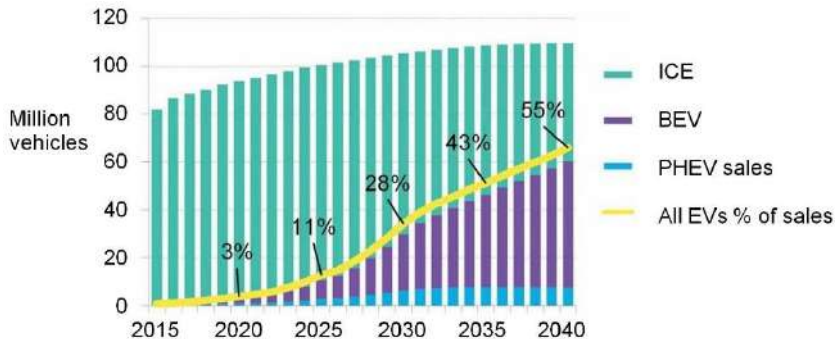


Figure 13: Share of vehicles with new powertrain systems in the worldwide sale of new vehicles (Bloomberg New Energy Finance, 2018).

SCENARIO 1: Medium rate of fleet renewal.

Diffusion of electric vehicles (BEV + PHEV) in the fleet of first-time registered vehicles in 2030 reached 28%, according to Bloomberg assessment. This 28% in 2030 consist of three groups (powertrain types) that are estimated from the diagram and they are distributed approximately in this way:

$$28 \% = (5.5 + 19 + 3.5) \% - (\text{PHEV} + \text{BEV} + \text{HEV}) \%$$

Diffusion of new powertrain systems is modelled with a logistic model. The results of the analysis according to this scenario are shown in Figures 14 and 15.

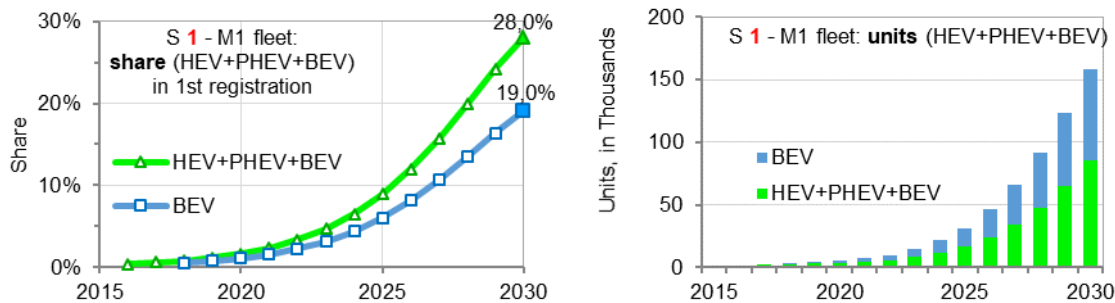


Figure 14: Scenario 1: Share of new powertrains in first-time registered vehicles (left) and their total number in passenger cars fleet – M1 (right).

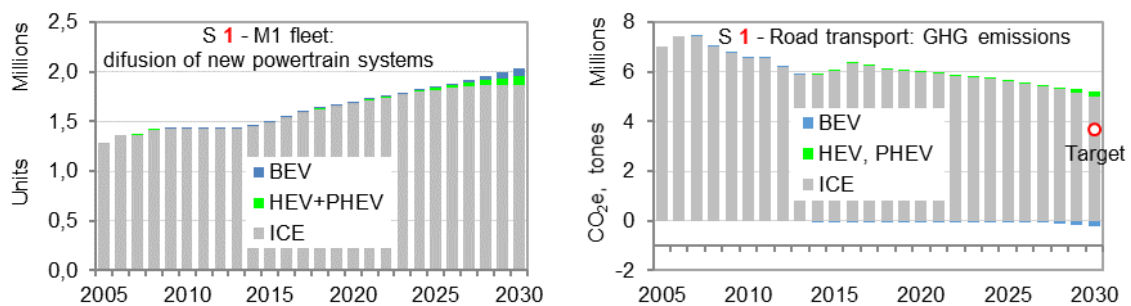


Figure 15: Scenario 1: Number of vehicles in the Croatian passenger cars fleet - M1 (left) and GHG emissions of the entire road transport sector (right).

Blue columns in the right diagram in Figure 15 represent a reduction in emissions due to the diffusion of battery electric vehicles instead of vehicles powered by an internal combustion engine.

SCENARIO 1 – Results

Bloomberg's forecast for the Republic of Croatia is very optimistic. Likewise, the medium rate of passenger cars fleet renewal is also quite optimistic. Thus, a number of vehicles registered for the first time in the passenger cars fleet – M1 in 2030 would reach a figure of almost 386 thousand units (19% of passenger cars fleet), of which over 73,000 would be battery electric vehicles and almost 35,000

would be hybrids. Despite, GHG emissions in the target year 2030 are even 39% higher than the target value.

SCENARIO 2: Fastest rate of fleet renewal.

Diffusion of hybrid and electric vehicles (1:1 ratio) in the fleet of first-time registered vehicles in 2030 have reached a level sufficient to lower the emissions of the road transport sector to the targeted value. Diffusion of new powertrain systems in scenario 2 was also modelled with a logistic model. In 2030, passenger cars (M1 category) fleet consist of 50.5% of IC powered vehicles, 24.8% of hybrid electric vehicles (HEV + PHEV) and 24.7% of battery electric vehicles (BEV). The share of vehicles registered for the first time in 2030 accounts for 19.0% of all passenger cars (M1), while the share of out-of-service amounts to 17.2%. In 2030, even four-fifths (79.5%) of the first registration are vehicles with new powertrain systems, and only one-fifth of the first registration are conventional vehicles powered by internal combustion engines. Results are shown in Figures 16 and 17.

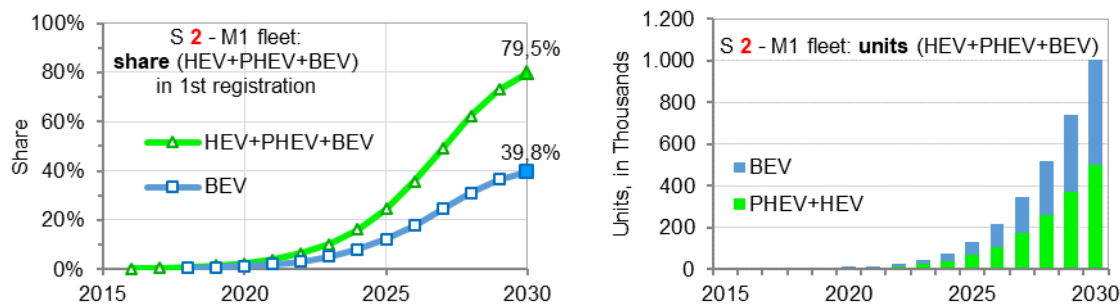


Figure 16: Scenario 2: Share of new powertrains in first-time registered vehicles (left) and their total number in passenger cars fleet – M1 (right).

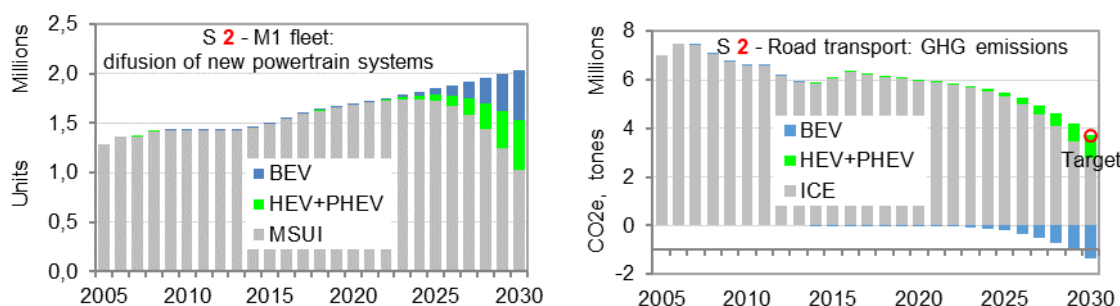


Figure 17: Scenario 2: Number of vehicles in the Croatian passenger cars fleet - M1 (left) and GHG emissions of the entire road transport sector (right).

Like shown in Figure 17 on the right, GHG emissions of the road transport sector in the Republic of Croatia are lowered to the 2030 target value. Like described before, blue columns in the right diagram in Figure 17 represent a reduction in emissions due to the diffusion of battery electric vehicles.

SCENARIO 2 – Results

The 2030 emission goal is met only due to the extremely high diffusion of battery electric vehicles. The diffusion and the share of vehicles with new powertrain systems in the overall fleet reached incredibly high values, higher than in the most optimistic forecasts.

In such a scenario in the Republic of Croatia, in the year 2030, there would be about two million passenger cars, where about one million of them should be vehicles with new powertrain systems (BEV + HEV + PHEV). That means that in the next 11 years approximately 91,000 new electric vehicles per annum should enter the Croatian passenger cars fleet, but the current market renewal trends will not reach that level for a next few years (Rešetar et al., 2018).

Conclusion

With the 682 PHEV and BEV passenger cars in the Republic of Croatia in 2018, which represents a market share of 0.04% of the total number of passenger cars, it can only be concluded that diffusion of

EVs in the Croatian market is practically negligible. After analysing the number of new registrations, it can be seen that significant changes occur only when incentives for the purchase of EVs are given, but unfortunately, they are not continuous over the years. With such EV diffusion rate a significant share of electric and hybrid vehicles in the Croatian fleet will not be expected for a long time. This is also supported with the fact that in the ownership approximately 65% of EVs in the Republic of Croatia are company owned which suggests that electric vehicles are too expensive for most of the Croatian citizens. However, to enable diffusion of EVs and shape the market in the right direction, EVs should become more affordable, or GDP should have to grow up significantly.

According to the current regulations, in which only tailpipe GHG emissions are observed, electric vehicles do not have any emissions and therefore are in the undoubted advantage over all other powertrain systems. Scenario analysis conducted, showed that the battery electric vehicles could be very effective in reducing GHG emissions (exhaust) of road motor vehicles, only under the condition that their diffusion in the fleet would be fast enough and accompanied by an appropriate network of charging stations. If Croatian prospects of GHG emissions reduction are evaluated, after analysis made, it can be concluded that there is no least possibility for the Republic of Croatia to fulfil EU GHG emission goals.

Acknowledgements

We would like to thank Vehicle Centre of Croatia for support without which the realization of this research would not be possible.

References

- Armstrong J.S. ed. (2002). Extrapolation for Time-Series and Cross-Sectional Data, in *Principles of Forecasting: A Handbook for Researchers and Practitioners*, Kluwer Academic Publishers, pp. 217–243.
- Box G.E.P., Jenkins G.M. and Reinsel G.C. (2008). Time Series Analysis, Forecasting and Control, 4th ed., Wiley.
- EEA (2018). European Environment Agency greenhouse gas - data viewer
<https://www.eea.europa.eu/data-and-maps/data/data-viewers/greenhouse-gases-viewer>
(accessed: 2018-12-05)
- EEA (2019). European Environment Agency CO2 emission intensity - data viewer
<https://www.eea.europa.eu/data-and-maps/daviz/co2-emission-intensity-5/>
(accessed: 2019-04-15)
- Electric Vehicle Outlook 2018, *Bloomberg New Energy Finance*, 2018.
- Energy in Croatia - Annual Energy Report 2010. Ministry of Economy, Labour and Entrepreneurship. Republic of Croatia.
- Energy in Croatia - Annual Energy Report 2014. Ministry of Economy. Republic of Croatia.
- Energy in Croatia - Annual Energy Report 2016. Ministry of Environment and Energy. Republic of Croatia.
- EPEEF (2015). Environmental Protection and Energy Efficiency Fund: National public calls and tenders http://www.fzoeu.hr/hr/nacionalni_javni_pozivi_i_natjecaji/ (accessed 2019-01-25).
- EPEEF (2018). Environmental Protection and Energy Efficiency Fund: Co-financing the purchase of energy efficient vehicles
http://www.fzoeu.hr/en/energy_efficiency/energy_efficient_transportation/cofinancing_the_purchase_of_energy_efficient_ve_hicles/ (accessed 2018-12-19).
- European Automobile Manufacturers Association, 2018. Study: Making the Transition to Zero-emission Mobility <https://www.acea.be/publications/article/study-making-the-transition-to-zero-emission-mobility> (accessed: 2019-01-17)
- European Council (2014). Conclusions - 23/24 October 2014. *EUCO 169/14*.
<https://www.consilium.europa.eu/media/24561/145397.pdf> (accessed: 2018-04-18).
- European Commission, 2014. Directive 2014/94/EU of the European Parliament and of the Council of 22 October 2014 on the deployment of alternative fuels infrastructure <https://eur-lex.europa.eu/legal-content/EN/TXT/PDF/?uri=CELEX:32014L0094&from=EN> (accessed 2018-12-19).
- Gómez Vilchez, J., Harrison, G., Kelleher, L., Smyth, A., Thiel, C., Lu, H., Rohr, C (2017). Quantifying the factors influencing people's car type choices in Europe: Results of a stated preference survey, EUR 28975 EN, Publications Office of the European Union,

Hyndman R. and Athanasopoulos G. Forecasting: Principles and Practice, <https://otexts.org/fpp2/> (accessed: 2018-08-13).

Jackson N. (2017). Future Automotive Challenges & Opportunities, presented at the Ricardo Plc, <http://peter-ftp.co.uk/aviation/misc-euroga/2017-Future%20Automotive%20Challenges%20Issued.pdf> (accessed: 2018-10-22).

Kucharavy D. and De Guio R. (2011). Application of S-shaped curves. *Procedia Engineering*, Vol. 9, pp. 559–572.

Kwon Y., Son S., Jang K. (2018). Evaluation of incentive policies for electric vehicles: An experimental study on Jeju Island, *Transportation Research Part A: Policy and Practice*, Vol. 116, 404–412

Linden A., Adams J.L. and Roberts N. (2003). Evaluating Disease Management Program Effectiveness: An Introduction to Time-Series Analysis, *Disease Management*, Vol. 6, no. 4, pp. 243–255.

Meade N. and Islam T. (1988). Technological Forecasting—Model Selection, Model Stability, and Combining Models. *Management Science*, Vol. 44, no. 8, pp. 1015–1130.

Mercure J.-F., Pollitt H., Chewpreecha U., Salas P., Foley A.M., Holden P.B., Edwards N.R. (2014). The dynamics of technology diffusion and the impacts of climate policy instruments in the decarbonisation of the global electricity sector, *Energy Policy*, vol. 73, pp. 686–700.

Minitab. Interpret the partial autocorrelation function (PACF),
<https://support.minitab.com/en-us/minitab/18/help-and-how-to/modeling-statistics/time-series/how-to/partial-autocorrelation/interpret-the-results/partial-autocorrelation-function-pacf/> (accessed: 2018-08-25).

Mock P. (2016). Summary, 2020–2030 CO₂ standards for new cars and light-commercial vehicles in the European Union. ICCT. <http://www.theicct.org/2020-2030-co2-standards-cars-lcv-s-eu-briefing-nov2016> (accessed: 2017-08-17).

National Inventory Report 2009, Croatian greenhouse gas inventory for the period 1990-2007. Ministry of Environmental Protection, Physical Planning and Construction. Republic of Croatia.

National Inventory Report 2018, Croatian greenhouse gas inventory for the period 1990-2016. Croatian Agency for the Environment and Nature. Republic of Croatia.

Oh H.-S. (1988). The selection of technological forecasting models in life analysis, *Iowa State University*.

Radas S. (2005). Diffusion Models in Marketing: How to Incorporate the Effect of External Influence?. *Privredna kretanja i ekonomska politika*, Vol. 105, pp. 31–51, 2005.

Rešetar M., Pejić G. Lulić Z (2017). Road Transport Emissions of Passenger Cars in the Republic of Croatia. *Digital Proceedings of the 8th European Combustion Meeting*, Dubrovnik, 2017, pp. 2553–2558.

Rešetar M., Pejić G. Lulić Z (2018). Changes and trends in the Croatian road vehicle fleet – Need for change of policy measures. *Transport Policy*, Vol. 71, pp. 92–105.

Rogers E.M. (1983). Diffusion of innovations, 3rd ed. New York, London, Free Press, Collier Macmillan.

Sokele M. (2008). Growth Models for the Forecasting of New Product Market Adoption, *Telektronikk*, Vol. 3/4, pp. 144–154.

SPSS Trends 10.0, 1999, SPSS Inc., ISBN 013-017905-1.

Zaiontz C. Performing Real Statistical Analysis Using Excel, *Real Statistics Using Excel*, <http://www.real-statistics.com/> (accessed: 2018-08-05).

Wallis, N., Lane, B., 2013. Electric vehicles: Improving consumer information to encourage adoption, European Council for Energy Efficient Economy, Tech. Rep. 4-514-13.

2.7 Remote sensing of vehicle emissions

This section includes papers presented in the context of the “Remote sensing of vehicle emissions” sessions of the TAP conference. Table 8 provides an overview of these papers, as they are listed in the following sub-sections.

Table 8. Titles and authors of “Remote sensing of vehicle emissions” papers

	Paper Title	Authors
2.7.1	Finding NOx-cheaters on the spot with Remote Sensing Devices	J. Buhigas, J. Fuente and J. Montero
2.7.2	A Novel Method for Comparing Passenger Car Fleets and Identifying High-Chance Gross Emitting Vehicles using Kerbside Remote Sensing Data	C. E. Rushton, J. E. Tate and S. P. Shepherd
2.7.3	NOx RDE measurements with Plume Chasing - Validation, detection of high emitters and manipulated SCR systems	D. Pöhler, T. Engel, U. Roth, J. Reber, M. Horbanski, J. Lampel and U. Platt
2.7.4	Multi-instrument enhancement of remote sensing on-road vehicle emissions measurements	R. Smit, S. Bainbridge, P. Kingston, M.K. Brown and G. Shaw
2.7.5	NOX emissions from Euro 5 and Euro 6 light-duty diesel vehicles as measured by remote sensing, PEMS and in legislative laboratory test cycles	M. Jerksjö, Å. Sjödin, R.A. Varella and C. Sandström-Dahl
2.7.6	Study on the durability of UK diesel and petrol passenger car emission control systems utilising remote sensing data	N. J. Farren, D. C. Carslaw, J. Borken-Kleefeld, A. R. Vaughan and Å. Sjödin

2.7.1 Finding NOx-cheaters on the spot with Remote Sensing Devices

J. Buhigas, J. de la Fuente and J. Montero¹

¹ Opus Remote Sensing Europe, Madrid, 28015, Spain, info@opusrse.com

Introduction

It is known that many heavy-duty vehicles (HDV) circulating on European roads may have some form of emission control manipulation⁴. These vehicles constantly cross the borders of many countries, making the problem a very serious one, that must be resolved by all Europe together.

The most common manipulation nowadays is to disconnect the AdBlue injection that reduces NO_x emissions in diesel trucks. AdBlue is a colourless, synthetically produced 32.5% solution of very pure urea in demineralised water. European legislation requires that the diesel vehicle monitors the level of AdBlue in the tank. If the tank is empty, the engine is prevented to be started.

This manipulation is done thanks to many different tricks, some of them with the so-called "AdBlue killers", which are devices that can be purchased for a very low price on the Internet and can be easily installed into driver's cabin⁵. The AdBlue killer makes the computer believe that it is injecting AdBlue when it is not. The most sophisticated manipulations on Euro VI trucks are carried out by software, so it is not possible to find a cheating device in a roadside inspection. In other cases, the device is very well hidden and finding the infraction is cumbersome. These NO_x manipulations are always hard to find for two reasons: (1) they can be very different from truck to truck and (2) in many cases the manipulations are hidden in the compact engine of the truck. Thus, the only practical option is catching the cheaters in the act, with on-road inspections, measuring their real-driving emissions in real-time with Remote Sensing Devices (RSD).

Finding this infraction on the spot can, depending on the national law, result in an immediate sanction to the driver. A European legislation is already in place to carry out technical emissions inspections of commercial vehicles on the road: Commission Directive 2010/47/EU of 5 July 2010, transposed into different national laws in the different Member States. This directive protects the security forces and traffic control for the use of RSDs to find manipulated vehicles. The directive details that significant non-compliance of emissions measured by the RSD is by itself a proof of defect of the vehicle. However, the law does not quantify this deviation, so there is no legal limit that implies an immediate sanction. Similarly, it is known that the average real-driving emissions from motor vehicles are higher than the Euro Standard, so it is also unclear what the limit against which these measurements should be compared is.

Police enforcement campaign in Spain within the LIFE GySTRA project

Coordinating a police deployment to find these cheaters is complex and randomly pulling over trucks is not cost-efficient. Without relying on mobile RSDs the police spent a lot of resources to find these offenders. In addition, due to the difficulty of finding the cheating, the police often only spent a couple of minutes looking for manipulations for each vehicle (as there was no previous hint), so the operations gave very poor results.

During the years 2017 and 2018, OPUS RSE has used Opus mobile RSDs to find NOx-cheaters in the act. In September 2017 a small pilot was done in Austria, in collaboration with the national police, to find heavy-duty vehicles with NOx-cheating devices. Tampering devices were found in around 15% of the trucks inspected. The exercise first proved that the screening method with RSD works. In December 2017 another pilot was done in Denmark, close to the border with Germany. The chosen location was near a border control point, where the trucks had to drive through a slightly constant positive slope road.

⁴ <https://trans.info/en/controls-great-britain-relation-adblue-manipulation-every-twelfth-truck-subject-control-78983>

⁵ <https://www.cardiag.com/support/adblue-emulator-installation-manual-renault/>

The success was very high and the conclusion for the Danish Police was that the RSD and the methodology used is valid⁶.

After these two pilots, it was decided to create a more extensive program in Spain. As part of the EU-funded LIFE program, in the GYSTRA⁷ project, OPUS RSE has collaborated with GUARDIA CIVIL, Spain's national police force, to find on the spot and remotely illegally manipulated commercial HDVs during 2018, thanks to remote sensing portable devices.



Figure 1: Pictures of the remote sensing program in Spain, 2018

Methodology

In the programme carried out with the GUARDIA CIVIL in Spain, it has been possible to define a methodology for coordinated and efficient operations to find cheating trucks in Europe.

Measurement and alert process:

The trucks are obliged to accelerate when measured by the RSD, either at a slightly constant positive slope road or at the exit of a toll station. The RSD measures the truck's emissions as it passes in front of the device. In less than half a second, real-time control software displays NO emission on a screen. If the NO emission is above a certain limit, it is considered that there is a high probability that the truck has some sort of tampering. A radio alert is sent immediately to a police agent, who is some distance away. The officer receives the notice and stops the vehicle for a detailed inspection. The process is shown in Figure 2.

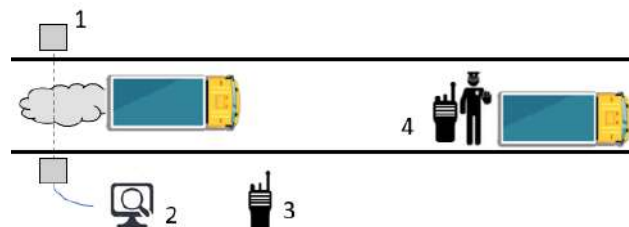


Figure 2: Remote sensing measurements and alert process

1. The RSD measures the vehicle's exhaust emissions.
2. Real-time control software displays NO emissions.
3. If the emissions are greater than a certain limit, the truck is considered to be highly likely to have some sort of manipulation. Only Euro V and Euro VI trucks are considered (visual identification of the license plate). A radio warning is sent to an agent some distance away. A technician also makes a manual record of this event in case there is a legal fine.

⁶ Measurements of cheating with SCR catalyst on heavy duty vehicles; Ministry of Environment and Food of Denmark, EPA; June 2018 - <https://www2.mst.dk/Udgiv/publications/2018/06/978-87-93710-42-9.pdf>

⁷ www.lifegystra.eu/

4. The agent who receives the alert orders the vehicle to be stopped and proceeds to inspect the vehicle for tampering. He/she also registers the time of the inspection, the license plate and the Euro standard according to the paperwork.

Sanctioning process:

The remote sensing measurement is for now only indicative. The sanction is only issued if the officer, who has sanctioning power, encounters a manipulation during the inspection. Thanks to the RSD alert, however, the police officer knows that the vehicle's emissions are very high and that the vehicle is therefore not operating correctly.

Surprise checks:

It has been observed that after 4 hours of measurement, the number of offenders found drops drastically, making the operation useless. It is believed that drivers alert each other to avoid being measured. Similarly, measuring more than two days at the same location appears to have similar effects. Therefore, it is recommended to coordinate and plan well the operations in advance (about 3-4 hours each day). It is recommended to change location every two days and preferably at different times of the day as well. A mobile RSD should be deployed and calibrated in about 20 minutes to quickly start the inspections.

Location and operative coordination:

Finding a good location is crucial. The site must be such that the trucks accelerate slightly and therefore emit gases through the exhaust pipe, either because the road has a positive slope or because the vehicle stopped before being measured (stop and go). The site must be such that the trucks are measured under a normal VSP level (between 2-30 KW/Ton). Low speeds are also recommended. Obviously, it must be a place where many trucks pass by per hour, so that the operation is cost-effective.

There should be enough space to deploy the RSD correctly. There must be a large area ahead where the trucks can be pulled-over for inspection. It is common that 4 or 5 trucks must wait in the inspection area until they are attended to by the police. This activity requires very close coordination with the police, as they are responsible for inspecting the vehicles. It is recommended to choose with them the site and to know before the inspection day how they are going to arrange the operation.

The correct positioning of the camera is also important, as trucks have different lengths depending on the type of vehicle. In addition, the number plate may be placed in different zones of the truck depending on the vehicle's country.

Emission limit

In this program the search for infractions has been focused on AdBlue manipulations and therefore the pollutant that was analyzed during the controls has been NO_x. The NO emitted by the vehicle is eventually transformed into NO₂ in the air. There is also a variable amount of NO₂ that is emitted just as it exits the exhaust. To simplify the analysis and the alert system for the police, for now we only look at the emission of NO. Specifically, through the RSD software, we visualize the NO in ppm to give an alert.

There is no limit that defines when a vehicle is tricked or not. An unmanipulated vehicle can emit large amounts of NO_x for different reasons, such as poor maintenance, a vehicle defect, manufacturer negligence, etc. On the other hand, since the measurement is only indicative, the limit must have a practical purpose. If a very high limit is set, many trucks that are tricked may not be inspected. If a low limit is set, many unmanipulated vehicles may be inspected. This limit must therefore be set in agreement with the police and must be a compromise solution. After several trial-error operations, in Spain a limit of 1000ppm of NO was defined as the convenient alert for inspecting the trucks. This study only presents data when this limit was established.

The Euro Standard for heavy-duty trucks is in g/kW-h, while direct RSD emissions are expressed in concentrations (ratios or ppm). In order to be able to compare the alert limit with the Euro Standard limits, the latter have been converted to ppm. To perform the conversion, a correlation has been made with a series of measurements to find the next transformation in HDVs. The emissions in ppm and in g/kW-h of each measurement have been plotted to find a linear regression for this system, so that a simple unit transformation equation can be obtained from real data.

$$\text{NO}_x \text{ [g/kW-h]} = 0.004 \cdot \text{NO [ppm]} - 0.0402 \quad R^2=0.9924$$

Table 1: Average NO and NO_x emissions of the trucks of this study

Limit	Euro I	Euro II	Euro III	Euro IV	Euro V	Euro VI
NO _x (g/kW-h)	9	7	5	3.5	2	0.4
NO (ppm)	1965	1530	1096	770	444	96

As can be seen in Figure 3, the limit set in Spain implies that trucks that exceed this value, emit almost as allowed in the Euro III Standard.

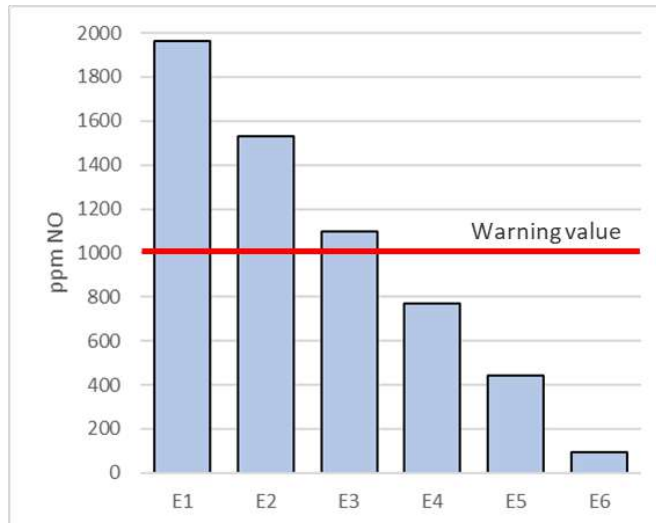


Figure 3: Equivalence of the Euro Standards for heavy-duty trucks at ppm and comparison with the established alert (warning value)

Results of the roadside inspections

From the campaign carried out during 2018, for this study only a set of days is considered, when the cut-point limit was fixed at 1000 ppm and the operative was done under controlled conditions, compiling a total of 1815 measured trucks. The average NO and NO_x emissions of these trucks are shown in Table 2. The RSD calculates automatically the concentrations expressed in ratio (NO/CO₂) and in parts per million (ppm). All further transformations are made assuming the following:

- All the trucks operate on diesel fuel. A fuel density of 0.81 kg/l is used for all this study.
- NO_x is calculated directly from NO, assuming NO_x = NO · (46/30).
- The combustion equation is used to transform concentrations to g/kg of fuel burned⁸.
- A diesel efficiency factor of 0.26 l/kW-h is used to transform emissions in g/kg to g/kW-h, according to Volvo Trucks recommendation.

⁸ FEAT Equations for CO, HC and NO. G. A. Bishop Last updated Feb. 2014.

Table 2: Average NO and NO_x emissions of the trucks of this study

	Number of vehicles	NO/CO ₂	NO (ppm)	NO (g/Kg)	NO _x (g/Kg)	NO (g/l)	NO _x (g/l)	NO (g/kW-h)	NO _x (g/kW-h)
All	1815	39,42	587,60	8,29	12,71	6,71	10,29	3,07	4,71
Valid VSP ⁹	1192	39,09	582,75	8,22	12,61	6,66	10,22	3,10	4,75

In Figure 4 the emissions of NO_x are shown in g/kW-h, from highest to lowest, in order to compare them with the same units as the limits defined in the Euro Standards. It can be seen that a large proportion of the heavy-duty trucks (22%) exceed the limit allowed in Euro I certification, a regulation that dates back more than 23 years.

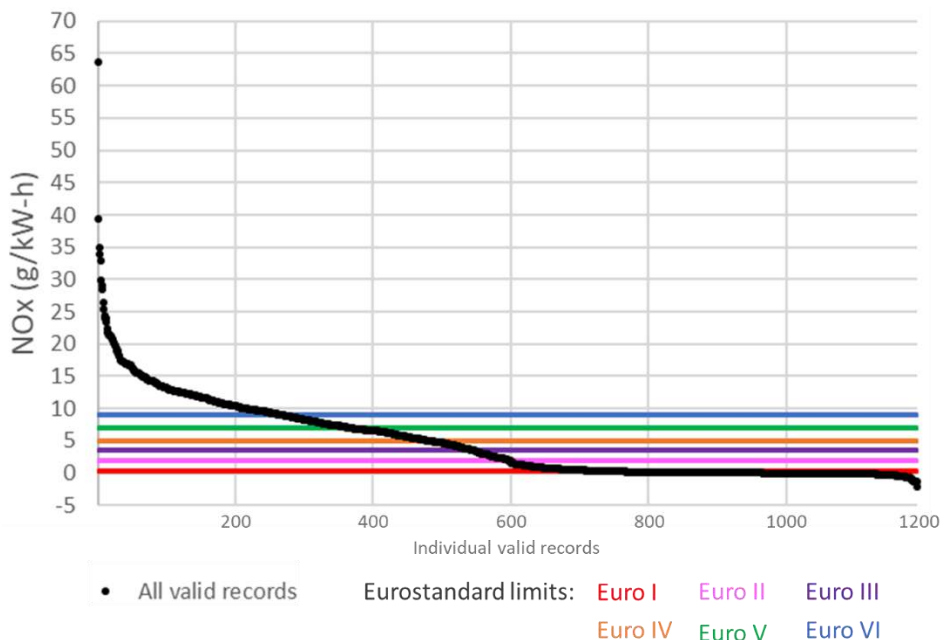


Figure 4: NO_x in grams per kW-h ranked from highest to lowest and compared to Euro Standard NO_x limits

Figure 5 shows the same data as above in a diagram of boxes and whiskers. It can be seen that there are statistically outliers that are far from the interquartile mean. In the diagram on the right, the outliers (more than 1.5 times the interquartile range) have been removed in order to correctly visualize the mean, median and quartiles. The NO_x median of these trucks is 2.04, almost exactly the limit of the Euro II standard (2 g/kW-h).

⁹ 2-30 KW/Ton, according to ISO-17025 accreditation of OPUS RSE.

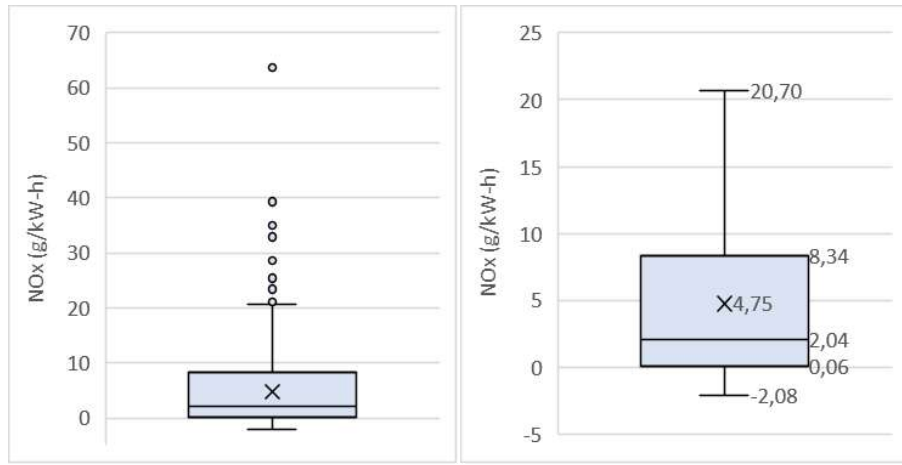


Figure 5: Boxplot of NO_x in grams per kW-h. All valid VSP records. Left: All valid VSP records, Right: Valid VSP records removing outliers

Figure 6 shows the relationship between the NO_x and the VSP (in the range 2-30). No clear relationship is observed between those two parameters, although there appears to be a fairly constant range of NO_x between 2 and 7.5 VSP.

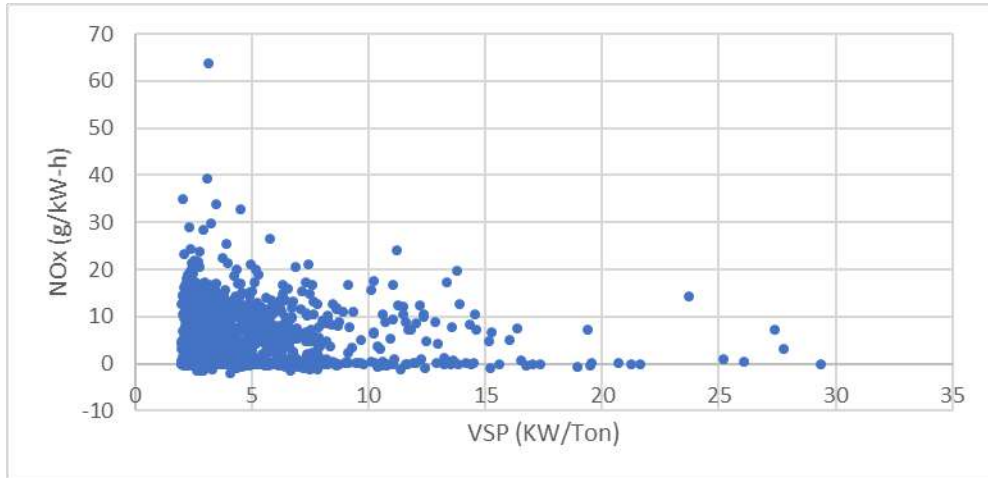


Figure 6: NO_x in grams per kW-h and compared to VSP

Figure 7 shows the average emissions classified by Euro Standard. Most of the measured trucks are Euro V and Euro VI, amounting to 75.6% of the total. It is also observed that the average emissions of Euro III, Euro IV and Euro V trucks are much higher than the homologation limits, while the average emission of Euro VI trucks almost complies with the regulations and also represents a huge reduction compared to the previous standard.

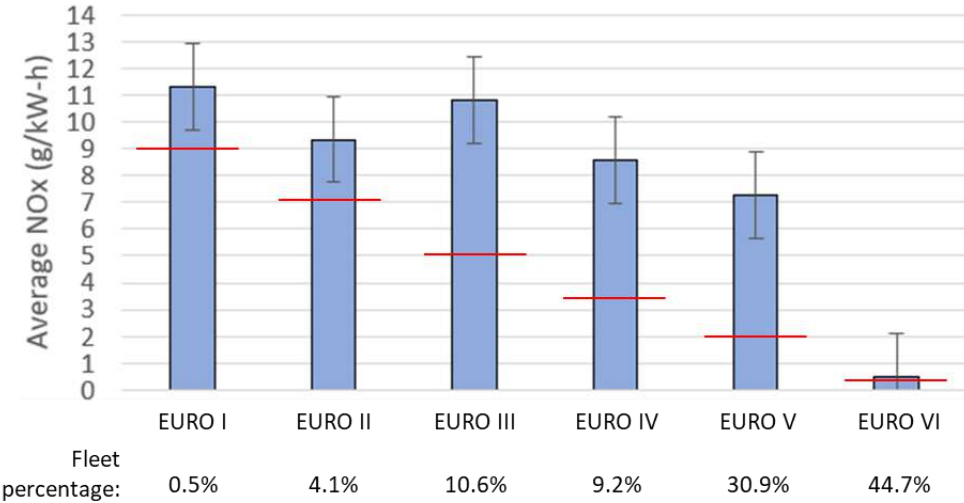


Figure 7: Average NOx in grams per kW-h by Euro Standard and compared to Euro Standard NOx limits

The Spanish police are mostly looking for manipulations on Euro V trucks. Of all the Euro V lorries inspected, **47% were found to have been illegally tampered**. This indicates that the RSD warning to find manipulated trucks is extremely useful and that the 1000 ppm limit used in Spain gave a very high success rate. It should also be noted that in some of the trucks that were inspected no definite proof of cheating was found by the police, despite seeing tampered fuses or other evidence that strongly indicated SCR tampering.

As can be seen in Figure 8, many Euro V trucks that were not reported had very high emissions as well.

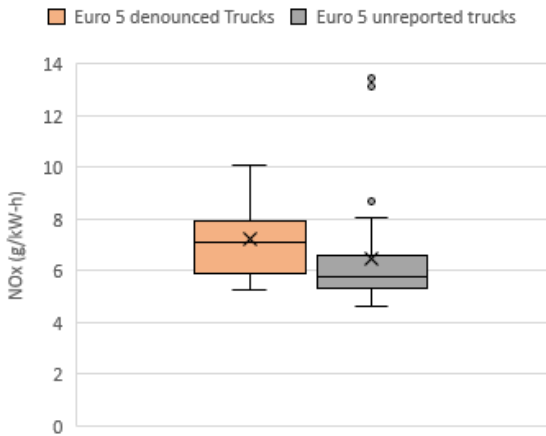


Figure 8: Boxplot of NOx in grams per kW-h. Reported and unreported Euro V trucks

Analysis of 3 manipulated Euro IV trucks

This chapter shows the analysis of three trucks that GUARDIA CIVIL ordered to be further inspected after a manipulation was found in the roadside inspection. They are three Euro IV Volvo trucks with an obvious manipulation of the SCR system. These vehicles were measured several times by the RSD, circulating at different speeds and accelerations within the VSP range of 2 to 30 kW/ton. The Figures 9, 10 and 11 show the NO_x emissions measured for the three trucks with the RSD. It can be seen that in all records the emissions are at least twice the limit of their associated Euro Standard. It is therefore shown that the measurement was not a one-off episode but that these trucks' NO_x emissions are consistently high for a wide range of VSP.

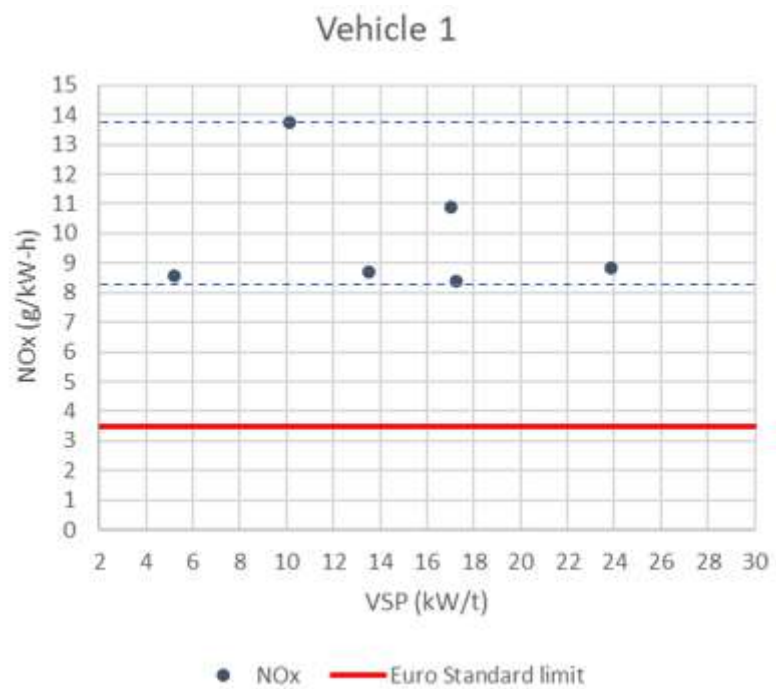


Figure 9: NOx emissions in relation to VSP of vehicle 1

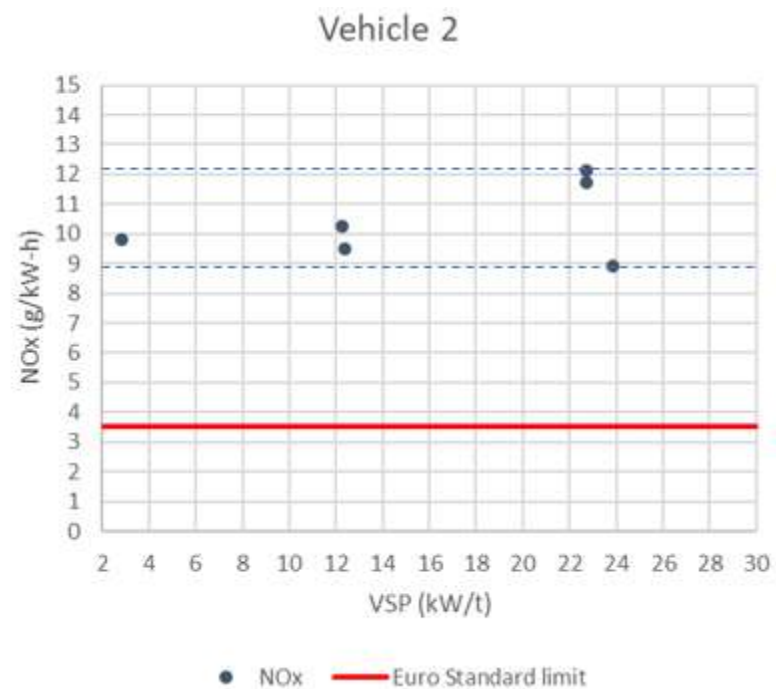


Figure 10: NOx emissions in relation to VSP of vehicle 2

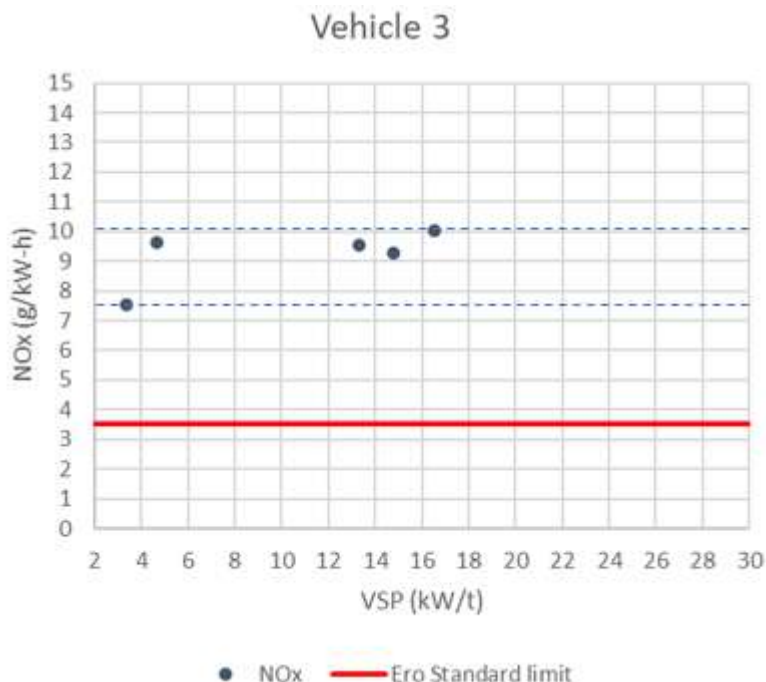


Figure 11: NOx emissions in relation to VSP of vehicle 3

The police recorded the exact average fuel consumption of these three vehicles as well as their actual mileage in the year 2017. With these data, an estimated calculation is made of the tons of NO_x that are emitted to the atmosphere every year by these vehicles above their Euro Standard limit. The lowest measured emission for each vehicle is considered to be representative of an average emission. Table 3 shows that these vehicles emit more than 1 ton of NO_x per year above the allowed Euro Standard NO_x limit.

Table 3: Estimation of excess of NOx over Euro Standard

Vehicle	Fuel consumption (litres/100km)	Mileage in 2017 (km)	Minimum measured NOx (ton/year)	Excess NOx over Euro Standard (ton/year)
1	27.99	236888	2.14	1.25
2	27.17	271850	2.53	1.53
3	23.90	281933	1.95	1.04

It is not known how much of this high NO_x emission (in these vehicles and also in all those reported in the police controls) is produced by the manipulation of the AdBlue injection and how much may be due to other reasons (negligence of the manufacturer, bad maintenance, irregular driving style, etc.). Trucks reported in Spain are currently undergoing legal proceedings and cannot be modified to undo the manipulation to re-measure them without the tampering.

It is therefore interesting to review the results of the study carried out by the Swedish Environmental Research Institute (IVL) in the year 2018. Two Euro VI trucks (of two different manufacturers) were measured several times by the RSD before and after connecting an AdBlue emulator. Figure 12 and Figure 13 shows some preliminary results that have been ceded by IVL¹⁰. As can be seen in the graphs, the installation of an emulator drastically increases the emission of NO_x.

¹⁰ <https://www.ivl.se/>

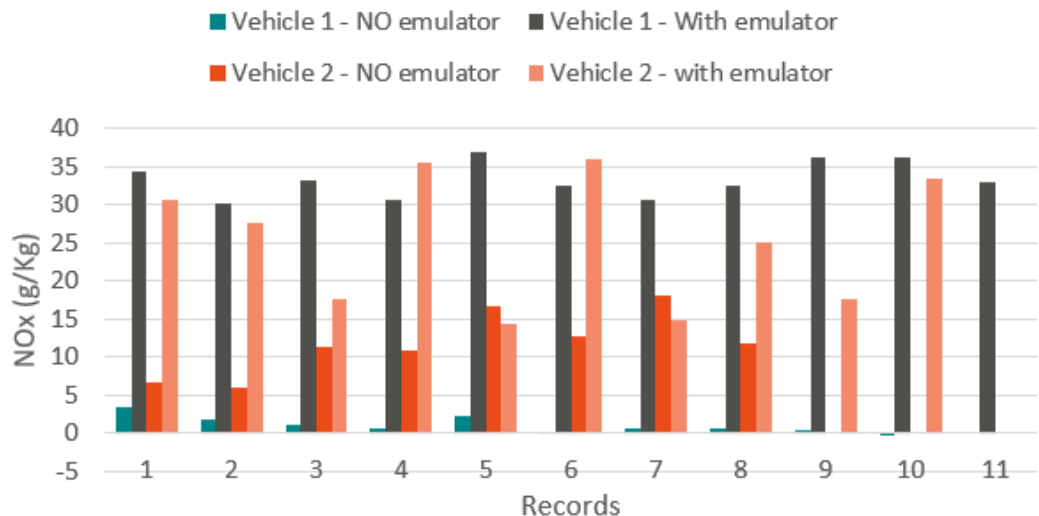


Figure 12: NOx emissions of two Euro VI trucks measured different times (records) with and without emulators. Data granted by IVL.

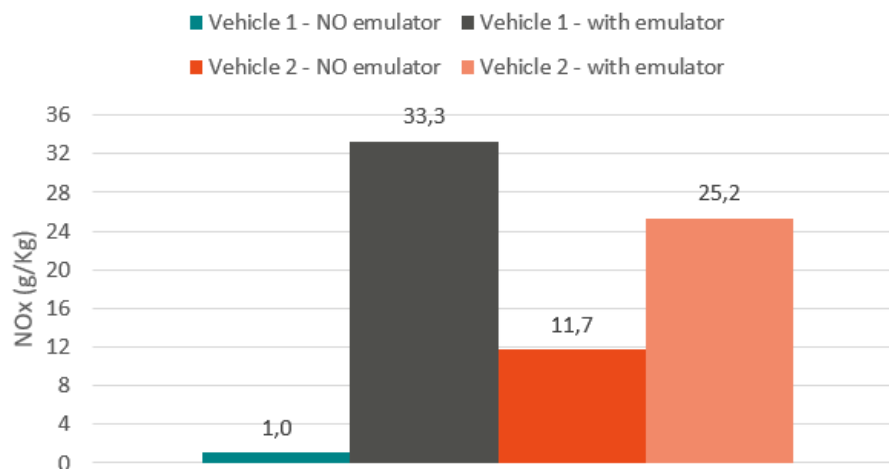


Figure 13: Average NOx emissions of two Euro VI trucks with and without emulators. Data granted by IVL.

Further characterization of NOx emissions in heavy-duty trucks

In addition to roadside checks for individual illegal HDVs, measurements have also been made to characterise the average emissions of large groups of trucks. A total of 2209 trucks have been measured in different locations, of which their NO_x emissions are classified by manufacturer and Euro Standard, according to the technical data received by the Spanish Vehicle Registry Database.

Figure 14 shows the average emissions by Euro Standard of the seven main truck manufacturers: DAF, Iveco, MAN, Mercedes, Renault, Scania and Volvo. The horizontal red line represents the limits of NO_x in the corresponding Euro Standard. These values do not necessarily indicate that one manufacturer emits more NO_x than another, as it may be the case that one type of truck model is frequently more manipulated than another. For instance, it could be that Scania Euro V trucks are more commonly manipulated by drivers or fleet owners than other Euro V trucks. Something similar could be hypothesized for MAN Euro VI trucks. These data do not separate how much of the vehicle's NO_x emissions are purely due to normal operation and how much is related to the SCR manipulation, which could be a massive practice in some HDV models.

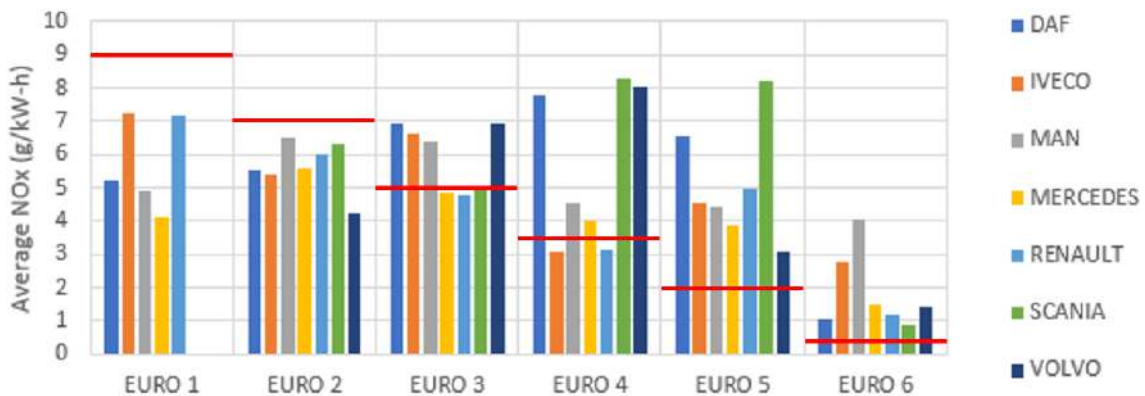


Figure 14: NOx emissions by manufacturer and by Euro Standard

Figure 15 shows the NO_x emissions in a diagram of boxes and whiskers classified by the different Euro Standards. Outliers have been removed in the graphic of the right. These data show that the average and median emissions of Euro V trucks are higher than those of Euro IV trucks. This situation has also been reported in passenger cars¹¹.

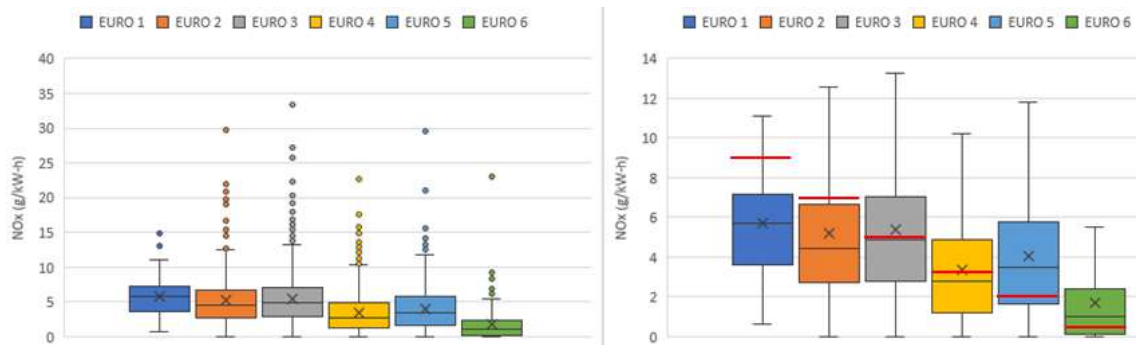


Figure 12: Boxplot of NOx in grams per kW-h classified by Euro Standard. Left: all records including outliers. Right: removing outliers. Horizontal red lines show NOx limit in corresponding Euro Standard

Next steps

A series of next steps have been identified to continue investigating this illicit and allegedly mass practice in Europe:

1. Find clean trucks, that are proven not to be tampered with in any way or form and measure them several times with the RSD. Trucks from the main manufacturers (Volvo, Scania, DAF, Renault, etc.) and at least for the Euro Standards VI, V and preferably IV should be measured. After this, it will be possible to define what is the legitimate and real emission range of these trucks so that other analogous trucks that clearly exceed these levels can be immediately sanctioned, as stated in Directive 2010/47/EU.
2. Analyse NO₂ emissions in greater depth, in case the direct measurement of this pollutant could also give a direct warning of manipulation, in combination with the direct NO.
3. Refine the current NO_x limit if possible or develop a model that can estimate a limit according to the circulating fleets of the different countries.

¹¹ https://www.trueinitiative.org/media/596931/true_remote_sensing_data.pdf

4. Investigate emissions of particulate matter (PM), which is also measured by the RSD, to study possible widespread manipulations in the Diesel Particulate Filter (DPF).
5. Investigate a potential dependency between NO_x and PM in cheating-trucks. Investigate whether improper operation of the DPF (manipulation or wear) has an influence on real-driving NO_x emissions as well.
6. To study at European level the different illicit practices being carried out by truck drivers and fleet owners, which go beyond the connection of emulators, and may be going unnoticed by policemen when inspecting these vehicles.
7. Further study the dependence on NO_x emission and VSP in heavy-duty trucks. The current results do not show a clear dependence, but more dedicated experimentation is needed.
8. To investigate with relevant experts the possible manipulations in the trucks that are currently circulating on European roads and the effects that these actions have on the different components of the vehicle and therefore on the actual emissions emitted.

Conclusions

The following conclusions can be drawn from the study:

1. For this application the remote sensing system measures horizontally, from side to side of the road and at a height of about 20 centimetres above the road. Most lorries in Europe are articulated, with a tractor cabin and one or more semi-trailers. The exhaust gases from these vehicles come out of the cabin and pass underneath the entire vehicle. It has been demonstrated that emissions are correctly measured this way, but if trucks are measured in a top-down manner, it should be evaluated if their emissions can be measured properly if they are emitted under the trailer. Some eastern lorries have the exhaust pipe at the top. These vehicles can be measured cross-road placing the RSD on a scaffold. This has been tested successfully in the past in Spain and USA.
2. Old trucks may have very high NO_x emissions without the vehicle being tampered in any way. SCR systems were only introduced in some Euro IV and were mandatory in Euro V. During inspections, the approximate Euro Standard of the vehicle should be visually assessed from the number plate. It is possible to implement a software that estimates this standard in almost real time. This would make it possible to set a warning level depending on the Euro Standard.
3. The quick and easy deployment of the RSD has been fundamental to the success of these projects, as if these devices were installed in a fixed way, drivers could be aware of their presence and avoid being measured. It was recommended from the police that the operations must have a maximum duration of 4 hours and, if possible, not repeat the place in two consecutive days. It has been seen that drivers warn each other by radio of the presence of the RSD and avoid being measured without passing through the measuring point.
4. The mobile capability of the RSD and the applied methodology have allowed the police to find manipulations in 47% of the Euro V trucks sent for inspection. The success of this application to prosecute illegal activities in Europe is demonstrated. Guardia Civil¹² and Europol¹³ have published Press Releases.
5. It has been shown that a manipulated truck always and consistently emits well above its corresponding Euro Standard when VSP is within 2-30 kW/Ton.
6. It has been shown that a Euro VI truck with a tampered SCR emits 2 to 32 times more NO_x than without tampering.

¹² <http://www.guardiacivil.es/es/prensa/noticias/6944.html>

¹³ <https://www.europol.europa.eu/newsroom/news/haulier-in-spain-caught-cheating-emission-regulations-designed-to-prevent-air-pollution>

Acknowledgements

This project was funded by the European Commission within the LIFE programme in the GySTRA project: <https://lifegystra.eu>.

The authors thank the Spanish Guardia Civil for their excellent and professional collaboration both in road inspections and in subsequent investigations.

The authors also thank IVL Swedish Environmental Research Institute for ceding their results of the study carried out in 2018 evaluating NO_x emissions from two Euro VI trucks with and without emulator.

References

- Bernard Y., Tietge U., German J., Muncrief R. (2018). Determination of real-world emissions from passenger vehicles using remote sensing data.
- Borken-Kleefeld, J., Bernard, Y., Carslaw, D., Sjödin, Å. (2018). Contribution of vehicle remote sensing to in-service/real driving emissions monitoring - CONOX Task 3 report.
- Dorado-Chiliquinga W., Ona-Quispe D., Castro-Clavijo J., Urrutia-Goyes R. (2018) Opacity and NOx Sensing on a Diesel Engine with AdBlue injected in a SCR system. 1-4. [10.1109/EEEIC.2018.8494222](https://doi.org/10.1109/EEEIC.2018.8494222).
- Jiménez J.L., McClintock P., McRae G.J., Nelson D.D., Zahniser M.S. (1999). Vehicle Specific Power: A Useful Parameter for Remote Sensing and Emission Studies, *9th CRC On-Road Vehicle Emissions Workshop San Diego*, April 21st, 1999.
- Sjödin, Å., Carslaw, D.C., Tate, J.E., de la Fuente, J., Alt, G.-M., Borken-Kleefeld, J., Gentala, R.A., McClintock, P.M., Vescio, N., Hausberger, S., Bernard, Y., Jenk, H. (2017). Pan-European study on real-driving NOX emissions from late model diesel cars as measured by remote sensing. In: *Proc. 22nd International Transport & Air Pollution Conference*, Zürich, 15-16 November 2017.

2.7.2 A Novel Method for Comparing Passenger Car Fleets and Identifying High-Chance Gross Emitting Vehicles using Kerbside Remote Sensing Data

C.E. Rushton^{1}, J.E. Tate², S.P. Shepherd²*

¹Transport Systems Catapult, 3rd Floor The Pinnacle, Midsummer Boulevard, Milton Keynes, MK91BP

²Institute for Transport Studies, University of Leeds, LS29JT

Introduction

The quantification and comparison of NOX emission from in-situ car fleets, and identification of the highest emitters is an ongoing challenge. The challenge will become more important as new and increasingly complex emissions control technologies and their associated countermeasures penetrate the market. In this paper real-world data is combined with new-to-the-field statistical methods to robustly describe the fleet behaviour and identify gross-emitter candidate vehicles. The analysis techniques presented and demonstrated in this paper intend to extend the knowledge and understanding that can be gleaned from remote sensing measurements.

Kerbside remote sensing devices (RSDs) allow for indirect and unobtrusive inspection of vehicles subject to real duty cycles and driven by real drivers in a naturalistic way, with minimal disruption to infrastructure. Remote Sensing Devices (RSDs) have been used in studies across the UK, Europe and world-wide to assess the emissions of in-situ vehicles for several years. These studies have shown that there has been little to no change in NOX emissions from Euro 3 to Euro 5 diesel powered PCs, light commercial and heavy commercial vehicles, despite the incrementally increasing strictness of type approval limit values (Rushton et al., 2018; Carslaw and Rhys-Tyler, 2013; Tate, 2013a,b; Carslaw et al., 2011b,a; Bishop et al., 2003, 2001; Bishop and Stedman, 1996, 1990).

The RSD was initially developed in 1989 as part of the United States clean air programme (EPA, 1999) to measure Carbon Monoxide (CO) (Bishop et al., 1989) and has been developed further to include Hydrocarbons (HC) (Popp et al., 1999) and NO with prototype Fuel Efficiency Automobile Test (FEAT) devices able to record Ammonia (NH_3) and NO_2 (Burgard et al., 2006). Measurements of the abundance of these species are made by infra-red (IR) and ultraviolet (UV) photometry at frequencies where the species are known to have absorption lines (Bishop et al., 1996). The RSD instrument consists of an open-path non-dispersive IR and dispersive UV light sources tuned to frequencies that interact with NO and CO_2 molecules in the exhaust plume to report a ratio between NO and CO_2 . To take a measurement the source and detector module (SDM) directs a multi-frequency beam of light across a single lane of traffic which is reflected using a corner cube mirror. The SDM calculates the difference in intensity between the sent (I_0) and the received (I) beam. The difference in intensity varies in accordance with the Beer-Lambert law (Lambert, 1760). The instrument returns the ratio of emissions between CO_2 and NO_x . The instrument is constantly operating and the pollution background level, subtracted from the observed tailpipe emission, is calculated using the last measurements before the beam is broken. The remaining difference is appointed to the vehicle. Measurement of NO and NO_2 is especially problematic as there are other species with strong absorption lines at similar frequencies to those used to measure NO_2 and have a high potential for interference. The most noticeable source of interference in NO_2 measurements is water (H_2O). Water vapour in the plume, a by-product of combustion, and also present in the atmosphere, can cause interference. The high spectral resolution of the RSD4600 and RSD5000 instruments allow the impact of interference to be minimised (Jimenez-Palacios, 1998).

Methodology

In the summer of 2015 the RSD was deployed for ten days across five sites, two days per site, distributed around central Aberdeen (Tate, 2016), a port city in East Scotland. The observation sites were pre-selected to represent a range of arterial, circulatory and city centre streets, whilst also meeting ease of accessibility and other practical constraints. The RSD was deployed from 08:00 to 18:00 where possible to capture the AM, PM, and inter peak periods, and to maximise the sample size of vehicles observed. The number of PC observations per vehicle category can be found in Tate (2016) and Rushton (2016).

The RSD was set up in a standard on-road configuration as described in the user manual provided with the equipment (ESP, 2005). An in-depth description of the setup including location map and survey site photographs can be found in Rushton (2016) and Tate (2016). A speed and acceleration module (SAM) consisting of three light beams was used to capture the vehicle dynamics. The SAM was placed between 3 and 5 metres before the SDM to ensure that the vehicle dynamics were representative of the emissions being observed. The operation of all the devices was controlled automatically by the RSD. The captured license plate data was converted to vehicle-specific metadata using a lookup service provided by CarWeb (<http://www.carweb.co.uk>). The RSD was calibrated twice daily, or whenever significant changes were observed in ambient weather conditions (Rushton, 2016), using an internal reference gas cell. Measurements were also audited every hour using blended calibration gas with known concentrations of pollutants broadly representative of what would be expected in the plume of a petrol-powered vehicle. The calibration gas measurements are compared to the known bottle gas concentrations and lock out further measurements if the instrument does not remain within an acceptable tolerance range (ESP, 2005).

A series of events with rare but high value events can be characterised by extreme value distributions. Various forms of extreme value distribution have been applied to many real-world scenarios where the distribution of the events' magnitude does not follow a normal distribution. The use of the extreme value distribution extends from finance (Poon et al., 2004; Bensalah et al., 2000) to hydrological data (Martins et al., 2000). There are three different types of extreme value distribution. These are called Weibull, Frechet and Gumbel (Frechet, 1928; Rosin, 1933; Gumbel, 1941, 1935). It has been previously hypothesised that a small number of vehicles contribute an excess amount of pollution to the overall inventory (Bishop et al., 2016; Zhang et al., 1994). This behaviour is compatible with the behaviours of extreme value distribution functions. This behaviour can be seen in the observed data histograms presented in Figure 1 and Figure 2.

A good distribution function for describing vehicle emissions must fit the data well and be parameterised in terms that are easily understandable in a real-world context. The Gumbel distribution meets these criteria. The Gumbel function is parameterised by the modal (or highest observation frequency in this context) value and a shape parameter that is related to the spread of the data and can be used to predict extreme flooding (Martins et al, 2000). It is possible to compare both the peak emissions and the spread of the data of different population subsets in a meaningful way using these parameters. The Gumbel probability density function $P(x)$ is defined, where $z = \frac{x - a}{b}$ and a and b are the modal value and the shape parameter respectively, in the following equation.

$$P(x) = \frac{1}{b} e^{-(z + e^{-z})}$$

Results

Analysis of Distribution Functions

Each Euro class and fuel type pair were fitted to normal and Gumbel distributions with probability density functions (PDFs) and the theoretical / empirical Quantile plots, or Q-Q Plots (Wilk and Gnanadesikan, 1968) were calculated. The distribution fit parameters were estimated using the Maximum Likelihood Estimation (MLE) method from the *fitdistplus* package in R (Wilks, 1938; Delignette-Muller and Dutang, 2015; R Core Team, 2015). The PDF and Q-Q plot types show the difference between the Gumbel and Normal distributions compared to the observed data. A Q-Q plot demonstrates the relationship between the expected and observed values in a distribution. A well modelled distribution will correlate strongly along the 1:1 line.

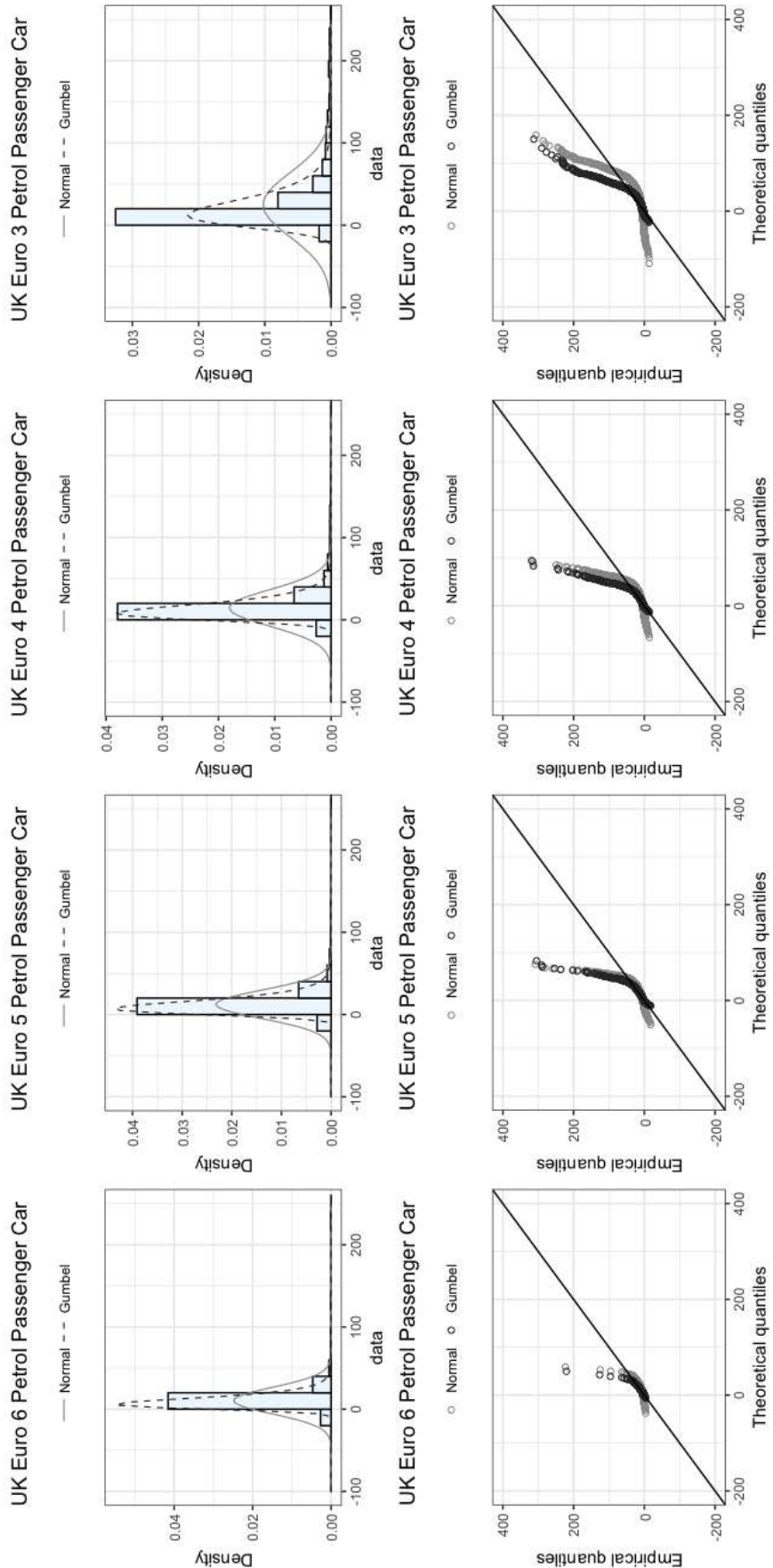


Figure 1: Distribution of petrol passenger car emission ratios compared to theoretical Gumbel distribution

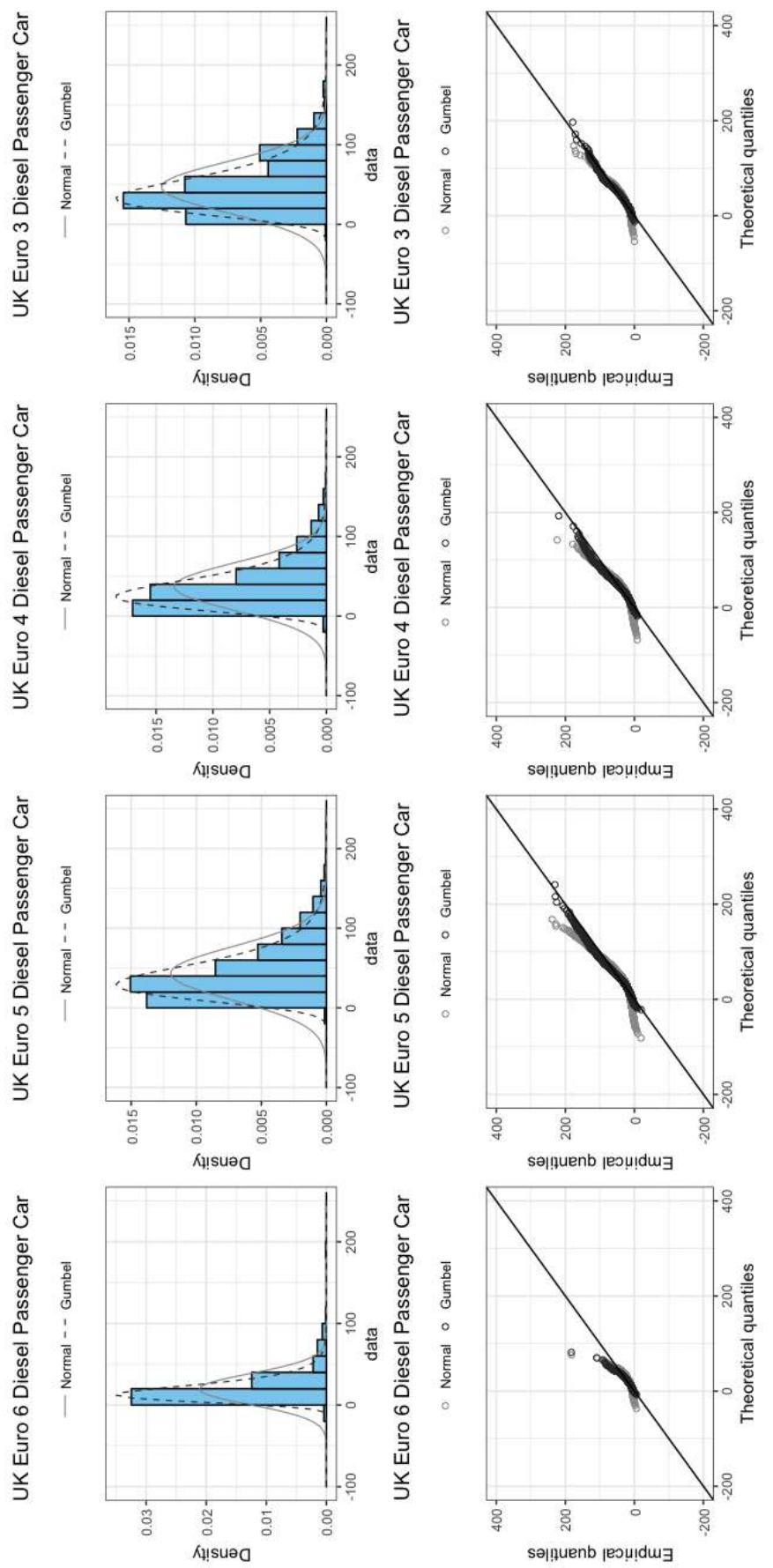


Figure 2: Distribution of diesel passenger car emissions compared to theoretical Gumbel distribution

Figure 1 and Figure 2s show the fits for the fleets of petrol and diesel-powered passenger cars respectively. For the diesel-powered vehicles, the Gumbel distribution fits the data more consistently than the normal distribution showing reasonable agreement across the whole range of percentiles. In contrast, the normal distribution underestimates both the number of highest emitters and lowest emitters in the population and fails to correctly identify the most frequent value for emissions. The population of observed emissions ratios for petrol powered vehicles mostly fit the Gumbel distribution. There is a small subset of the population that deviate from the Gumbel distribution. The higher quantiles side of the distribution begins to depart from the 1:1 line most noticeable in the petrol-powered fleets but also in the Euro 6 diesel fleets. It is hypothesised that most of the fleet follow the Gumbel distribution and a small percentage of vehicles that do not. The fraction of vehicles that do not follow the Gumbel distribution are termed 'off model' and may represent high-chance gross emitting vehicles.

To test the hypothesis that most of the vehicle population conformed to the Gumbel distribution and quantify the magnitude of the off-model behaviour the data was cut by quantiles, in steps of 1% and the distribution re-fitted. An R^2 value was calculated for the relationship between the theoretical and empirical quantiles observed for each cut using the re-fitted model. Cuts of data from 99% to 1% in steps of 1% were performed with the highest percentile, maximal R^2 value was chosen as the best model for that fleet subset. This percentile, P_{off} , was reported as the off-model fraction. The process was iterated a second time with the off-model fraction to determine the parameters that define the off-model fraction. The variation in R^2 statistic for each cut is shown in Figure 3. The line for $R^2 = 0.98$ is shown for comparative purposes. The convergence to the model with well-chosen cuts is graphically demonstrated in Figure 6 as the Q-Q line best matches the 1:1 line and agrees with the result generated using the maximising R_2 value approach. The large increase in R^2 values as the cut percentile decreases is likely an artefact of the algorithm over-fitting the distribution function to the available data.

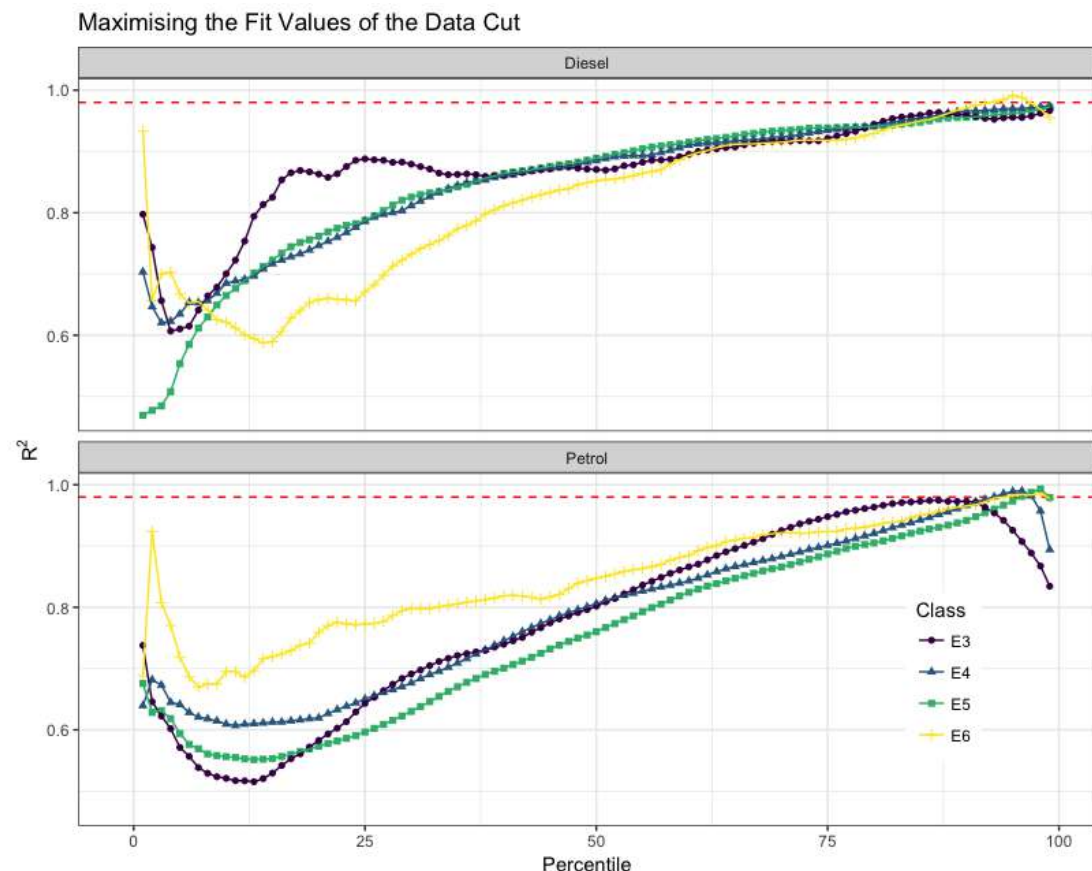


Figure 3: R^2 variation as a function of percentile cut showing the point of best fit for a theoretical Gumbel distribution

Parameterising the distribution of NOx emission ratios in this way allows for more realistic and representative comparisons to be made between the various fleets because it robustly quantifies a behaviour of the vehicle using transferrable and meaningful variables. By developing this method of

analysis, it allows for a better understanding of what has changed regarding emissions as they relate to euro class and fuel type. Given a sufficient sample size this method can be applied to vehicles of a specific make, manufacturer, engine capacity or chassis platform. In all but one case, Euro 3 diesel, cutting the data correctly results in an R^2 parameter greater than 0.970. This result suggests that the majority of the vehicles observed in each class can be parameterised by a Gumbel distribution fitted to appropriately cut data. The implication of this is that vehicle fleets with greater levels of NOX control exhibit two-type behaviour and that the fleet is comprised of two or more component parts. For the purpose of this paper they can be thought of as normal and grossly emitting vehicles relative to their category.

There is a known association between Vehicle Specific Power (Jimenez-Palacios, 1998) and high NO_x emission (Carslaw et al., 2013). To ensure that the analysis is identifying gross-emitter candidate vehicles rather than vehicles with high vehicle specific power (VSP) the emission rates for Euro 3 - 6 petrol and Euro 6 diesel were cut into two different subsets. These two subsets are referred to as an under-cut and an over-cut population based on their VSP percentile, P_{VSP} and the cut point is defined as $P_{VSP} = P_{off}$. The under-cut subset is the vehicles where $P_{VSP} < P_{off}$ and the over-cut subset is where $P_{VSP} \geq P_{off}$. For example the 98th percentile of VSP was used as the cutting point for Euro 5 petrol vehicles. The results of this analysis are shown in Figure 4. If VSP was the dominant factor for causing off-model behaviour clustering would be expected in the upper and lower panels. No such clustering is observed and the over-cut VSP follow the trends of the under-cut VSP vehicles. The over-cut, off-model vehicle the highest in population NO_x emitter in only one case from the current limited sample of six. There is no evidence of strong systematic bias towards high VSP vehicles and off-model behaviour observed in any of these samples. Previous result alongside this analysis suggests that whilst the VSP of a vehicle is a contributing factor to its emissions it is not a systematic dominant factor when considering which vehicles are gross emitter candidates. Gross-emitter candidates appear to be unrelated to the driving dynamics. The lack of strong relationship to driving dynamics suggests that the solution to the problem of gross-emitter vehicles will be predominantly mechanical rather than behavioural.

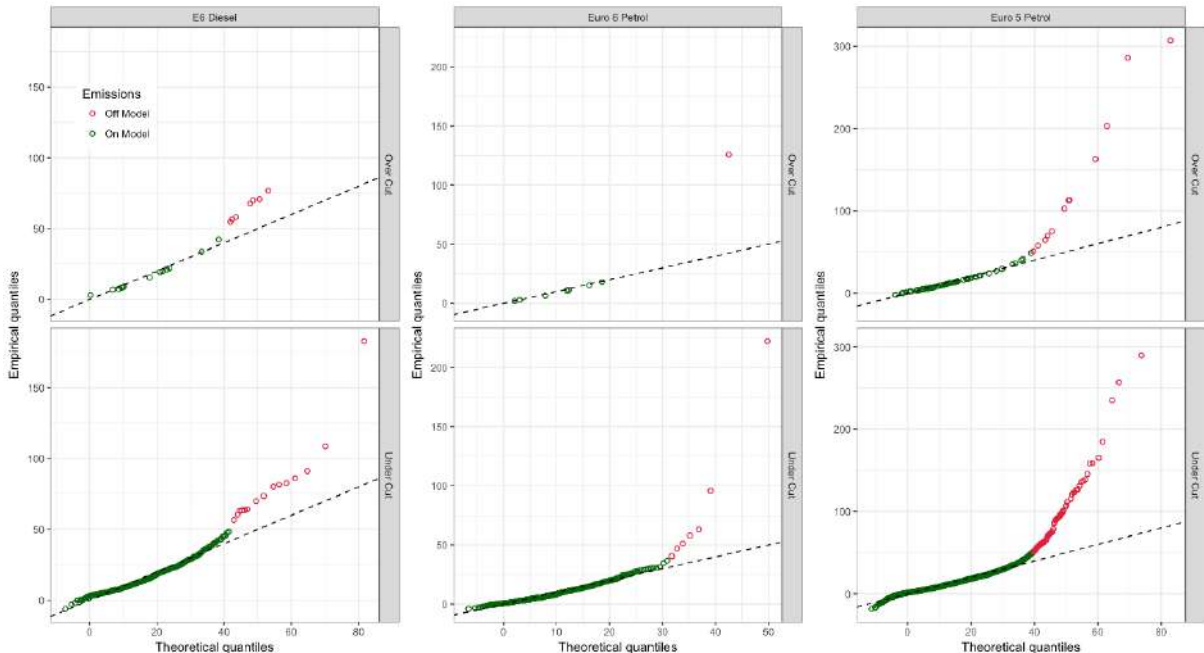


Figure 4: Q-Q plot showing on and off model vehicles split by Euro and fuel type, and an over and under-cut for VSP. On and off model vehicles are coloured green and red respectively.

Parameterisation of Observed Gross-Emitter Candidates

The existence of off-model vehicles presents a problem for modelling the fleet as the modeller cannot simply fit the Gumbel distribution to the data and move on to the next step. The modeller must now understand the nature of off-model vehicles or risk not accounting for some of the most important

contributors to total emissions. Physically these vehicles might be thought of as having sub-optimal emission control systems due to their higher NO:CO₂ emissions ratios. There are multiple reasons for why a vehicle's emissions control systems would not perform optimally. Cold starts, ambient temperatures or defeat devices may all contribute by some degree to the off-model fraction of newer fleets. Catalyst poisoning, sintering or physical damage may all contribute in varying degrees to reduction in catalyst efficiency in older fleets. Those vehicles exhibiting off-model behaviour were grouped into separate subclasses of their euro and fuel class of vehicles, parameterised independently, and their contribution was added to the on-model component of the fleet.

The off-model fractions of the Euro 3 and Euro 4 passenger car petrol fleet subsets were chosen for initial parameterisation because they had the largest sample sizes of 222 and 150 respectively. Euro 6 diesel is included despite the small sample size of 19 as they are the most relevant vehicle class to this analysis and the observed distribution was assessed to be qualitatively similar to a Gumbel distribution. The Euro 5 and 6 petrol vehicle subsets with identified off-model contributions did not contain enough off-model vehicles to fit distribution functions to with any degree of confidence.

Table 1: Gumbel distribution function parameters for selected off-model vehicle subsets

Vehicle Type	Sample Size	Location Parameter	Shape Parameter
Euro 3 Petrol	150	80.9	38.7
Euro 4 Petrol	222	78.2	31.1
Euro 6 Diesel	19	70.5	13.1

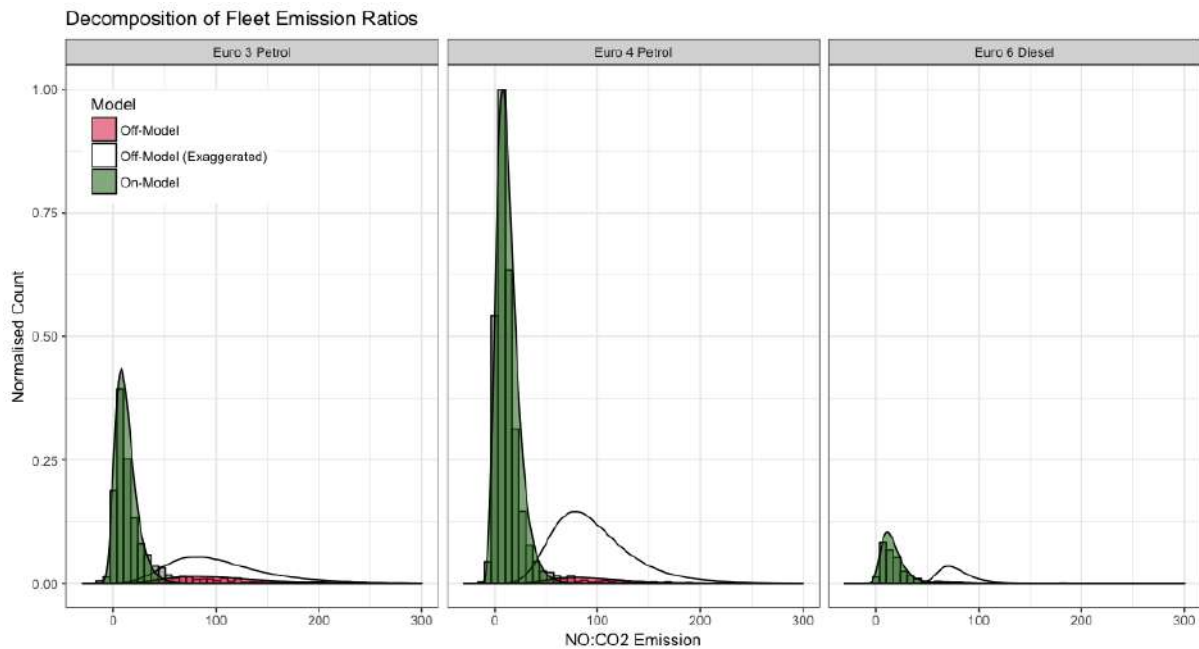


Figure 5: Decomposed fleet distribution functions (coloured) with illustrative exaggerated distribution function plotted over real data (grey histogram)

The functions for the on and off model components were plotted and normalised then overlaid on the data. The off-model fraction is small for both the Euro 4 petrol and Euro 6 diesel fleets so an additional and exaggerated off-model component has been added to the data. The exaggerated component was calculated based on the assumption that 50% of the vehicles in the fleet were off-model and is for illustrative purposes only. These distributions are shown in Figure 9. Two-sample KS tests were performed on the function and the data to determine the similarity between the model predictions and the data. The p statistics for the Euro 3 petrol vehicles were $p = 1.69 \times 10^{-3}$ and for the Euro 4 petrol vehicles were $p < 2.2 \times 10^{-16}$. The p -values generated suggests that there is good agreement between the predicted distribution of both the normally emitting vehicles and the gross-emitters, suggesting that this methodological approach can provide useful insight to distribution of emission ratios in these fleets.

The number of vehicles in the Euro 6 diesel category was not large enough to generate a reliable p-value however the qualitatively successful application of this methodology suggests that given a bigger data set this feature could be replicated in a more robust statistical manner.

Conclusions, Discussion and Further Work

Conclusions

The results presented in this paper suggest that the clear majority (87% to 100%) of NOx remotely sensed emission ratios for vehicles in any given euro or fuel subset can be described using a well-fitted Gumbel distribution function. In fleet subsets where significant work has been done to reduce NOX emissions a small number of gross-emitter candidate vehicles can be observed in their deviation from this model. For the normally behaving vehicles the fitted parameters from the Gumbel distribution function can be used to compare and contrast fleet emission rates in a more precise way. This new methodology allowed the level of Euro 6 emissions to be tested and compared to other Euro and fuel-type fleet subsets for the first time ignoring high emitters. It can now be shown that a new Euro 6 diesel vehicle is likely to emit slightly more NO:CO₂ than a Euro 3 petrol powered vehicle when passing through a remote sensing device. This is approximately half the emission of a Euro 5 or 4 diesel vehicle. Given that a Euro 3 petrol powered vehicle is not an ultra-low emission zone (ULEZ) compliant vehicle there should be some concern that the introduction of ULEZ into city centres may not lead to a significant reduction in ambient NOx concentration. No significant change was observed between Euro 3, 4 or 5 diesel cars.

It is now possible to state with some confidence the magnitude of impact that a legislative change has had on the emissions ratios of nitric oxide. The method developed here will allow for almost instantaneous appraisal of new legislation Euro 6c+ vehicles as they enter the fleet.

Discussion

Remote sensing studies have previously demonstrated their value in observing the differences between in-situ vehicles and laboratory and PEMS based testing environments. The results and methodologies demonstrated in this paper build on this work and increase the knowledge surrounding this methodology by identifying the best method to parameterise this data, using a Gumbel distribution. Use of the Gumbel distribution to describe the observation improves the diagnostic information that RSD observations can generate. The RSD methodology can now further contribute to the emissions factor debate. It also allows for more naturalistic and granular descriptions of the fleets to be produced which both account for the natural variation in emissions between similar vehicles and those vehicles with abnormally high emission performance.

A quantitative method for assessing the differences between fleet sub-categories, in this case by Euro class but extendable to any observed vehicle parameter, has been described and defined in a robust and repeatable way. This paper investigated Euro class however make, marque, year of first introduction, level of WLTP or RDE compliance if not stated explicitly, engine size or other parameters can be analysed in the same way given a large enough dataset. Using the mean emission value has been demonstrated to be unreliable as it does not encapsulate the underlying distribution of fleet emissions. The new method using the Gumbel distribution can be used to make strong assessments about the differences between fleet subsets at any level of granularity. The difference between cities or sub-regions within cities and temporal differences could also be assessed. The results of these assessments are more robust and useful than a simple average because they encapsulate the underlying behaviour of the fleet in a much more representative way.

The characterisation of the on-model and off-model fleets mean that an observer can now assess the likelihood that a vehicle is operating in a sub-optimal way. With appropriate underlying infrastructure the vehicles that are performing within the expected window can easily be identified using a real-time, big-data approach that compares each vehicle observed to every other vehicle. Vehicles suspected as having SCR emulators (OEM defeat devices or customer fitted) may be identifiable.

Improving the statistical framework around individual vehicle emissions and how they are positioned within the fleet presents a further use case related to clean air zone enforcement. It may be desirable in the course of enacting and enforcing future clean air zones to penalise drivers of excessively highly

emitting vehicles on a case by case basis. One-off individual measurements may struggle to identify the worst emitters and may be further confounded by idiosyncrasy in vehicle emission control systems and driver behaviour. Repeated measurements of the same vehicle may be able to identify those vehicles that are consistently emitting higher than the rest of the fleet. Repeated measurements

of the same vehicle become more likely if remote sensing devices are more widely deployed in the future. Targeted schemes to remove the most highly emitting vehicles would become more realistic. This methodology, coupled with the correct infrastructure, could provide a useful tool for identification of candidate gross-emitter vehicles. These vehicles could then be flagged as a gross emitter candidate, potentially triggering a more thorough emissions test at next routine inspection. This type of fleet surveillance and targeted intervention, when coordinated with more targeted RDE testing by type approval, could give authorities some of the tools they need to reduce the number of high emitting new diesel cars on the road whilst minimising the disruption to those vehicles that are performing at a level consistent with the requirements of the legislation.

Further Work

Further important use cases of this methodology include assessing the effectiveness of emissions reduction systems on Euro 6c, 6d-temp and 6d vehicles as they enter the fleet. Each of these legislative changes are changes to the test procedure with Euro 6d-temp and Euro 6d requiring real driving emissions tests to be within a conformity factor of legislation ($CF_{d\text{-temp}} = 2.1$ and $CF_d = 1.5$) and this is expected to result in real-world reduction in tailpipe emission. Using the methods developed in this paper a more representative and useful comparison could be made between these new type approval classes, each other, and those currently on the road. These comparisons could be completed reasonably quickly after the vehicles are introduced to the fleet as a sample size of the order 100 will give statistics that are comparable to the current Euro 6 fleet.

Bibliography

- Bensalah, Y., et al., 2000. Steps in applying extreme value theory to finance: a review. Bank of Canada.
- Bishop, G., Stedman, D., 1996. Measuring the emissions of passing cars. Accounts of Chemical Research 29 (10), 489–495.
- Bishop, G. A., Burgard, D. A., Stedman, D. H., 2003. On-road remote sensing of automobile emissions in the La brea area: Year 3, october 2003.
- Bishop, G. A., Morris, J. A., Stedman, D. H., Cohen, L. H., Countess, R. J., Countess, S. J., Maly, P., Scherer, S., 2001. The effects of altitude on heavy-duty diesel truck on-road emissions. Environmental science & technology 35 (8), 1574–1578.
- Bishop, G. A., Starkey, J. R., Ihlenfeldt, A., Williams, W. J., Stedman, D. H., 1989. Ir long-path photometry: a remote sensing tool for automobile emissions. Analytical Chemistry 61 (10), 671A–677A.
- Bishop, G. A., Stedman, D. H., 1990. On-road carbon monoxide emission measurement comparisons for the 1988-1989 colorado oxy-fuels program. Environmental Science & Technology 24 (6), 843–847.
- Bishop, G. A., Stedman, D. H., Ashbaugh, L., 1996. Motor vehicle emissions variability. Journal of the Air & Waste Management Association 46 (7), 667–675.
- Bishop, G. A., Stedman, D. H., Burgard, D. A., Atkinson, O., 2016. High-mileage light-duty fleet vehicle emissions: Their potentially overlooked importance. Environmental science & technology.
- Burgard, D. A., Dalton, T. R., Bishop, G. A., Starkey, J. R., Stedman, D. H., 2006. Nitrogen dioxide, sulfur dioxide, and ammonia detector for remote sensing of vehicle emissions. Review of scientific instruments 77 (1), 014101.
- Carslaw, D., Beevers, S., Westmoreland, E., Williams, M., Tate, J., Murrells, T., Stedman, J., Li, Y., Grice, S., Kent, A., et al., 2011a. Trends in nox and no2 emissions and ambient measurements in the uk. Defra, London.
- Carslaw, D., Rhys-Tyler, G., 2013. Remote sensing of no2 exhaust emissions from road vehicles. A report to the City of London Corporation and London Borough of Ealing, Version 16th July.
- Carslaw, D. C., Beevers, S. D., Tate, J. E., Westmoreland, E. J., Williams, M. L., 2011b. Recent evidence concerning higher no x emissions from passenger cars and light duty vehicles. Atmospheric Environment 45 (39), 7053–7063.
- Carslaw, D. C., Williams, M. L., Tate, J. E., Beevers, S. D., 2013. The importance of high vehicle power for passenger car emissions. Atmospheric Environment 68, 8–16.
- Delignette-Muller, M. L., Dutang, C., 2015. fitdistrplus: An R package for fitting distributions. Journal of Statistical Software 64 (4), 1–34. URL <http://www.jstatsoft.org/v64/i04/>
- EPA, 1999. Nitrogen oxides (nox), why and how they are controlled.
- ESP, 2005. RSD 4600 Operator's Manual Edition 3.0.
- Frechet, M., 1928. Sur la loi de probabilité de l'écart maximum. In: Annales de la societe Polonaise de Mathematique. [sn].
- Gumbel, E. J., 1941. The return period of flood flows. The annals of mathematical statistics 12 (2), 163–190.
- Jimenez-Palacios, J. L., 1998. Understanding and quantifying motor vehicle emissions with vehicle specific power and tildas remote sensing. Ph.D. thesis, Massachusetts Institute of Technology.

- Lambert, J. H., 1760. Photometriae de mensura et gradibus luminis, colorum et umbrae. Klett.
- Martins, E. S., Stedinger, J. R., et al., 2000. Generalized maximum-likelihood generalized extreme-value quantile estimators for hydrologic data. *Water Resources Research* 36 (3), 737–744.
- Poon, S.-H., Rockinger, M., Tawn, J., 2004. Extreme value dependence in financial markets: Diagnostics, models, and financial implications. *Review of financial studies* 17 (2), 581–610.
- R Core Team, 2015. R: A Language and Environment for Statistical Computing. R Foundation for Statistical Computing, Vienna, Austria. URL <https://www.R-project.org/>
- Rosin, P., 1933. The laws governing the fineness of powdered coal. *J. Inst. Fuel.* 7, 29–36.
- Rushton, C. E., 2016. Measuring and modelling vehicle nox emissions using a remote sensing device.
- Rushton, C. E., Tate, J. E., Shepherd, S. P., Carslaw, D. C., 2018. Interinstrument comparison of remote-sensing devices and a new method for calculating on-road nitrogen oxides emissions and validation of vehicle-specific power. *Journal of the Air & Waste Management Association* 68 (2), 111–122.
- Tate, J., 2016. Vehicle emission measurement and analysis - aberdeen city council.
- Tate, J. E., 2013a. Vehicle emission measurement and analysis - cambridge city council.
- Tate, J. E., 2013b. Vehicle emission measurement and analysis - sheffield city council.
- Wilk, M. B., Gnanadesikan, R., 1968. Probability plotting methods for the analysis of data. *Biometrika* 55 (1), 1–17.
- Zhang, Y., Bishop, G. A., Stedman,
- WHO, 2006. Who air quality guidelines for particulate matter, ozone, nitrogen dioxide and sulfur dioxide: global update 2005: summary of risk assessment.
- WHO, 2013. Review of evidence on health aspects of air pollution: Revihaap project: final technical report.
- Wilk, M. B., Gnanadesikan, R., 1968. Probability plotting methods for the analysis of data. *Biometrika* 55 (1), 1–17.
- Wilks, S. S., 1938. The large-sample distribution of the likelihood ratio for testing composite hypotheses. *The Annals of Mathematical Statistics* 9 (1), 60–62.
- William, J. C., 1971. Practical nonparametric statistics.
- Wyatt, D. W., Li, H., Tate, J. E., 2014. The impact of road grade on carbon dioxide (co 2) emission of a passenger vehicle in real-world driving. *Transportation Research Part D: Transport and Environment* 32, 160–170.
- Zhang, Y., Bishop, G. A., Stedman, D. H., 1994. Automobile emissions are statistically gamma distributed. *Environmental science & technology* 28 (7), 1370–1374

2.7.3 NO_x RDE measurements with Plume Chasing - Validation, detection of high emitters and manipulated SCR systems

D. Pöhler^{1,2*}, T. Engel¹, U. Roth¹, J. Reber¹, M. Horbanski^{1,2}, J. Lampel^{1,2} and U. Platt^{1,2}

¹ Institute of Environmental Physics, University of Heidelberg, Heidelberg, 69120, Germany,
denis.poehler@iup.uni-heidelberg.de

² Airyx GmbH, Eppelheim, 69214, Germany
airyx@airyx.de

Introduction

Vehicles, especially Diesel, are the most relevant NO_x (NO + NO₂) source in urban areas which cause large environmental problems. The EURO Norm define the allowed emissions (e.g. EURO VI since 1.1.2013 for vehicles >3.5t emission limit is 400mg/kWh). The best technology to achieve low NO_x emissions is the SCR (selective catalytic reduction), consuming AdBlue®. For vehicles above 3.5t (trucks and busses) all EURO VI and most EURO V use the SCR system. For vehicles below 3.5t, SCR systems become also widely used since EURO 6.

RDE (real driving emissions) can significantly vary from EURO Norm emissions in the lab. Thus RDE measurements have become an important topic in recent years to improve the true emissions on the road and not only in the lab. For vehicles above 3.5t RDE measurements have become mandatory but allow a higher emission with a conformity factor of 1.5 (resulting in 600mg/kWh). Typically, PEMS (portable emission measurement systems), installed on an individual vehicle are used to investigate RDE. But PEMS measurements are very expensive, time consuming and investigation of only very few individual vehicles are possible. They are thus not practical to investigate a large number of vehicles or even a complete fleet. On the other hand, remote sensing (RS) emission measurements are possible to investigate the emissions of a large quantity of passing vehicles. However, the measurement is a snap shot of the emission and not representative for an individual vehicle. Thus an individual high emitter cannot reliable be identified (see next chapter).

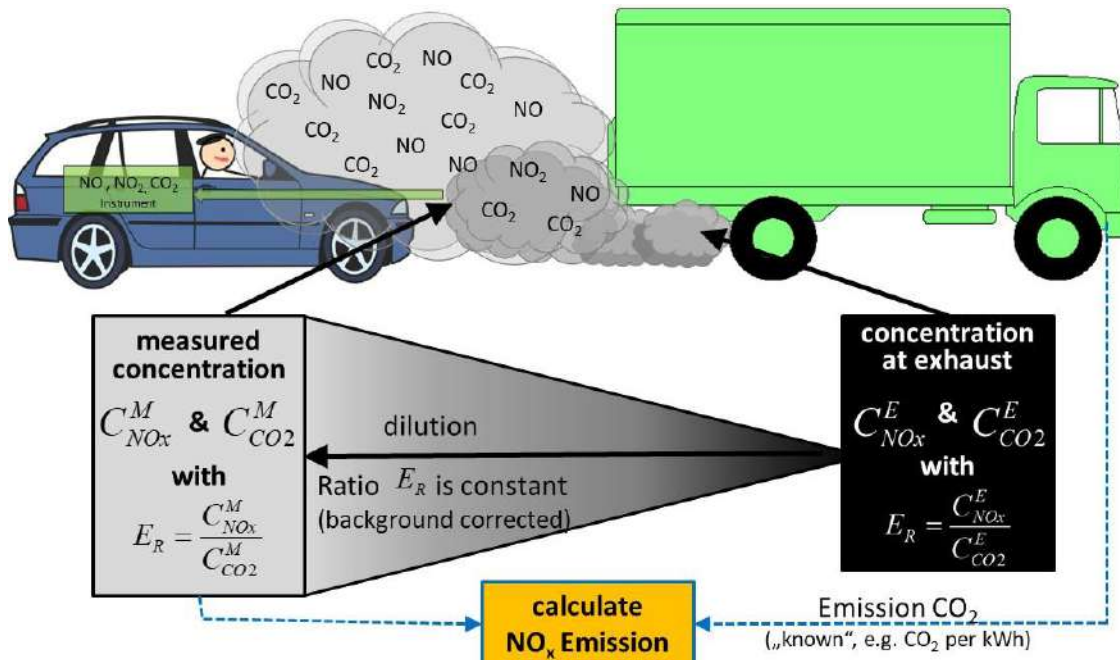


Figure 1: Plume Chasing measurement principle illustrated for NO_x. In a chasing vehicle the investigated pollutants (e.g. NO_x, PM) are measured together with CO₂. After correction of background concentration, the ratio of pollutant to CO₂ allow the calculation of the emission value with known CO₂ emission.

To fill the gap between PEMS and RS, we apply and further develop the new Plume Chasing method (Figure 1). It allows to investigate reliable the emission of individual vehicles with a lower demand than PEMS. Main applications are the real driving emissions of a vehicle fleet to indicate high emitters. For example, public busses can be studied to derive the high emitters which need to be repaired or exchanged. Also the reliable detection of high emitters due to a malfunction in the emission cleaning system or even manipulation are possible. We here present validation studies of the Plume Chasing method and different applications.

Requirements for individual vehicle emission measurements

The emission regulation defines the maximum allowed emission averaged over a complete test cycle. On a short time scale the emissions can vary significantly from its average value, not only due to varying engine power (or fuel consumption), but also in the ratio to CO₂. The main reason is the strong fluctuation of emissions and needed regulations of the emission cleaning system leading to a variability of the emission reduction. Thus also a correct working EURO VI or V truck can on short time show emission values of a EURO III or II truck. Different studies show that NO_x RDE of EURO V show on short periods large variability, also significantly above the EURO Emission norm (e.g. TNO 2014, TNO, 2016). But lower variability and average emissions below the EURO Norm are found on the highway where more constant driving conditions are found (Kleinebrahm, 2008; TNO 2014, TNO, 2016). EURO VI trucks show typically emission values with lower variability and they better agree to the EURO Norm (e.g. TNO 2014, TNO, 2016).

The statistical variance (and thus accuracy) of the emission ratio in dependence of the averaging time is shown in Figure 2 for two trucks derived with PEMS. Note this is the statistical variance, individual emission values can vary even more. The derived short term emission values are compared with the average emission of a complete test cycle. A short averaging like for RS measurements (left end of the plot, yellow shaded area) feature a large deviation and thus a large error on the investigated emission. Different colour lines indicate two different trucks one EURO V and one EURO II and also measurements at different road sections or exclusion of cold start. Trucks without SCR systems like the EURO II show a lower variability like expected. Emissions vary less at relative constant driving conditions like on a highway. Blue shaded area indicate the typical averaging period for plume chasing (3 to 10 minutes) for each investigated vehicle.

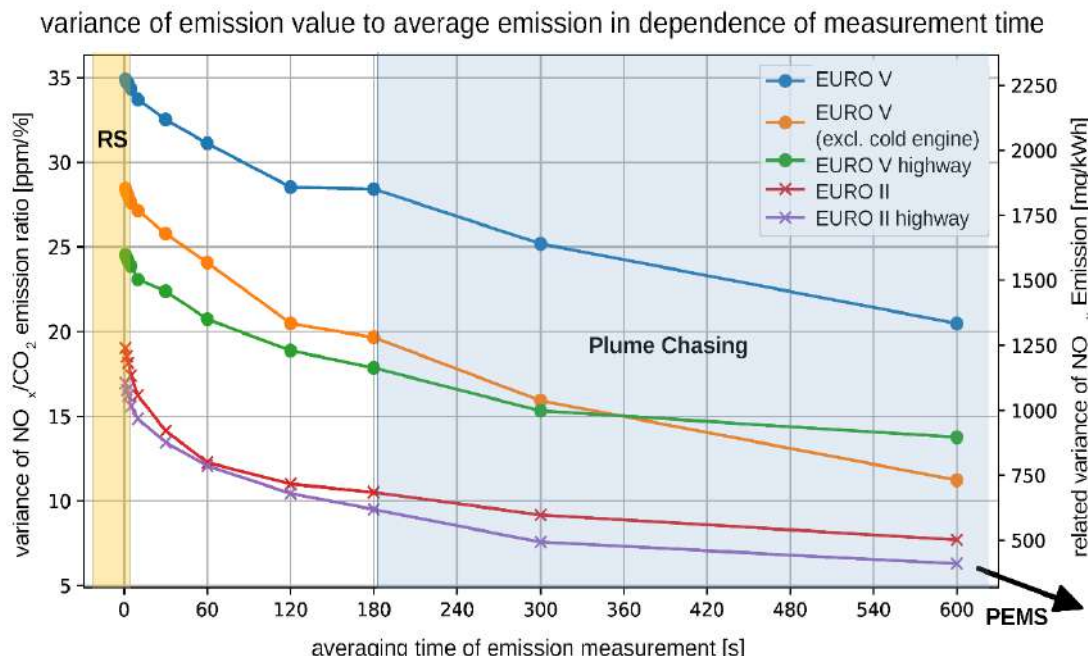


Figure 2: Statistical variance of an individual emission value to the average emission in dependence of the averaging time of the value for a EURO V and EURO II truck.

That mean to derive a reliable emission value of an individual vehicle the measurement has to average over a representative period and should be performed at driving condition with relative constant conditions like on the highway. For example, to identify a EURO V truck with a defective emission

system, and thus on average higher emissions, the derived emission value should have an accuracy of typ. 1000mg/kWh. For a measurement on the highway (green curve in Figure 2) this requires a measurement over 300s (=5min). A snap shot measurement of the emission, like done with RS technique, does not fulfil these criteria. Plume Chasing can easily measure over several minutes and even on the highway to achieve these accuracies.

Plume Chasing

Plume Chasing measurements (sometimes also called sniffer car) is based on a gas observation in the diluted emission plume of the investigated vehicle. A chasing car samples air in the diluted plume behind the investigated vehicle (Chui et al., 2016; see Figure 1) and analyse the gas sample. Due to dilution of the air, the observed concentrations do not provide a direct emission value and additional the measurement of a reference gas is required. The reference gas is CO₂. Its emission value is well defined over the fuel consumption. The calculation of emissions (emission ratios) is similar to the well-established Remote Sensing (RS) technique, by using the ratio of the desired trace gas or particle to the CO₂ (Bishop and Stedman, 1996). First the measured concentrations are corrected by its background level outside the plume. Afterwards the ratio E_R of the pollutant to CO₂, e.g. NO_x / CO₂, is derived. The ratio E_R is constant in the plume, directly at the exhaust pipe or few meters behind the vehicle, as all gases have the same dilution. With strong dilution the concentrations cannot sufficiently be separated from the background any more. Thus we define a threshold of 30ppm CO₂ above background concentration to indicate sampling inside the emission plume. Measurements at lower concentration are not used for the emission calculation. From sensitivity studies we observed this 30ppm as best compromise. A higher threshold would reduce the amount of valid measurement points, but no significantly difference in the average emission ratio for an individual vehicle was found. If even lower threshold would be chosen we observe a change in the observed emission ratio, likely as than other emission from other vehicles more influence the measurements. Background concentrations needed for the data analysis are taken automatically from the measurement time series as in between the vehicle regularly show low emissions (concentrations are than similar to background levels) or we observe the background before approaching the vehicle or while overtaking. In practice the algorithm searches the data point with lowest CO₂ concentration while measuring a vehicle plus a time window of 2 minutes. The CO₂ and NO_x concentration during this time are used as background value. But it needs to be considered that changing different background concentrations need to be considered or excluded. Therefore, we exclude measurements in tunnels and treat measurements on different road times separately (e.g. a country road separated from a high way). Also other background measurements are possible (e.g. measurement background concentration over a separate inlet, different selection of background concentration), but extensive investigations show, that the selection of the correct background only minor influence the derived emission value and is thus not critical (Roth, 2018). However, plume sampling can still be optimised to measure higher concentrations of the emission, as than the error of the background correction plays a minor role and influence of other vehicle emissions can be reduced. Optimising the sampling for plume changing is thus still topic of current investigations.

If emissions of other vehicles dilute into the investigated emission plume a measurement error arises according to its proportion. This is especially a problem in dense stop and go traffic with multiple driving rows. Emissions of a vehicle driving in front of the investigated vehicle has only a minor influence of up to 10%. This is typically uncritical, but can in extreme cases (e.g. very high emitter in front of a low emitter) cause significant measurement errors with an overestimated emission up to a factor of two. It is thus obvious that Plume Chasing cannot achieve the accuracy of PEMS.

From the emission ratio E_R an emission factor of the pollutant, e.g. E_{NO_x} , can be calculated using the known CO₂ emission E_{CO_2} . For vehicles >3.5t (trucks and busses) E_{CO_2} per kWh is needed to calculate the emission per kWh. E_{CO_2} can be estimated over the engine efficiency and the carbon content of diesel. We apply an engine efficiency of 40%, which is a very optimistic energy efficiency of a truck and corresponds to a best case emission calculation (lower efficiency result in higher emission factor). For vehicles <3.5t (cars) E_{CO_2} per km is needed to calculate the emission per km. E_{CO_2} is measured or estimated from data bases (HBEFA). This estimation may introduce errors of 20% which are still lower than typical emission variations.



Figure 3: Mobile ICAD NO_x instrument of Airyx GmbH used for Plume chasing. The instrument fits in the easily in any car boot.

We apply a IR CO₂ Sensor and a ICAD-NO_x instrument from Airyx GmbH for our plume chasing studies. In the ICAD NO is converted to NO₂ so that all NO_x is in the form of NO₂. Afterwards it is optically measured by its characteristic differential absorption features which has the large advantage to avoid interferences with other emitted gases. The measurement with 2 seconds time resolution has an accuracy of ~0.5ppb. The used instruments feature perfect mobile performance with high time resolution, high accuracy, large measurement range and low power consumption and are thus ideal for this application.

Validation

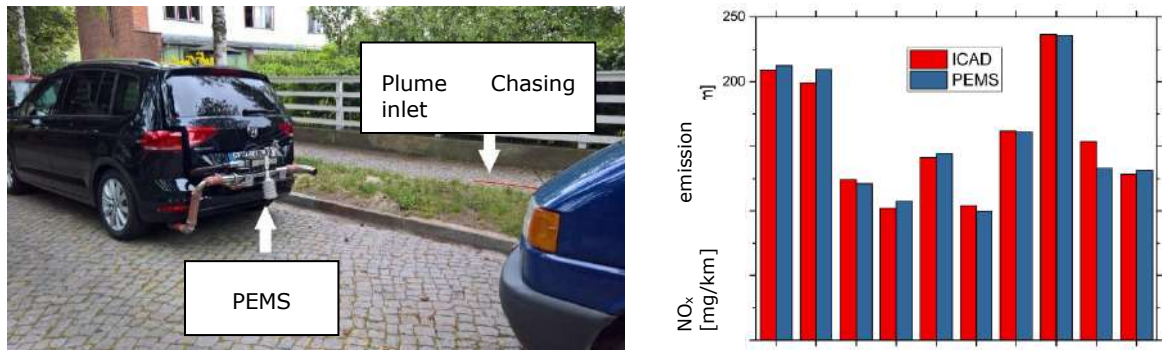


Figure 4: Validation measurements of Plume Chasing passenger diesel cars. Emissions were compared over a test cycle of 31km. The NO_x emissions derived for each cycle are compared for the two instruments (right plot).

We performed several different validation campaigns of NO_x emissions derived with Plume Chasing vs. PEMS for passenger cars (vehicles <3.5t) as well as trucks (vehicle > 3.5t). General a good correlation can be observed. Figure 4 show the measurement for two different EURO 6 passenger cars over a real driving test cycle of 31km in urban and suburban area (Krufczik, 2017). PEMS and Plume Chasing (ICAD instrument) derive for each test a very similar NO_x emission with an agreement typical of ~5% (10mg/km). The variation between the test cycle is due to a variation of the emission, but observed by both techniques. In cycle 9 (Figure 4 right plot) Plume Chasing observes a higher emission caused by a disturbance from an old diesel van with very high emissions driving a long distance in front of the investigated car.

In another study we investigated how good Plume Chasing can also capture short term emission variations like measured with PEMS (Reber, 2018). Figure 5 show one example of pulsed accelerations. We achieve best correlation for small and moderate speeds and distance to the vehicle up to 25m. For larger distance and high driving speed of min. 80km/h often only 30% of the measurements are in the emission plume. This directly result in larger error of short term emission values up to 25%. The result show that at good measurement conditions with small vehicle distance and moderate speed Plume Chasing can observe short term emission variations with time resolutions of ~10s. But data also show that short measurements are more affected by disturbances from other vehicles than this is the case for the average value.

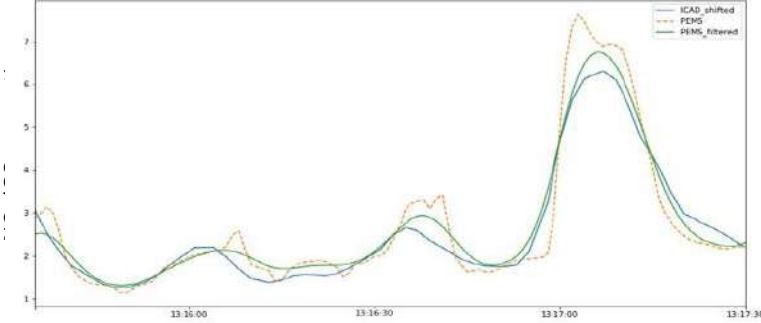


Figure 5: Validation measurements of Plume Chasing (ICAD instrument) with PEMS for short term emission variations during incremental acceleration. We average the PEMS data over 10s (filtered) and shift to get agreement with Plume Chasing.

Beside validations with cars also extensive validation studies for truck NO_x emissions were performed for BAFU (Bundesamt für Umwelt, Switzerland) together with EMPA (Switzerland) (Roth, 2018). The emissions of 3 test trucks ranging from EURO II with high emissions, EURO V (moderate emission) to EURO VI (low emissions). The goal was to investigate how reliable Plume Chasing can separate high from low emitters at different conditions. This would allow to detect defective or manipulated emission cleaning systems of EURO V and EURO VI trucks. Unfortunately, the PEMS measurement in the study did not derive realistic emission values. They were over long distances unrealistic 0mg/kWh. Thus only a comparison of EURO II and V was possible. An example of a EURO V is shown in Figure 6 where different road sections with very different driving behaviour and traffic load are included.

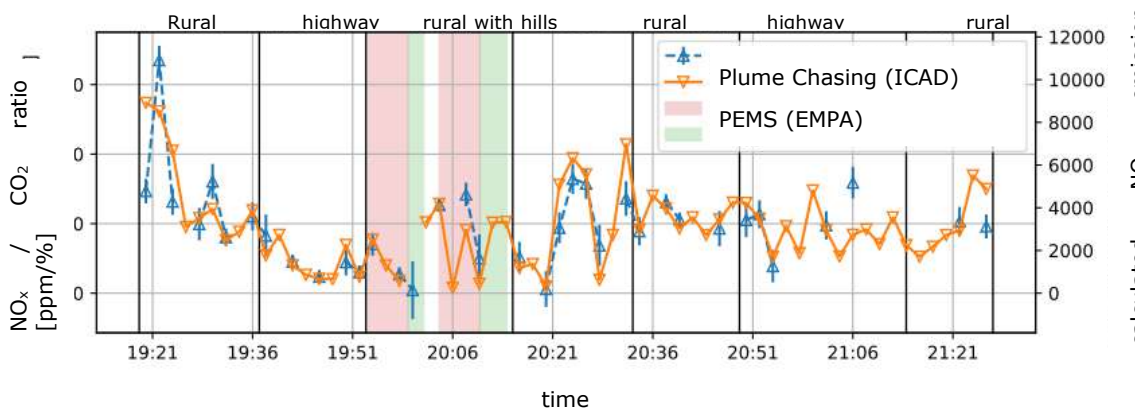


Figure 6: Validation measurements of Plume Chasing (ICAD instrument) with PEMS of a EURO V truck over different road sections. Compared are 2-minute average emission ratios.

Compared are emissions ratios of NO_x/CO₂ averaged over 2 minutes ranging up to 160ppm/% (correspond to 12.000mg/kWh). If the signal of the plume was too weak for the plume chasing method (less than 30ppm CO₂ above background) no emission value is derived. A good agreement between the two methods is observed, even if measurement conditions were difficult at dense highways, hilly roads and even urban sections. Over all truck measurements a correlation of R=0.88 is achieved with slope of 0.83 (lower emissions with plume chasing). Especially for the EURO II PEMS derives higher emission values. Reasons can be uncertainties in the Plume Chasing method or interferences of the PEMS technique. Best agreement was achieved on rural roads and uphill (R=0.91 and R=0.93 respectively) and also good agreement on highways (R=0.89). For a measurement over several minutes an agreement of 100mg/kWh can be achieved.

All validation studies show that Plume Chasing can derive NO_x emission values relatively simple and reliable, but not with accuracies like PEMS. No significant overestimation was observed. Thus it can be used to simply investigate emission of individual vehicles and to identify high emitters. They also show that PEMS can feature problems and observe wrong emission values which need to be further investigated.

Study emissions of a public bus fleet

We analysed the emissions of public busses in few German cities. Examples are shown in Figure 7 for the city of Reutlingen and Figure 8 for Heidelberg. Real emissions of the busses are often unknown and thus it is not precisely known how much the public busses contribute to total NO_x emissions and NO₂ air pollution problems in the city.

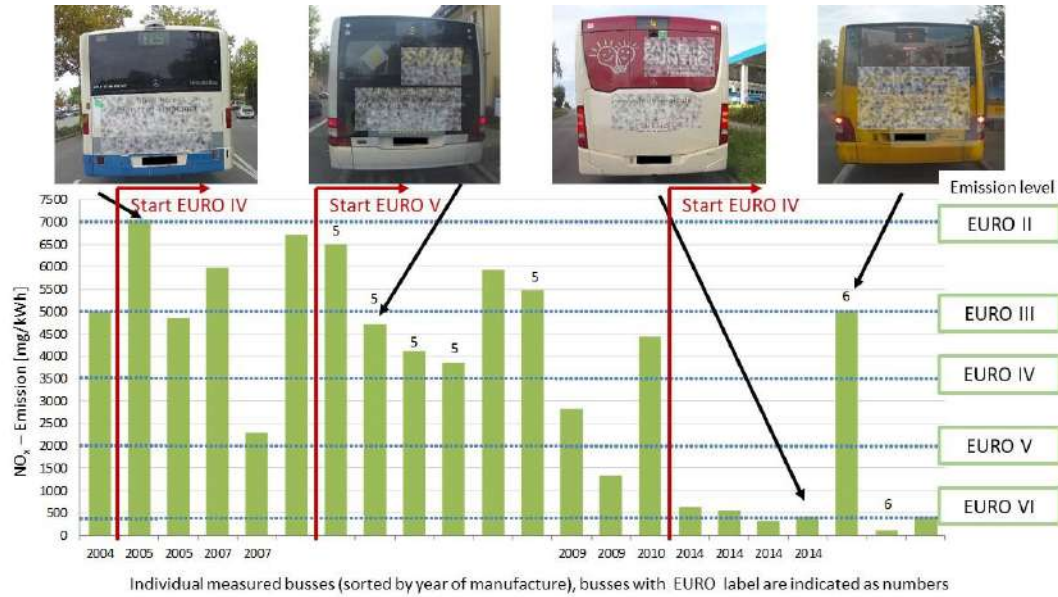


Figure 7: Public bus NO_x emissions in Reutlingen. Each column represents an individual bus, sorted by year of construction. If precise construction date or EURO class are known, they are indicated. Dotted lines indicate the EURO emission Norm.

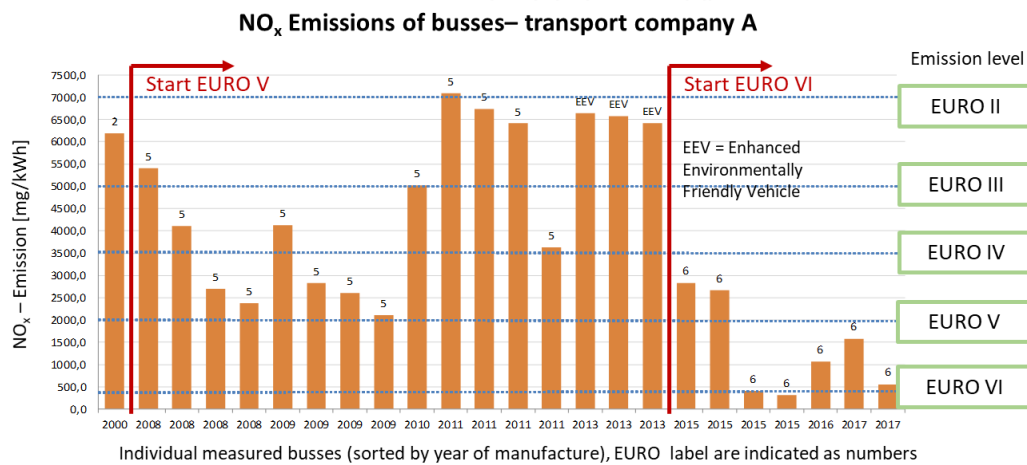


Figure 8: Public bus NO_x emissions in Heidelberg (similar to Figure 7) of one specific transport company where bus data are provided.

Figure 7 and Figure 8 show that real driving emissions in the city up to EURO V are much higher than the EURO emission norm which is related to the old emission test procedure. Interesting is that even newer EURO V – EEV (Enhanced Environmental Friendly) busses show often the highest emission value up to 7000mg/kWh (EURO II level). A significant reduction can be observed for EURO VI busses (on average 663mg/kWh), often even below the EORO VI emission norm. The reason for this improvement are stronger emission test procedures introduced for EURO VI including real driving emissions. Few individual EURO VI busses feature much higher emissions (see Figure 7) indicating a defective emission system. Also some older EURO VI seem to feature higher emissions (see Figure 8) indicating a degradation of the SCR system. These studies demonstrate that investigations of the public bus fleet allow cities to perform decisions on the fleet to effectively reduce its emission. For example,

we estimate that the NO_x bus emissions in Heidelberg could be reduced by 80% if all busses with emissions above 2000mg/kWh are upgraded or exchanged to EURO 6 level with real driving emissions observed in the study.

Truck emission studies – identification of manipulated emission systems

For truck emissions we focus on the identification of high emitters due to manipulated or defective SCR systems. So called AdBlue® emulators simply switch off the SCR systems to save AdBlue® consumption (up to 2000€/year), but also to avoid an expensive maintenance exchange of the SCR system. As a result, truck emissions increase significantly. AdBlue® emulators are already available for 25€ and are easy to install. There are two kinds, hardware and software emulators. Hardware emulators are a small electronic which is installed in the truck. They can be located at positions which are difficult to reach (below the trailer) and thus they are difficult to find in a control. The software emulators are a manipulated engine software which is uploaded to the truck and popular for EURO VI trucks. There is no physical modification of the truck. So far it is not possible to detect these emulators. Modern emulators have many features which additionally make it difficult to detect them, e.g. emission reduction is applied only above a certain speed so that detection requires a higher driving speed. Additionally, AdBlue® consumption arise even if it is much lower. Also optional DPF or EGR manipulation is possible. Current controls focus on the observation a physical hardware emulator. It is obvious that only a small portion of the hardware emulators are found due to its small size, and no possibilities to observe software emulators. Thus official numbers of manipulations arising from these controls (1-3%) underestimate the number of manipulated trucks.

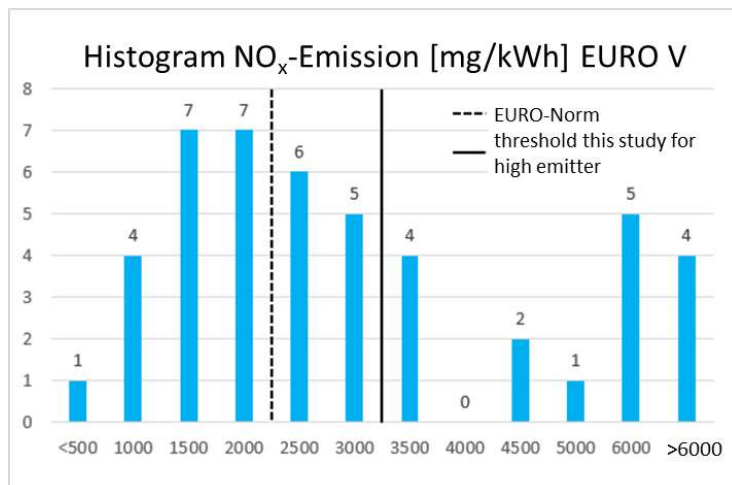


Figure 9: Histogram of observed EURO V truck emissions in Austria, 2018.

With Plume Chasing we can reliable identify high emitters and thus quantify the amount of potentially manipulated trucks. In the last years we performed studies in Germany (254 trucks), Austria (215 trucks) and Switzerland (39 trucks) mainly performed on high ways. Due to warm engine and relative constant driving behaviour, reliable emission measurements can be observed (see Figure 2, TNO 2014; TNO 2016). On the other hand, this mean that at such driving conditions a high emission over several minutes cannot be explained with an engine effect, but mainly due to a defective or manipulated emission system. As threshold for such a high emitter we use the EURO Norm emission value + a tolerance of 1000mg/kWh (resulting in 3000mg/kWh for a EURO V, 1400mg/kWh for a EURO VI).

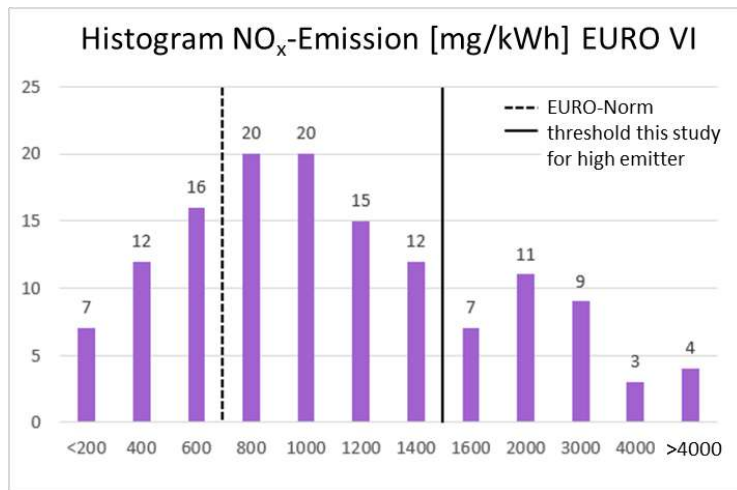


Figure 10: Histogram of observed EURO VI truck emissions in Austria, 2018

Figure 9 and Figure 10 show the histogram of observed emissions for the study in Austria 2018. A good separation between low and high emitters is visible. Many trucks show consistently high emissions and use potentially AdBlue® emulators. These trucks originate mostly from east and south Europe. Up to 35% of EURO V trucks are affected and up to 25% of EURO VI trucks (Table 1). It clearly shows that also EURO VI trucks are often manipulated. The higher percentage in Austria may be due to a different truck fleet or to an increase in manipulations. The percentage is much higher than for controls due to the mentioned difficult observation. Plume Chasing is probably currently the most reliable method to easily and reliably identify these individual high emitters. We also observe a correlation of the high emitters with transport agencies. In the study in Austria few suspicious trucks could also be investigated in a police control. For half of these trucks a suspicious electronic device like a hardware emulator could be observed or errors in the SCR system. The later could also originate from an emulator. The large amount of high truck emitters has a significant impact of total NO_x Emissions of the transport sector.

Table 1: Percentage of observed high emitting trucks with potentially manipulated SCR emission systems.

Percentage of high emitters	EURO V	EURO VI
Germany, 2016		
German trucks	0%	6.9%
non German trucks	26%	19%
Austria, 2018	35%	25%

Acknowledgements

We acknowledge for scientific contribution, measurements and data EMPA (Dr. Thomas Büttler group), Dr. Axel Friedrich and Deutsche Umwelthilfe (DUH). For financing we acknowledge EXIST Forschungstransfer Project (FKZ: 03EFGBW121), Land Tirol (Austria), BAFU (Switzerland), Camion Pro e.V., ZDF, SRF.

References

- Bishop G.A., and Stedman D.H. (1996). Measuring the Emissions of Passing Cars, *Acc. Chem. Res.*, 29, 489-495.
- Kleinebrahm, M. et al. (2008). On-Board Measurements of EURO IV / V Trucks, *Final Report, a research project of the Federal Environmental Agency (FKZ: 204 45 144)*, Germany, TUV NORD Mobilität.
- Krufczik C. (2017). Mobile NOx-Emissionsmessungen an Fahrzeugen mit einem ICAD-Messinstrument, *Bachelor thesis, University of Heidelberg*.
- Pöhler D. and Adler T. (2017). Bestimmung von realen Lkw NOx Emissionen (Real Driving Emissions) auf deutschen Autobahnen, *public report, Institute of Environmental Physics, University of Heidelberg*.

Pöhler D. and Engel T. (2018), Bestimmung von LKW NOx Emissionen (Real Driving Emissions) auf Tiroler Autobahnen und potenziellen Abgasmanipulationen, *Final report, Institute of Environmental Physics, University of Heidelberg*.

Reber J. (2018). Mobile NOx-Emissionsmessungen an Stadtverkehrsbussen mit einem ICAD-Messinstrument, *Bachelor thesis, University of Heidelberg*.

Roth U. (2018). Optimierung und Validierung des "Plume Chasing" Verfahrens bei LKWs, *Bachelor thesis, University of Heidelberg*.

TNO (2014). The Netherlands In Service Emission Testing programme for Heavy-Duty 2011-2013, *TNO 2014 R10641*.

TNO (2016). The Netherlands In-Service Emissions Testing Programme for Heavy-Duty Vehicles 2015-2016 – Annual report, *TNO 2016 R11270*.

2.7.4 Multi-instrument enhancement of remote sensing on-road vehicle emissions measurements

R. Smit¹, Bainbridge, S.², Kingston, P.¹, Brown, M.K.¹, Shaw, G.¹

¹ Emission and Air Modelling, Department of Environment and Science (DES), GPO Box 2454, Brisbane, QLD 4001, Australia, robin.smit@des.qld.gov.au

² Strategic Policy, Department of Water and Environmental Regulation (DWER), Locked Bag 33, Cloisters Square, Perth, WA 6850, Australia

Introduction

The use of remote sensing to measure vehicle emissions is not new, dating back to 1971. Remote sensing has been used extensively over the last decades for various purposes around the world, including but not limited to identification of high-emitting vehicles, examination of on-road vehicle emissions distributions, trend analysis and model validation (NIWA, 2015).

An on-road measurement campaign was conducted at two locations in Brisbane, Australia: a freeway on-ramp (Macgregor 4-5 September 2018, denoted as FWY) and a heavily trafficked urban road (Taringa 6-7 September 2018, denoted as URB). Figure 1 shows the test sites.



Figure 1: Instrumented road sections at two test sites (left FWY, right URB).

This work is a follow up research project from an earlier tunnel study (Smit et al., 2017) and part of a larger validation program for the Australian vehicle emissions software programs COPERT Australia and PΔP. This study has used a RSD (remote sensing device) to provide snapshot information on vehicle emission distributions, as well as instantaneous pollutant-to-CO₂ emission ratios for individual vehicles. However, the program was taken a step further than 'conventional' RSD programs, with the specific aim to examine data accuracy, enhance data capture rates, better understand reliability and usability and potentially address specific issues (bias) that relate to the use of RSD. Remote sensing has specific strengths and certain limitations, when compared with e.g. dynamometer and on-road PEMS testing (and vice versa). They are not further discussed here as other publications have done so comprehensively (Smit and Bluett, 2011; NIWA, 2015).

Equipment and Methods

The road sections were instrumented with a RSD and a range of additional measurement devices, namely automatic pneumatic loop detectors, a dedicated license plate camera, a thermal imaging camera, a network of Bluetooth MAC address units, two integrated air quality monitoring stations and speciated VOC (volatile organic compounds) sampling equipment. The additional equipment provides for independent verification of the robustness and accuracy of RSD monitoring data (emissions, driving behaviour), provision of additional information, and correlation with on-road air quality.

An Accuscan RSD4600 was used to measure vehicle emission concentrations of CO, NO, HC, 'UV smoke' and CO₂, and includes a Source Detector Module (SDM), a speed-acceleration bar and a video camera to capture an image of the vehicle's license plate (LPN). The remote sensing system uses the principle that the majority of gases will absorb light at particular wavelengths. It measures on-road emissions by absorbance of ultraviolet (UV) and infrared (IR) light across an open (optical) path using wave-length specific detectors for different air pollutants. The RSD consists of an IR component for detecting CO, CO₂ and HC, together with an UV spectrometer for measuring NO.

Three sets of automatic pneumatic loop detectors were installed at each site for a period of two weeks to collect traffic count data and speed and acceleration data for individual vehicles. The loop pairs (i.e. two closely spaced loops) had a separation distance of 1m. The distance between the loop pairs was 15m and 20m for the URB and FWY sites, respectively. The middle loop set was located as close to the RSD acceleration/speed bar as possible (about 2m upstream). Data loggers were set to an atomic clock.

A specialised license plate number camera (Reconyx MS7 Microfire) was purchased and installed about 15m upstream from the RSD to provide complete information of the on-road traffic composition. Bluetooth MAC address units were installed in the road network around the measurement sites, with the aim of tracking individual vehicle movements in time and space before the RSD measurement took place (cold vehicle detection). In addition, a thermal imaging camera (Noptic Thermal Camera, Strategic Innovations, STH1000) was used at the RSD site to record, visualise and analyse the thermal profiles of individual vehicles.

Two integrated air quality monitoring stations (AQM65) were installed at the urban site only, 7m upstream of the RSD SDM and on both sides of the road (1m from road markings and on the kerb) to monitor on-road minute-by-minute ambient concentrations of CO, NO_x, NO₂, O₃, VOCs, PM₁, PM_{2.5}, PM₁₀ and CO₂. Local meteorology (wind speed/direction, temperature, humidity, etc.) was measured using a Vaisala WXT520. Summa canisters were also installed on site to provide VOC speciation of on-road emissions.

The collective set of measurements provides a rich and unique database that can be analysed in various ways. This paper presents the results of selected and specific analyses. It is noted that this is by no means exhaustive, considering the amount of data and information that has been generated. Therefore future publications will further elaborate and expand on this work.

RSD Database

A total of 11,376 vehicles were measured by the RSD in September 2018, with 7,668 valid samples with recorded LPNs (67%). Cross-referencing LPNs with the Queensland vehicle registration database resulted in 6,850 vehicles with a valid LPN, i.e. a 60% overall capture rate in the RSD data as defined as a proportion of the total number of RSD samples.

The RSD measurements contain valid concentration and speed-acceleration readings, but may contain invalid RSD vehicle images. RSD images can be illegible (e.g. dirty LPN) or out of view. An error can also be made during manual LPN entry. The second LPN (Reconyx) camera is located further away from the road, provides good picture quality and has a wider view. Hence it is able to capture vehicles that are out of view for the RSD camera or suffer from poor picture quality. Images taken with the specialised license plate camera were used to verify and supplement the RSD database. The dedicated LPN camera provided LPN information for an additional 518 vehicles, leading to a significant increase in overall RSD capture rate from 60% to 65%.

Vehicle images collected by both the RSD and LPN camera were put through an automated LPN recognition process. The Open ALPR (ALPR, 2018) open source software library was used to automate the identification of vehicle number plates from a total of 53,576 images (RSD 11,374 and LPN Camera 42,202 images) within a Microsoft Windows operating environment. The Open ALPR API was chosen for its advanced configuration options and availability in many popular software languages. Adobe Photoshop was used to pre-process images in order to convert images to grayscale and increase the levels of contrast and brightness to improve readability by Open ALPR. Python was used to automate the collection of the output from Open ALPR, extract image file metadata and summarise results into CSV format. The process was completed with a manual check where missing LPNs were determined by visual inspection of the images.

The automatic loop detectors provided vehicle count data, as well as speed and acceleration data for individual vehicles. Loop detector data were synchronised with the RSD measurements to supplement

the RSD database and to compare speed/acceleration data. The RSD collected 810 valid concentration measurements with invalid speed and acceleration readings, representing a significant loss of data (7%). Loop detector data can be used to provide valid speed and acceleration data for these missed vehicles. The loop detectors provided data for an additional 611 vehicles of which 584 had valid LPNs. Hence, overall RSD capture rate increased significantly from 65% to 70%. As a consequence, valid RSD emissions data were collected for a total of **7,952 vehicles**. This is a good overall result since capture rates for RSD studies are typically about 30-70% (NIWA, 2015).

RSD does not capture all vehicles passing the RSD, i.e. a proportion of the on-road fleet is missed. This means that the actual capture rate in terms of the on-road fleet is lower than 70% (defined as the proportion of the total number of RSD samples). Figure 2 shows traffic count data derived from three types of equipment (loop detectors, LPN camera and RSD), and broken down by vehicle type (light duty vehicle - LDV and heavy duty vehicle - HDV).

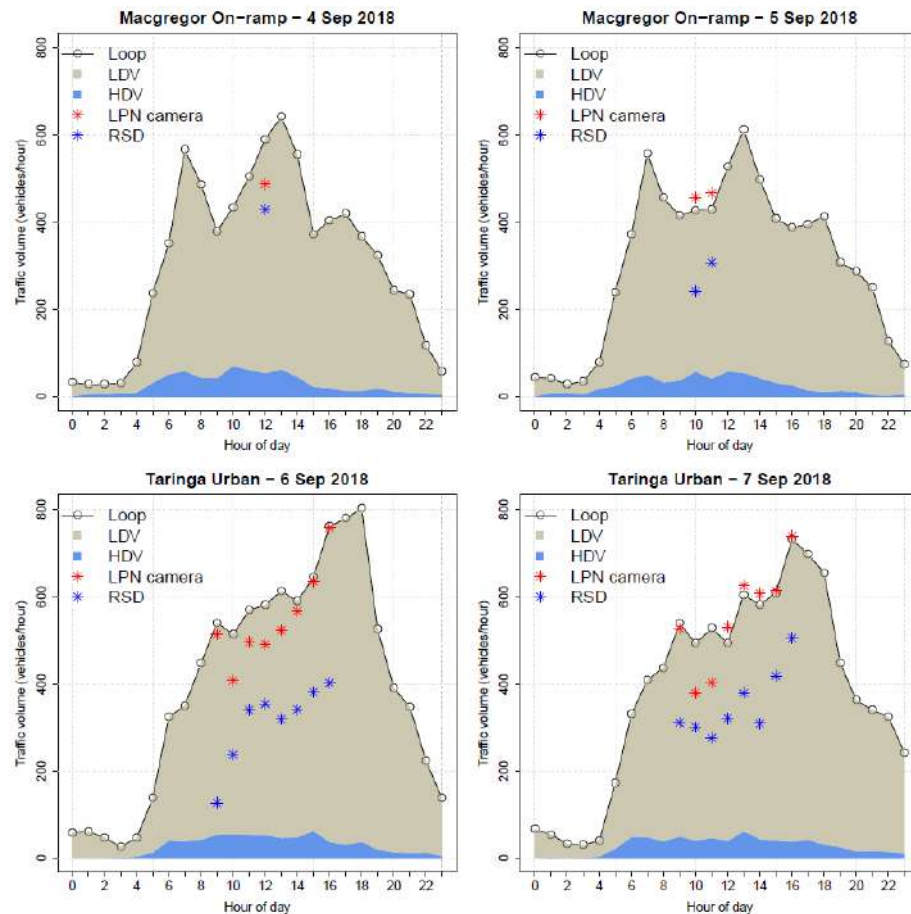


Figure 2: Hourly traffic volumes by day, site and different types of equipment.

The loop detectors provide classified vehicle count data. These data show that the proportion of heavy-duty vehicles (HDVs) varies with time and location but is, on average, 10% at the FWY site and 7% at the URB site. Count data derived from tallying the number of images taken with the LPN camera within a particular hour are generally comparable with the hourly loop counts with an average capture rate of 94% and an hourly variation of about $\pm 15\%$. This implies that the LPN camera tends to capture most on-road vehicles and should provide a good understanding of the on-road fleet, provided that valid license plates are extracted from the images.

It suggests that the dedicated LPN camera could also be used as an alternative vehicle count device, for example in the absence of loop detectors, which are relatively expensive to install and operate. It is noted that count data derived from tallying the number of images taken with the RSD camera (not shown in Figure 2) within a particular hour gives slightly lower performance as compared with the LPN camera with an average capture rate of 90% and an hourly variation between 40% and 97%.

Figure 2 shows that count data derived from tallying the number of RSD images with valid samples within a particular hour leads to an actual capture rate (expressed as proportion of vehicle counts) of

62%, which is lower than 70% mentioned before (expressed as proportion of the total number of RSD samples), and a significant hourly variation between 24% and 74%.

Speed and acceleration data

Speed and acceleration data are used to compute vehicle specific power (VSP) to quantify driving conditions, as will be discussed later. Figure 3 shows the measured loop detector and RSD speeds and accelerations for individual vehicles in the RSD database, including a 45° line.

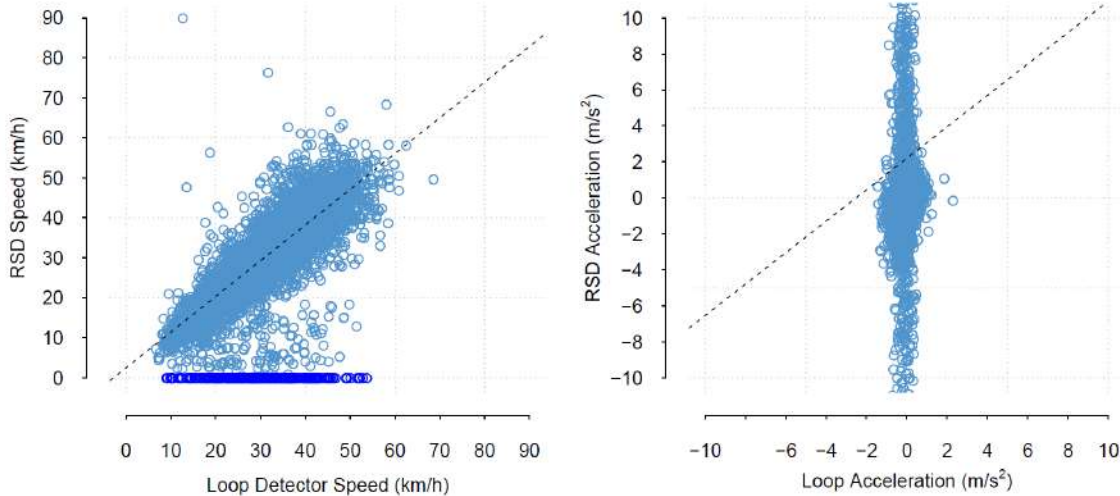


Figure 3: Comparison of RSD and loop detector speed and acceleration data.

RSD speeds vary between 0 and 90 km/h and have a larger range compared with the loop detector data (6-69 km/h). The difference is (partly) explained with the short distance of the RSD speed-acceleration bar (0.9 m) versus the longer distance loop detector distances (30-40 m). For a travel speed of 50 km/h, it will take a vehicle about 0.05 seconds to pass the RSD bar and 2-3 seconds to pass the loop detectors, providing longer averaging times (and hence reduced variability) in the loop speed measurements. Nevertheless, RSD speeds exceeding 70 km/h appear unrealistic, and indeed these speeds are flagged as invalid by the RSD.

About 3% of the RSD measurements are recorded as zero speed (dark blue dots, left plot), and are also flagged as invalid, whereas the loop detectors report vehicle speeds between 9 and 54 km/h for these vehicles. The left plot in Figure 3 suggests there is tendency for the RSD to report speeds that are too low, which will affect the accuracy of VSP estimates.

The RSD reports extreme and unrealistic accelerations varying from -110 m/s² to +138 m/s², which are flagged as invalid by the RSD. Valid RSD accelerations vary between -6.0 and +4.0 m/s², whereas the loop detectors have a much narrower range and vary between -1.4 and +2.3 m/s², as is shown in Figure 3. Note that the acceleration axis range in Figure 3 is capped at ± 10 m/s² for readability purposes, but that 4% of the RSD data are not shown as a result.

It is clear that the use of loop detector speed and acceleration data instead of RSD data will lead to substantially different VSP estimates. In this paper the VSP values provided by the RSD have been used. However, in future papers the impact of loop detector data on the analysis results will be explored.

Data analysis

The RSD reports concentration levels in the exhaust gas, i.e. CO₂ (%), CO (%) and HC (ppm) and NO (ppm), corrected for water and excess oxygen not used in the combustion process. However, the exhaust plume path length and the density of the observed plume are highly variable from vehicle to vehicle and are a function of the height of the vehicle's exhaust pipe, wind direction and speed, and turbulence behind the vehicle, amongst other factors. The RSD can therefore only reliably measure ratios of CO, HC and NO to CO₂. These ratios are assumed to be constant in a particular vehicle's exhaust plume. Due to the short time period involved in the measurement, this is expected to hold true

for reactive species such as NO as well. However, RSD data are naturally noisy and sufficiently large sample sizes are required to obtain significant results.

The RSD data were classified by vehicle category (vehicle type, fuel type, euro standard) and vehicle specific power (VSP). VSP normalises RSD data for ‘driving conditions’ and is commonly used as an explanatory variable in emission simulation, particularly in the USA (e.g. ISSRC, 2019). VSP (kW) is calculated by the RSD using speed and acceleration for each individual vehicle. Six VSP bins were used to classify the data. They are defined as $VSP < 0$ kW, $0 \leq VSP < 5$ kW/(metric) tonne, $5 \leq VSP < 10$ kW/tonne, $10 \leq VSP < 20$ kW/tonne, $20 \leq VSP < 40$ kW/tonne, $VSP \geq 40$ kW/tonne. It is noted that other researchers have used a larger number of VSP bins, e.g. 14 bins (Frey et al., 2003) and 2 kW/tonne bins (IVL, 2018). However, NIWA (2015) found that the difference between a 6 or 14 bin classification is not statistically significant when the variability in the RSD emissions data is considered. The six bins and their boundaries use a logical distinction in driving behaviour and generally ensure a sufficient sample sizes for each bin (Smit and Bluett, 2011).

As an example Figure 4 shows the results for a particular vehicle class, i.e. light commercial petrol vehicles (LCVP). Colour intensity is used to show the sample size for each VSP-Euro class bin. Single measurements ($n = 1$) were removed and are not presented. Figure 4 includes 95% confidence intervals for each bin. It is noted that for some small sample sizes, confidence intervals are very large and exceed the scale of the y-axis. No data were measured in the higher VSP bins for this vehicle class and are therefore not shown in Figure 4.

There is generally a downward trend in pollutant-to-CO₂ ratios, demonstrating the progressive impacts of improved vehicle emission control with progressive Euro emission standards. Although NO₂ measurement has recently become a feature of remote sensing (IVL, 2018), remote sensing studies have traditionally used RSDs that measure NO only, as is the case in this study. In contrast, on-road or laboratory measurements, as well as emission factors used in vehicle emission predictions, relate to the sum of NO and NO₂ (i.e. NO_x, expressed as NO₂ equivalents). For the particular vehicle class considered in this paper (LCVP), this is not a significant issue as petrol cars exhibit low NO₂/NO_x shares in the order of 2-5%, which are approximately independent of emissions standard (NIWA, 2015). Therefore, RSD NO data can be used as a reasonable proxy measurement of NO_x for this vehicle class.

High emitters

Vehicle fleet emissions are dominated by a small percentage of ‘high-emitters’ with excessive emission levels. This has been confirmed by laboratory test programs (e.g. Choo et al., 2007), remote sensing studies (Zhang et al., 1995) and tunnel studies (e.g. Smit et al., 2017). This skewness in emission distributions is – at least to some extent – due to the variability in emission profiles by vehicle type, the progressive introduction of cleaner engine and catalyst technology into the vehicle fleet and ageing effects of the in-use fleet.

Park et al. (2012) reported that the skewness of (~1 Hz) emission distributions for CO, hydrocarbons (HC) and NO_x as measured with RSD has increased over the last decade, whereas fleet-averaged emissions have decreased considerably. Bishop et al. (2012) noted that 1% of on-road vehicles in the USA contributed about 10% to total vehicle emissions in the late 1980s, and that this contribution of 1% of on-road vehicles now has increased to about 30%.

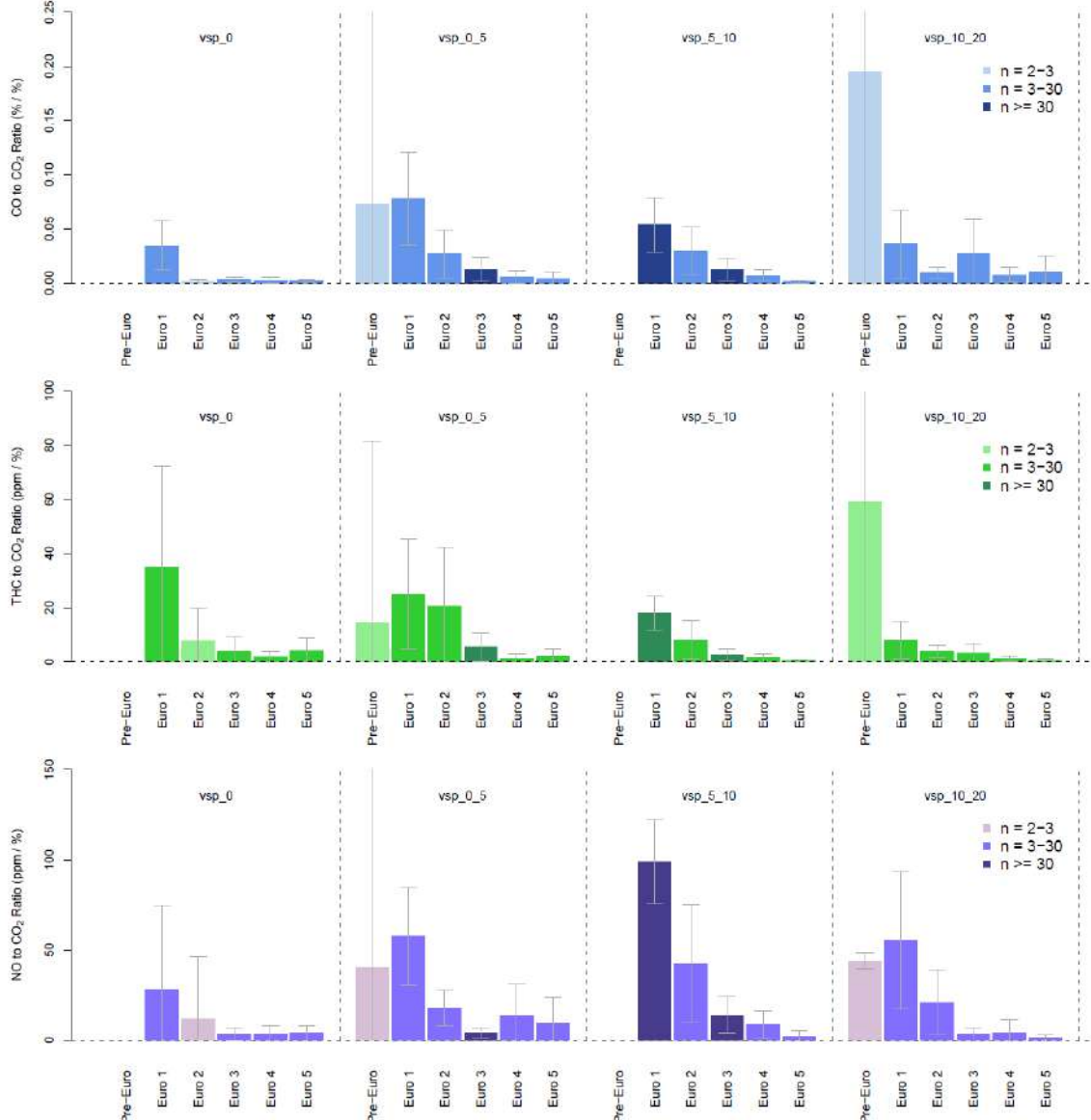


Figure 4: Binned mean pollutant-to-CO₂ RSD results for LCVP by pollutant and Euro class.

This change in on-road emission profiles reflects two main trends:

- 1) the penetration of cleaner vehicles into the fleet over time due to increasingly strict emission standards and improved control technologies with emissions behaviour that is characterised with generally low emission levels and brief and large emission peaks; and
- 2) the presence of vehicles that have excessive emissions, for example due to engine issues, malfunctioning or partly functioning emission control systems, incorrect repairs, lack of servicing and maintenance, poorly retrofitted fuel systems or even tampering.

Remote sensing has been used as a roadside real-time vehicle emissions information system to identify these high-emitting vehicles (e.g. Sjödin et al. 1997; Bishop and Stedman, 2008). However, there are other reasons that can lead to (temporarily) elevated emission levels. For instance, vehicle ageing has a significant and unavoidable effect (increase) on vehicle emissions, which is aggravated by poor maintenance and tampering.

Cold starts also lead to short periods with high emissions. Cold start emissions, and CO and HC in particular, are of increasing relative importance, due to strong reduction in hot running emissions on a per vehicle kilometre basis (Smit and Ntziachristos, 2013). Other reasons for excessive emission levels can be heavy vehicle loads or aggressive driving, where the latter can be identified with high VSP values.

It is thus important to find a method to identify true high emitters with technological issues that require repair, and not incorrectly identify vehicles in cold start mode or vehicles that have undergone 'normal' ageing. This last aspect is usually covered by analysing emission distributions for individual technology classes (e.g. Euro standards).

It is challenging to accurately determine if a vehicle is in cold start mode. Indeed, very few researchers have attempted to determine which specific vehicles operate in cold start mode. Monateri et al. (2004) reported on the (manual) use of an infrared camera to measure the heat signature of passing vehicles (exhausts, tyres, underbody) and determine if a vehicle is in cold start mode. A common approach is to make rather bold assumptions regarding on-road cold start modes. For instance, CRC (2006) simply excluded specific hours of RSD data for sites where "5% of newer vehicles had excessive HC emissions".

Two independent methods are used in this study to identify and explore the impact of cold start conditions on vehicles with significantly elevated emission levels.

- 1) Assessing the likelihood that a particular RSD site is impacted by cold start vehicles by employing a network of Bluetooth monitoring units at and around each location.
- 2) Using a statistical method to identify outliers/high emitters in the data, and subsequently analysing the thermal signatures of these individual vehicles.

Bluetooth Units

Six Bluetooth MAC (media access control) address units were installed at specific points in the road network, one at the measurement site (site 1) and the other units at sufficient distances away from the measurement sites, as is shown in Figure 5 (URB location).

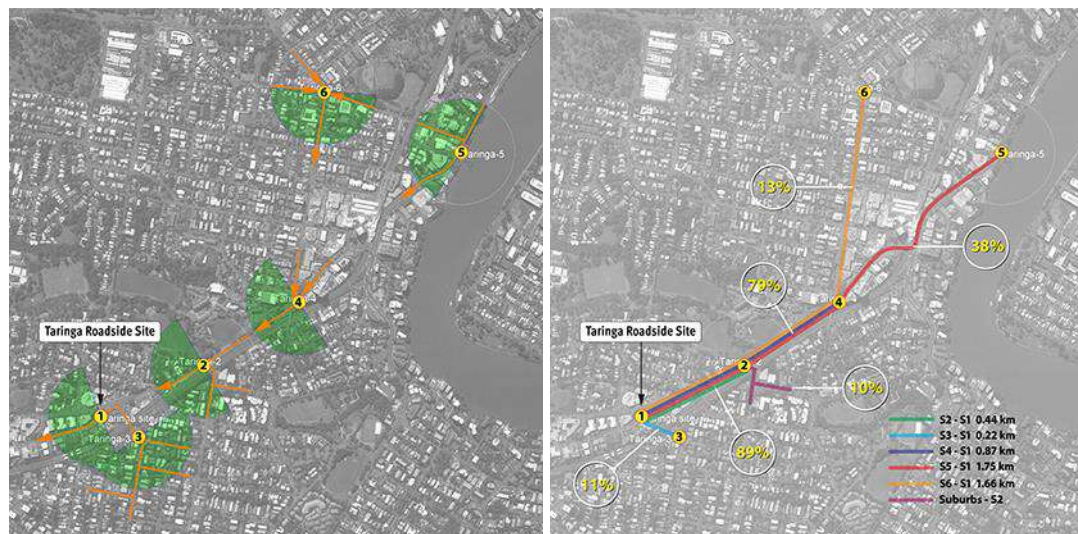


Figure 5: Network of Bluetooth devices (left); results of vehicle movement analysis (right).

The units record time stamps and log the unique MAC address of any Bluetooth device inside a vehicle (e.g. audio system) that is scanned by the unit when the vehicle passes by. This also includes the unique MAC address of the audio system from the vehicle itself. With this unique identification of the vehicle individual vehicle movements in time and space can be tracked before the RSD measurement took place at site 1. The method is relatively new and primarily used to calculate travel times between 2 or more nodes. The units typically capture about 15% of total vehicles passing a given point, and should therefore be regarded as a indicative sample of vehicle movements in the road network.

For this study, vehicles coming out of nearby suburbs are of particular interest as they could potentially be in cold start mode. Movements from/past sites 3 and 2 capture local traffic just before the RSD test site. It can be seen that a significant number of vehicles (about 20%) could potentially be driving in cold start conditions for the urban site. As a consequence, the RSD results are likely to be affected to some extent by cold start vehicles and analysis of thermal images is warranted.

Thermal imaging

High emitters are considered to be outliers in a statistical sense, i.e. observations with characteristics that are identified to be distinctly different from the other observations. Outliers can be determined in various ways e.g. through examination of univariate and multivariate distributions and at different scales. Outliers are determined as those observations that fall at the outer ranges of the distributions. Observations may occur normally in the outer ranges of a distribution, so the analysis will attempt to identify the truly distinctive observations and designate them as outliers. Outliers can be detected using 'standard z-scores'. A z-score represents the distance between the observation and the mean in terms of the number of standard deviations. The z-score is negative when the observation is below the mean and positive when above.

There is, however, one issue with this approach. Vehicle emissions are typically highly skewed with long tails to the right, reflecting occasional emission spikes. Outlier detection using z-scores assumes an (approximate) normal distribution. As a consequence, RSD emissions data need to be transformed before outlier detection can be applied. The aim is to achieve a more or less symmetrical and normal distribution of observed emission rates.

The Box-Cox procedure has been used to automatically select the best data transformation from a family of power transformations.¹⁴ Transformed data equals the actual data to the power of the transformation variable λ where, by definition, $\lambda = 0$ suggests a log-transformation. The z-scores are computed for each combination of vehicle category (e.g. LCVP Euro 3) and pollutant-to-CO₂ ratio, using these equations:

$$d_i^* = (1 + d_i + |\min(d_i)|)^\lambda$$

$$z_i = (d_i^* - \bar{d}_i^*)/s$$

Where d_i is the vehicle-specific RSD observation i , d_i^* represents a vector of shifted and transformed d_i values, \bar{d}_i^* is the mean of vector of values, z_i represents the computed z-score for the transformed vehicle-specific RSD observation i , and s is the standard deviation of the vector of d_i^* values. A log transformation may be suggested so d_i^* is shifted to be greater than unity. Z-scores have a mean of zero and a standard deviation of one. The value of λ is determined automatically by profile likelihood minimisation.

Z-score values larger than 4 standard deviation (SD) away from the mean qualifies as an outlier and are identified as a high emitter. Figure 6 visualises the approach. The left chart shows the original emissions distributions, and the right chart shows the same distribution after transformation using $\lambda = -0.7$. No observations with z-scores larger than 4 SDs were found for this vehicle category and pollutant.

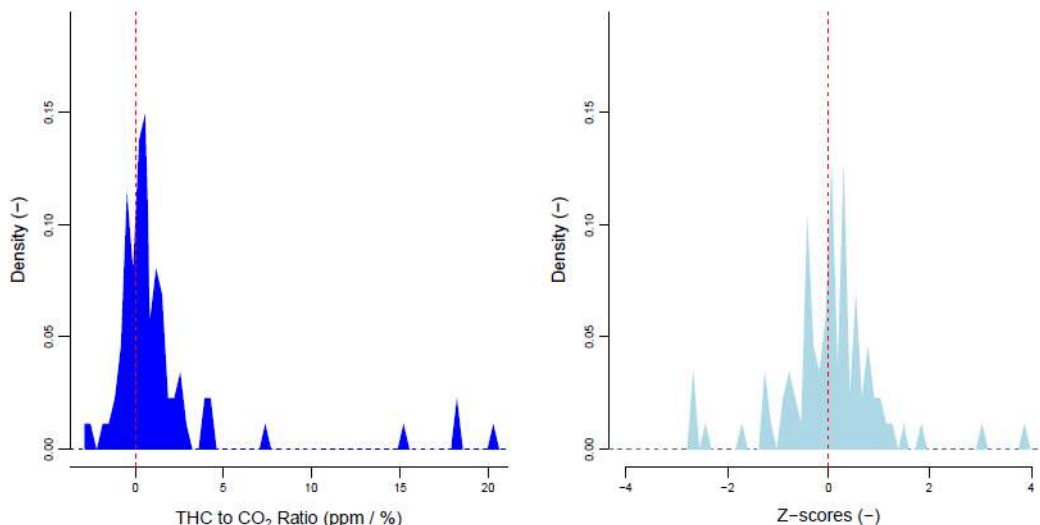


Figure 6: Example (LCVP Euro 4): transforming emission distributions for outlier detection.

¹⁴ While the Box-Cox transformation corrects for positive or negative skewness, the resulting transformed data is not guaranteed to be normally distributed. It is therefore recommended that the empirical quantiles of the z-scores be checked graphically against the theoretical quantiles of the standard normal distribution.

In fact, only six LCVP vehicles out of 386 (2%) were identified as high emitters using this method, and mainly for CO. No NO high emitters were identified. Obviously the 4 SD criterion can be relaxed to identify more high emitting vehicles, but the point is that several vehicles can have high emissions but can still be considered part of the natural distribution of emissions of the on-road fleet for the same technology class. It is noted that classification for outlier testing could also be refined and include VSP bins, however this would require a larger database. For now identified outliers with high VSP values \geq 40 kW/tonne could be removed from the list of identified high emitters on the basis of high speed/acceleration conditions causing high emission levels. None of the six identified vehicles had VSP values \geq 40 kW/tonne.

After identification, the date-time stamped heat signature images were retrieved for analysis. A small test program was conducted where the thermal imaging camera was set up on a quiet stretch of road with roundabouts at either side, to replicate the URB site and driving conditions, with periods of constant speed driving close to the speed limit and regular stops and turns (Smit and Kingston, 2019). Cold vehicles were then driven in loop past the thermal imaging camera where images were recorded. It became clear that cold vehicles produce a dark image and that it takes several minutes to record hot exhaust, underbody and wheels (braking). As a consequence, thermal images can be used to verify if a vehicle is producing high emissions due to cold start conditions.

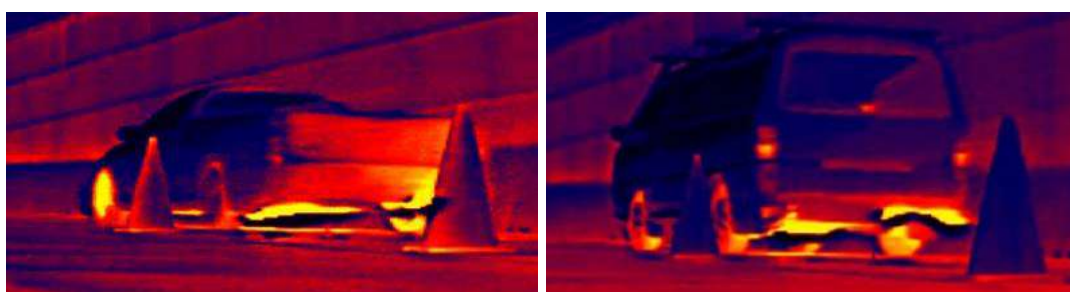


Figure 7: Heat signature images of measured vehicles identified as 'hot high emitters'.

All of the identified high emitting LCVs had distinctive hot thermal profiles and are unlikely to be affected by cold start conditions. Two examples are shown in Figure 7.

As a final note the number of high-emitters in the on-road fleet is typically small and their emissions are highly variable – more so than properly functioning vehicles (Schulz et al., 2000). In terms of identifying high emitters and consideration of this variability it would be recommended to have identification of the same vehicle at multiple dates/times before the owner is contacted and instructed to have the vehicle repaired.

Conclusion

This paper has discussed and presented some of the results from and methods used in a short but comprehensive on-road emission measurement program. The results show that supplementing RSD equipment with a range of additional traffic and air quality equipment can significantly increase sample size (LPN camera, loop detectors) and provide useful new information that assists in the analysis of on-road emissions data (thermal imaging camera, MAC address units, loop detectors).

References

- ALPR (2018). Automated License Plate Recognition, <https://github.com/openalpr/openalpr>, accessed 9 October 2018.
- Bishop, G.A., Stedman, D.H. (2008). A decade of on-road emissions measurements, *Environ. Sci. Technol.*, 42, 1651-1656.
- Bishop, G.A., Schuchmann, B.G., Stedman, D.H., Lawson, D.R. (2012). Multispecies remote sensing measurements of vehicle emissions on Sherman Way in Van Nuys, California, *J. Air & Waste Manage. Assoc.*, 62 (10), 1127-1133.
- Choo, S., Shafizadeh, K., Niemeier, D. (2007). The development of a prescreening model to identify failed and gross polluting vehicles, *Transpn Res.-D*, 12 (3), 208-218.
- CRC (2006). *Analysis of Remote Sensing Data to Determine Deterioration Rates for OBDII Equipped Vehicles*, Coordinating Research Council (CRC), CRC Report No. E-23-8, September 2006.

Frey, H.C., Unal, A., Chen, J., Li, S. (2003) Evaluation and recommendation of a modal method for modelling vehicle emissions, 12th International Emission Inventory Conference – “Emission Inventories - Applying New Technologies”, San Diego, April 29 - May 1, 2003.

ISSRC (2019). International Vehicle Emissions Model. <http://www.issrc.org/ive/>; accessed 7 February 2019.

IVL (2018). *Comparing Emission rates Derived from Remote Sensing with PEMS and Chassis Dynamometer Tests – CONOx Task 1 Report*, IVL Swedish Environmental Research Institute, ISBN 978 91 88787 28 6.

Monateri, A. M., Stedman, D. H., Bishop, G. A. (2004). Infrared thermal imaging of automobiles, Poster presented at the 14th CRC On-Road Vehicle Emissions Workshop, San Diego, March 2004, <http://www.feat.biochem.du.edu/reports.html>.

NIWA (2015). *The Use of Remote Sensing to Enhance Motor Vehicle Emission Modelling in New Zealand*, prepared by Robin Smit and Elizabeth Somervell, Report No. AKL2015-012, National Institute of Water & Atmospheric Research, New Zealand.

Park, S.S., Kozawa, K., Fruin, S., Mara, S., et al. (2012). Emission factors for high-emitting vehicles based on on-road measurements of individual vehicle exhaust with a mobile measurement platform, *J. Air & Waste Manage. Assoc.*, 61, 1046-1056.

Schulz D, Younglove T, Barth M. (2000). Statistical analysis and model validation of automobile emissions, *Journal of Transportation and Statistics*, 29-38.

Sjödin, Å, Andréasson, K., Wallin, M., Lenner, M., Wilhelmsson, H. (1997). Identification of high-emitting catalyst cars on the road by means of remote sensing, *Int. J. of Vehicle Design*, 18 (3/4), 326-339.

Smit, R., Bluett, J. (2011). A new method to compare vehicle emissions measured by remote sensing and laboratory testing: High-emitters and potential implications for emission inventories, *Science of the Total Environment*, 409, 2626–2634.

Smit, R., Kingston, P., Wainwright, D., Tooker, R. (2017). A tunnel study to validate motor vehicle emission prediction software in Australia, *Atmospheric Environment*, 151, 188-199.

Smit, R., Kingston, P. (2019). Detecting cold start vehicles in the on-road fleet, *Air Quality and Climate Change*, 53 (2), (*submitted for publication*).

2.7.5 NO_x emissions from Euro 5 and Euro 6 light-duty diesel vehicles as measured by remote sensing, PEMS and in legislative laboratory test cycles

M. Jerksjö^{1}, Å. Sjödin¹, R. Varella², C. Sandström-Dah^P*

¹ IVL Swedish Environmental Research Institute, SE-411 33, Göteborg, Sweden, martin.jerksjo@ivl.se

² AVL MTC, SE-136 23, Haninge, Sweden

Introduction

There are presently two mechanisms for monitoring emission performance of road vehicles in Sweden, the national in-use compliance program and the periodic technical inspection (PTI). The aim of the Swedish in-use compliance program is to monitor that the durability of exhaust aftertreatment systems complies with the legal requirements according to the EU regulations and to ensure that vehicle manufacturers are aware of that the in-use emissions of the fleet are monitored. Around 70 randomly chosen vehicles are tested every year in the program and tests are conducted both in the laboratory and on-road. In the Swedish PTI the emission performance of diesel cars newer than 2004 are judged only by an inspection via the OBD-system and an additional measurement of soot (by an opacity measurement) if it is required by the initial OBD check. No other tests are conducted to assess the emissions from the car. Within both the in-use compliance program and the PTI there is a need for making the vehicle emission testing more efficient. The vehicle models selected for tests within the in-use compliance program could for example be chosen not by random but instead by using available knowledge on emission rates for specific makes or models. One way to obtain such information is to use remote emission sensing. The method has been used for more than 25 years to measure emissions from passing vehicles in real world driving. It is commonly used to determine emission rates, for distinct vehicle makes and models, evaluate the durability of emissions control systems (Sjödin et al., 2018), track the emissions performance of vehicle fleets over time (Chen and Borken-Kleefeld, 2014) and in addition it can be used to identify high-emitting vehicles and detect individual tampering (Borken-Kleefeld and Dallman, 2018). Remote sensing has been used in Sweden for many years but mainly for research applications (Sjödin et al., 2017). However, since there is a need for improved real-world control of vehicle emissions, remote sensing may be an interesting option as a supplement to existing test methods used in the PTI and within the in-use compliance program.

Objectives and methodology

Within an ongoing project (November 2017 - December 2019), remote sensing (RS) is evaluated as a method to be used for achieving higher emission testing efficiency in both the Swedish in-use compliance program and the periodic technical inspection. One potential use of RS in the in-service testing is for screening out high- and/or low-emitting vehicles, either on an individual level or on group level (e.g. by engine families). These vehicles or vehicle groups can then become subject for further PEMS and laboratory tests or other test methods suiting regulatory purposes.

This paper presents the first preliminary results from remote sensing, PEMS and laboratory measurements carried out in the project to study the potential of remote sensing to support the Swedish in-use compliance program regarding the compliance of light-duty diesel vehicles. For this purpose, a remote sensing device (RSD) was used to measure the emissions of NO, NO₂, CO, HC and particles (as opacity) from passing vehicles during 14 days at a site in Haninge, Sweden. The measured NO_x emissions were then used to classify diesel passenger cars and diesel light commercial vehicles of Euro standard 5 and 6 as high-, intermediate- or low-emitters. To evaluate how well the on-road NO_x emissions measured by remote sensing correspond to emissions measured with PEMS in the Real Driving Emission (RDE) procedure, owners of measured vehicles were contacted by mail and phone with a request to lend out their vehicles for emission testing. So far in the project 12 vehicles have been tested with PEMS of which 7 also have been tested in the laboratory for further comparison between RDE, RS and the NEDC and WLTC driving cycles. More tests will be conducted during 2019 with the aim of testing in all about 30 vehicles with PEMS, of which about 10 also on a chassis dynamometer.

When analyzing the RS results for identifying candidates for further tests only, with a few exceptions, measurements where the vehicle specific power (VSP) was in the range 2-30 kW/t have been included. This to be sure to exclude vehicles that have been tested when the engine was operating under loads higher than what is considered as normal operation. VSP is a measure of the instantaneous engine power per unit of mass of the vehicle and is calculated from the speed and acceleration of the vehicle,

road slope, aerodynamic drag, rolling resistance and friction losses in bearings, (Borken-Kleefeld et al., 2018).

Further, three main criteria have been used when classing vehicles as high emitters:

1. At least two valid measurements and average NO_x emission over the 95th percentile for the euro standard.
2. At least two valid measurements and average NO_x emission over the 90th percentile for the euro standard.
3. Only one valid measurement which is over the 98th percentile.

Vehicles with average NO_x emissions below 2 gNO_x/kg fuel were classified as low-emitters and vehicles with emissions close to the average emission for the Euro standard were classified as intermediate emitters.

Remote sensing measurements

Remote sensing measurements were conducted on seven workdays during the period 30 May to 8 June and seven workdays during the period 28 August to 7 September 2019. The instrument used was an Opus AccuScan™ RSD 5000 with NO₂ capability. In addition to air pollutant emissions the RSD measures also parameters such as vehicle speed and acceleration and ambient air temperature. Furthermore, a camera is included in the system for taking photos of the license plate of each passing vehicle, enabling retrieving detailed vehicle information, such as make, model, fuel type, Euro standard, model year, etc., from national vehicle registers. Calibration of the detector is done by means of both fixed gas cells and gas bottles, both containing known concentrations of the measured pollutants. Cell calibration in the measuring campaign were commonly conducted once or a few times every day and gas audits using the gas bottles were conducted every second hour. The measurement site is located in Haninge, a suburb to Stockholm, Sweden. The instrument was placed about 40 meters after a roundabout in a road section that is almost flat. The proximity to the exit of the roundabout means that most vehicles accelerated past the RSD providing good measuring conditions.



Figure 1: Photos from the RS measuring site in Haninge, Sweden.

Laboratorial and PEMS testing

Laboratorial tests were conducted at a one-axis roller dynamometer at AVL MTC site in Haninge, Sweden. The exhaust gas was connected to the full dilution tunnel with a constant volume sampling. For the emissions acquisition, sampling bags were filled with the diluted exhaust and analyzed at the end of the test. Also, diluted gas was measured by one AVL AMA i40. For PEMS and laboratory equipment correlation, an AVL M.O.V.E. PEMS was installed in the exhaust line together with an exhaust flow meter (EFM). Attention was given to leave enough tube diameter length before and after the EFMs to ensure their proper operation, and additionally, not to cause a significant pressure drop by reducing the tailpipe inner diameter (European Commission, 2018). That way, a correlation was possible to be performed. Figure 2 presents an example of a correlation acquired for the PEMS and laboratorial

gas analyzers. According to the RDE regulation r^2 should be higher than 0.9 and the slope between 0.9 and 1.1. Thus, the example in Figure 2 complies with the current regulation (European Commission, 2018) for RDE tests.

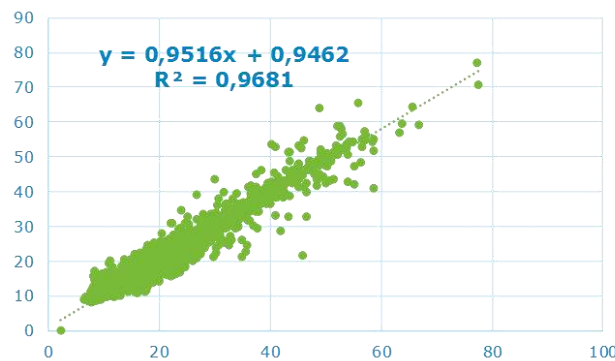


Figure 2: PEMS and laboratorial correlation results in terms of CO₂ emissions (g/s).

The zero and span calibration of the analyzers was conducted before each test with the PEMS and the zero and span drift of the PEMS was checked only after the RDE tests. All results were well within the regulation requirements (NO_x zero drift <5 ppm, NO_x span drift <2%) and there was no systematic drift (positive or negative). Table 1 presents a quick description of the equipment specifications used for the tests.

Table 1: Characteristics of the used equipment.

Technology	PEMS	Bags
Manufacturer	AVL	AVL
Model	M.O.V.E. iS	AMA i40
Principle CO ₂	NDIR	NDIR
Range CO ₂	20%	1%, 20%
Principle NO _x	NDUV	CLD
Range NO _x (ppm)	5 000	10, 100, 1 000
EFM	Pitot 2" & 2.5"	-

PEMS Route characterization

The route, designed to follow RDE regulations rules, was performed in the Stockholm Metropolitan Area, under on-road conditions. It was planned to cover different conditions of driving, respecting the driving shares stipulated by the EC regulation (European Commission, 2018), (1/3 in urban condition, 1/3 in rural condition and 1/3 in motorway condition) and stop time periods. The first part of the route was a preparation cycle route, where all vehicles were able to "warm-up". This initial driving cycle allows to analyze cold-start, specifically, coolant temperature and catalytical temperature for the regulated cold-start period of 5 minutes. The route starts and ends at the same location and under urban conditions at the AVL MTC site in Haninge. Each trip took approximately 6000 s, to perform and the length was around 75 km.

Results and discussion

The remote sensing measurement campaign resulted in approximately 4 000 valid measurements on diesel passenger cars of Euro 6 and around 3 400 of Euro 5. The number of valid measurements on diesel light commercial vehicles were around 1 500 of Euro 6 and around 2 000 of Euro 5. The numbers of valid measurements together with emissions as gNO_x/kg fuel burnt are presented in Table 2.

Table 2: Number of valid RS measurements for diesel passenger cars (PC) and diesel light commercial vehicles (LCV) together with average VSP, average NO_x and percentiles. Uncertainties are presented as 95% confidence intervals.

Vehicle type	Emission Standard	Valid measurements	Average VSP (kW/t)	Average NO _x (g/kg)	NO _x percentiles (g/kg)		
					98 th	90 th	95 th
PC	Euro 5	3382	12 ± 0.2	12 ± 0.4	27	34	42
PC	Euro 6	4046	13 ± 0.2	6 ± 0.2	14	18	27
LCV Class II	Euro 5	587	12 ± 0.5	17 ± 0.9	33	40	43
LCV Class III	Euro 5	1372	12 ± 0.3	15 ± 0.6	32	38	45
LCV Class II	Euro 6	518	13 ± 0.5	7 ± 0.8	19	27	31
LCV Class III	Euro 6	1012	12 ± 0.3	6 ± 0.5	16	22	31

Information on the 12 cars tested with PEMS and on the chassis dynamometer are presented in Table 3. The biggest constraint so far in the study has been the difficulty to recruit vehicles to the tests. Most people have not been willing to let their car be tested even though a temporary replacement car together with an economic compensation for the inconvenience has been offered. In addition to that a considerable share of the vehicles passing the RS site were owned by companies, this was especially the case for the light commercial vehicles. Vehicles owned by companies have been even more difficult to recruit for testing than vehicles owned by private persons. The consequence has been that vehicles tested with PEMS and in laboratory so far not have been the highest prioritized vehicles based on data from the RS measurements.

Table 3: Information on the diesel cars tested with PEMS and on chassis dynamometer .

Vehicle	Emission Standard	Displacement volume (l)	Mass ¹ (kg)	Exhaust Aftertreatment ²	Conducted tests
#1	E 6	2.0	1902	LNT+DPF	RDE
#2	E 6	1.7	1619	LNT	NEDC/WLTC/RDE
#3	E 6	2.0	1865	LNT+DPF	NEDC/RDE
#4	E 6	2.0	1832	LNT+DPF	NEDC/WLTC/RDE
#5	E 6	2.0	1839	LNT+DPF+SCR	RDE
#6	E 5	1.6	1419	DPF	NEDC/RDE
#7	E 5	1.5	1469	DPF	RDE
#8	E 5	1.5	1504	DPF	NEDC/RDE
#9	E 5	1.6	1526	DPF	NEDC/WLTC/RDE
#10	E 5	1.7	1490	DPF	RDE
#11	E 5	1.6	1494	DPF	NEDC/WLTC/RDE
#12	E 5	2.0	1664	DPF	RDE

¹ mass in running order

² In addition to EGR+DOC

A comparison for Euro 6 cars between NO_x measured with RS, PEMS and in laboratory test are presented in Figure 3. RDE emissions are presented as g/kg fuel and g/km for making a comparison with RS, laboratory tests and emission limits possible.

None of the tested Euro 6 cars had such high NO_x emissions when tested with RS that they clearly could be identified as suspected high emitters. Vehicle #4 was identified as a possible high emitter but the VSP of this car when measured with RS was 48 kW/t which is higher than the upper limit of 30 kW/t that has been used to define normal driving conditions in this project. This exception was made to study the effect of high VSP when it comes to identifying high emitters with RS.

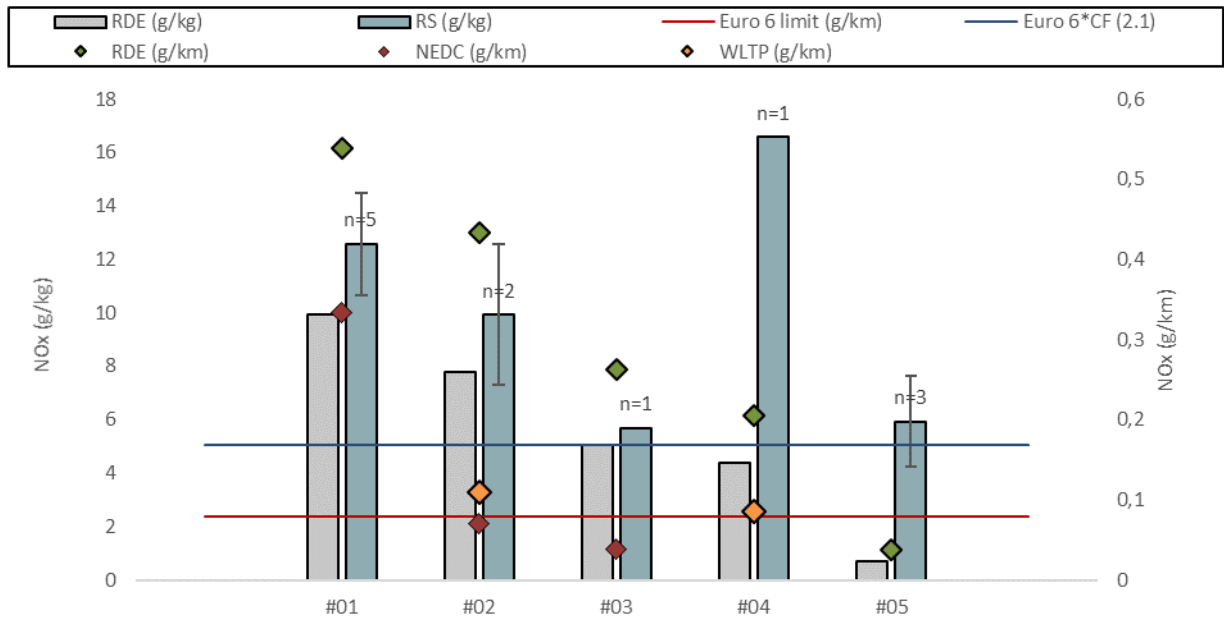


Figure 3: NO_x emission from Euro 6 cars measured with RS, PEMS and during the NEDC and WLTP. Lines represent the Euro 6 limit and the Euro 6 RDE limit with a conformity factor of 2.1. Error bars represent 95% confidence intervals.

Conformity between remote sensing and RDE are for three of the vehicles relatively good but for vehicles #4 and #5 the differences in measured emissions are quite large. A likely explanation for the differences for vehicle #4 is the high vehicle specific power in the remote sensing test. One plausible explanation for the difference in measured NO_x from vehicle #5 lies in the fact that the car has an SCR-catalyst. During most parts of the RDE route the catalyst reduced the emissions efficiently but when passing the RS site, the temperature may not have been high enough for activation of the SCR. Vehicles #1 and #2 showing high NO_x emissions when measured with RS were also well above the NO_x RDE emission limit using a conformity factor of 2.1.

A comparison for Euro 5 cars is presented in Figure 4. Emissions measured with RS and PEMS are at the same level for four of the tested Euro 5 cars. The biggest difference is seen for Vehicle #12 for which the RDE emissions were much lower than the emissions measured with RS. Interesting to mention is that Vehicle #5 and Vehicle #12 are of the same model but different Euro Standards and they both have low RDE emissions but intermediate (Euro 6) or high (Euro 5) emissions compared to the RS averages for the Euro standards.

Figure 5 shows a plot of NO_x emissions measured with RS versus PEMS. All vehicles tested with PEMS except #4, the vehicle with high VSP, are included.

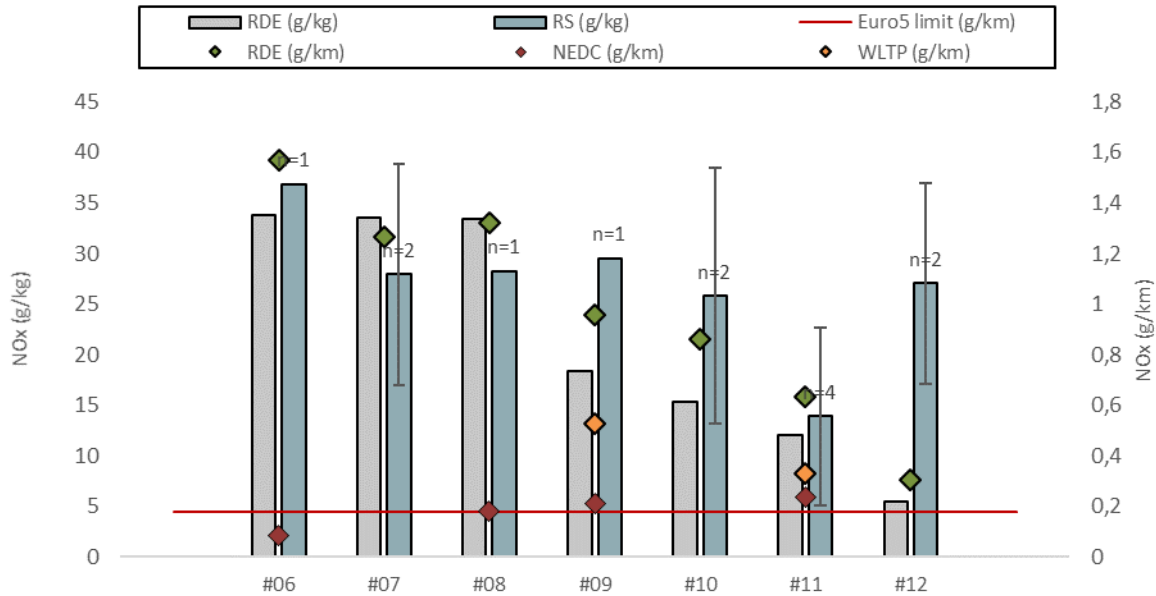


Figure 4: NOx emission from Euro 5 cars measured with RS, PEMS and during the NEDC and WLTP. The line represent the Euro 5 limit. Error bars represent 95% confidence intervals.

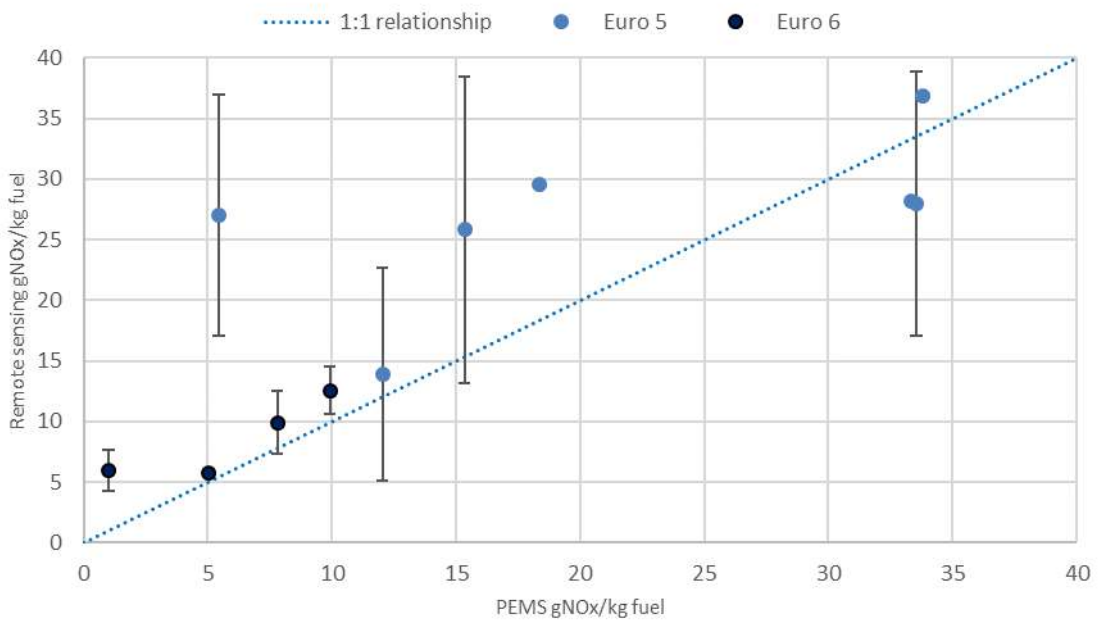


Figure 5: RDE NOx versus NOx emissions measured with RS. Error bars represent 95% confidence intervals.

The results so far in the study indicates that in most cases NOx emissions measured with RS can be used as an indication of the NOx emission performance as measured using the RDE procedure. One exception seen so far is the car with a SCR catalyst which had the lowest RDE levels of NOx among the tested cars but was classified as an intermediate emitter from the RS measurements. This indicates that NOx emissions from Euro 6 cars with SCR catalyst measured with RS may only be representative for driving conditions when the catalyst is not working efficiently e.g. due to low catalyst temperature. But this can to a large extent be avoided by using a site where all passing cars should be warm enough for the SCR-system to work efficiently. The site used in this project was not optimal from that point of view. On the other hand, the emission measured with RS from the SCR equipped vehicle was still on an

average level for a Euro 6 car meaning that in this case, even if the SCR may not have been activated the emissions were still not close to the levels of high emitting Euro 6 cars.

One other aspect that must be considered for the method used in this project for comparison of different emission testing methods is the time lapse between the RS measurement and the PEMS and laboratory tests. Around three to five months passed between the RS measurement and the other tests conducted so far. This has been mainly due to the difficulties in recruiting vehicles for the tests. For the planned tests during 2019 the time lapse between the RS tests and the other tests will be even longer. This means a greater risk that some parameters may have changed from the RS measurement to when the vehicles are tested again. This fact can be handled to some extent by asking the owner if they are aware of any changes on the vehicle that may have had effect on the emissions performance, e.g. service. In addition, to even increase the precision of the analysis, further VSP and driving categories analysis will be performed. In this way, good indications on how to analyze data and where to position the RS equipment can be given, improving the overall results.

Further work

In the first part of the project that is presented in this paper focus has been on conducting remote sensing measurements and to start with the RDE and chassis dynamometer tests. The study continues until the end of 2019 and there still are several activities to be conducted. In the first two quarters of 2019 more cars will be recruited and tested with PEMS and on chassis dynamometer. No more Euro 5 cars will be tested only Euro 6 cars and if some will be available for tests, also light commercial Euro 6 vehicles. In total 18 more vehicles will be tested with PEMS and two more on the chassis dynamometer. In the second quarter of the year measurements with remote sensing and other methods will be conducted in connection to the periodic vehicle inspection with the aim to evaluate different methods that in the future can be used to make the emission testing in the periodic inspection more efficient. The latter half of the year will be used for evaluating and reporting results.

Acknowledgements

This project is fully financed by the Swedish Road Administration and the Sweden's Innovation Agency. We also especially want to thank Opus Remote Sensing Europe for the support on the remote sensing measurements.

References

- Borken-Kleefeld J., Bernard Y., Carslaw D., Sjödin Å. (2018) Comparing emission rates derived from remote sensing with PEMS and chassis dynamometer tests – CONOX Task 1 report, Commissioned by the Federal Office for the Environment (FOEN), Switzerland, IVL C 293
- Borken-Kleefeld J and Dallman T., (2018) Remote sensing of motor vehicle exhaust emissions, (ICCT: Washington, DC, February 2018)
- Chen, Y. and J. Borken-Kleefeld (2014), Real-driving emissions from cars and light commercial vehicles - Results from 13 years remote sensing at Zurich/CH, *Atmos. Environ.* 88, 157-164.
- European commission (2018). Commission Regulation (EU) 2018/ 1832
- Sjödin, Å., Jerksjö, M., Fallgren, H., Salberg, H., Parsmo, R., Hult, C., Yahya, M-R., Wisell, T., Lindén, J. (2017) On-Road Emission Performance of Late Model Diesel and Gasoline Vehicles as Measured by Remote Sensing, IVL B 2281
- Sjödin, Å., Borken-Kleefeld, J., Carslaw, D., Tate, J., Alt, G.-M., De la Fuente, J., Bernard, Y., Tietge, U., McClintock, P., Gentala, T., Vescio, N., Hausberger, S. (2018), Real-driving emissions from diesel passenger cars measured by remote sensing and as compared with PEMS and chassis dynamometer measurements- CONOX Task 2 report, Commissioned by the federal Office for the Environment (FOEN), Switzerland, IVL C294

2.7.6 Study on the durability of UK diesel and petrol passenger car emission control systems utilising remote sensing data

N. J. Farren^{1*}, D. C. Carslaw^{1,2}, J. Borken-Kleefeld³, A. R. Vaughan¹, Å Sjödin⁴

¹ Wolfson Atmospheric Chemistry Laboratories, University of York, York, YO10 5DD, UK,
naomi.farren@york.ac.uk

² Ricardo Energy & Environment, Harwell, Oxfordshire, OX11 0QR, UK

³ International Institute for Applied Systems Analysis (IIASA), Schlossplatz 1, 2361, Laxenburg, Austria

⁴ IVL Swedish Environmental Research Institute, Gothenburg, Sweden

Introduction

The quantity and chemical composition of pollutants emitted from the vehicle tailpipe depend on both engine-out emissions and the operation of the vehicle after-treatment system. Over time, several deterioration processes can occur, including wear of the engine and its components, wear of catalyst coatings and poisoning of the catalyst. This can result in changes in exhaust emission behaviour with increasing use. Standard knowledge regarding the deterioration of emissions was established during two major European research programs conducted in the 1990s, MEET and ARTEMIS.

However, the deterioration functions are based on a limited number of chassis dynamometer measurements that do not include high mileages. Long-term deterioration is based on extrapolation of data rather than actual measurements. Deterioration is represented as a linear increase with vehicle mileage, with two sets of estimated deterioration rates: one for Euro 1 and 2 cars and one for Euro 3 and 4 cars. It is also assumed that emissions do not change beyond 120,000 and 160,000 km respectively for these two sets of vehicles. These assumptions are currently incorporated into Europe's standard vehicle emission models, COPERT (Ntziachristos et al., 2009) and HBEFA (HBEFA, 2017).

Vehicle emission remote sensing (RS) measurements offer the potential to update and significantly improve the accuracy of vehicle emission deterioration factors. RS data provides 'snapshot' measurements of pollutants emitted from thousands of vehicles under real-world driving conditions, capturing a comprehensive picture of the emission performance of the vehicle fleet. Recent studies have made promising progress in terms of better characterising deterioration effects (Borken-Kleefeld and Chen, 2015; Chen and Borken-Kleefeld, 2016) but have been forced to rely on vehicle age as a proxy for vehicle mileage. This approach can mask a lot of potentially important information regarding vehicle use, as vehicles of a specific age can in fact be associated with a large range in mileage.

In 2018, a new study on the durability of European passenger car (PC) emission control systems was carried out (DETERS project, Carslaw et al. 2018). The study aimed to better understand the effects of deterioration of PCs on vehicle emissions, using a comprehensive RS dataset containing around 1 million vehicle emission measurements from across Europe. A new and important development emerging from this study was the acquisition of vehicle mileage information for individual vehicles, allowing a direct measure of mileage effects on vehicle emissions without the need to use vehicle age as a proxy for mileage. In this paper, we use UK 2017-2018 RS measurements (for which a direct measure of vehicle mileage is available) to demonstrate how various data analysis approaches can be used to examine the deterioration of emissions for the UK passenger car fleet.

Experimental

Instrumentation. Two spectroscopic remote sensing (RS) instruments were used to make vehicle emission measurements in this study: the Fuel Efficiency Automobile Test (FEAT) instrument developed by the University of Denver (UoD) and the Opus AccuScan RSD 5000 (UoD, 2011; Opus, 2018). The development and operation of the FEAT instrument has been described extensively in the literature (Bishop and Stedman, 1996; Popp et al., 1999; Burgard et al., 2006a; Burgard et al., 2006b) and previous instrument comparison studies between the UoD and Opus systems revealed well correlated NO measurements, showing a linear relationship with a gradient of 0.93 and an R^2 of 0.85 (Rushton et al., 2018). Both RS instruments consist of a light source (collinear beams of IR and UV light) and a detector unit. The setup of the FEAT instrument is such that the source and detector are placed either side of a single lane road, whereas the source and detector are housed within the same unit for the

Opus RSD 5000. Therefore the RSD 5000 relies on a corner cube mirror on the opposite side of the road to reflect the light beams back to the detector. Carbon monoxide (CO), carbon dioxide (CO₂) and hydrocarbons (HCs) are measured via non-dispersive IR absorption, whilst dispersive UV spectrometers are used to measure nitric oxide (NO), nitrogen dioxide (NO₂) and ammonia (NH₃). A measurement is triggered each time a vehicle passes the RS setup; all species are quantified as a ratio to CO₂ to account for variation in the density, position and path length of the vehicle exhaust plume. The attenuation of light as it passes through the vehicle exhaust plume provides a measure of the absolute concentration of each pollutant. The amount of each pollutant from the vehicle exhaust plume is determined as the increment over the ambient background level measured prior to the vehicle passing by.

Parallel speed bar lasers placed alongside the source and detector provide a measurement of vehicle speed and acceleration. A video camera captures a photograph of the registration plate of each vehicle, which is used to obtain vehicle technical information. To account for possible changes in instrument performance and ambient CO₂ concentrations (caused by variations in local CO₂ sources, atmospheric conditions and instrument path length), the RS instruments are calibrated in situ every couple of hours. Certified gas cylinders (supplied by The BOC Group and Air Liquide for the FEAT and RSD 5000 respectively) containing known ratios of (1) CO, C₃H₈, CO₂, NO, SO₂, N₂ balance; (2) NH₃, C₃H₈, N₂ balance; and (3) NO₂, CO₂, air balance were used. A small amount of gas is released into the instrument's path to allow for a comparison of the measured ratios from the instrument to those certified by the gas cylinder manufacturer. Ratios of pollutants to CO₂ can be used to derive fuel-specific emission factors in g kg⁻¹ fuel (UoD, 2014).

Vehicle information. The vehicle registration plate images were digitised and sent to a commercial supplier (CDL Vehicle Information Services Limited) to obtain technical information for each individual vehicle measured using the RS device. The information details physical characteristics of the vehicle itself (e.g. engine size, fuel type, kerb weight) as well as the Euro emissions standard and the dates the vehicle was manufactured and registered. The information provided by CDL is acquired from data collected by the Driver and Vehicle Licensing Agency (DVLA) and data queried from the Society of Motor Manufacturers and Traders (SMMT) Motor Vehicle Registration Information System (MVRIS). The mileage of a vehicle at its most recent annual MOT inspection test was also provided by CDL. Limitations of this data include the fact that vehicles under three years old are not required to take an annual MOT inspection, and that the vehicle mileage represents the date of the most recent MOT test rather than the emission measurement date. Nevertheless, these official annual inspection values are considered to be substantially more robust than mileage estimates based on the age of the vehicle and can be used as a proxy for individual vehicle usage and the associated potential effects of vehicle ageing on emissions.

Measurement surveys. RS measurement surveys were performed in two UK cities (York and London) during 2017 and early 2018. The RSD 5000 was operated at six measurement sites in London. The FEAT instrument was deployed at three of the London sites and an additional three locations in York. A total of 116,285 vehicle emission measurements were recorded using the RSD 5000, and a further 35,344 measurements were made using the FEAT instrument. The data were combined into a single data set comprising 151,629 measurements. Measurement surveys were carried out on weekdays during daylight hours (approximately 0900-1700 h) apart from during periods of rain. Ambient temperatures ranged from around 15 to 21 °C during the York survey period, whilst temperatures were considerably lower during the London measurement period (approx. 0-16 °C). Overall, the surveys represented a wide range of urban-type driving conditions, with average vehicle speed by site location ranging from 17.6 to 47.4 km h⁻¹. In total, 107,974 measurements were made of passenger cars. The passenger car fleet was comprised of 53,985 petrol cars, 48,398 diesel cars, 5,218 petrol hybrids and 123 diesel hybrids. The remainder of the vehicle fleet was comprised mainly of buses (3,986), light commercial vehicles (LCVs, 30,803) and heavy goods vehicles (HGVs, 4,690).

Data treatment. Generalised Additive Models (GAMs) were used to establish the relationship between emissions and vehicle mileage. GAMs are a highly flexible 'data-driven' modelling approach that is suited to the analysis of vehicle emission remote sensing data (Wood, 2004). The GAM approach allows non-linear relationships between independent and dependent variables to be considered and makes no a priori assumptions about the nature of the relationship. The thin-plate regression spline method available in the R package mgcv was used (Wood, 2003). The default options of the mgcv package were used without modification, which produced interpretable models with smooth relationships between the dependent and independent variables. The uncertainty intervals shown in the plots of this paper are estimated standard errors, which show higher uncertainties where there are fewer data (typically at high or low mileages). Quantile regression, developed by Koenker and Bassett (1978), has

also been used to model the distribution of vehicle emissions. This technique considers the conditional quantiles of distributions, e.g. the 95th percentile, to provide a more complete picture of the conditional distribution compared to 'ordinary' regression models. Quantile regression was performed using the B-spline function in the splines R package (Bates and Venables, 2019).

Results

A direct measure of individual vehicle mileage at the last annual MOT inspection was obtained for 71,650 of the 107,974 measured passenger cars (PCs). The annual occurrence of MOT tests (inspection of vehicle safety and roadworthiness) in the UK means that the recorded mileage is accurate to the nearest 12 months. Most of the remaining PCs for which a direct measure of vehicle mileage was not available were Euro 6 vehicles less than 3 years old, and therefore not yet required to undergo a MOT test.

Previous studies have proven the usefulness of RS data for investigating the changes in emission behaviour over vehicle age, indicating that emission control systems become less effective over time (Borken-Kleefeld and Chen, 2015; Chen and Borken-Kleefeld, 2016). However, these studies have relied on vehicle age as a proxy for its cumulative mileage, rather than on a direct measure of mileage itself. This approach relies on using estimated vehicle mileage values, largely derived from national statistics rather than direct measurements. This can disguise a lot of potentially important variability, as a vehicle of a certain age can be associated with a large range in mileage. For example, a petrol car that is 10 years old suggests a mean mileage of approximately 100,000 km. However, the recent UK data shows that in reality, vehicles of this age can have vastly different mileages. The range from 5th to 95th percentile is from 50,000 to 200,000 km, with minimum and maximum mileages reaching <10,000 km and >500,000 km respectively. This information can be lost when using age-derived mileages, therefore an important development in this study is the acquisition of direct vehicle mileage information for individual vehicles, enabling a more detailed investigation of the relationship between emissions and vehicle mileage for UK petrol and diesel passenger cars.

Vehicle emission RS data is comprised of short duration (~ 0.5 s) measurements of vehicle exhaust plumes. On their own, individual exhaust plume measurements are not particularly informative, but the aggregation of several thousand RS measurements derives useful insight into vehicle emission behaviour across a range of driving conditions. Most commonly this is achieved by calculating the mean emission of a pollutant by some sort of categorical such as Euro standard or year of manufacture. Alternatively, continuous variables such as vehicle mileage can be 'binned' into intervals to produce categories, but this process is somewhat arbitrary; it is uncertain how wide each bin should be and how many measurements there should be in each bin. This study relies on the use of Generalized Additive Models (GAMs) to determine the relationships between two variables i.e. vehicle emission and vehicle mileage (Wood, 2004). The GAM approach is useful for analysing RS data for two principal reasons. Firstly, GAMs can be used to analyse non-linear relationships between variables, and secondly, RS data does not need to be aggregated to establish these relationships.

Figures 1 and 2 show the change in emissions with mileage for nitrogen monoxide (NO) for Euro 3 to 6 petrol and diesel cars respectively. NO has been considered separately to total NO_x (NO + NO₂) because recent studies have revealed important differences in the relationships of NO and NO₂ emissions with vehicle mileage. For example, Carslaw et al. (2019) report a decrease in NO₂ emissions with vehicle mileage for Euro 3 to Euro 6 diesel PCs. The strongest evidence for a decrease in NO₂ is shown for Euro 5 diesel vehicles, partly due to the larger sample sizes of these vehicles. The evidence for a NO₂ decrease for Euro 6 vehicles is weaker due to the limited vehicle mileage information available for these newer vehicles (PCs in the UK do not undergo an annual MOT inspection until they are over 3 years old). Further details of the trends of other important pollutants (e.g. CO and hydrocarbons) with vehicle mileage can be found in the DETERS report (Carslaw et al., 2018). As shown in Figure 1, NO emissions for Euro 3 to 5 petrol cars increase with mileage and the slope is steeper for earlier Euro standards. Interestingly, low mileage early Euro class vehicles (e.g. Euro 3 and 4) can be relatively low-emitting. There is more certainty in the behaviour of low mileage Euro 5 vehicles relative to Euro 3 and 4, as more low mileage Euro 5 vehicles were present on the roads (and therefore measured) during the recent 2017-2018 RS survey period. For Euro 5 petrol cars, NO emissions increase gradually until around 150,000 km, at which point the slope becomes steeper i.e. NO emissions increase more rapidly above 150,000 km. This is a potentially important finding considering that deterioration functions currently used assume that emissions do not change above 160,000 km. There are currently insufficient numbers of Euro 6 cars to robustly understand any high mileage effects – and no evidence yet of any

deterioration for emissions of NO. The change in NO emissions with mileage for Euro 3 to 6 diesel passenger cars is shown in Figure 2. When comparing diesel and petrol PCs, absolute emissions of NO from diesel cars are higher than for petrol cars. In fact, even modern diesel vehicles can have higher NO emissions than old petrol cars. Furthermore, emissions of NO from diesel cars gradually increases with vehicle mileage for all Euro standards shown (although there is limited evidence for Euro 6 at this stage).

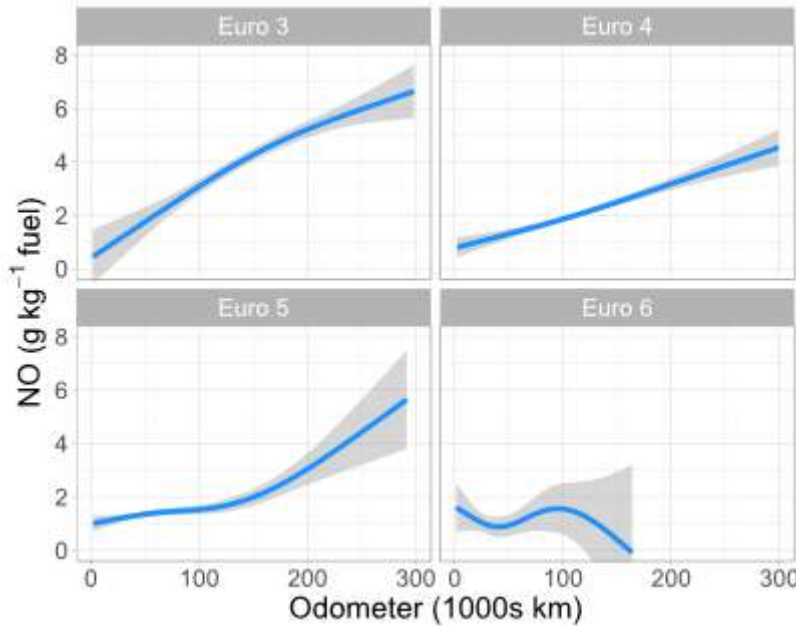


Figure 1: Emissions of NO (g kg^{-1} fuel) as a function of vehicle mileage for UK petrol passenger cars, split by Euro standard. The smooth lines show the results of fitting a GAM to the data and the shaded area represents the 95% confidence interval.

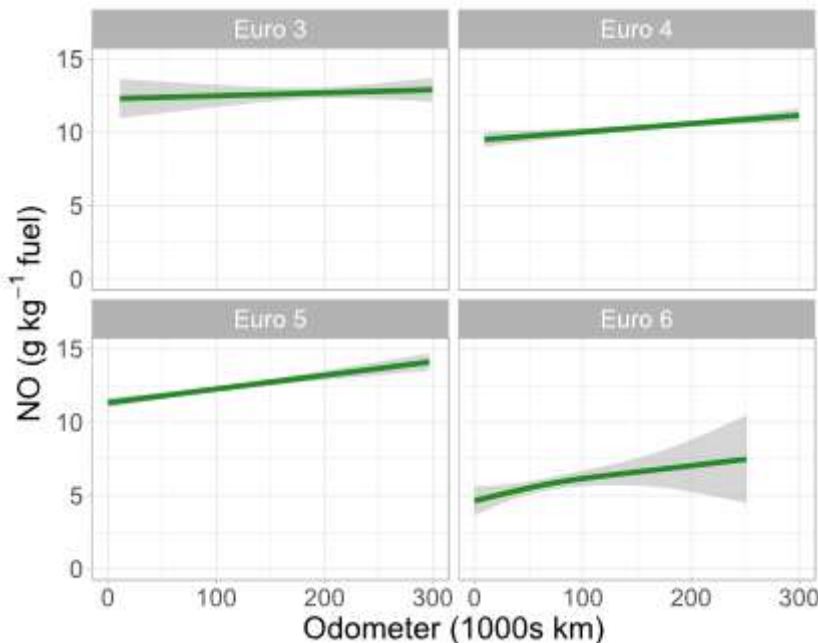


Figure 2: Emissions of NO (g kg^{-1} fuel) as a function of vehicle mileage for UK diesel passenger cars, split by Euro standard. The smooth lines show the results of fitting a GAM to the data and the shaded area represents the 95% confidence interval.

Most commonly with data analysis such as the use of GAMs, the mean response between the predictor and predictand is considered. However, in reality there is a distribution of responses, which have

interpretable meaning. These responses can be investigated using quantile regression, which extends the ordinary regression model to conditional quantiles of the response variable, e.g. the 95th percentile. In the case of vehicle emissions deterioration, the question can be asked whether all vehicles deteriorate by a similar amount or whether (for example) the mean response is driven by a relatively small number of higher emitting vehicles. A better understanding of the vehicle operating conditions under which high emissions are produced is essential for achieving more effective emission control and reducing atmospheric concentrations of key pollutants. The technique also has the advantage of producing a continuous function, rather than for example, splitting the mileage data into arbitrary intervals and considering the interval distributions. To further investigate the relationship between NO emissions and vehicle mileage for petrol and diesel passenger cars, quantile regression has been applied to illustrate how the median, 5th and 95th quantiles of emissions vary with mileage.

For petrol cars (Figure 3) the 5th percentile and median show relatively constant NO emissions with vehicle mileage for all Euro standards, with a maximum NO increase of 1 g kg⁻¹ fuel between 0 and 300,000 km. These results suggest that at the median level, there is little evidence of a deterioration effect. However, very different behaviour is observed for the 95th percentile (i.e. the highest 5% of NO emitted by the petrol cars) whereby NO emissions drastically increase with vehicle mileage. For example, for Euro 5 petrol cars the 95th percentile shows an increase from approximately 5 to 40 g kg⁻¹ fuel over 300,000 km. This suggests that a small fraction of high emitting petrol cars is largely responsible for the overall average increase in NO emissions with vehicle mileage shown previously in Figure 1.

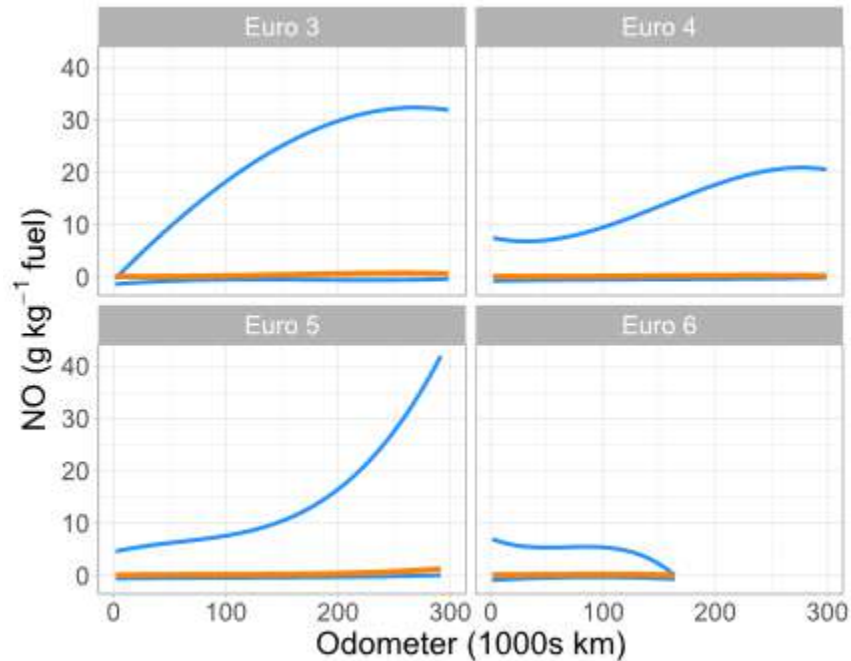


Figure 3: Variation of NO emissions with vehicle mileage for petrol passenger cars in the UK. The orange line shows the median value and the blue lines show the 5th and 95th percentile values as determined by quantile regression.

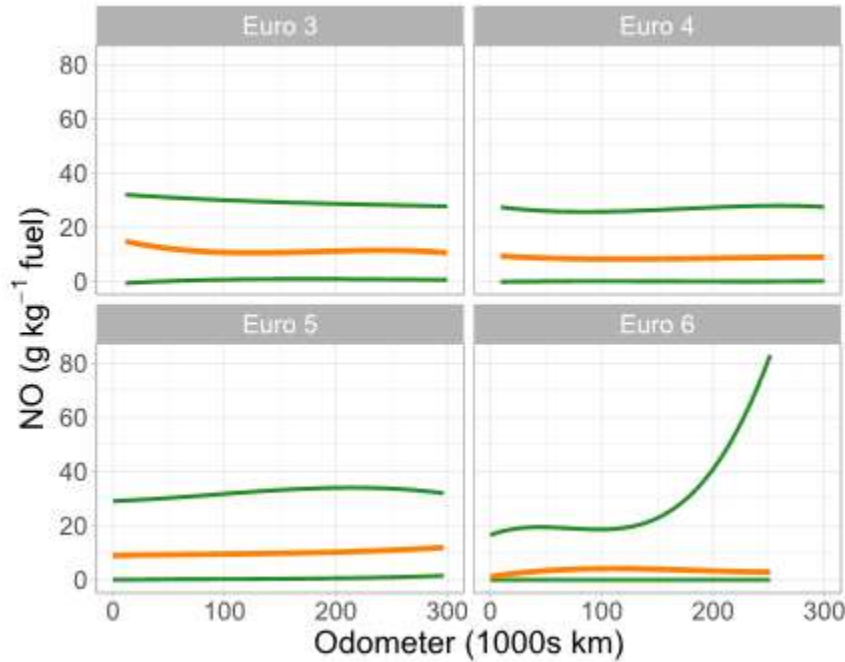


Figure 4: Variation of NO emissions with vehicle mileage for diesel passenger cars in the UK. The orange line shows the median value and the green lines show the 5th and 95th percentile values as determined by quantile regression.

The situation for diesel cars (Figure 4) differs in important ways. Except for the 95th percentile for Euro 6 cars, the quantiles shown (5th, median and 95th) are roughly parallel to each other, and show either no change or a gradual increase in NO emission with vehicle mileage. Note however, that in the case of Euro 6 vehicles there are very few high mileage data. More data is needed to robustly understand high mileage effects for Euro 6 diesel cars. The QR analysis shows firstly that the relationship between NO emission and vehicle mileage is consistent across each Euro class of diesel cars. Secondly, it shows that unlike petrol cars, the range in NO emissions is not drastically affected by vehicle mileage. For example, the 5th and 95th percentile values for a Euro 4 diesel car at 0, 100,000 and 200,000 km are all approximately 0 and 26 g kg⁻¹ fuel respectively. This means that the NO emission behaviour at the start of the vehicle's lifetime appears largely representative of how the vehicle will behave as mileage increases (up to 300,000 km at least).

Overall, the QR analysis shows contrasting behaviour for the variation in NO emissions with vehicle mileage for Euro 3-5 petrol and diesel vehicles. The highly skewed relationship for petrol cars suggests that whilst catalyst-equipped petrol cars perform well for NO emissions at low mileages, emission control of NO will fail at higher mileages for a small fraction of cars and dramatically influence the mean relationship between NO emission and vehicle mileage. This effect is strong for Euro 3 to 5 vehicles, but more high mileage Euro 6 measurements are needed to establish a robust relationship for these vehicles. Diesel vehicles on the other hand, show median, 5th and 95th percentiles that are roughly parallel to each other, contributing uniformly to a very gradual average increase in NO emissions with vehicle mileage. This suggests that the performance of the NO emission control can vary significantly at the point of manufacture and do not tend to diverge with increasing mileage. These results suggest that there is a wide range in behaviour of vehicle NO emission performance from new; consistent with vehicles have a large differential performance in emissions, as reported elsewhere (Bernard et al., 2018).

In summary, comprehensive RS data has been analysed to better understand deterioration effects from passenger cars on vehicle emissions. There are several additional factors that can influence vehicle emissions, such as ambient temperature and vehicle specific power, and these will be published in a separate study. At this stage, these factors have been accounted for to ensure that the findings reported in this study remain valid. An important development has been the acquisition of vehicle mileage information from UK data for individual vehicles. This information provides a direct measure of mileage effects on vehicle emissions without the need to use vehicle age as a proxy for mileage. A GAM approach has been used to analyse non-linear relationships between emissions and vehicle mileage;

this has proven useful for RS data as relationships can be established without needing to aggregate continuous variables such as vehicle mileage. In addition, quantile regression techniques have been applied to gain further insight into the emission-mileage relationship by considering the full distribution in emissions. This allows for a better understanding of the vehicle operating characteristics under which high emissions are produced, which is essential for achieving more effective emission control in the future. Many Low Emission Zone (LEZ) restrictions are currently based on the Euro standard of a vehicle. Results from this study indicate that factors such as vehicle mileage can also have an important influence on emissions and should be taken into consideration when planning effective emission control strategies.

Acknowledgements

We would like to thank the Swiss Federal Office for the Environment (FOEN, represented by H. Jenk) for funding the durability of emission control systems project. Special thanks to G. Bishop for access to and use of the FEAT instrument. N. Farren would like to thank A. Vaughan, W. Drysdale and S. Young for their assistance with the RS surveys. The Opus RSD 5000 data provided by Ricardo and the financial support of the International Council on Clean Transportation (ICCT) are also gratefully acknowledged.

References

- Bates, D. M., and Venables, W. N.: (2019). splines: Regression Spline Functions and Classes. R package version 3.4.4.
- Bernard, Y., Tietge, U., German, J. and Muncrief, R.: Determination of real-world emissions from passenger vehicles using remote sensing data. [online] Available from: https://www.theicct.org/sites/default/files/publications/TRUE_Remote_sensing_data_20180606.pdf, 2018.
- Bishop, G. A., and Stedman, D. H.: (1996). Measuring the emissions of passing cars, *Accounts Chem Res*, 29, 489-495, Doi 10.1021/Ar950240x.
- Borken-Kleefeld, J., and Chen, Y.: (2015). New emission deterioration rates for gasoline cars - Results from long-term measurements, *Atmos. Environ.*, 101, 58-64, 10.1016/j.atmosenv.2014.11.013.
- Burgard, D. A., Bishop, G. A., Stadmuller, R. S., Dalton, T. R., and Stedman, D. H.: (2006a). Spectroscopy applied to on-road mobile source emissions, *Appl Spectrosc*, 60, 135a-148a, Doi 10.1366/000370206777412185.
- Burgard, D. A., Dalton, T. R., Bishop, G. A., Starkey, J. R., and Stedman, D. H.: (2006b). Nitrogen dioxide, sulfur dioxide, and ammonia detector for remote sensing of vehicle emissions, *Rev Sci Instrum*, 77, Artn 014101 10.1063/1.2162432.
- Carslaw, D. C., Farren, N. J., Vaughan, A. R., Drysdale, W. S., Young, S., Lee, J. D.: (2019). The diminishing importance of nitrogen dioxide emissions from road vehicle exhaust, *Atmos. Environ.* X, 1, 100002.
- Carslaw, D. C., Farren, N. J., Borken-Kleefeld, J., Sjödin, Å.: (2018). Study on the durability of European passenger car emission control systems utilizing remote sensing data. IVL Swedish Environmental Research Institute, preliminary final report. Commissioned by: Federal Office for the Environment (FOEN), Switzerland.
- Chen, Y. C., and Borken-Kleefeld, J.: (2016). NOx Emissions from Diesel Passenger Cars Worsen with Age, *Environ. Sci. Technol.*, 50, 3327-3332, 10.1021/acs.est.5b04704.
- HBEFA: 2017, Handbook Emission Factors for Road Transport Version 3.3: <http://www.hbefa.net/e/index.html>, access: 05-02-2019.
- Koenker, R., and Bassett, G.: (1978). Regression Quantiles, *Econometrica*, 46, 33-50, Doi 10.2307/1913643.
- Ntziachristos, L., Gkatzoflias, D., Kouridis, C., and Samaras, Z.: (2009). COPERT: A European Road Transport Emission Inventory Model, *Environ Sci Eng*, 491-+, 10.1007/978-3-540-88351-7_37.
- Opus: 2018, Remote Sensing Technology: <https://www.opus.global/vehicle-inspection/remote-sensing/>, access: 28-01-2019.
- Popp, P. J., Bishop, G. A., and Stedman, D. H.: (1999). Development of a high-speed ultraviolet spectrometer for remote sensing of mobile source nitric oxide emissions, *J Air Waste Manage*, 49, 1463-1468, Doi 10.1080/10473289.1999.10463978.
- Rushton, C. E., Tate, J. E., Shepherd, S. P., Carslaw, D. C.: (2018). Inter-instrument comparison of remote-sensing devices and a new method for calculating on-road nitrogen oxides emissions and validation of vehicle-specific power, *J Air Waste Management*, 68:2, 111-122, Doi 10.1080/10962247.2017.1296504.
- UoD: 2011, What's a FEAT?: <http://www.feat.biochem.du.edu/whatsafeat.html>, access: 28-01-2019.
- UoD: 2014, FEAT Equations for CO, HC and NO : http://www.feat.biochem.du.edu/assets/reports/FEAT_Math_II.pdf, access: 28-01-2019.
- Wood, S. N.: (2003). Thin plate regression splines, *J Roy Stat Soc B*, 65, 95-114, Doi 10.1111/1467-9868.00374.
- Wood, S. N.: (2004). Stable and efficient multiple smoothing parameter estimation for generalized additive models, *J Am Stat Assoc*, 99, 673-686, 10.1198/016214504000000980.

2.8 Particulate Matter

This section includes papers presented in the context of the “Particulate Matter” sessions of the TAP conference. Table 9 provides an overview of these papers, as they are listed in the following subsections.

Table 9. Titles and authors of “Particulate Matter” papers

	Paper Title	Authors
2.8.1	Vertical profiles of lung deposited surface area concentration of particulate matter measured with a drone in a street canyon	H. Kuuluvainen, M. Poikkimäki, A. Järvinen , J. Kuula, M. Irlala, Miikka Dal Maso, J. Keskinen, H. Timonen, J.V. Niemi and T. Rönkkö
2.8.2	How much tyre wear (microplastic) is effectively contributing to PM10? Insights from automated SEM/EDX single particle analysis	J. Rausch, D. Jaramillo Vogel and B. G. Purghart
2.8.3	Numerical study of particle dispersion emitted from train brakes in underground station	A. Durand, A. Mehel, F. Murzyn, S. Puech and F. Larrarte

2.8.1 Vertical profiles of lung deposited surface area concentration of particulate matter measured with a drone in a street canyon

H. Kuuluvainen^{1}, M. Poikkimäki¹, A. Järvinen¹, J. Kuula², M. Irlala³, Miikka Dal Maso¹, J. Keskinen¹, H. Timonen², J.V. Niemi⁴, and T. Rönkkö¹*

¹ Aerosol Physics, Faculty of Natural Sciences, Tampere University of Technology, Tampere, Finland
heino.kuuluvainen@tuni.fi

² Atmospheric Composition Research, Finnish Meteorological Institute, Helsinki, Finland

³ Aeromon Ltd, Helsinki, Finland

⁴ Helsinki Region Environmental Services Authority (HSY), Helsinki, Finland

Introduction

Street canyons are interesting and important environments in urban areas with respect to the dispersion of traffic emissions and human exposure. Because of the reduced natural ventilation, pedestrians, cyclists, and people inside vehicles are exposed to relatively high concentrations of particles and gaseous pollutants on the ground level of street canyons. In addition, the vertical dispersion of pollutants affects the human exposure above the ground level in buildings and contributes to regional background concentrations. In previous studies, the emissions have been measured in street canyons at a few different heights, mainly restricted to the ground level and the rooftop. More detailed information on the vertical dispersion is needed, for instance, for the use of urban planning and the design of ventilation systems in buildings. Lung deposited surface area (LDSA) concentration is a relevant metric for particulate matter with respect to negative health effects especially in urban areas and it can be measured with different electrical particle sensors.

All the results presented here in this conference paper are originally published in Environmental Pollution by Kuuluvainen et al. (2018). Only a general background, a short description of the methods and the most important results are shown here. Please, see the original publication (Kuuluvainen et al., 2018) for further references to literature and previous studies as well as a more detailed description of the methods and results of this study.

Methods

The drone measurements were carried out in a busy street canyon in Helsinki next to an urban supersite measurement station (Mäkelänkatu 50) during two days, on November 14th and 15th, 2016. These measurement days are referred as Day 1 and Day 2, respectively. In addition to them, stationary measurements at two different heights were carried out during the afternoon on November 17th, referred as a stationary day, and a two-week period of measurements between 7th and 23rd. Furthermore, simultaneous measurements were also carried out at an urban background measurement station nearby in Kumpula.

Figure 1 shows a schematic cross-section of the street canyon which can be classified as an avenue canyon with an aspect ratio of 0.45. The drone was operated vertically starting from the ground on the southeast side of the measurement station up to an altitude of 50 m. During the drone measurements, simultaneous reference measurements were carried out with different instruments at the measurement station, on the other side of the street at the kerbside, and at the urban background measurement station. In addition, meteorological data, including the wind speed and direction, was measured at a weather station located nearby.

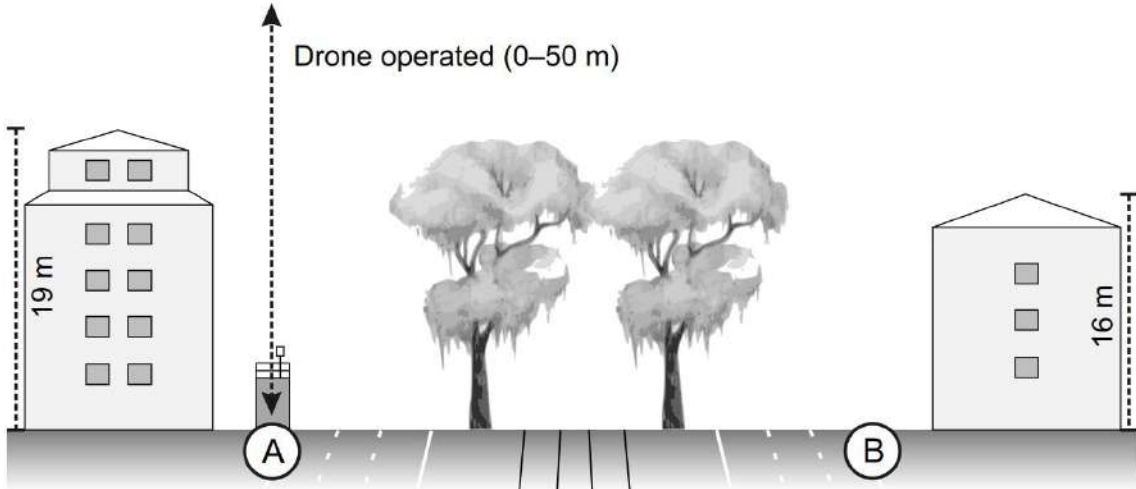


Figure 1: A schematic cross-section of the street canyon in which the measurements were carried out. The drone was operated next to an urban supersite measurement station and simultaneous ground level measurements were conducted at the station (A) and on the other side of the street (B). See Kuuluvainen et al. (2018).

An unmanned aerial vehicle (UAV) used as a moving measurement platform in the experiments was a quadrotor drone, and the particle sensor installed into the drone was a Partector (Naneos GmbH), which measures the LDSA concentration. A pressure altimeter was used to track the altitude of the drone. The drone was able to operate 3–5 subsequent up-and-down flights before the battery has to be changed or recharged. Altogether, 48 up-and-down flights were conducted during the two days. In addition to the sensor installed into the drone, reference data was measured at different locations with another Partector and other devices such as a DiSCmini (Testo Ltd.), an electrical low pressure impactor (ELPI+, Dekati Ltd.), and an AQ Urban (Pegasor Ltd.). In the data analysis, the obtained measurement data on the vertical concentration profiles were fitted with a mathematical equation to find a functional form for the LDSA concentration versus the measurement altitude.

Results and discussion

In order to estimate the representativeness of the drone measurement days and the stationary day with respect to the two-week period, Figure 2 shows the diurnal variation of the LDSA concentration measured at the street level of the street canyon along with a wind rose for the different measurement days and the two-week period of measurements. In the LDSA concentrations, the two-week data showed a strong diurnal pattern as expected at an urban traffic site. Even though the wind conditions were very different during the two drone measurement days, namely a relatively strong south wind during Day 2 and a much weaker north-east wind during Day 1, the LDSA concentrations measured at the ground level were very similar during these days and close to the two-week averages during daytime. This indicates that the vortex caused by the predominant wind had only a minor influence on the LDSA concentrations compared to the turbulent mixing caused by the traffic. The average LDSA concentrations of the stationary day were also close to the two-week averages and other measurement days during daytime. The drone measurements and the stationary measurements were carried out during daytime, and the exact measurement periods and the corresponding wind conditions are illustrated with light-colored plots and markers in Figure 1.

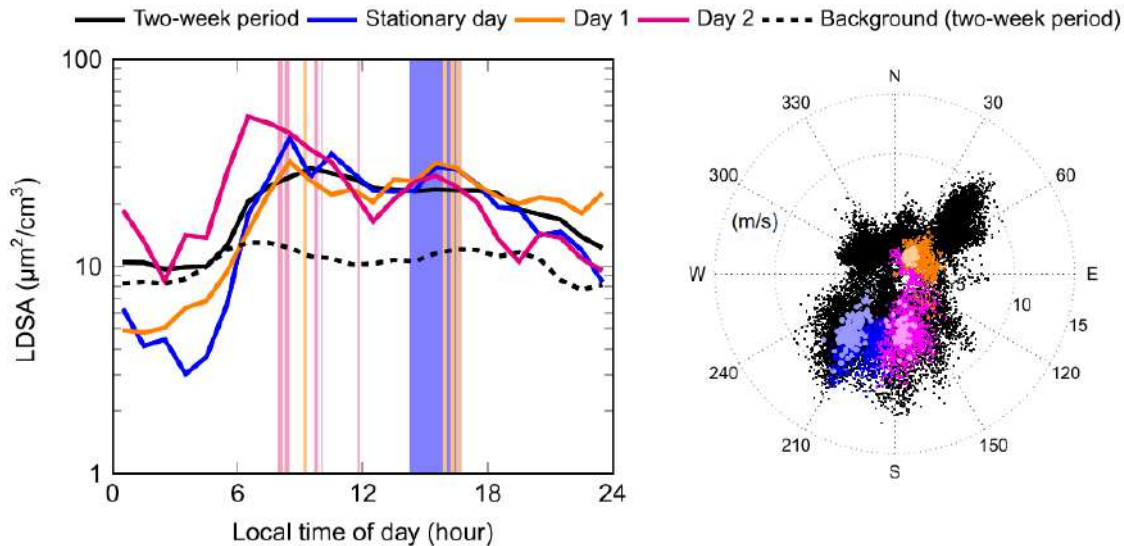


Figure 2: Diurnal variations of the lung deposited surface area (LDSA) concentration measured at the ground level of the street canyon for different measurement days and for the two-week period. Also the two-week data from the background station is shown. The drone and stationary measurement times are illustrated with the shaded color plots on the background. A wind rose on the right shows the wind direction and speed with an averaging time of 10 min. The data is classified according to the measurement day and the light-colored markers represent the actual measurement times. See Kuuluvainen et al. (2018).

Figure 2 shows the vertical profiles of the LDSA concentration measured with the Partector installed into the drone, separately for the two drone measurement days. The shapes of the averaged vertical profiles were similar for both the measurement days. Two different dilution profiles were seen - one of them inside the street canyon with the LDSA concentration approaching the background level in the street canyon, and the other above the rooftop level with the LDSA concentration approaching the urban background. The greatest difference between the data of these two days was observed in the magnitude of the deviation for all the data points and in the averaged profiles right below the rooftop level. During the drone measurements of Day 2, the wind speed was much higher compared to Day 1, which may cause more efficient advection of emissions and the breakage of the rooftop level concentration as seen in the averaged vertical profiles during Day 2 but not during Day 1. Despite the very different wind directions during these two days, the effect of the vortex caused by the predominant wind on the vertical profiles and the LDSA concentrations at the ground level seemed to be insignificant. The stationary measurements at two different heights supported the vertical LDSA profiles measured with the drone. Based on a detailed data analysis (Kuuluvainen et al., 2018), the role of turbulent mixing caused by traffic, induced by the measurement station container located right next to a bus line of the street, was concluded to be the most important factor affecting the vertical dispersion of particles. With the mathematical fits on the vertical profiles, the results could be compared to previous studies and they seemed to be in line with other studies at least those of focusing on similar type of wide street canyon environments.

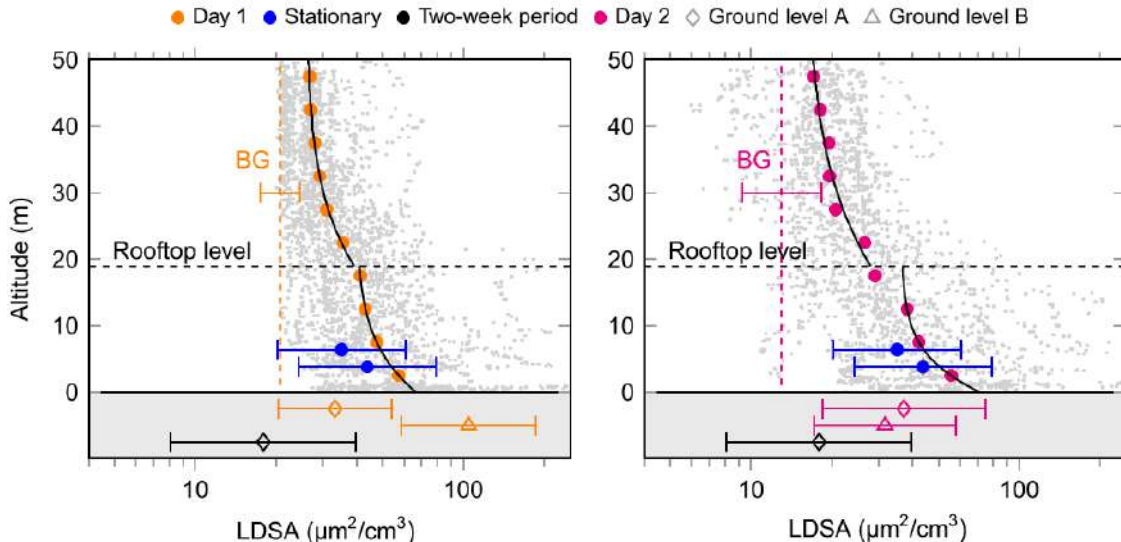


Figure 3: Vertical profiles of lung deposited surface area (LDSA) concentrations for Day 1 and Day 2. All the measured data is presented with gray dots, the geometric means for different altitudes with colored circles, and the mathematical fits with solid lines. In addition, reference data are shown for the two-week period, ground level measurements and background measurements (BG) simultaneously with the drone measurements, as well as for the stationary measurements at different heights. See Kuuluvainen et al. (2018).

Summary and conclusions

The vertical profiles of alveolar lung deposited surface area (LDSA) concentration were measured for the first time in an urban street canyon by using a drone as a moving measurement platform. In spite of different wind conditions, the averaged vertical profiles of LDSA measured during two different days were found to be close to each other. The role of turbulent mixing caused by traffic was emphasized compared to the street canyon vortex as a driving force of the dispersion. The mathematical fits on the high-resolution measurement data of this study showed that also the concentration over the rooftop level decreased exponentially approaching the urban background concentration. This important result should be taken into account to improve current street canyon models, many of which predict zero concentrations above the rooftop level. Models should be able to explain the dispersion in different scales starting from the source at the ground level to the level where pollutants are fully mixed to the urban background air. The high-resolution measurement data obtained in this study can be then used in the verification of models. In addition, the methodology based on the use of a drone as a moving measurement platform can be used to characterize the vertical profiles in various urban street canyons as such or support model development for example in different meteorological conditions.

Acknowledgements

This work was conducted in the INKA-ILMA/EAKR project funded by Tekes, European Union, Helsinki Region Environmental Services Authority (HSY), City of Tampere, City of Kuopio, Dekati Ltd., Genano Ltd., Nordic Envicon Ltd., Pegasor Ltd., Sandbox Ltd., Suomen Terveysilma, TreLab Ltd., and Vallox Ltd., as well as in the Cityizer project funded by Tekes, HSY, and Pegasor.

References

- Kuuluvainen, H., Poikimäki, M., Järvinen, A., Kuula, J., Irjala, M., Dal Maso, M., Keskinen, J., Timonen, H., Niemi, J.V., Rönkkö, T. (2018). Vertical profiles of lung deposited surface area concentration of particulate matter measured with a drone in a street canyon, *Environmental Pollution*, 241, pp. 96-105.

2.8.2 How much Tyre Wear (Microplastic) is Effectively Contributing to PM10? Insights from Automated SEM/EDX Single Particle Analysis

J. Rausch^{1*}, D. Jaramillo Vogel¹, B. Gälli Purghart²

¹Particle Vision GmbH, c/o Fri Up, Annexe 2, Passage du Cardinal 11, Fribourg, 1700, Switzerland,
juanita.rausch@particle-vision.ch

²Federal Office for the Environment (FOEN), 3003 Bern, Switzerland

Introduction

Increasingly more attention is focused on non-exhaust particle emissions as previous and actual efforts have been leading to successful reduction of exhaust particle emissions. The major contributors to non-exhaust particle emissions derived from road traffic are tyre, break and road surface wear, as well as the resuspension of those particles (e.g. Pant and Harrison, 2013). Break wear particles are known to be present in the Particular Matter (PM) fractions PM10 and PM2.5. However, the amount of tyre wear in these health-relevant fractions is still highly debated. One of the difficulties in quantifying tyre wear is the heterogeneity of tyre rubber and road wear compositions and their variable degree of mixing, which depends on many factors (e.g. vehicle behaviour, road characteristics, etc.) resulting in complex ambient tyre wear particles. Furthermore, bulk analytical techniques do not enable a straightforward identification, differentiation and quantification of the amount of tyre wear, respectively tyre/road wear mixtures in environmental samples due to ambiguous tracers (e.g. Zn is used as tracer for brake as well as for tyre wear). In this study, we present the results of the quantification of tyre wear and its proportion in the PM10-2.5 and PM2.5-1 fractions of environmental samples collected with Sigma-2 passive samplers and analyzed with automated SEM/EDX single particle analysis.

Sampling and analytical Methods

Samples of the PM80-1 fraction were collected passively on self-made boron substrates with the Sigma-2 passive sampler (VDI 2119:2013) (Fig. 1). The advantage of boron substrates is that - unlike on conventional carbon-bearing SEM substrates - the element carbon (C) can be semi-quantitatively analysed by EDX (energy dispersive x-ray spectroscopy). The inclusion of C in the analysis is essential because it can be diagnostic for the identification of tyre wear. In addition, the material contrast between the collected particles and the substrate is strongly enhanced resulting in an optimized particle recognition for single particle analysis and in better images, allowing a more detailed morpho-textural characterization of the particles.



Figure 1: Sigma-2 passive sampler (left) and adhesive surface exposed within the Sigma-2 (right) containing various substrates for microscopic analysis (boron: bottom right, C-Pad: top right, both for SEM, and glass surface for light microscopy: left).

The samples collected on boron substrates were analyzed by automated SEM/EDX (Scanning Electron Microscopy coupled to Energy Dispersive X-ray spectroscopy) single particle analysis with a Zeiss

Gemini SEM 300 equipped with an Oxford X-MAX 80 mm² EDS detector, a high efficiency 4 quadrant BSE detector and the newest particle analysis software of Oxford (Aztec Feature) at the Particle Vision SEM lab (Fribourg, Switzerland). The elemental composition and morphological parameters of at least 700 particles per sample were determined. The data sets obtained by single particle analysis were treated with the particle classifier PACLA software (Meier et al., 2018), which enables particle classification based on their chemical composition. Subsequently, chemical classes can be assigned to a specific source (e.g. tyre wear) if they match one of the previously characterized and archived chemical source composition in the particle library of PACLA (Fig. 2).

For particle classification a three-stage procedure is applied. The first stage consists a rule-based filter grouping particles consisting of the same elements into so called main classes. In the second stage, a robust model-based clustering method using the R package tclust is applied to each main class resulting in subclasses. Outliers are excluded automatically and hence have no effect on the shape of the subclasses. Recently, a third stage, which considers the content of carbon as a further parameter for chemical classification, was introduced. Since carbon determination by EDX is semiquantitative, it was decided to give carbon a different weighting in the classification schema compared to the more quantitative elements (starting from Na). Therefore, three carbon classes were defined (c1: low carbon particles containing 0-30 wt.% C; c2: medium carbon particles containing >30 <70 wt.% C and c3: high carbon particles containing > 70 wt.% C) (Fig. 2). The boundaries of these three classes can be modified in PACLA based on the aim of the study and the particles that are to be grouped. However, the boundaries mentioned above resulted to be ideal for the specific question of this study (i.e. detection and quantification of tyre wear in airborne samples).

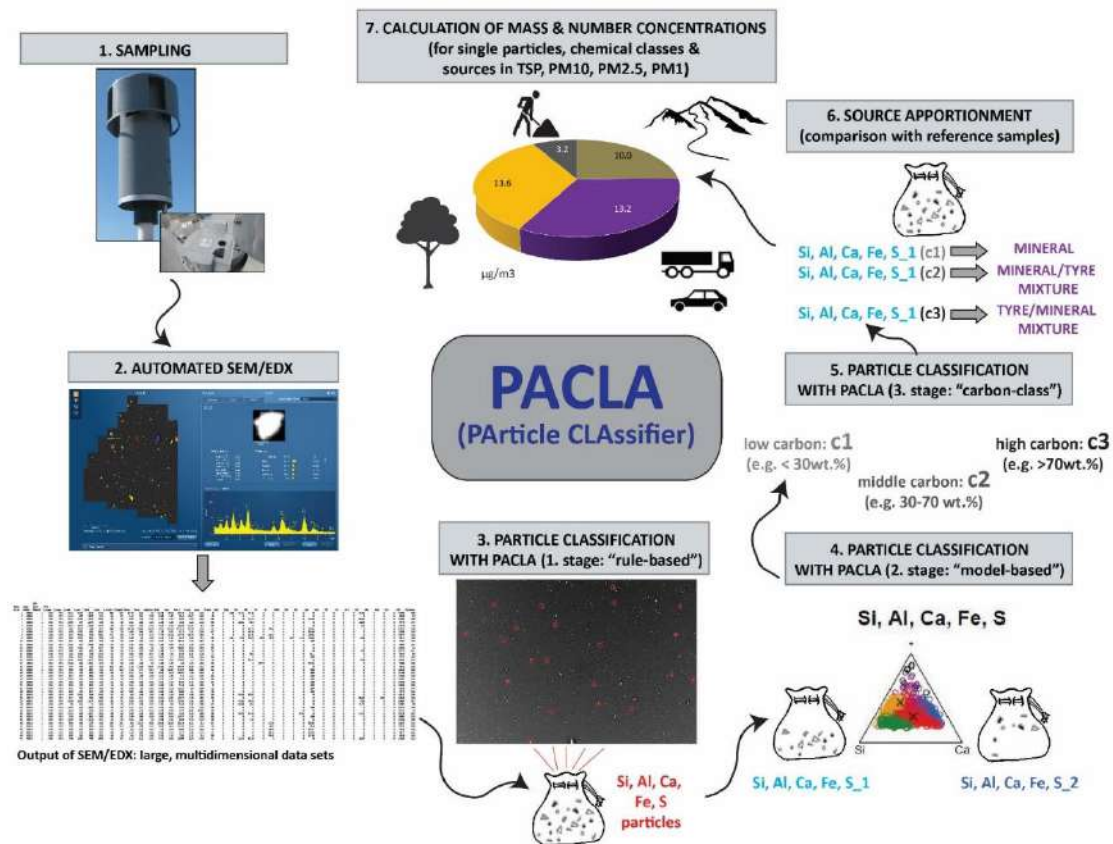


Figure 2: Schematic representation of the methodological procedure applied in this study for sampling, analysis, chemical classification and source assignment for each single particle.

Description and definition of tyre wear for this study

Tyre wear in environmental samples does not match the original composition of tyres. Once the tyres interact with the road there is always a contamination or mixing process between the tyre and the road material (e.g. Sommer et al., 2018). This explains why tyre wear particles practically always show mineral encrustations (Fig. 3). However, our studies have shown that the relative amount of these encrustations generally decreases with decreasing size of the tyre wear particles. This implies that the relative concentration of elements added by mineral particles (e.g. Si, Al, Ca, K, Na, Mg, etc) decreases with decreasing particle size as well. In contrast, the relative amount of carbonaceous material, which is one of the principal components of the rubber, seems to increase with decreasing tyre wear particle size (Fig. 4). In addition, it has also been proposed that the tyres suffer a chemical modification when they get into contact with the road and natural dust, resulting in tyre wear particles of modified composition with respect to the original composition of tyres (Panko et al. 2013). Due to all these difficulties it has been extremely challenging to identify tyre wear in environmental samples.

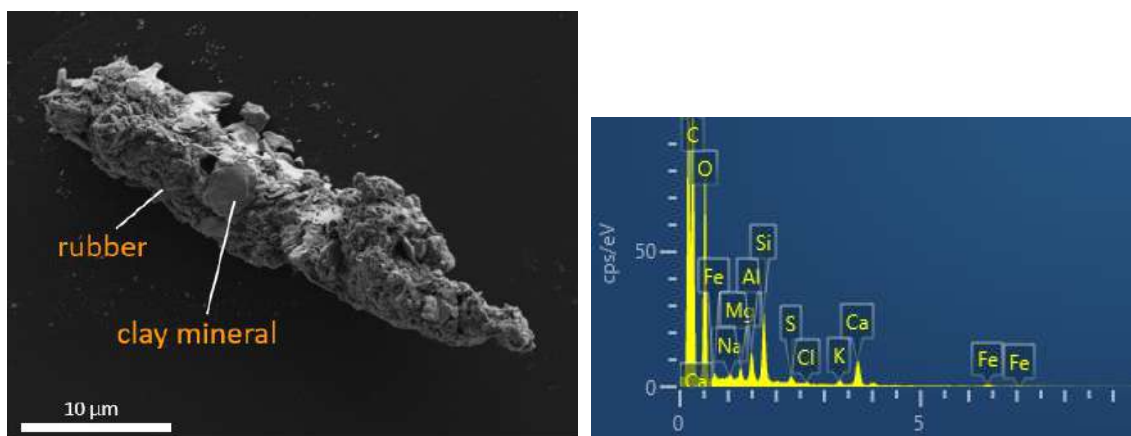


Figure 3: Detailed SEM image of a tyre wear particle showing the typical heterogeneity due to road wear incrustations, especially in coarser fractions (left). Example of an EDS spectrum from a tyre/road wear particle (right). Note that the carbon peak originates to 100% from the particle itself and is not influenced by the substrate since the substrate is made of boron.

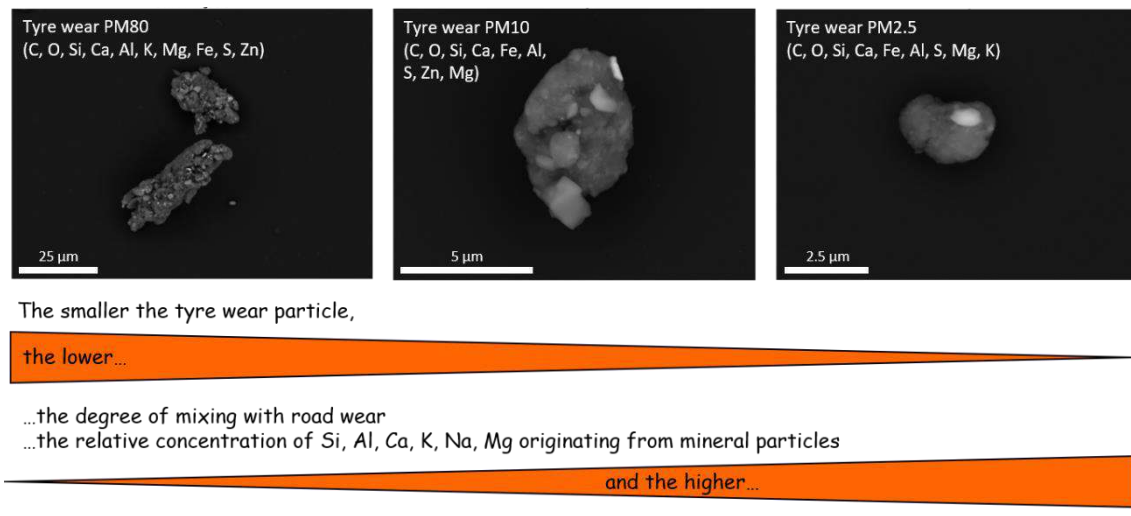


Figure 4: SEM images of tyre wear particles within different PM fractions with their corresponding elemental composition.

(Airborne) tyre wear particles are mixtures that fall within a line between two ideal end-members: one end-member corresponds to pure tyre rubber without any influence from the road and the environment and the other end-member corresponds to pure road wear without any share of tyre material. Tyre wear in environmental samples is practically always found as mixed tyre/road wear particles showing different degrees of mixing. The final composition is obviously also influenced by the chemical composition of the specific type of tyre and the road itself (Fig. 5). In this study, we opted to define tyre wear as all tyre/road

wear mixtures with more than 30% of C, which implies that these particles have a substantial rubber component.

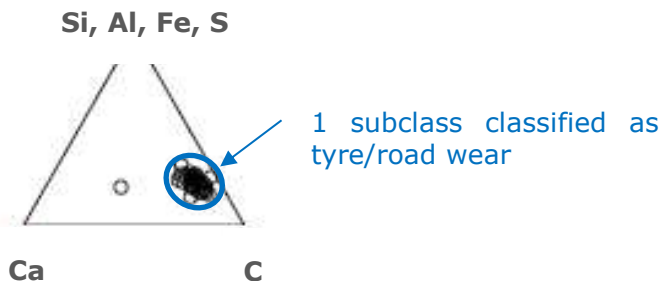


Figure 5: Ternary diagram showing one of the multiple chemical compositions (in this case: C, Si, Al, Ca, Fe, S) that has been identified as tyre/road wear mixtures by the SEM/EDX/PACLA classification schema. Chemical compositions are normalized excluding oxygen. Particles (= dots) plotted in this diagram do not contain further elements with a concentration > 1 wt.%.

Results: Quantification of mixed tyre/road wear particles by automated SEM/EDX single particle analysis and PACLA

Here, we present an estimation for the contribution of tyre/road wear particle immissions in PM80-10, PM10-2.5 and PM2.5-1 from selected sites. The samples were collected either beside a main road or in the centre of a highly transited town in three different countries (Switzerland, CH; Colombia, CO; and Mexico, ME). The results of the sites Orbe and Villeneuve (Fig. 6) were extracted from two PM10 characterization campaigns performed for the Environmental Office of the Canton of Vaud in Switzerland in 2017 and 2018, respectively. Each sample was collected during 14 days.

The sites Bern Bollwerk and Zurich Kaserne (Fig. 6) belong to the National Air Pollution Monitoring Network (NABEL) of Switzerland and are being studied in the frame of a PM10 characterization and source apportionment campaign taking place between June 2018 and June 2019. This study is being performed under the mandate of the FOEN (Swiss Federal Office for the Environment). The sampling interval is 16 days for each sample.

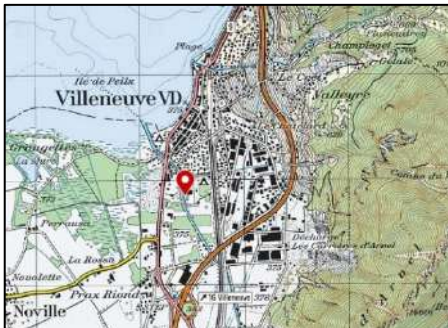
The measurements performed in Mexico took place in 2016 in collaboration with the UNAM (National Autonomous University of Mexico) on the roof of the Center for Atmospheric Sciences with a sampling duration of 14 days.

The measuring site in Medellin (Colombia) was located in one of the monitoring stations of the SIATA (Sistema de Alerta Temprana de Medellín y el Valle de Aburrá) at the Politécnico Jaime Isaza Cadavid (Fig. 6). The sampling interval was 10 days. These measurements have been done in the frame of an ongoing collaboration with the University EAFIT.

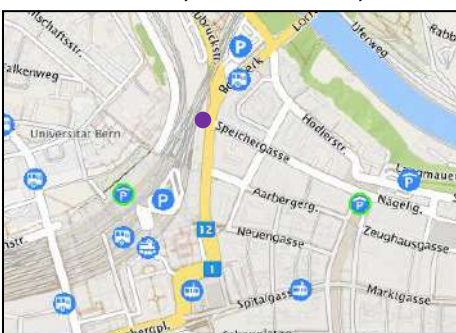
Orbe, Canton Vaud, Switzerland



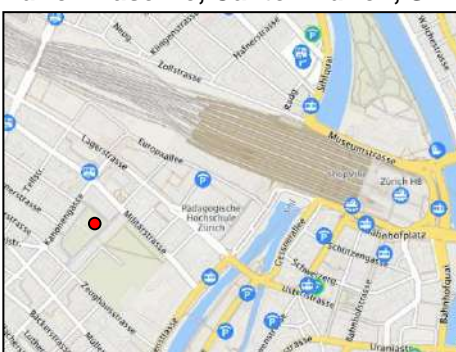
Villeneuve, Canton Vaud, Switzerland



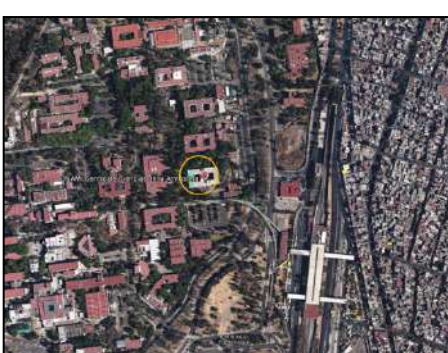
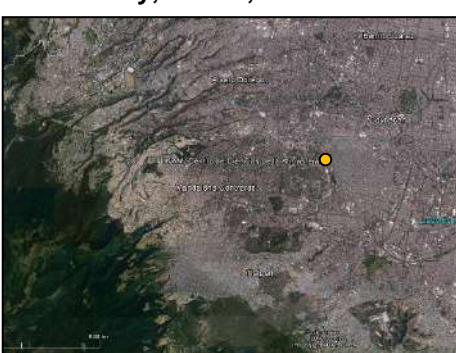
Bern Bollwerk, Canton Bern, Switzerland



Zurich Kaserne, Canton Zurich, Switzerland



Mexico City, UNAM, Mexico



Medellín, Valle de Aburrá, Colombia

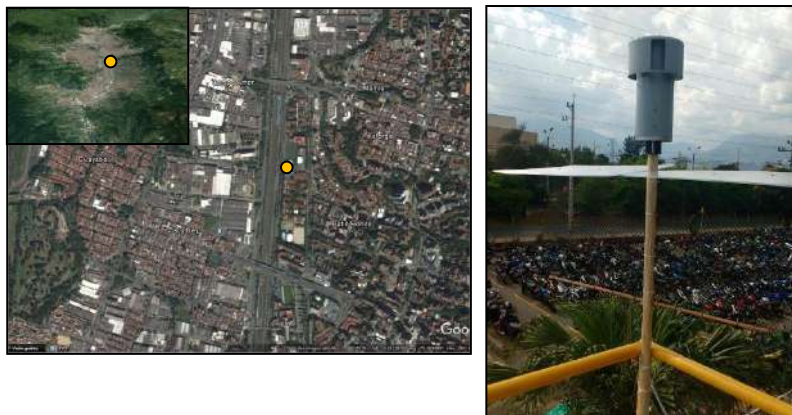


Figure 6: Sampling sites in Switzerland (Orbe, Villeneuve, Bern Bollwerk and Zurich Kaserne), Mexico (UNAM, Mexico City) and Colombia (Medellín).

Table 1. Examples of mass concentration and contribution in % of mixed tyre/road wear particles to PM10-2.5 and PM10 measured at different sites worldwide. The values are from one sampling period at each locality. The total PM2.5 and PM10 concentrations from the FOEN (CH), Canton of Vaud (CH), Medellín (CO) and Mexico City (ME) studies are derived from continuous optical single particle measuring devices (e.g. FIDAS 200) and are partially validated by gravimetry.

Country	Sites	Site typology	Tyre wear in PM10-2.5 ($\mu\text{g}/\text{m}^3$ / %)	PM10-1 tyre wear in PM10 ($\mu\text{g}/\text{m}^3$ / %)
CH	Orbe, VD	Urban, parking	1.20 / 23	1.25 / 9
	Villeneuve, VD	Urban, autoroute	0.83 / 8	0.92 / 6
	Bern Bollwerk, BE	Urban/traffic	5.01 / 35	5.91 / 20
	Zurich Kaserne, ZH	Urban background	0.43 / 9	0.53 / 4
CO	PJIC, Medellin	Urban/traffic	7.86 / 25	9.04 / 20
ME	UNAM, Mexico City	Urban/traffic	10.35 / 35	11.90 / 22

The results show that mixed tyre-road wear particles can contribute to up to 35% ($10.35 \mu\text{g}\cdot\text{m}^{-3}$) in the coarse mode fraction (PM10-2.5) and >22 % in PM10 (table 1 and fig. 7). The tyre/road wear estimations for PM10 represent minimum values since the fraction PM1 was not included in the measurements. The analytic approach to identify and quantify these particles in PM1 respectively PM2.5 samples (i.e. polycarbonate filters) is under improvement (see perspectives chapter).

The temporal variability of the **absolute concentration ($\mu\text{g}/\text{m}^3$)** of tyre/road wear in the studied sites shows very different behaviours. For instance, the results obtained from Zurich Kaserne show very low variabilities (standard deviation (s) of $0.06 \mu\text{g}/\text{m}^3$ with an average value of $0.39 \mu\text{g}/\text{m}^3$ over 12 periods, each period (=sample) with a duration of 16 days, i.e. a total sampling interval of ca. 6 months). In contrast, the standard deviation for the tyre/road wear concentrations in Bern Bollwerk was much higher ($s = 0.97 \mu\text{g}/\text{m}^3$) with an average value of $2.5 \mu\text{g}/\text{m}^3$ for the same time period (June-November 2018) and number of samples as in Zurich Kaserne.

However, the **relative concentration (%)** of tyre/road wear within the studied fractions does not vary significantly as lower tyre/road wear concentrations correlate with lower total PM10-2.5 and PM10 concentrations.

Hence, the actual results evidence that tyre/road wear is an important source of pollution in PM10, especially in heavily traffic-loaded areas.

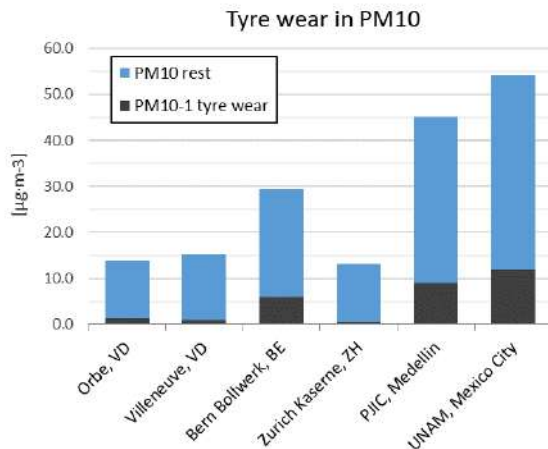


Figure 7: Comparison of the proportion of tyre wear in PM10 among all studied sites for one exemplary sampling period (see data in table 1).

The contribution of tyre/road wear to the different size fractions (PM80-10, PM10-2.5 and PM2.5-1) is shown exemplarily for the site of Orbe (parking activity), Bern Bollwerk (heavy traffic) and Zurich Kaserne (urban background) (Fig. 8). The results evidence that the driving behaviour and the distance to the road influences the size distribution of the tyre/road wear particles measured in the respective immission sites. Parking activities seem to mainly generate tyre/road wear particles of large size (> PM2.5). The proportion of small (PM2.5-1) tyre/road wear particles resulted to be higher close to highly transited roads (e.g. Bern Bollwerk) than in parking areas. Furthermore, the relative proportion of PM2.5-1 particles is the largest in the site Zurich Kaserne. This site is located at the furthest distance to the road among the three sites, suggesting that the relative proportion of the PM2.5 particles is highly dependent on the distance to the road. This effect is due to the long residence time of small particles in the air because of their small weight, and hence, low sedimentation velocity.

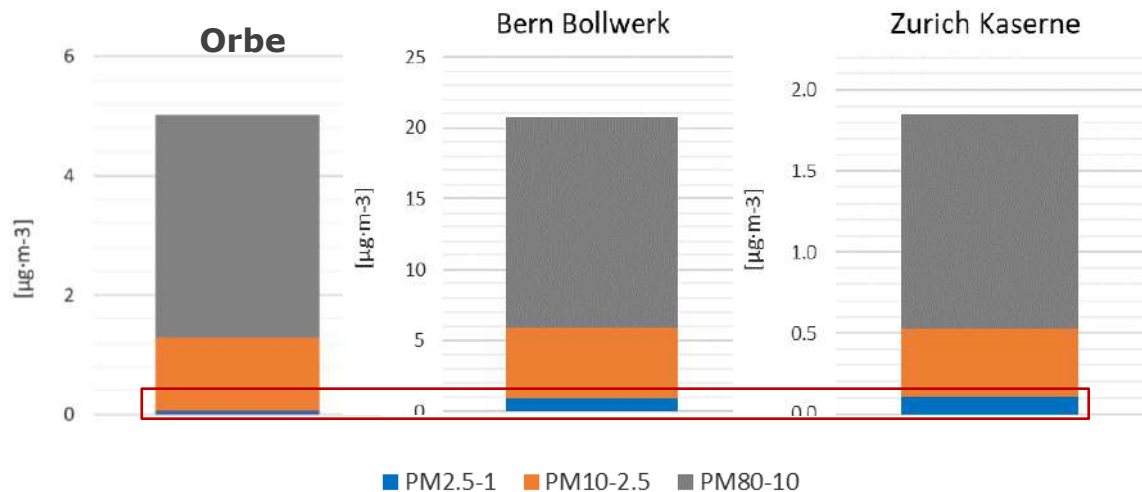


Figure 8. Examples of mass concentration of mixed tyre-road wear particles in the different size fractions (PM80-10, PM10-2.5, PM2.5-1) for Orbe, Bern Bollwerk and Zurich Kaserne. Note the differences in the relative proportion of tyre wear in PM2.5-1 depending on the measuring site.

Discussion and conclusions

The results presented in this study clearly show that tyre/road wear is an important source of pollution in the coarse mode fraction of PM10 (PM10-2.5), especially in heavily traffic-loaded areas, such as the studied sites in Bern, Mexico City and Medellín.

Even though the absolute mass concentration of tyre/road wear within the PM2.5-1 fraction is low, the number concentration can be very high. Considering the negative health effects of PM2.5 and specially the potential toxicity of the rubber components (Grigoratos & Martini, 2014), these particles and their

contribution to the respirable fractions should be studied in more detail. In addition, strategies aiming to reduce the emission of tyre wear must be included in the action plans for air quality improvement. Assessing the impact of tyre wear on our environment is not only relevant because of its worth mentioning contribution to air pollution but also because it is considered to be one of the most important sources of microplastic in the oceans worldwide (Kole et al., 2017). Therefore, detailed studies aiming to quantify the amount of tyre wear and its geographic distribution in the water systems are also of large relevance.

Perspectives: Quantification of tyre wear in active PM2.5 samples and differentiation of rubber

In order to extend the quantification of tyre wear to the finest fraction (PM1) by means of SEM/EDX, this fraction needs to be actively sampled on polycarbonate filters. To overcome the difficulties of C quantification on the polycarbonate filters (due to the signal interference between the C from the particles and the C of the substrate itself), calibrated grey values can be used as a further proxy for an approximate estimation of the carbon content and subsequent particle differentiation. The lower the carbon content the lower the gray value, and the higher the metal content, the higher the gray value of the particle. By combining this principle with the elemental composition obtained by automated SEM/EDX analysis (excluding C) and the morphological information of the single particles, the detection and quantification of tyre wear within the PM2.5 fraction is becoming more reliable. An automatization and integration in the particle classifier software PACLA of this classification schema specifically adapted for PM2.5 is in progress.

In addition, a differentiation of the proportion of rubber vs. mineral particles encrusted in the rubber by image analysis is under development. This will enable a better estimation of the amount of the more harmful component of the tyre/road wear mixtures (i.e. rubber) in the PM samples.

Acknowledgements

We thank the Swiss Commission for Technology and Innovation (CTI) for financial support (CTI project 16675.1 PFIW-IW), Prof. Bernard Grobéty and the Department of Geosciences at the University of Fribourg (CH) for their analytical support and René Locher and his team from the Zürcher Hochschule für Angewandte Wissenschaften (ZHAW) for the statistical support to develop the particle classifier (PACLA) software. We are very grateful to the Federal Office for the Environment (FOEN) and the Environmental Office of the Canton of Vaud for their financial contribution, for the great cooperation and for the open communication policy. We also thank Telma Gloria Castro Romero and her research team from the Atmospheric Science Center (CCA) of the National Autonomous University of Mexico (UNAM) and Jose Duque and his collaborators from the University EAFIT and from the SIATA for helping us with the sampling campaigns.

References

- Grigoratos, T., & Martini, G. (2014). Non-exhaust traffic related emissions. Brake and tyre wear PM. *Report no. Report EUR, 26648.*
- Kole, P. J., Löhr, A. J., Van Belleghem, F., & Ragas, A. (2017). Wear and tear of tyres: A stealthy source of microplastics in the environment. *International journal of environmental research and public health, 14(10)*, 1265.
- Meier, M. F., Mildenberger, T., Locher, R., Rausch, J., Zünd, T., Neururer, C., Ruckstuhl, A., Grobéty, B. (2018) A model based two-stage classifier for airborne particles analyzed with CCSEM. *J Aerol Sci 123: 1-16.*
- Panko, J. M., Chu, J., Kreider, M. L., & Unice, K. M. (2013). Measurement of airborne concentrations of tire and road wear particles in urban and rural areas of France, Japan, and the United States. *Atmospheric environment, 72*, 192-199.
- Pant, P., & Harrison, R. M. (2013). Estimation of the contribution of road traffic emissions to particulate matter concentrations from field measurements: a review. *Atmospheric environment 77: 78-97.*
- Sommer, F., Dietze, V., Baum, A., Sauer, J., Gilge, S., Maschowski, C., & Gieré, R. (2018). Tire abrasion as a major source of microplastics in the environment. *Aerosol and Air Quality Research, 18(8)*, 2014-2028.VDI, VDI2119:2013-06, Beuth Verlag, 10772, Berlin, Germany, 2013.

2.8.3 Numerical study of particle dispersion emitted from train brakes in underground station

A. Durand^{1, 2*}, A. Mehe¹, F. Murzyn³, S. Puech¹ and F. Larrarte⁴

¹ Department of Environment, SNCF, 72000, Le Mans, France

² Department of Mechanical Engineering, Estaca'Lab, 78180, Montigny-Le-Bretonneux, France, antoine.durand-ext@estaca.fr

³ Department of Mechanical Engineering, Estaca'Lab, 53000, Laval, France

⁴ Department of Geotechnical Engineering, Environment, Natural hazards and Earth sciences, IFSTTAR, 44344, Bouguenais, France

Introduction

Air pollution has become a major issue since it is responsible for several adverse health effects. Among pollutants, exposure to particle matter (PM) including ultrafine (UFP) and nanoparticles has been defined as particularly hazardous. It was shown (Oberdörster, 2001; Pope et al., 2003) that PM exposure increases the risks of cardiovascular and respiratory diseases. Particles size is strongly linked to their dangerousness. The smaller they are, the higher their deposition rate and their ability to penetrate respiratory and blood system are. Former studies carried out in underground train stations across the world revealed that particle concentration rates can reach higher levels than outdoor (Braniš, 2006 ; Kim et al., 2008 ; Kam et al., 2011). Thus, commuting is one of the main contribution to daily personal exposure to particulate pollutants (Chillrud et al., 2004; Knibbs et al., 2011; Querol et al., 2012). Particles being in subway platforms are mostly ferruginous compounds. They are mostly emitted by friction between wheels and rail and by mechanical braking systems while trains are stopping at stations (Moreno et al, 2015; Airparif, 2017).

However, most of the studies investigating PM levels was undertaken to monitor global PM rates inside stations rather than the exact contribution of each PM source. To achieve this goal, one approach consists in studying the particles dynamics from their emission to their complete dispersion. To date, little is known about wear particles dynamics inside train stations (Octau et al., 2017), while flow turbulence resulting from passing trains have a strong influence on PM levels at the platform (Salma et al., 2007; Querol et al., 2012). This work aims to increase our knowledge about particle dynamics issued from trains brake discs in the context of an underground station.

Then, the influence of the flow surrounding a train passing a station at low speed is investigated. Three different particle sizes emitted from brakes are considered. Size ranges are fine particles (FP), ultrafine particles (UFP) and nano-sized particles (NSP), with mean diameters of $d_p=2.5\mu\text{m}$, $d_p=0.8\mu\text{m}$ and $d_p=0.07\mu\text{m}$, respectively. The first two sets of particles have been identified by both published studies (Olofsson et al., 2009; Olofsson, 2011) and SNCF (French National Railways Company) tribology experiments. The exact diameter peaks in a Particle Size Distribution (PSD) depends on friction materials and sliding velocity. However, their order of magnitude remains the same. Concerning the NSP peak, it seems to be correlated with the temperature increase of materials resulting from the sliding contact (Sundh et al., 2009; Namgung et al., 2016).

To assess the particle dynamics for these three specific size ranges, three-dimensional numerical simulations are conducted using the commercial code Fluent 19.2. The Eulerian-Lagrangian approach is used allowing a fine tracking of particles in the flow around the rolling stock. The turbulent mean flow is computed using Unsteady Reynolds-Averaged Navier-Stokes (URANS) through the RNG k- ε turbulence model. Particles dispersion from disks brakes to the station is computed with the Discrete Phase Model.

Our methodology is described in the first part of this paper, followed by the results of flow computation. Train-induced flow influence on brake particle dispersion is discussed in the third section. This paper ends with our conclusions about regions of interested highlighted by the present study and perspective for further studies to assess properly particle dispersion in underground stations.

1. Methodology

1.1 Geometry and boundary conditions

This study is based on a full-scale SNCF Z20500 french commuter train (Figure 1a), which is widely used by this company for underground commuting. Computer-Aided Design (CAD) was achieved with the help of SNCF blueprints and existing partial CADs (Figure 1b). Although details such as ventilation units, pantographs or accessibility equipment are not considered, the main geometry is kept similar to the original. The full trainset is made of a front-end motor car, two trailer cars and a tail-end motor car. Model length, width and height are respectively $L_t=98.76\text{m}$, $W_t=2.82\text{m}$ and $H_t=4.32\text{m}$. The train is located in an underground station with a 7.2m wide (including 0.3m overhang at both sides) and 0.6m high central platform, which is a common architecture for SNCF underground stations. Station length, width and height are $L_s=240\text{m}$, $W_s=17.6\text{m}$, $H_s=6\text{m}$. Rail width is extended to wheel thickness in order to simplify the contact between wheels and rails.

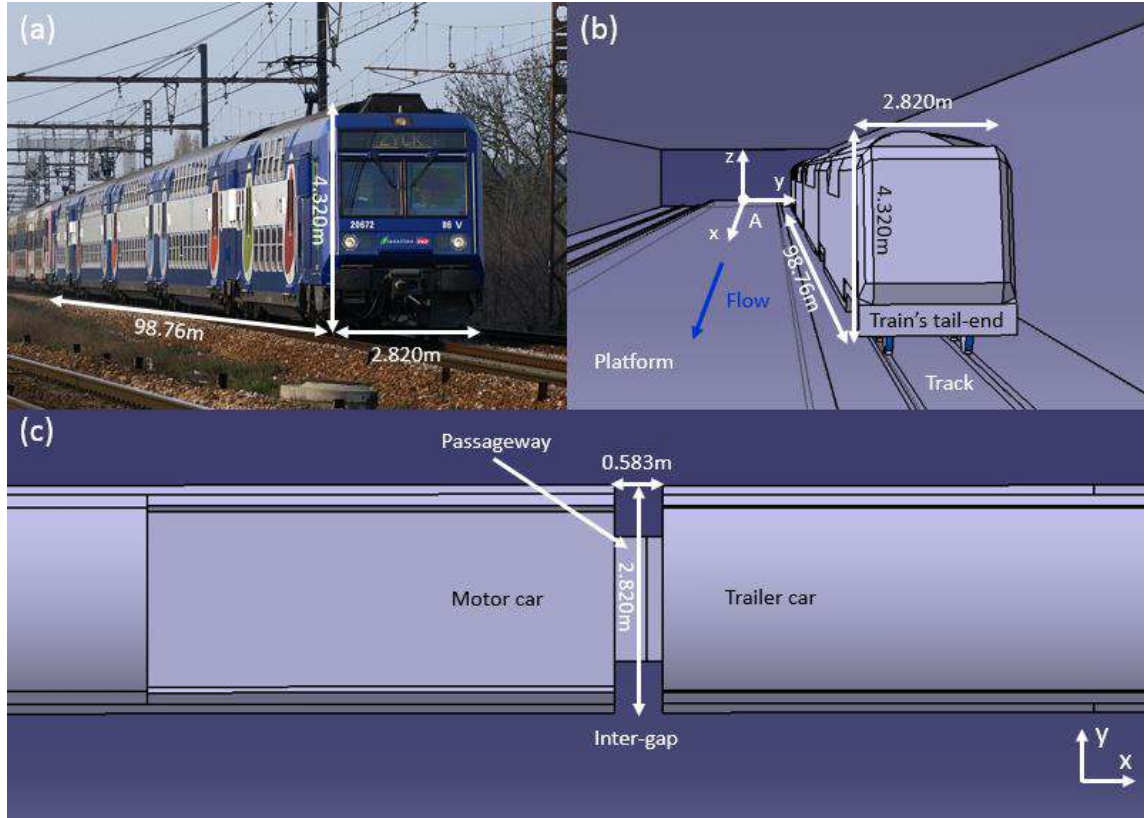


Figure 1: SNCF Z20500 trainset (a) (photo from Romain Martin shared under CC BY-SA 2.5 license), full-scale train CAD model inside a station with central platform (b) and a closer look at the inter-gap between cars (c).

The origin of the coordinate system is defined in the mid-plane of the platform, $x=0$ corresponds to the exit of the station (the nearest side from train's front-end) and $z=0$ at the bottom level of the track. Thus, in Figure 1b, point A is located at $x=0\text{m}$, $y=0\text{m}$, $z=0.6\text{m}$. A uniform velocity $U_0=12.5\text{m.s}^{-1}$ with a turbulent intensity of 10% are set at the inlet. This is supposed to be representative of the train approach speed in underground stations. The Reynolds number based on H_t is 3.10^6 . A zero gauge pressure is set at the outlet. No-slip condition in the direction of the flow is set to station's wall to avoid non-realistic boundary layer development induced by the freestream velocity. Stationary walls and no-slip conditions are set at train's surfaces. Time step is calibrated following Wang et al. (2017) recommendations for high-speed train CFD using URANS as no studies has been found so far for low-speed train aerodynamics. With the boundary conditions above mentioned, $T_{ref}=H_t/U_0$, is about 0.35s. Thus, time step is set at $\Delta t=0.05T_{ref}$ to ensure step independence (Wang et al., 2017; Niu et al., 2018).

Particles are generated for $8.5T_{ref}$ after $26T_{ref}$ single-phase computation to ensure the flow has advected more than the entire train length ($22T_{ref}$) with a margin for the slipstream. No particle is

generated from motor bogies, as there is no disc brake and one trailer bogie has been only considered. Both injection time and locations have been chosen to be in agreement with a reasonable computation time. The last trailer bogie has been chosen for particles injection to limit the number of time step required for the particles to reach the platform and the train wake flow. Injection time has been set to ensure a sufficient number of particles emitted with acceptable calculation cost. Total particle mass flow is based on former SNCF internal experiments for brake materials similar to those used for a Z20500 trainset. The mass flow for each particle size class is calibrated according to Olofsson (2011) assuming all particles emitted from brakes are made of steel dust.

1.2 Meshing

Domain meshing is made of tetrahedral elements combined with fine element in terms of size at face conditions in order to capture geometry details of cars and bogies. Three different levels of refinement zones, summarized in Table 1, are used to ensure the accuracy of predictions in critical regions. Far field is meshed with relatively coarse elements, while the train near-wake zone has finer elements and bogies areas are the most refined. Inflation layers are used at all domain surfaces to capture the boundary layer development resulting from the flow induced by the train.

The mesh used for this study, shown in Figure 2 (a), (b) and (c), is within the requirement for medium refinement (Wang et al., 2017), which is the better compromise between computation cost and results accuracy.

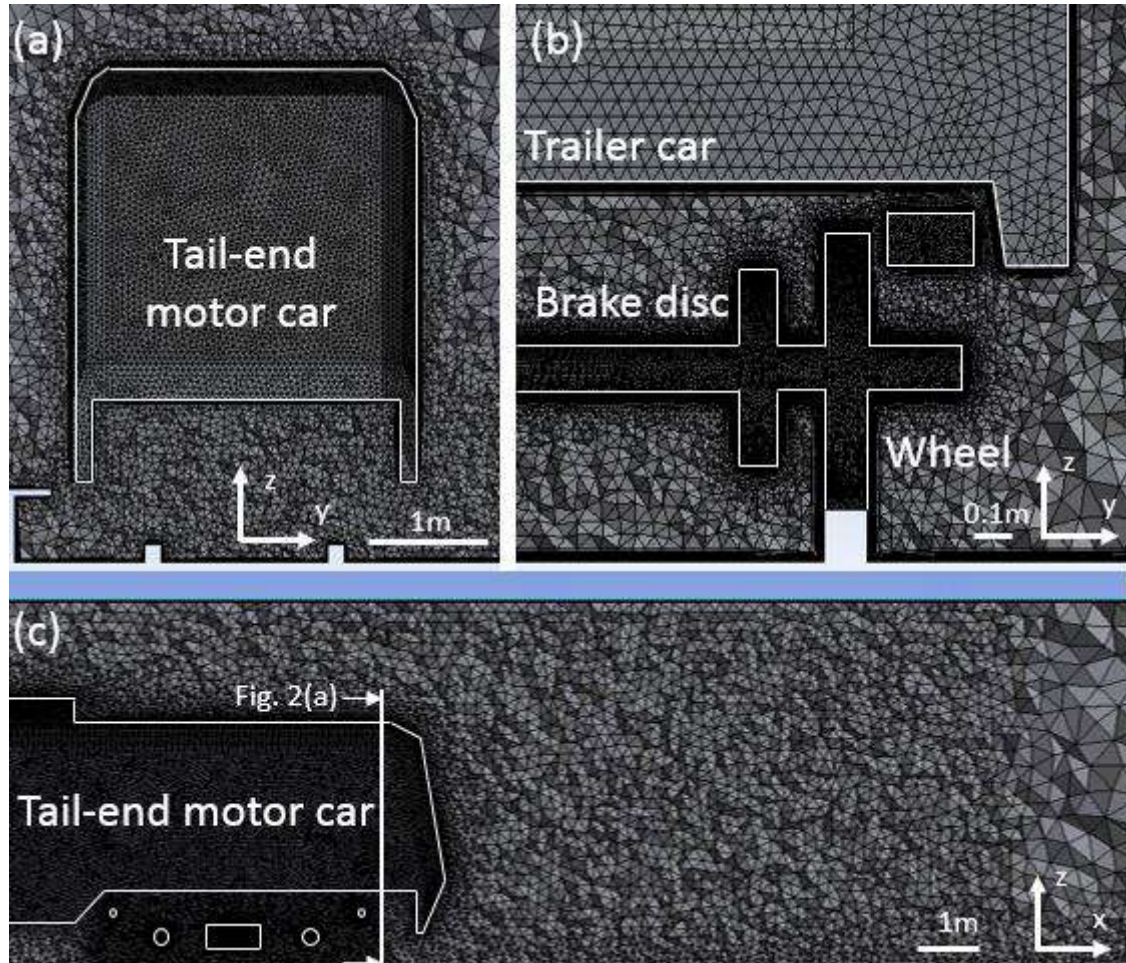


Figure 2: Transverse cross section views of the mesh refinement around the full-scale train model: at the tail-end (a), around a trailer bogie (b) and in a longitudinal cross section view in the wake where far-field sized cells can be seen at the extreme right (c).

Table 1: Meshing parameters

Mesh	Zone	Value
Cell size	Train surface	$0.01H_t$
	Platform surface	$0.01H_t$
	Rail surface	$0.01H_t$
	Bogies region	$0.002H_t - 0.01H_t$
	Wake region	$0.01H_t - 0.05H_t$
	Far-field region	$0.05H_t - 0.12H_t$
Inflation layers	All surfaces	12
Wall y^+	Train surface	1-35
Number of cells (millions)		113

1.3 Flow simulation

The flow around the train is governed by Navier-Stokes continuity (1) and momentum (2) equations. URANS equations are given by:

$$\frac{\partial \bar{u}_i}{\partial x_i} = 0 \quad (1)$$

$$\frac{\partial \rho_f \bar{u}_i}{\partial t} + \frac{\partial \rho_f \bar{u}_i \bar{u}_j}{\partial x_j} = - \frac{\partial \rho_f \bar{p}}{\partial x_i} + \frac{\partial}{\partial x_i} \left[\mu_f \left(\frac{\partial \bar{u}_i}{\partial x_j} + \frac{\partial \bar{u}_j}{\partial x_i} \right) \right] + \frac{\partial}{\partial x_j} \left(-\rho_f \bar{u}'_i \bar{u}'_j \right) \quad (2)$$

Where μ_f is the fluid dynamic viscosity, ρ_f the fluid density, \bar{p} the mean pressure, \bar{u}_i represents the mean flow velocity components and \bar{u}'_i is for fluctuating values. The term $-\rho_f \bar{u}'_i \bar{u}'_j$ represents the Reynolds stress tensor, whose components are unknowns. Thus, k- ϵ model aims to approximate the Reynolds stresses by solving two further equations. One accounts for the turbulent kinetic energy (k) and the other one for the turbulent dissipation rate (ϵ). Morden et al. (2015) suggested that RNG k- ϵ model has a better behaviour than SST k- ω outside the boundary layer region. The RNG k- ϵ model was used for various studies of train's aerodynamics performances in tunnels (Huang and Gao, 2010; Rabani and Faghah, 2015). In this work, the interaction between particles and wake coherent structures is investigated. Thus, the k- ϵ model combined to the Enhanced Wall Treatment were chosen to perform flow simulations.

1.4 Discrete phase simulation

Particle dispersion is simulated by tracking a large number of particles injected from discs brakes. The Lagrangian approach consists in computing each particle trajectory considering the forces acting on it. For submicron particles, Brownian motion has to be considered besides drag force (Li and Ahmadi, 1992). Within the size range investigated here, the influence of other forces such as Saffman lift force (Wang et al., 1997), virtual mass force or pressure gradients (Ounis and Ahmadi, 1990) can be neglected. Thus, the particle instantaneous velocity u_p is given by equation (3):

$$\frac{du_p}{dt} = \frac{C_D Re_p}{24\tau} (u - u_p) + F_B \quad (3)$$

Where, C_D is the particle drag coefficient, Re_p the particle Reynolds number and τ the particle relaxation time defined in equation (4). The term F_B accounts for Brownian force. It is expressed in equation (6) as a white noise process, where G is a zero mean, unit variance, normally distributed random number and S_0 the spectral intensity.

$$\tau = \frac{Sd_p C_c}{18\nu_f} \quad (4)$$

In equation (4), S is the particle-to-fluid density ratio, ν_f the fluid kinematic viscosity and C_c the Stokes-Cunningham slip correction factor, which is computed from equation (5):

$$C_c = 1 + \frac{2\lambda}{d_p} (1.257 + 0.4e^{-(1.1d_p/2\lambda)}) \quad (5)$$

Where λ is the mean free path of air, which is equal to $0.07\mu\text{m}$ (Jennings, 1988). In the present case, $C_c=1.07$ for $d_p=2.5\mu\text{m}$, $C_c=1.22$ for $d_p=0.8\mu\text{m}$ and $C_c=3.98$ for $d_p=0.07\mu\text{m}$.

$$F_B = G \sqrt{\frac{\pi S_0}{\Delta t}} \quad (6)$$

Instantaneous flow fluctuations are the main mechanism for particle dispersion. However, by using URANS equations, instantaneous fields are not depicted. In order to take into account turbulent diffusion by flow fluctuating components, the Discrete Random Walk Model (DRW) combined with the Fluent Random Eddy Lifetime (REL) model is used. DRW is a stochastic method, which models the effect of instantaneous turbulent velocity fluctuations to track the statistical evolution of a cloud of particles, which successively encounters different eddies (Gosman and Ioannides, 1983). Fluctuation velocities are given as:

$$u'_i = G \sqrt{\overline{u_i'^2}} \quad (7)$$

In equation (7), $\sqrt{\overline{u_i'^2}}$ RMS local fluctuation velocity. For k- ε model, $\overline{u_i'^2}$ is assumed to be equal to $\frac{2}{3}k$. The time scale of each eddy τ_e , which is called eddy life time is given in the REL model by equation (8):

$$\tau_e = -T_L \ln(r) \quad (8)$$

Here, T_L is the local turbulence Lagrangian time scale, which is equal to $0.15\frac{k}{\varepsilon}$ (Oesterlé and Zaichik, 2004) and r a random number greater than zero and less than one (Tian and Ahmadi, 2007; Fluent User's Guide, 2018). The interaction time of a particle with an eddy depends on the time taken for this particle to cross the eddy (Gosman and Ioannides, 1983) and is defined by equation (9):

$$t_c = -\tau \ln \left[1 - \left(\frac{L_e}{\tau |u - u_p|} \right) \right] \quad (9)$$

Where L_e is the eddy length scale, $|u - u_p|$ is the magnitude of relative slip velocity.

2. Flow topology

Figure 3 presents a 2D (xy) vector map of the dimensionless velocity magnitude at the centreline of the train. It depicts the apparition of a recirculation zone in the near-wake of the train characterized by negative horizontal velocities. This structure has been formerly found at higher freestream velocities for trains with high roof angle and sharp-edged nose (Weise et al., 2006; Bell et al., 2017), which is a common design for commuter trains.

The recirculation length (L_r) corresponds to the length for which the sign of the streamwise velocity changes from negative to positive. In the present case, L_r is equal to $0.54H_t$ at $Z^*=z/H_t=0.37$ (between the two vortices). The lowest value of the horizontal velocity component ($U_x/U_0=-0.25$) is recorded at a dimensionless distance $0.16H_t$ downstream of the tail-end nose. The maximum vertical velocity component ($U_y/U_0=0.20$) is found at $Z^*=0.19$ and $X^*=x/H_t=0.42$ downstream of the tail-end. It is consistent with our former preliminary study in wind tunnel (Durand et al., 2017). Scale effects and the presence of the bottom sleeve, which could not be reproduced at the scale used for our former wind tunnel study, may explain the differences.

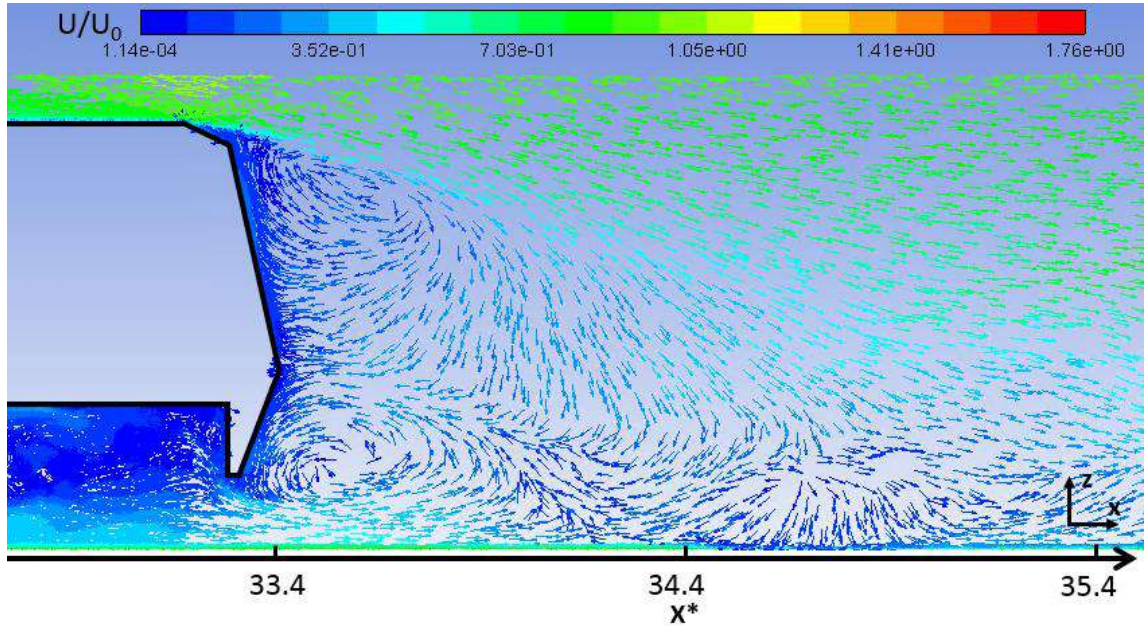


Figure 3: Dimensionless velocity magnitude (U/U_0) vectors at the centerline of the train ($Y^*=1.20$).

Figure 4 shows 2D maps (yz) of the dimensionless velocity magnitude in the wake of the last trailer bogies (where particles are injected) at 4 dimensionless distances X^* . The first pair of brake discs is not visible here and is located just before the plane $X^*=26.8$. The second pair can be seen at $X^*=27.2$ between the wheels. The platform (not displayed) is at the left of the rolling stock. Our results point out an asymmetric flow around the bogie, influenced by the presence of the platform at the left side and the station wall at the right side. The presence of the platform affects the flow topology in its proximity and reduce the streamwise velocity component. Thus, maximum velocity magnitudes are seen at the right side of the bogie.

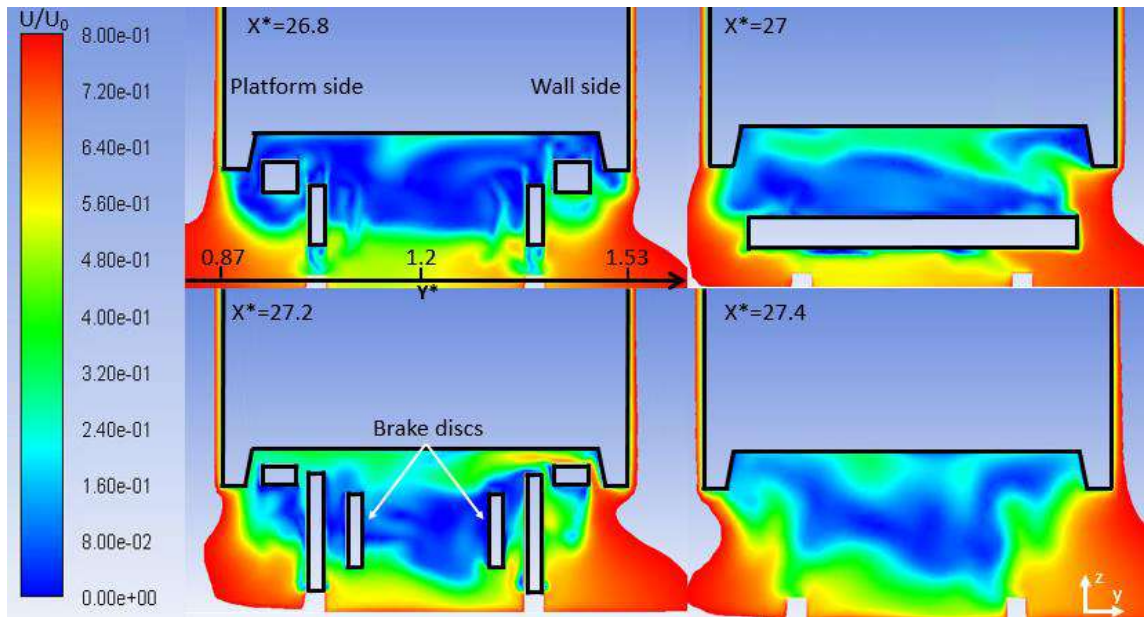


Figure 4: Dimensionless velocity magnitude (U/U_0) contours at different (yz) planes at the level of the last trailer bogie.

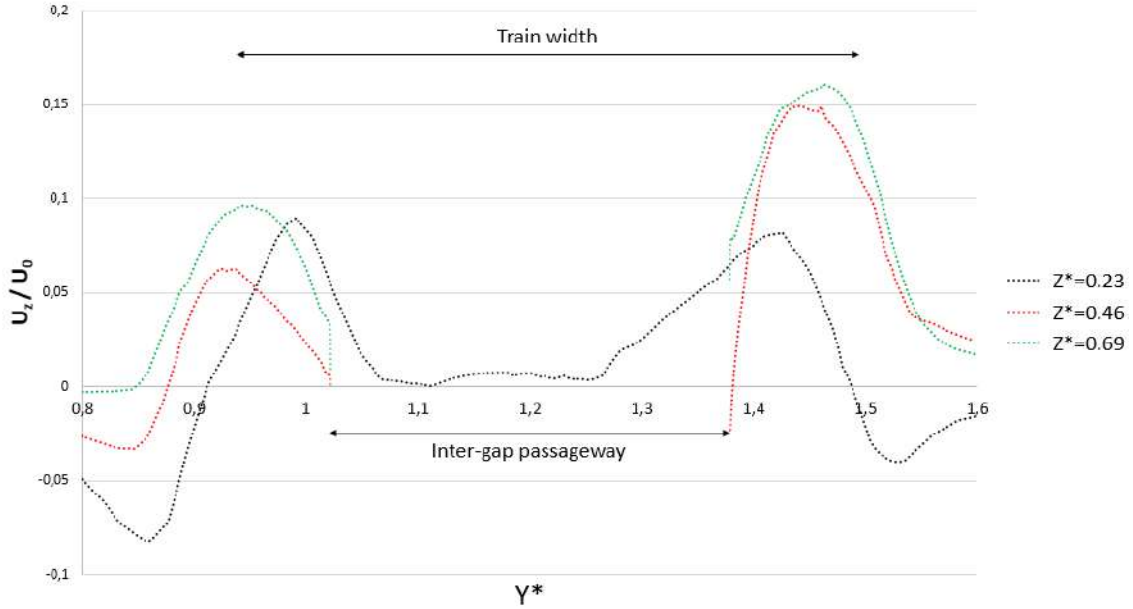


Figure 5: Vertical dimensionless velocity component (U_z/U_0) at the level of the inter-gap between carriages.

Inter-gaps present a particular flow topology, depicted in Figure 5. In these regions, the flow is redirected upwards. Negative vertical velocity components are found outside of train boundaries and more particularly at low Z^* . However, these negative components can be found all along the train, where positive components at this magnitude are only found at inter-gaps. Under the passageway (at $Z^*=0.23$) the maximum vertical velocity components (U_z/U_0)=0.089 and (U_z/U_0)=0.082 are respectively found at $Y^*=y/H_t=1.00$ and $Y^*=1.43$. Width of the left peak is constraint by the vicinity of the platform (the top of the platform reaches $Z^*=0.14$); however, the order of magnitude of the vertical velocity is roughly the same for both peaks. At $Z^*=0.46$ and $Z^*=0.69$, a clear vertical velocity asymmetry is shown. Vertical velocities remain quite similar on the platform side. In this region, the flow is no more influenced by the platform (that may explain the larger peak length). Vertical velocity reaches (U_z/U_0)=0.16 at $Z^*=0.69$ at the station wall side, which may be explained by the proximity between inter-gap passageway side wall and station wall.

The structure and the dynamic of the flow in the regions described above are of great importance and will have a significant influence on particle dispersion, as it will be described in the next section.

3. Brake particles dispersion

Figure 6 presents 2D maps (yz) of dimensionless velocity vectors colored by their velocity magnitude overlaid with filled contours of dimensionless particle concentration in a streamwise brake disc cross-section. In this figure, particles have been continuously injected for $5.7T_{ref}$. In order to make the figure readable, maximum dimensionless concentration values are not clipped to range, which means that in black-colored zones concentration can reach higher levels than the scale presented. A clear accumulation area is visible at the top of the front braking discs. It is correlated with the presence of a vortex, which traps freshly emitted particles. Other remarkable concentration zone are located either at vortices cores (particles are trapped by the vortex) or at the periphery of the vortices (in which case, particles are transported along the flow). It denotes that vortices induced by bogies strongly influence particles accumulation regions and their dispersion. Nevertheless, particles remains confined under the rolling stock in bogies regions by the flow transversal and vertical components.

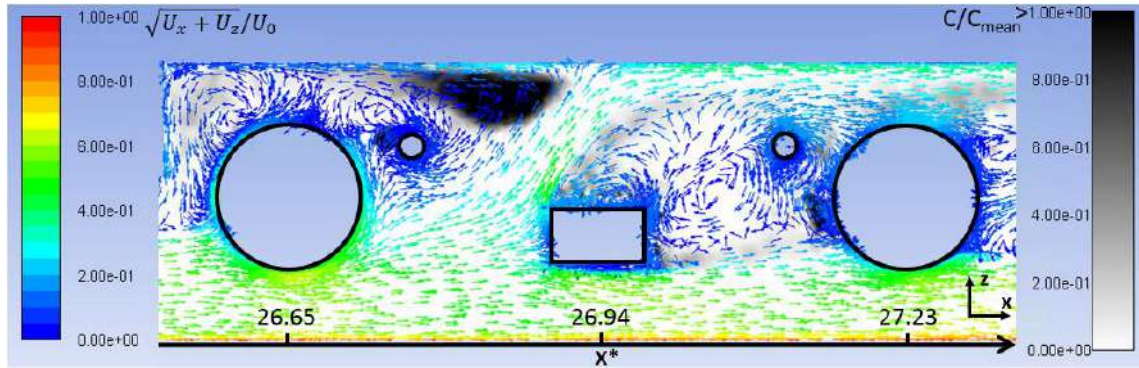


Figure 6: Dimensionless contours of particles concentration ($C^*=C/C_{\text{mean}}$) in a brake disc cross-section of the bogie and (xz) velocity vectors colored by their velocity magnitude ($\sqrt{U_x + U_z}/U_0$), $5.7T_{\text{ref}}$ after injection start (flow from left to right).

Particles generated from the last trailer bogies are then transported by the flow under the rolling stock. As soon as they reach the inter-gap between the carriages, some of them are raised up around the passageway, where the flow has remarkable positive vertical velocity components. Dimensionless particle concentrations ($C^*=C/C_{\text{mean}}$) around the inter-gap at $t=5.7T_{\text{ref}}$ after the start of injection are provided in herein below Figure 7. A clear asymmetry of concentrations is observed depending on the side (platform side at left, station wall side at right). The height reached by particles is higher at the station wall side. This is coherent with the higher vertical velocities found in the previous section. A puff phenomenon is visible on this side (low concentrations $Z^*=0.46$ and high concentrations $Z^*=0.69$). It may result from flow unsteadiness. At some given time, the flow can release particles trapped in previous vortices. However flow unsteadiness characteristics require further post-processing to be properly assessed.

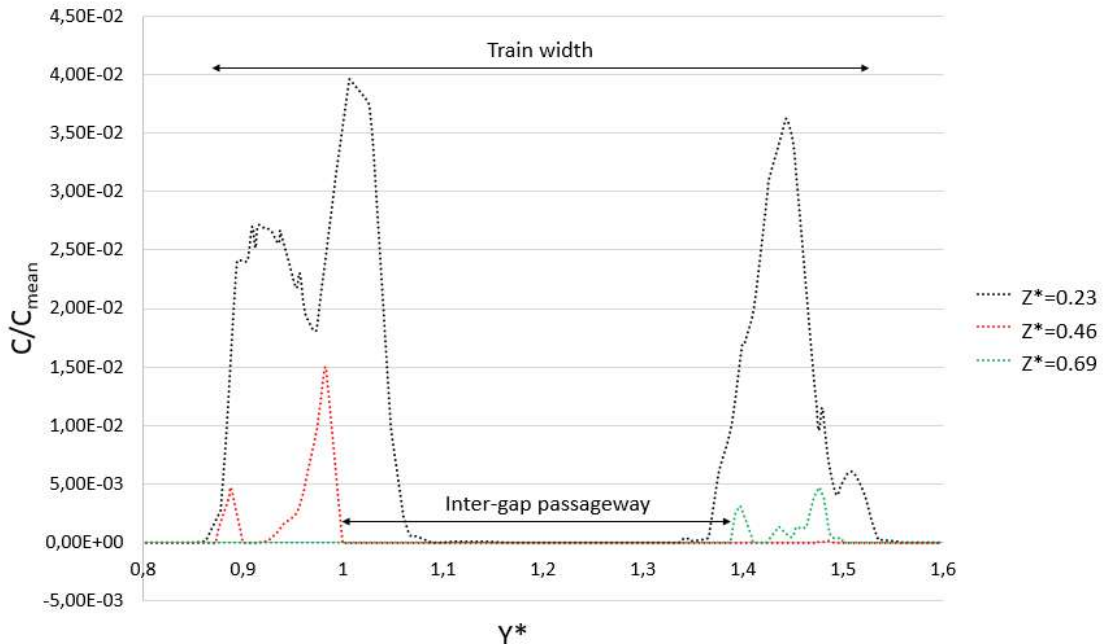


Figure 7: Dimensionless particles concentration ($C^*=C/C_{\text{mean}}$) around the inter-gap passageway $5.7T_{\text{ref}}$ after injection start.

Once particles have reached the near wake of the train (at $t=11.5T_{\text{ref}}$), they are sucked up by the lower vortex located in the recirculation zone as depicted in Figure 8. The $Z^*=0.46$ line, where a concentration peak appears around $X^*=33.7$, is located just above this vortex and before the zone with the maximal vertical flow. Once particles are raised up, they are redirected towards train tail-end nose, as horizontal velocity components are negative between the two vortices. After that, they reach the tail-end. Some of them stay stuck in the lower vortex while others are captured by the upper one. Others peaks are visible

in Figure 8, particularly around $X^*=34.1$ and $X^*=34.4$. It corresponds to the particles formerly lifted above the train at inter-gaps or by the recirculating region. These particles are transported by the flow to the far field after the recirculation zone (as shown in Figure 3). However, we acknowledge that the computation may not have last sufficient time to observe the complete influence of the wake on particle dispersion.

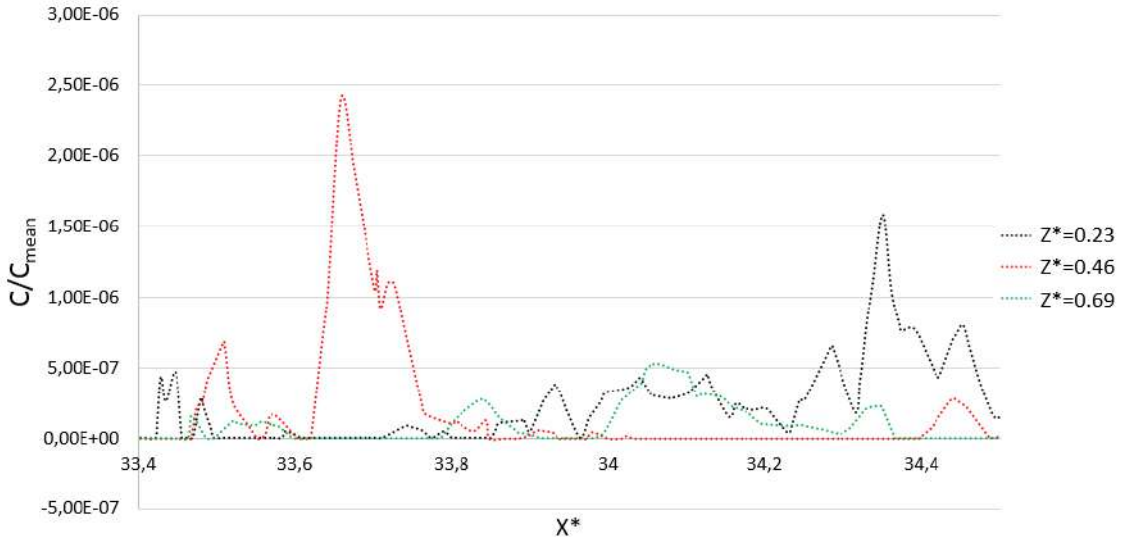


Figure 8: Dimensionless particles concentration ($C^*=C/C_{\text{mean}}$) in the near-wake of the train $17T_{\text{ref}}$ after injection start.

4. Conclusions and perspectives

In the present paper, a preliminary numerical study has been undertaken to assess particle dispersion from railway rolling stock brakes in an underground station. Three regions of interest were highlighted.

The first one is the region around bogies. Coherent structures induced by bogies may trap particles or, at least, slightly influence their trajectory. It creates clear accumulations areas inside vortex core. Concentrations rates are higher in vortices close to the point where particles are released and at the boundaries of the vortices.

The second one corresponds to the inter-gaps between carriages. Remarkable vertical velocity components are found in these regions. It leads to a rise of the particles passing under the passageway before being conveyed to the wake flow by the mean stream above the train.

The last one is the $0.54H_t$ long recirculation zone in the near-wake of the train, which has the ability to suck up and trap particles coming from under the last carriage of the train.

The present study does not show high lateral dispersion of particles in any of the above mentioned regions. However we only considered the flow induced by the train itself. As wake influence may have been underestimated, further computational resources will be added soon to investigate this point. Piston effect induced by the train displacement in a confined place (Khayrullina et al., 2015) or station ventilation design (Moreno et al., 2014) may also significantly affects particle dispersion. While station ventilation conditions are quite easy to set up for further assessment, piston effect requires dynamic layering method to be assessed. This kind of technique may be used in the future to assess its effect on particle dispersion. This may be combined with heavier geometrical simplification to reduce the high computation costs. The last limit of our study is related to the isotropy of the turbulence in the model we used. Turbulence anisotropy has an important effect on particles dispersion particularly close to walls. This point will be taken into account using second order turbulence models (Tian and Ahmadi, 2007).

Acknowledgements

This work was funded by SNCF Transilien and supported by ANRT CIFRE (Grant N°2017/1599).

References

- Airparif (2017). Mesures de la qualité de l'air intérieur sur les quais du RER C en gare SNCF d'Austerlitz, *Résultats des campagnes de mesure*, 1-41
- Bell J.R., Burton D., Thompson M.C., Herbst A.H., Sheridan J. (2017). The effect of tail geometry on the slipstream and unsteady wake structure of high-speed trains, *Experimental Thermal and Fluid Science*, 83, 215-230.
- Braniš (2006). The contribution of ambient sources to particulate pollution in spaces and trains of the Prague underground transport system, *Atmospheric Environment*, 40, 348-356.
- Chillrud S.N., Epstein D., Ross J.M., Sax S.N., Pederson D., Spengler J.D., Kinney P.L. (2004). Elevated airborne exposures of teenagers to manganese, chromium and iron from steel dust and New York City's subway system, *Environmental Science & Technology*, 38(3), 732-737.
- Durand A., Mehel A., Murzyn F., Fokoua G., Puech S. (2017). Particle dispersion from railway rolling stock: preliminary results from wind tunnel experiments and CFD, *Poster Proceedings of the 22nd International Transport and Air Pollution Conference*, 106-114.
- Fluent User's Guide (2018). Lebanon, NH: Fluent Inc.
- Gosman A.D., Ioannides E. (1983). Aspects of computer simulation of liquid-fueled combustors, *Journal of Energy*, 7(6), 482-490.
- Huang Y.D. and Gao W. (2010). A numerical study of the train-induced unsteady airflow in a subway tunnel with natural ventilation ducts using the dynamic layering method, *Journal of Hydrodynamics*, 22(2), 164-172.
- Jennings S.G. (1988). The mean free path of air, *Journal of Aerosol Science*, 19(2), 159-166.
- Kam W., Cheung K., Daher N., Sioutas C. (2011). Particulate matter (PM) concentrations in underground and ground-level rail systems of the Los Angeles Metro, *Atmospheric Environment*, 45(8), 1506-1516.
- Khayrullina A., Blocken B., Janssen W., Straathof J. (2015). CFD simulation of train aerodynamics: train-induced wind conditions at an underground railroad passenger platform, *Journal of Wind Engineering and Industrial Aerodynamics*, 139, 100-110.
- Kim K.Y., Kim Y.S., Roh Y.M., Lee C.M., Kim C.N. (2008). Spatial distribution of particulate matter (PM₁₀ and PM_{2.5}) in Seoul Metropolitan Subway stations, *Journal of Hazardous Materials*, 154, 440-443.
- Knibbs L.D., Cole-Hunter T., Morawska L. (2011). A review of commuters exposure to ultrafine particles and its health effects, *Atmospheric Environment*, 45(16), 2611-2622.
- Li A. and Ahmadi G. (1992). Dispersion and deposition of spherical particles from point sources in a turbulent channel flow, *Aerosol Science and Technology*, 16(4), 209-226.
- Moreno T., Pérez N., Reche C., Martins V., de Miguel E., Capdevila M., Centelles S., Minguillón M.C., Amato F., Alastuey A., Querol X., Gibbons W. (2014). Subway platform air quality: Assessing the influences of tunnel ventilation, train piston effect and station design, *Atmospheric Environment*, 92, 461-468.
- Namgung H.G., Kim J.B., Woo S.H., Park S., Kim M., Kim M.S., Bae G.N., Park D., Kwon S.B (2016), Generation of nanoparticles from friction between railway brake disks and pads, *Environmental Science & Technology*, 50(7), 3453-3461.
- Öberdörster G. (2001). Pulmonary effects of inhaled ultrafine particles, *International Archives of Occupational and Environmental Health*, 74(1), 1-8.
- Octau, C., Lippert M., Dbouk T., Watremez M., Keirsbulck L., Dubar L. (2017), Etudes expérimentales et numériques d'un jet de particules : application au freinage ferroviaire, *Proceedings of the 23^{ème} Congrès Français de Mécanique*.
- Oesterlé B., Zaichik L.I. (2004). On Lagrangian time scales and particle dispersion modeling in equilibrium turbulent shear flows, *Physics of Fluids*, 16(9), 3374-3384.
- Olofsson U., Olander L., Jansson A. (2009). A study of airborne wear particles generated from a sliding contact, *Journal of Tribology*, 131(4), 044503-044503-4.
- Olofsson U. (2011). A study of airborne wear particles generated from the train traffic – Block braking simulation in a pin-on-disc machine, *Wear*, 271, 86-91.
- Ounis H., and Ahmadi G. (1990). Analysis of dispersion of small spherical particles in a random velocity field, *Journal of Fluids Engineering*, 112(1), 114-120.
- Pope III C.A., Burnett R.T., Thurston G.D., Thun M.J., Calle E.E., Krewski D., Godleski J.J. (2003). Cardiovascular Mortality and long-term exposure to particulate air pollution, *Circulation*, 109, 71-77.

- Querol X., Moreno T., Karanasiou A., Reche C., Alastuey A., Viana M., Font O., Gil J., de Miguel E., Capdevila M. (2012). Variability of levels and composition of PM₁₀ and PM_{2.5} in the Barcelona metro system, *Atmospheric Chemistry and Physics*, 12, 5055-5076.
- Rabani M. and Faghih A.K. (2015). Numerical analysis of airflow around a passenger train entering the tunnel, *Tunnelling and Undergroud Space Technology*, 54, 203-213.
- Salma I., Weidinger T., Maenhaut W. (2007). Time-resolved mass concentration, composition and sources of aerosol particles in a metropolitan underground railway station, *Atmospheric Environment*, 41(37), 8391-8405.
- Sundh J., Olofsson U., Olander L., Jansson A. (2009). Wear rate testing to airborne particles generated in a wheel-rail contact, *Lubrication Science*, 21, 135-150.
- Tian L., Ahmadi G. (2007). Particle deposition in turbulent duct flows – Comparisons of different model predictions, *Journal of Aerosol Science*, 38, 377-397.
- Wang Q., Squires K.D., Chen M., McLaughlin J.B. (1997). On the role of the lift force in turbulence simulations of particle deposition, *International Journal of Multiphase Flow*, 23(4), 749-763.
- Wang S., Bell J.R., Burton D., Herbst A.H., Sheridan J., Thompson M.C. (2017). The performance of different turbulence models (URANS, SAS, DES) for predicting high-speed train slipstream, *Journal of Wind Engineering and Industrial Aerodynamics*, 165, 46-57.
- Weise M., Schober M., Orellano A. (2006). Slipstream velocities induced by trains, *Proceedings of the 4th WSEAS International Conference on Fluid Mechanics and Aerodynamics*, 26-28.

2.9 Special Session on H2020 projects

This section includes papers presented in the context of the “Special Session on H2020 projects” sessions of the TAP conference. Table 10 provides an overview of these papers, as they are listed in the following sub-sections.

Table 10. Titles and authors of the “Special Session on H2020 projects” papers

	Paper Title	Authors
2.9.1	Application of DC-sensors to measure ultrafine particles from combustion engines	T. Rüggeberg, M. Fierz and H. Burtscher, A.D. Melas, D. Deloglou, E. Papaioannou and A.G. Konstandopoulos
2.9.2	The PEMS4 Nano project: measuring engine emissions below 23 nm	C. Focsa, D. Duca, J. A. Noble, M. Vojkovic, Y. Carpentier, C. Pirim, P. Desgroux, A. Manz, R. Grzeszik, T. Tritscher, J. Spielvogel, M. Rahman, A. Boies, K. F. Lee, A. Bhavé, S. Legendre, P. Kreutziger and M. Rieker
2.9.3	Particle Reduced, Efficient Gasoline Engines: A Second Year Report on the PaREGEN Project	S. Edwards, J. Gidney, N. Freisinger, N. Turner, A. Perez and C. van der Zweep
2.9.4	GPF model-based optimization methodologies supporting RDE conformity	M. Mitsouridis, G. Koltsakis, Z. Samaras and C. Martin
2.9.5	Particle emissions measurements on CNG vehicle focusing on, sub-23nm	Z. Toumasatos, A. Kontses, S. Doulgeris, Z. Samaras and L. Ntziachristos

2.9.1 The PEMS4Nano project: measuring engine emissions below 23nm

C. Focsa^{1,*}, D. Duca¹, J. A. Noble^{1,†}, M. Vojkovic¹, Y. Carpentier¹, C. Pirim¹, C. Betrancourt^{2,‡}, P. Desgroux², T. Tritscher³, J. Spielvogel³, M. Rahman⁴, A. Boies⁴, K. F. Lee⁵, A. Bhave⁵, S. Legendre⁶, O. Lancy⁶, P. Kreutziger⁷, and M. Rieker⁷

¹Université de Lille, CNRS, UMR 8523 – PhLAM – Laboratoire de Physique des Lasers Atomes et Molécules, F-59000 Lille, France

²Université de Lille, CNRS, UMR 8522 – PC2A – Laboratoire de Physico-Chimie des Processus de Combustion de l'Atmosphère, F-59000 Lille, France

³TSI GmbH, 52068 Aachen, Germany

⁴University of Cambridge, CB2 1PZ Cambridge, United Kingdom

⁵CMCL Innovations, CB3 0AX Cambridge, United Kingdom

⁶HORIBA Scientific, 231 Rue de Lille, 59650 Villeneuve d'Ascq, France

⁷HORIBA Europe GmbH, Hans-Mess-Strasse 6, D-61440 Oberursel, Germany

*Corresponding author: cristian.focsa@univ-lille.fr

†Current address: CNRS, Aix Marseille Université, PIIM, UMR 7345, 13397 Marseille cedex, France

‡Current address: Ecole Centrale Supélec, 91190 Gif-sur-Yvette, France

Keywords: internal combustion engine, nanoparticles, physico-chemical characterization, model-guided application

Abstract

Particulate emissions from on-road motor vehicles are currently the focus of intensive research due to the impact of ambient particulate matter levels on climate and human health. Constant improvement in engine technology has led to a significant decrease in the number and mass of emitted particles, but a particular concern is raised nowadays by the ultrafine particles. In this context, there is a critical lack of certification procedures for the measurement of these smallest-sized (<23 nm) particulate matter emissions. The goal of the H2020 PEMS4Nano project is to develop robust, reliable and reproducible measurement technology, supporting the engine development process as well as future certification procedures on the chassis dyno and during real driving emissions (RDE) measurements. The measurement procedure for sub-23 nm sized particles also entails developing an understanding of the formation and evolution of particles from the engine through to the tailpipe via multiple experimental particle characterization techniques and theoretical model guided application (MGA).

On the experimental characterization side, an extensive database has been built up using a gasoline direct injection single-cylinder engine (operated in various regimes) as the particle generator. Particulates produced by the engine were sampled using a cascade impactor which allows size-separation of the sampled particles into 13 different size bins. Chemical characterization of the collected size-selected particles was performed using mass spectrometry, which gives access to detailed molecular information on chemical classes of critical interest such as organosulfates, oxygenated hydrocarbons, nitrogenated hydrocarbons, metals, and polycyclic aromatic hydrocarbons. Additionally, the morphology of the emitted particles was probed with atomic force and scanning electron microscopy. Tip-Enhanced Raman Spectroscopy (TERS) was applied, for the first time, to sub-10nm combustion-generated particles to gather information on their nanostructure. On the theoretical side, the MGA combines physico-chemical internal combustion engine simulation with advanced statistical analytics, and has been used to simulate and validate engine-out gas phase and particulate emissions, including the influence of the sampling method (e.g. dilution, temperature, etc.) on the evolution of the physical and chemical characteristics of the emitted nanoparticles.

1 Introduction

Particulate matter (PM) is a ubiquitous air pollutant, consisting of a mixture of solid and liquid particles that can remain suspended in the air, on timescales ranging from a few minutes up to days or even weeks (WHO, 2013) depending on their size, and hence can undergo long-range transport. Primary PM can have anthropogenic sources that include PM produced by internal combustion (IC) engines (e.g. on-road vehicles), wear of vehicle components, or industrial activities. Traffic is therefore a significant

source of PM emission with a mass size distribution ranging from coarse mode ($PM_{10} < 10 \mu m$) to fine mode ($PM_{2.5} < 2.5 \mu m$) particles (Atkinson et al., 2010), and often dominated by submicron particles (e.g. $PM_{0.5} < 0.5 \mu m$, Alves et al., 2015). Major improvements in engine technology and the use of alternative fuels over the last few years have helped lessen the environmental harm caused by motor vehicle emissions. While NO_x and hydrocarbons emissions, along with particulate mass and number of emitted particles, have been reduced, one of the downsides has been the shift in the particle size distribution toward smaller sizes (lower than 100 nm, Karjaleinen et al., 2014), thus likely increasing their contribution to air pollution, i.e. a public health issue (e.g. Kim et al., 2015; Shah et al., 2013; Manke et al., 2013, Sager et al., 2009, Seaton et al., 2009, EPA 2009). European legislation (EURO6) limits both the mass and number of emitted particulates, and this regulation is followed by 17 members of the G-20 countries (which account for 90% of global vehicle sales). Therefore, information about the particle number (PN) of ultrafine particles is becoming more and more valuable for vehicle certification. Specifically, sub-23 nm particles have attracted a lot of attention recently for two main reasons. First, sub-23 nm particles can be produced, sometimes in high concentrations, in both diesel and gasoline direct-injection (GDI) engines (e.g. Giechaskiel et al., 2014). Second, the harmfulness of the particles has been shown to correlate better with surface area than with mass (Donaldson et al., 1998; Oberdörster 1996), which becomes important for ultrafine particles even though their residence time in the atmosphere is shorter. However, it has been estimated that the percentage of sub-23 nm solid particles that is not measured by current certification procedures (that have a cut-off size of 23 nm) could reach 30-40% for gasoline vehicles utilizing direct injection, and be potentially higher when alternative fuels are being used (Giechaskiel et al., 2017). The critical lack of certification procedures for the measurement of ultrafine (< 23 nm) particulate matter emissions provides an impetus to develop reliable measurement systems for sub-23 nm particles. To address this need, three projects focused on reducing the lower size limit of measurement systems (PEMs4Nano, DownToTen, and Sureal-23) were awarded funding from the Horizon 2020 call for 'Technologies for low emission light-duty powertrains'.

The goal of the H2020 PEMs4Nano project (www.pems4nano.eu) is to develop robust, reliable and reproducible measurement technology, supporting the engine development process as well as future certification procedures on the chassis dyno and during real-driving conditions (RDC) measurements. The specificity of our project lies in a bottom-up approach, based on a model guided application (Lee et al., 2019), which contributes to the understanding of particle formation and dynamics and supports the optimization of the newly developed particle emission monitoring systems (PEMS). This theoretical simulation workflow needs operational (engine-level and/or vehicle level) inputs and measurements data for calibration as well as validation, in order to offer reliable evaluations of the particle formation and loss mechanisms. Therefore, an extensive database was built up via the thorough size-dependent physico-chemical characterization of a wide variety of combustion-generated particles. A gasoline direct-injection single-cylinder engine (SCE) was employed in a multitude of operating regimes (different injection timing, applied load, etc) as a stable and versatile particle generator. Particulates generated in these various regimes simulate the engine exhaust as a representation of real driving conditions, while presenting the advantage of having been produced in a controlled environment.

The experimental set-up built around the SCE allows both on-line measurements (e.g. size-distribution, volume fraction through SMPS, EEPS, LII) and particulate sampling for subsequent off-line characterization. This paper addresses mainly the off-line characterization, in terms of morphology, nanostructure and chemical composition, with a particular emphasis on the latter. Specifically, chemical characterization of size-selected collected particles is performed using high-performance mass spectrometry, which gives access to detailed molecular information on chemical classes of critical interest such as organosulfates, oxygenated hydrocarbons, nitrogenated hydrocarbons, metals and polycyclic aromatic hydrocarbons. Recently developed advanced statistical methodologies (Irimiea et al., 2018, 2019), based on principal component analysis (PCA) and hierarchical clustering analysis (HCA), are used to highlight subtle differences, as well as similarities, between different-sized particles. In addition, the particle morphology is probed with a scanning electron microscope (SEM) and an atomic force microscope (AFM), while unprecedented tip-enhanced Raman spectroscopy (TERS) measurements on individual combustion-generated particles down to a few nm are performed to gather insights about their nanostructure.

2 Experimental details

2.1 Single cylinder engine and sampling line

The particulate matter investigated in this work was produced by a generic gasoline direct-injection single-cylinder test engine, whose specifications are given in Table 1. The temperature conditioning of the engine is set to 80°C for coolant flow and oil (Agip SIGMA TFE, 10W-40). In addition to gasoline (EURO5), gaseous fuels such as methane (CH_4) can be employed e.g. for conditioning the engine to ensure the cleanliness of the combustion chamber. The specific operating points studied here are described in Table 2.

Table 1 Engine specifications (b/aTDC – before/after Top Dead Center)

Specification	Value	
Cylinder head	Pentroof type	
Compression ratio	12.5:1	
Bore	82 mm	
Stroke	85 mm	
Stroke volume	449 cm ³	
Fuel direct injection system	Central mounted generic six-hole injector	
Injection pressure	150 bars	
Spark plug location	Exhaust side	
Intake valve timing:	Open	334 deg. bTDC
	Close	166 deg. bTDC
Exhaust valve timing:	Open	154 deg. aTDC
	close	330 deg. aTDC

Monitoring and sampling of particles from the generic single-cylinder test engine was performed using a home-built sampling line. A partial flow is taken from the exhaust duct approximately 5 cm after the exhaust port (Figure 1) and is then supplied to the particle measurement system, via the DEKATI FPS 4000 (Fine Particle Sampler) dilution system to prevent condensation of volatile particles. The overall dilution ratio of the DEKATI FPS 4000 is 30:1. The stability of the engine operation is monitored using an EEPS (Engine Exhaust Particle Sizer; TSI, model 3090) connected to the dilution stage through a thermodiluter ($T=350^\circ\text{C}$), thus ensuring that particle production is constant during the period of

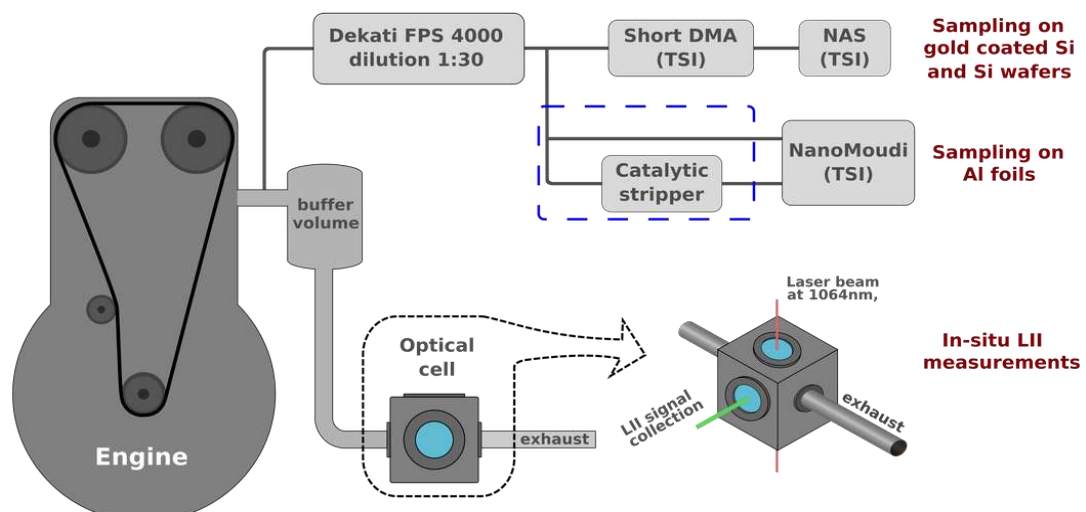


Figure 1 Schematic representation of the sampling line. Sampling with NanoMoudi on Al foils can be done with or without the catalytic stripper (dashed blue rectangle).

measurements. The rest of the exhaust flows through an optical cell for on-line study by laser-induced incandescence (LII).

The characterization techniques used for structural and morphological analysis (described in section 2.3.1) require samples with a low coverage, i.e. isolated individual particles. At the same time, chemical characterization requires more loaded samples, ideally with a homogeneous layer of particles fully covering the deposition substrate. Consequently, the sampling time in case of the samples used for chemical characterization was much longer. Moreover, the time is optimized for each engine operation regime, in order to obtain similar coverages, the longest (12h) being for the **NHC** regime and the shortest (6h) for the **EM** one, respectively (see below). Regarding the samples intended for the structural and morphological analysis, the collection time varies between 30 minutes and 1h, depending on engine conditions.

The collection of particles for the chemical analysis is performed with a NanoMOUDI II cascade impactor (TSI/MSP, model 125R) connected through a stainless-steel line to the dilution stage. Being a "Micro-Orifice Uniform-Deposit Impactor", the NanoMoudi works on the well-known principle of inertial impaction (Marple et al., 1991; Marple 2004). The MOUDI impactors have sharp cut characteristics with steep cut-off curves per stage and low inter-stage wall losses. The model we used comprises 13 stages, with nominal cut sizes of 10000, 5600, 3200, 1800, 1000, 560, 320, 180, 100, 56, 32, 18, 10, and 0 nm. Particles are deposited on aluminum foils (for the 13 size-selected stages) and a quartz fiber filter (for the last stage). In order to avoid surface contaminants that would interfere with our chemical analysis, no coating was applied to the substrates and Al foils were thermally treated in an oven at 300°C prior to sampling. For structural and morphological analyses particles are collected on either Au-coated or bare Si wafers using a combination of a short Differential Mobility Sizer (short DMA, TSI) and a Nanometer Aerosol Sampler (NAS, TSI, Figure 1), enabling the sampling of different-sized particles within very narrow size bins. Parallel sampling is performed for subsequent chemical, structural and morphological analyses.

Table 2 Studied engine operating points (λ : ratio of the actual air/fuel ratio to stoichiometric)

Set-point	Load	$\lambda \pm 0.01$	Injection, deg. BTDC	Description
NS	low	1.01		Optimal engine conditions, low load
NM	medium	1.01		Optimal engine conditions, medium load
NH	high	1.01		Optimal engine conditions, high load
NHC	high	1.01	270	Optimal engine conditions, high load with a catalytic stripper
OM	medium	1.01		Optimal engine conditions, medium load with an addition of oil
EM	medium	0.70		Low air/fuel ratio, medium load
EI1	high	1.01	305	Early injection, high load
EI2	high	1.01	311	Early injection, high load

2.2 On-line characterization by Laser-Induced Incandescence

LII measurements are performed in-situ while the test engine runs with the objective of studying the evolution of the soot volume fraction with engine conditions. The principle of LII consists first in heating combustion-generated particles, generally using a pulsed laser up to 3500-4200K, and then recording the radiation associated with the thermal emission while they cool down. This incandescence emission follows the Planck law and depends on the emission properties of particles at the detection wavelength. This technique is used to monitor soot concentration, e.g. in flames (Schulz et al., 2006), aeronautics (Delhay et al., 2009), automotive engines (Bachalo et al., 2002). LII is mainly used to determine the soot

volume fraction (f_v) and the primary particle diameter (Schulz et al., 2006). Soot volume fraction can be determined from the time-resolved LII peak signal as follows:

$$f_v \propto \left(\frac{LII}{E(m_\lambda) \cdot B(T, \lambda)} \right)$$

where $B(T, \lambda)$ is the Planck function, T is the peak reached temperature, λ - the emission wavelength, m_λ - the refractive index of the particle and $E(m_\lambda)$ - soot absorption function.

The decay of the LII signal is related to the cooling time of particles and therefore to their size. Primary particle diameter can hence be determined, provided a model of the energy transfer during laser heating is available (Michelsen et al., 2007).

An LII setup was coupled to the single cylinder engine via an optical cell mounted on the exhaust duct, as illustrated in Figure 1. The choice of the optimum cell location took into consideration the layout and space constraints of the test bed. LII measurements were performed simultaneously with the collection of particulates. LII measurements were performed with an excitation wavelength of 1064 nm generated by a Nd:YAG pulsed laser (Quantel Brilliant, 10Hz repetition rate, 5 ns pulse duration). An optical attenuator is used to adjust the energy of the laser between 0 and 350 mJ/pulse. The excitation laser beam has a Gaussian profile and a diameter of 6 mm. A laser fluence of 0.32 J/cm² was used for excitation, thus maximizing the LII signal and limiting its dependence on laser fluctuations. The LII signal is collected by two achromatic lenses ($f_1=200$ mm, $f_2=100$ mm) and focused on the collection slit (100 x 0.2 mm). The signal, in the 400-825 nm spectral range, is then detected with a photomultiplier tube (PMT) (Hamamatsu R2257) and recorded by an oscilloscope (LeCroy 6050A, 500 MHz bandwidth, 5 GS/s sampling rate) triggered with a photo-diode (Hamamatsu S1722-02). The PMT is equipped with a short-pass filter with a cut off at 825 nm.

2.3 Off-line characterization

2.3.1 Morphology and structure

For structural and morphological studies, particles collected on Au-coated or bare Si wafers are analyzed with a SEM (Scanning Electron Microscope) and AFM/TERS (Atomic Force Microscope / Tip Enhanced Raman Spectrometry). The SEM Merlin (Zeiss) is used for the morphology analysis of collected particles; it features a spatial resolution of 1 nm and high detection efficiency. Since the focus of this work is the study of ultra-fine particles, a low accelerating voltage (1kV) was chosen, thus decreasing the size of the interaction volume and improving the spatial resolution. Moreover, it enables the study of ultra-fine combustion-generated particles without the need of a conductive coating. Additionally, SEM images are used to determine the surface coverage and adjust, if needed, the sampling time.

The AFM (SMART SPM, HORIBA Scientific) features high-resolution cantilever-based tips (Hi'Res-C14/Cr-Au, μ masch, typical 1 nm-radius) for a high lateral resolution. A NanoRaman system that combines a SMART-SPM (HORIBA Scientific) with a Raman spectrometer (LabRAM HR Evolution Nano, HORIBA Scientific) is used for tip-enhanced Raman measurements (TERS). The system is based on a reflection configuration allowing the use of a 100x objective lens (NA 0.7) with a 60° angle. The incident laser (633 nm, p-polarized) is focused through the objective onto the apex of the cantilever-based silver TERS probe (Ag coated OMNI TERS probe). The collection of the back-scattered signal is performed through the same objective.

2.3.2 Chemical composition

Two-step laser mass spectrometry

The two-step laser mass spectrometry (L2MS) technique has been extensively developed (at the University of Lille, PhLAM laboratory) over the last decade to specifically probe the chemical composition of combustion byproducts (Popovicheva et al., 2017; Delhaye et al., 2017; Faccinetto et al., 2011, 2015; Moldanova et al., 2009). The main advantages of L2MS are its high sensitivity and selectivity with regards to specific classes of compounds owing to the resonant ionization processes that can be adapted, by using different ionization wavelengths, thus targeting different classes of compounds and

reaching sub-fmol limit of detection, e.g. for PAHs (Faccinetto et al., 2008, 2015). Systematic studies (Mihesan et al., 2006, Mihesan et al., 2008) have led to the optimization of the laser desorption process (and its coupling with the subsequent ionization step, Faccinetto et al., 2008), which ensures a soft removal (with minimum internal excess energy) of molecules adsorbed on the particle surface, and thus avoids/limits both their fragmentation and the in-depth damaging of the underlying carbon matrix (Faccinetto et al., 2015). In this work, a new mass spectrometer (Fasmatech S&T) is used, combining ion cooling, Radio Frequency (RF) guiding and Time of Flight (ToF) analyzer, which allows us to reach a mass resolution of $m/\Delta m \sim 15000$.

In this new experimental setup, the sample, placed under vacuum (10^{-8} mbar residual pressure), is irradiated at 30° angle of incidence by a frequency doubled Nd:YAG laser beam (Quantel Brilliant, $\lambda_d = 532$ nm, 4 ns pulse duration, ~ 100 mJ cm^{-2} fluence, 10 Hz repetition rate) focused to a 0.07 mm^2 spot on the surface. The desorbed compounds form a gas plume expanding in the vacuum normally to the sample surface, and are ionized by an orthogonal UV laser beam (Quantel Brilliant, $\lambda_i = 266$ nm, 4 ns pulse duration, 10 Hz repetition rate, $\sim 0.3 \text{ J cm}^{-2}$ fluence). At this ionization wavelength, a high sensitivity is achieved for PAHs through a resonance enhanced multiphoton ionization process 1+1 REMPI (Zimmermann et al., 2001; Haefliger and Zenobi 1998; Thomson et al., 2007). The generated ions are then RF-guided to a He collision cell for thermalization and subsequently mass analyzed in a reflectron time of flight mass spectrometer (ToF-MS). A high sensitivity for aliphatic compounds was achieved with a similar instrument where the desorbed plume is ionized by a single photon ionization (SPI) process at $\lambda_i = 118$ nm. The ninth harmonic of the YAG:Nd laser is generated in a coherent nanosecond source by frequency-tripling of a 355 nm pump beam (Continuum Surelite, 10 ns, 10 Hz) in a low-pressure Xe cell (Popovicheva et al., 2017).

Secondary Ion Mass Spectrometry

The particles were also analyzed with a commercial IONTOF TOF.SIMS⁵ secondary ion mass spectrometer (SIMS) with maximum resolving power of $m/\Delta m \sim 10\,000$. The sample is placed on a holder and introduced into a vacuum chamber with residual pressure of $\sim 10^{-7}$ mbar. The surface of the sample is probed by a Bi_3^+ pulsed ion beam at 25 keV. The primary ion source delivers a pulsed current of 0.3 pA. The penetration depth of the primary ions is typically 1-3 nm. In the static mode, used for the surface molecular analysis, the ion dose is limited to a level at which every primary ion should always hit a fresh area of the sample. A small fraction of the ejected atoms/molecules are ionized (secondary ions) and can thus be analyzed using a time of flight tube (V mode). Mass spectra are recorded in both positive and negative polarities, to obtain the maximum amount of information on the sample (Irimiea et al., 2018, 2019).

3 Experimental results

3.1 LII measurements within the exhaust duct

The LII technique was used in this work to monitor the evolution of the particle size and volume fraction (assumed to be proportional with the LII peak signal, see section 2.2) upon various engine regimes. Figure 2a shows the evolution of the LII signal (f_V) with five engine set points. One can clearly see that the main parameter inducing a strong effect on the soot volume fraction is the timing of injection, leading to a 150-fold increase between the **NH** (270 deg. BTDC, see Table 2) and the **EI2** (311 deg. BTDC) regimes. This trend is correlated with the occurrence of pool fires (i.e. liquid fuel burning on the top of the piston) observed only for the points **EI1** and **EI2**. Occurrence of pool fires was observed using endoscopic imaging of the combustion chamber. This observation is consistent with the ones revealed by Velji et al., (2010) who experimentally identified that the main source of soot in the homogeneous combustion in a gasoline engine is due to the pool fires, while in the stratified mode the soot may also originate from local rich regions in the combustion chamber. On the other hand, a moderate increase (four-fold) is recorded when the pressure mean indicator (PMI) doubles, from 5 (**NS**) to 10 bar (**NH**). This is consistent with the work of Wang et al. (2014) who suggested that this trend could be due to slightly longer combustion duration for a clean injector.

The LII signal time decays exhibit significant variations depending on the engine regime (see Figure 2b). The “normal regimes” (**NS**, **NM**, **NH**) show similar decay times (i.e. relatively low influence of the PMI on the particle size), whereas the non-optimal engine operation conditions (early injection, **EI1** and **EI2**) clearly show longer decay times i.e. larger primary particle sizes. The interpretation of these time-resolved LII decays in terms of soot primary particle diameter requires complex energy transfer

modeling, especially since size distributions of the particles are expected to be bimodal. Thus Wang et al., (2014) measured on line the size distributions of the particles in different GDI conditions by scanning mobility particle sizing (SMPS) and highlighted that most of the electrical mobility diameter distributions were bimodal. Particularly they showed that the smallest mode which was attributed to the nucleation mode could be prevalent in some engine conditions. Thus, the combination of LII and SMPS or EEPS offers promising perspectives in view of measuring the smallest particles and to better understand their nucleation. Once the nucleation mode has been favored thanks to the particle sizer control, engine conditions might be selected in view of reducing the number of small particles as low as possible, as controlled by the highly sensitive LII technique.

These observations provide precious information for optimizing the simultaneous sampling of the particulates for off-line analyses. Further efforts will be devoted to calibrate f_v using an extinction technique at a given engine set-point (Betancourt et al., 2019) and to combine LII with particle sizers as mentioned above in a context of very small particles (down to 10 nm).

3.2

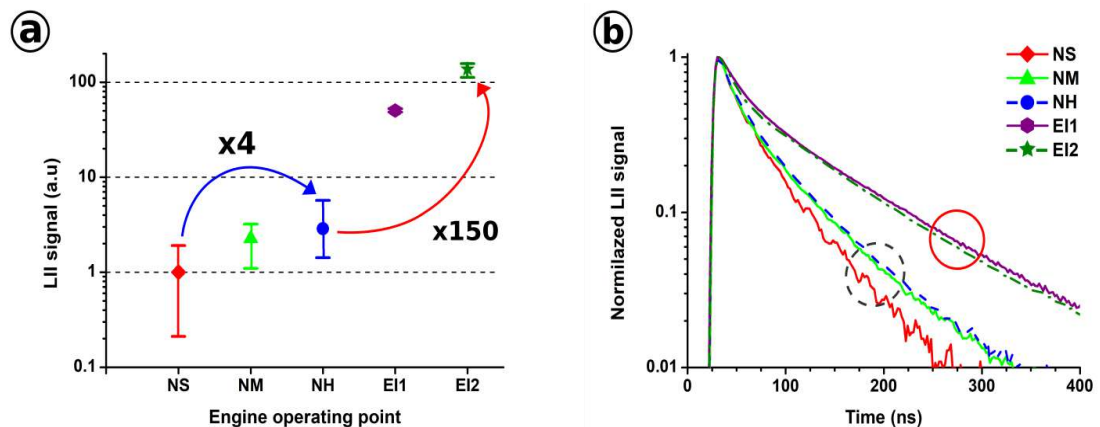


Figure 2 LII peak signal (a.u.) (a) and time-resolved LII signal (b) measured at different engine set-points.

Structure and morphology

One of the biggest challenges in collecting and studying combustion-generated particles is avoiding the agglomeration of the smallest ones during sampling. As small particles are the focus of this work, proper sampling is crucial to avoid the aggregation of small particles that would result in their collection on a different impaction stage (with a higher cut-off size compared to the dimensions prior to aggregation). Several samples of particles are analyzed with SEM, Figure 3, in order to ensure that our experimental setup is able to sample and collect small single particles. The particles are collected on Au-coated Si wafers with a combination of a short DMA, set to pass particles with a mobility diameter of 18 nm (± 5 nm), and a NAS.

One can see that the samples (obtained in different engine regimes) contain predominantly single, spherical particles with a diameter ranging from 17 to 23 nm, Figure 3, and are presumably primary soot particles. This is in agreement with previous studies on the emitted particles from GDI engines (Gaddam and Wal 2013; Price et al., 2007). The fact that there are no aggregates observed on these samples confirms that the experimental setup is able to minimize the aggregation of particles to an extent that should not affect the subsequent chemical analysis.

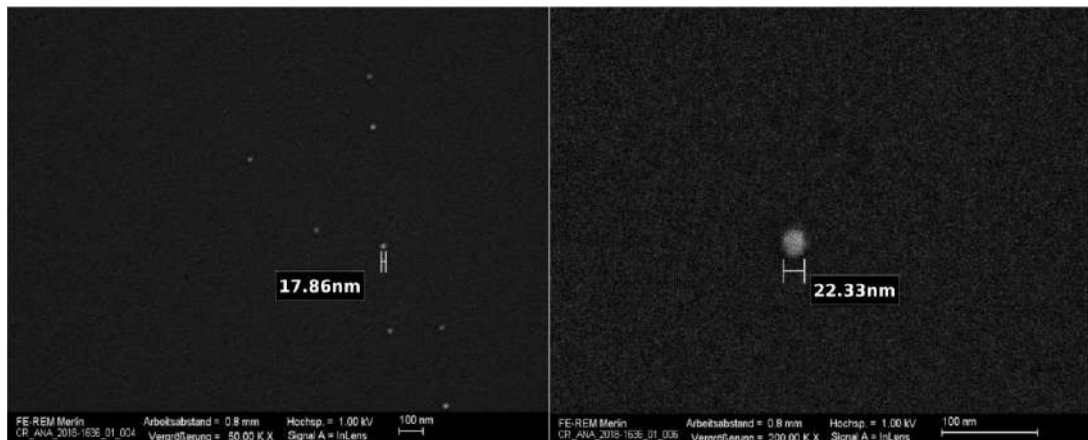


Figure 3: SEM images of size-selected particles (size bin centered at 18 nm) collected with a NAS in the **NH** (left panel) and **NM** (right panel) engine operating regimes.

AFM analysis is performed on samples collected in the **NH** engine regime (optimal conditions, high load), Table 2. The technique is used to determine the distribution and the size of single particles. AFM measurements are performed on a $1.2 \times 1.2 \mu\text{m}$ region (300 x 300 pixels), Figure 4a. The heights of particles 1 and 2 were determined to be 10 nm and 6 nm, Figure 4d. The measured diameter is highly dependent on the used tip, especially when the radius of the scanned object is close to the one of the tip. The Full Width at Half Maximum (FWHM) diameters of particles 1 and 2, obtained with a sharp tip ($r=1 \text{ nm}$), are <48 nm and <43 nm, respectively.

Two smaller zones have been characterized by TERS with a resolution of 7 nm/pixel (zone I) and 5 nm/pixel (zone II) and with a Raman integration time of 100 ms (one spectrum/pixel). The TERS maps of zones I and II are presented in Figures 4b and 4c, respectively. Raman spectra of carbon materials contain two main features (see Figure S1 in Supplementary Material): the G band, derived from in-plane motion of carbon atoms (around 1580 cm^{-1}) and the D band (D1), attributed to lattice motion away from the center of the Brillouin zone (around $1270 - 1450 \text{ cm}^{-1}$). The TERS maps displayed in Figure 4b,c are obtained by integrating the G band only.

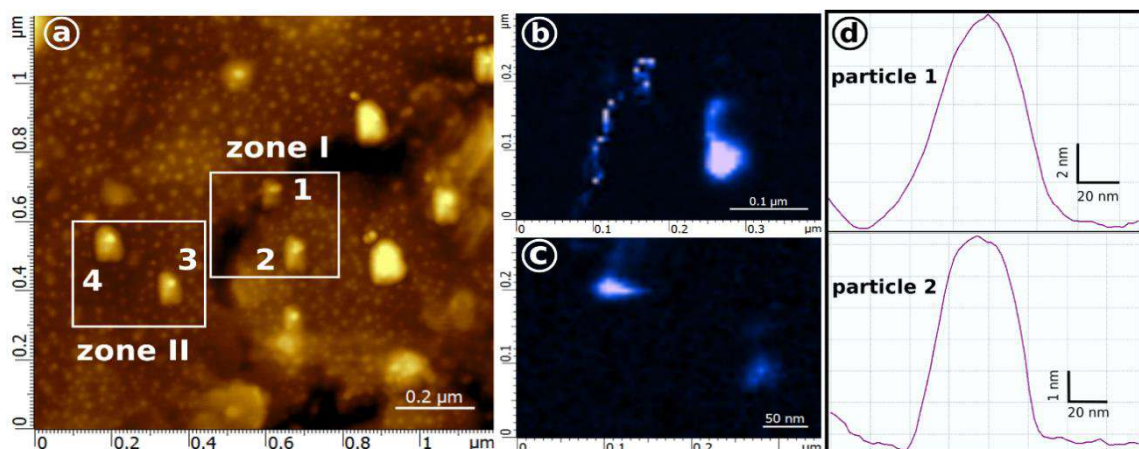


Figure 4 AFM and TERS study of nanoparticles collected in the **NH** engine regime (optimal conditions, high load). Topography image ($1.2 \times 1.2 \mu\text{m}$) (a), TERS mapping of zone I, particles 1 and 2 (b), and zone II, particles 3 and 4 (c), topographic cross-section of particles 1 and 2 (d).

Besides TERS maps, TERS spectra were obtained for particles 2, 3, and 4 and are displayed in Figure S1. The three spectra (Figure S1) exhibit very different profiles (for example, the relative intensity of the D band to the G band is higher for particle 2 and lower for particles 3 and 4) which is indicative of major

structural variations between particles collected in the same engine regime and the same size bin. A more quantitative approach involves a five-band fitting method, often applied to Raman spectra of soot particles (Sadezky et al., 2005), in which the G, D1, D2, and D4 bands are fitted with a Lorentzian profile, whereas the D4 band is fitted with a Gaussian profile. The fit results are presented in Figure S1. The spectral parameters determined by curve fitting are highly variable across the three particles (Table S1), confirming our first observation. For instance, the ratio of the integrated areas of D1 to those of (G+D2) bands is usually considered as a good indicator of the order in the soot structure (Carpentier et al., 2012). This value increases from 1.5 (particle 4) to 2.5 (particle 3) and to 3 (particle 2), suggesting that particle 2 has a much more disordered structure compared to particles 3 and 4. In addition, the presence of strong signatures at 1208 and 1278.6 cm⁻¹ on the spectra of particles 3 and 4 could be an indicator of organic molecules present on the surface of the particles.

These TERS measurements, performed, to the best of our knowledge, for the first time on ultra-fine combustion-generated particulate matter, reveal the diversity (at least in terms of nanostructure) of soot particles generated by the same engine, operating in the same conditions, and collected in the same size bin. This observation is of paramount importance for the interpretation of our off-line chemical composition measurements discussed in section 3.3., which, conversely, do not probe individual particles but rather a high number of them because of the diameter of the laser or ion beam used in the experiments. Therefore, the properties and trends we derive in section 3.3. are averaged over many (different) particles. Nevertheless, we demonstrate that the measured trends are statistically significant and do offer valuable input for the theoretical model, also operating with statistical approaches on particles ensembles.

3.3 Chemical characterization

To obtain a comprehensive chemical characterization and thus provide valuable inputs for building and validating the theoretical model, size-selected particles are analyzed with L2MS and SIMS. Data-treatment was performed according to our recently developed comprehensive methodology (Irimiea et al 2018, Irimiea et al., 2019) which includes powerful statistical techniques such as PCA and HCA. Since the particles emitted in a certain engine regime are size-selected, a notation scheme that indicates the size of collected particles, in addition to the engine regime will be used from here forth (<engine regime>:<upper size limit>-<lower size limit>), e.g. **OM:180-100**. The layer of particles deposited on aluminum foils is very thin and since the adhesion of particles to aluminum is rather weak, several desorption laser pulses is all it needs to clear the aluminum surface from the particles. This phenomenon caused the formation of Al⁺ and Al₂O⁺ ions, detected at *m/z* 27 and 70, respectively. Consequently, even though the presence of Al compounds in such samples is typically a marker of engine wear, these peaks will rather be associated with the aluminum substrate in our case.

3.3.1 Size discrimination

One of the major points that need to be determined is whether the chemical composition of emitted particles varies with their size. On that ground, size-selected particles produced in the **OM** engine regime (optimal conditions with an addition of oil, medium load) are analyzed with L2MS. This particular engine regime was chosen as it simulates a malfunction, i.e. an extreme case of operation, equivalent to a “worn out” engine with a high oil consumption. This information, along with similar analyses performed on size-selected particles emitted in other operation conditions, allows for a more precise calibration of the theoretical model.

When the ionization of laser-desorbed compounds is performed at 266 nm (Figure 5) mass spectra contain mostly aromatic species. They are visually separated into two groups: one of lower and one of higher mass compounds. The first group is comprised of aromatic compounds with one to two aromatic rings and their alkylated species (*m/z* 78 – 170) and is present in the spectra of all the samples with varying relative intensities. The second group is composed of aromatic compounds with three and more rings. According to Bari et al., (2010), the first group can be considered as volatile species, as they are mostly present in the gas phase. The second group is comprised of semi and non-volatile compounds. Therefore, the intensity ratio of the first to the second group is related to the overall volatility of the organic layer on the surface of particles. Species with masses between *m/z* 178 and 398 are detected on larger **OM** particles, i.e. on samples **OM:180-100**, **OM:100-56**, and **OM:56-32**, while for the sample **OM:32-18** the highest detected mass is only *m/z* 278. A table encompassing the detected mass peaks is presented in SI (Table S2).

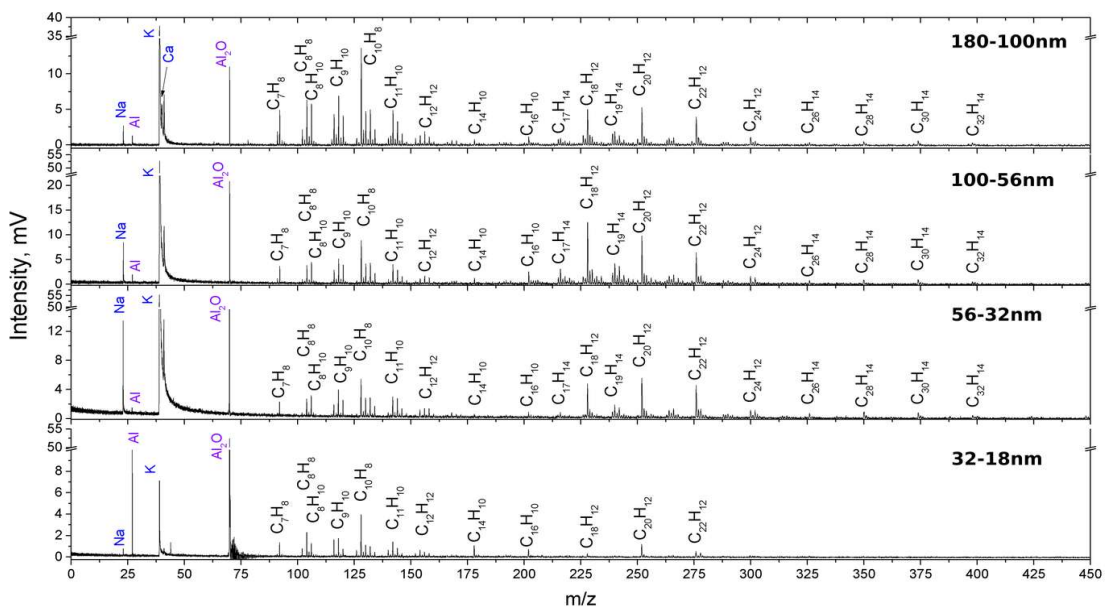


Figure 5 Mass spectra of four samples (particle size 180-18nm) obtained in the **OM** engine conditions (optimal operation, medium load). The analyses were performed with an ionization wavelength $\lambda_i=266$ nm to target aromatic compounds.

The intensity ratio of species belonging to the second group to those in the first one changes from sample to sample, within the **OM** regime. For the largest particles (**OM:180-100**) as well as for the smallest (**OM:32-18**), the first group ($78 \leq m/z \leq 170$) shows a higher intensity. However, for samples **OM:100-56** and **OM:56-32**, the second group ($m/z \geq 178$) exhibits a higher contribution. Within the first group, the base peak is at m/z 128 for all samples and the group features fairly constant peak and intensity distributions across samples. The second aromatic group shows a distinct behavior, where the base peak is m/z 252 for samples **OM:180-100**, **OM:56-32**, and **OM:32-18**, but m/z 228 for sample **OM:100-56**. However, with the exception of the peak at m/z 228, peak and intensity distributions change only slightly from sample to sample. The change in the relative intensity of the m/z 228 peak is probably linked to a $C_{18}H_{12}^+$ isomer present on particles in the size range 100 – 32 nm. The fact that only species up to m/z 278 can be seen on sample **OM:32-18** might be explained by an overall lower intensity, as this sample had the lowest coverage of deposited particles. However, since the contribution from the highest masses (e.g. $m/z \geq 275$) does not exceed a few percent of that given by the whole distribution of aromatic compounds making up the second group (≥ 3 -ring aromatic compounds), we can still derive the intensity ratio of species from the second group to those belonging to the first one. The fact that this ratio is low suggests that smaller particles contain mostly light aromatic species.

Along with organic species, some metals were also detected (Na^+ , K^+ and Ca^+). While Na^+ and K^+ are mostly associated with fuel, they can also be present in the lubricating oil as trace elements (Huang et al., 1994; Cadle et al., 1997; Cross et al., 2012; Dallmann et al., 2014). In addition, the origin of Ca^+ is most likely the lubricating oil, since Ca^+ is a component of detergent additives, widely used in modern motor oils (Cadle et al., 1997; Dallmann et al., 2014).

When the same samples are analyzed with a different ionization scheme ($\lambda_i=118$ nm) (Popovicheva et al., 2017), predominantly aliphatic species are detected, as seen in Figure S2. Ion series with the formula $C_nH_{2n-1}^+$ is typical of cycloalkanes and alkenes while the $C_nH_{2n+1}^+$ series (alkyl fragments) is typical of linear or branched alkane compounds (McLafferty and Tureek 1993). The series at m/z 67, 81, 95, and 109 ($C_nH_{2n-3}^+$ fragments of bicycloalkanes) is also present, however with a very low intensity. The asymmetrical shape of the peaks is a sign of fragmentation. The fragmentation pattern is characteristic of the presence of aliphatic hydrocarbons, alkanes ($C_nH_{2n+2}^+$). As alkane cations are not stable, especially if the excess internal energy is high after ionization, they can easily fragment.

Since lubricating oils tend to be dominated by cycloalkanes due to the deliberate removal of *n*-alkanes during a de-waxing process (Tobias et al., 2001), an intense signal for cycloalkanes is usually a sign of oil contribution. The main source of aliphatic compounds can be derived from the ratio of *n*-alkanes to

cycloalkanes. The signal corresponding to alkanes is superior to that of neighboring cycloalkanes in the mass range $m/z = 67 – 71$ and $81 – 85$ when the fuel is the main source of these compounds, and inferior for the lubricating oil (Dallmann et al., 2014; Sakurai et al., 2003; Tobias et al., 2001). Ion signals at m/z 71 and 85 are lower than signals at m/z 69 and 83, suggesting that the measured exhaust particles mainly consist of unburnt lubricating oil (in case of diesel particles this pattern would be caused by at least 95% oil and 5% fuel, while in the case of gasoline, the ratio should be higher (Dallmann et al., 2014; Sakurai et al., 2003)). The one exception is observed for the sample **OM:100-56** where the signal at m/z 69 is lower than that of m/z 71 ($r = S_{69}/S_{71} \approx 0.8$), while the m/z 83 to 85 ratio is close to unity. The ratio of cycloalkanes to acyclic alkanes is the lowest for sample **OM:100-56**. Since the source of organic species in the exhaust includes fuel, lubricating oil, and their partially oxidized products, it is possible that particles containing the most unburnt fuel are concentrated in the size bin associated with sample **OM:100-56**.

Peaks at m/z 50, 64, 66 and 78 can be attributed to aromatic species and their fragments, that are known to be present on the **OM** samples. Series of highly unsaturated aliphatic compounds are present as well: $C_{2n}H_2^+$ and $C_{2n}H_4^+$. These series were attributed to polyylic fragments, known to be present in rich premixed flames and play an important role in combustion-generated particles formation (Hansen et al., 2008; Li et al., 2009). Just like above, when the ionization wavelength of 266 nm was used, Na^+ , K^+ and Ca^+ were detected.

To classify the samples and to uncover differences and similarities between them, the principal component analysis (PCA) was used (Irimiea et al., 2018, Irimiea et al., 2019). This statistical method is able to reduce the number of dimensions of complex mass-spectrometric data, thus increasing its readability, while still preserving most of the original information. Before applying the PCA, all peaks associated with the substrate were disregarded. Each principal component (PC) accounts for a defined percentage of the variance within the dataset. For both ionization schemes, the first two components are responsible for most of the variation between samples (containing particles of different sizes) ($\approx 97\%$), and therefore the number of dimensions of the original data was reduced to only two. The contribution of mass peaks to each principal component is represented by their loading (Figure S3), which reflects the interpretation of individual components. For 266 nm ionization, PC1 can be associated with the total number of different aromatic species, since it receives a high negative contribution from both alkylated and non-alkylated PAHs. The first group of aromatic compounds ($78 \leq m/z \leq 170$) shows a high positive contribution to the second principal component (PC2) while the second group ($m/z \geq 178$) is related to the negative PC2 value.

For spectra obtained with 118 nm ionization, PC1 is linked to all detected aliphatic species and it can also be seen as an indicator of the homogeneity of aliphatic signal throughout the mass spectrum. PC2 has a strong contribution from highly unsaturated hydrocarbons ($C_nH_2^+$, $C_nH_4^+$, positive PC2) and several aliphatic species (negative PC2), Figure S3. Moreover, since contributions to PC2 from $C_nH_2^+$, $C_nH_4^+$, and aliphatic species ($C_{n+1}H_{2n+1}^+$, $C_nH_{2n}^+$, $C_nH_{2n+1}^+$) have the opposite sign, PC2 represents the ratio of highly unsaturated hydrocarbons to aliphatic species. In addition, the fact that peaks at m/z 50, 52, 74 and 78 have a high contribution to PC2 proves that these species have the same origin, which is in agreement with soot formation models (Hansen et al., 2008; Li et al., 2009).

Data in terms of PC1 and PC2 are presented in Figure 6. Data points for each sample are clustered together, proving that the sample surface is homogeneous and the reproducibility of the method is high. In the case of 266 nm ionization, sample **OM:180-100** shows a large number of aromatic species, with a higher contribution coming from the light-weight compounds ($78 \leq m/z \leq 170$). In contrast, sample **OM:100-56** exhibits a higher contribution from the second group of aromatic compounds ($m/z \geq 178$). Sample **OM:56-32** seems to have fewer species, however heavier compounds ($m/z \geq 178$) still dominate. For the smallest analyzed particles, i.e. sample **OM:32-18**, the contribution of lighter aromatic compounds increases considerably, with only a few species detected from the second group (high PC1).

For 118 nm ionization, sample **OM:32-18** exhibits the most peaks, although they have a low intensity, including peaks in the mass range m/z 64 – 112 (which reflects as a high PC1, the latter being representative of all detected aliphatic species in Figure 6). At the same time, highly unsaturated hydrocarbons ($C_nH_2^+$ and $C_nH_4^+$) have a low contribution compared to the aliphatic species. Sample **OM:56-32** has a fairly inhomogeneous-looking spectrum (Figure S2), with well-separated groups of peaks. The contribution of highly unsaturated hydrocarbons is the highest (higher PC2). Sample **OM:100-56** also has an inhomogeneous spectrum with the lowest contribution from highly unsaturated hydrocarbons. In contrast, sample **OM:180-100** has the highest contribution from them, while having a more homogeneous spectrum (with peaks in the mass range $78 \leq m/z \leq 398$).

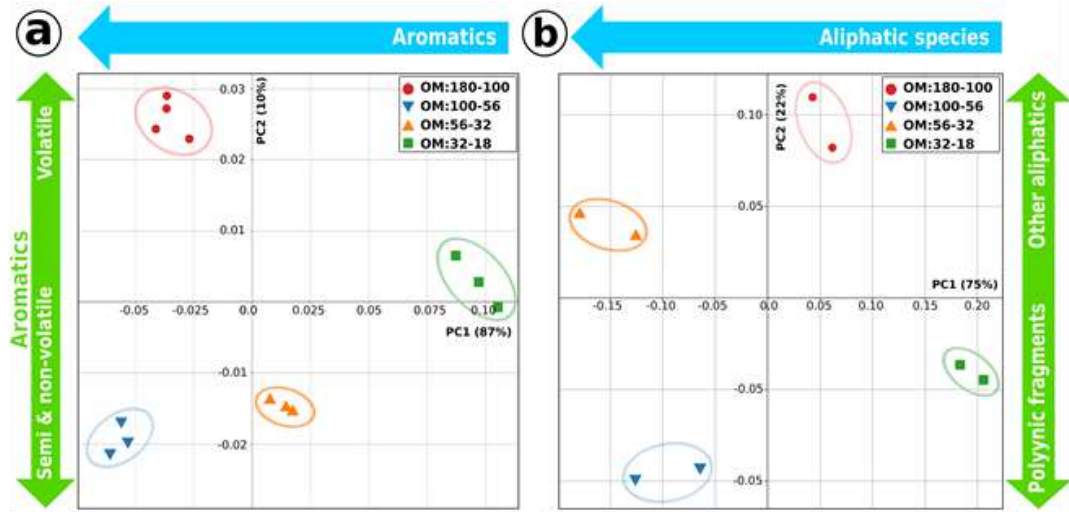


Figure 6 PCA applied to combustion generated samples obtained in the OM engine regime (optimal operation with addition of oil, medium load) discriminates PM composition by particle size for ionization wavelengths of $\lambda_i=266 \text{ nm}$ (a), or $\lambda_i=118 \text{ nm}$ (b). Species were classified as volatile, semi- and non-volatile compounds according to Bari et al. (2010).

It appears that aromatic species with a lower mass (first group on spectra obtained with 266 nm ionization) are present on all samples and are not bound to a specific particle size. In contrast, there is a clear increase in the contribution from higher mass aromatic species on sample **OM:100-56**, suggesting that these compounds preferably adsorb on particles in this size range (100 – 56 nm). The ratio of the signals of *n*-alkanes to those of cycloalkanes implies that the main source of aliphatic compounds is the unburnt lubricating oil. The contribution of aliphatic compounds from the fuel is maximal on sample **OM:100-56** and decreases toward both smaller and larger particles. Oil contribution was also confirmed by the presence of metals associated with various additives as well as trace elements that are present in the lubricating oil. There is a notable separation between different samples, thus demonstrating the capability of our PCA method to discriminate between samples that present, at first glance, similar mass spectra.

Another engine regime that simulates a malfunction is **EM** (low air/fuel ratio, medium load), which acts as one more extreme operation point, this time with a normal oil consumption. Particle emissions obtained in this engine regime are analyzed with SIMS in both positive and negative polarity (Figure S4 and Figure S5, Table S3 contains all the detected peaks in the positive and negative polarity). All spectra are dominated by hydrocarbon fragments $C_nH_m^+$. Masses between m/z 128 and 300 can be mostly attributed to PAHs. Metallic and metalloid ions such as Na^+ , Mg^+ , Al^+ , Si^+ , K^+ , Ca^+ and Cu^+ are also present, however, their intensity is higher for the blank aluminum foil, and therefore they will be assumed to be coming from the underlying substrate rather than from the collected particles. Additional minor signals correspond to NH_4^+ and oxygenated species such as C_3HO^+ (m/z 55), $C_2H_4O_2^+$ (m/z 60) and CHO_4^+ (m/z 77). CH_3O^+ can be associated with methyl esters or ethers. Alternatively, it can correspond to primary alcohols or methyl-carbinols. The oxygenated positive ions, CH_3O^+ and $C_2H_4O_2^+$ present the highest correlation ($R = 0.98$) between the integrated areas of their peaks (normalized with respect to total ion count, TIC), thus indicating a common source. For instance, isopropanol, which is used as a gas dryer additive in gasoline for fuel system protection (Patil et al., 2014), could be a common source for these two ions. Ferrocene ($Fe(C_5H_5)_2$) is believed to be present in the fuel, since its fragment ($FeC_5H_5^+$) was detected. Ferrocene is sometimes used as a fuel additive that acts as an antiknock agent. Hopanes and *n*-alkanes ($C_{26} - C_{36}$) were also detected, they are believed to be linked to unburned lubricant oil (Wang et al., 2009). The high correlation between these peaks ($R = 0.85 - 0.98$) also suggests a common source. The correlation between PAHs and hopanes is almost non-existent, therefore we can conclude that PAHs are formed during the combustion process and are not remnants of oil/fuel.

Negative SIMS spectra, as presented in Figure S5, are dominated by H^- , O^- , and OH^- fragments. Additional strong features correspond to the C_n^- and C_nH^- ($n = 1 - 9$) series with the hydrogenated carbon cluster C_nH^- being more intense compared to C_n^- when n is an even number (except in the case

of $n = 1$). C_n^- ($n = 2 - 4$) fragments are considered to be a marker for elemental carbon (EC) in aerosol mass spectrometry (AMS) data (Pagels et al., 2013). The fact that detected carbon clusters have the same source is confirmed by the high positive correlation factors between C_2^- , C_3^- , and C_4^- . The correlation between C_3^- and C_4^- is the highest ($R_{\max} = 0.95$), while the lowest is between C_2^- and C_4^- ($R_{\min} = 0.74$).

For the positive polarity SIMS spectra, the first two main components account for 92% of the variation. All samples can be easily separated by PCA, Figure S5a, and by hierarchical clustering analysis (HCA), Figure 7. For PCA, the first principal component receives a high negative contribution from aliphatic compounds ($C_nH_{2n+1}^+$ and $C_nH_{2n+1}^{+}$, negative PC1), while other aliphatic species show a positive contribution. PC2 can be seen as the ratio of aliphatic species (positive PC2 value) to aromatic compounds, such as PAHs and their fragments (negative PC2 value). The PCA clearly shows that aliphatic species are concentrated predominantly on samples **EM:180-100**, **EM:56-32**, and **EM:32-18** while aromatics are present in comparable amounts on the lower four stages (**EM:100-56**, **EM:56-32**, **EM:32-18** and **EM:18-10**).

HCA is a statistical technique able to group samples according to the distance between them in a multidimensional space while also accounting for the total variance within the dataset (Alvin et al., 2000; Pei et al., 2008). The distances between the samples are represented in form of a dendrogram, Figure 8. We can see that samples **EM:180-100**, **EM: 56-32**, and **EM:32-18** form a relatively small cluster (small distance between data-points), thus indicating their similarity. Likewise, **EM:100-56** and **EM:18-10** samples are grouped together hence forming a second cluster well separated from the first cluster. Samples in these two clusters are thus very different, primarily due to the high contribution of $C_nH_{2n+1}^+$ and $C_nH_{2n+1}^{+}$ ions to **EM:100-56**, and **EM:18-10** samples (as already shown by PCA). Interestingly, the distance between the blank and the second cluster (**EM:100-56** and **EM:18-10** samples) is relatively small, which can be explained by the lower coverage of these samples.

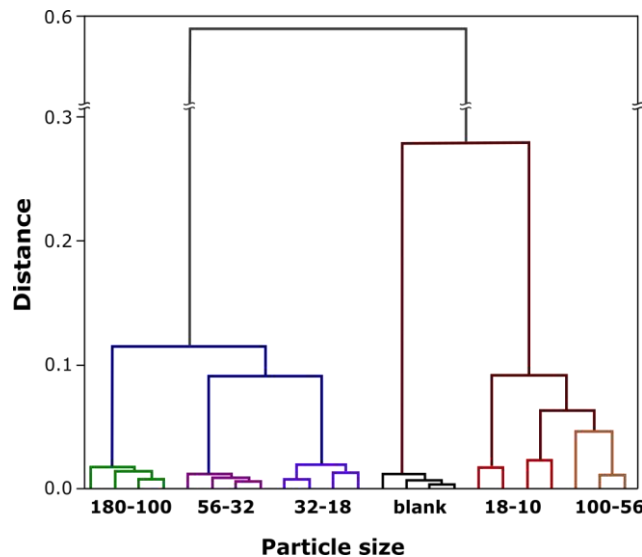


Figure 7 Separation of combustion-generated particles obtained in the EM (low air/fuel ratio) engine regime into size groups by HCA.

The same statistical technique was applied to SIMS mass spectra in negative polarity. Only the first two components were kept as they account for 95% of the variations within the data set. The results are presented in Figure S7b. In this case, PC1 is related to the ratio of the amount of oxygenated species to the C_n^- , C_nH^- family (with a positive PC1 contribution linked to a high fraction of oxygenated species while a negative PC1 value indicates a high amount of C_n^- , C_nH^- , i.e. a high amount of elemental carbon (EC)). PC2 is linked to oxygenated species (positive for hydrocarbon-based compounds and negative for oxygenated species containing S, P and N). Samples **EM:100-56**, **EM:56-32**, and **EM:32-18** exhibit the highest amount of C_n^- and C_nH^- ions, and therefore have a high EC content. Sample **EM:180-100** has the highest contribution from oxygenated compounds that contain elements other than carbon and hydrogen (e.g. PO_3^- , SO_3^- , SO_4^- , PO_4^- , $NaSO_4^-$), while samples **EM:100-56** and **EM:18-10** contain the lowest. From Figure S7, it is clear that PCA can easily distinguish between samples, implying that size-selected particulates are also chemically different in the **EM** regime. Eventually, negative polarity SIMS data extracted from **EM** samples (Figure S7b) can be divided into three main clusters according to the amount and nature of oxygenated species present on the samples. Specifically, the first cluster

encompasses the two samples which exhibit the most oxygenated species, i.e. **EM:100-56** and **EM:18-10**. The second cluster gathers the two samples which bear much less oxygenated species compared to the others, along with more elemental carbon, i.e. **EM:56-32** and **EM:32-18**. Lastly, the third cluster is sample **EM:18-10**, which contains the most inorganic oxygenated species of all samples.

3.3.2 Source discrimination

We showed in section 3.3.1 that some chemical compounds of different provenience are preferentially found on particles featuring a distinct size range. It is now possible to determine the contribution of major sources to the formation of particulates. Determining the impact of various sources to the chemical composition of particulates will help further improve the theoretical model. On that basis, samples obtained in engine operation regimes (**OM**, **EM**, **NM**, and **NH**) with different contribution from fuel and oil (main sources of particulates) are analyzed and compared using PCA.

The first two PCA components, PC1 and PC2 (~98%) are presented in Figure 8. It is clear that particles produced in an optimized engine regime (medium and high load) are chemically very different from the ones produced in non-optimal ones and, therefore, can be easily separated by their principal components (Figure 8a). PC1 alone (~91%) allows the separation of regimes, based on the abundance of aliphatic fragments (positive contribution to PC1, Figure S8). Consequently, samples produced in non-optimal regimes are characterized by a higher relative contribution from aliphatic fragment ions compared to optimized engine regimes. PC2 is linked to the aliphatic fragment ions and aromatic species (positive PC2 value), however some aliphatic fragment ions ($C_5H_7^+$, $C_5H_9^+$, $C_3H_7^+$, $C_4H_7^+$) contribute to the negative value of PC2. Data points corresponding to optimal engine regimes form a smaller cluster, implying that particles produced in non-optimal conditions exhibit a much larger variability in their chemical composition.

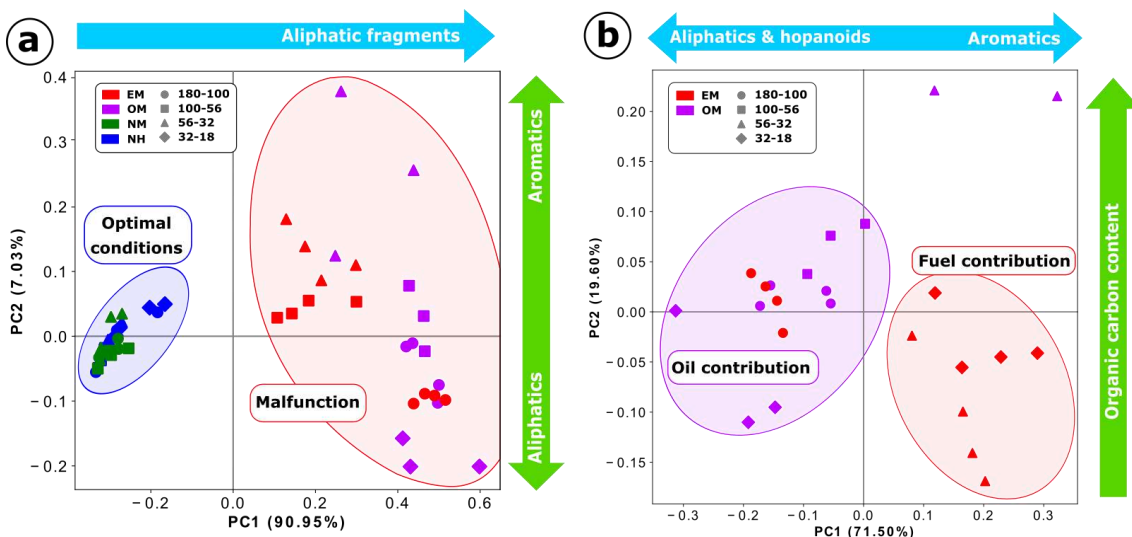


Figure 8 Discrimination of different engine regimes (a) and main sources of particles (b) achieved by application of PCA.

The two non-optimal regimes have been compared using the same statistical method, which further enables the distinction between the two main contributors to particulate emissions from the internal combustion engine: fuel and oil, Figure 8b. PC1 (~71%), which is accountable for the separation of the two regimes (and consequently sources), is linked to the contribution of hydrogen-rich hydrocarbons on one side (negative contribution) and to fragment ions and aromatic species on the other (positive contribution, Figure S8). This reveals that oil-related particles feature more hydrogen-rich hydrocarbons, while an excess of gasoline leads to the production of more aromatic species. The increase in the contribution of fragment ions in the latter is probably linked to the increase in the aromatic contribution, since the majority of fragments can be associated to the fragmentation of PAHs (McLafferty and Tureek 1993). PC2 (~20%) is associated with the presence of aromatic hydrocarbons, thus confirming that the presence of aromatic species is related to fuel combustion. Two data-points, corresponding to **OM:56-32**, show a rather high contribution from organic carbon, and aromatic compounds in particular, unlike other **OM** samples. Since these compounds are linked to the

contribution of fuel, we can infer that, for the **OM** regime, particles in this size (56-32nm) mostly originate from fuel combustion.

3.3.3 Influence of the catalytic stripper

We have previously shown the analysis of collected particles from the “raw exhaust” (at the exhaust port), and thus gathered information about the chemical composition of emitted particles that will serve as inputs to test and improve the theoretical model. However, particles present in the “raw exhaust” contain a multitude of organic species (as is shown above), with various degrees of volatility, and since the current regulation limits only the number of non-volatile particles, one should also study PN emissions after the removal of the volatile fraction. This is especially important in this study as this information will also help characterize and model the catalytic stripper (CS) that will be used to remove volatile compounds in the PEMS measuring system – whose development is the ultimate goal of the Pems4Nano project. For such a system, volatile removal efficiency of the CS should be in accordance with European regulations, that is to say >99% removal of $\geq 30\text{nm}$ tetracontane ($\text{CH}_3(\text{CH}_2)_{38}\text{CH}_3$) particles with an inlet concentration of $\geq 10000 \text{ cm}^{-3}$ at the minimum dilution (European commission 2017). However, supplementary efforts are currently being made to better understand how the CS that complies with these regulations affects other individual organic compounds that are commonly present on the surface of combustion generated particles (such as PAHs) – important information for modeling the non-volatile fraction leaving the CS and entering the counting stage of the instrument. To study the influence of the CS, two sets of exhaust particles are collected and subsequently analyzed. One set was sampled with and one without the catalytic stripper. The engine regime was exactly the same for both sets of samples. Here we only show some preliminary results on the influence of the CS to the chemical composition of emitted particles, however, a more complete and detailed study will be presented in an upcoming paper.

From the mass spectra (L2MS) of the two sets we can already see the difference in the absolute intensity of all the peaks corresponding to organic species (considerably smaller for the samples obtained with the catalytic stripper). However, the signal which corresponds to carbon clusters is considerably higher for particulates sampled after the catalytic stripper (Figure S9). PCA clearly shows that the catalytic stripper removed the volatile particles as well as the organic species from the surface of nonvolatile particles and, as a result, the contribution of EC (carbon clusters) increased, Figure 9. Accordingly, particles present in the “raw exhaust” have a higher contribution from organic components (OC), Figure S10. The only exception are the particles in the size range 56-18 nm (**NHC:56-32** and **NHC:32-18**), which might be the result of a combination of (i) a high contribution from organic components to particles in this size-range (as previously shown), and (ii) a lower efficiency of the catalytic stripper in this size-range (Swanson et al.,2013). Positive value of PC2 is linked to the organic fraction and small mass carbon clusters (C_{10}^+ and C_{11}^+), while the negative value is related to the contribution of carbon clusters with a higher mass and a few PAHs, Figure S10. Eventually, the catalytic stripper was effective in removing most of the organic fraction from the surface of the particles.

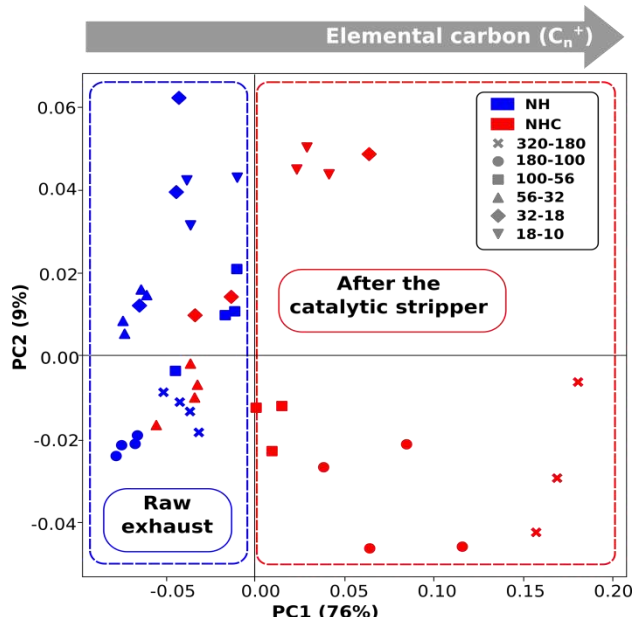


Figure 9 Discrimination between particles sampled from the raw exhaust and after the catalytic stripper.

3.3.4 Outputs for the theoretical model

To uncover general trends in the chemical composition, as well as to provide chemical data as useful input to the theoretical model (for calibration and validation purposes) individual species are grouped into classes. Compounds are grouped based on their chemical family (aromatics⁺, C_nH_{2n-1}⁺, C_nH_{2n-3}⁺, hopanes⁺, n-alkanes⁺) as well as their connection to the elemental carbon content (C_n⁻) (Gilardoni et al., 2007; Kirchner et al., 2003). Moreover, the organic carbon content (OC) can be expressed as the sum of the former groups of organic compounds (Pagels et al., 2013; Delhaye et al., 2017). These chemical families/groups have been chosen as they have different sources and roles in the formation and ageing mechanism of combustion-generated particles (e.g. PAHs are associated with the combustion of gasoline, while hopanoid compounds are seen as markers of unburnt lubricating oil). The contribution of a group to a mass spectrum is equal to its normalized intensity (to TIC). This is illustrated in Figure 10, where the error bars correspond to the standard deviation associated with multiple zones of each sample. The normalized signals obtained for the blank filter are given for comparison. For most of the fragments, relative intensities of the blank filter are negligible. The total amount of aromatic compounds increases toward sample **EM:32-18**, and exhibits similar variation as found for the C_n⁻ family. Aliphatic families (C_nH_{2n-1}⁺ and C_nH_{2n-3}⁺) are the most abundant on samples **EM:180-100**, **EM:56-32** and **EM:32-18**, when only a small contribution is observed for the other two samples (peak intensities comparable to those of the blank aluminum foil). Hopanes and n-alkanes are mostly present on sample **EM:180-100** and since they are attributed to the lubricating oil, one can conclude that the unburnt oil is found predominantly on bigger particles. This is slightly different compared to the **OM** engine regime where the oil contribution is the highest on sample **OM:100-56**. This difference might be linked to the state of the oil. In fact, for the **EM** regime, the oil originates from an oil film present on the cylinder liner while for **OM** regime, oil was deliberately added to the combustion chamber, forming a mist.

The relative abundance of the C_n⁻ fragments, compared to the TIC in the negative polarity SIMS spectra is shown in Figure 10. The relative proportion of these fragments increases from the sample made of the largest particles (180-100 nm) to that holding the smallest ones, reaching its maximum for sample **EM:32-18** and then dropping significantly for **EM:18-10**. Figure 10 shows, once again, that the chemical composition of emitted particles changes with their size because of a size-dependent contribution from different sources of particle emission (e.g. fuel/oil combustion, unburnt oil). These trends represent essential information for the development of a precise and reliable model for the formation of particles in an internal combustion engine.

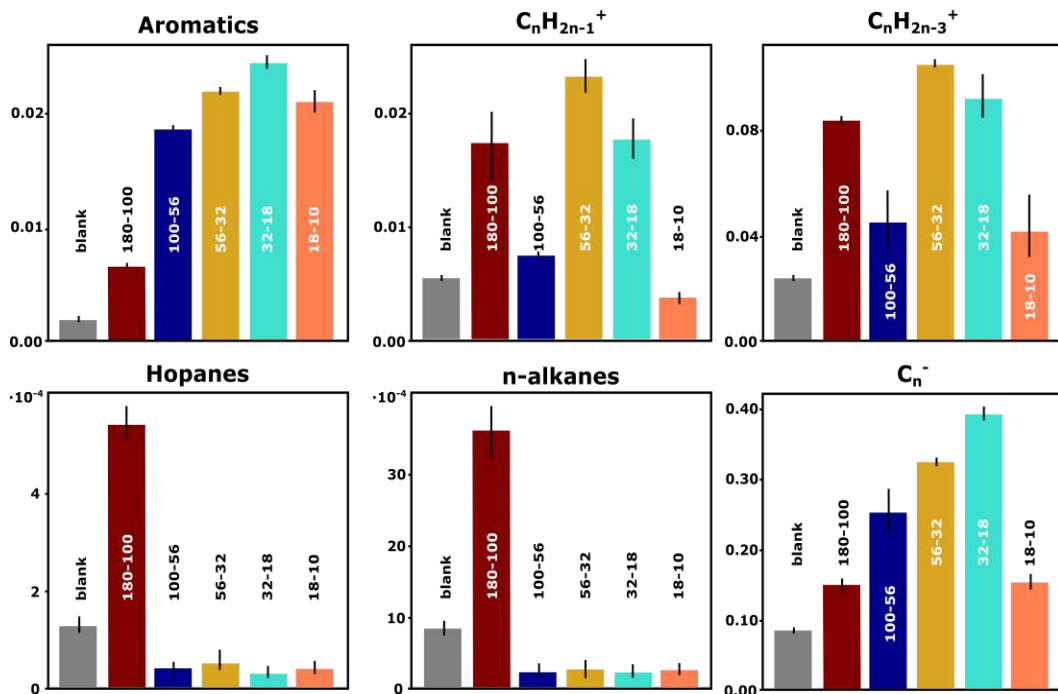


Figure 10 Integrated peak areas of positive and negative SIMS fragment ions of interest normalized to the total ion count (TIC) for particles produced in the EM engine regime (low air/fuel ratio). The error bars represent the standard deviation among all analyzed zones.

4 Theoretical model

Within PEM4Nano, the MGA combines detailed physico-chemical simulation together with advanced statistical techniques of parameter estimation, computational surrogate generation and sensitivity analysis (Lee et al., 2019). MGA supports the understanding of the particle characteristics (composition, morphology, and size distribution that have a major influence on the resulting particle number) in the system that then is fed back into the methodology by demonstrating the use of simulation models to guide the application of measurement technology, especially in this area of ultra-fine particles in harsh automotive exhaust. The evolution of the detailed particle population is evaluated at engine-out and as a function of sampling characteristics such as dilution ratios, temperatures of the sampling stream, etc. This is essential to ensuring robust and reliable measurements in both domains, stationary and mobile, and creates a valuable opportunity to demonstrate the use of these procedures to support the development process of new technologies for internal combustion engines.

The physico-chemical IC engine simulator in this case is the SRM Engine Suite which uses a probability density function (PDF) based stochastic reactor model library to simulate gasoline fuel oxidation, chemical pathways of emission formation, and the key engine sub-processes such as turbulent mixing, direct injection, flame propagation, etc. (Bhave and Kraft 2004; Etheridge et. al. 2011, Smallbone et al., 2011, Lai et al., 2018). The model captures the inhomogeneities in equivalence ratio and temperature composition space, which is important in order to evaluate gas phase and particulate emissions. The model contains a novel population balance sub-model to account for solid, carbonaceous (soot) particles alongside organic SOF liquid particles. This sub-model is directly coupled with the gas phase chemistry within the SRM Engine Suite. The model considers solid particles containing carbon with SOF compounds condensed on their surfaces. Additionally, the model allows for separate tracking of liquid-like particles composed of SOF compounds.

The SRM Engine Suite was first applied to model 12 steady state operating conditions of the gasoline direct-injection single-cylinder test engine. The in-cylinder pressure profile, gas phase emissions (e.g. CO, uHC, NO_x) and PN concentrations are compared with measurements as described in the previous sections. The model evaluations match well with the measurements, for example, in-cylinder pressure

shown in Figure 11 and NOx emissions shown in Figure 12. The dependencies of the engine-out emissions on the load-speed and other engine operating conditions are captured well by the simulation.

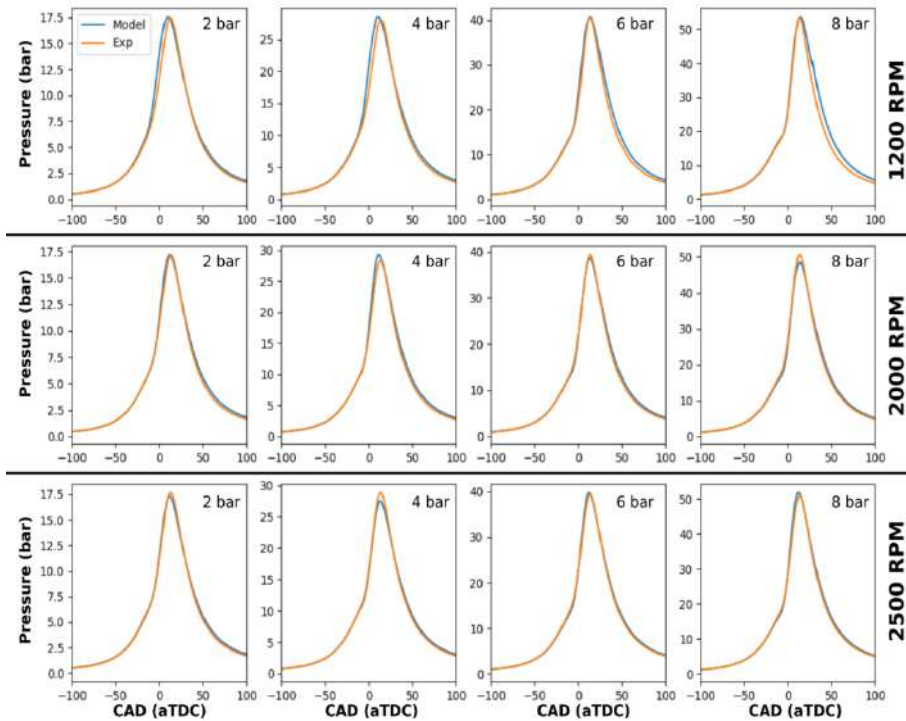


Figure 11 In-cylinder pressure profile (bar): SRM Engine Suite calibrated against measurements for 12 steady state operating conditions in a GDI single cylinder test engine. (CAD - Crank Angle Degree, aTDC - after Top Dead Center).

Furthermore, the engine-out chemical composition obtained from the calibrated and validated SRM Engine Suite was used as a boundary condition to simulate the Dekati FPS 4000 as described in Section 2.1 above. The sampling system was simulated as an equivalent chemical reactor network while accounting for particle coagulation, adsorption, etc., thus enabling the study of the influence of dilution ratios, pipe lengths and temperatures on the evolution of the particle size distribution. Figure 13a shows the reduction of SOF mass fraction with the increase in dilution from the current 30:1 (set during experiments) to as high as 600:1. On the contrary, the increase in the length of the dilution pipe (at the particles sample out location in the diluter) resulted in a surge in the SOF mass fraction (see Figure 13b) in the sub-23 nm size range. Note that the presence of SOF mass fraction can adversely affect the robustness of the “solid” particle number (PN) measurement.

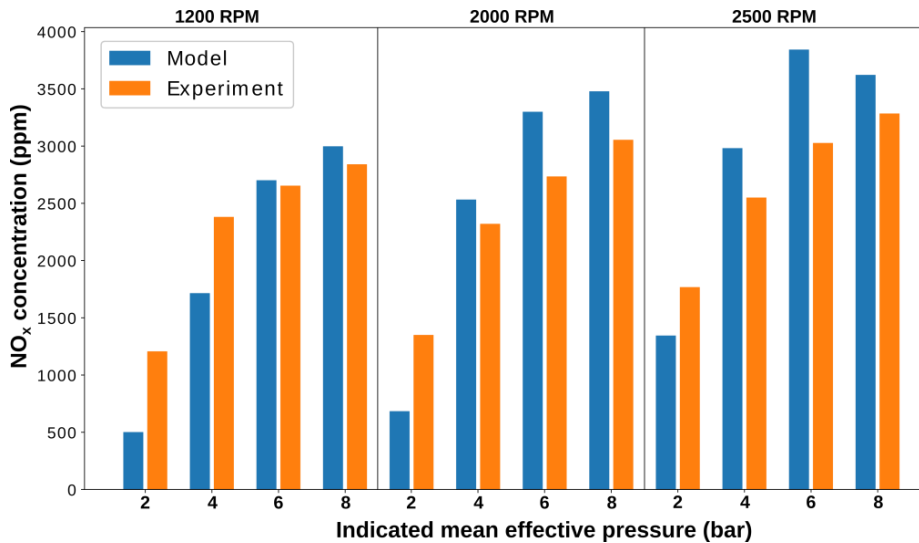


Figure 12 Engine-out NOx emissions: SRM Engine Suite calibrated against measurements for 12 steady state operating conditions in a gasoline direct injection single cylinder test engine.

From the perspective of the chemical characterization of the particles, the model is validated by comparing the SOF layer thickness with the experimentally measured organic carbon content (Figure 13c and Figure 13d). The bump in the SOF layer thickness observed in the measurements was mimicked well by the model. The measurements and the model results confirmed that surface composition is not a measure of bulk characteristics. This is further supported by the decreasing carbon trend shown in the mass spectra as it has been concluded that the nuclei mode particles should have higher SOF. Within the PEMs4Nano project, the MGA is being further applied to gasoline multi-cylinder engine data along with after-treatment, the results from which will be part of a future paper.

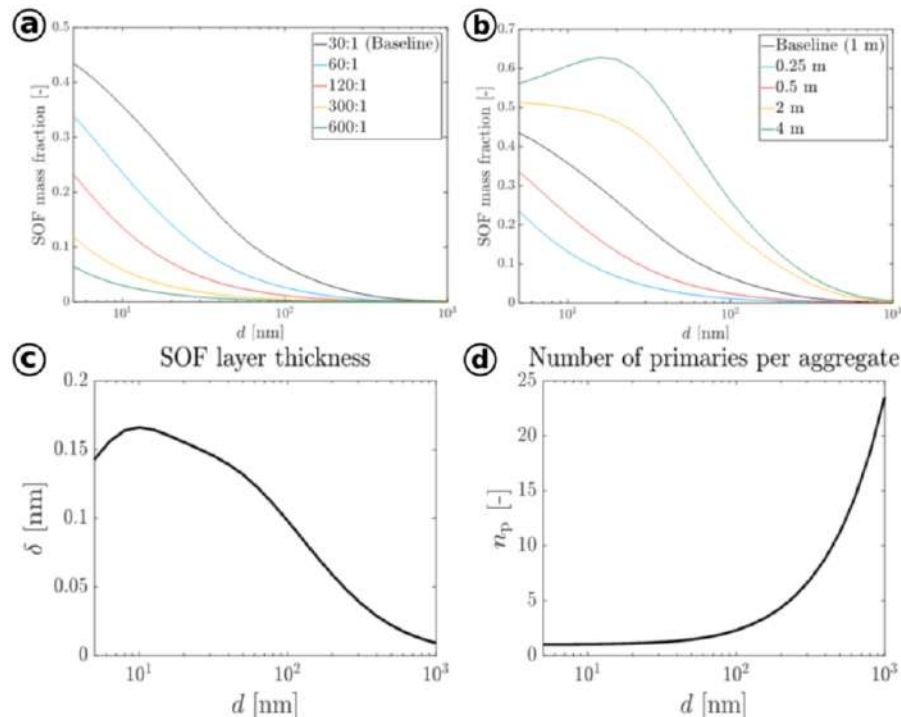


Figure 13 SRM Engine Suite together with kinetics reactor network applied to investigate sensitivity of particle size distribution to dilution ratios (a), and pipe lengths (b). Model evaluated soluble organic fraction (SOF) layer thickness (c) and number of primaries per aggregate (d) at a given operating point.

5 Conclusions

This paper presents an overview of the bottom-up approach used in the PEMS4Nano project to optimize the measurement of sub-23nm particles emitted by internal combustion engines. A GDI single cylinder engine was employed as a particle generator to build up an extensive database of particulates with various characteristics with the aim of testing and validating the Model Guided Application (MGA) proposed by the project. A combination of multiple techniques (online and offline) enabled extensive information to be gathered relative to the structure, morphology and composition of the particulate matter, and their variation with size. Detailed molecular-level characterization of size-selected particulates by mass spectrometric techniques coupled with statistical procedures showed decisive evidence for the variation of the chemical composition with particle size. Moreover, identification of key chemical markers allowed clear discrimination of particles by source (fuel, lubricant, engine wear) or engine operating regime. Atomic force and scanning electron microscopies were used to monitor the morphology of the collected particles, while Tip-Enhanced Raman Spectroscopy was used for the first time to probe the nanostructure of sub-10nm combustion-generated particles.

MGA comprising physico-chemical simulation and advanced statistics has been formulated as part of the development of measurement procedures to support the understanding of the formation and evolution of the particles, as well as the aforementioned physical and chemical characteristics. The results demonstrate the ability to use a model-based framework to assess the performance of an experimental setup as well as the nature of the experimental data. A range of dilution ratios and sampling pipe lengths were investigated for the sampling system and the results indicate the threshold for the dilution ratios as well as the pipe lengths that are necessary to reduce the amount of soluble organic fraction (SOF) adsorbed on the particles in the sampling stage. Lastly, the surface characterization of organic carbon using the mass spectrometry analysis and the SOF layer thickness tracked by the digital engineering workflow indicate that the surface composition of a particle is not a measure of its bulk characteristics.

The multiple experimental particle characterization techniques and theoretical model guided application (MGA) employed in this work provided solid foundations to support the understanding of the formation and evolution of sub-23nm particles from the engine through to the tailpipe, critical to the optimization of the newly developed particle emission monitoring systems.

Acknowledgements

This project has received funding from the European Union's Horizon 2020 research and innovation programme under Grant Agreement no. 724145.

References

- Bachalo W. D., Sankar S. V., Smallwood G. J., Snelling D. R. (2002). "Development of the Laser-Induced Incandescence Method for the Reliable Characterization of Particulate Emissions William", *The 11th International Symposium on Applications of Laser Techniques to Fluid Mechanics: Lisbon, Portugal: July 8-11*. <https://doi.org/10.1111/j.1349-7006.2001.tb02146.x>
- Bari M. A., Baumbach G., Kuch B., Scheffknecht G. (2010). "Particle-Phase Concentrations of Polycyclic Aromatic Hydrocarbons in Ambient Air of Rural Residential Areas in Southern Germany", *Air Quality, Atmosphere and Health*, 3, 103–116. <https://doi.org/10.1007/s11869-009-0057-8>
- Betrancourt C., Mercier X., Desgroux P. (2019). "Quantitative Measurement of Volume Fraction Profiles of Soot of Different Maturities in Premixed Flames by Extinction-Calibrated Laser-Induced Incandescence", *Applied Physics B: Lasers and Optics* 125, 1-18. <https://doi.org/10.1007/s00340-018-7127-2>
- Bhave A., Kraft M. (2004). "Partially Stirred Reactor Model: Analytical Solutions and Numerical Convergence Study of a PDF/Monte Carlo Method", *SIAM Journal of Scientific Computing*, 25, 93-104. <https://doi.org/10.1137/S1064827502411328>
- Cadle S. H., Mulawa P., Ball J., Donase C., Weibel A., Sagebiel J. C., Knapp K. T., Snow R. (1997). "Particulate Emission Rates from in Use High Emitting Vehicles Recruited in Orange County, California", *Environmental Science and Technology*, 31, 3405–12. <https://doi.org/10.1021/es9700257>

- Carpentier Y., Féraud G., Dartois E., Brunetto R., Charon E., Cao A. T., d'Hendecourt L., Bréchignac Ph., Rouzaud J.N., Pino T. (2012). "Nanostructuration of Carbonaceous Dust as Seen through the Positions of the 6.2 and 7.7 μ m AlBs", *Astronomy & Astrophysics*, 548, 40-54. <https://doi.org/10.1051/0004-6361/201118700>
- Cross E. S., Sappok A., Fortner E. C., Hunter J. F., Jayne J. T., Brooks W. A., Onasch T. B., et al. (2012). "Real-Time Measurements of Engine-Out Trace Elements: Application of a Novel Soot Particle Aerosol Mass Spectrometer for Emissions Characterization", *Journal of Engineering for Gas Turbines and Power*, 134, 72801-10. <https://doi.org/10.1115/1.4005992>
- Dallmann T. R., Onasch T. B., Kirchstetter T. W., Worton D. R., Fortner E.C., Herndon S. C., Wood E. C., et al. (2014). "Characterization of Particulate Matter Emissions from On-Road Gasoline and Diesel Vehicles Using a Soot Particle Aerosol Mass Spectrometer", *Atmospheric Chemistry and Physics* 14, 7585–99. <https://doi.org/10.5194/acp-14-7585-2014>
- Delhay J., Desgroux P., Therssen E., Bladh H., Bengtsson P. E., Hönen H., Black J. D., Vallet I. (2009). "Soot Volume Fraction Measurements in Aero-Engine Exhausts Using Extinction-Calibrated Backward Laser-Induced Incandescence", *Applied Physics B: Lasers and Optics*, 95, 825–38. <https://doi.org/10.1007/s00340-009-3534-8>
- Delhaye D., Ouf F. X., Ferry D., Ortega I. K., Penanhoat O., Peillon S., Salm F., et al. (2017). "The MERMOSE Project: Characterization of Particulate Matter Emissions of a Commercial Aircraft Engine", *Journal of Aerosol Science*, 105, 48–63. <https://doi.org/10.1016/j.jaerosci.2016.11.018>.
- Donaldson K., Li X., MacNee W. (1998). "Ultrafine (Nanometre) Particle Mediated Lung Injury", *Journal of Aerosol Science*, 29, 553-560. [https://doi.org/10.1016/S0021-8502\(97\)00464-3](https://doi.org/10.1016/S0021-8502(97)00464-3)
- EPA, (2009) "Integrated Science Assessment for Particulate Matter (Final Report)," U.S. Environmental Protection Agency, Washington, DC, EPA/600/R-08/139F.
- Etheridge J., Mosbach S., Kraft M., Wu H., Collings N. (2011). "Modeling Soot Formation in a DISI Engine", *Proceedings of the Combustion Institute*, 33, 3159-3167. <https://doi.org/10.1016/j.proci.2010.07.039>
- European commission, (2017). "Commission regulation (EU) 2017/1154", *Official Journal of the European Union*, 1154, 708-732. <https://doi.org/10.1097/OLQ.0b013e3181bf9b2d>
- Faccinetto A., Thomson K., Ziskind M., Focsa C. (2008). "Coupling of Desorption and Photoionization Processes in Two-Step Laser Mass Spectrometry of Polycyclic Aromatic Hydrocarbons", *Applied Physics A: Materials Science and Processing*, 92, 969–74. <https://doi.org/10.1007/s00339-008-4605-0>
- Faccinetto A., Desgroux P., Ziskind M., Therssen E., Focsa C. (2011). "High-sensitivity detection of polycyclic aromatic hydrocarbons adsorbed onto soot particles using laser desorption/laser ionization/time-of-flight mass spectrometry: An approach to studying the soot inception process in low-pressure flames", *Combustion and Flame*, 158, 227. <https://doi.org/10.1016/j.combustflame.2010.08.012>
- Faccinetto A., Focsa C., Desgroux P., Ziskind M. (2015). "Progress toward the Quantitative Analysis of PAHs Adsorbed on Soot by Laser Desorption/Laser Ionisation/Time-of-Flight Mass Spectrometry", *Environmental Science and Technology*, 49, 10510–20. <https://doi.org/10.1021/acs.est.5b02703>
- Gaddam C. K., Vander Wal R. L. (2013). "Physical and Chemical Characterization of SIDI Engine Particulates", *Combustion and Flame*, 160, 2517–28. <https://doi.org/10.1016/j.combustflame.2013.05.025>
- Giechaskiel B., Manfredi U., Martini G. (2014). "Engine Exhaust Solid Sub-23 nm Particles: I. Literature Survey", *SAE International Journal of Fuels and Lubricants*, 7, 950–964. <https://doi.org/10.4271/2014-01-2834>
- Giechaskiel B., Vanhanen J., Väkevä M., Martini G. (2017). "Investigation of vehicle exhaust sub-23 nm particle emissions", *Aerosol Science and Technology*, 51, 626-641. <https://doi.org/10.1080/02786826.2017.1286291>
- Gilardoni S., Russell L. M., Sorooshian A., Flagan R. C., Seinfeld J. H., Bates T. S., Quinn P. K., et al. (2007). "Regional Variation of Organic Functional Groups in Aerosol Particles on Four U.S. East Coast Platforms during the International Consortium for Atmospheric Research on Transport and Transformation 2004 Campaign", *Journal of Geophysical*

- Haefliger O. P., Zenobi R. (1998). "Laser Mass Spectrometric Analysis of Polycyclic Aromatic Hydrocarbons with Wide Wavelength Range Laser Multiphoton Ionization Spectroscopy", *Analytical Chemistry*, 70, 2660–65. <https://doi.org/10.1021/ac971264f>
- Hansen N., Klippenstein S. J., Westmoreland P. R., Kasper T., Kohse-Höinghaus T., Wang J., Cool T. A. (2008). "A Combined Ab Initio and Photoionization Mass Spectrometric Study of Polyyne in Fuel-Rich Flames", *Physical Chemistry Chemical Physics*, 10, 366–374. <https://doi.org/10.1039/B711578D>
- Huang X., Imez I. O., Aras N. K., Gordon G. E. (1994). "Emissions of Trace Elements from Motor Vehicles: Potential Marker Elements and Source Composition", *Atmospheric Environment*, 28, 1385–1391. [https://doi.org/10.1016/1352-2310\(94\)90201-1](https://doi.org/10.1016/1352-2310(94)90201-1)
- Irimie C., Faccinetto A., Carpentier Y., Ortega I. K., Nuns N., Therssen E., Desgroux P., Focsa C. (2018). "A Comprehensive Protocol for Chemical Analysis of Flame Combustion Emissions by Secondary Ion Mass Spectrometry", *Rapid Communications in Mass Spectrometry*, 32, 1015–25. <https://doi.org/10.1002/rclm.8133>
- Irimie C., Faccinetto A., Mercier X., Ortega I. K., Nuns N., Therssen E., Desgroux P., Focsa C. (2019). "Unveiling Trends in Soot Nucleation and Growth: When Secondary Ion Mass Spectrometry Meets Statistical Analysis." *Carbon*, 144, 815–830. <https://doi.org/10.1016/j.carbon.2018.12.015>
- Kirchner U., Vogt R., Natzeck C., Goschnick J. (2003). "Single Particle MS, SNMS, SIMS, XPS, and FTIR Spectroscopic Analysis of Soot Particles during the AIDA Campaign", *Journal of Aerosol Science*, 34, 1323–46. [https://doi.org/10.1016/S0021-8502\(03\)00362-8](https://doi.org/10.1016/S0021-8502(03)00362-8).
- Lai J., Parry O., Mosbach S., Bhave A., Page V. (2018). "Evaluating Emissions in a Modern Compression Ignition Engine Using Multi-Dimensional PDF-Based Stochastic Simulations and Statistical Surrogate Generation", *SAE Technical Paper*, 2018-01-1739. <https://doi.org/10.4271/2018-01-1739>
- Lee K. F., Eaves N., Mosbach S., Ooi D., Lai J., Bhave A., Manz A., et al. (2019). "Model Guided Application for Investigating Particle Number (PN) Emissions in GDI Spark Ignition Engines." *SAE International*, 26, 1–13. <https://doi.org/10.4271/2019-26-0062>
- Li Y., Zhang L., Tian Z., Yuan T., Zhang K., Yang B., Qi F. (2009). "Investigation of the Rich Premixed Laminar Acetylene/Oxygen/Argon Flame: Comprehensive Flame Structure and Special Concerns of Polyyne", *Proceeding of the Combustion Institute*, 32, 1293–1300. <https://doi.org/10.1016/j.proci.2008.07.009>
- Manke A., Wang L., Rojanasakul Y. (2013). "Mechanisms of Nanoparticle-Induced Oxidative Stress and Toxicity", *BioMed Research International*, 2013, 1–15. <http://dx.doi.org/10.1155/2013/942916>
- Marple V. A. (2004). "History of Impactors—The First 110 Years", *Pakistan Textile Journal*, 38, 247–92. <https://doi.org/10.1080/02786820490424347>
- Marple V. A., Rubow K. L., Behm S. M. (1991). "A Microorifice Uniform Deposit Impactor (Moudi): Description, Calibration, and Use", *Aerosol Science and Technology*, 14, 434–36. <https://doi.org/10.1002/pssc.201600009>
- McLafferty F. W., Tureek F. (1993). "Interpretation of Mass Spectra", *University Science Books*, California.
- Michelsen H. A., Liu F., Kock B. F., Bladh H., Boiarciuc A., Charwath M., Dreier T., et al. (2007). "Modeling Laser-Induced Incandescence of Soot: A Summary and Comparison of LII Models", *Applied Physics B: Lasers and Optics*, 87, 503–21. <https://doi.org/10.1007/s00340-007-2619-5>
- Mihesan C., Ziskind M., Therssen E., Desgroux P., Focsa C. (2006). "IR Laser Resonant Desorption of Polycyclic Aromatic Hydrocarbons", *Chemical Physics Letters*, 423, 407–412. <https://doi.org/10.1016/j.cplett.2006.04.032>
- Mihesan C., Ziskind M., Therssen E., Desgroux P., Focsa C. (2008). "Parametric study of polycyclic aromatic hydrocarbon laser desorption", *Journal of Physics: Condensed Matter*, 20, 025221–9. <https://doi.org/10.1088/0953-8984/20/02/025221>

Moldanová J., Fridell E., Popovicheva O., Demirdjian B., Tishkova V., Faccinetto A., Focsa C., (2009). "Characterisation of particulate matter and gaseous emissions from a large ship diesel engine", *Atmospheric Environment*, 43, 2632-2641. <https://doi.org/10.1016/j.atmosenv.2009.02.008>

Oberdörster G. (1996). "Significance of Particle Parameters in the Evaluation of Exposure-Dose Relationships of Inhaled Particles", *Inhalation Toxicology*, 8, 73-90. <https://doi.org/10.1080/02726359608906690>

Pagels J., Dutcher D. D., Stolzenburg M. R., McMurry P. H., Gälli M. E., Gross D. S. (2013) "Fine-Particle Emissions from Solid Biofuel Combustion Studied with Single-Particle Mass Spectrometry: Identification of Markers for Organics, Soot, and Ash Components", *Journal of Geophysical Research Atmospheres*, 118, 859-70. <https://doi.org/10.1029/2012JD018389>

Patil N., Poul A., Patil A., Yerrawat R. N. (2014). "Literature Review on Effect of Oxygenated Additives on S.I. Engine Performance & Emissions", *International Journal of Engineering, Business and Enterprise Applications*, 10, 73-76. ISSN: 2279-0039.

Pei L., Jiang G., Tyler B. J., Baxter L. L., Linford M. R. (2008). "Time-of-Flight Secondary Ion Mass Spectrometry of a Range of Coal Samples: A Chemometrics (PCA, Cluster, and PLS) Analysis" *Energy and Fuels*, 22, 1059-72. <https://doi.org/10.1021/ef7003199>

Popovicheva O. B., Irimiea C., Carpentier Y., Ortega I. K., Kireeva E. D., Shonija N. K., Schwarz J., Vojtíšek-Lom M., Focsa C. (2017). "Chemical Composition of Diesel/Biodiesel Particulate Exhaust by FTIR Spectroscopy and Mass Spectrometry: Impact of Fuel and Driving Cycle", *Aerosol and Air Quality Research*, 17, 1717-34. <https://doi.org/10.4209/aaqr.2017.04.0127>

Price P., Stone R., Oudenijeweme D., Chen X. (2007). "Cold Start Particulate Emissions from a Second Generation DI Gasoline Engine", *SAE International*, 1931, 1738-52. <https://doi.org/10.4271/2007-01-1931>

Rencher A. (2000). "Methods of Multivariate Analysis", *Journal of Statistical Planning and Inference*, 59, 183-194. [https://doi.org/10.1016/S0378-3758\(96\)00098-5](https://doi.org/10.1016/S0378-3758(96)00098-5)

Sadezky A., Muckenhuber H., Grothe H., Niessner R., Pöschl U. (2005). "Raman Microspectroscopy of Soot and Related Carbonaceous Materials: Spectral Analysis and Structural Information", *Carbon* 43, 1731-42. <https://doi.org/10.1016/j.carbon.2005.02.018>

Sager T., Castranova V. (2009). "Surface Area of Particle Administered Versus Mass in Determining the Pulmonary Toxicity of Ultrafine and Fine Carbon Black: Comparison to Ultrafine Titanium Dioxide", *Particle and Fibre Toxicology*, 6, 1-15. <https://doi.org/10.1186/1743-8977-6-15>

Sakurai H., Tobias H. J., Park K., Zarling D., Docherty K. S., Kittelson D. B., McMurry P. H., Ziemann P. J. (2003). "On-Line Measurements of Diesel Nanoparticle Composition and Volatility", *Atmospheric Environment*, 37, 1199-1210. [https://doi.org/10.1016/S1352-2310\(02\)01017-8](https://doi.org/10.1016/S1352-2310(02)01017-8)

Schulz C., Kock B. F., Hofmann M., Michelsen H., Will S., Bougie B., Suntz R., Smallwood G. (2006). "Laser-Induced Incandescence: Recent Trends and Current Questions", *Applied Physics B: Lasers and Optics*, 83, 333-54. <https://doi.org/10.1007/s00340-006-2260-8>

Seaton A., Tran L., Aitken R., Donaldson K. (2009). "Safety of Nanomaterials Interdisciplinary Research Centre Nanoparticles, Human Health Hazard and Regulation". *Journal of the Royal Society Interface*, 7(supl_1), S119-S129, <https://doi.org/10.1098/rsif.2009.0252.focus>

Smallbone A., Bhave A., Coble A., Mosbach S., Kraft M., Morgan N., Kalghatgi G. (2011). "Simulating PM Emissions and Combustion Stability in Gasoline/Diesel Fuelled Engines", *SAE Technical Paper 2011-01-1184*. <https://doi.org/10.4271/2011-01-1184>

Thomson K., Ziskind M., Mihsan C., Therssen E., Desgroux P., Focsa C. (2007). "Influence of the Photoionization Process on the Fragmentation of Laser Desorbed Polycyclic Aromatic Hydrocarbons", *Applied Surface Science*, 253, 6435-41. <https://doi.org/10.1016/j.apsusc.2007.01.050>

Tobias H. J., Beving D. E., Ziemann P. J., Sakurai H., Zuk M., McMurry P.H., Zarling D., Waytulonis R., Kittelson D. B. (2001). "Chemical Analysis of Diesel Engine Nanoparticles Using a Nano-DMA/Thermal Desorption Particle Beam Mass Spectrometer", *Environmental Science and Technology*, 35, 2233–43. <https://doi.org/10.1021/es0016654>

Velji A., Yeom K., Wagner U., Spicher U., Roßbach M., Suntz R., Bockhorn H. (2009). "Investigations of the formation and oxidation of soot inside a direct injection spark ignition engine using advanced Laser-Techniques", *SAE Paper*, 2010-01-0352. <https://doi.org/10.4271/2010-01-0352>

Wang G., Kawamura K., Xie M., Hu S., Gao S., Cao J., An Z., Wang Z. (2009). "Size-Distributions of n-Alkanes, PAHs and Hopanes and Their Sources in the Urban, Mountain and Marine Atmospheres over East Asia", *Atmospheric Chemistry and Physics*, 9, 8869–82. <https://doi.org/10.5194/acp-9-8869-2009>

World Health Organization (WHO) (2013). "Health effects of particulate matter. Policy implications for countries in eastern Europe, Caucasus and central Asia", Copenhagen: WHO Regional Office for Europe

Zimmermann R., Blumenstock M., Heger H. J., Schramm K. W., Kettrup A. (2001). "Emission of Nonchlorinated and Chlorinated Aromatics in the Flue Gas of Incineration Plants during and after Transient Disturbances of Combustion Conditions: Delayed Emission Effects", *Environmental Science and Technology*, 35, 1019–30. <https://doi.org/10.1021/es0001431>

Supplementary information

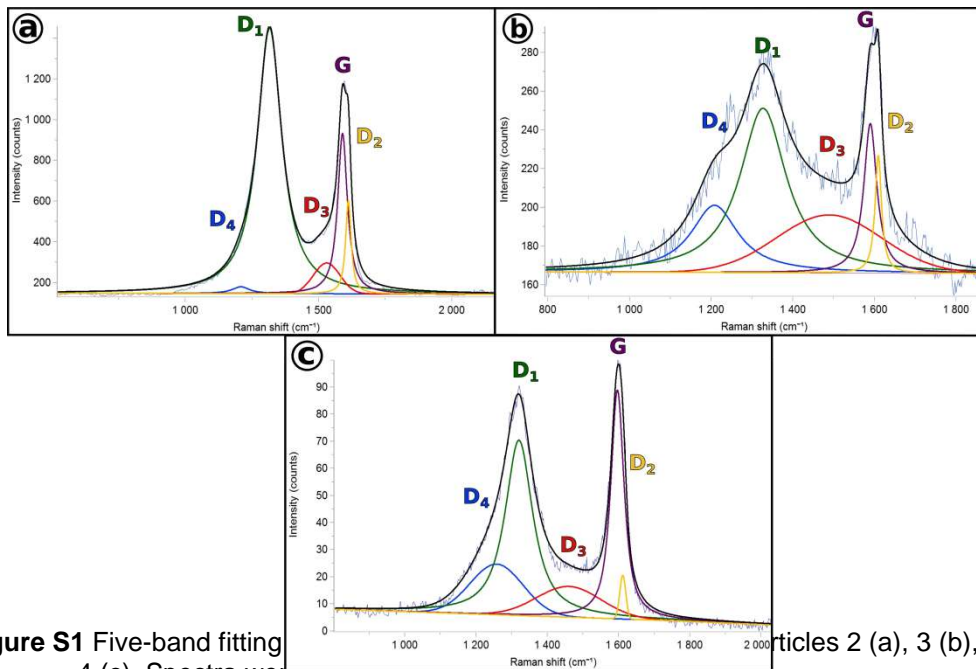


Figure S1 Five-band fitting of the TERS spectra for particles 2 (a), 3 (b), and 4 (c). Spectra were fitted using tools available in LabSpec 6.

Table S1 Deconvolution of the TERS spectra for particles 2, 3, and 4

Particle	Band	Position, cm^{-1}	Width, cm^{-1}
Particle 2	G	1589.7	43.4
	D1	1315.5	111.4
	D2	1611.5	24.7
	D3	1530.7	117.8
	D4	1208.0	80.4
Particle 3	G	1589.4	38.5
	D1	1326.8	137.1
	D2	1608.5	19.0
	D3	1489.0	304.1
	D4	1208.0	140.0
Particle 4	G	1596.6	44.6
	D1	1320.2	92.8
	D2	1611.7	20.1
	D3	1460.6	213.9
	D4	1257.8	175.1

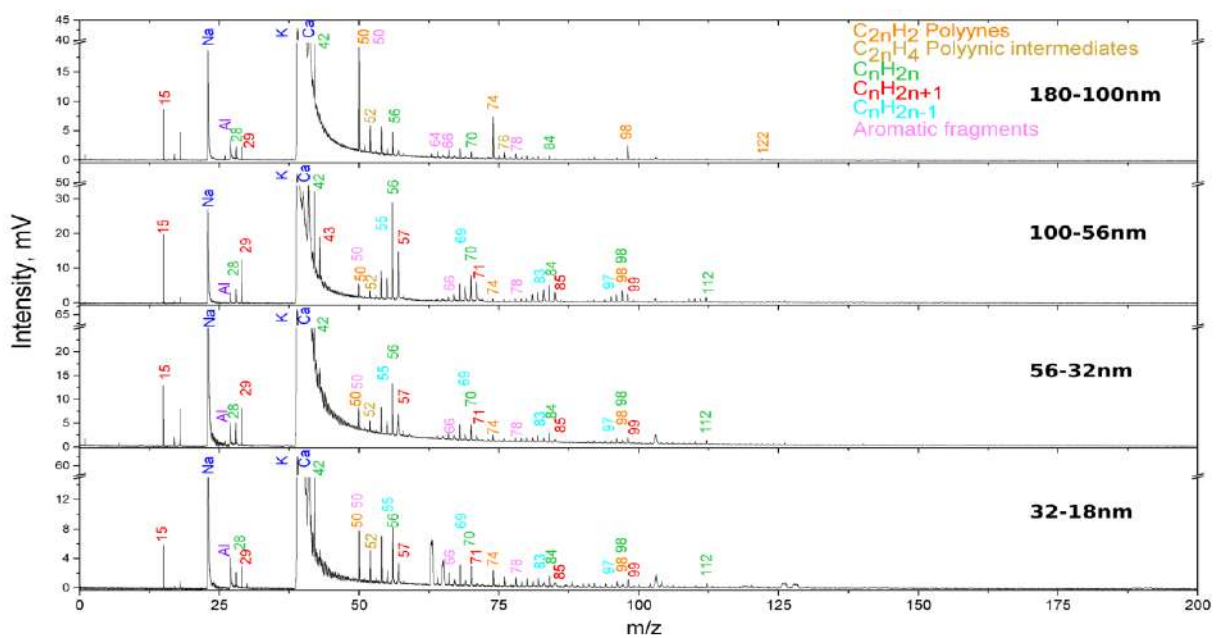


Figure S2 Mass spectra of the four samples (particle size 180-18nm) obtained in the **OM** engine conditions. The analyses were performed with the ionization wavelength $\lambda_i=118\text{nm}$ for its high sensitivity toward aliphatic compounds.

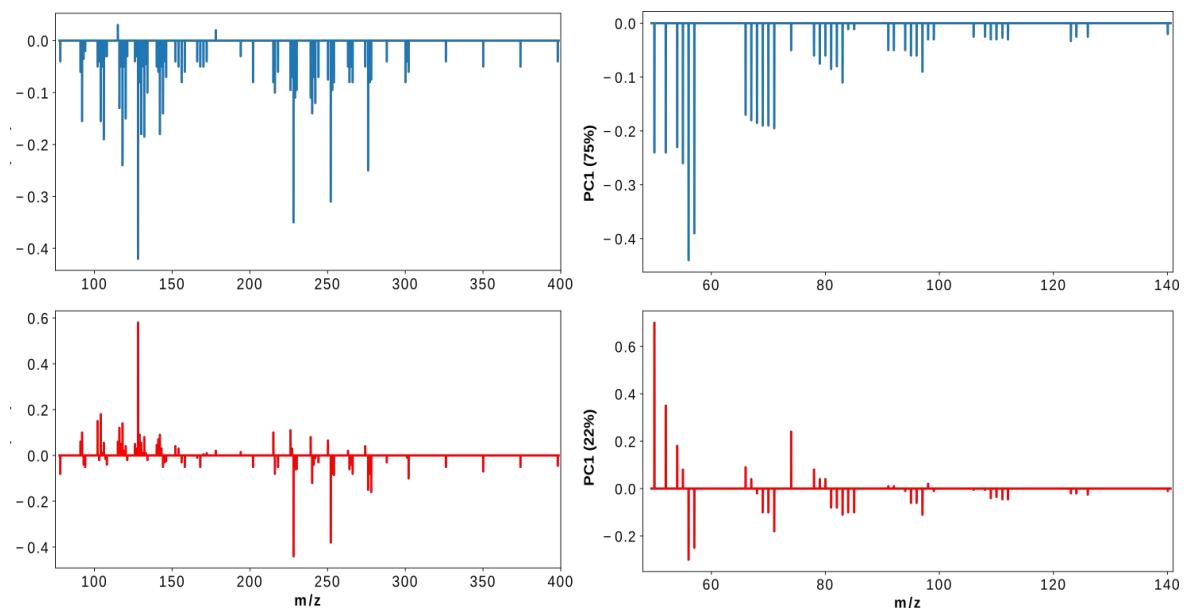


Figure S3 Contribution of different masses to PC1 and PC2 for the **OM** engine regime. Left panel - ionization at 266 nm, right panel - 118 nm.

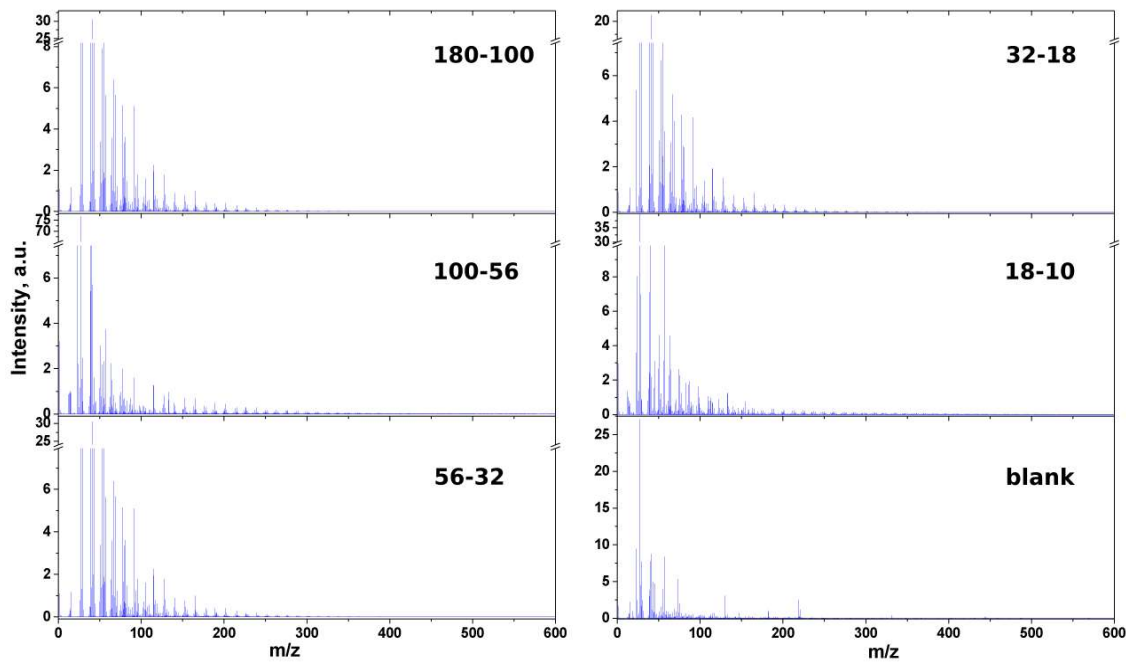


Figure S4 Positive polarity SIMS spectra of samples obtained in the **EM** engine regime (low air/fuel ratio) and a blank aluminum foil.

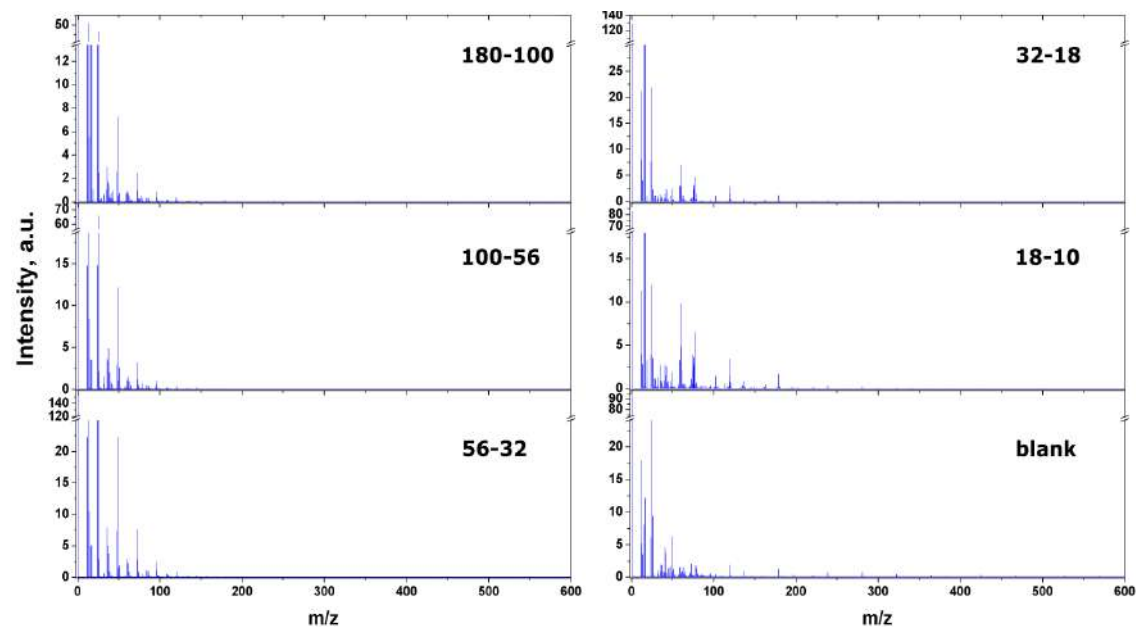


Figure S5 Negative polarity SIMS spectra of samples obtained in the **EM** engine regime (low air/fuel ratio) and a blank aluminum foil.

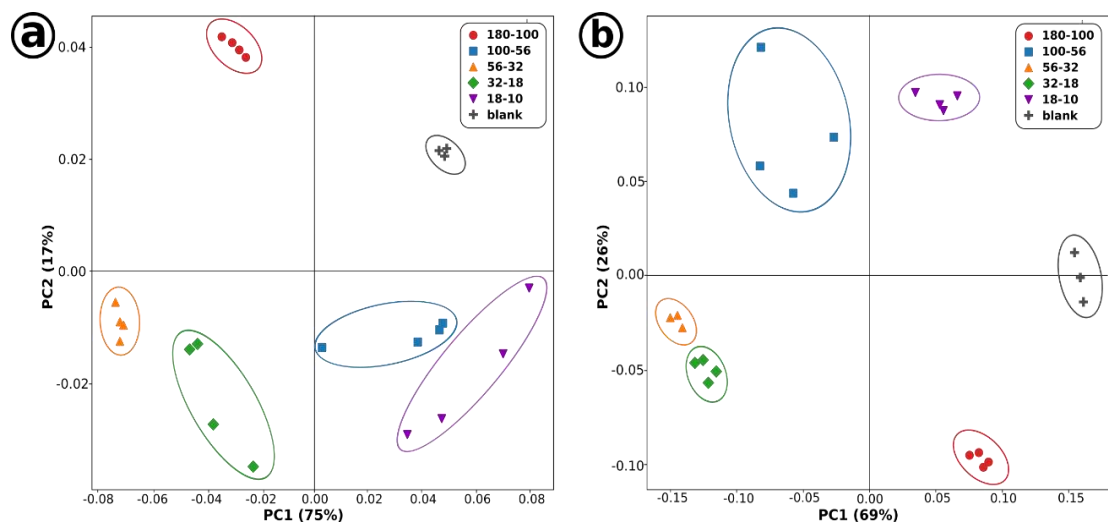
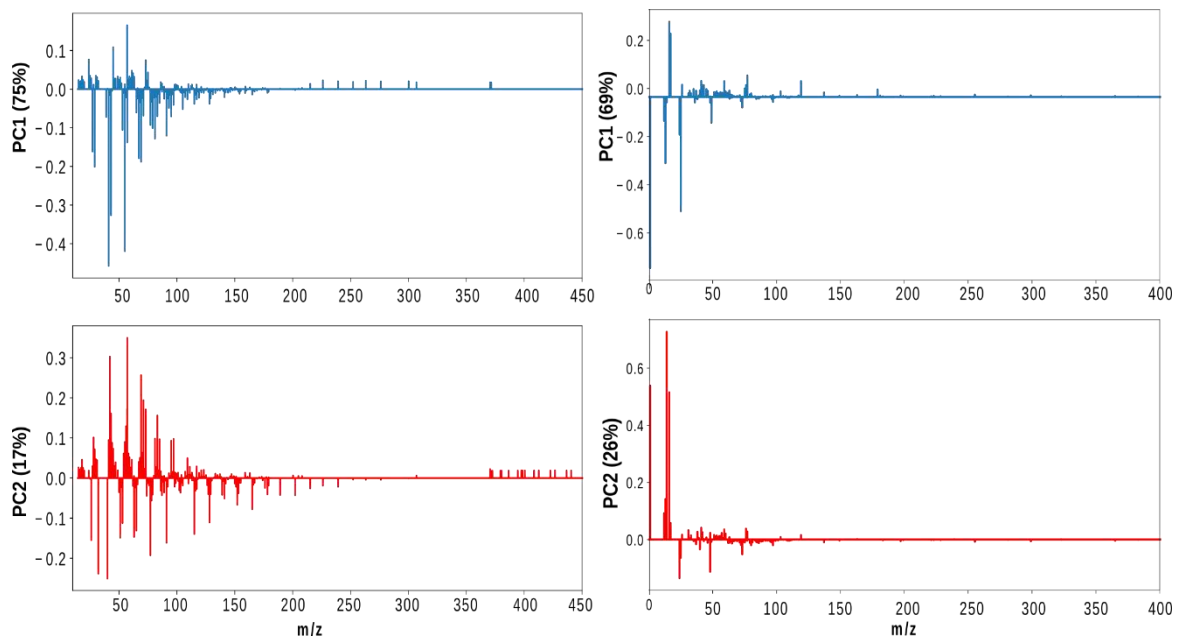


Figure S6 Size discrimination of collected particles obtained in the **EM** (low air/fuel ratio) engine regime based on the positive (a) and negative (b) SIMS spectra.

Figure S7 Contribution of different masses to PC1 and PC2 for the **EM** engine regime. Left panel - positive SIMS polarity, right panel - negative SIMS polarity.



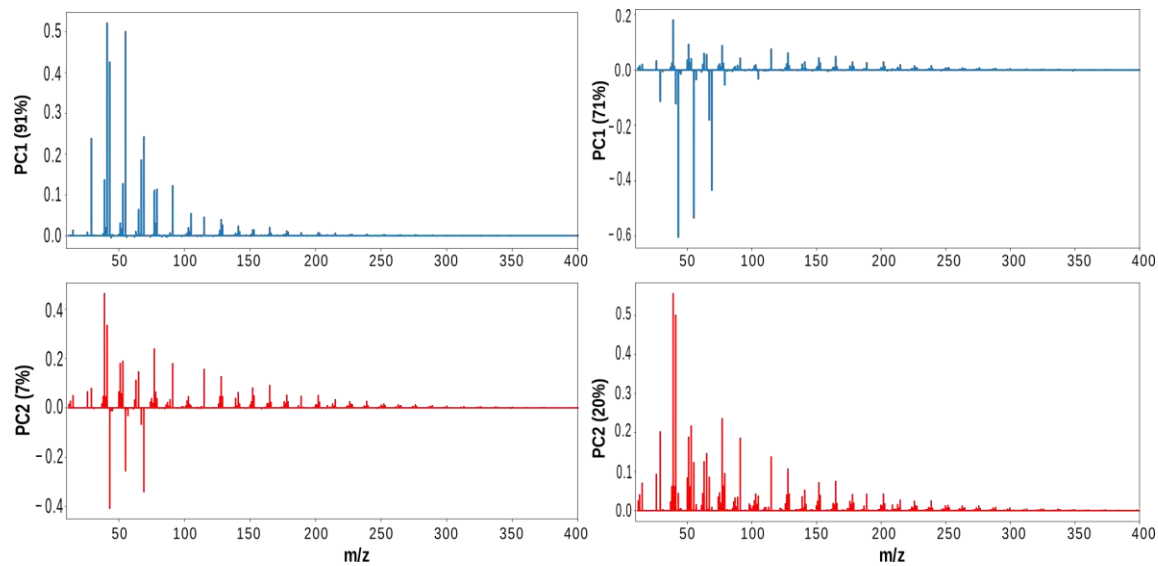


Figure S8 Contribution of different masses to PC1 and PC2 when discriminating between different engine regimes (left panel) and main sources of particles (right panel).

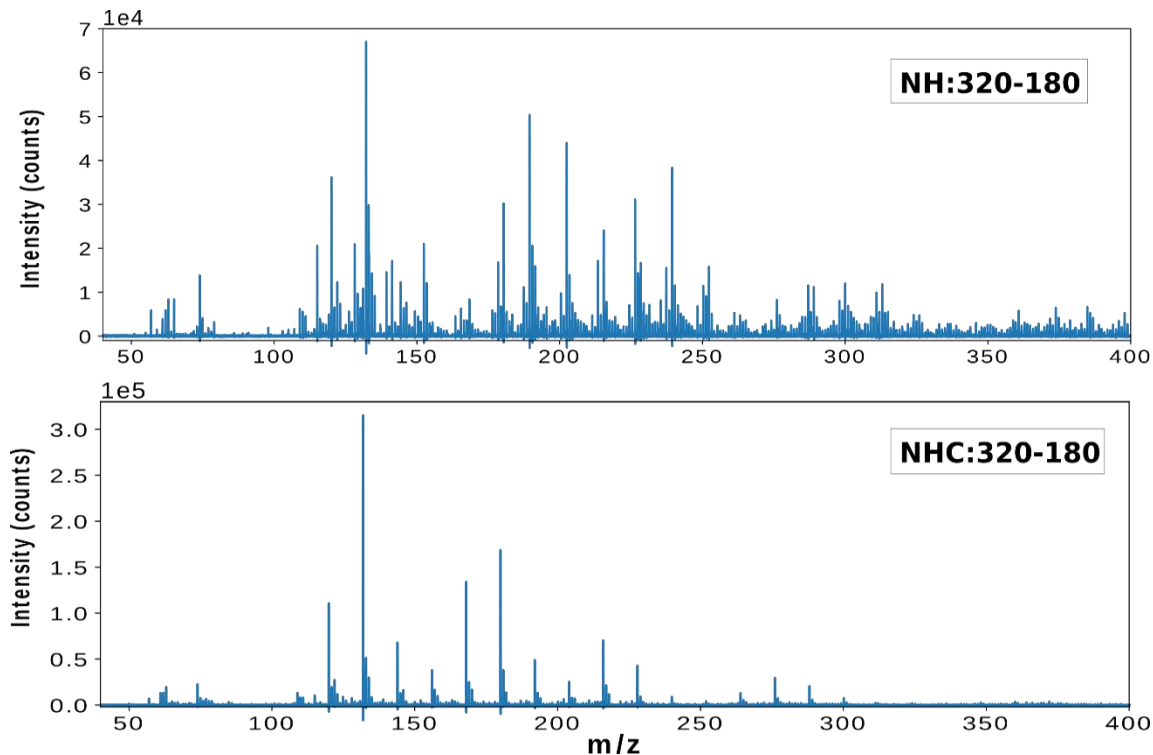


Figure S9 Comparison between mass spectra of collected particles (320-180nm) sampled without (upper panel) and with the catalytic stripper (lower panel). Mass spectra of particles in other size bins show a similar picture.

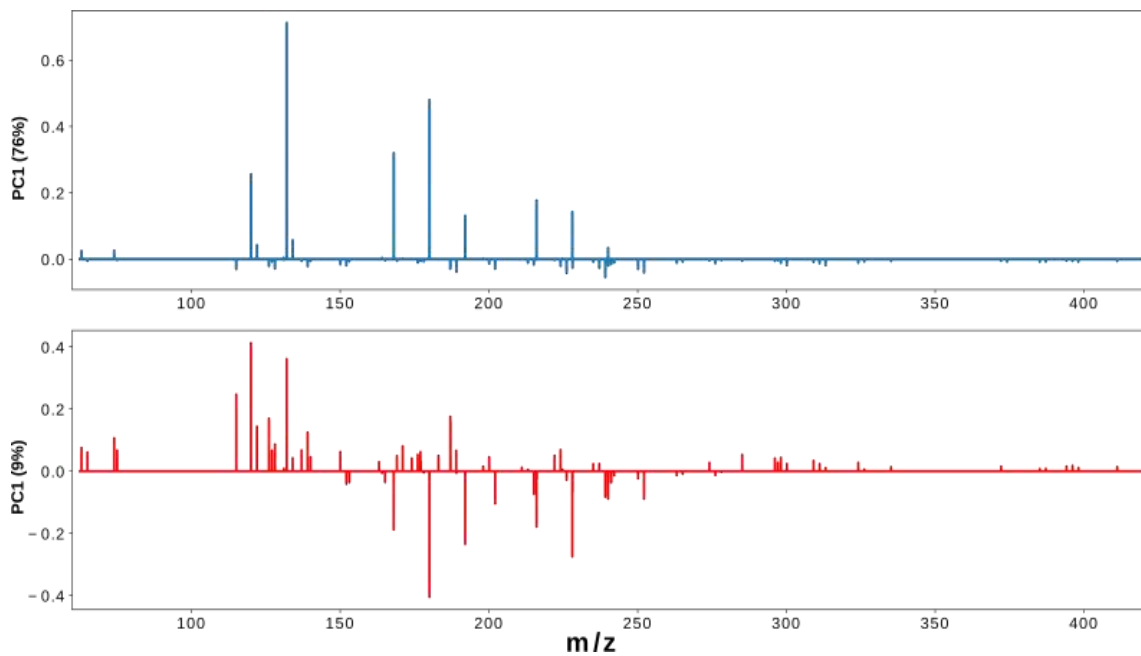


Figure S10 Loading plot for the first and second principal components allowing the separation

Table S2 List of molecular and atomic species detected by L2MS with different ionization wavelengths. Accuracy better than 20 ppm for all assigned species. Only peaks with a relatively high signal are shown.

m/z	Formula	m/z	Formula	m/z	Formula	m/z	Formula	m/z	Formula
266 nm ionization									
22.99	Na^+	120	C_{10}^+	154.078	$C_{12}H_{10}^+$	204	C_{17}^+	276.094	$C_{22}H_{12}^+$
26.982	Al^+	120.094	$C_9H_{12}^+$	156.094	$C_{12}H_{12}^+$	216.094	$C_{17}H_{12}^+$	278.11	$C_{22}H_{14}^+$
38.964	K^+	128.063	$C_{10}H_8^+$	158.11	$C_{12}H_{14}^+$	218.11	$C_{17}H_{14}^+$	300.094	$C_{24}H_{12}^+$
39.963	Ca^+	130.078	$C_{10}H_{10}^+$	166.078	$C_{13}H_{10}^+$	226.078	$C_{18}H_{10}^+$	302.11	$C_{24}H_{14}^+$
69.958	Al_2O^+	132	C_{11}^+	178.078	$C_{14}H_{10}^+$	228	C_{19}^+	326.11	$C_{26}H_{14}^+$
78.047	$C_6H_6^+$	132.094	$C_{10}H_{12}^+$	168.094	$C_{13}H_{12}^+$	228.094	$C_{18}H_{12}^+$	350.11	$C_{28}H_{14}^+$
92.063	$C_7H_8^+$	134.11	$C_{10}H_{14}^+$	168	C_{14}^+	240	C_{20}^+	374.11	$C_{30}H_{14}^+$
101.948	$Al_2O_3^+$	142.078	$C_{11}H_{10}^+$	170.11	$C_{13}H_{14}^+$	240.094	$C_{19}H_{12}^+$	398.11	$C_{32}H_{14}^+$
104.063	$C_8H_8^+$	144	C_{12}^+	178.078	$C_{14}H_{10}^+$	242.11	$C_{19}H_{14}^+$		
106.078	$C_8H_{10}^+$	144.094	$C_{11}H_{12}^+$	180	C_{15}^+	252.094	$C_{20}H_{12}^+$		
116.063	$C_9H_8^+$	146.11	$C_{11}H_{14}^+$	192	C_{16}^+	264.094	$C_{21}H_{12}^+$		
118.078	$C_9H_{10}^+$	152.063	$C_{12}H_8^+$	202.078	$C_{16}H_{10}^+$	266.11	$C_{21}H_{14}^+$		
118 nm ionization									
15.023	CH_3^+	52.031	$C_4H_4^+$	70.078	$C_5H_{10}^+$	84.094	$C_6H_{12}^+$	108.094	$C_8H_{12}^+$
22.99	Na^+	54.034	$C_2H_4CN^+$	71.086	$C_5H_{11}^+$	85.102	$C_6H_{13}^+$	110.11	$C_8H_{14}^+$
26.982	Al^+	55.047	$C_4H_7^+$	74.016	$C_6H_2^+$	95.086	$C_7H_{11}^+$	112.125	$C_8H_{16}^+$
28.031	$C_2H_4^+$	56.063	$C_4H_8^+$	76.031	$C_6H_4^+$	96.094	$C_7H_{12}^+$	122.016	$C_{10}H_2^+$
29.039	$C_2H_5^+$	57.07	$C_4H_9^+$	78.047	$C_6H_6^+$	97.102	$C_7H_{13}^+$	124.031	$C_{10}H_4^+$
38.964	K^+	66.047	$C_5H_6^+$	79.055	$C_6H_7^+$	98.016	$C_8H_2^+$	126.047	$C_{10}H_6^+$
39.963	Ca^+	67.055	$C_5H_7^+$	80.063	$C_6H_8^+$	98.11	$C_7H_{14}^+$	140.063	$C_{11}H_8^+$
42.047	$C_3H_6^+$	68.06	$C_3H_6CN^+$	82.078	$C_6H_{10}^+$	99.117	$C_7H_{15}^+$		
50.016	$C_4H_2^+$	69.07	$C_5H_9^+$	83.086	$C_6H_{11}^+$	106.078	$C_8H_{10}^+$		

Table S3 List of molecular and atomic species detected with SIMS in positive and negative polarity. Accuracy better than 20 ppm for all assigned species. Peaks associated with the substrate not shown.

m/z	Formula	m/z	Formula	m/z	Formula	m/z	Formula	m/z	Formula
Positive polarity									
12	C^+	77.039	$C_6H_5^+$	158.016	$C_{13}H_2^+$	287.086	$C_{23}H_{11}^+$	396.094	$C_{32}H_{12}^+$
13.008	CH^+	78.047	$C_6H_6^+$	163.055	$C_{13}H_7^+$	289.102	$C_{23}H_{13}^+$	398.11	$C_{32}H_{14}^+$
14.016	CH_2^+	79.055	$C_6H_7^+$	164.063	$C_{13}H_8^+$	290.11	$C_{23}H_{14}^+$	399.117	$C_{32}H_{15}^+$
15.023	CH_3^+	80.063	$C_6H_8^+$	165.07	$C_{13}H_9^+$	296.026	$C_{23}H_4O^+$	400.125	$C_{32}H_{16}^+$
24	C_2^+	81.07	$C_6H_9^+$	166.078	$C_{13}H_{10}^+$	298.053	$C_{22}H_6N_2^+$	401.133	$C_{32}H_{17}^+$
26.016	$C_2H_2^+$	82.066	$C_5H_8N^+$	170.016	$C_{14}H_2^+$	300.094	$C_{24}H_{12}^+$	407.086	$C_{33}H_{11}^+$
27.023	$C_2H_3^+$	83.037	$C_4H_5NO^+$	174.047	$C_{14}H_6^+$	301.102	$C_{24}H_{13}^+$	409.102	$C_{33}H_{13}^+$
28.031	$C_2H_4^+$	85.008	C_7H^+	176.063	$C_{14}H_8^+$	302.11	$C_{24}H_{14}^+$	411.117	$C_{33}H_{15}^+$
29.039	$C_2H_5^+$	86.016	$C_7H_2^+$	178.078	$C_{14}H_{10}^+$	303.117	$C_{24}H_{15}^+$	412.125	$C_{33}H_{16}^+$
31.018	CH_3O^+	87.023	$C_7H_3^+$	179.086	$C_{14}H_{11}^+$	309.033	$C_{22}H_3N_3^+$	413.133	$C_{33}H_{17}^+$
36	C_3^+	88.031	$C_7H_4^+$	184.035	$C_{12}H_8S^+$	311.086	$C_{25}H_{11}^+$	420.094	$C_{34}H_{12}^+$
37.008	C_3H^+	89.039	$C_7H_5^+$	187.055	$C_{15}H_7^+$	313.102	$C_{25}H_{13}^+$	422.11	$C_{34}H_{14}^+$
38.016	$C_3H_2^+$	91.055	$C_7H_7^+$	189.07	$C_{15}H_9^+$	314.11	$C_{25}H_{14}^+$	423.117	$C_{34}H_{15}^+$
39.023	$C_3H_3^+$	92.063	$C_7H_8^+$	200.063	$C_{16}H_8^+$	315.117	$C_{25}H_{15}^+$	424.125	$C_{34}H_{16}^+$
40.031	$C_3H_4^+$	93.07	$C_7H_9^+$	202.078	$C_{16}H_{10}^+$	322.078	$C_{26}H_{10}^+$	425.133	$C_{34}H_{17}^+$
41.039	$C_3H_5^+$	98.016	$C_8H_2^+$	203.086	$C_{16}H_{11}^+$	324.094	$C_{26}H_{12}^+$	431.086	$C_{35}H_{11}^+$
43.018	$C_2H_3O^+$	99.023	$C_8H_3^+$	211.055	$C_{17}H_7^+$	325.102	$C_{26}H_{13}^+$	433.102	$C_{35}H_{13}^+$
43.055	$C_3H_7^+$	100.031	$C_8H_4^+$	213.07	$C_{17}H_9^+$	326.11	$C_{26}H_{14}^+$	435.117	$C_{35}H_{15}^+$
49.008	C_4H^+	100.987	$C_3HO_4^+$	215.086	$C_{17}H_{11}^+$	327.117	$C_{26}H_{15}^+$	436.125	$C_{35}H_{16}^+$
50.016	$C_4H_2^+$	101.039	$C_8H_5^+$	216.094	$C_{17}H_{12}^+$	333.07	$C_{27}H_9^+$	437.133	$C_{35}H_{17}^+$
51.023	$C_4H_3^+$	102.047	$C_8H_6^+$	224.063	$C_{18}H_8^+$	335.086	$C_{27}H_{11}^+$	444.094	$C_{36}H_{12}^+$
52.031	$C_4H_4^+$	103.055	$C_8H_7^+$	226.078	$C_{18}H_{10}^+$	337.102	$C_{27}H_{13}^+$	446.11	$C_{36}H_{14}^+$
53.039	$C_4H_5^+$	105.07	$C_8H_9^+$	227.086	$C_{18}H_{11}^+$	338.11	$C_{27}H_{14}^+$	448.125	$C_{36}H_{16}^+$
55.018	$C_3H_3O^+$	109.008	C_9H^+	228.094	$C_{18}H_{12}^+$	339.117	$C_{27}H_{15}^+$	449.133	$C_{36}H_{17}^+$
57.034	$C_3H_5O^+$	110.019	$C_6H_6S^+$	229.102	$C_{18}H_{13}^+$	346.078	$C_{28}H_{10}^+$	450.141	$C_{36}H_{18}^+$
57.07	$C_4H_9^+$	111.023	$C_9H_3^+$	237.07	$C_{19}H_9^+$	348.094	$C_{28}H_{12}^+$	457.102	$C_{37}H_{13}^+$
58.066	$C_3H_8N^+$	113.039	$C_9H_5^+$	239.086	$C_{19}H_{11}^+$	350.11	$C_{28}H_{14}^+$	459.117	$C_{37}H_{15}^+$
59.05	$C_3H_7O^+$	115.055	$C_9H_7^+$	240.094	$C_{19}H_{12}^+$	351.117	$C_{28}H_{15}^+$	461.133	$C_{37}H_{17}^+$
60.021	$C_2H_4O_2^+$	120.974	$C_5H_5Fe^+$	248.063	$C_{20}H_8^+$	352.125	$C_{28}H_{16}^+$	468.094	$C_{38}H_{12}^+$
61.008	C_5H^+	122.016	$C_{10}H_2^+$	250.078	$C_{20}H_{10}^+$	357.07	$C_{29}H_9^+$	470.11	$C_{38}H_{14}^+$
62.016	$C_5H_2^+$	123.023	$C_{10}H_3^+$	251.086	$C_{20}H_{11}^+$	359.086	$C_{29}H_{11}^+$	472.125	$C_{38}H_{16}^+$
63.023	$C_5H_3^+$	126.047	$C_{10}H_6^+$	252.094	$C_{20}H_{12}^+$	361.102	$C_{29}H_{13}^+$	473.133	$C_{38}H_{17}^+$
64.031	$C_5H_4^+$	127.055	$C_{10}H_7^+$	253.102	$C_{20}H_{13}^+$	363.117	$C_{29}H_{15}^+$	474.141	$C_{38}H_{18}^+$
65.039	$C_5H_5^+$	128.063	$C_{10}H_8^+$	261.07	$C_{21}H_9^+$	370.078	$C_{30}H_{10}^+$	481.102	$C_{39}H_{13}^+$
66.047	$C_5H_6^+$	139.055	$C_{11}H_7^+$	263.086	$C_{21}H_{11}^+$	372.094	$C_{30}H_{12}^+$	483.117	$C_{39}H_{15}^+$
67.055	$C_5H_7^+$	141.07	$C_{11}H_9^+$	264.094	$C_{21}H_{12}^+$	374.11	$C_{30}H_{14}^+$	485.133	$C_{39}H_{17}^+$
69.07	$C_5H_9^+$	142.078	$C_{11}H_{10}^+$	265.102	$C_{21}H_{13}^+$	375.117	$C_{30}H_{15}^+$	487.149	$C_{39}H_{19}^+$
70.066	$C_4H_8N^+$	146.016	$C_{12}H_2^+$	44.026	$C_2H_4O^+$	376.125	$C_{30}H_{16}^+$	494.11	$C_{40}H_{14}^+$
73.053	$C_3H_7NO^+$	150.047	$C_{12}H_6^+$	274.078	$C_{22}H_{10}^+$	377.133	$C_{30}H_{17}^+$	496.125	$C_{40}H_{16}^+$
74.016	$C_6H_2^+$	151.055	$C_{12}H_7^+$	276.094	$C_{22}H_{12}^+$	383.086	$C_{31}H_{11}^+$	498.141	$C_{40}H_{18}^+$
75.023	$C_6H_3^+$	152.063	$C_{12}H_8^+$	277.102	$C_{22}H_{13}^+$	385.102	$C_{31}H_{13}^+$		
76.031	$C_6H_4^+$	153.07	$C_{12}H_9^+$	278.11	$C_{22}H_{14}^+$	387.117	$C_{31}H_{15}^+$		
76.987	CHO_4^+	155.086	$C_{12}H_{11}^+$	285.043	$C_{18}H_7NO_3^+$	388.125	$C_{31}H_{16}^+$		
Negative polarity									
12	C^-	44.998	CHO_2^-	78.959	PO_3^-	110.016	$C_9H_2^-$	168	C_{14}^-
13.008	CH^-	45.993	NO_2^-	79.957	SO_3^-	118.941	$NaSO_4^-$	169.008	$C_{14}H^-$
15.995	O^-	48	C_4^-	80.965	HSO_3^-	120	C_{10}^-	170.016	$C_{14}H_2^-$
17.003	OH^-	49.008	C_4H^-	84	C_7^-	121.008	$C_{10}H^-$	180	C_{15}^-
24	C_2^-	50.003	C_3N^-	85.008	C_7H^-	122.016	$C_{10}H_2^-$	181.008	$C_{15}H^-$
25.008	C_2H^-	55.018	$C_3H_3O^-$	86.016	$C_7H_2^-$	132	C_{11}^-	182.016	$C_{15}H_2^-$
26.003	CN^-	56.026	$C_3H_4O^-$	94.953	PO_4^-	134.016	$C_{11}H_2^-$	193.008	$C_{16}H^-$
31.018	CH_3O^-	57.034	$C_3H_5O^-$	95.952	SO_4^-	135.023	$C_{11}H_3^-$	204	C_{17}^-
31.972	S^-	60	C_5^-	96	C_8^-	144	C_{12}^-	205.008	$C_{17}H^-$
36	C_3^-	61.008	C_5H^-	96.96	HSO_4^-	145.008	$C_{12}H^-$	206.016	$C_{17}H^-$
37.008	C_3H^-	61.988	NO_3^-	97.008	C_8H^-	146.016	$C_{12}H_2^-$	217.008	$C_{18}H^-$
38.016	$C_3H_2^-$	62.016	$C_5H_2^-$	98.016	$C_8H_2^-$	156	C_{13}^-		
40.019	$C_2H_2N^-$	62.996	HNO_3^-	99.023	$C_8H_3^-$	157.008	$C_{13}H^-$		

41.003	C_2HO^-	72	C_6^-	108	C_9^-	158.016	$C_{13}H_2^-$
42.011	$C_2H_2O^-$	73.008	C_6H^-	109.008	C_9H^-	159.023	$C_{13}H_3^-$

2.9.2 Particle Reduced, Efficient Gasoline Engines: A Second Year Report on the PaREGEN Project

Simon Edwards^{1}, Jeremy Gidney², Normann Freisinger³, Niall Turner⁴, Antonio Perez⁵ and Cor van der Zweep⁶*

¹Ricardo GmbH, Schwäbisch Gmünd, Germany. Contact: Simon.Edwards@Ricardo.com

²JohnsonMatthey, UK

³Daimler, Germany

⁴Jaguar Land Rover, UK

⁵IDIADA, Spain

⁶Uniresearch, Netherlands

Abstract

The PaREGEN project (supported by EC Grant No. 723954) is addressing the research and innovation topic GV-02-2016, “Technologies for low emission light duty powertrains”, under the European Horizon 2020 framework programme. This project works on the short-term aspects of that call, through the further development of gasoline engines used in mid to premium sized passenger cars. The innovations therein are planned to be realized during the first part of the critical transition period (2020-2030) for transport that is the focus of this conference. Hence, the vehicles that use the results of the project’s research will be in operation up to and beyond the coming decade. The project is being realized by a seventeen-partner consortium representing all parts of the European Automotive Industry. At the point of the TAP2019 results will be presented relating to the first two years of project progress.

Introduction

Growing road traffic in Europe results in detrimental effects on the environment and public health, to a level that is becoming unsustainable, despite increasingly stringent emission standards. In particular, carbon dioxide (CO₂) and noxious emissions may not be sufficiently reduced in real driving, whilst some engine technologies may have led to increases in the emissions of nanoparticles that are undetected by current certification procedures. The challenge is to develop a new generation of engine technologies that is truly and significantly more fuel efficient than the best 2015 equivalent under real driving conditions, and to demonstrate pollutant emissions levels compliant with the Euro 6 real driving emissions (RDE) limits and particle number emissions measured to a 10nm size threshold.

Globally, the gasoline engine remains the dominant passenger car prime mover, with more than 80% of light-duty vehicles using these engines (International Energy Agency (2012)). A comparison of the vehicles shows approximately 10% higher CO₂ emissions for those with gasoline engines compared to diesel fuelled vehicles. Improvements in gasoline engines have an intrinsically greater potential to lower the CO₂ emissions than improvements with diesel engines: there are many more gasoline engines and the potential for improvement for gasoline engines is larger than for diesel engines. Furthermore, those vehicle classes with the higher annual mileages, namely D and E class vehicles, are often those with higher CO₂ emissions. The challenge for the automotive industry is, therefore, to develop highly fuel efficient (gasoline) engines and to improve exhaust gas aftertreatment systems, in order to meet (forthcoming) EU legislation on emission standards and fuel economy under real driving conditions. At the same time, the European automotive industry has to improve competitiveness in order to successfully maintain substantial market volumes of high-quality cars with attractive designs, driving characteristics and fuel economy.

In PaREGEN, further development of gasoline engines used in mid to premium sized passenger cars is being made. With the electrification of powertrains in smaller vehicles, suitable for zero emissions in urban environments, addressing mid to premium sized cars is especially important: the requirement for ultra-low emission, efficient and economic engines for cars regularly used for inter-urban and regional transport becomes more urgent as well as more effective to address the societal challenges of air quality, energy efficiency (decarbonization) and cost-effective mobility.

Through the use of state of the art development techniques, like optical single cylinder engines, a range of modelling and simulation tools from 0D to 3D (for understanding of in-cylinder particle formation process) and the application of novel engine componentry (next generation fuel or water injection and ignition equipment, boosting systems and exhaust gas aftertreatment technology), the optimal trade-offs between ultra-low emissions and efficiency are being identified. Of special attention throughout this

process is the contribution of such technologies to the reduction and control of particle numbers, including those particles between 10 and 23 nm in size.

This learning is being used for the generation of two demonstration vehicles. The two approaches to achieving the efficiency targets are different in each, using different combustion system, injection (fuel and water), ignition and diluent technologies, different engine air handling systems and different aftertreatment packages. As such, progress within the project is giving insight into the best way forward to meet the requirements for these gasoline engines in all vehicle classes in the coming decade.

The project PaREGEN has committed to show a 15% CO₂ reduction along with real driving emissions targets. If successful and adopted across all light vehicle classes, these short-term gasoline engine developments have been projected to reduce the European vehicle parc CO₂ emissions by about 2.0 Mtonnes CO₂ in 2025 and up to 10 Mtonnes CO₂ together with around a 10% reduction in PN >10 nm in 2030. In addition, one of the most valuable contributions from this project will be that the new modelling and simulation tools benefit engine design, development and control in general long after the project is completed.

Project Objectives

The specific objectives of the work being conducted within the PaREGEN project can be stated briefly as:

- 1: Establish the solid basis for model-supported engine design and control, based on an in-depth understanding of the Cause and Effect Relationship (CER) of particle formation during the in-cylinder processes;
- 2: Realise robust aftertreatment technology for high performance gasoline engines, which comply with the upcoming Euro 6(c) RDE emission standard;
- 3: Realise the optimal combination of advanced engine componentry for stoichiometric and lean burn gasoline engines by validation on engine test rigs;
- 4: Realise two demonstration vehicles by integrating the advancements in gasoline direct injection engines, aftertreatment systems and control systems;
- 5: Verification of the targeted achievements by independent testing of the demonstrator vehicles.

Further details relating to these objectives have been given previously (Edwards et al. 2018).

Project Approach

The overall concept, approach and project delineation of the PaREGEN project have also been shown previously (Edwards et al. 2018). Briefly, the overall concept comprises three major elements:

- An element of research for improved understanding: to acquire in-depth knowledge of the relationships between combustion processes, engine design aspects, engine operation, emissions (including CO₂) and particle control over the engine operation map; and to include this understanding in new models, simulation tools and control strategies for future application in engine development and calibration processes;
- An element of innovation and demonstration, where the developed know-how, software and control strategies are integrated and implemented in two novel optimised gasoline engines together with new engine components; both engines using high compression ratio, the Miller Cycle and highly

- diluted combustion, but different in dilution methods: water injection with stoichiometric or dry with lean (homogeneous or stratified) combustion;
- An independent assessment of the technologies' impact through tracking the progress of the project in reaching the targets and to assess the impact in terms of societal goals: CO₂ reduction (potential) and air quality improvement.

Each element interacts with the others, to ensure that the knowledge gained and technology improvements made can be applied to series production road vehicles in the short-term.

The project is divided into two different types of activity: 'horizontal' and 'vertical'. The 'horizontal' type (Work Packages (WP) 1, 2, 5, 6 and 7) relates to generic and collaborative activities that are key to realising synergies through the project and achieving the goals of research, evaluation and dissemination. The 'vertical' type relates to specific component and demonstrator vehicle development plus validation activities: these are discrete in their nature (WPs 3 and 4). All WPs are led by industry partners. The project WPs, the leader and collaborating partners in each and the tasks planned within each WP, plus the full list of the project consortium membership can be found under www.paregen.eu.

Results Achieved to Date

Work Package 1 (Advanced Combustion Technologies).

The overall aim of this WP is to determine the optimal combination of measurement technologies and simulation methods for understanding the CER of particle emissions, with a focus on a model supported design and calibration approach to get closer to the optimal combination of engine and robust aftertreatment technologies. This is represented pictorially in Figure 1.

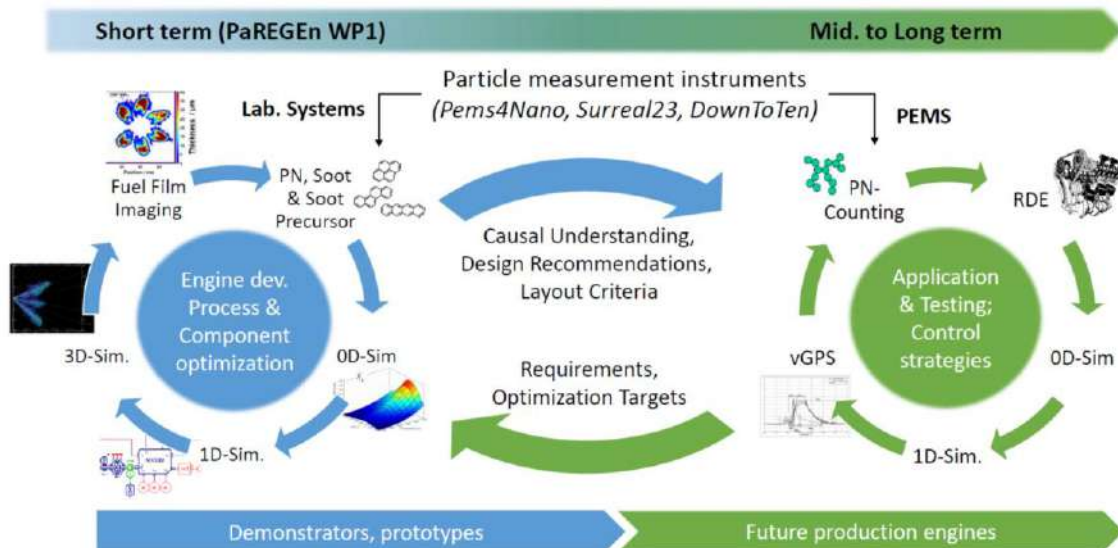


Figure 1: A representation of the activities in WP1, their possible links with other Horizon 2020 projects and potential future application in vehicle powertrain development

The overall hypothesis is that fuel films within the cylinder can be related to subsequent particle emissions. Therefore, optical engine measurements, looking at the fuel film thickness on the piston surface have been made and the effects of the injection pressure on the distribution of the film thickness on the piston surface have been assessed (see Figure 2). These measurements were enabled by advances in calibration of the LIF methods, considering the photo-physical properties of the fuel tracers in the liquid phase (see Geiler et al. (2017) and (2018)). Further, a two colour LIF was developed to give film thickness and temperature simultaneously, providing important comparative data for 3D CFD simulation validation.

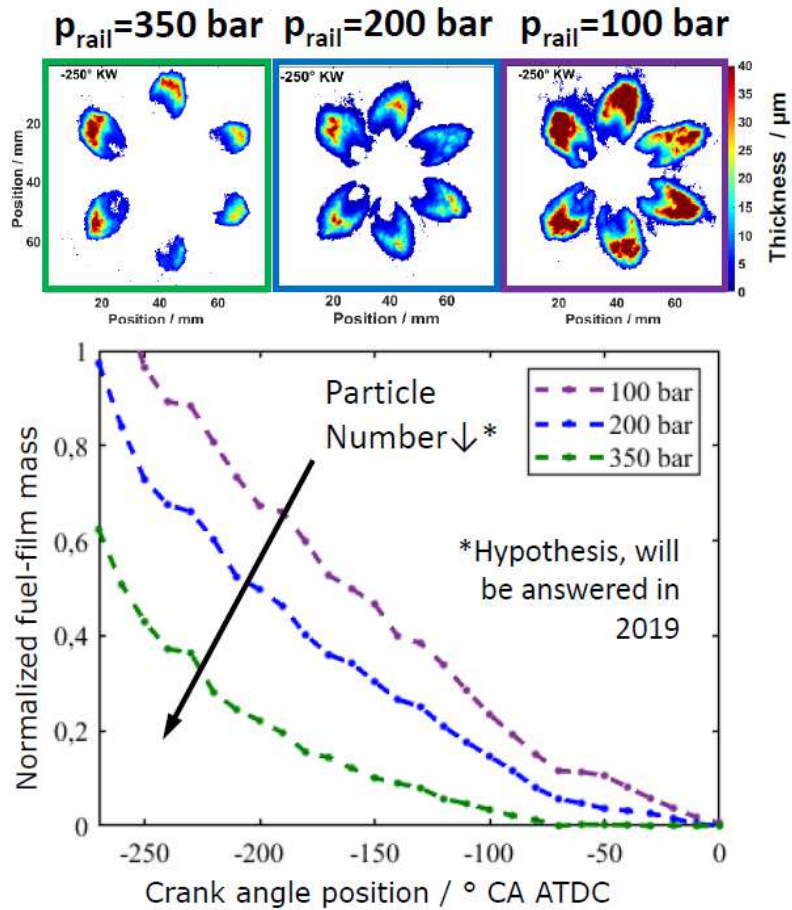


Figure 2: Fuel film thickness measured on the piston crown at a given crank angle for three different injection pressures (top image) and the temporal variation in the fuel mass therein (lower image)

Further, validation data for CFD simulation has been obtained using an optical combusting flow bench together with LII and LIF techniques (see Edwards (2018) for the general arrangement). This has enabled the temporal and spatial variations between different PAH and subsequent soot particle amounts to be determined and linked to the fuel film properties (see Figure 3).

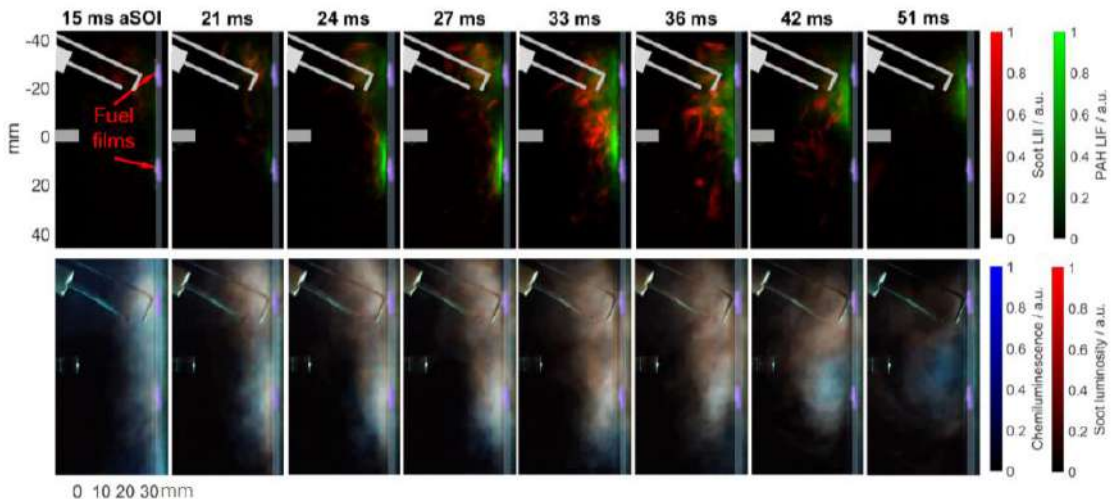


Figure 3: PAH LIF and soot LII ensemble averaged images compared with high speed combustion images from an optical flow bench.

3D CFD simulation of the optical engine conditions has been found to give excellent quantitative prediction of the fuel film thickness, together with fair representation of their spatial extent and variation, under stationary piston conditions. With varying operating conditions and rig geometry, the quantitative prediction of the fuel films has been found to be good, with measured trends well predicted in the simulation. Furthermore, the predicted temporal, crank angle variation of fuel film mass, area and median thickness evolution is found to be in good agreement with the experimental measurements, both in the optical engine and the flow bench. These results are encouraging for the overall development of combustion system design recommendation tools based upon simulation.

The 3D CFD simulation and single cylinder engine soot emissions results are being used as validation data sets for the virtual gasoline particle sensor (vGPS) development, which is also being undertaken in this WP (see the right-hand side of Figure 1). To date, the models under development within this sensor have been found to give reasonable agreement of both the fuel evaporation rate during the cycle (including the wall film evaporation) and, via a simplified combustion model, soot generation under a wide variety of operating conditions. Since these models are running within 10ms per cycle, there is some confidence that such sensor can be developed and practically applied for future engine control systems.

The experimental measurements are also being used to calibrate 0D combustion and emissions models. The resultant Spark Ignited Stochastic Reactor Model (SI-SRM) employs detailed chemistry and considers inhomogeneities in the combustion chamber, assuming a stochastic distribution of enthalpy and gas composition. Once calibrated on a few engine operating points, the SI-SRM has been used to extrapolate combustion and emissions behaviour over the full engine map. This has then been coupled, in the form of a look-up table, to crank-angle based and Mean Value Engine Models (MVEM) to allow fast and yet predictive system simulation, such as used within vehicle simulations.

Work Package 2 (Advanced Aftertreatment Systems).

In this WP, a TWC+GPF combination is being developed (for WP3) and a lean NO_x filter combination (for WP4). Much of the emphasis of WP2 has been aimed at the particulate filter, since not much was known about sub 23nm particle emissions and their control. Progress towards this goal has been reported (see Edwards (2018) and Osborne (2019)).

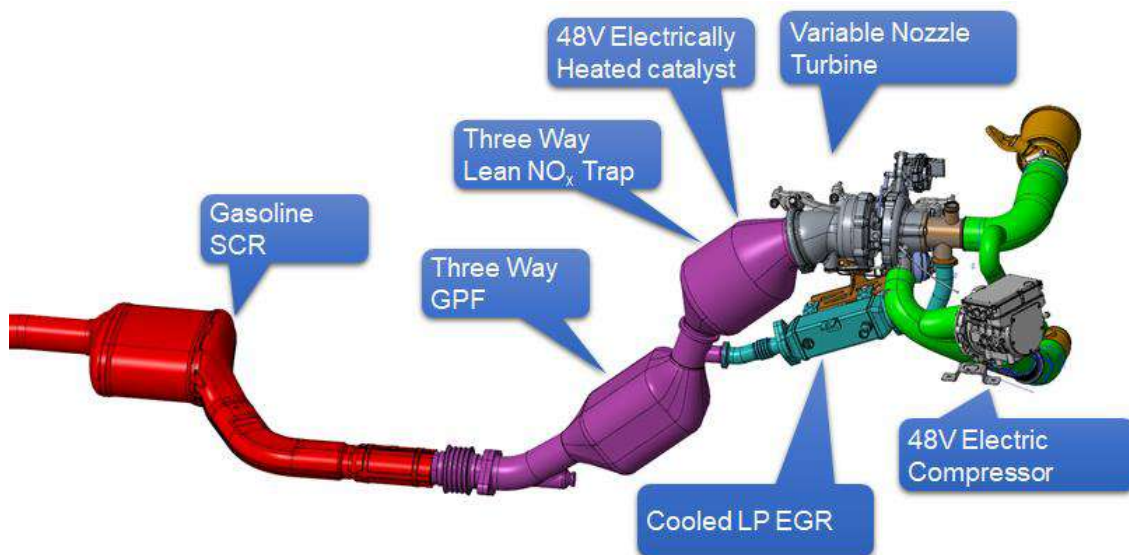


Figure 4: The air handling and exhaust aftertreatment system arrangement as applied within the WP4 demonstrator vehicle

Recent activities have concentrated on the development of the complete aftertreatment system for WP4, the arrangement of which for the vehicle is shown in Figure 4 (above) and includes:

- a TWLNT for both stoichiometric performance and lean NOx conversion;
- which is coated onto a 48V 3kW electrically heated catalyst for improved light-off performance;
- a TWGPF, giving additional CO and HC conversion and high filtration efficiency; plus
- a Selective Catalytic Reduction (SCR) catalyst, for lean NOx conversion with ammonia (urea) dosing.

Gas temperatures at the inlet to the SCR are expected to be approximately 140C cooler than those typical at the exhaust manifold. An iron-based (Fe-SCR) technology has been chosen because of its higher durability under low-oxygen conditions (e.g. stoichiometric combustion) and its low selectivity toward forming N₂O when compared to copper-based technology. The ratio of NO₂:NO can have significant bearing on the SCR conversion efficiency: a higher proportion of NO₂ greatly improves the efficiency, especially at lower temperatures. However, for the lean-burn combustion system the ratios are likely to be so low, such that a NO₂-make functionality has been added to the GPF. Such a system has been tested in the vehicle over a WLTC, see Figure 5: the resulting PN filtration efficiency has been found to be approximately 90%.

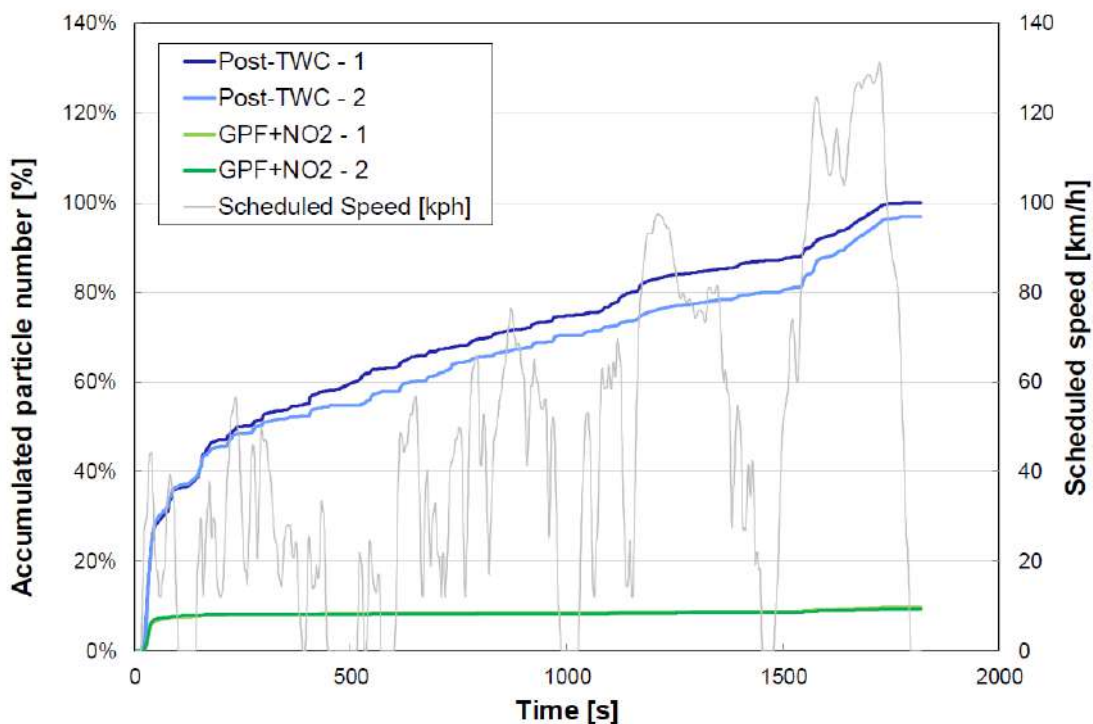


Figure 5: Aftertreatment system filtration efficiency over the WLTC for the WP4 demonstrator vehicle

Work Package 3 (Stoichiometric small TC-VVA-DI water injection engine).

The path towards lower CO₂ emissions for the demonstrator vehicle in WP3 is represented in Figure 6. To date the hardware selection for the base engine and aftertreatment has been completed. The control function development and the engine calibration are almost done, with the engine having been on the test bed and now being installed into the vehicle, to be ready for independent evaluation starting in the Spring of 2019.

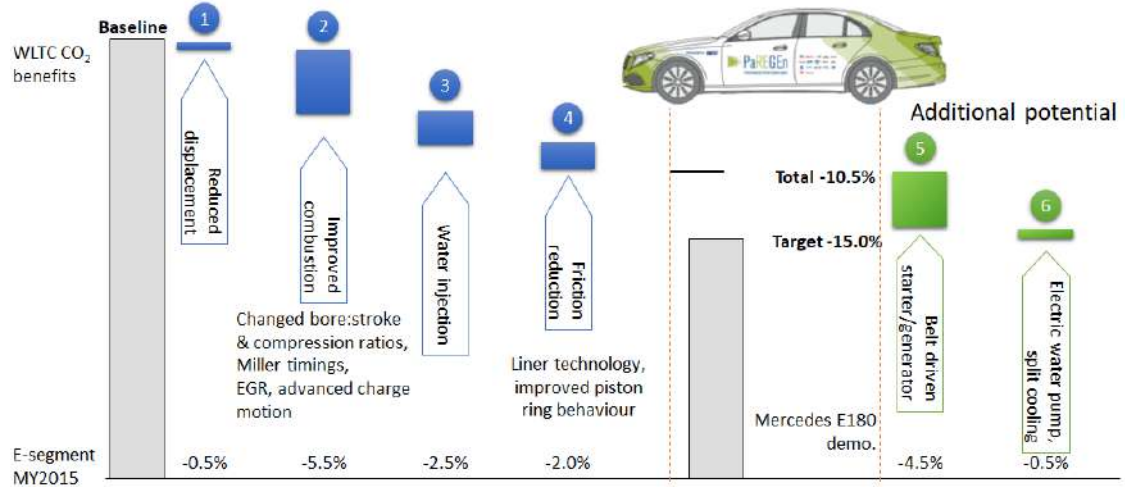


Figure 6: A WLTC CO₂ emissions benefit waterfall diagram for the stoichiometric small TC-VVA-DI water injection engine (WP3) demonstrator vehicle.

Of particular novelty within the WP3 developments, is the use of water injection and harvesting. Rig and engine comparative tests, including optical investigations, have shown that direct water injection has the better trade-off between fuel economy and emissions, including PN emissions, when compared with port water injection, hence DI technology will be pursued further. The water harvesting system has been assembled and is ready now for evaluation on the engine test bench.

Work Package 4 (Dry Dilute Combustion Demonstrator)

The path towards lower CO₂ emissions for the demonstrator vehicle in WP4 is represented in Figure 7. Detailed information in relation to the engine and component development has been published in Lane A. (2019) and, for example related to the air handling system, in Pohorelsky et al. (2018). To date, single cylinder engine testing has been completed, allowing the range of suitably stable lean operation to be mapped. Multi-cylinder engine testing is on-going and showing specific fuel consumption improvements of up to 15% in specific areas of operation (Osborne et al. (2019)). The engine and aftertreatment transient control and calibration is currently being refined (initial results have also been shown in Osborne et al. (2019)). The demonstrator vehicle has been assembled and first emissions testing, including the measurement of PN down to 10nm in size, has been made.

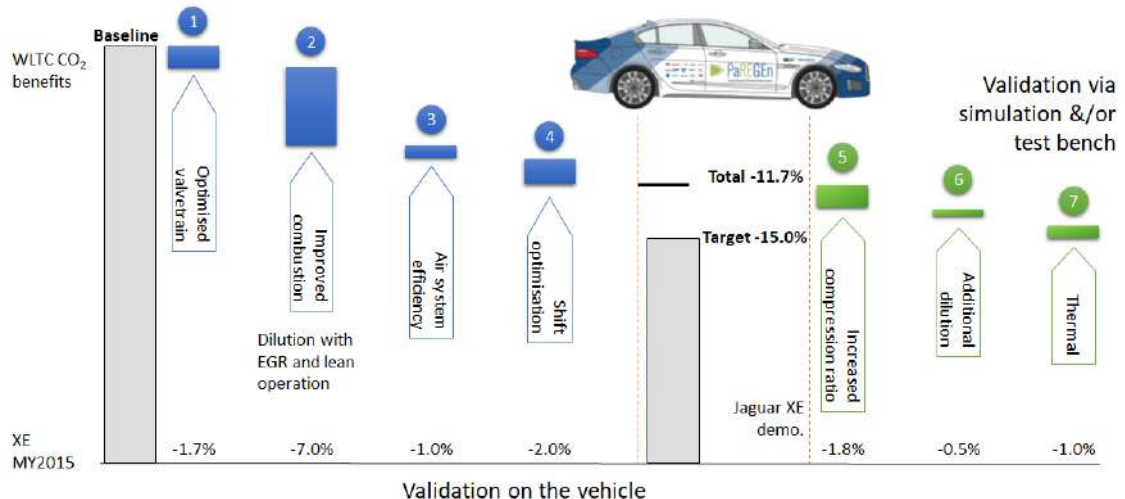


Figure 7: A WLTC CO₂ emissions benefit waterfall diagram for the dry dilute combustion (WP4) demonstrator vehicle.

Work Package 5 (Target Setting, Tracking and Impact Assessment)

The overall targets for the two demonstrator engines and vehicles have been set, based on the project objectives and the state of the art prior to the project start. The baseline vehicles have been tested to give a reference for WPs 3 and 4. Of particular interest were the PN measurements of different sized particles, made over a variety of test cycles and with a variety of instruments, as shown in Figure 8. The cycles included the NEDC, WLTP (high and low) and RDE (on-road and on-chassis-dynamometer) using the AIRMODUS and EEPS instruments, which have the capability to measure particles below 23nm in size over the wide range of tests. The baseline vehicles were seen to be well below the relevant legislative PN levels. The relationship between the PN₂₃ and PN₁₀ measurements was consistent with the other measurements made within the DownToTen project. Currently, the progress of the two engine and vehicle developments is being tracked; the independent final demonstrator vehicle assessment is planned for Summer 2019. During this testing, the impact of the fuel-efficient engine technology on the PN₁₀ will be established.

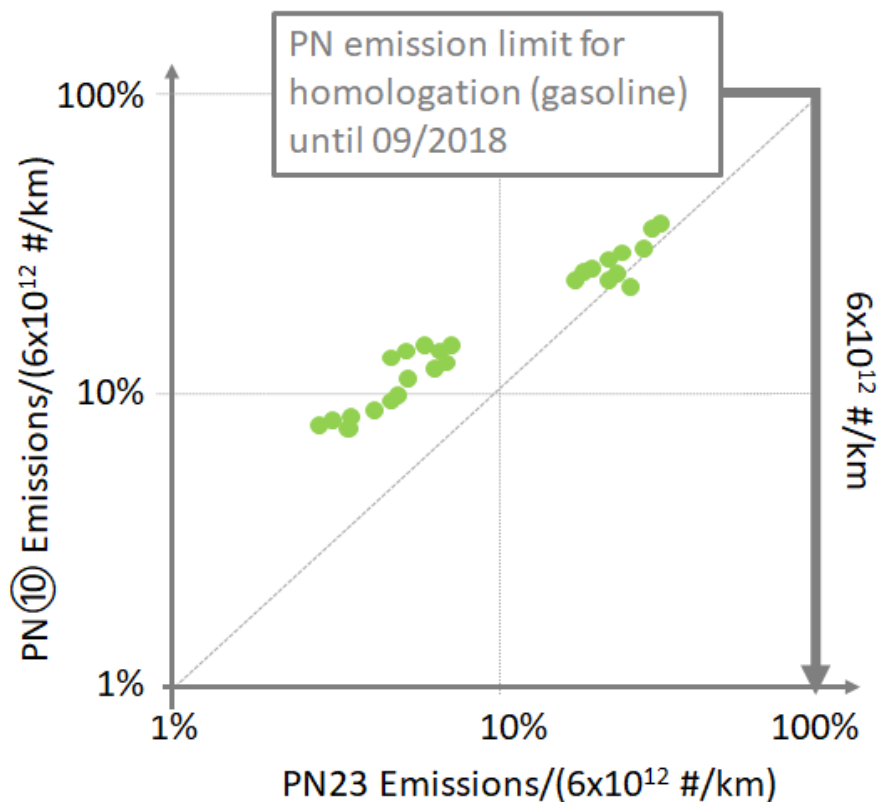


Figure 8: PN measurement results with the baseline PaREGEn vehicles (various test cycles and instruments).

Conclusions

In the PaREGEn project, the further development of gasoline engines for mid to premium sized passenger cars within the coming decade is being undertaken. The project is currently two years into its plan and is on track to reach its objectives. Specifically, the cause and effect relationships between in-cylinder engine conditions and particle emissions are being deduced. The findings are being integrated into updated simulation tools and a new virtual sensor for improved engine development and control in the future. Further, two technology demonstrators are well on the way to showing the route toward a 15% reduction in CO₂ emissions together with emissions compliance at Euro 6d RDE and PN emissions measured down to 10nm in size.

Acknowledgements

The authors would like to thank their Directors and the project partners for permission to publish this paper. The contributions from the various work package teams, in particular the individual WP leaders, in preparing this paper are gratefully acknowledged.

This project has received funding from the European Union's Horizon 2020 research and innovation programme under grant agreement No. 723954. The information and views set out in this publication do not necessarily reflect the official opinion of the European Commission. Neither the European Union institutions and bodies, nor any person acting on their behalf, may be held responsible for the use which may be made of the information contained therein.

References

- Edwards S.P. and Verschragen E. (2018). Particle Reduced, Efficient Gasoline Engines: A First-Year Report on the PaREGEN Project. *Proceedings of 7th Transport Research Arena TRA 2018, April 16th-19th 2018, Vienna, Austria*.
- Edwards S. (2018). Particle Reduced, Efficient Gasoline Engines. *Presented at the Road Transport Research conference, 29th November, Brussels*.
- Geiler J., Grzeszik R., Quaing S., Manz A. and Kaiser S. (2017). Development of Laser Induced Fluorescence to Quantify In-Cylinder Wall Films. *"International Journal of Engine Research"*, Academic Press, New York, p. 387.
- Geiler J.N., Grzeszik R., Manz A., Mansbart M. and Kaiser S. (2018). Further Development of Laser Induced Fluorescence (LIF) to Quantify In-Cylinder Wall Films. *"14th International Congress Engine Combustion and Alternative Concepts"*, 13th-14th March, Essen, Germany.
- International Energy Agency (2012). *Energy Technology Perspectives*, Paris, France.
- Lane A. (2019). A New Generation of Lean Gasoline Engines for Premium Vehicle CO₂ Reduction. *Presented at the Future Powertrain Conference, Birmingham, UK*.
- Miller R.H. (1956). High Expansion, Spark Ignited, Gas Burning, Internal Combustion Engines. *USA Patent No. 2773490*.
- Osborne R., Turner N., McWilliam L., Hinton N., Geddes J., Gidney J., Cleeton J., Atkins P. and Morgan R. (2019). A New-Generation Lean Gasoline Engine for Reduced CO₂ in an Electrified World. *Vienna Motor Symposium, May 16th-17th 2019, Austria*.
- Pohorelsky L., Vondrak A., Turner N., Luard N., Cooper B., Lane A. and Osborne R. (2018). The coupling of Advanced Gasoline Combustion and a fast-transient Boost System to produce a Low CO₂ vehicle Concept. *ATK Conference, Dresden, Germany*.

Abbreviations

CER	Cause and Effect Relationship
CFD	Computational Fluid Dynamics
CO ₂	Carbon dioxide
CVVL	Continuous Variable Valve Lift
DI	Direct Injection
EGR	Exhaust Gas Recirculation
EU	European Union
eIVC	early Intake Valve Closing
GDI	Gasoline Direct Injection
GPF	Gasoline Particulate Filter
HC	Hydrocarbon(s)
LIF	Laser Induced Fluorescence
LII	Laser Induced Incandescence
MVEM	Mean Value Engine Model
NEDC	New European Drive Cycle
NO _x	Oxides of Nitrogen
N ₂ O	Dinitrogen oxide
PAH	Poly-Aromatic Hydrocarbon(s)
PEMS	Portable Emissions Measurement System

PN	Particle Number (PN ₂₃ are measured to 23nm, PN ₁₀ are measured down to 10nm in size)
PWI	Port Water Injection
RDE	Real Driving Emissions
SI-SRM	Spark Ignited Stochastic Reactor Model
TC	Turbocharged
TRL	Technology Readiness Level
TWC	Three Way Catalyst
TWLNT	Three Way Lean NO _x Trap
vGPS	Virtual Gasoline Particle Sensor
VVA	Variable Valve Actuation
WLTC	World Light-duty Test Cycle
WP	Work Package
0D	Zero-dimensional
3D	Three-dimensional

2.9.3 GPF model-based optimization methodologies supporting RDE conformity

M. Mitsouridis¹, G. Koltsakis¹, Z. Samaras¹, S.-H. Veit², C. Martin²*

¹Laboratory of Applied Thermodynamics, Aristotle University of Thessaloniki, Thessaloniki, 54124, Greece

²AVL List GmbH, Graz, 8020, Austria

Introduction

The Gasoline particulate filter (GPF) technology is considered as a very efficient technology to meet the Particulate Number (PN) legislation limits (Richter et al., 2012). Depending on the engine-out emissions which are highly dependent on operating mode and temperature, filtration efficiencies in the order of 90% or more may be required over the whole range of operating conditions throughout the useful life of a vehicle. To meet this target, the macro-geometry as well as the microstructure geometry of the filter media need to be carefully engineered. High filtration efficiency is usually associated with high pressure drop which needs to be minimized in order to maintain the desired engine power output and fuel efficiency. The accumulation of soot in the filter drastically increases both pressure drop and filtration efficiency whereas passive or active regenerations should not entail overheating and potential filter damage (Koltsakis et al., 2009). The filter design optimization needs to account for the operating conditions of each particular vehicle class under real driving modes, including flow rate, temperature and particle emissions.

In order to cope with the above numerous and conflicting challenges, the exhaust system engineer has a multitude of design freedom degrees, including the GPF positioning, its volume, wall porosity and pore size distribution as well as washcoat loading amount and coating technology (Thier et al., 2015). However, to achieve a cost-efficient solution in a timely manner, experimental methods need to be supported by mathematical modeling of the filtration, thermal and reaction phenomena under steady-state and transient conditions. The main target of this paper is to demonstrate how engine tests can be combined with simulation models that can be used as predictive tools to reduce the development efforts and costs for system design and engine control.

In a first step, quasi-steady engine tests will be presented to examine the pressure drop and filtration efficiency behavior of three GPFs with different wall microstructure, washcoat loading and positioning in the exhaust line. The data are then used to parameterize a physico-chemical model, using the axisuite® platform. In a next step, a series of transient engine tests simulating real driving modes with filters under various soot loading states will be shown. The filtration efficiency and the passive regeneration behavior will be evaluated and compared with respective model predictions.

Experimental setup

The first filter characterization tests were performed on an engine testbed using a 2.0l TGDI engine.

The driving cycle validation tests were performed on a chassis dynamometer using a mid-size class vehicle equipped with a 1.8l TGDI engine.

Engine-out (EO) and tailpipe (TP) pressure and particle emissions were measured simultaneously to evaluate the instantaneous pressure drop and filtration performance of each system. The instrumentation, indicated in Figure 1, was used:

APC: Measures Particle number emissions. Two such instruments were placed in each measurement position. The lower size threshold is 10 nm and 23 nm respectively.

MSS: Measures Particle mass emissions.

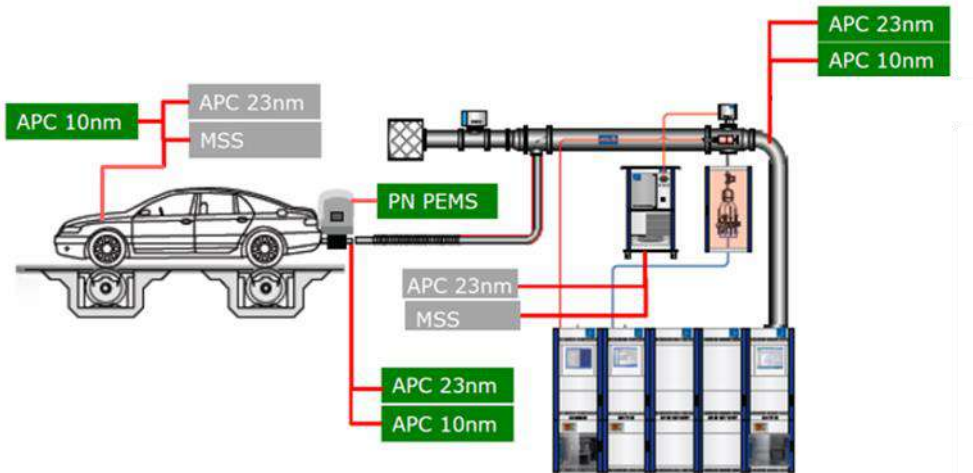


Figure 1: Chassis dynamometer experimental setup

The original exhaust system was removed and replaced with exhaust systems of two different variants as shown in Figure 2.

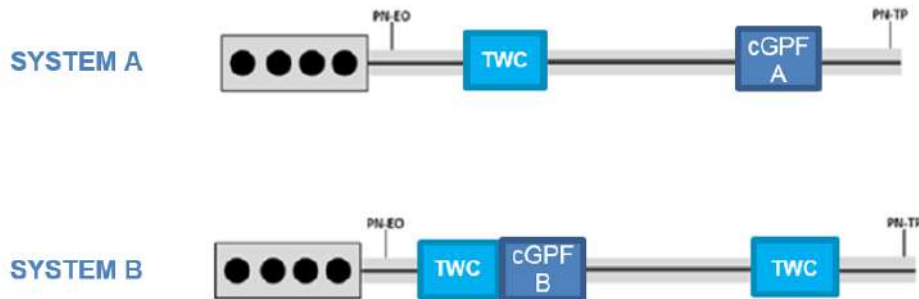


Figure 2: Exhaust line layout for pressure drop and filtration efficiency measurements

In the first system, the GPF is placed underfloor (UF) whereas in the second system the GPF is placed right after the close coupled (CC) TWC.

Both filters have the same wall thickness and cell density, i.e. 8mils and 300cpsi respectively, as well as a medium-large mean pore size and a high porosity. The exact microstructure information cannot be disclosed due to confidentiality reasons. The only difference of cGPF A and B is their washcoat loading, i.e. 100 and 50g/l respectively.

GPF characterization and model development

Model calibration by load ramp tests

The pressure drop and filtration model parameters were calibrated based on “load-ramp” tests. A load ramp test consists of step-wise changes of the engine operating point, scanning the complete engine operating map, hence exposing the GPF in a large variety of feed gas temperatures and flow rates.

A mean effective pressure (bmep) vs engine speed graph schematically depicting the scanned engine operating points, is presented in Figure 3 below:

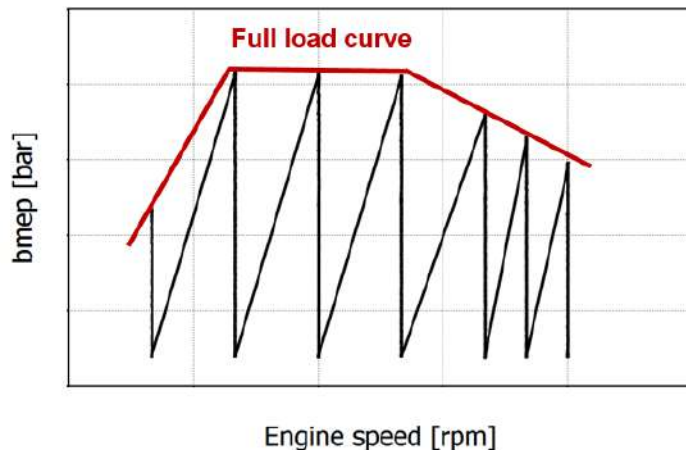


Figure 3: bmep vs engine speed during a load ramp test sketch.

The actual bmep and engine speed range is deliberately hidden due to confidentiality issues.

Pressure and PN concentrations were measured upstream and downstream the initially soot-free GPFs. Then, the filters were loaded with soot and the same tests were performed again.

The accelerated soot loading procedure must be defined very specifically for every engine. The delta pressure behavior of the accelerated soot must be matched with the delta pressure behavior from real vehicle soot accumulation. Usually the accelerated soot loading point is defined by modified engine parameters e.g. injection settings.

The process of soot loading on the engine testbed is done in following steps:

1. Engine start, set operation point
2. Activation of soot loading settings
3. Hold the point for a certain time or until a target delta pressure is reached
4. Deactivation of settings and Cooldown
5. Stop engine without unintended soot regeneration

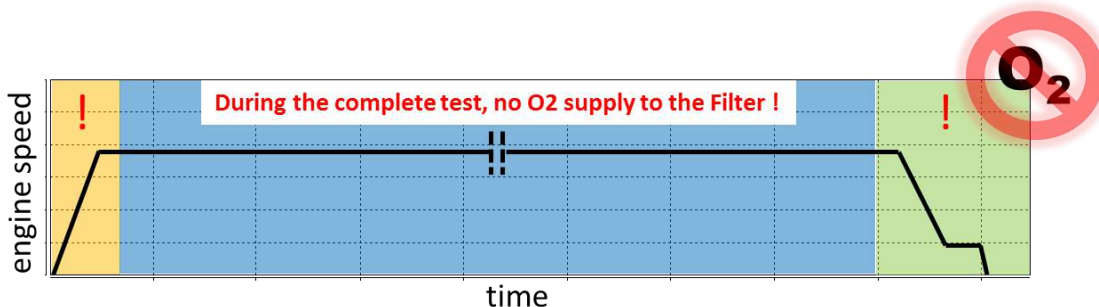


Figure 4: Soot loading process on the engine testbed

To minimize the uncertainties during weighing the GPF, a well-established process, which has to be repeated precisely is the key element of high-quality measurement result. The filter weight is measured in hot conditions over a temperature range from 300°C to 200°C in the filter. The soot load is then identified as the average over time in this temperature range minus the reference weight in empty condition. Weighing in hot conditions ensures that there is no influence of condensed droplets e.g. water. The whole weighing procedure is performed in a well-conditioned room without any airflow and constant temperature. To ensure the correctness of the reference weight the filter mass is determined several times (e.g. every week) in empty conditions. In case the soot loading target is below 1g/l, only the

pressure correlation is taken into account as soot mass estimation via filter weighing is not reliable any more.

For the case of GPF modeling, a special challenge is the accuracy of filtration model predictions at soot-free and slightly soot loaded filter state. Contrary to their Diesel Filter counterparts, the gasoline filters are frequently operated at low-soot loadings where the surface filtration via the formation of the 'soot-cake' is not predominant (Saito et al., 2011). Under such conditions, the depth filtration mechanism in the pores of the wall is the main mechanism which involves particle diffusion and interception processes (Mitsouridis et al., 2019). Given that the microstructure of the porous wall does not correspond to an ideal filter geometry (e.g. packed bed or fiber), it is necessary to include some semi-empirical correction factors in order to achieve a good agreement between model predictions and filtration efficiency data (Exothermia SA, 2018).

The results for both exhaust line layouts examining GPF A and B at both soot-free and soot loaded state, are presented in Figure 5.

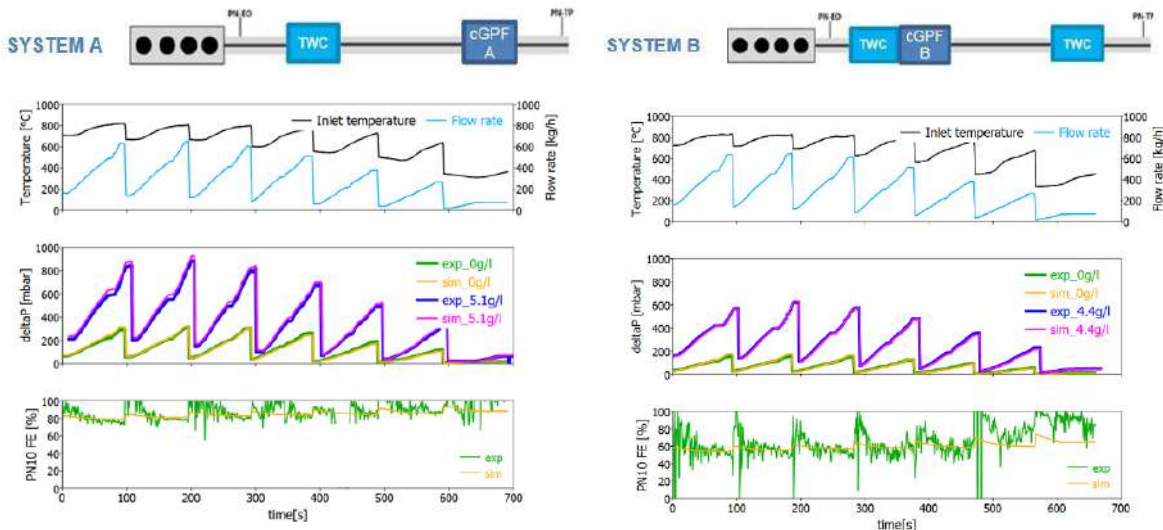


Figure 5: Pressure drop and filtration efficiency results during load ramp tests for the two exhaust system variants. Respective simulation results after model calibration are included.

The model solves the mass, momentum, energy and species equations in the inlet and outlet channels of the GPF, as summarized in Figure 6.

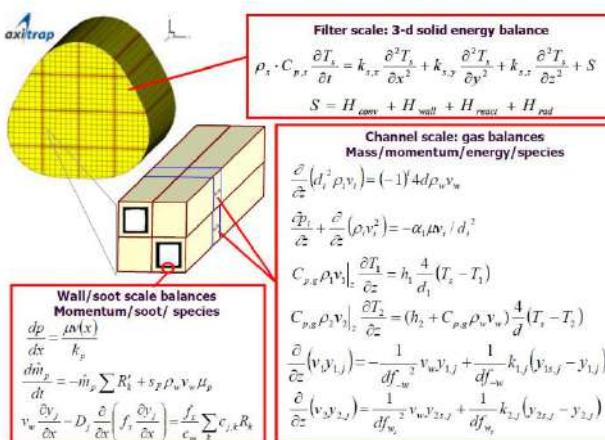


Figure 6: GPF model scales and balance equations

The foundation of the model and examples of model validation can be found in earlier works (Koltsakis et al., 2013). To model the chemical reactions on the active impregnated washcoat, a standard library of the axisuite software was used. The accuracy of CO, HC, NOx conversion prediction (Spiess et al., 2013) was of secondary importance in this work. Nevertheless, the inclusion of the 3-way reactivity was important to account for O₂ availability and exotherm generation, as presented in earlier studies (Mitsouridis et al., 2019), (Boger et al., 2015).

A simple soot oxidation mechanism was implemented as described by the following reactions:



The respective rate expressions of the above reactions are formulated as:

$$R'_1 = A_1 \cdot \exp^{\frac{-E_1}{RT}} \cdot P_{O_2}^{\alpha_1} \quad \text{Eq. 1}$$

$$R'_2 = A_2 \cdot \exp^{\frac{-E_2}{RT}} \cdot P_{O_2}^{\alpha_2} \quad \text{Eq. 2}$$

where the pre-exponential factor A, the activation energy E and the reaction order α are tunable parameters to match the oxidation reaction properties of the soot under consideration.

Model validation under transient conditions

The pressure drop and filtration models predictivity was validated in a series of transient cycle tests corresponding to the legislated WLTC and two types of RDE tests, i.e. moderate and dynamic. The difference between moderate and dynamic RDE cycles lies on the driving style which is mild or aggressive respectively, leading to higher temperatures and mass flow rates for the latter case. Filters A and B were tested at both initially soot-free and soot loaded state. The tests are summarized in Table 1 below:

Table 1: Transient tests

Filter	WLTC	RDE moderate	RDE dynamic	RDE dynamic w/o FCOFF phases
A	soot-free & 0.1g/l soot	soot-free & 0.2g/l soot	soot-free & 0.1g/l soot	-
B	soot-free & 0.4g/l soot	soot-free	soot-free & 0.4g/l soot	0.5g/l soot

Experimental vs simulated pressure drop results for filters A and B are presented in Figure 7, demonstrating the pressure drop models predictivity under both soot-free and soot loaded conditions. For simplicity, only the RDE dynamic results are included.

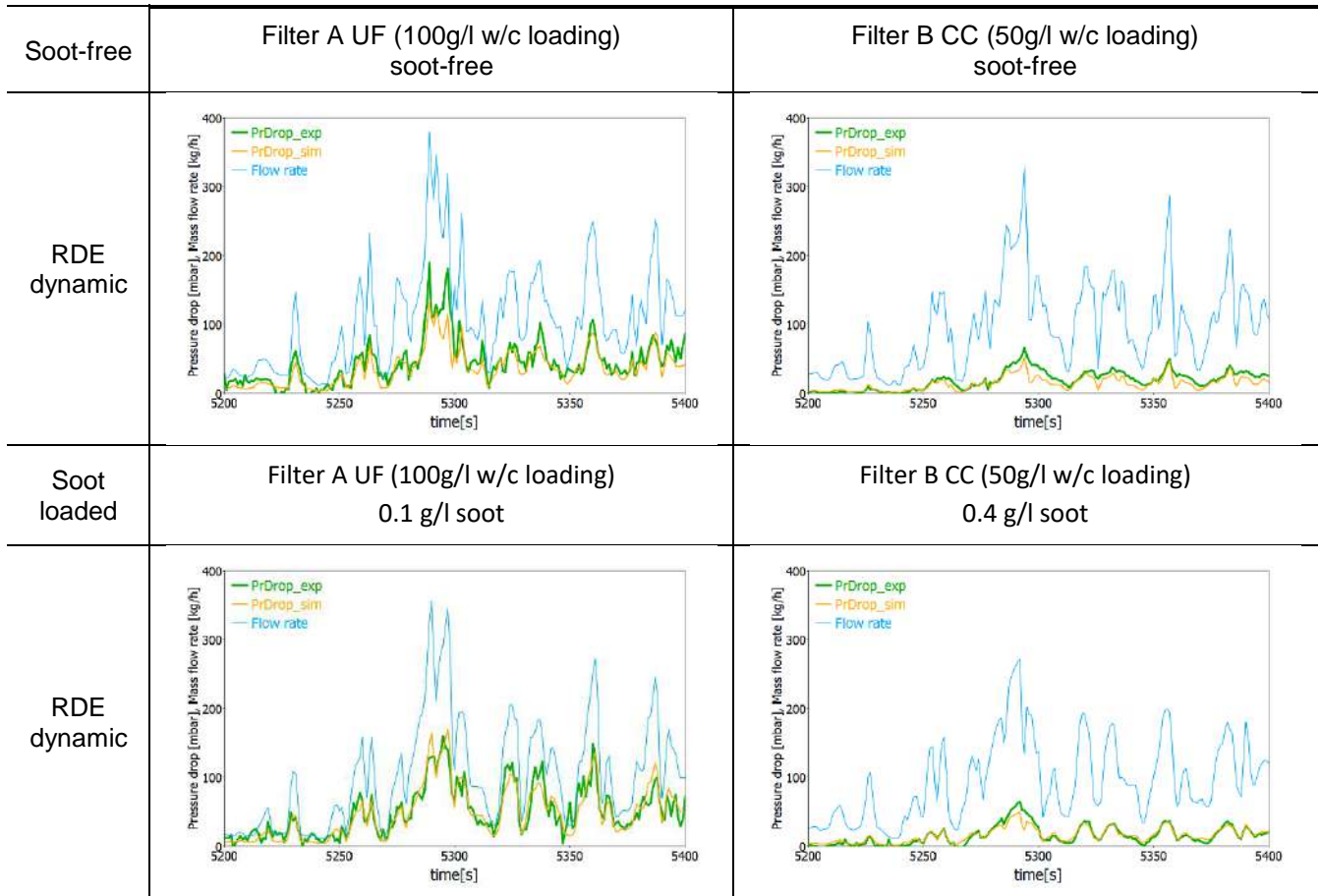


Figure 7: Experimental and simulation pressure drop results for filters A and B at both initially soot-free and soot loaded state

The initiative behind exclusively presenting the high flow areas at the end of the RDE dynamic cycles is to present data carrying the smallest possible inaccuracy. At higher flow rates, the experimental pressure drop is higher, hence less affected by any measurement-related issues.

In order to demonstrate the filtration model predictivity, a comparison between experimental and simulated cumulative TP PN emissions was performed. The instantaneous cumulative TP PN data were normalized based on the cumulative EO PN value at the end of the respective cycle and are presented in Figure 8 below:

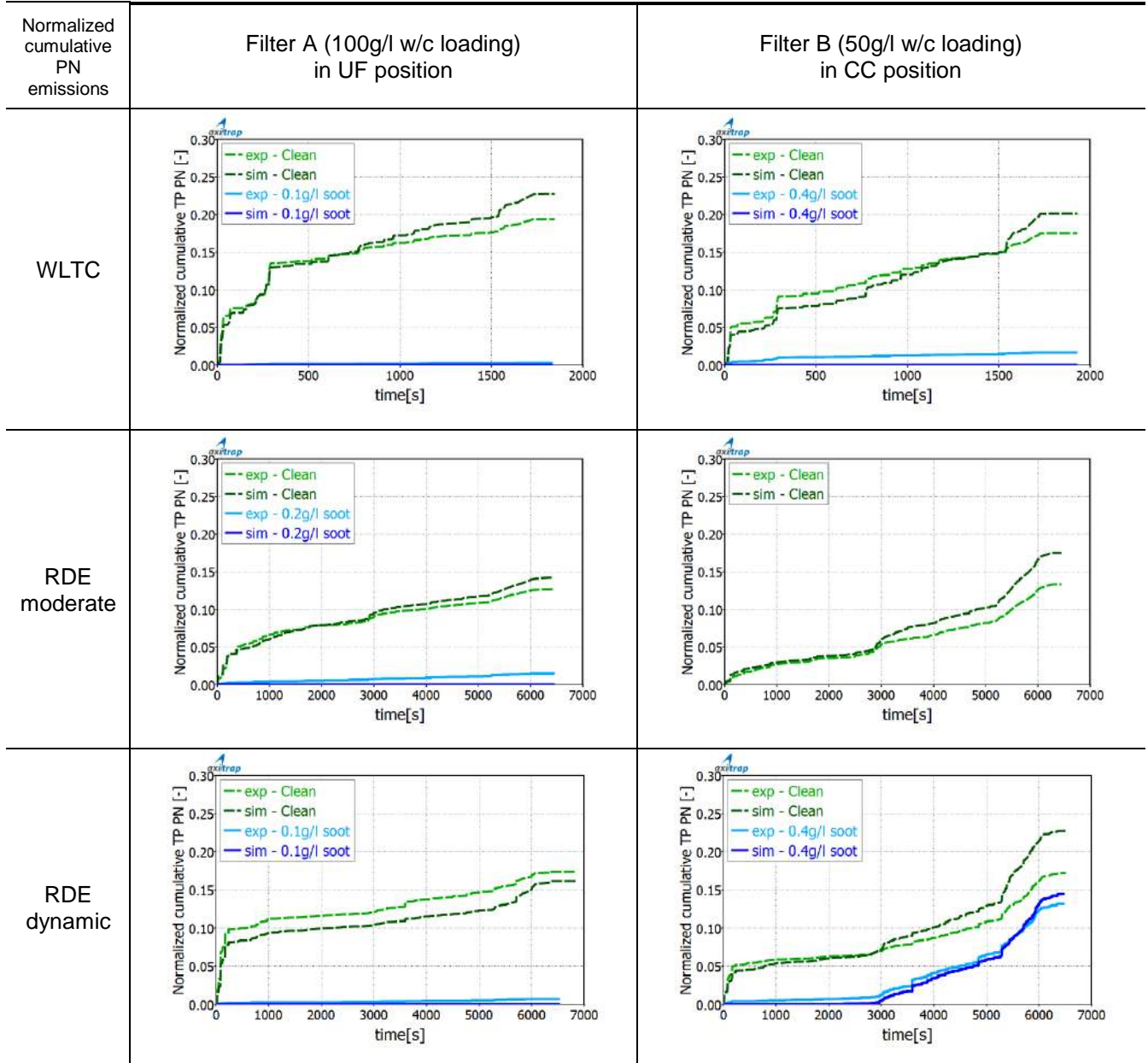


Figure 8: Experimental and simulation normalized, cumulative PN results for filters A and B at both initially soot-free and soot loaded state

This normalization permits us to compare any of the above presented results and draw direct conclusions about the total filtration efficiency. The lower the normalized curve values, the higher the respective total filtration efficiency.

In this respect, the impact of soot accumulation on the cGPF's filtration performance is highlighted. Comparing the initially soot-free vs soot loaded cumulative TP PN results in any of the above graphs, it is manifested that soot accumulation can drastically increase a GPF's filtration efficiency performance.

Nevertheless, after running the WLTC protocol on loaded filter A and B, the latter showed a worse filtration performance even though it was loaded with significantly more soot. This may be attributed to either filter's B CC placement which may have boosted passive filter regeneration leading to decreased filtration performance, or to particle measurement inaccuracy.

It is interesting to mention that for the regenerated filter A, lower experimental total filtration efficiency results are obtained for WLTC and RDE dynamic tests as opposed to the RDE moderate test, while the model is able to capture this trend.

The soot loaded filter B RDE dynamic results that step out of the norm, are analytically discussed in the following section.

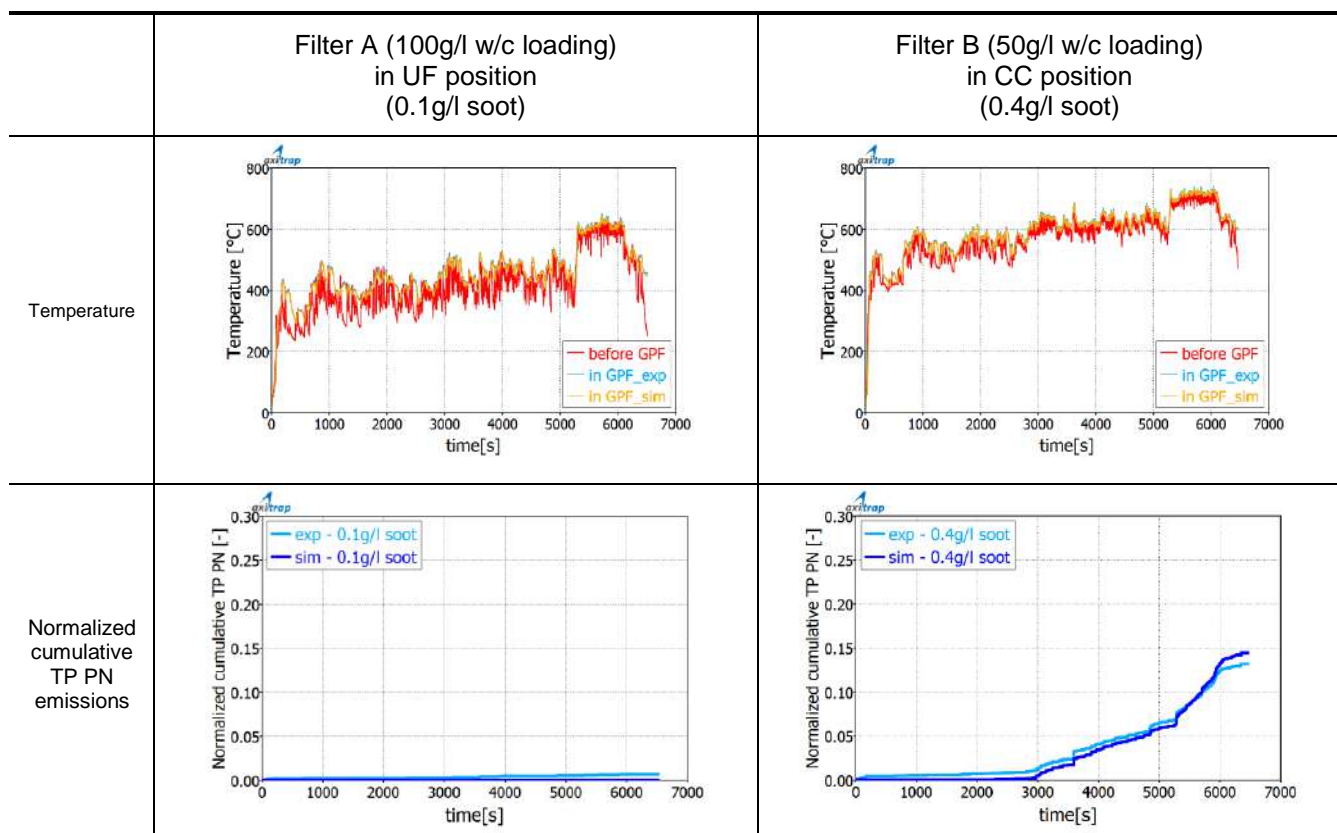
Effect of filter positioning on filtration efficiency

A filter located in CC position is subjected to significantly higher temperatures and therefore has a higher passive regeneration potential, compared to a filter located in UF position.

On the one hand, filter A can maintain a high filtration efficiency as its UF placement favors soot accumulation. Its filtration performance is additionally enhanced by its higher washcoat loading compared to filter B, which reduces its effective wall porosity.

On the other hand, the filtration efficiency of the initially loaded filter B starts at ~100% and gradually drops as the test progresses. The reason is that after ~3000 seconds, the passive regeneration conditions of high temperature and oxygen availability are met. Thus, the previously accumulated soot is oxidized and the filtration performance deteriorates. This is highlighted in Figure 9, where the soot loaded filters A and B filtration performance under RDE dynamic conditions is compared.

These experimental data are very interesting, as they provide valuable information for the soot oxidation model calibration. In fact, the introduced soot oxidation model, described in the previous section, was calibrated based on the initially loaded filter B RDE dynamic experimental data.



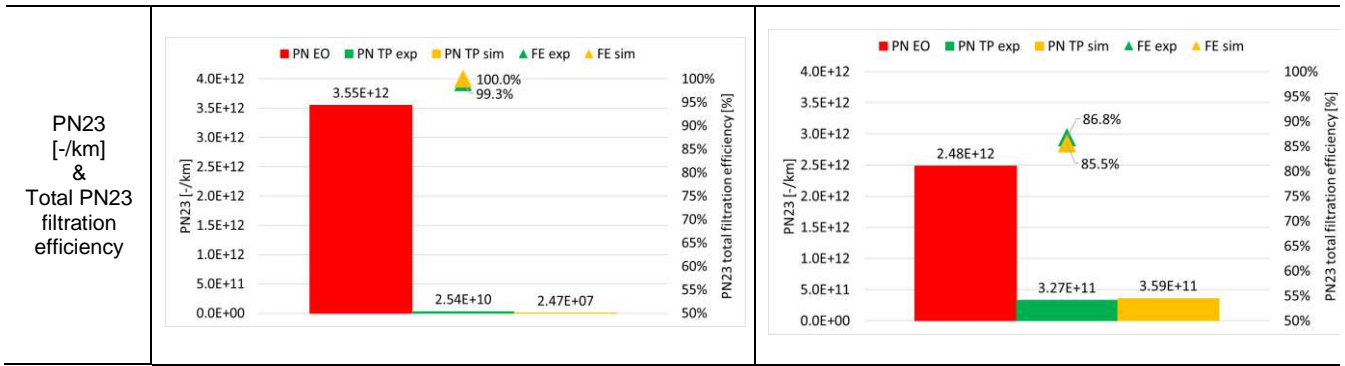


Figure 9: Experimental and simulation temperature, normalized cumulative TP PN emissions and total PN filtration efficiency results of Filters A and B at initially loaded state under RDE dynamic conditions

When loaded with an initial soot amount, both filters A and B TP PN emissions are below the legislated EU 6d limits, i.e. 6×10^{11} particles/km, under all the tested transient driving cycle conditions.

The simulation results showed that the lower filtration efficiency of the close coupled filter could be associated with the enhanced passive regeneration that removes the soot from the wall eventually reducing the filtration efficiency.

To validate the above hypothesis, an additional RDE dynamic test was performed for System 3. However, in this test the fuel-cut off events were de-activated. This means that during vehicle deceleration, the engine is fueled stoichiometrically, therefore O₂ availability for soot oxidation is extremely low compared to the fuel cut case where O₂ concentration was close to ambient air levels. The results of this test along with the respective simulation results are presented in Figure 10.

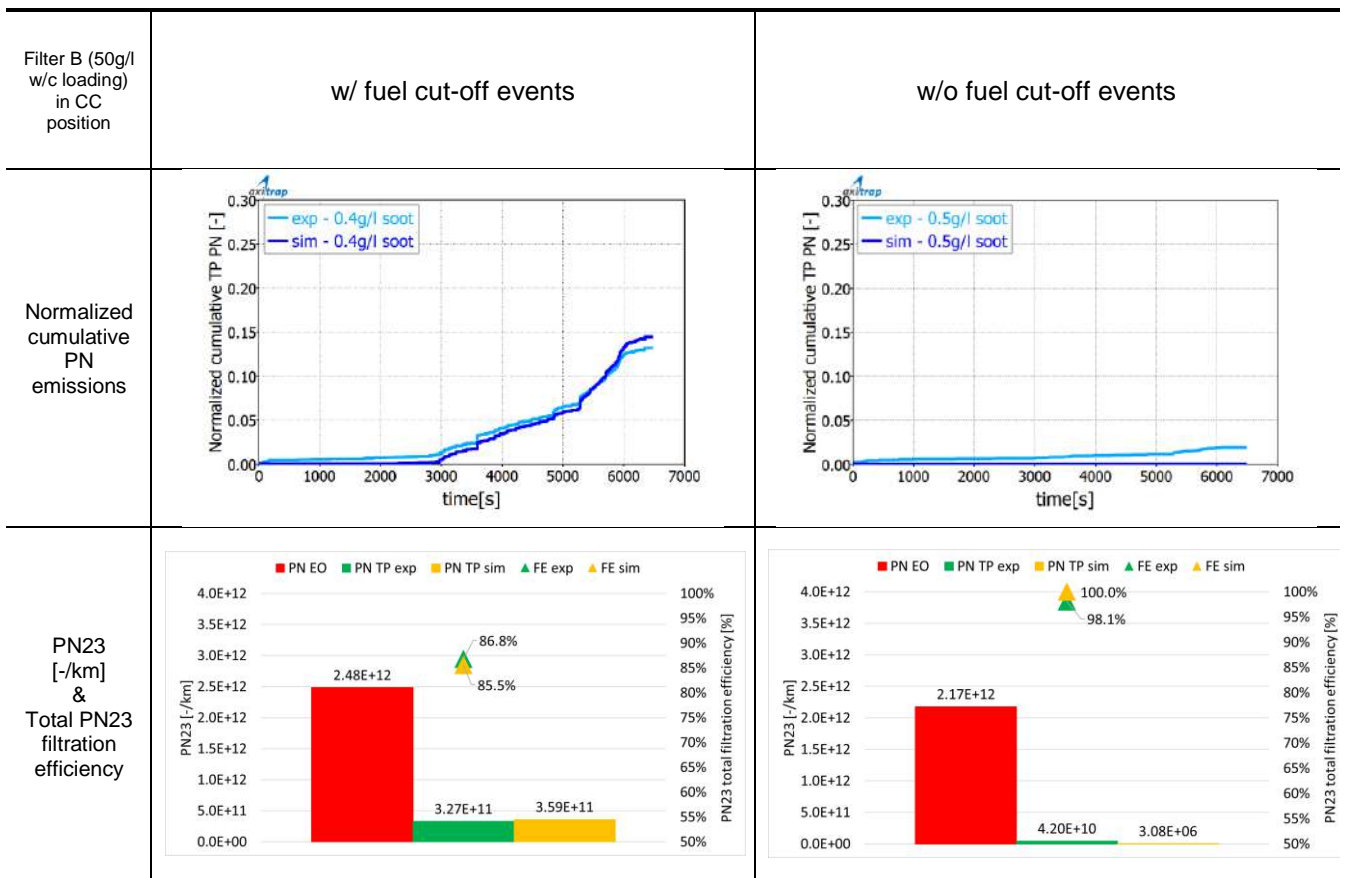


Figure 10: Experimental and simulation instantaneous and total PN filtration efficiency results of Filter B at initially loaded state under RDE dynamic conditions, w/ vs w/o fuel cut-off events

Without fuel cut-off events, no soot oxidation takes place and the cGPF's high filtration performance is maintained.

Summary & Conclusions

In this work, we performed a series of measurements to characterize the performance of two cGPF system configurations. The measurements were used to develop predictive models that could be used later on as system design tools. In parallel, the models were used to identify and explain the trends observed in the system benchmarking process.

The filtration efficiency obtained with both systems was sufficiently high to meet the legislative requirements provided that a minimum amount of soot is accumulated in the wall. A soot loading in the order of 0.1 g/l, was sufficient to reach the legislative target filtration efficiency for the conditions studied here. This would ideally involve a careful management of the regeneration events to avoid complete regenerations.

The accumulated soot has therefore an important beneficial effect to maintain RDE compliance. On the other hand, high soot amounts increase pressure drop and pose a risk for the filter integrity under uncontrolled regeneration. In this respect, passive regenerations occurring during fuel cut off events assist in maintaining the soot amount to a low level. However, we showed that such passive regenerations may lead to undesirably low soot levels that result in low filtration efficiency.

Maintaining the balance between filtration efficiency and pressure drop is a delicate engineering challenge. In this work, we illustrated a number of design parameters involved: filter positioning affecting temperature levels, washcoat amount affecting backpressure and filtration, engine fueling strategies. Employment of model-based methodologies would be an efficient way to tackle the complexity and reach optimum design solutions.

Acknowledgements

The results presented here were obtained within the project UPGRADE. This project has received funding from the European Union's Horizon 2020 research and innovation programme under grant agreement No 724036.

References

- Boger et al. (2015). Oxidation of Soot (Printex® U) in Particulate Filters Operated on Gasoline Engines. *Emiss. Control Sc. Technol.*, 49-63.
- Exothermia SA. (2018). User's Manual of axitrap Version 2017A_sp3.
- Koltsakis et al. (2009). Flow Maldistribution Effects on DPF Performance. *SAE International*.
- Koltsakis et al. (2013). Catalyzed Diesel particulate filter modeling. In *Reviews in Chemical Engineering* (pp. 1-61). De Gruyter.
- Mitsouridis et al. (2019). Model-based analysis of TWC-coated filters performance aspects. *Emission Control Science and Technology*.
- Mitsouridis et al. (2019). System integration and application for a three way catalyst coated gasoline particulate filter. In T. a. Boger, *Reducing Particulate Emissions in Gasoline Engines*. SAE International.
- Richter et al. (2012). Application of Catalyzed Gasoline Particulate Filters to GDI Vehicles. *SAE Int. J. Engines*.
- Saito et al. (2011). New Particulate Filter Concept to Reduce Particle Number Emissions. *SAE International*.
- Spies et al. (2013). Investigations of Emission Control Systems for Gasoline Direct Injection Engines with a Focus on Removal of Particulate Emissions. In *Topics in Catalysis* (pp. 434-439). Springer.
- Thier et al. (2015). Novel GPF Concepts with Integrated Catalyst for Low Backpressure and Low CO₂ Emissions. In *Proceedings* (pp. 217-232).

2.9.4 Particle emissions measurements on CNG vehicle focusing on, sub-23nm

Zisis Toumasatos¹, Anastasios Kontses¹, Stylianos Doulgeris¹, Zissis Samaras¹, Leonidas Ntziachristos²*[leon@auth.gr],

¹Laboratory of Applied Thermodynamics, Aristotle University of Thessaloniki, P.C. 54124, Thessaloniki, Greece

²Laboratory of Heat Transfer and Environmental Engineering, Aristotle University of Thessaloniki, P.C. 54124, Thessaloniki, Greece

Abstract

Current study aims to investigate sub-23nm solid particles (SPN<23nm) from spark ignition engine using compressed natural gas (CNG) as a primary fuel working in port fuel injection (PFI) mode and gasoline working as direct injection (GDI). For that reason, a state-of-the-art exhaust gas sampling system used for solid particle detection up to 2.5nm. Vehicle tested in various driving cycles. The SPN<23nm investigation have shown particle emissions beyond EURO 6 limits for both fuels. During tests, Particle Size Distribution (PSD) profiles reveal nucleation mode characteristics for both fuels. Though geometric mean diameter (GMD) for CNG operation was smaller, indicating that different combusting phenomena can formulate smaller in size particles.

Introduction

CNG market penetration increased over the years, reaching on average 6% annual increase with over 1.1 million vehicles running with natural gas in Europe (NGVA Europe, 2017) (Transport & Environment, October 2018), with future trends to be more optimistic since natural gas vehicle registrations for 2018 doubled from previous year (ACEA, October 2018). CNG yields lower CO, CO₂ in comparison to gasoline and lower CO, CO₂ and NOx emissions in comparison to diesel (Owen, et al., 1995) (Yusaf, et al., 2010) (Jahirul, et al., 2010) (Cachón, et al., 2009). Lower price as well as lower gaseous emission impact, are the main drivers for increasing market share of natural gas.

Gaseous emissions of CNG equipped passenger cars have been thoroughly investigated over the years, but for particle emissions perspective research is limited. Generally, exhaust tailpipe particle emissions below 100nm are harmful to public health as they can easily penetrate via breathing into the pulmonary system (Stone, 2012) (Eastwood, 2008) (Hinds, 1982). Research on sub-23nm particle emission in CNG passenger cars is limited. To this moment, studies on CNG particle emissions, focus on retrofitted engines (Kento T. Magara-Gomez, 2014), heavy-duty vehicles (Xue, et al., 2018) (Nylund, et al., 2004) or CNG-Diesel and CNG-Gasoline combined operation, with parallel investigation of engine operation characteristics (Jahirul, et al., 2010) (Yusaf, et al., 2010) (Nithyanandan, et al., 2016). In one case, experimental optical engine was used to conduct particle emission study performance in dual fuel operation with various blends including CNG in direct injection mode (Catapano, et al., 2017). Recent and most relevant research in the field investigated the potential difference between CVS and tailpipe particle emissions measurements including CNG equipped passenger cars (Giechaskiel, et al., 2019). In general, the previous results have shown a general trend of higher particle emissions towards nucleation mode region in CNG operation as compared to Gasoline operation.

As regards testing methodologies of previously mentioned studies, those, were restricted to steady state points or outdated driving cycles (NEDC) (Catapano, et al., 2017) (Mayer, et al., 2012) using indirect methods of sampling (CVS) (Schreiber, et al., 2007) in most of the cases. Indirect method of sampling poses a potential risk of lab to lab high measurement variability (Mamakos, et al., 2004) (Mathis, et al., 2004) and can lead to misunderstanding of actual PSD and thus to different aggregated particle emissions from tailpipe to CVS (Cedric, et al., 2017) (Giechaskiel, et al., 2019). Current work addresses these issues by implementing direct tailpipe sampling technology, which minimize the potential risk of particle losses. This work aims to investigating sub-23nm particle emissions using direct tailpipe measurement. For that reason, the DownToTen (DTT) sampling system was developed and funded under the framework of the European Commission's HORIZON 2020 program (Samaras, et al.) (Loctier, 2019).

Methodology

Current study is focusing on sub-23nm particle emissions investigation on a CNG equipped vehicle. To accomplish this, a bi-fuel passenger car investigated. The vehicle has CNG as the primary fuel and Gasoline as a secondary fuel that used when CNG is depleted. Fuel injection technology differs from CNG to Gasoline, the primary fuel injection is PFI and the secondary, is GDI technology. Gasoline interinjection, when the engine is running in CNG, is not required since the combustion chamber designed to disperse excessive heat (Markowski, 2017). To have a holistic view of particle emissions, a combined measurement campaign was adopted using both fuels in series, during experiments. Testing protocol included series of driving cycles in the chassis dyno first with CNG and then with Gasoline fuel. Engine characteristics are presented below (Table 1).

Table 1 Test vehicle characteristics

Vehicle segment	C
Engine	Spark-ignition 4-cyl, 16-valve
Model Year	2018
Fuel	CNG (PFI) and Gasoline (GDI)
Drive, Transmission and Number of gears	FWD, Manual, 6
Maximum power [kW] / Torque [Nm]	81 at 4800-6000rpm / 200 at 1500-3500rpm
Engine capacity [cm ³]	1395
Engine Stop-Start system	Yes
Emission Standard	Euro 6b
Aftertreatment system	TWC

SPN<23nm particle detection acquired using DTT exhaust gas sampling system. The system consists of two porous tube dilutors, the first dilutor is heated to avoid condensations, along with a catalytic stripper (CS) and ejector diluter (ED). In the DTT sampling system three particle detection devices attached. Two of them were CPC based and the other one using particle charging technology (EEPS). The DTT system addresses the issues that previous researchers raised regarding the sub-23nm measurement feasibility (Giechaskiel, et al., 2014). Thus, DTT system yields a dilution system with low particle losses in the sub-23nm region with a CS optimized for accurate determination of sub-23nm particles. In particular, by introducing porous tube dilutor, thermophoretic losses were reduced to almost zero. The dominating source of diffusional losses are reduced by optimizing – downsizing the CS. Artefact formation was very low proving excellent performance.

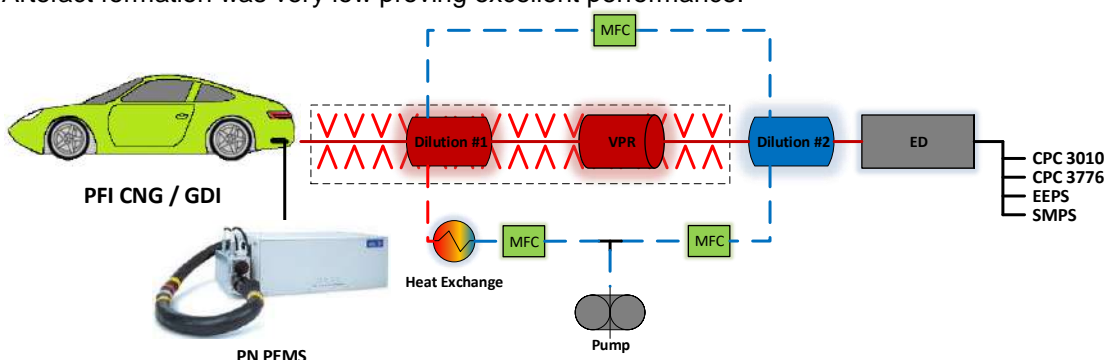


Figure 1 E.U. HORIZON 2020 DownToTen sampling system attached to the exhaust tailpipe. PN PEMS connected to the tailpipe for SPN>23nm measurements.

In addition to the DTT system that was sampling in the exhaust line, a PN PEMS device was installed to the tailpipe for SPN>23nm measurements. The PN PEMS is a PMP compliant device, based on diffusion charging technology. During steady state runs an SMPS classifier also used to acquire particle size distributions. In order to avoid artefacts during measurements, the exhaust line was covered with

insulation. Technical specifications of the measurement devices are included in the following table (Table 2).

Table 2 Technical characteristics of particle detection instrumentation

	AVL PN PEMS	SMPS, TSI 3080	CPC, TSI 3776	CPC, TSI 3010	EEPS, TSI 3090
Particle size (nm)	SPN>23 (PMP)	10 - 1000	2.5	10	5.6 - 560
Concentration range (#/cm³)	3000 – 2*10 ⁷	108	0 – 3*10 ⁵	0 - 10000	300 – 107 (5.6nm) 3 – 105 (560nm)
Time resolution	10Hz	30-120s	1Hz	1Hz	10 Size distributions/s
Particle detection technology	Diffusion Charging	Neutralizer and CPC	CPC based	CPC based	Unipolar charging

The Bi-fuel passenger car considered for this study was tested on steady state runs as well as under several driving cycles. Tests performed on a one-axis chassis dynamometer using road load settings calculated from a coast down test. Three types of test cycles were used, including WLTC, NEDC and SRC. Main idea was to conduct measurements in various test cycles to have a better understanding of particle emission performance under different engine loads.

In order to acquire a large amount of experimental data, 23 laboratory tests were performed on the chassis dynamometer. Engine preconditioning and soaking was mandatory prior to each measurement day. Warm up time, calibration and zeroing it was applied to every device so as to maintain high level of measurement validity. Prior the chassis dyno testing, a coast down test was performed to acquire the real-world road load. Regarding fuel testing sequence, CNG fuel tested at first since it was the primary fuel since no selection capability between two fuels was applicable. After depletion of CNG, engine ECU switched automatically to Gasoline. Typical fuel properties of CNG and gasoline are listed in Table 3 as extracted from literature (Heywood, 1988) (Vogler, et al., 2018).

Table 3 Fuel characteristics

Parameter	Gasoline E0	CNG
Chemical formulae	C4-C12	CH4
State at NTP conditions	Liquid	Gas
Density at STP [kg/m ³]	730	0.79
Octane number [-]	84-95	120+
Lower Heating Value [MJ/kg]	43.5	48.5
H/C ratio [-]	2.0:1	3.9:1

Results and discussion

In Figure 2, the aggregated particle emissions [#/km] for both fuels are depicted. With light green background colour are the CNG results whereas with light yellow background colour are the Gasoline ones. As it can be seen, blue bars which correspond to SPN>23nm particle emissions measured with PMP compliant PN PEMS, are all within current EURO 6 limits (6×10^{11} #/km). As the particle emission investigation expands to a greater range, emission results are increasing for both fuels. Emissions results for SPN>10nm, SPN>5.6nm and SPN>2.5nm, are in the same level for both fuels. This indicates that PFI CNG operation reveals comparable particle emissions with GDI mode in the sub-23nm region. In addition to that, sub-23nm particle emissions are beyond EURO 6 limits in almost all particle size ranges.

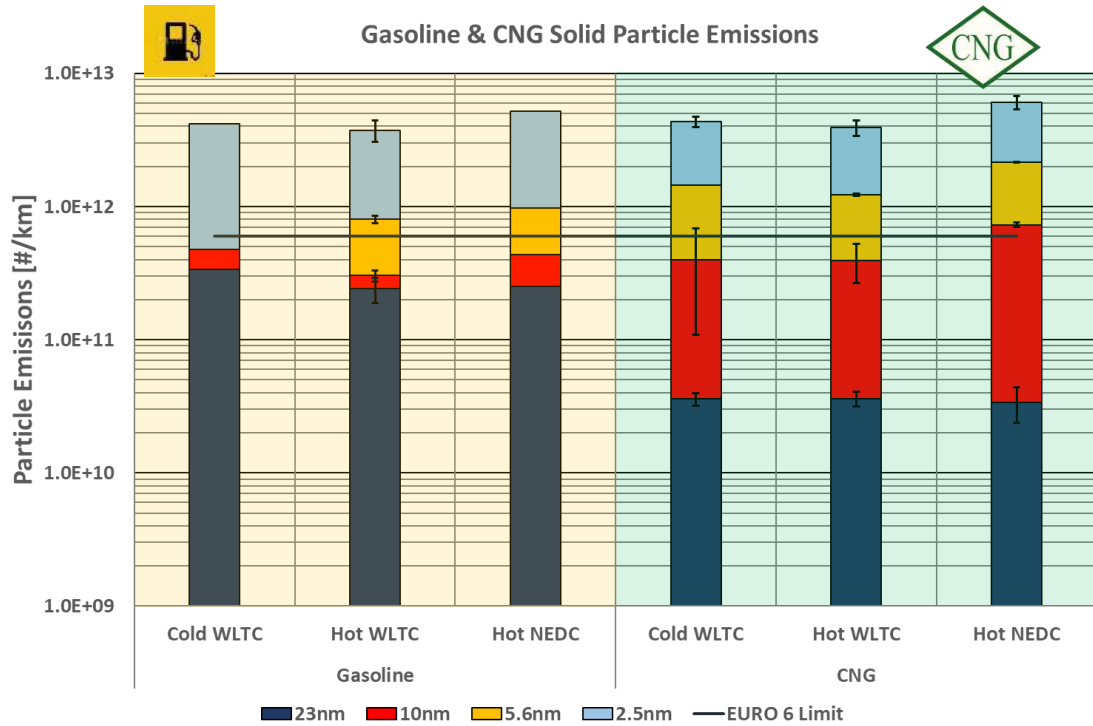


Figure 2 Aggregated SPN emissions for Gasoline (light yellow) and CNG (light green). Error bars shown the standard error of the mean including 2 to 4 repetitions. Emission bars with no error bar indicating unique measurement. Emission limit corresponds to EURO 6 (6×10^{11} #/km)

Figure 3 illustrates the SPN ratios together with mean particle concentration values of SPN>23nm. In particular, SPN10nm/SPN23nm, SPN5.6nm/SPN23nm and SPN2.5nm/SPN23nm are presented from darker to lighter green. As can be seen, CNG SPN10nm/SPN23nm ratios are much higher compared to Gasoline values. This is indicative of higher sub-23nm particle emissions during CNG than Gasoline operation. In other words, GMD of CNG is shifted towards nucleation mode particles.

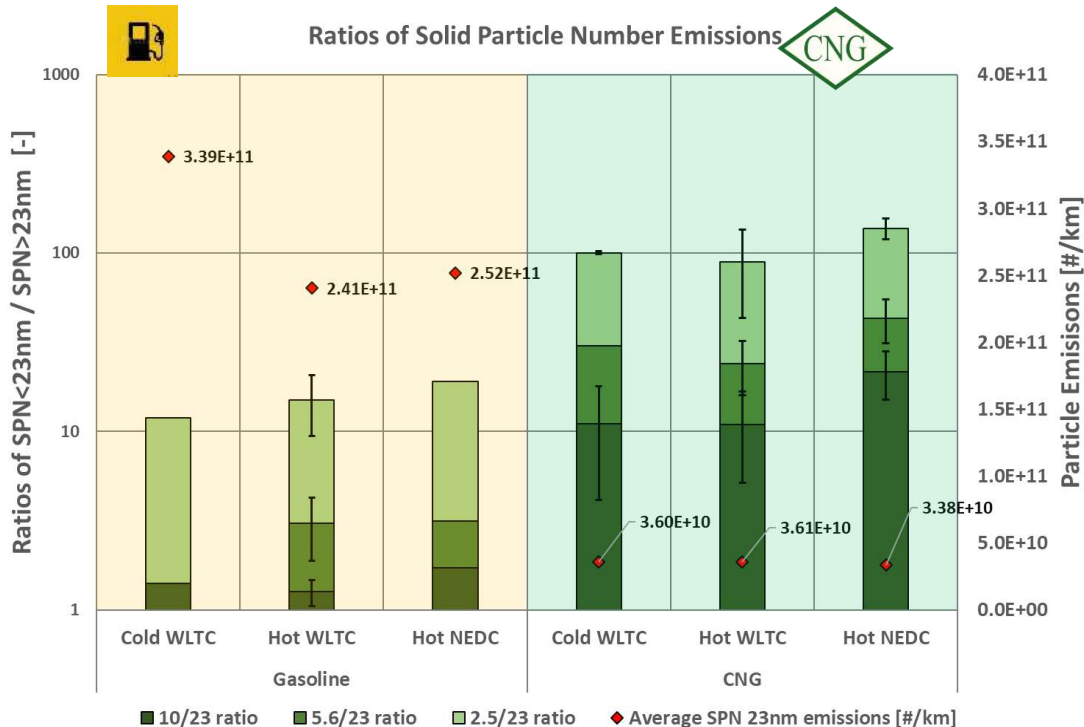


Figure 3 SPN ratios bars are depicted from darker to lighter green. Average values of SPN>23nm particle emissions are presented with red diamonds. Error bars show the standard error of 2 to 4 repetitions. Emission bars with no error bar indicating unique measurement.

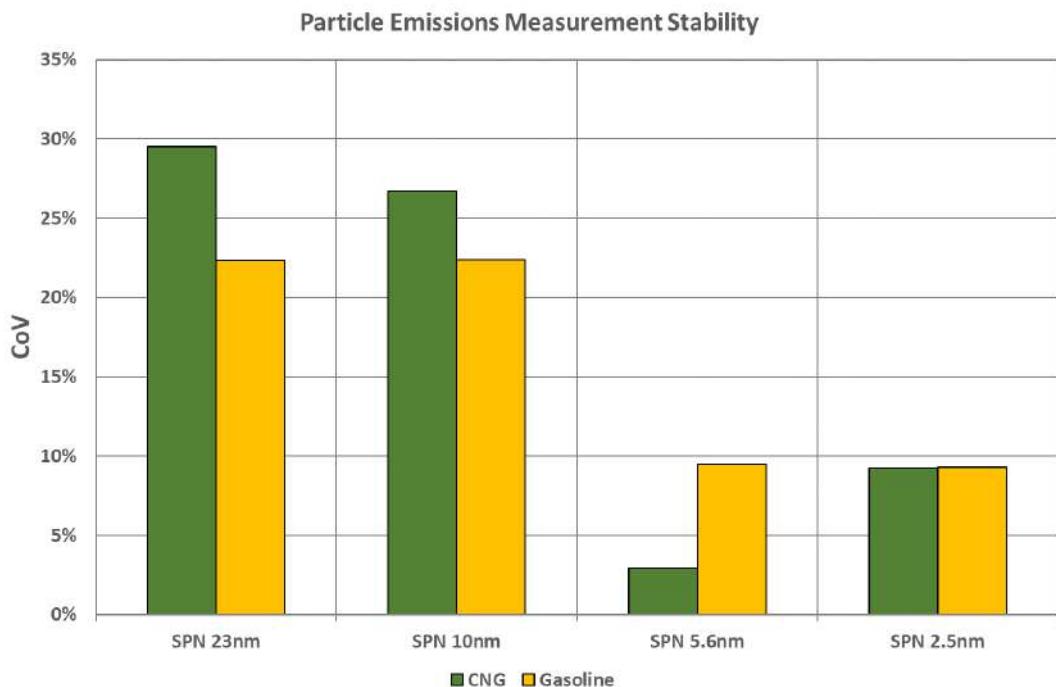


Figure 4 Particle emission measurement stability for each cut off size category.

In Figure 4 the measurement repeatability is depicted. For that reason, the statistical parameter of covariance (CoV) was used, which is the standard deviation of each measurement category over the average value of all measurements in the same category. There are four categories that correspond to different cut-off particle sizes. CoV function is presented herein.

$$CoV_{SPN} = \frac{S_{SPN}}{SPN}$$

Figure 4 results, after outlier removal, shown significant drop from 30% for CNG and 22% for Gasoline to 9% for both fuels. Since this engine produces particles in the ultrafine region below 23nm, as the measurement widens to sub-23nm particle detection, measurement reproducibility is getting optimized since the nucleation mode captured better from the sub-23nm particle detection devices. Same trend also revealed from other researchers that were investigating in the sub-23nm region (Giechaskiel, et al., 2019). CoV of Gasoline has better reproducibility than CNG from early stages, since Gasoline PSD is

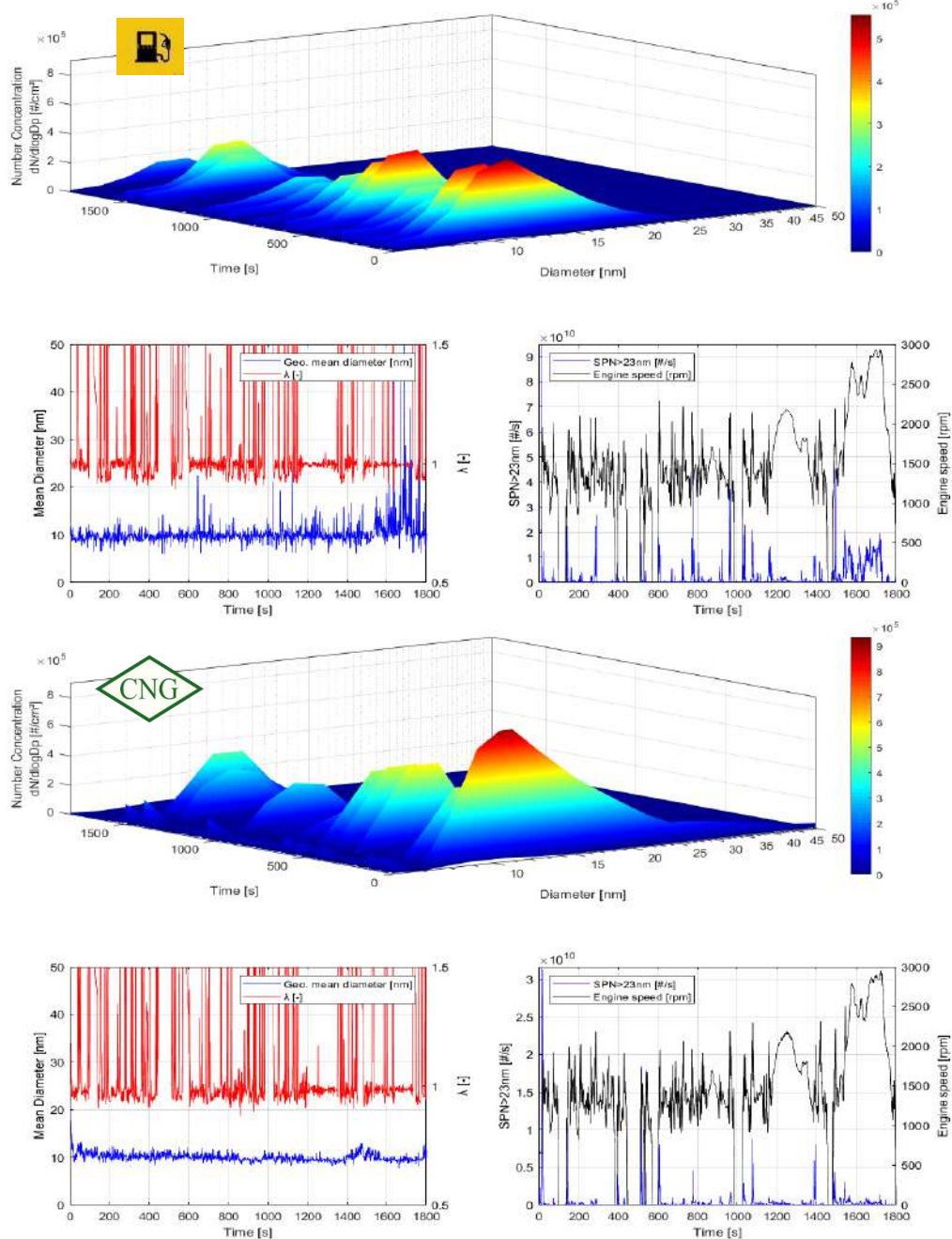


Figure 5 PSD profiles (3D map), with Lamda (red, bottom left) Dg (blue, bottom left) and SPN>23nm particle emissions (blue, bottom right) for Gasoline (top) and CNG (bottom) during Hot WLTC

shifted towards a greater GMD and thus, particle detection with reproducible manner from early stages. CoV parameter for both fuels was constantly below 10% after SPN<5.6nm.

In Figure 5 the time series of particle concentration, GMD and PSD profiles are presented. Figure data referred to Hot WLTC measurements for Gasoline (top) and CNG (bottom). GMD of gasoline is higher

than CNG, as it can be seen at the bottom left graph, that confirms initial finding of CNG smaller particles. What is remarkable is that GMD of GDI tends to increase in higher loads in contrast to CNG PFI which is getting slightly lower during high loads. In addition, large peaks of GMT being observed under heavy loads, immediately after fuel cut events, during fuel enrichments (equivalence ratio in red) that is leading to the fact that fuel impingement is prevalent when engine is running under GDI mode. In CNG PFI operation same events cannot be seen.

Those two trends indicate that the PSDs of GDI and PFI CNG change during the cycle and strongly depended to the engine load. As regards GDI GMD behaviour, this, mainly has to do with higher carbon content of gasoline which corresponds to soot related particles during rich mode and high engine loads. Wall impingement of fuel spray should not be neglected, as it is largely affecting pool fire events and thus soot related particles. Regarding GDI engine particle emission performance there is ample piece of information that reader may find in the literature (Raza, et al., 2018).

On the other hand, the absence of C-C bonds in CNG PFI and the low carbon content (Table 3) aren't able to promote particles in larger diameters. One possible explanation of nucleation mode particle emissions during CNG PFI operation is the lubrication. Lubrication related particle emissions can be attributed to escaping oil from valve stems and piston rings which could be a sign of engine wear. Another source is the exposed bore oil during combustion which could be evaporate in the exhaust line (Eastwood, 2008), that potentially generate nucleated particles under intense combustion process (Mayer, et al., 2010). Since no significant particle emissions can be observed during deceleration phases (Figure 6 deceleration phase within red dashed circle), which can be attributed to escaping lube oil, high sub-23nm particle emissions can be attributed to exposed lube oil during combustion. The combination of different CNG fuel characteristics when compared to gasoline and the exposed bore oil under different combusting phenomena that occurring in CNG (Vogler, et al., 2018) (Catapano, et al., 2017), is able to magnify sub-23nm particle emissions.

Instantaneous particle emissions measurements are presented in Figure 6. Sub 23nm particle emissions including SPN>2.5nm (orange) and SPN>10nm (red) are also depicted. In red dashed circle the final phase of WLTC cycle (extra high) is underlined for both fuels. What can be seen here is that PFI CNG operation reveals higher SPN>2.5nm emissions than GDI engine operation. The extra high WLTC phase corresponds to higher engine loads, thus, it can be concluded that CNG PFI engine operation emits higher sub-23nm particle emissions than GDI during high engine demand.

As regards ignition timing, illustrated in blue dots, the studies that includes both particle emissions measurement and ignition timing evaluation are limited. The majority of these studies are focused on GDI engines without GPF, along with or without TWC under steady state operating points instead of transient ones, such as the current case (Ketterer, et al., 2014) (Price, et al., 2007) (Qin, et al., 2014). The general trend, as previous researchers discovered, is that as the ignition timing advances, particle emissions increase during steady state operation. Having in mind the measurements conducted under transient conditions during this study, no clear evidence of strong correlation between ignition timing and particle emissions can be seen until the three quarters of the cycle. Advanced ignition timing promotes higher exhaust gas temperature inside the cylinder, which can also contribute to nucleation mode. This trend also revealed during CNG PFI operation. From Figure 5, in the 1200s – 1600s region, as the ignition timing advances and towards higher exhaust gas temperature, engine load and speed, GMD decreases. Similar trend cannot be observed in GDI, in fact it's the opposite behavior that may indicate fuel impingement in cylinder walls that promotes soot related particles.

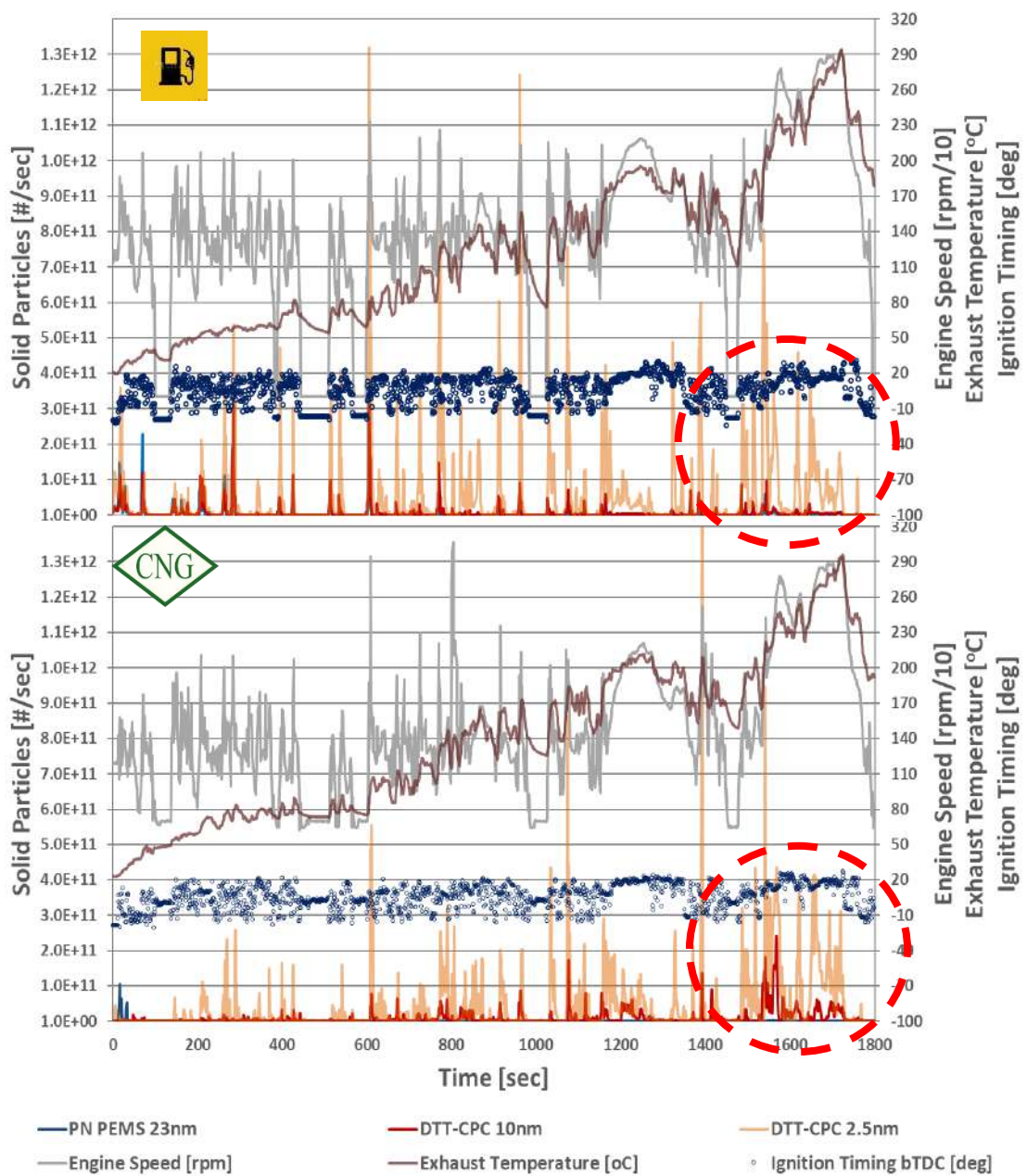


Figure 6 Instantaneous particle emissions including sub 23nm cut of sizes. The blue dots represent ignition timing events given in degrees of bTDC. The negative values represent retard ignition while the positive ones represent advance ignition. Exhaust

Summary and Conclusions

The purpose of this study was to investigate a CNG equipped passenger car in terms of sub-23nm particle emissions. Measurements performed using E.U. Horizon 2020 DownToTen sampling system that allows tailpipe testing using different particle detection devices. Conclusion of measurement campaign listed herein.

- CNG PFI engine operation reveals beyond EURO 6 limits particle emissions in the sub-23nm area. During measurements at the sub-23nm particle detection level, emissions were comparable to GDI engine operation.
- During CNG combustion, GMD was smaller compared to GDI operation, indicating that CNG PSD were located closer to nucleation mode particles.
- During high load GDI engine operation, the GMD was getting larger in contrast to PFI CNG operation which was getting smaller.
- During WLTC cold measurements, CNG operation has revealed higher sub-23nm SPN emissions in the extra high phase of WLTC in contrast to gasoline operation, this corresponds to higher sub-23nm SPN emissions than gasoline at higher engine loads.
- Sub-23nm particle emissions can be attributed to exposed lube oil during combustion. Further chemical characterization of sub-23nm particle emissions is needed.
- GPF installation considered as mandatory if the current regulation EURO 6 limit for sub-23nm particle emission is to be met.

Abbreviations

PSD: Particle size distribution

GMD: Geometric mean diameter

PFI: Port Fuel Injection

GDI: Gasoline Direct Injection

SPN: Solid Particle Number

CNG: Compressed Natural Gas

EEPS: Engine Exhaust Particle Sizer

CPC: Condensation Particle Counter

GPF: Gasoline particulate filter

TWC: Three-way catalyst

PEMS: Portable emission measurement system

ECU: Electronic control unit

CVS: Constant Volume Sampling

ED: Ejector diluter

CS: Catalytic stripper

WLTC: Worldwide harmonized Light vehicles Test Cycles

NEDC: New European driving cycle

SRC: Standard Road Cycle

PMP: Particle measurement programme

Acknowledgement

This work is conducted in the framework of the H2020 DownToTen project. This project has received funding from the European Union's Horizon 2020 research and innovation programme under grant agreement Nr. 724085

Conflict of Interest

The authors declare that there is not any conflict of interest with this work.

References

- ACEA** Economic and Market Report EU automotive Industry Quarter 2 2018 [Report]. - October 2018.
- Barouch Giechaskiel Giorgio Martini** Engine Exhaust Solid Sub-23 nm Particles: II. Feasibility Study for Particle Number Measurement System [Article] // SAE Int. J. Fuels Lubr. - [s.l.] : SAE International, November 2014. - 3 : Vol. 7.
- Barouch Giechaskiel Tero Lähde, Yannis Drossinos** Regulating particle number measurements from the tailpipe of light-duty vehicles: The next step? [Article] // Environmental Research. - [s.l.] : ELSEVIER, 4 February 2019. - pp. 1-9.
- Cachón L., Tóth D. and Pucher E.** Real-world Emission Measurements of a High Efficient Monofuel CNG Light Duty Vehicle [Conference]. - [s.l.] : SAE International, 2009.
- Catapano Francesco, Di Iorio Silvana and Sement Paolo** Particle Formation and Emissions in an Optical Small Displacement SI Engine Dual Fueled with CNG DI and Gasoline PFI [Article] // SAE International. - 2017.
- Cedric Louis Yao Liu, Simon Martinet, Barbara D'Anna, Alvaro Martinez Valiente, Antoinette Boreave, Badr R'Mili, Patrick Tassel , Pascal Perret, Michel Andre** Dilution effects on ultrafine particle emissions from Euro 5 and Euro 6 diesel and gasoline vehicles [Article] // Atmospheric Environment. - [s.l.] : ELSEVIER, 2017. - 169. - 80-88.
- Eastwood Peter** Particulate emissions from Motor Vehicles [Book]. - [s.l.] : Wiley, 2008.
- Heywood John B.** Internal Combustion Engine Fundamentals [Book]. - New York : McGraw-Hill Book Company, 1988. - ISBN 0-07-028637-X.
- Hinds William C.** Aerosol Technology: Properties, Behavior, and Measurement of Airborne Particles [Book]. - 1982.
- Jian Xue Yin Li, Joshua Peppers, Chao Wan, Norman Y. Kado, Peter G. Green, Thomas M. Young, and Michael J. Kleeman** Ultrafine particle emissions from natural gas, biogas and biomethane combustion // Environ. Sci. Technol.. - [s.l.] : DOI: 10.1021/acs.est.8b04170, 2018.
- Kento T. Magara-Gomez Michael R. Olson, Jerome E. McGinnis, Mang Zhang, James J. Schauer** Effect of Ambient Temperature and Fuel on Particle Number Emissions on Light-Duty Spark-Ignition Vehicles. - Madison Wisconsin : Aerosol and Air Quality Research, 2014. - doi: 10.4209/aaqr.2013.06.0183.
- Ketterer Justin E. and Cheng Wai K.** On the Nature of Particulate Emissions from DISI Engines at Cold-Fast-Idle [Article] // SAE International Journal Engines. - July 2014. - 2 : Vol. 7.
- Loctier Denis** Measuring pollution: the tiny nanoparticles causing big health problems [Article] // EURNEWS . - [s.l.] : EURNEWS, 20 02 2019.
- M.I.Jahirul H.H.Masjuki, R.Saidur, M.A.Kalam, M.H.Jayed, M.A.Wazed** Comparative engine performance and emission analysis of CNG and gasoline in a retrofitted car engine [Article] // Applied

Thermal Engineering. - [s.l.] : ELSEVIER , October 2010. - 14 -15 : Vol. Volume 30. - pp. Pages 2219-2226.

Mamakos Athanasios, Ntziachristos Leonidas and Samaras Zissis Comparability of particle emission measurements between vehicle testing laboratories: a long way to go [Article] // Measurement Science and Technology. - [s.l.] : Institute of Physics Publishing, 6 August 2004. - 15. - pp. 1855-1866.

Markowski Robert gazeo.com [Online]. - 25 07 2017. - 21 01 2019. - <https://gazeo.com/up-to-date/reportages-interviews-road-tests/road-tests/Skoda-Octavia-G-TEC-makes-sense-but-doesn't-report,9857.html>.

Mayer Andreas [et al.] Metal Oxide Particle Emissions from Diesel and Petrol Engines [Article] // SAE International. - [s.l.] : SAE International, 16 04 2012. - 2012-01-0841.

Mayer Andreas, C. [et al.] Metal-Oxide Particles in Combustion Engine Exhaust [Article]. - 2010. - SAE International.

NGVA Europe Statistical Report 2017 [Report]. - 2017.

Nils-Olof Nylund Kimmo Erkkilä, Maija Lappi & Markku Ikonen TRANSIT BUS EMISSION STUDY: COMPARISON OF EMISSIONS FROM DIESEL AND NATURAL GAS BUSES [Report]. - [s.l.] : VTT, 2004.

Nithyanandan Karthik [et al.] Characterization of soot from diesel-CNG dual-fuel combustion in a CI engine [Article] // Fuel. - [s.l.] : Elsevier BV, 2016. - Vol. Vol. 184. - pp. Pages 145-152. - ISSN: 0016-2361.

Owen Keith and Coley Trevor Automotive Fuels Reference Book [Book]. - [s.l.] : Society of Automotive Engineers, 1995. - 1-56091-589-7.

Price Philip [et al.] Particulate and Hydrocarbon Emissions from a Spray Guided Direct Injection Spark Ignition Engine with Oxygenate Fuel Blends [Article] // SI Combustion. - [s.l.] : SAE International, 2007.

Qin Jing, Li Xiang and Pei Yiqiang Effects of Combustion Parameters and Lubricating Oil on Particulate Matter Emissions from a Turbo-Charged GDI Engine Fueled with Methanol/Gasoline Blends [Article] // SAE Technical Paper. - 13 10 2014. - 2014-01-2841.

Raza Moshin [et al.] A review of Particulate Number (PN) Emissions from Gasoline Direct Injection (GDI) Engines and Their Control Technologies. - [s.l.] : Energies, 2018. - Vol. 11. - doi: 10.3390/en11061417.

Schreiber D. [et al.] Particle Characterisation of Modern CNG, Gasoline and Diesel Passenger Cars [Conference] // 8th International Conference on Engines for Automobiles / ed. Empa Swiss Federal Laboratories for Materials Testing and Research, Laboratory for I.C. Engines. - [s.l.] : SAE Technical Paper, 2007.

Stone Richard INTRODUCTION TO INTERNAL COMBUSTION ENGINES [Book]. - New York : PALGRAVE MACMILLAN, 2012. - 4th Edition : pp. 171-172. - ISBN 978-0-230-57663-6.

Transport & Environment CNG and LNG for vehicles and ships - the facts [Report]. - Brussels : [s.n.], October 2018.

Urs Mathis Jyrki Ristimaki, Martin Mohr, Jorma Keskinen, Leonidas Ntziachristos, Zissis Samaras, and Pirlita Mikkonen Sampling Conditions for the Measurement of Nucleation Mode Particles in the Exhaust of a Diesel Vehicle [Article] // Aerosol Science and Technology. - Dubendorf, Switzerland : ELSEVIER, 2004. - 1521-7388.

Vogler Christian [et al.] Downsized Engine optimised for CNG Operation [Article] // 11. Tagung Einspritzung und Kraftstoffe 2018. - [s.l.] : Springer Fachmedien Wiesbaden, 2018. - pp. 499-513.

Yusaf Talal F., Buttsworth D. R. and Khalid Saleh H. CNG-diesel engine performance and exhaust emission analysis with the aid of artificial neural network [Article] // Applied Energy. - 2010. - Issue 5 : Vol. Vol. 87. - pp. Pages 1661-1669. - ISSN: 0306-2619.

Zissis Samaras Leonidas Ntziachristos, Georgia Parpori Down To Ten [Online]. - <http://www.downtoten.com/>.

2.10 New sensors and techniques

This section includes papers presented in the context of the “New sensors and techniques” sessions of the TAP conference. Table 11 provides an overview of these papers, as they are listed in the following sub-sections.

Table 11. Titles and authors of the “New sensors and techniques” papers

	Paper Title	Authors
2.10.1	Development and test of a new device collecting at source airborne particles issued from rolling stocks brakes systems	P. Clement, L. Adamczak, A. Maistre, F. Ghozzi and V. Nicot
2.10.2	Real-E: Robust and affordable IoT solution for market surveillance	P. Dégeilh, J. Kermani, S. Rodríguez, L. Thibault, A. Frobert and G. Corde
2.10.3	Development of a Low-Cost Quartz-Enhanced Photoacoustic Spectroscopy Nitrogen Dioxide Sensor Network for Air Pollution Measurements	P. Breitegger, M. Knoll and A. Bergmann
2.10.4	Making sense of variability in real-world vehicles emissions	C. Le Cornec, N. Molden and M. Stettler
2.10.5	Ultrafine particle dispersion in the wake of a squareback vehicle model	R.Rodriguez, F.Murzyn, A.Mehel and F.Larrarte

2.10.1 Development and test of a new device collecting at source airborne particles issued from rolling stocks brakes systems

Philippe CLÉMENT¹, Loïc ADAMCZAK², Adrien MAISTRE², Fayes GHOZZI³ and Vincent NICOT¹

¹Rolling stock engineering, SNCF Mobilités, Le Mans, Pays de la Loire, 72100, France

²Tallano Technologie, Boulogne-Billancourt, Boulogne, Ile de France, 92100, France

³Rolling stock engineering, SNCF Mobilités, Vitry/Seine, Ile de France, 94400, France

Keywords: railway, underground station, air quality, brake wear, emission, particle matter, collection

Presenting author email: philippe.clement@sncf.fr

Introduction

The paper exposes the studies realised on air quality measurements and on conception, development and experimentation of a new device that collects particles emitted by trains braking systems.

Railway transportation is well known to be the most effective mode in term of environmental impacts. This public transportation mode reduces traffic congestion and pollutants emissions by limiting the use of personal vehicles (Martins et al., 2015a; Xu and Hao, 2017). Energy loss free of wheel / rail contact, efficient aerodynamic of convoys, huge load capacity of mobiles on track and long-life duration give an unbeatable advantage in term of energy and raw materials consumption per passenger.km or ton.km.

With the responsible will to lower even more its impacts, the rail sector sets out specific environmental objectives on four key environmental topics: climate protection, energy efficiency, exhausts emissions and noise¹⁵. 28 European members of UIC (Union Internationale des Chemins de fer) have thus collectively committed with CER (the Community of European Railway and Infrastructure Companies) to reduce by 2030 their CO₂ emissions per passenger.kilometre and ton.kilometre by 50%, and their diesel engines exhaust emissions of NOx and PM10 by 40% in absolute terms even with projected traffic growth compared to 2005. They are well on track to meet this target. However, engines exhaust emissions from trains are not their only source of air pollution.

In underground railway surroundings, a specific pollution exists in addition to contaminants entering from the outside atmosphere, bound to rolling stock exploitation that generates fine particles, and their evacuation is strongly limited by the confinement (Martins et al., 2015a). Most of the particles in underground stations are issued from mechanical braking of the rolling stocks (Burkhard 2007). Studies have mainly focused on the understanding of phenomena: characterisation of airborne particles (Fortin 2005 - Abbasi 2011) and simulation of air flow in underground stations (Durand 2017). Though it is still necessary to clarify the sanitary impact of the dusts, it is necessary to decrease levels of concentration. Several solutions to improve air quality in underground stations are under experimentations:

- Ventilation in stations with new motors for smoke extraction to improve the renewal of air,
- Air treatment experimentation, one by ionization and the other one by humid filtration,
- Selection of the less emissive brake shoes and pads,
- Collecting at source airborne particles issued from rolling stocks brakes systems.

Other solutions are also studied as the use of hybrid traction systems for work trains operating in tunnels or the modification of the combination between electrical and mechanical braking of trains.

Air quality in underground stations - Stakes and challenges

Air quality is a growing concern in the world. Air pollutant exposure has been extensively studied by Pope and Dockery, 2006; Dockery et al. 1993; Araki et al.; 2010 and approved to be a vital cause of increased perceivable health risk (Xu and Hao, 2017). More recently, outdoor air pollution is considered as a leading environmental cause of cancer deaths (Loomis, 2013). The World Health Organisation

¹⁵ Moving towards Sustainable Mobility: European Rail Sector Strategy 2030 and beyond (UIC-CER)

(WHO) has established in 2005¹⁶ that air pollution is a major environmental risk to health. The WHO provides an assessment of health effects of air pollution and thresholds for health-harmful pollution levels (example in Table 1).

Coarse Particulate Matter (PM10)	20 µg/m ³ annual mean 50 µg/m ³ 24-hour mean
Fine Particulate Matter (PM2.5)	10 µg/m ³ annual mean 25 µg/m ³ 24-hour mean

Table 1 - WHO Particulate matter guideline values Numerous studies concerning levels of PM have been reported in many subway systems in the world (Xu and Hao, 2017; ANSES, 2015 and references therein): Barcelona, London, Rome, Milan, Taipei, Seoul, Guangzhou, Los Angeles, Mexico City, New York, Shanghai, Paris, etc. All the results are not always directly comparable because of specificities of sampling and measurements methods, data analysis, duration of the measurements and type of environment studied (Martins et al., 2015a).

Air quality measurements revealed that PM are composed up to 50% of metallic elements, originating railway material wears: braking systems (mostly), wheel, rail, pantograph and catenary (AEF, 2017). The influence on health of this specific composition of air in underground station has not yet been established (ANSES, 2015 and references therein). It appears that in underground stations, the air quality depends mainly on the following factors: length and design of the station and tunnels; depth; system of ventilation (performances and maintenance); number of travellers; speed and frequency of trains; system age (Martins et al., 2015a and references therein; AEF, 2017).

Annual and continuous measurements in several underground stations in Paris-France have been realised since 2016 by SNCF Mobilités (AEF, 2017) and AirParif to characterise the air quality (AirParif is an organization accredited by the Ministry of Environment to monitor the air quality in Paris and in the Ile de France region). Figure 1 shows two French underground stations Magenta and Avenue Foch where measurements were conducted. For example, the PM10 and PM2.5 annual average concentration in Magenta (Paris) during year 2016 were respectively 38µg/m³ and 13 µg/m³. In Avenue Foch (Paris) the average concentration was 207µg/m³ for PM10 and 79 µg/m³ for PM2.5 during the measurement week in October 2016.

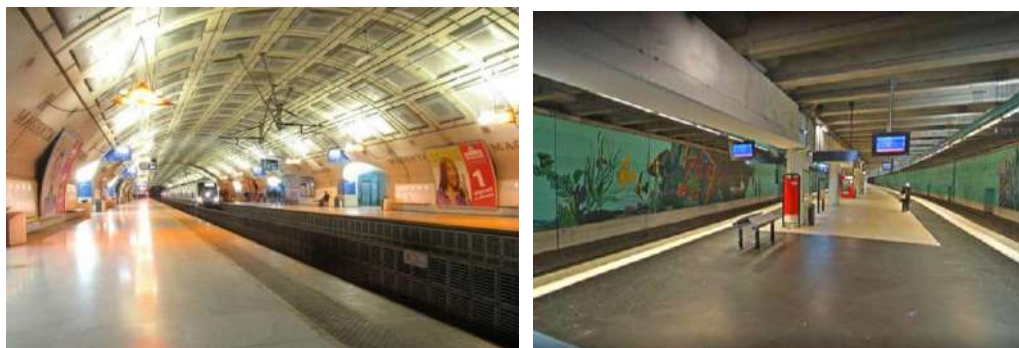


Figure 1: Magenta station (left - built in 1999) / Avenue Foch station (right - 1st built in 1854)

For the same year, the average values for ambient air in Paris were 21µg/m³ for PM10 and 13 µg/m³ for PM2.5. As said above, differences in air composition between ambient air in Paris, ambient air for the WHO studies, and air in underground stations don't permit to formulate any conclusion on health impacts for the moment.

The daily profiles (Figure 2) reveal two peaks of concentrations in particles measured during rush hours in the morning (8h-12h) and in the evening (18h-22h). PM concentrations are correlated to the number of trains and number of travellers in Magenta station. These profiles also revealed a fall of concentration at night when the station is closed. A decrease of 20% for the PM10 and 15% for the PM2.5 is observed during the weekends. (AEF, 2017)

¹⁶ The WHO Air Quality Guidelines: Global Update 2005

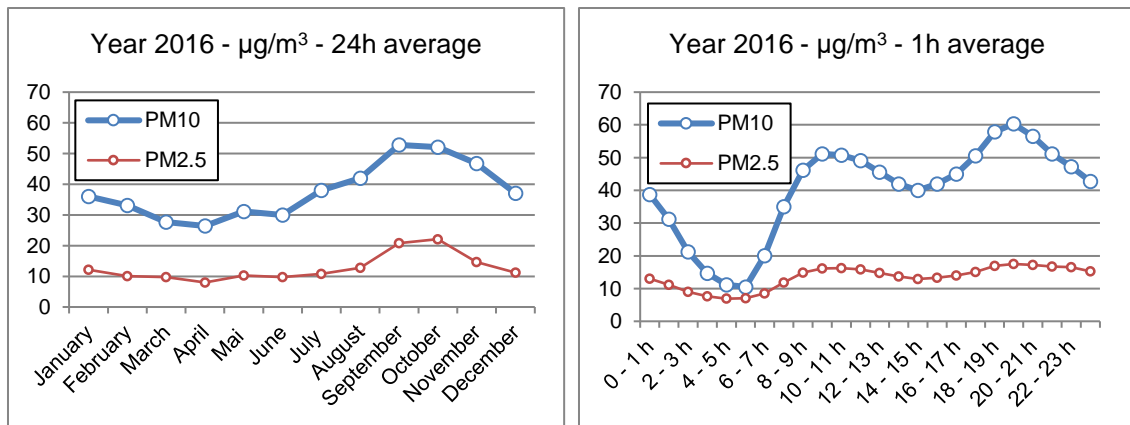


Figure 2: Daily concentration of PM in Paris Magenta station

Air quality measurements on bench

The braking systems being the main source of emission, it has been developed test benches to quantify and to analyse pollutions emitted out by the wear of braking pads + discs and of braking shoes + wheels of trains (Figure 3).

The bench permits to test real operating conditions or specific ones at speed up to 500 km/h.

The installation is design to:

- Assess braking performance and endurance for “disc-pad” and “wheel-shoe” combinations,
- Conduct tests for wheel thermomechanical resistance and failure,
- Estimate life cycle costs: Weighing of pads and shoes + measuring disc and wheel profiles.

The usual measurements realised during the tests are:

- Friction and stress coefficients,
- Noise during braking (initial noise and dBA level),
- Temperature,
- Wheel deflection by means of optical sensors,
- Surface roughness,
- Pollutant emissions into the air.

To qualify air pollutants emitted by a brake block, tests are conducted during raw material characterizations on brake pads in laboratory and during braking sequences on a brake testing bench.

An aeraulic system on a bench capture dusts emitted out by braking systems and drive them through a tube in which are done the different withdrawals and analysis (Figure 4):

- Composition of particles and gases: metallic elements, volatile organic compounds, fibres...,
- Real time measurement of emissions according to the different parameters of braking,
- Determination of the size and/or number of particles: from some nanometer to several tens of microns.



Figure 3: Test rig for railway braking systems



Figure 4: Measurement device of emissions due to braking systems

The tests can also be used to evaluate the impact of braking parameters on emissions (succession, strength...). Data can serve for the development of numeric models to simulate the particle scattering.

At source collection system: Operating principle

The brake pads and disc wear out during contact and release particles (Figure 5). To remedy this, it has been developed an at source collection system to meet the challenges of railway of today and tomorrow.



Figure 5: Visualization of particles released during braking

The train when braking automatically triggers a signal, which is transmitted to an electronic card controlling high performance suction turbines (Figure 6).



Figure 6: High performance turbines

The brake pads are modified to maximize the capture at the source of the micro particles emitted by the braking system (Figure 7).

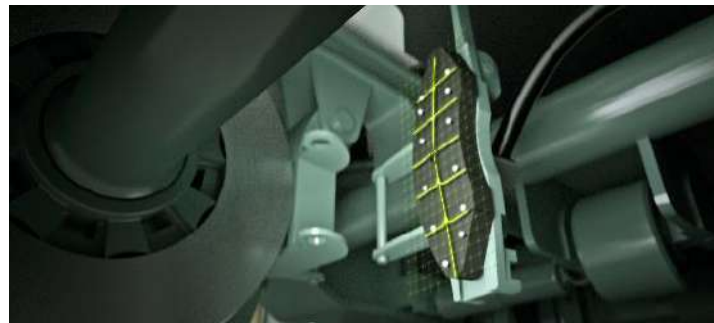


Figure 7: Modified brake pads

Two suction channels allow the collection and transportation of the aspirated dust (Figure 8).

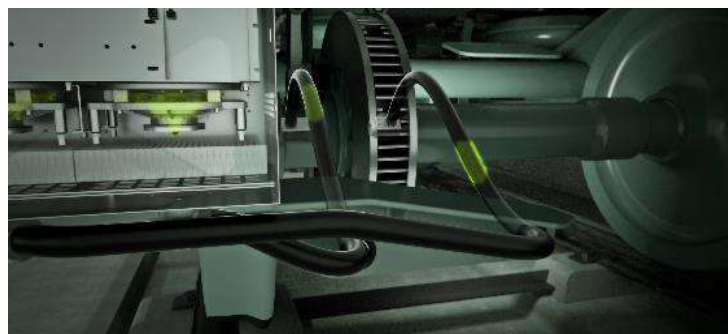


Figure 8: Suction channels

The dust is trapped and stored in specifically developed filters (Figures 9 and 10).

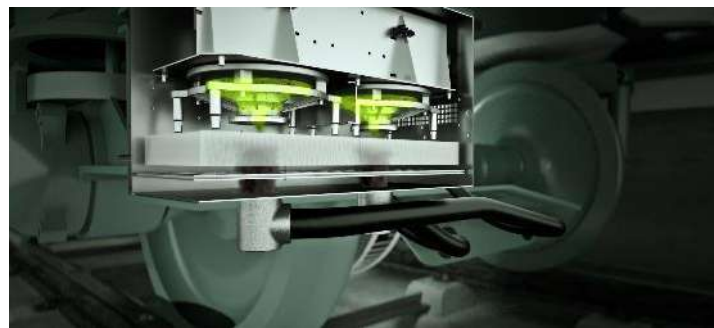


Figure 9: Filtration



Figure 10: Filter replacement

Automotive background

The system was first developed for automotive applications. Whatever the application, railway or automotive, braking is a quite complex process. Depending on speed, weight and deceleration levels,

and so on pressure and temperature induced, different amounts of gases are emitted. Metals oxidation may occur or not. And different amounts of ultrafine, fine and coarse particles are emitted.

Concerning airborne particles emitted during braking, more and more studies are now available. They all show that mainly PM10 particles are emitted during braking and the size distribution varies with the braking conditions (Olofsson 2010; Namgung et al. 2017). So, there is a need to collect and retain such a broad distribution. From nano to micro particles.

To collect these particles, we did study the prior art and different solutions were developed. The best results were obtained with the solution presented on Figure 11. A groove is machined at the trailing edge of the pads. Particles are collected before they leave the pad-disc contact.

Based on CFD simulations and designs of experiments, we optimized the shape and location of this groove. And we defined the negative pressure and the flow rate levels needed to collect most of the big and small particles.

This allowed us to design our aspiration system. It relies on pipes connected to a turbine equipped with a filter to trap wear particles. The filter developed with our filtration partner allows to cope with the large distribution of brake dust particle size. Figure 12 shows the efficiency levels for different particle sizes obtained with normalized ISO/TS 11155-1 testing procedure at 10 cm/s, which is the actual air speed in our filters.

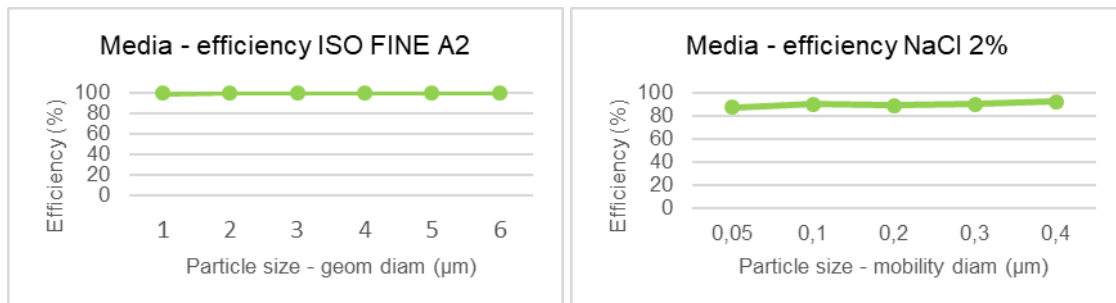


Figure 12: Media filter efficiency at 10 cm/s

The whole system is driven by an embedded electric brushless motor powered by the vehicle battery (Figure 13)



Figure 13: System mounted on a car

It has been tested on bench (>1800 hours) and vehicles (>700 hours on 3 different cars).

A mass efficiency above 85% has been achieved on both bench and car. So, more than 85% of the weight lost by the braking pads and disc rotor were collected by our system. No difference between bench and vehicle tests results shows that our solution is not influenced by the aerology within the wheel arch. As our system was added on existing callipers, to avoid any influence of additional drag torque, the entire tests presented here were performed with a continuous aspiration. The serial version of our system will only aspirate during braking events.

We also did implement particle number efficiency tests at Ilmenau University. The protocol is described in (Augsburg et al. 2018). A constant volume sampling system has been used with an inlet air filtered by an HEPA filter. The measurement devices were the following:

- Horiba Mexa-2100SPCS: Condensation Particle Counter – size range: 10 – 2500nm / Modified sub 23nm version
- Dekati ELPI+: Electrical low-pressure impactor – size range: 6 – 10000nm

A standard serial brake calliper with ECE pads has been used for the test. We did compare serial pads and pads and calliper modified to integrate our system.

For each test, a first run-in procedure of 150 brakes AK-Master section 3 (80->30km/h; 30 bar) was performed (SAE International, 2003). Then section 4.1 (40->5km/h; 10-80bar), 4.2 (80->40km/h; 10-80bar), 4.3 (120->80km/h; 10-80bar) and 4.4 (160->130km/h; 10-80bar) of AK master were performed. System efficiency compared to serial pads is displayed on Figure 14. A reduction potential of 50-90% with low mechanical stress and 50-80% with high mechanical stress could be proved. The highest reduction potentials were obtained in urban driving conditions. Which is very positive as pollution concerns are the highest in cities.

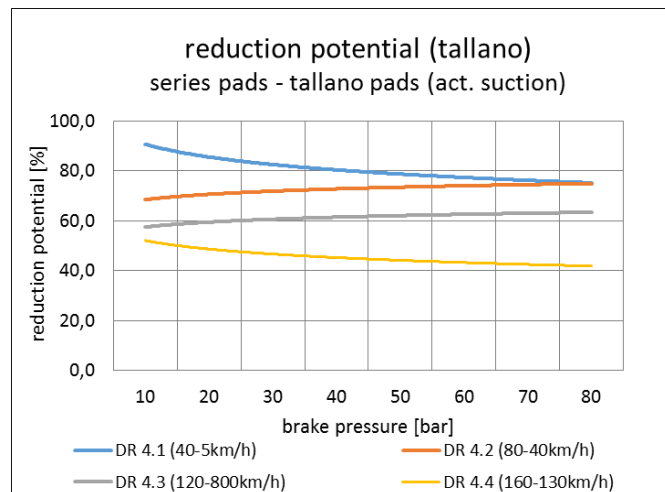


Figure 14: Number reduction potential in different driving conditions

We also did perform Laser Images in Ilmenau University in order to visualize the efficiency of our system. We could visualize the particles emitted during a braking event with and without our system (Figure 15). The high efficiency measured with the particle counters is confirmed.

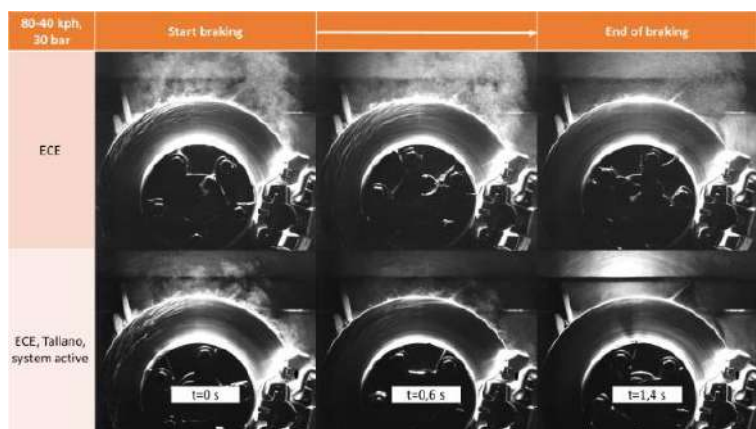


Figure 15: Laser Images with and without our system

Railway development

Building on our experience in automotive, we did the same for a suburban railway application. The main difference and challenge in railway applications is that our system must work in both directions on the contrary of automotive applications.

We first tried to modify as little as possible the actual groove pattern of standard railway pads used for suburban trains presented on Figure 16a. So, we designed the groove pattern presented on Figure 16b and modified the pads carrier (Figure 17) in order to connect a hose to aspirate the wear particles collected by the grooves. A specific suction housing with one turbine and one filter for each pad carrier has been designed.



Figure 16: (a) Standard groove pattern of suburban train pads
 (b) First groove pattern tested

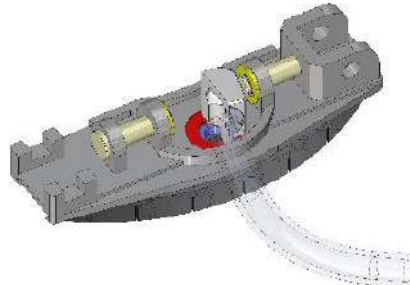


Figure 17: Pads carrier modification

In order to assess the collection efficiency of our system, a testing protocol has been defined based on Ile-de-France suburban trains operated on line C (called RER C). It consists of 10 cycles of 33 stop breakings, 2 speed hold breakings and 1 slow-down braking (Figure 18).

2x stop brakings 120 – 0 km/h, VOM	4x stop brakings 100 – 0 km/h, CN
1x slow-down braking 120 à 60 km/h, VOM	8x stop brakings 80 – 0 km/h, CN
2x stop brakings 120 – 0 km/h, VOM	5x stop brakings 60 – 0 km/h, CE
1x speed hold braking 120 km/h during 30 s at 8 KN	1x stop brakings 90 – 0 km/h, CE
2x stop brakings 90 – 0 km/h, VOM	1x speed hold braking 120 km/h during 30 s at 8 KN
2x stop brakings 60 – 0 km/h, VOM	7x stop brakings 100 – 0 km/h, CN

VOM: Inertia 5 375 kg & 18KN per disc
 CN: Inertia 8 313 kg & 28KN per disc
 CE: Inertia 9 375 kg & 37KN per disc
 Number of cycles: 10
 Restarting T°: 80°C
 Air flow: 35 km/h

Figure 18: RER C brake testing protocol

The groove pattern presented on Figure 16b was tested with this protocol. We did obtain a 33% mass efficiency. Namely, we did only collect 33% of the weight lost by the pads and the disc during the test. So far from automotive results. The main reason is our turbines were not powerful enough and consequently we were not able to aspirate particles collected by the groove which were far from the central aspiration hole. It made no sense to increase the power of the turbines, as the electrical consumption would be too high.

So, we decided to optimize the groove pattern and the air flow circuit. We knew from previous studies (Benseddiq and Al., 1996) that the groove pattern has a huge impact on the real contact area between pads and disc and then the surface conformation between these 2 rubbing parts. According to this study, the optimal groove pattern for real contact surface maximization is presented on Figure 19a.

According to our know how for automotive applications, assuming that the real contact area is 100% of the pads area during braking, the best design for particles collection would be the one presented on Figure 19b. Unfortunately, the 100% real contact area is far to be true for this design. Actually, we did collect less than 30% of the weight lost by the pads and the disc this this groove design. So, the aim of the study presented here was finding the best compromise between particle collection maximization and pads-disc real contact area maximization through the groove pattern design.

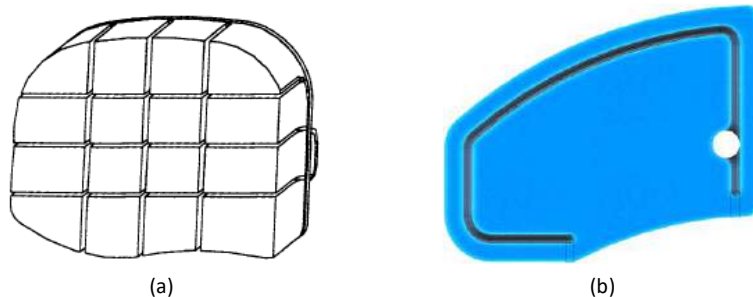


Figure 19: (a) Optimal groove pattern (4.1) to maximize disc-pads real contact area
(b) Optimal groove pattern (1.0) to maximize particles collection

To achieve this goal, we first decided to simplify the air flow circuit equilibration. On the first design presented on Figure 16, we tried to aspirate particles through a single hose for the 2 half pads mounted on the pad carrier. To simplify, we decided to separate the air flow circuit of the 2 half pads as presented on Figure 20.

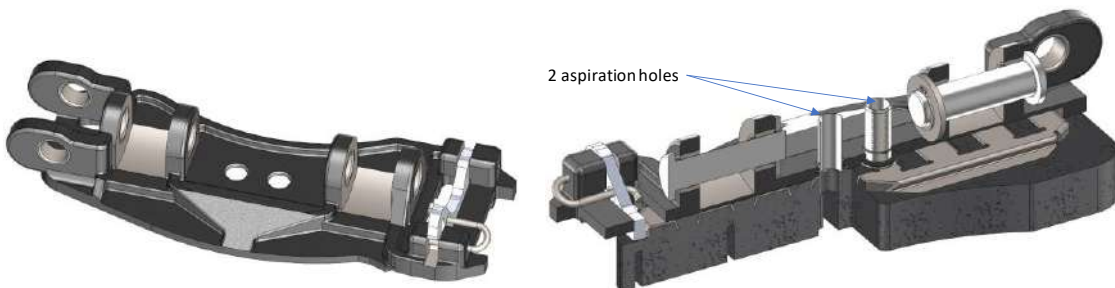


Figure 20: Pads carrier with 1 aspiration hole per half pad

Then we implemented a simplified finite element analysis calculation, with Solidworks Simulation software, in order to assess the pad deformation during braking. Using standard parameters for railway organic friction materials, we did apply 300°C at the surface of the pad and ambient temperature at the rear. This allowed us to simulate the vertical distortion at the surface induced by a thermal gradient.

Results are displayed on Figure 21 for different groove patterns. Vertical elevation is displayed taking the initial plane of the pad surface as a reference. When the elevation is positive the point is above the initial surface plane.

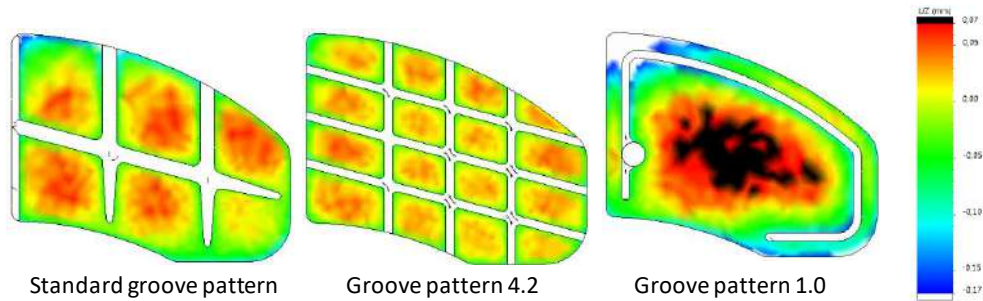


Figure 21: Influence of groove pattern on thermal distortion

From a thermal distortion point of view, we could confirm that groove pattern 4.2 (based on optimal groove pattern 4.1 presented on Figure 19a) is better than standard design which is much better than groove pattern 1.0 (optimal for wear particles collection).

Thanks to this tool we could simulate more than 60 different groove patterns combining grooves for wear particles collection and grooves to reduce distortion.

We also did optimize groove shape and air inlet holes dimension with Solidworks Flow Simulation software (Figure 22). The main target was the homogenization of air speed and pressure levels all along the groove pattern.

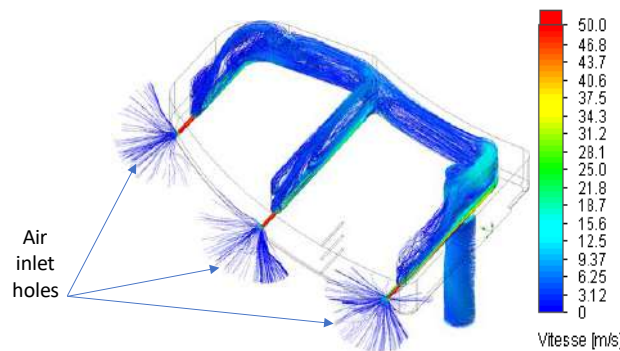


Figure 22: Air flow simulation

The 3 designs presented on Figure 23 were selected to be tested on bench.

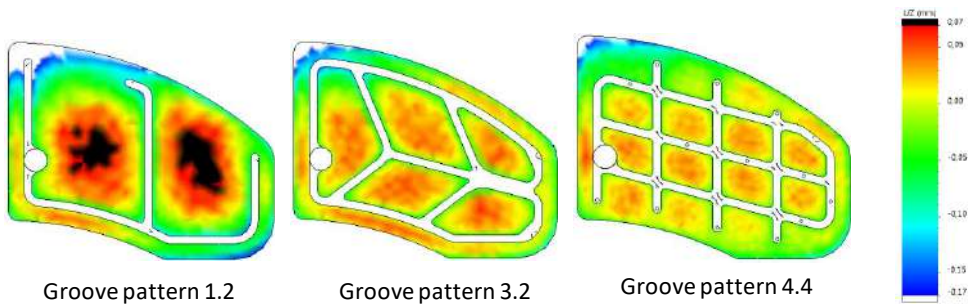


Figure 23: Selected groove pattern designs

We first tested groove pattern 1.0 as a reference with RER C testing protocol (figure 24). Mass efficiency of the different groove patterns are reported in Table 2. Groove pattern 1.0 had the lowest efficiency. This can be explained by the high distortion of the pad during the test, which was confirmed by the observation of the pads after the test. We could notice a high amount of wear particles deposited on the inner and outer surface of the pads, indicating that these areas were not in contact with the disc during the test. This means that the air flow circuit in the groove is not closed. There is a leakage and non-polluted air enters through the void created between the pads and the disc. Depression within the groove is then non-homogeneous and collection efficiency is reduced.

Groove pattern	Testing protocol	Mass efficiency
1.0	RER C	21%
1.2	RER C	70%
1.2	100km/h middle energy	79%
3.2	100km/h middle energy	83%
3.2	100km/h middle energy	85%
4.4	100km/h middle energy	90%
1.2	100km/h high energy	60%
3.2	100km/h high energy	68%
4.4	100km/h high energy	76%

Table 2: Particle collection efficiency of the different groove patterns in continuous aspiration



Figure 24: Groove pattern 1.0 pad after RER C testing

We also did test groove pattern 1.2 with RER C protocol and got a much more encouraging mass efficiency at 70%.

In order to better understand the phenomena, we decided to simplify the testing procedures. We first did use what we call a middle energy testing procedure (400 braking cycles; 100km/h to 0km/h; Inertia per disc: 5375kg; braking force: 18kN). We defined these conditions in order to get enough wear during a 400 cycles test and not too severe to limit distortion during the test. The results of the different groove patterns are reported in Table 2. The lower the simulated distortion is the higher the mass efficiency is.

In order to further verify this correlation, we did test these groove patterns with high energy conditions (400 braking cycles; 100km/h to 0km/h; Inertia per disc: 9375kg; braking force: 37kN). The energy dissipated in these conditions is much higher than the average one encountered in suburban exploitation, where brake particle emission is today the biggest concern. But we wanted to amplify distortion and check the effect on collection efficiency. Once again, the lower the simulated distortion is the higher the mass efficiency is (Table 2). In these latter conditions a higher contact temperature during braking might also explain part of the collection efficiency reduction, as gases might be emitted through phenolic resin oxidation. These gases are not collected by our filters.

Conclusion

The groove design developed to collect brake particles at source for automotive applications could not be simply implemented for rolling stock brake systems. A specific groove pattern has been designed thanks to the scientific approach described in this paper. This basic study, based on finite element distortion analysis, air flow circuit optimisation and tests on a braking bench, shows a strong correlation between thermal distortion and brake particles mass collection efficiency.

This scientific approach allowed us to save time and reach the same brake particles mass collection efficiency than the one we did achieve for automotive applications (>80%).

Next steps

The best design will be tested with RER C testing protocol next months. A one-month campaign of tests will be proceeded to evaluate braking performances and particles collection efficiency.

Test on trains will start in October 2019 to measure performances in real operating conditions, with preliminary test without passengers to ensure that braking performances of the train are maintained.

Acknowledgements

Région Ile de France, administrating the most populous region of France.

Ile de France Mobilités, the transport authority of Région Ile-de-France, and its major transport operator, SNCF TRANSILIEN.

References

- Abbasi (2011), Characterisation of airborne particles from rail traffic, *Royal Institute of Technology - Sweden*
- AEF (2017), Site de mesures de particules en continu en gare de Magenta (2016), *Rapport n°DOC047931/MES016241 de l'Agence d'Essai Ferroviaire*
- ANSES (2015), Pollution chimique de l'air des enceintes de transports ferroviaires souterrains et risques sanitaires associés chez les travailleurs. Rapport d'expertise collective de l'Agence nationale de sécurité sanitaire de l'alimentation, de l'environnement et du travail, septembre 2015, 382 pages.
- Araki A., Kawai T., Eitaki Y., Kanazawa A., Morimoto K., Nakayama K., Shibata E., Tanaka M., Takigawa T., Yoshimura T., (2010) Relationship between selected indoor volatile organic compounds, so-called microbial VOC, and the prevalence of mucous membrane symptoms in single family homes, *Sci. Total Environ.* 408, 2208-2215
- Augsburg K., Hesse D., Kuhn U., Leicht R., (2018) Comparison of the run-in and emission behavior of different disc concepts, PMP-47-20 rev1
- Benseddiq N., Weichert D., Seidermann J., Minet M., (1996) Optimization of Design of Railway Disc Brake Pads, *Journal of Rail and Rapid Transit*.
- Burkhard, L. Rossi, M. Boller, (2007), Diffuse release of environmental hazards by railways, *ScienceDirect – Switzerland*
- Dockery D.A., Pope C.A., Xu X., Spengler J.D., Ware J.H., Fay M.E., Ferris Jr., B.G., Speizer F.E., (1993) An association between air pollution and mortality in six US cities. *New Engl. J. Med.* 329, 1753-1759.
- Durand, A. Mehel, F. Murzyn, G. Fokoua1, S. Puech (2017) Particle dispersion from railway rolling stock, *TAP Conference - France*
- Fortin (2005), Caractérisation des particules en gares souterraines, *PhD Université de la Rochelle - France*
- Loomis (2013) The carcinogenicity of outdoor air pollution, *The Lancet Oncology*
- Martins V., Moreno T., Minguillón M.C., Amato F., De M.E., Capdevila M., Querol X., (2015a.) Exposure to airborne particulate matter in the subway system. *Sci. Total Environ.* 511, 711-722.
- Namgung H. G., Kim J. B., Kim M. S., Kim M., Park S., Woo S. H., Bae G. N., Park D., Kwon S. B., (2017), Size distribution analysis of airborne wear particles released by subway brake system, *Wear* 2017 372-373, 169-176
- Olofsson, U. (2010) A study of airborne wear particles generated from the train traffic – block braking simulation in a pin-on-disc machine. *Wear*, 2010, 271(1–2)
- Pope C.A., Dockery D.W., (2006) Health effects of fine particulate air pollution: lines that connect. *J. Air Waste Manage. Assoc.* 56, 709-742
- SAE International. (2003) Dynamometer global brake effectiveness. *SAE, J2522*
- Xu B., Hao J., (2017), Air quality inside subway metro indoor environment worldwide: A review.

2.10.2 REAL-e: Robust and affordable IoT solution for market surveillance

P. Dégeilh^{1*}, J. Kermani¹, S. Rodríguez¹, L. Thibault¹, A. Frobert¹, and G. Corde¹

¹ IFP Energies nouvelles, Institut Carnot IFPEN TE, 1-4 avenue de Bois-Préau, 92852 Rueil-Malmaison, France

philippe.degeilh@ifpen.fr

Context and state of the art

Automotive emission regulations have known major evolutions over the past years and still face a few important challenges. With the deployment of Euro 6d Temp regulation, from September 2017, vehicle type-approval certification is now closer to the real-world driving conditions thanks to the introduction of new measuring procedures: the Worldwide harmonized Light vehicles Test Procedure (WLTP) and the Real Driving Emissions (RDE). In-Service Conformity (ISC) is newly applied with RDE Work Package 4 (WP4) since early 2019 (Regulation EU 2018/1832) and Market Surveillance (MS) will be mandatory from 2020 (Regulation EU 2018/858). Both ISC and MS will make extensive RDE testing mandatory.

On the other hand, RDE testing remains a complex and costly procedure (Cuelenaere et al., 2016). Indeed, on-road vehicle emissions are necessarily driver and conditions dependent (Giechaskiel et al., 2018), but the test protocol must remain fair in order to make unbiased comparisons between vehicles. As a consequence, an experimental-only approach needs de facto a rigorous protocol: the use of a complex and costly PEMS analyzer (Portable Emission Measurement System), constrained trip and ambient conditions, as well as driving behavior limitations. This ensures the representativeness and the comparability of the results between different vehicles, labs, drivers, and environmental conditions. The proper setup of the RDE testing procedure requires at least half a day of work and an expensive PEMS device, nonetheless the RDE compliance rate is usually under 50%.

For ISC and MS, it is challenging to identify on the market the vehicles with the highest pollutant emissions because of the wide range of possible driving conditions and RDE experimental limitations. This is why complementary tools are needed: to detect and focus on the specific situations with elevated emissions due to technical reasons, control strategies, road conditions or driving behavior. In RDE WP4, Remote Sensing Devices (RSD) or Simplified on-board Emissions Monitoring Systems (SEMS) are cited as probable tools for providing information to the type approval authorities to guide the selection of vehicles to test. On the one hand, RSD allows a large-scale deployment of measurements, but on a limited number of locations and associated driving conditions. On the other hand, SEMS proposes easier and more affordable embedded solutions than PEMS, and allows a growing deployment of on-road emission tests. However, SEMS results are trip dependent and a single test cannot be enough to ensure vehicle conformity to any driving conditions. Operators can try to approach the RDE limits to make sure of it, but the compliance rate of the tests decreases significantly once again, even though there is no tool to establish that these boundary conditions are the most critical for the technologies of the considered vehicle.

Contribution

In this context, this work presents an innovative approach, named REAL-e, consisting in coupling an affordable on-board gas measurement system and cloud emission modeling in order to promote a robust and affordable IoT (Internet of Things) solution for ISC and MS. This approach aims to overcome the aforementioned limitations in order to multiply real-driving tests and get a consolidated market overview. The main added value of the contribution is to propose a complementary tool to improve state of the art solutions, allowing large-scale deployment of measurements thanks to simplification and characterization of vehicle behavior in real driving conditions.

This paper first presents the proposed methodology. Secondly, the hardware setup for data collection is described. Furthermore, the software framework is detailed, including focus on (i) the microscopic generic vehicle model, (ii) the pollutant mass flow calculation by coupling measurements and modeling, (iii) the learning algorithms developed in order to re-calibrate vehicle models, and (iv) the process retained to highlight and contextualize abnormal behaviors of vehicles in terms of pollutant emissions. Each part includes a discussion of the state of the art, contributions and main results. Finally, perspectives and future works are discussed.

An experimental campaign has been operated on Euro 5 and Euro 6 gasoline and diesel vehicles. Vehicles were equipped with both the proposed solution and a reference PEMS system. The performance is discussed regarding:

- in-house hardware solution vs. PEMS to validate the accuracy of concentration measurements;
- proposed calculation method of pollutant mass flow vs. PEMS equipped with EFM;
- capability of the proposed methodology to highlight and contextualize abnormal pollutant emissions behavior in order to raise a High Emitter (HE) status.

1. Methodology

Figure 1 represents the whole methodology, that consists of:

- (i) A simple exhaust emission measurement device to allow large scale testing campaigns. The hardware setup allows a quick and easy installation and setup (avoiding the need of complex and costly sensors, such as the Exhaust Flow Meter (EFM) that must be fitted to the tailpipe with an adaptation part and a bracket). The operated trip(s) do not have specific restrictions, and a real time driving guide can maximize the utility of generated data to characterize vehicle behavior on a wide range of real driving use cases;
- (ii) Data enrichment using modeling to provide pollutant mass flow from concentration measurement. A vehicle and powertrain modeling framework has been developed. It allows to estimate fuel consumption on the current operating conditions and to convert the measured pollutant over CO₂ ratio into pollutant mass flow. Measured data are used to successively refine the calibration of models of vehicle related components (vehicle driving resistance, gear box staging, engine consumption);
- (iii) An analysis using modeling to characterize the behavior deviation in different life cases. A nominal vehicle emissions model is used to visualize the expected behavior of the vehicle on the current driving conditions. The comparison of this nominal model to the measurements, taking the form of a dynamic conformity factor, allows to go deeper in the analysis of the operated data: emission behavior characterization does not depend only on the final cumulated emission value but is relative to each use case encountered. In this way, abnormal behaviors are highlighted and contextualized. A second step of auto-calibration using measured data can be used for engine-out emissions and after-treatment efficiency, in order to highlight the degradation of the system efficiency needed to reproduce the measured behaviors and fit a reliable pollutant emission model of the vehicle;
- (iv) Projection of observed behaviors on RDE boundaries: when an abnormal behavior is highlighted on a given life case, this step aims to study the possible occurrence and severity of this life case. Taking into account both behavior deviation and life case criticality on RDE boundaries, a High Emitter (HE) status is computed. It does not include the provision of a quantified value of NOx emissions or associated CF on a given RDE, but a justified indication of the level of confidence about respect of regulatory thresholds in the RDE perimeter.

The potential of going further on the simulation on non-operated cycles, at least for vehicles that demonstrate a quite nominal behavior during tests,, is currently studied. This model could for example simulate a wide range of RDE cycles and compute a consolidated distribution of RDE results with their associated uncertainties. Those results could be used to point out the RDE conditions that are likely to reveal a High Emitter vehicle and also to generate the route to perform to measure it.

This global approach fits in the ISC and MS workflow and more specifically into the Information Gathering step defined in RDE WP4 to improve the vehicle selection process.

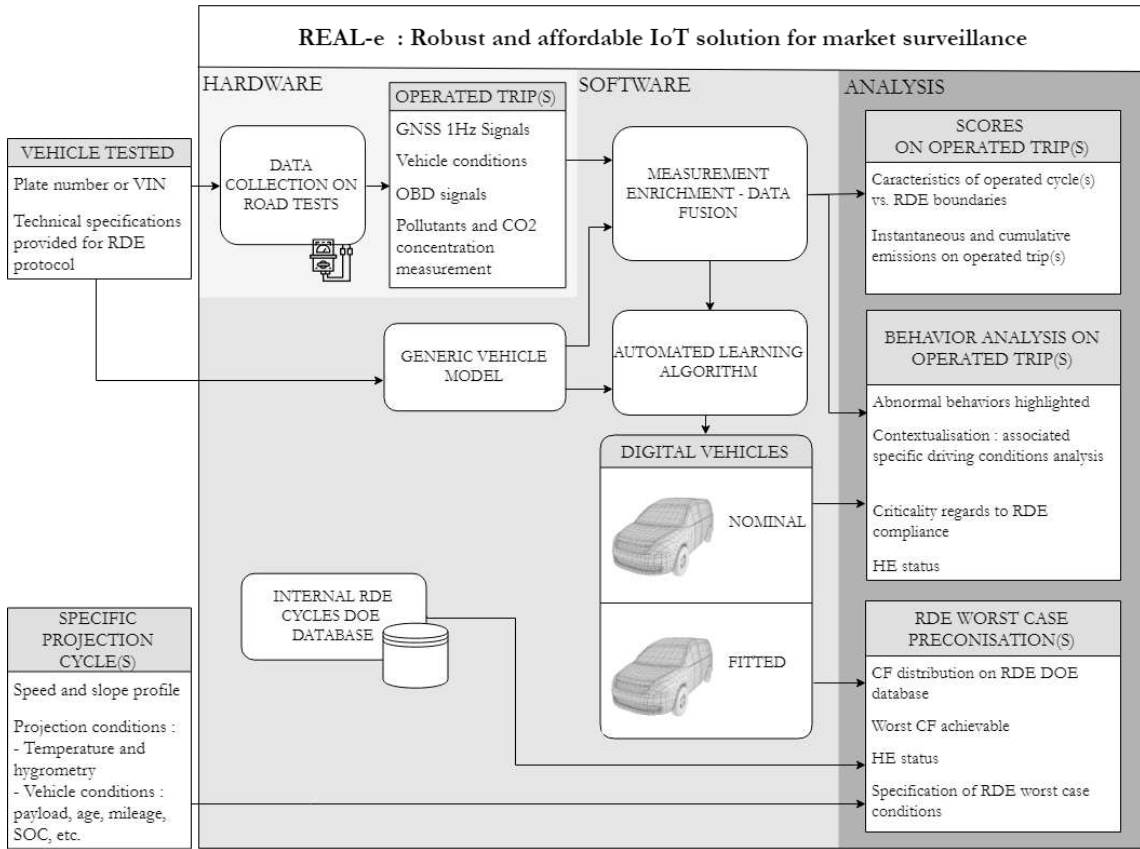


Figure 1: REAL-e whole process diagram

2. Hardware setup for data collection

The sensors used in REAL-e are derived from off-the-shelf Periodical Technical Inspection (PTI) analyzers. It is based on Non Dispersive Infra-Red (NDIR) and Electro Chemical Cell (ECC) sensors, more details are given in Table 1. The power supply has been replaced by a battery, offering enough energy to cover a full test day. Everything is packaged into a briefcase to simplify the handling. For safety purposes, an ambient CO detector is added. Figure 2 shows an example of use of the REAL-e solution in a car. All those upgrades make it ready and cost-efficient for on-board measurement of regulated pollutants. The use of REAL-e is simplified compared to a conventional PEMS. It does not need tools nor a drawbar. The operating of REAL-e does not depend on laboratory span gases on a daily basis, the ambient air is sufficient. Table 1 compares the specificities of REAL-e with regards to a conventional PEMS. In addition, an On-Board Diagnostic (OBD) dongle registers standard available OBD signals: vehicle speed, engine speed, load and coolant temperature for instance. Finally the GPS-chip of the OBD dongle provides 1 Hz speed and elevation data. All signals are centralized on a cloud database in real-time using a 3G-chip also integrated in the OBD dongle.



Figure 2: REAL-e in use

Table 1: REAL-e vs PEMS analyzers and prerequisites

	REAL-e	PEMS		
[CO2]	Heated NDIR ¹	✓	Heated NDIR	✓
[HC]	Heated NDIR	✓ (propane only)	-	Not mandatory
[CO]	Heated NDIR	✓	Heated NDIR	✓
[NOx]	ECC ²	✓	Heated Dual-CLD ³	✓
PN	Ionization	(under development)	CPC ⁴	✓
Exhaust Flow Meter	From model	✓		✓
Emission mass flow	From consumption model and pollutant over CO ₂ ratio		RDE method : From concentration and EFM	
GPS info	OBD Dongle	✓	Aux. device	✓
Weather info	Web service	✓	Aux. device	✓
OBD data	OBD Dongle	✓	Aux. device	✓ (Not mandatory)
Need of span gas	Every 6 months	✓	Every trip	✓

¹ NonDispersive InfraRed

² Electro Chemical Cell

³ ChemiLuminescence Detector

⁴ Condensation Particle counter

The raw concentration measurements of REAL-e have been compared to the ones from a PEMS on a panel of vehicles driven on different trips and driving styles (RDE-like around 80 km and 90 minutes, short urban trips around 7 km and 15 to 20 minutes). Figure 3 shows the results of this comparison, with the density plot of all the measurements performed on the test campaign for CO₂ and NO_x for more than 30 trips and 1200 km driven. In addition, performance indexes have been computed in the form of the coefficient of the trend curve, showing a good match between the two measurement devices and also the standard deviation that remains low regarding the range of measurement.

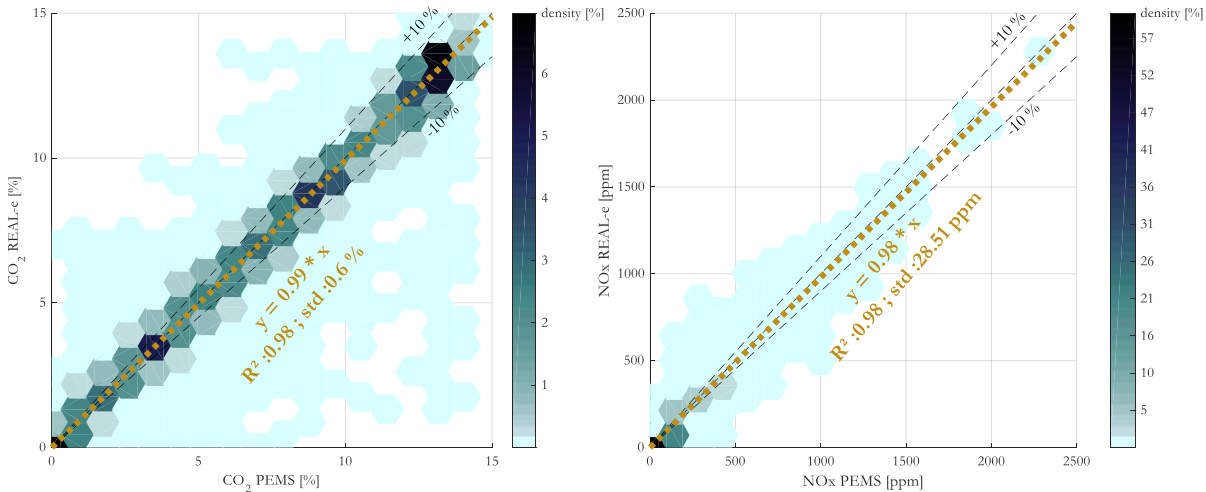


Figure 3: Comparison between REAL-e and PEMS CO₂ and NO_x volumetric concentrations : % density of measurements per hexagonal section

3. Software framework

Modeling is used at different steps of the approach with quite different aims. A vehicle modeling framework has been developed, including consumption and pollutant emissions. Modeling is first used for the enrichment of available data on the operated tests. Then, considered as a reference of nominal behavior, the vehicle pollutant emission model is used to highlight abnormal behaviors on measurement and contextualize the associated driving conditions. In the future steps of the project, a projection of vehicle behavior on non-operated trips could be allowed when there will be a good prediction capability. The next paragraphs detail the introduction of modeling in the REAL-e workflow.

3.1. Microscopic generic vehicle model

The state of the art in terms of vehicle emissions models is made up of two large families, macroscopic and microscopic. Among the macroscopic models, the most widespread approach considers Emission Factors (EF). EF are average values that relate the quantity of a pollutant released to the atmosphere to its source, car driving in our case. In most cases, these factors are simply averages of all available data of acceptable quality, and are generally assumed to be representative of long-term averages for all facilities in the source category. They are suitable for average emissions on long trips but not for real traffic emissions which need to take into account the impact of local infrastructure and of the driving style. Their major cause of error comes from the impact of the driving style and slope as studied in (Sentoff et al., 2015). To take into account these phenomena, it is necessary to use a finer level of modeling, called microscopic, whose input is generally a 1 Hz vehicle speed profile.

Several microscopic models already exist and the most widespread are: the Comprehensive Modal Emission Model (CMEM) of University of California (Barth et al., 2000), the Passenger car and Heavy duty Emission Model (PHEM) of Graz University of Technology (Hausberger et al., 2003) and the Virginia Tech Microscopic energy and emissions model (VT-Micro) of Virginia Tech (Rakha et al., 2004). They use different approaches: the CMEM model was developed as a power-demand model, the VT-Micro model was developed as a regression model from experimentation with numerous polynomial combinations of speed and acceleration levels. A validation of CMEM and PHEM can be found in (Rakha et al., 2003) and (Nam et al., 2003), showing a good consistency with experimental results. PHEM is also used to generate a standard of EF called HBEFA. These microscopic models are designed for offline studies.

The purpose of the contribution of this paper is to couple a microscopic model with on road pollutant measurement to improve model accuracy and predictability, on a large vehicle scale. For this objective, it was chosen to develop new microscopic models, in order to be suitable for the real-world emissions estimation of a large vehicle fleet, and designed to be recalibrated from dedicated embedded measurements. The purpose of this section is to present our general approach to estimate real-world emissions from Global Navigation Satellite System (GNSS) measurements. Figure 4 shows the cloud computing architecture used to estimate pollutant emissions. The four inputs of this calculation are the registration number of the vehicle (ID) and GNSS measurements automatically recorded (pos_{GNSS} , $\text{speed}_{\text{GNSS}}$ and $\text{slope}_{\text{GNSS}}$).

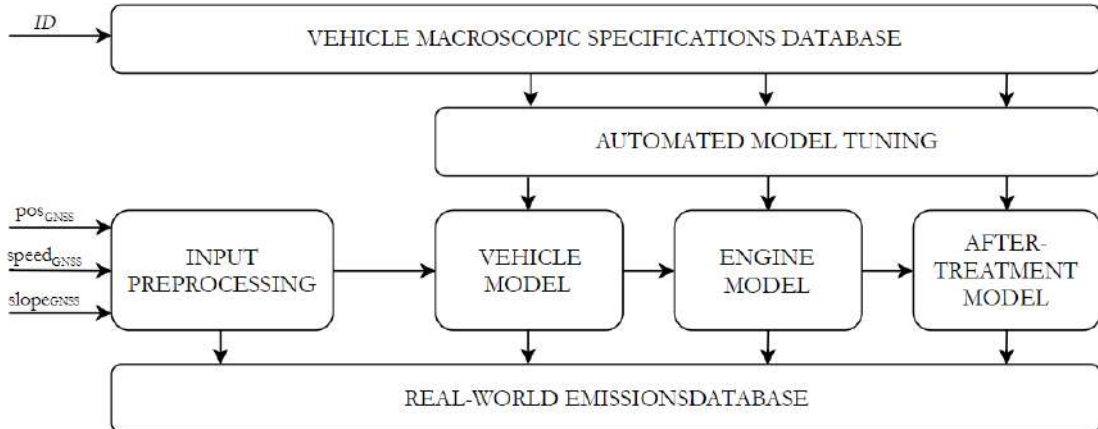


Figure 4: generic vehicle model scheme

The choice of the right modeling level is a trade-off between precision, number of input parameters, and computation time. The desired models should be able to catch the impact of real-world driving conditions and allow identifying situations where pollutant emissions are particularly high or low. Moreover, to be adapted to data provided by standard GNSS systems and OBD, the model has to deal with inputs sampled at low rates, typically 1Hz. This critical point has to be related to physics of pollutant creation which occurs during an engine cycle, typically few milliseconds. Each of the bricks of this approach will not be detailed in this paper, the interested reader can refer to (Thibault et al, 2017) for more details (only some elements will be included in the rest of the paper to illustrate the methods of recalibration). Models are developed to represent state-of-the-art calibration and control strategies for each technology. They do not take into account and report on OEM specific control strategies and calibrations, as well as vehicle specific defaults or tampering. Depending on the usage of models, it can be considered as an advantage (to represent a nominal behavior) or a limitation (to predict the emission

level of a specific vehicle). In this case, this weakness is overcome thanks to an enrichment with specific measurement data and learning algorithms as described in the dedicated section.

3.2. Pollutant mass flow calculation coupling measurement and modeling

One of the main constraints of state-of-the-art pollutant on-board measurement is the measurement of exhaust mass flow to convert pollutant measurement from concentration to mass flow. With REAL-e, we use a methodology based on the monitoring of instantaneous pollutants over CO₂ concentration ratio and the estimation of CO₂ emissions (CO₂_{est}). The CO₂ estimation comes from the addition of two bricks:

- Vehicle dynamics model: using the GNSS trip signals (vehicle speed and altitude), this model is able to estimate the engine power. First, power at the wheels is computed through longitudinal dynamics equations. Then, with the transmission efficiency and the reduction ratio between the wheel and the engine crankshaft, the velocity and torque from wheels can be converted into engine speed and torque. Available OBD signals gathered by REAL-e (engine speed, coolant temp, vehicle speed and engine load) help to refine the models and specifically the transmission layout.
- Internal physical quantities model: this part of the model evaluates the internal physical quantities for the current engine operating point, based on the following basic assumptions:
 - Maximum torque curve of the engine estimated from maximum torque, maximum power and air-path architecture;
 - Friction Mean Effective Pressure (FMEP) generic law (function of engine speed) depending on engine architecture;
 - Constant gross indicated efficiency;
 - Fuel air equivalence ratio equal to 1 in spark ignition engine (except at high load where it increases linearly with load), and varying between two values for compression ignition engine;
 - EGR (Exhaust gas rate) fraction is assumed for each point of the engine map.

These assumptions allow to calculate the Pumping Mean Effective Pressure, and later, fuel consumption, total intake mass flow rate and exhaust mass flow which take into consideration the EGR and the hybridization level if necessary, and also pressure and temperature conditions, for the instantaneous engine operating point. The CO₂ emissions are directly calculated from the fuel consumption. As introduced previously this estimation of CO₂ is used to calculate pollutant emissions from pollutant over CO₂ concentration ratio, as depicted in Figure 5.

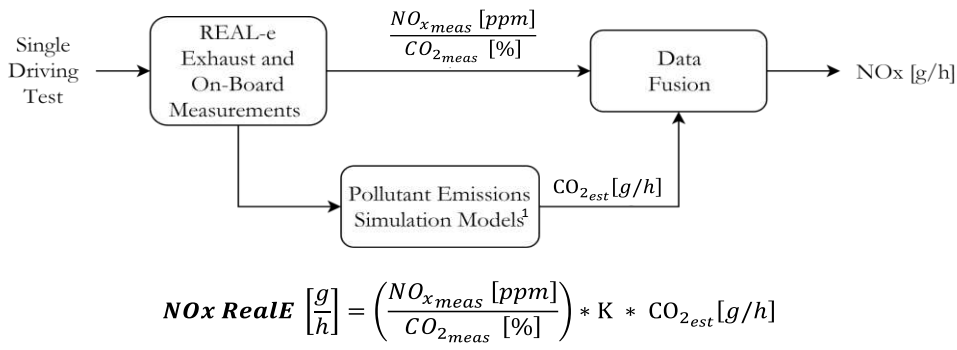


Figure 5: Pollutant mass flow calculation coupling measurement and modeling

Thereby, this methodology for mass flow calculation from pollutant over CO₂ ratio is near from RSD process (Bernard et al., 2018), but all over the trips operated instead of in a single area of the road.

The performance of this approach has been evaluated on an experimental campaign operated on a panel of vehicles (various engine types, After-Treatment Systems and standard levels). An example is given in Figure 6, showing the performance of REAL-e data enrichment against PEMS for NOx emissions, expressed on conformity factor relative to each vehicle respective standard level. It shows consistent results compared to the PEMS on a wide range, with a mean relative error of 16%, mainly due to low NOx values.

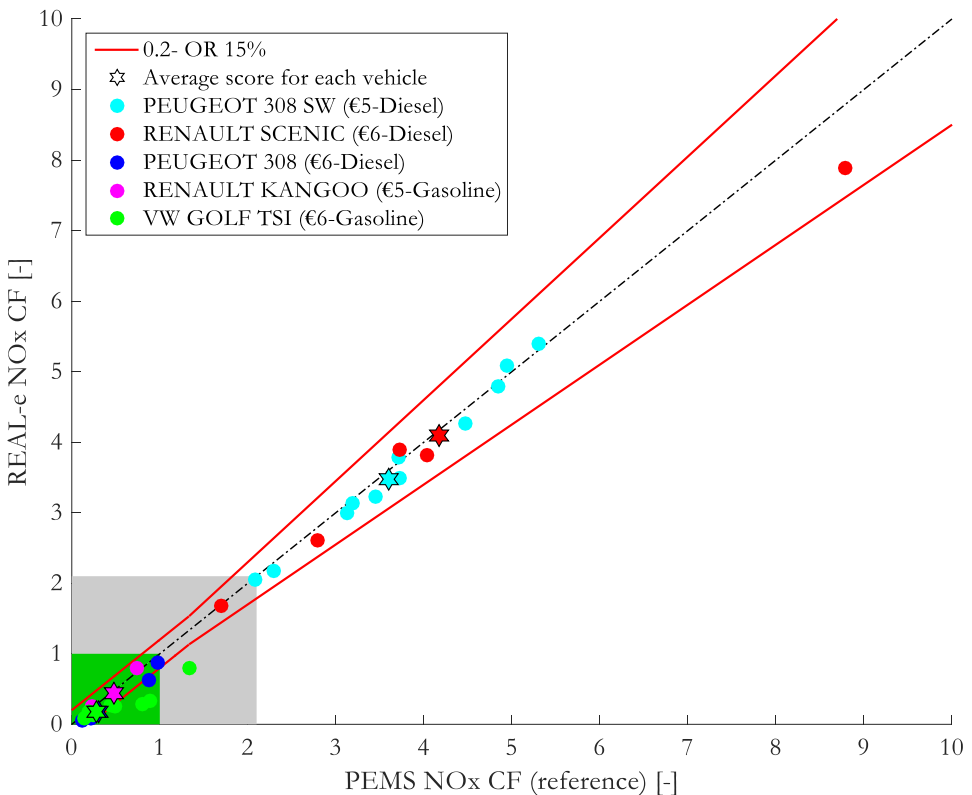


Figure 6: Performance of REAL-e enriched data against PEMS

3.3. Algorithms for model re-calibration : nominal & fitted models

In order to fit the vehicle pollutant emission model on determined target and real driving conditions, automated learning algorithms have been developed. Figure 7 represents the model calibration procedure.

The first step using data from approval tests is computed independently of experimental test availability and allows refining the generic pollutant emissions model for each vehicle. This contribution proposes to go a step further using:

- on the one hand nominal RDE emissions target in order to recalibrate a nominal pollutant emission model of the vehicle, that means a model that fits the Euro standard requirements on the homologation cycle and RDE tests;
- on the other hand the experimental measurement on the considered vehicle to fit the behavior of the vehicle measured during one or several operated trip(s) performed with the REAL-e hardware. These learning trips do not have specific restrictions such as the RDE requirements, meaning that there is no invalidation of the measurement because of the severity of the driving nor the altitude etc. These data are used to auto-calibrate models, i.e. refine the settings of each submodel to fit to the vehicle driven in its current state of use.

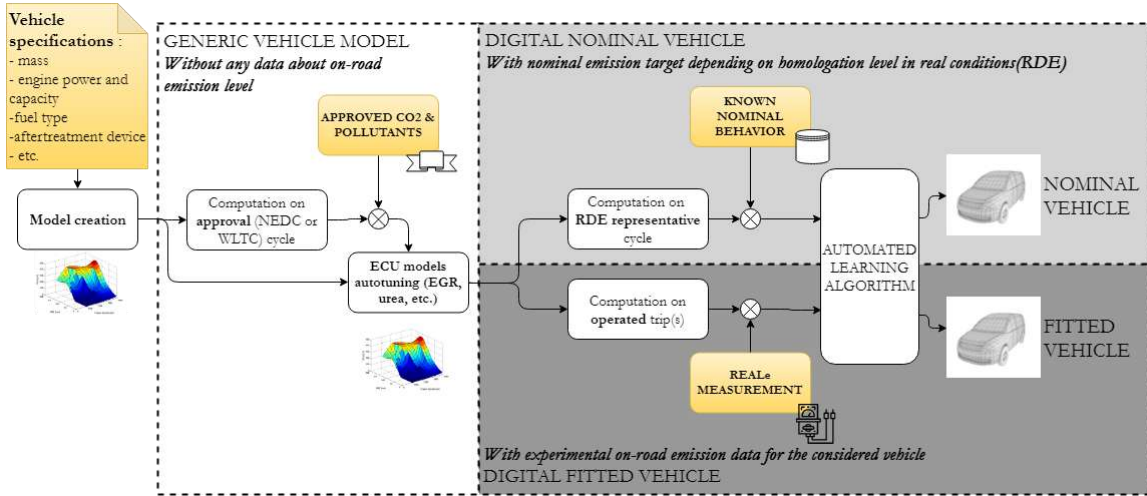


Figure 7: Model flowchart: From generic to nominal and realistic calibrated models

3.3.1. Gear box staging learning

As an example of a learning implementation, the gearbox staging model is recalibrated using OBD vehicle and engine speeds signals. The generic gearbox model is calibrated thanks to the power of the vehicle and the maximum speed achievable, then the staging is deduced from common design principles. Based on REAL-e measurements, a clustering method allows identifying the ratios staging and the gearbox ratio engaged throughout the cycle, as illustrated in Figure 8.

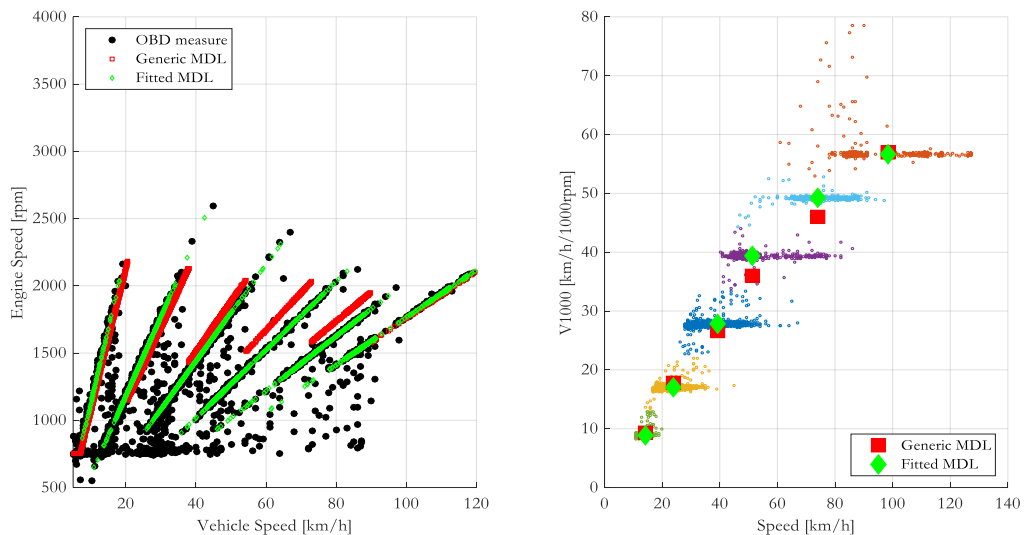


Figure 8: Clustering method on OBD signals for gearbox staging identification

3.3.2. NOx Engine Out (EO) and NOx Tail-Pipe (TP) learning method

Another learning capacity that offers the use of REAL-e hardware is the improvement of the NOx Tailpipe estimation for diesel vehicles. To estimate pollutants emission at the tailpipe, the generic model relies on:

- Engine-out emissions model

The estimated internal physical quantities are used to obtain the engine-out emissions, which are Nitrogen Oxides, Particulate Matter, Carbon Monoxide and Carbon Dioxide, as a result of equations from the literature with some adjustments to the available data (Sabiron et al., 2018). This modeling is based on steady state assumptions for most parameters but transient phenomena such as the air path settling time or thermal behaviors are also taken into account through dynamic models. In particular for the case of NOx Engine Out (NOx EO), the model depends on the Fuel flow rate (Q_{fuel}) and the Burnt Gas Ratio (BGR) level and is described as follows:

$$\frac{NOx EO}{\eta_{fuel}} = e^{\alpha * BGR + \beta}$$

- Exhaust after-treatment model

An after-treatment model library with several sub-models has been developed: Diesel Oxidation Catalyst, Diesel Particulate Filter, Selective Catalyst Reduction, Lean NOx Trap, Three-Way-Catalyst and Gasoline Particulate Filter. With these elements it is possible to describe most existing exhaust line architectures. The output of all these sub-models is the pollutants emissions at tail-pipe.

Thanks to the level of pollutants registered for the vehicle and to the data fusion with the models, those two parts can be improved to better estimate the pollutants at the tailpipe. For example, Figure 9 describes how the measurement can help to tune the NOx Engine Out via BGR and the After-Treatment System (ATS) efficiency for a Euro 6 vehicle equipped with a SCR system from a generic model.

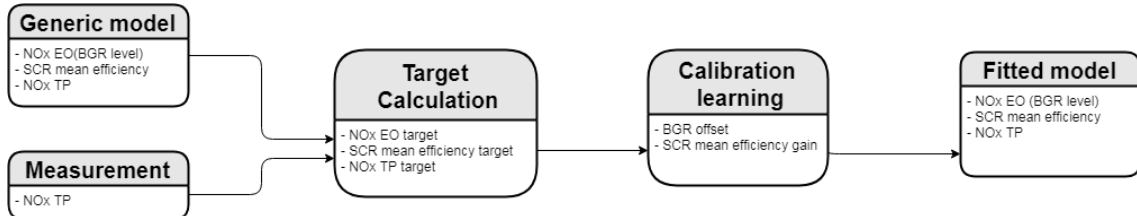


Figure 9: NOx Engine Out (EO) and NOx Tail-Pipe (TP) learning diagram

In Figure 9, for the target calculation:

- $NOx TP target = NOx TP meas$
- $NOx EO target = NOx EO generic + Prop EO \times \frac{NOx TP target - NOx TP generic}{1 - SCR Eff generic}$
- $SCR Eff target = 1 - \frac{NOx TP target}{NOx EO target}$

To calculate the BGR offset, the NOx model described before is inverted to obtain,

$$BGR_{offset} = 1/\alpha \times \log\left(\frac{NOx EO target}{NOx EO generic}\right) \times K_0$$

For the ATS efficiency, a ratio between the generic efficiency and the targeted efficiency allows to recalibrate the model.

3.4. Behavior analysis: highlight and contextualize abnormal behaviors using modeling

The approach consists in taking a nominal vehicle as reference in order to visualize a “normal” emission behavior on the current operating conditions and to highlight potential abnormal behaviors of the vehicle recorded on the measurement. The comparison of measured data and the nominal model results is expressed itself as a dynamic Conformity Factor (CF -Measurement / Nominal) over the test. Emissions are aggregated using a statistical binning method, in order to distinguish driving situations throughout the trip. Each segment is then categorized depending on this dynamic CF value along five thresholds arbitrarily defined (see Table 2).

Table 2: Dynamic Conformity Factors thresholds

Color	Threshold	Behavior	Prediction capability
Light Green	0 – 1.43	Very good	Good
Dark Green	1.43 – 2.1	Good	Good
Orange	2.1 – 3	Poor	Limited
Red	3 – 5	Bad	Non possible but HE status
Black	5 or more	Very bad	Non possible but HE status

Figure 10 shows the NOx emission analysis for one Euro 6b vehicle, called Vehicle A. It consists in the comparison of measurements (dark blue) to the nominal model (light blue) representing a nominal average behavior. The upper left plot compares the NOx level by segments of 10 km, the bottom left one represents the accumulated NOx. The middle left bargraph illustrates the conformity factor for NOx for each 10 km segment using the thresholds described in Table 2. It allows an evaluation of the vehicle behavior on the happening driving situations. On the given example, the methodology highlights that the vehicle has a worse cold start emission level than expected, then a nominal behavior for the next 50 km and finally exceeded pollution level under highway conditions.

A further step of the analysis is the characterization of the segments in order to contextualize observed behavior deviation and investigate possible High Emitter causes. In the studied cases, the analysis of the segments offers an explanation for the high conformity factors. The three plots on the right are proposing analysis of the NOx emissions vs. V^*A_{pos} (positive vehicle power), T_{SCR} (Internal temperature of the SCR catalyst) and GHSV (Gas Hourly Space Velocity in the SCR catalyst). Each star represents a 10 km segment of the considered trip. It indicates that for this application there is a reduced window of performance for the SCR after-treatment, defined by the temperature and GHSV boundaries. For low SCR temperature and GHSV, the vehicle behavior is categorized as “poor”, and for high SCR temperature and GHSV, it is declared as “very bad”.

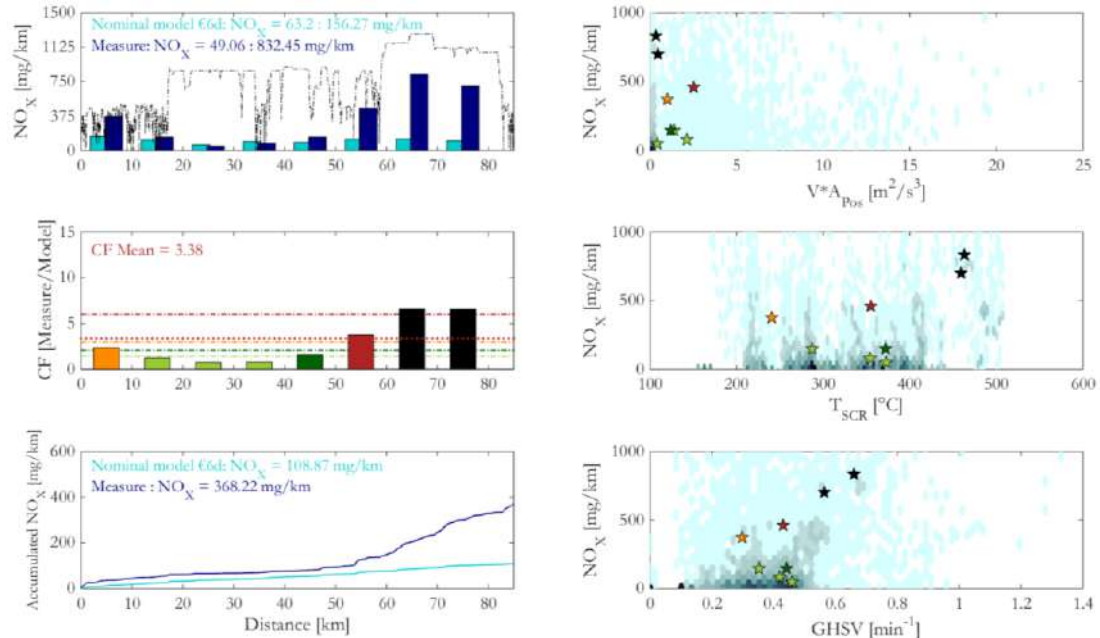


Figure 10: Dynamic Conformity Factor and segment analysis for Vehicle A

On the other hand, Figure 11 shows the NOx tail-pipe results for another Euro 6b vehicle tested, called Vehicle B, on the same itinerary, with the same representation of binned NOx each 10 km. The similarity between measurements and nominal model highlights the good performer status of the tested application, having always lower levels emitted than the model. The CF are almost constant and always lower than one. In the studied case, the characterization of the segments shows that its good performer

status is explained by its capacity to maintain low emissions over a large variation of the SCR temperature or GHSV.

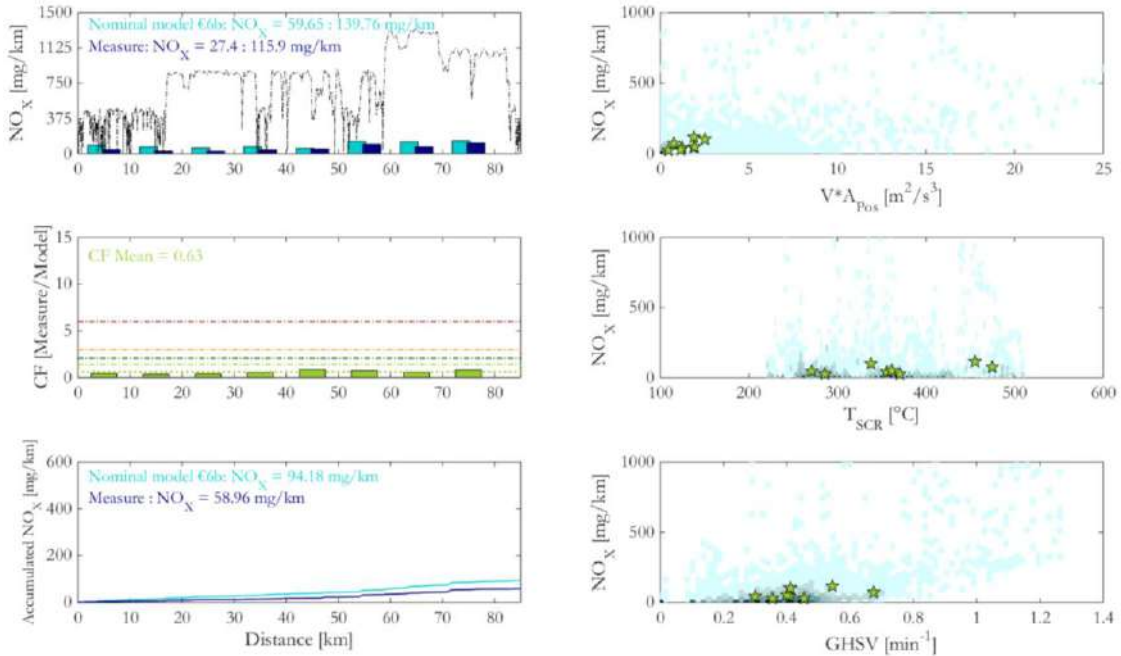


Figure 11: Dynamic Conformity Factor and segment analysis for Vehicle B

When an abnormal behavior is highlighted on a given life case, the possible occurrence and severity of this life case upon RDE boundaries is studied. Taking into account both behavior deviation and life case criticality on RDE boundaries, a HE status is computed. It does not include the provision of a quantified value of NOx emissions or associated CF on a given RDE, but a justified indication of the level of confidence about respect of regulatory thresholds in the RDE perimeter. Such analysis can help to understand why the application tested differs in real life from a nominal expected behavior. This ability of the REAL-e system helps to focus on the real driving situation that creates abnormal behaviors and to understand why an application can be declared as a High Emitter.

3.5. Using fitted models for emission level projections

The potential of going further on the simulation on non-operated cycles, at least for vehicles that demonstrate a quite nominal behavior during tests, is currently studied. The model fitted on experimental measurement could for example simulate a wide range of RDE cycles and compute a consolidated distribution of RDE results with their associated uncertainties, estimating the sensitivity of the vehicle tested to the RDE boundaries. Those results could be used to point out the RDE conditions that are likely to reveal a High Emitter vehicle and also to generate the route to perform to measure it. It may allow the third parties and the Granting Type Approval Authorities (GTAA) to focus on those conditions and applications to realize the ISC or MS tests. These calibrated models, available for cloud computing simulation, may be questioned to predict the emissions on customer, approval and RDE cycles. The collection of digital twins represents a consolidated market overview over the time.

Conclusion

This paper describes an innovative tool for market surveillance and In Service Conformity. Compared to the state-of-the-art it is more affordable and easy-to-use thanks to the coupling of minimalist hardware sensors and an advanced software framework. Hardware sensors have been adapted from proven off-the-shelf components, and validated on a wide range of vehicles by comparison with reference PEMS analyzers, showing good accuracy. Microscopic vehicle models are used to enrich measurements and convert pollutant concentrations into pollutant mass flows. They also serve as a reference to visualize expected nominal behavior of vehicles in various real-driving conditions encountered during the experimental campaign, and to highlight abnormal behaviors recorded in measurements. When such a behavior is detected, its generating conditions are analyzed in view of RDE boundaries (criticality, possible occurrence, etc.). In this way, this methodology is able to highlight and contextualize vehicle failures regarding pollutant emissions. It identifies vehicles that require further investigations and PEMS

testing, and refer to specific driving conditions likely to highlight these abnormalities for each vehicle. To resume, the proposed REAL-e solution offers capabilities to evaluate a High Emitter status more easily than with restricted RDE trips with PEMS, to help GTAA and Third parties to reduce the time and cost to evaluate vehicles and avoid false-positive, to improve experimental surveillance at a larger scale. Current work activities aim to continue the validation of the approach on a wider range of real-life scenarios in order to further confirm the relevance of the proposed approach. A particular attention will be given to guarantee a low rate of false-positive or false-negative HE detections.

Acknowledgments

The authors wish to thank CAPELEC team and especially Georges PETELET for the fruitful collaboration on REAL-e development.

References

- Barth, M., et al. (2000). "Comprehensive Modal Emission Model (CMEM), version 2.0 user's guide" University of California, Riverside.
- Bernard, Y., et al (2018). "Determination of real-world emissions from passenger vehicles using remote sensing data", *TRUE*, The Real Urban Emissions Initiative.
- Commission Regulation (EU) 2018/858 of the European Parliament and of the Council of 30 May 2018 on the approval and market surveillance of motor vehicles and their trailers, and of systems, components and separate technical units intended for such vehicles, amending Regulations (EC).
- Commission Regulation (EU) 2018/1832 of 5 November 2018 amending Directive 2007/46/EC of the European Parliament and of the Council, Commission Regulation (EC) No 692/2008 and Commission Regulation (EU) 2017/1151 for the purpose of improving the emission type approval tests and procedures for light passenger and commercial vehicles, including those for in-service conformity and real-driving emissions and introducing devices for monitoring the consumption of fuel and electric energy.
- Cuelenaere et al. (2016). "Assessment of the strengths and weaknesses of the new Real Driving Emissions (RDE) test procedure", *TNO*.
- Giechaskiel, B et al. (2018). "Framework for the assessment of PEMS (Portable Emissions Measurement Systems) uncertainty", *Environ. Res.*, 166, 251–260.
- Hausberger, S., et al. (2003). "Emission factors for heavy-duty vehicles and validation by tunnel measurements," *Atmospheric Environment*, vol. 37, no. 37, pp. 5237-5245.
- Nam, E. K., et al. (2003). "A Comparison of real-world and modeled emissions under conditions of variable driver aggressiveness" *82nd Annual Meeting of the Transportation Research Board*, Washington.
- Rakha, H., et al. (2003). "Comparison of MOBILE5a, MOBILE6, VT-MICRO, and CMEM models for estimating hot-stabilized light-duty gasoline vehicle emissions" *Canadian Journal of Civil Engineering*, vol. 30, no. 6, pp. 1010-1021.
- Rakha, H., et al. (2004). "Development of VT-Micro model for estimating hot stabilized light duty vehicle and truck emissions" *Transportation Research Part D: Transport and Env.*, vol. 9, no. 1, pp. 49-74.
- Sabiron, G., et al. (2018). "Pollutant emissions estimation framework for real-driving emissions at microscopic scale and environmental footprint calculation." *IV'18, 2018 IEEE Intelligent Vehicles Symposium*.
- Sentoff, K. M., et al. (2015) . "Implications of driving style and road grade for accurate vehicle activity data and emissions estimates" *Transportation Research Part D: Transport and Env.*, vol. 35, p. 1756188.
- Thibault, L., et al. (2017). "GNSS data-based Approach to Monitor Real-World Exhaust Emissions at Microscopic Resolution." *TAP*, 22st International Transport and Air Pollution Conference.

2.10.3 Development of a Low-Cost Quartz-Enhanced Photoacoustic Spectroscopy Nitrogen Dioxide Sensor Network for Air Pollution Measurements

P. Breitegger^{1*}, M. Knoll¹ and A. Bergmann¹

Affiliation of authors, include e-mail address for corresponding author (Arial 9). [style: Affiliation]

¹ Institute of Electronic Sensor Systems, Graz University of Technology, Graz, 8010, Austria,
p.breitegger@tugraz.at

Introduction

Air pollution adversely affects the environment and is one of the biggest health risks. This is pertained also for Europe, with its relatively clean cities and strict air quality limits. In 2015 in Europe, it is estimated, that 422,000 premature deaths were due to PM_{2.5} and 79,000 in connection with NO₂ (Guerreiro et al., 2018). Therefore, possibilities to monitor air quality at high spatial resolution are of high interest to better understand air pollution, assess the impact of air quality improvement measures, and inform citizens on air quality. At present, air pollution monitoring is carried out at low spatial resolution due to high costs coming along with high accurate measurement equipment. To achieve high-resolution pollution maps, these point measurements assist dispersion models, which however, only deliver approximate values of pollution levels. To overcome this issue, a much denser sensor network of low-cost sensors is required, which is directly able to monitor air pollution values (Breitegger and Bergmann, 2016).

In the EU, limit values and measurement techniques are described in the 2008/50/EG und 2015/1480/EC directive. These limit values are depicted for NO₂ and PM_{2.5} in Table 1. Present low-cost sensors are unable to detect such low concentrations without implications, such as drift, noise or cross-interferences to other pollutants (Castell et al., 2017).

Table 1: Air pollution limits for PM_{2.5} and NO₂

Pollutant	Short term limit ($\mu\text{g}/\text{m}^3$)	Long term limit ($\mu\text{g}/\text{m}^3$)
PM _{2.5}	-	25 (calendar year) 20 (three calendar years)
NO ₂	200 (1 hour) Should not be exceeded on more than 25 days per year averaged over 3 years	40 (calendar year)

To inform citizens on air quality, a common air quality index (CAQI) was established, which ranges from 0 (very low pollution) to 100 (very high pollution). The CAQI for NO₂ and PM_{2.5} is depicted in Table 2.

Table 2: Common air quality index for NO₂ and PM_{2.5} (same values for roadside and background measurements) according to (van den Elshout, 2012)

Index Class	NO ₂ ($\mu\text{g}/\text{m}^3$)	PM _{2.5} ($\mu\text{g}/\text{m}^3$)	
		1 hour	24 hours
Very High (> 100)	400	>110	>60
High (75-100)	200-400	55-110	30-60
Medium (50-75)	100-200	30-55	20-30
Low (25-50)	50-100	15-30	10-20
Very Low (0-25)	0-50	0-15	0-10

In this work, we suggest the use of an embedded quartz-enhanced photoacoustic spectroscopy (QEPAS) sensor, equipped with a wireless sensor network (WSN) module, as a well-suited candidate for low-cost air quality sensing. QEPAS can be used to sense a wide variety of pollutants, even soot (Breitegger et al., 2019a), by simply changing to a different wavelength light source.

To date, QEPAS sensors have solely relied on high cost laboratory equipment, without accomplished field measurement campaigns or WSN connectivity for dense spatial detection. Therefore, to

demonstrate the capabilities, the results of a QEPAS sensor for NO₂ are discussed (Breitegger et al., 2019b). Then, a possible system architecture is discussed together with concepts to replace the laboratory equipment with custom solutions. Further, a power efficient, long-range technology named LoRa is employed in urban environment, which shows the capability to provide spatially dense connectivity (Knoll et al., 2018).

Sensor Principle

In quartz-enhanced photoacoustic spectroscopy (Kosterev et al., 2002), modulated light is absorbed by the analyte, which results in the production of a sound wave. The principle is drawn in Figure 1. First, a modulated light source is chosen such that its wavelength matches one or more absorption bands of the analyte (1). Ideally, there is no cross-interference to other gas constituents. Then, the analyte will be periodically excited (2), which results in periodic heating of the surrounding gas (3) and in turn the generation of sound (4). This sound pressure wave is converted to a small current by a piezoelectric quartz-tuning fork (QTF) in QEPAS. Due to the high quality factor of QTFs (around 8000), this sound is only detected if the modulation frequency of the light source matches the resonance of the QTF. QTFs have resonance frequencies in the range of 32.768 kHz. Thanks to industrial mass production, they are available for prices in the cent range.

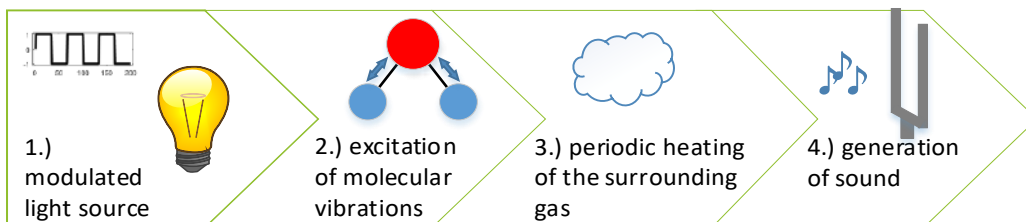


Figure 1: Principle of QEPAS.

The QEPAS signal S can be described as (Patimisco et al., 2014)

$$S \propto \frac{Q \cdot P \cdot \alpha}{f_0},$$

where Q is the quality factor, P the laser power, α the absorption coefficient of the analyte at the wavelength of the light source and f_0 is the resonance frequency of the QTF. Thus, the QEPAS signal is directly proportional to the analyte concentration.

A typical laboratory setup for QEPAS is shown in Figure 2. A laser is modulated with a signal generator and focused between the prongs of a QTF. The weak current signal is electronically amplified. By the use of a lock-in amplifier, only the frequency component matching the reference frequency of the lock-in amplifier is measured. Post-processing and control is typically handled with a computer. Although the main sensing element can consist of low-cost parts, signal generator and lock-in amplifier are far too expensive and bulky to be used in a sensor network.

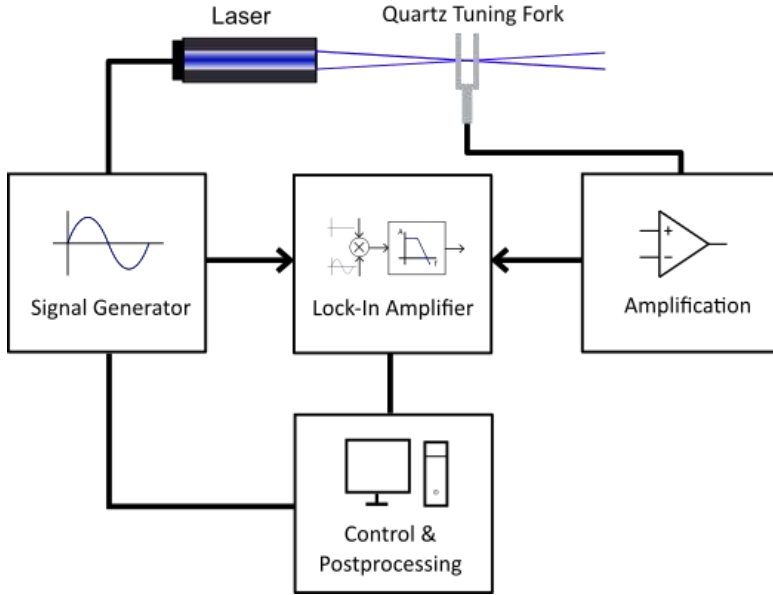


Figure 2: Typical laboratory setup for QEPAS.

Architecture

The simplest QEPAS setup uses a bare fork, where a laser is focused through. This setup allows easy correction of temperature and pressure dependence (Breitegger et al., 2019b). With this setup, a detection limit below $40 \mu\text{g}/\text{m}^3$ is reached with an averaging time of 30 sec. This is suitable for both, indicative values of the CAQI, but also to detect exceedance of the limit values. By using a laser diode with a peak-wavelength of 450 nm, cross-interference to other gas constituents is prevented.

In Figure 3, on the left, the laboratory QEPAS setup is shown. The laser driver is a commercial product (Thorlabs ITC4001). Sampling and signal generation are carried out with a PXI (National Instruments) system, which synchronizes signal generation as well as data acquisition. The QEPAS signal is sampled at 250 kSps and the lock-in amplifier is implemented on a dedicated computer.

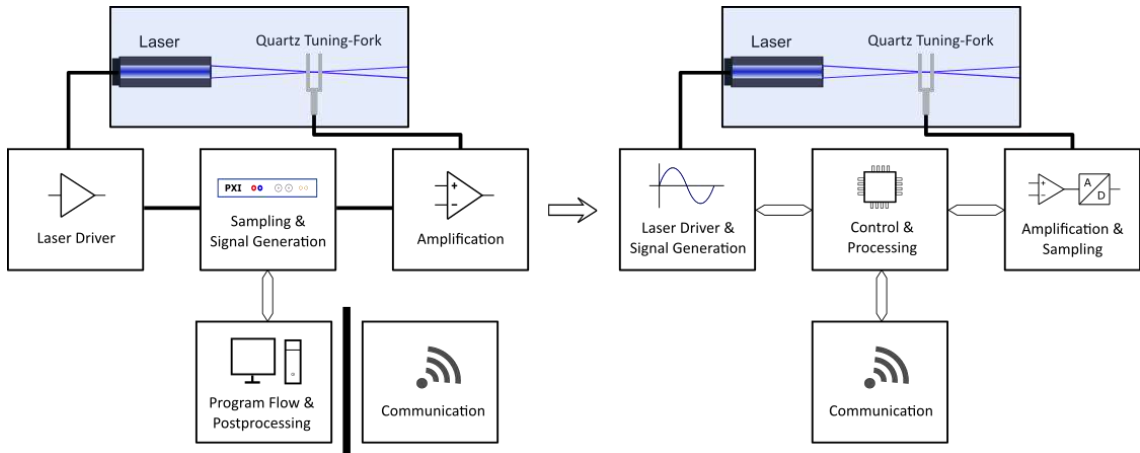


Figure 3: Transitioning from a lab setup and an LPWAN microcontroller to a sensor system suitable for a sensor network.

As previously described, lock in amplifier and signal generator, which run on the same time base, are the most urgent parts to be optimized in terms of price and size. Due to the high resonance frequency and Q-factor of the QTF, there are high requirements on the timing. For resonance detection, a minimum frequency resolution of 1 Hz is required. E.g., if the modulation signal is a square wave, which is generated by the use of a microcontroller, the clock rate must be well above 2 GHz for resonance frequencies around 32.768 Hz. This is not achievable with the current microcontroller technology. Another challenge is the need for dual phase detection, as the phase of the QEPAS signal can vary.

The right part of Figure 3 depicts the proposed embedded QEPAS setup with WSN connectivity. Therefore, a laser driver and a digital signal processor based lock-in amplifier were developed. The lock-in amplifier is able to detect the in-phase- and quadrature component of the QEPAS signal and also produces the modulation signal with a frequency resolution below 1 Hz (Kerschhofer et al., 2018). Due to the DSP based lock-in amplifier, a sampling frequency of 100 Hz is sufficient, which can easily be handled by microcontrollers.

An ARM-based microcontroller brings along the processing and control capability. The computing unit is responsible to control the lock-in amplifier, where it brings along the functionality to perform resonance detection and fast gas concentration tracking. Subsequent to the determination of the air pollution, the data is ready for collection at a central base station. This data gathering process needs to be reliable and at best feasible with low power consumption and across large distances for dense sensor meshes. Accordingly, the microcontroller is connected to a long range LoRa module, which features the above mentioned characteristics. LoRa networks are employed in a star topology, where the nodes directly send their messages to the base station. With the usage of LoRa, communication distances in the kilometer range in urban environment are achievable (Augustin et al., 2016). We performed an evaluation of the communication range in the urban area of Graz using LoRa (Knoll et al., 2018). In Figure 5, the positioning of the sensor nodes and the base station is depicted. The evaluation results are shown in Figure 4, where it can be seen that the connectivity range exceeded 1700 m. By applying a proper resending algorithm of lost packets, a reliable data transfer over wide areas can be achieved.

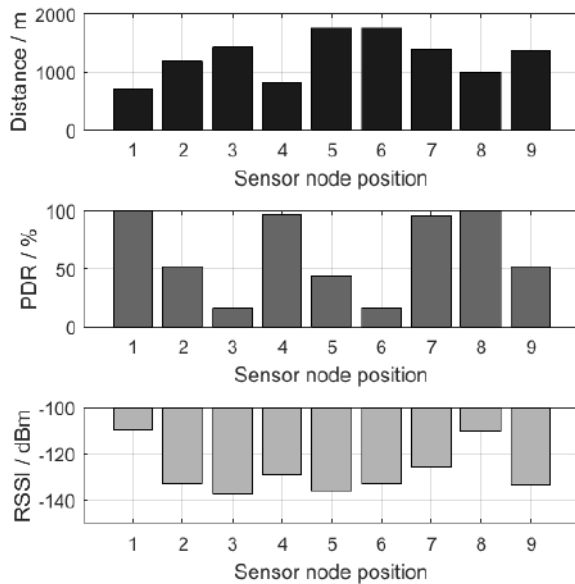


Figure 4: Communication distance measurement results in the urban area of Graz. From top to bottom: a) Distances between sensor node and base station b) Packet Deliver Ratio (PDR) from the individual positions c) Received Signal Strength Indicator (RSSI) from the different positions (Knoll et al., 2018)

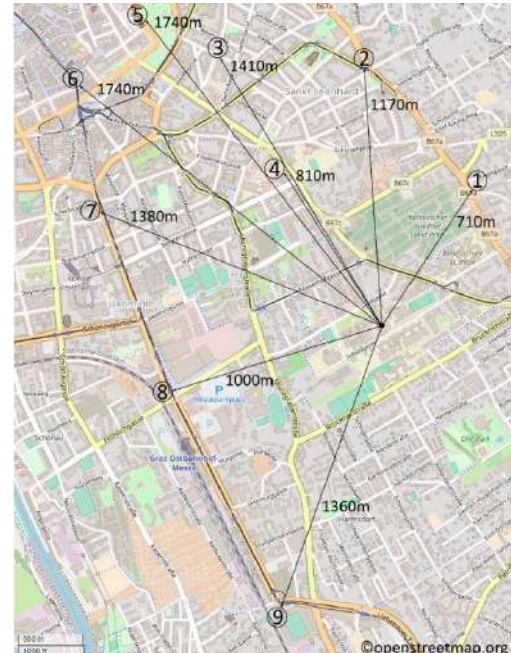


Figure 5: Placement of the base station, the sensor nodes and the distance in between them in Graz. (Knoll et al., 2018)

Conclusion and Outlook

In this work we presented an embedded architecture of a smart sensor node for the detection of nitrogen dioxide. QEPAS provides a trustworthy detection mechanism without cross-interference to other pollutants. By adding lasers with different wavelengths, a single QEPAS sensor could detect different pollutants. The embedded architecture enables the usage as a compact sensor platform, which can be manufactured on a large scale. The network connectivity enables the deployment in large scales to

accomplish dense spatial pollution maps without the need of modelling. With this sensor concept, air quality indexes can be calculated and air pollution exceedances can be reliably detected at high spatial resolution.

Ongoing work includes a co-location study at the legislative measurement station at Petersgasse in Graz to compare the sensor to a chemiluminescence detector and evaluate its performance under real-world conditions and the long-term performance. Future work will cover the placement of multiple nodes to investigate pollution patterns and interpolate 2D maps.

References

- Augustin, A., Yi, J., Clausen, T., Townsley, W.M., 2016. A study of Lora: Long range & low power networks for the internet of things. *Sensors (Switzerland)* 16, 1–18. <https://doi.org/10.3390/s16091466>
- Breitegger, P., Bergmann, A., 2016. Air quality and health effects — How can wireless sensor networks contribute? A critical review, in: 2016 International Conference on Broadband Communications for Next Generation Networks and Multimedia Applications (CoBCom). IEEE, pp. 1–8. <https://doi.org/10.1109/COBCOM.2016.7593507>
- Breitegger, P., Schriefl, M., Nishida, R., Hochgreb, S., Bergmann, A., 2019a. Soot Mass Concentration Sensor using Quartz-Enhanced Photoacoustic Spectroscopy. Manusc. Submitt. Publ.
- Breitegger, P., Schweighofer, B., Wegleiter, H., Bergmann, A., 2019b. Towards Low-Cost QEPAS Sensors for Nitrogen Dioxide Detection. Manusc. Submitt. Publ.
- Castell, N., Dauge, F.R., Schneider, P., Vogt, M., Lerner, U., Fishbain, B., Broday, D., Bartonova, A., 2017. Can commercial low-cost sensor platforms contribute to air quality monitoring and exposure estimates? *Environ. Int.* 99, 293–302. <https://doi.org/10.1016/j.envint.2016.12.007>
- Guerreiro, C., González Ortiz, A., Leeuw, F. de, Mar, V., Colette, A., 2018. Air quality in Europe — 2018 report, Report. Luxembourg. <https://doi.org/10.2800/777411>
- Kerschhofer, A., Breitegger, P., Bergmann, A., 2018. Laser Driver and Analysis Circuitry Development for Quartz-Enhanced Photoacoustic Spectroscopy of NO₂ for IoT Purpose. *Proceedings* 2, 1062. <https://doi.org/10.3390/proceedings2131062>
- Knoll, M., Breitegger, P., Bergmann, A., 2018. Low-Power Wide-Area technologies as building block for smart sensors in air quality measurements. *Elektrotechnik und Informationstechnik* 135, 416–422. <https://doi.org/10.1007/s00502-018-0639-y>
- Kosterev, A.A., Bakhirkin, Y.A., Curl, R.F., Tittel, F.K., 2002. Quartz-enhanced photoacoustic spectroscopy. *Opt. Lett.* 27, 1902. <https://doi.org/10.1364/OL.27.001902>
- Patimisco, P., Scamarcio, G., Tittel, F., Spagnolo, V., 2014. Quartz-Enhanced Photoacoustic Spectroscopy: A Review. *Sensors* 14, 6165–6206. <https://doi.org/10.3390/s140406165>
- van den Elshout, S., 2012. CAQI Air quliaty index: Comparing Urban Air Quality across Borders. Schiedam.

2.10.4 Making sense of variability in real-world vehicles emissions

Clémence M. A. Le Cor nec¹, Nick Molden² and Marc E. J. Stettler^{1*}

¹ Centre for Transport Studies, Department of Civil and Environmental Engineering, Imperial College London, London, SW7 2AZ, United Kingdom, m.stettler@imperial.ac.uk

² Emissions Analytics, Kimball Smith Limited, Kings Worthy House, Court Road, Kings Worthy, Winchester, SO23 7QA, United Kingdom

1. Introduction

Outdoor air pollution significantly affects public health and is responsible for about 428,000 premature death annually in Europe ([EEA, 2017](#)). Nitrogen oxides ($\text{NO}_x = \text{NO} + \text{NO}_2$) emissions substantially deteriorate air quality ultimately leading to adverse short and long term environmental and health effects ([EEA, 2017](#)). Exposure to NO_2 is associated with an increased risk of cardiovascular diseases, decreased lung functionalities, aggravated asthma, low birth weights and premature deaths ([EEA, 2017](#); [Andersen et al., 2012](#); [Vineis et al., 2006](#)). NO_2 and O_3 have also been linked with the degradation of natural ecosystems and reduction in biodiversity ([EEA, 2017](#)). Despite evidence of adverse impacts and the introduction by the EU of successively more stringent regulations on both air quality and emissions, NO_2 concentrations in European cities have remained significantly higher than the limits set for the protection of human life.

Road transport is the major source of NO_x in Europe, in 2015 it accounted for 39% of the total NO_x emissions ([EEA, 2017](#)). In London, [Roads Task Force \(2012\)](#) estimated that road transport contributed to 47% of the total NO_x emissions in 2012. Diesel engines, which show intrinsic higher distance-specific NO_x emissions than gasoline engines ([Grinham and Parry, 2018](#)), are responsible for approximately 80% of the NO_x emissions due to road transport. The market penetration of diesel vehicles, which represents 40% of the total fleet in the UK ([Grinham and Parry, 2018](#)), and the significantly higher emissions measured in real driving conditions, from one to twenty-two times compared to type approval, ([O'Driscoll et al., 2016, 2017](#)) partially explain the failure to reach air quality standards. A various number of mitigation strategies exist to control air pollution in urban areas. One popular strategy consists in the implementation of a charging system aiming at penalizing pollutant vehicles entering a polluted area.

In this context, emissions models have become of key importance in the assessment of road transport role in air quality issues. Estimated emissions are used to predict levels of air pollution along roads and therefore implement mitigation strategies. Existing emissions models achieve limited performance to estimate NO_x emissions in real-world driving conditions ([Smit et al., 2010](#)), which is partially due to a lack of understanding of the processes behind emissions. [O'Driscoll et al. \(2016\)](#) demonstrate that COPERT underestimates NO_x emissions in real-driving conditions by a factor 1.6 compared to real measurements. PHEM overestimates NO_x emissions in real-driving conditions by up to 25% ([Matzer et al., 2017](#)). Finally, [Ntziachristos et al. \(2016\)](#) show that VERSIT+ emission factors underestimate by a factor up to 1.5 NO_x emissions compared to emissions in real-world driving conditions. Real-time accurate estimation of NO_x emissions is therefore of key importance in the assessment of road transport responsibility in air quality issues. Existing emission models are not able to achieve a sufficient accuracy in real-world driving conditions and there is consequently a need for improving NO_x emissions models. This could probably only be achieved through a better understanding of the processes underlying emissions. To our knowledge, no studies have used unsupervised machine learning techniques to analyse the similarities in emissions behaviours of a large sample of vehicles and ultimately improve emission models.

The present study aims therefore to (i) explore a large dataset of real-world vehicle emissions by performing a clustering analysis that could be used to disaggregate emissions models that are currently usually based on Euro standard; and (ii) provide a description of the variability in real-world vehicles emissions in space and time.

2. Methodology

In this study, we present a clustering analysis on a vehicle emissions dataset in order to group together vehicles presenting similar emitting behaviours in similar operating conditions. Secondly, we present an analysis of external variables able to explain the results of the clustering. Thirdly, we explore the influence of driving style and road design on emissions across a set route.

2.1. Dataset description

The dataset used in this study was provided by Emissions Analytics (EA) and was already described in a previous study from [O'Driscoll et al. \(2017\)](#). A Portable Emissions Measurements System (PEMS) was used to measure real world driving emissions of 36 Euro 5 and 34 Euro 6 diesel passenger vehicles in the Greater London area between 2012 and 2016. All these vehicles were fitted with a Diesel Oxidation Catalyst (DOC), a Diesel Particulate Filter (DPF) and an Exhaust Gas Recirculation (EGR) system. The Euro 6 vehicles had a mixture of NO_x aftertreatment systems, 7 used EGR only, 16 EGR + Lean NO_x Trap (LNT) and 11 used EGR + Selective Catalytic Reduction (SCR). We study refer the interested reader to [O'Driscoll et al. \(2017\)](#) for a more detailed description of the data collection process.

A test route was extracted based on the instantaneous coordinates as measured by the embedded GPS and is depicted in Figure 1. The 10.3 km test route was in an urban area and the average vehicle speed was 23.47 (std 2.50) km/h. All the vehicles in the dataset travelled this journey one to three times and instantaneous speed, coordinates, external temperature and NO_x emissions were recorded. A total of 110 segments were extracted: 54 for Euro 5 vehicles and 56 segments for Euro 6 vehicles. The average dynamic characteristics of the segments of are given in Table 1.

Table 1: Segment dynamic characteristics

Parameter	Mean ± std
Duration [min]	27.55 ± 6.56
Distance [km]	10.30 ± 0.095
Average speed [km/h]	23.47 ± 2.50
% of idle [%]	20.75 ± 5.75
Relative Positive Acceleration (RPA) [m/s ²]	0.19 ± 0.03
95 th percentile of the product of positive instantaneous acceleration and speed [m ² /s ³]	12.49 ± 3.99

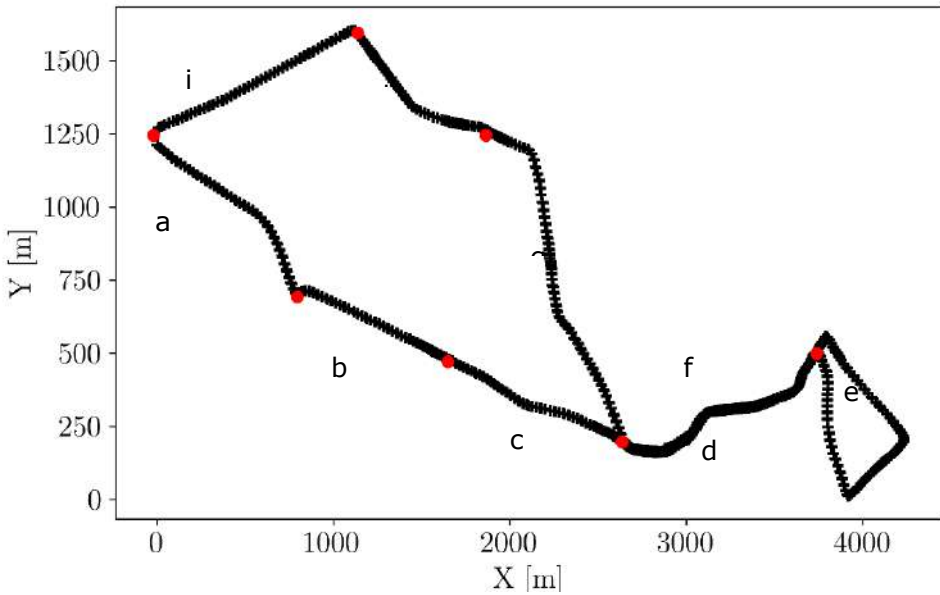


Figure 1: Test route. The main intersections are depicted by a red dot. Subsegments are labelled by the letters a to i.

2.2. Clustering

Clustering is the process of grouping a set of objects into clusters so that objects within clusters are similar to each other and dissimilar to objects in other clusters (Park and Jun, 2009). An important step in most clustering algorithms is the selection of a distance metric, which determines how the similarity between two elements is calculated (Velmurugan, 2012). This step is particularly challenging when working with time-series because a standard point by point distance metric is not appropriate to cope with potential variations in speed and length between two time-series that are compared. Dynamic Time Warping (DTW) is an algorithm designed to solve the aforementioned issue and estimate the distance between two time-series that may vary in speed and length. For a detailed description of the DTW algorithm, the interested reader is referred to Appendix A. In this study, DTW was applied on the instantaneous measured NO_x emissions of the 110 test route segments previously extracted. A distance matrix of the distances of each time-series with respect to the others in the dataset was built. Vehicles that have similar emitting behaviours are consequently situated close to each other while being further apart from the others. The defined distance matrix can therefore be used directly to cluster the dataset. The k-means++ algorithm, a popular unsupervised clustering algorithm, was identified as a suitable technique for this task. For a more detailed description of the k-means++ algorithm, the interested reader is referred to Appendix B. The k-means++ algorithm, using an euclidean distance evaluation, was applied to the previously defined distance matrix for 2 to 20 clusters. The optimal number of clusters was finally estimated using the Davies-Bouldin and the Calinsky-Harabatz indices. For more details about the Davies-Bouldin and the Calinsky-Harabatz indices, the interested reader is referred to Appendix C.

The resulting clusters were subsequently analysed with respect to emission factors, vehicle aftertreatment, vehicle engine size and vehicle weight in order to identify a physical variable able to explain the clusters. In addition, the defined clusters were used in the next steps of this study to update existing instantaneous emission models and develop a new emission model.

3. Results

The present study was conducted with two main points of focus. The results of the clustering are analysed. Analysis of the main clusters (clusters containing more than 3 tests) is provided in terms of driving dynamics and physical characteristics (vehicle weight, engine size, NO_x aftertreatment system) of the vehicles in each cluster. Special focus is given to the analysis of tests of the same vehicle classified in different clusters as well as the importance of spatial variability in emissions. Quantitative analysis of the driving dynamics was performed using the average speed, the Relative Positive Acceleration (RPA, minimum metric of the dynamic boundary conditions in (EU) 2016/646), the 95th percentile of v^*a_{pos} (v^*a_{pos} [95], the maximum metric of the dynamic boundary conditions in (EU) 2016/646) and the percentage of idling (percentage of the test where the engine was running while the vehicle was not in motion). In a second step, the test route was separated into subsegments delimited by major intersections and the variability of emissions on each subsegment was analysed in relationship with the road design.

3.1. General analysis of the main clusters

The best partition is achieved with 17 clusters. Six clusters (hereafter referred to as the main clusters) regroup 97 tests, which represent 88% of the dataset. The eleven other clusters regroup tests of vehicles presenting an emitting behaviour that differs significantly from those of the main clusters. Figure 1 presents the main clusters with respect to the NOx emission factor (a), the engine size (b) and the vehicle weight (c). Finally, the distribution of the NOx emission factors within each cluster is shown in (d). Figure 1d) suggests that clusters consist of tests presenting a similar emission factor. It can moreover be observed that neither the manufacturer, the aftertreatment system, the engine size nor the vehicle weight are able to fully explain these clusters even if some partial conclusions can be drawn. Clusters 4 and 10 contain the tests presenting the lowest emission factors, almost compliant with the Euro 6 test approval limit respectively with the Euro 5 test approval limit. With one exception, cluster 4 contains only vehicles equipped with LNT or SCR systems, which is in agreement with Weiss et al. (2012) who showed that vehicles equipped with EGR systems are not able to reach Euro 6 type approval limits in real-driving conditions. Cluster 10 contains four vehicles each equipped with an EGR system only, but these four vehicles have a significantly smaller engine compared to the rest of the vehicles in this cluster. At the other edge of the emission spectra, vehicles in cluster 8, which present the highest emission factors distribution are vehicles only equipped with an EGR system. A closer inspection of Figure 1 indicates that globally, vehicles equipped with the same aftertreatment system from the same manufacturer tend to be grouped together (with one exception, vehicles from Volkswagen equipped with an LNT system are grouped in cluster 4 while most of the vehicles from Volkswagen equipped with an EGR system only are grouped in cluster 5 and 11). The engine optimisation strategies of the different manufacturers are probably one of the main reasons for the discrepancies between the vehicles.

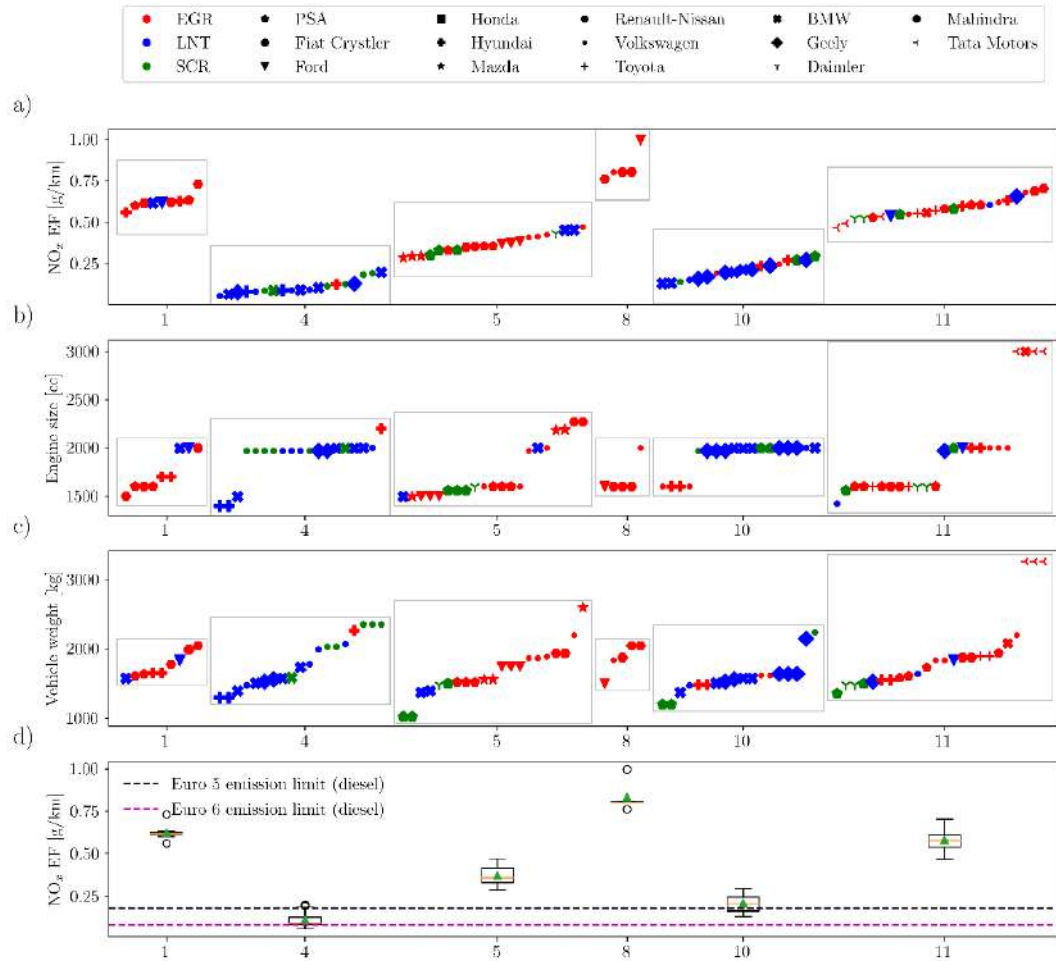


Figure 2: Vehicle manufacturer, NO_x aftertreatment technology and (a) emission factor, (b) engine size, and (c) vehicle weight of each vehicle in the cluster. (d) Boxplots of emission factors per cluster. Each manufacturer is depicted with a different marker, while the aftertreatment technology is displayed in red when the vehicle is equipped with an EGR system only, in blue when the vehicle is equipped with an LNT system in addition to the EGR system and in green when the vehicle is equipped with an SCR system in addition to the EGR system. Clusters containing less than three tests are not depicted here.

3.2. Intra-vehicle real-world driving variations in emissions

Surprisingly, further analysis reveals that for nearly half of the vehicles that were tested several times, the tests are classified in different clusters. Table 3 ([Appendix D](#)) summarizes all the vehicles concerned and gives, in addition to the emission factor and ambient temperature for each of the tests, driving dynamics metrics such as the percentage of mean speed, percentage of idling, the RPA and the 95th percentile of v^*a_{pos} . All the tests are compliant with the EU 2016/646 directive for RPA (which means that none of them were driven "too passively") while eight of the tests are not compliant with the EU 2016/646 directive for v^*a_{pos} [95] (which means that these tests were driven "too aggressively" and would not be RDE compliant). Most of the tests present somewhat lower RPA compared to the average real world RPA (approximately 0.35 m/s² at an average speed of 25 km/h) presented by [Pelkmans and Debal \(2006\)](#) and therefore the driving style can with few exceptions be described as "smooth". It can be clearly observed that the emission factors for the same vehicle can dramatically vary by up to a factor of 7 (vehicle 16) while variations up to a factor of 2 are not unusual (vehicles 1 and 8). Therefore, the overall variations in emission factors for the same vehicle are significant. It is not possible to ascertain the effect of ambient temperature on emissions of the same vehicle as it does not vary among tests of the same vehicle. Variations in percentage of idling (when all the other driving dynamic metrics remaining constant) do not present a systematic effect, even for vehicles from the same manufacturer, for example:

vehicle 4 presents a lower emission factor for a greater percentage of idling while vehicle 10 presents the exact opposite effect. With the exception of one vehicle (vehicle 14), tests of the same vehicle presenting a lower RPA also present lower emission factors (vehicles 3, 6 and 15). However, the inverse relationship with $v^*a_{pos}[95]$ is not true (higher $v^*a_{pos}[95]$ does not always result in higher emission factors). Therefore, while variations in driving dynamics do seem to have an effect on emissions, the data presented here shows clearly that it is unlikely to be the only factor. Previous studies found contradictory outcomes on the effect of driving dynamics: while [Gallus et al. \(2017\)](#) presented results indicating that aggressive driving lead to an increase in NO_x emissions, [Franco et al \(2014\)](#) showed that it is difficult to link an increase in NO_x emissions to driving dynamicity. The current dataset does not allow us to isolate an individual parameter that is able to explain these intra-vehicle real-world driving emissions variations.

In summary, the clustering analysis groups vehicles presenting similar emitting behaviours. However, it is not possible to find a simple relationship that is able to explain the clusters based on physical parameters such as vehicle weight, engine size and emissions control technology, even though some patterns can be identified. This indicates that manufacturer calibration strategies are likely to significantly contribute to the observed variations. The same vehicle does not always present the same emitting behaviour (variations by a factor of 2 are not unusual), even on the same road. Driving dynamics seems to influence emissions, however it is unlikely to be the only factor.

3.3. Influence of road layout on emissions

To further investigate the variability of real-world emissions in the spatial domain, we now explore variability of emissions along subsegments of the route. The layout of roads influences the driving dynamics and some designs may therefore enhance or worsen emissions. A comparison of the NO_x emission factors and mean speed distributions per subsegment are presented in Figure 3 and Figure 4 respectively. The comparisons of the CO₂ emission factors, acceleration, RPA, $v^*a_{pos}[95]$, percentage of idling distributions are available in [Appendix E](#). Table 3 presents the characteristics of each subsegment in terms of distance, cumulated altitude, number of traffic lights, speed bumps, pedestrian crossings, number of lane, number of bus stops and number of roundabouts. It can be observed that the lowest emission factors (mean = 0.37 g/km, median = 0.26 g/km) are obtained on subsegment c whereas the highest emission factors are obtained on subsegment f (mean = 0.50 g/km, median = 0.62 g/km). Interestingly, subsegments d and f, which have the same length (f is simply the reverse of subsegment d), present slightly different distributions of emission factors (NO_x and CO₂) despite presenting similar driving dynamics in terms of mean speed, mean acceleration, cumulative altitude (as approximately flat), RPA, percentage of idling, and $v^*a_{pos}[95]$, as shown in Table 2. As the differences in emissions between the two subsegments seem to be systematic, these are likely to be explained by another source of variability that has not been identified in this study (such as congestion). Subsegments d and f, which cross a commercial area characterised by the presence of numerous shops, present the lowest median and mean speed while the speed standard deviation indicates that these subsegments are characterised by numerous stops compared to the other subsegments. Subsegment c, in which lanes are separated by a central reservation and are only slightly obstructed by park spaces, present a higher average speed than subsegments d and f. These results show that a road designs that enable smoother driving, notably by clearly separating the lanes and removing obstructions caused by vehicle

parked on the sides of the road, could significantly reduce emissions (mean emission 48% lower on subsegment c compared to subsegment f).

Table 2: Subsegment characteristics.

	a	b	c	d	e	f	g	h	i
Length [km]	1.0	0.9	1.1	1.2	1.5	1.2	1.4	0.9	1.1
Cumulative altitude [m. km ⁻¹]	-3	0	-9.1	1.7	0	-1.7	-5	4.4	-0.9
Number of lanes [km ⁻¹]	2	2	2	2	1	2	2/4	2	2
Number of speed bumps [km ⁻¹]	0	0	0	0	2.7	0	0	0	0
Number of intersections [km ⁻¹]	3	7.8	10.9	10.8	4	10.8	7.9	3.3	7.3
Number of pedestrian crossings [km ⁻¹]	3	3.3	3.6	4.2	0.7	4.2	2.9	3.3	1.8
Number of traffic lights [km ⁻¹]	2	1.1	2.7	3.3	0.7	3.3	0.7	1.1	0.9
Number of bus stops [km ⁻¹]	2	1.1	3.6	3.3	1.3	3.3	0.7	1.1	3.6
Number of roundabouts [km ⁻¹]	0	0	0	1.7	0	1.7	0	0	0
Other	-	**	* , **	* , ***	* , ****	* , ***	*	* , ** , *	-

*Park spaces obstructing the road, **Central reservation, ***Commercial area with small shops, ****Residential area, *****Cycling lane

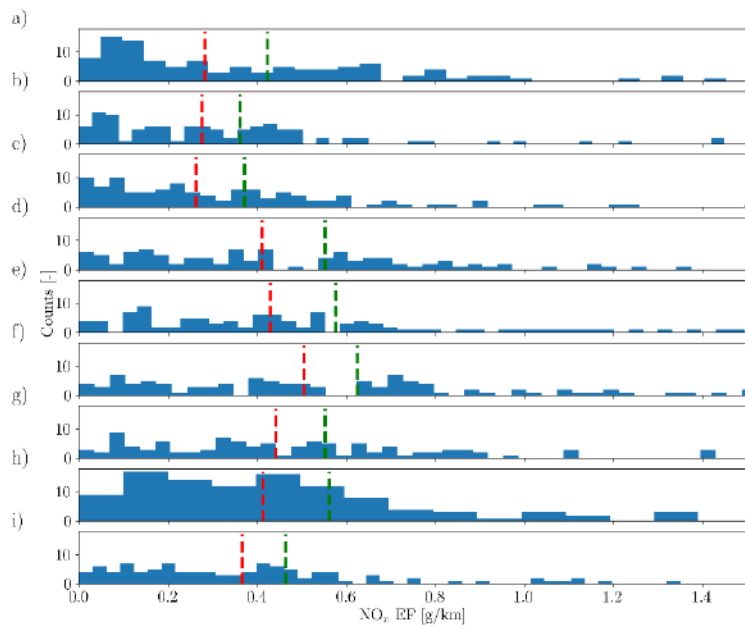


Figure 3: NO_x emission factors distribution on each subsegments. The red dashed line is the median of the distribution. The green dashed line is the mean of the distribution.

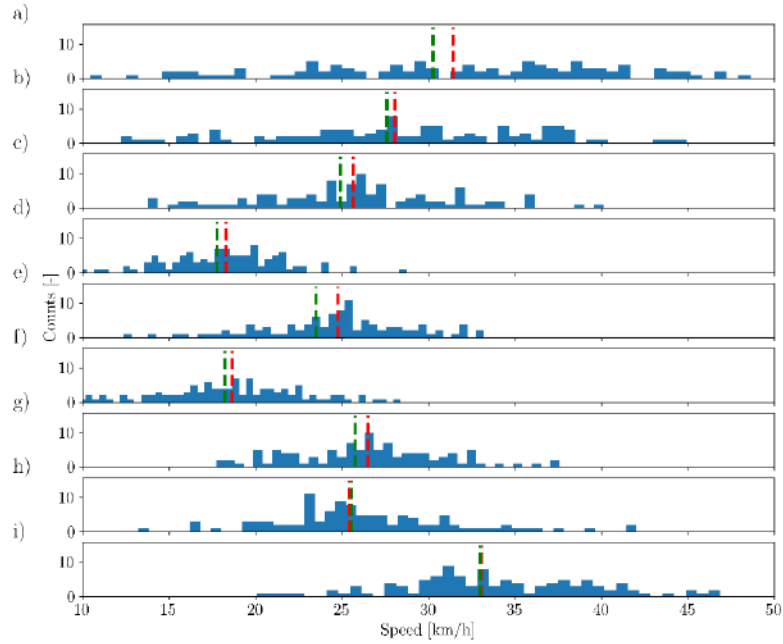


Figure 4: Mean speed distribution on each subsegments. The red dashed line is the median of the distribution. The green dashed line is the mean of the distribution.

4. Conclusion

In this study, machine learning techniques were applied on a large dataset of PEMS measurements (110 tests) in urban driving conditions. Firstly, a clustering analysis grouped vehicles according to their NO_x emission behaviours over a set test route. Analysis of the clusters reveals that: 1) vehicles within the same cluster present similar emission factors, 2) different tests of the same vehicle in the same conditions could result in very different emissions and therefore be assigned to different clusters. There is no relationship based on a priori knowledge that can predict in which cluster an unseen vehicle would fall, e.g. based on engine size, vehicle weight and emissions control technology. The defined clusters will be used in future work to develop more accurate emissions models. [Le Cor nec et al. \(in prep, 2019\)](#), will used the above developed framework to 1) update existing emission models, 2) compare the performances of the original and reformulated models and 3) explore the potential of neural networks to model NO_x emissions.

Analysis of subsegments of the test route reveals that: 1) the same portion of road, presenting the same dynamic characteristics can result in different emission factors probably due to another source of variability than those studied here (such as congestion), and 2) in residential areas, road designs that smooth traffic flow, notably by clearly separating the lanes and removing obstructions (such as vehicle park spaces) seem to have a positive impact on emissions. Further studies assessing the influence of road design and traffic management system on emissions, especially in more congested situations would be beneficial and further studies should be conducted in order to understand the underlying phenomena.

Acknowledgements

This work was supported by Innovate UK (project ref: 103304). Data was provided by Emissions Analytics.

References

- Andersen Z. J., Kristiansen L. C., Andersen K. K., Olsen T. S., Hvidberg M., Jensen S.S., Ketzel M., Loft S., Sorensen M., Tjonneland A., Overvad K. and Raaschou-Nielsen O. (2012). Stroke and long-term exposure to outdoor air pollution from nitrogen dioxide – a cohort study. *Stroke*, 43:320-325.
- Arthur D. and Vassilvitskii S. (2007). K-means++: The advantages of careful seeding. *Proceedings of the eighteenth annual ACM-SIAM symposium on Discrete algorithms*. 1027-1035.
- Commission Regulation (EU) 2016/646 of 20 April 2016 amending Regulation (EC) No 692/2008 as regards emissions from light passenger and commercial vehicles (Euro 6)
- Corradini A. (2001). Dynamic time warping for off-line recognition of small gesture vocabulary. *Proceedings IEEE ICCV Workshop on Recognition, Analysis, and Tracking of Faces and Gestures in Real-Time Systems*, 82-89.
- Czink N., Cera P., Salo J., Bonek E., Nuutinen J.-P. and Ylitalo J. (2006). A framework for automatic clustering of parametric mimo channel data including path power. *Vehicular Technology Conference, 2006. VTC-2006 Fall. 2006 2006 IEEE 64th*, 1-5.
- EEA (2017), Air quality in Europe – 2017 report. Technical report, European Environmental Agency.
- Franco V., Sanchez F.P., German J. and Mock P. Real-world exhaust emissions from modern diesel cars. (2014). *Communications*, 49 (30):847129-102.
- Gallus J., Kirchner U., Vogt R. and Benter T. (2017). Impact of driving style and road grade on gaseous exhaust emissions of passenger vehicles measured by a Portable Emission Measurement System (PEMS). *Transportation Research Part D: Transport and Environment*, 52:215-226.
- Grinham B. and Parry T. (2018). Vehicle licensing statistics: Annual 2017 (revised). Technical report, Department for Transport, UK government.
- Hagena J.R., Filipi Z. and Assassis D.N. (2006). Transient diesel emissions: Analysis of engine operation during a tip-in. *SAE 2006 World Congress and Exhibition*. SAE International.
- Izakian H., Pedrycz W. and Jamal I. (2015). Fuzzy clustering of time series data using dynamic time warping distance. *Engineering Applications of Artificial Intelligence*, 39:235-244.
- Jain A.K. (2010). Data clustering: 50 years beyond k-means. *Pattern Recognition Letters*, 31(8):651-666.
- Le Cor nec C. M. A, Molden N. and Stettler M. E. J. (2019, in prep). Modelling of instantaneous NO_x emissions from diesel vehicles: Insights from machine learning techniques.

- Ligterink N., Kadijk G., van Menschen P., Hausberger S. and Rexeis M. (2013). *Investigations and real-world emission performance of Euro 6 light-duty vehicles*. TNO Delft.
- Matzer C., Hausberger S., Lipp S. and Rexeis M. (2017). A new approach for systematic use of PEMS data in emission simulations. *Journal of Earth Sciences and Geotechnical Engineering*, 7(1):33-50.
- Maulik U. and Bandyopadhyay S. (2002). Performance evaluation of some clustering algorithms and validity indices. *IEEE Transactions on Pattern Analysis and Machine Intelligence*, 24(12):1650-1654.
- Muller M. (2007), Dynamic Time Warping, pages 69-84. Springer Berlin Heidelberg, Berlin Heidelberg.
- Myers C., Rabiner L. and Rosenberg A. (1980). Performance tradeoffs in Dynamic Time Warping algorithms for isolated word recognition. *IEEE Transactions on Acoustics, Speech, and Signal Processing*, 28(6):623-635.
- Ntziachristos L., Papadimitriou G., Ligterink N. and Hausberger S. (2016). Implications of diesel emissions control failures to emission factors and road transport NOx evolution. *Atmospheric Environment*, 141:542-551.
- O'Driscoll R., ApSimon H. M., Oxley T., Molden N., Stettler M.E.J. and Thiagarajah A. (2016). A Portable Emissions Measurement System (PEMS) study of NOx and primary NO₂ emissions from Euro 6 passenger cars and comparison with COPERT emission factors. *Atmospheric Environment*, 145:81-91.
- O'Driscoll R., Stettler M.E.J., Molden N., Oxley T. and ApSimon H.M. (2017), Real-world CO₂ and NOx emissions from 149 Euro 5 and Euro 6 diesel, gasoline and hybrid passenger cars. *Science of the Total Environment*, 621:282-290.
- Park H.-S. and Jun C.-H. (2009). A simple and fast algorithm for k-medoids clustering. *Expert Systems with Applications*, 36(2, Part 2):3336-3341.
- Pelkmans L. and Debal P. (2006). Comparison of on-road emissions with emissions measured on chassis dynamometer test cycles. *Transportation Research Part D: Transport and Environment*, 11(2):233-241.
- Petitjean F., Forestier G., Webb G.I., Nicholson A.E., Chen Y. and Keogh E. (2014). Dynamic time warping averaging of time series allows faster and more accurate classification. *2014 IEEE International Conference on Data Mining*, 470-479.
- Road Task Force (2012). What air quality on the road network and how does this vary by road type, location and time of day? Technical report. *Transport for London*.
- Sempena S., Martens J., Dahl G. and Hinton G. (2013). Human recognition using dynamic time warping. *Proceedings of the 2011 International Conference on Electrical Engineering and Informatics*, 1-5.
- Smit R., Ntziachristos L. and Boulter P. (2010). Validation of road vehicle and traffic emission models – a review and meta-analysis. *Atmospheric Environment*, 44:2943-2953.
- Velmurugan T. (2012). Efficiency of k-means and k-medoids algorithms for clustering arbitrary data points. *International Journal of Computer Technology and Applications*, 3(5):1758-1764.
- Vineis,P.,Gerard,H.,Michal,K.,Federica,V.T.,Fabrizio,V.,Luisa,A.,Herman,A.,Alison,D.,Seymour,G.,Pierre,H.,Christ ian,M.,Giuseppe, M., Kim, O., Ole, R.-N., Francoise, C.C., Jacob, L., Heiner, B., Antonia, T., Domenico, P., Marco, P., Vittorio, K., Rosario, T., Salvatore, P., Bas, B.-D.-M. H., H., P. P., Eylin, L. E., A., G. C., Carmen, M., Miren, D., Aurelio, B., Lluis, C., Ramon, Q. J., Goran, B., Bertil, F., E., D. N., J., K. T., Rodolfo, S., Rudolf, K., and Elio, R. (2006). Air pollution and risk of lung cancer in a prospective study in Europe. *International Journal of Cancer*, 119(1):169-174.
- Weiss M., Bonnel P., Kuhlwein J., Provenza A., Lambrecht U., Alessandrini S., Carriero M., Colombo R., Forni F., Lanappe G., Lijour P.L., Manfredi U. Montigny F. and Sculati M. (2012). Will Euro 6 reduce the NOx emissions of new diesel cars? Insights from on-road tests with Portable Emission Measurement Systems (PEMS). *Atmospheric Environment*, 62:657-665.

Appendix

A. Dynamic Time Warping (DTW)

Dynamic Time Warping (DTW) is a class of algorithms that allow comparing two (time-dependent) sequences with respect to their shape under certain restrictions ([Muller \(2007\)](#)). Intuitively, the two sequences are matched by distorting the time axis, stretching some segments while shrinking others. Similar dynamic patterns occurring at different timesteps of the sequences are matched together and consequently the algorithm is able to cope with time deformations and different speeds associated with time-dependent data ([Izakian et al. \(2015\)](#)). The optimal alignment of these two sequences should satisfy the following conditions: the first and the last indices of both sequences are matched together, the mapping of indices from the first to the second sequence must be monotonically increasing and

continuity should be insured ([Muller \(2007\)](#)). The monotonicity condition reflects to requirement for faithful timing (e.g. if an element in the first sequence precede a second, it should be the same in the second sequence) while the continuity condition forces the algorithm to consider all the data points. DTW algorithms were successfully applied to a wide range of problems, including speech recognition ([Myers et al. \(1980\)](#)), gesture recognition ([Sempena et al. \(2011\)](#), [Corradini \(2001\)](#)), clustering ([Petitjean et al. \(2014\)](#)), etc.

B. K-means ++ algorithm

k-means is a widely used clustering algorithm aiming at partitioning N observations into k clusters by minimizing the within-cluster sum-of-squares ([Arthur and Vassilvitskii \(2007\)](#)). The original algorithm begins with k centres, typically chosen randomly from the data points. Each point is then assigned to the nearest cluster and the cluster center is recomputed as the centre of mass of all the points assigned to it. These two stages are repeated until the clusters stabilize. Although simple and quick, accuracy is not insured and the results can converge to a suboptimal solution ([Jain \(2010\)](#)). [Arthur and Vassilvitskii \(2007\)](#) proposed an approximation is NP-hard problem, by choosing the initial values (seeds) randomly from the datapoints similarly than for the original algorithm but weights additionally the datapoints according to their squared distance from the closest center already chosen. This so called k-means++ is $O(\log k)$ -competitive and achieves performances 20% better and almost twice as fast than the original k-means algorithm for a real-world dataset ([Arthur and Vassilvitskii \(2007\)](#)).

C. Calinski-Harabatz and Davies-Bouldin indices

Evaluation of the optimal number of clusters, in the context of unsupervised clustering where little or none previous knowledge about the data is available, is a complicated task. Internal validation measures, based on separation and compactness, are a commonly used methodology. The Calinski-Harabatz (CH) index is based on the average sum-of-squared between and within each cluster while the Davies-Bouldin (DB) index is a function of the intra-cluster similarity and inter-cluster separation ([Maulik and Bandyopadhyay \(2002\)](#), [Czink et al. \(2006\)](#)). Both the CH and the DB indices allow to determine the partition with the most compact and separated clusters

D. Dynamics and emitting characteristics of the repeated tests falling in different clusters

	#	Cluster	EF [g/km]	Mean speed [km/h]	% of idle	RPA [m/s ²]	v*a _{pos} [95] [m ² /s ³]	Mean temp. [C]
BMW 220D SPORT 2015 - LNT	1	4	0.07	19.4	29.0	0.17	8.8	21.7
		10	0.13	25.7	16.7	0.18	9.9	22.8
Citroen Grand C4 Picasso - EGR	2	1	0.60	25.7	14.5	0.20	16.8	23.8
		11	0.53	25.8	13.8	0.17	15.5	23.9
Citroen DS5 DSTYLE BLUEHDI 2014 - SCR	3	5	0.31	27.3	20.5	0.17	10.7	28.4
		11	0.58	21.9	19.0	0.21	10.5	28.8
BMW 116D ED PLUS 2015 – LNT	4	4	0.11	20.0	28.3	0.23	21.0	17.5
		5	0.46	23.0	20.0	0.23	20.9	17.3
BMW 220d SE – LNT	5	5	0.45	23.3	18.8	0.16	16.1	15.0
		10	0.22	22.9	25.2	0.17	17.7	14.6
Volkswagen Passat - EGR	6	5	0.42	23.4	23.6	0.18	17.9	25.4
		11	0.55	21.1	24.8	0.22	25.0	25.4
Ford S-Max TDCi Duratorq Titanium X - LNT	7	1	0.62	27.9	13.3	0.20	16.9	24.3
		11	0.54	26.4	18.2	0.18	10.7	24.2
Volkswagen Golf SV SE TDi - LNT	8	4	0.09	26.3	16.2	0.16	8.3	22.3
		10	0.15	23.9	15.5	0.18	8.7	23.7
Volvo S60 R- DESIGN LUX NAV D3 2015 – LNT	9	4	0.08	19.8	33.1	0.16	7.9	22.0
		10	0.16	22.0	26.8	0.18	9.1	21.2
BMW X3 XDRIVE20D M SPORT AUTO 2014 – LNT	10	1	0.62	22.1	10.4	0.23	10.4	24.0
		6	0.97	23.8	16.2	0.23	11.0	25.0
Mercedes C200 AMG Line Blue Tec – SCR	11	5	0.44	20.9	23.2	0.21	9.7	22.4
		11	0.52	20.0	23.6	0.20	10.3	22.9
		11	0.53	22.0	22.6	0.21	11.2	19.3
Peugeot 308 – SCR	12	13	1.43	23.5	24.3	0.18	17.4	27.3
		14	1.17	25.8	17.3	0.17	19.0	27.7
		15	1.66	25.7	20.9	0.21	18.5	27.6
Nissan X-Trail – EGR	13	1	0.62	27.2	16.1	0.20	10.2	27.6
		8	0.80	25.0	18.2	0.21	11.3	27.3
		8	0.80	25.6	18.6	0.19	11.6	28.2
Nissan Qasqai – EGR	14	8	0.76	23.4	24.0	0.18	10.7	19.7
		11	0.70	16.2	36.3	0.15	8.2	19.0
		11	0.69	22.0	17.0	0.19	9.1	20.8
Audi Q3 – EGR	15	8	0.80	25.4	19.5	0.18	8.4	19.0
		11	0.62	27.1	10.2	0.11	5.9	19.8
		11	0.68	21.5	24.5	0.14	7.6	20.3
Volvo V40 CROSS COUNTRY SE NAV 2014 – LNT	16	4	0.13	18.5	30.1	0.18	9.6	21.3
		9	0.90	23.9	14.3	0.15	8.5	22.5
		10	0.22	23.2	16.9	0.17	9.5	21.6
	17	4	0.20	23.9	24.3	0.21	13.2	26.9

BMW 218D LUXURY 2014 - LNT		10	0.13	21.5	25.9	0.19	11.3	26.9
		10	0.20	23.4	22.9	0.18	11.0	26.6

Table 3: Dynamics and emitting characteristics of the repeated tests falling in different clusters.

E. Dynamic metrics distribution per subsegment

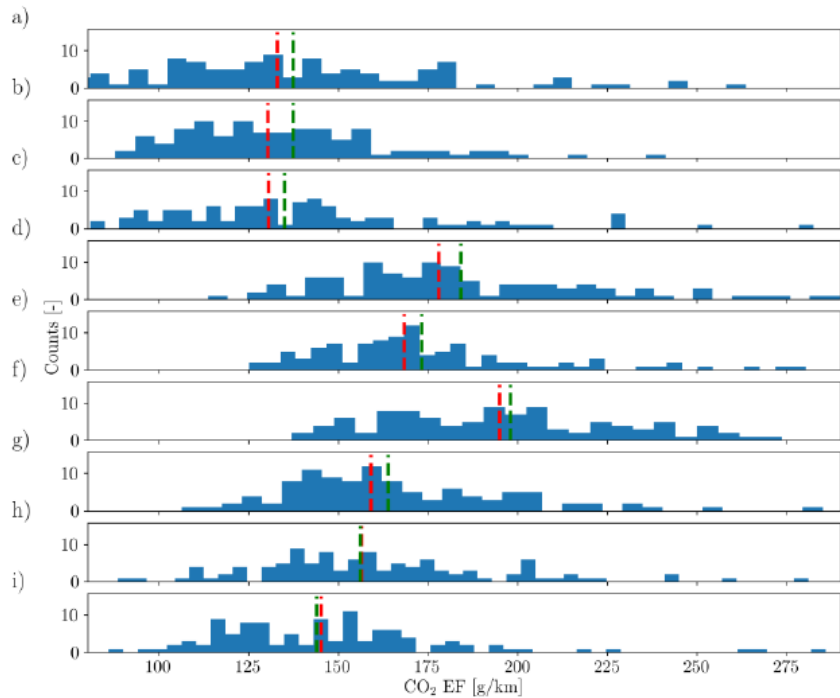


Figure 5: CO₂ emission factors distribution on each subsegments. The red dashed line is the median of the distribution. The green dashed line is the mean of the distribution.

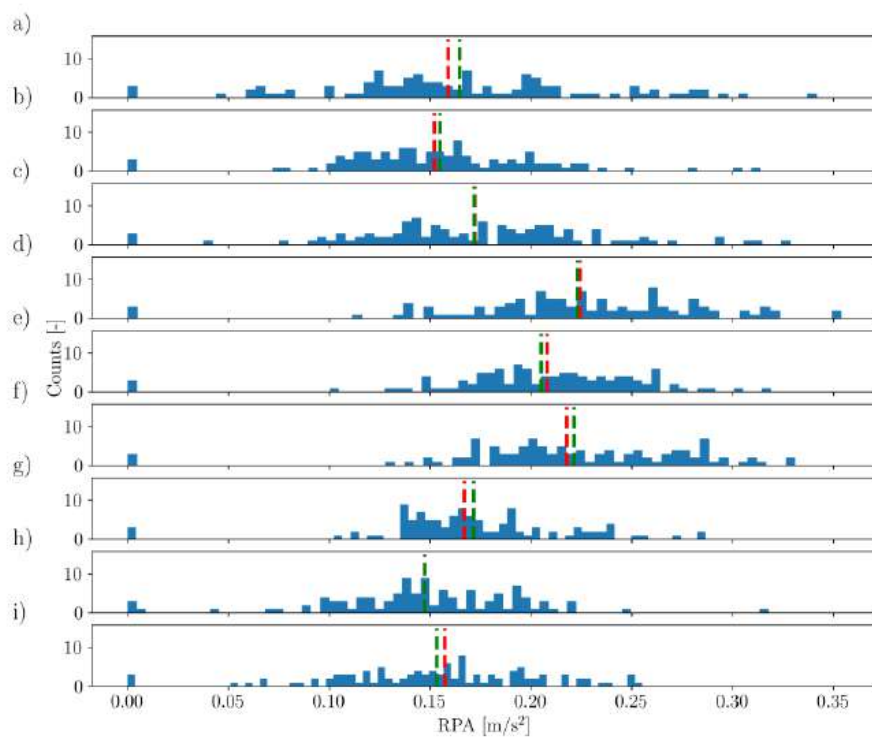
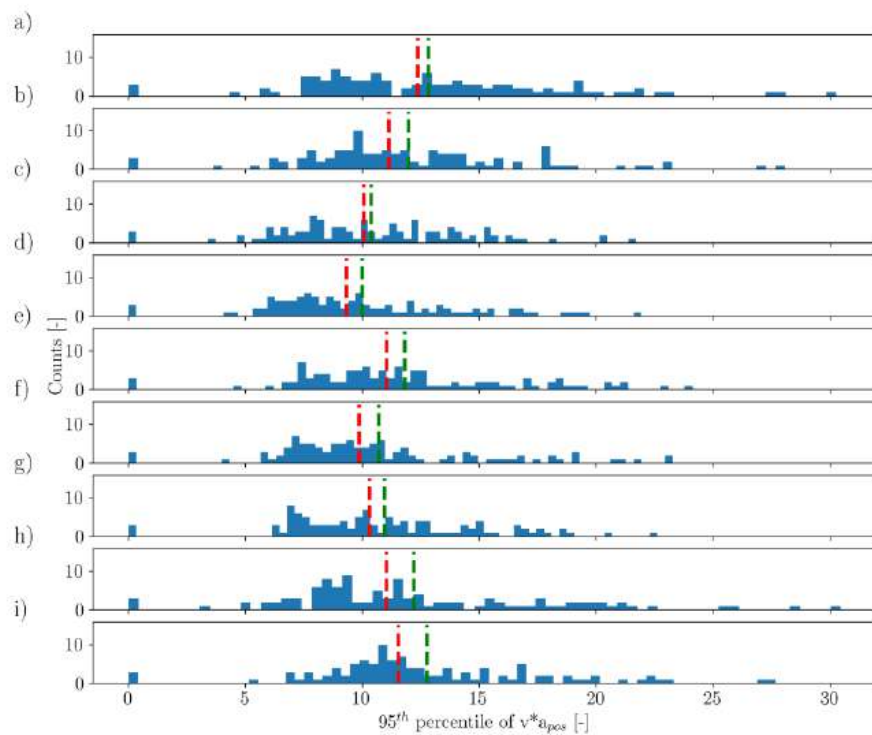


Figure 6: Distribution of RPA for each subsegment. The red dashed line is the median of the distribution. The green dashed line is the mean of the distribution.



*Figure 7: Distribution of v*a_{pos}[95] for each subsegment. The red dashed line is the median of the distribution. The green dashed line is the mean of the distribution.*

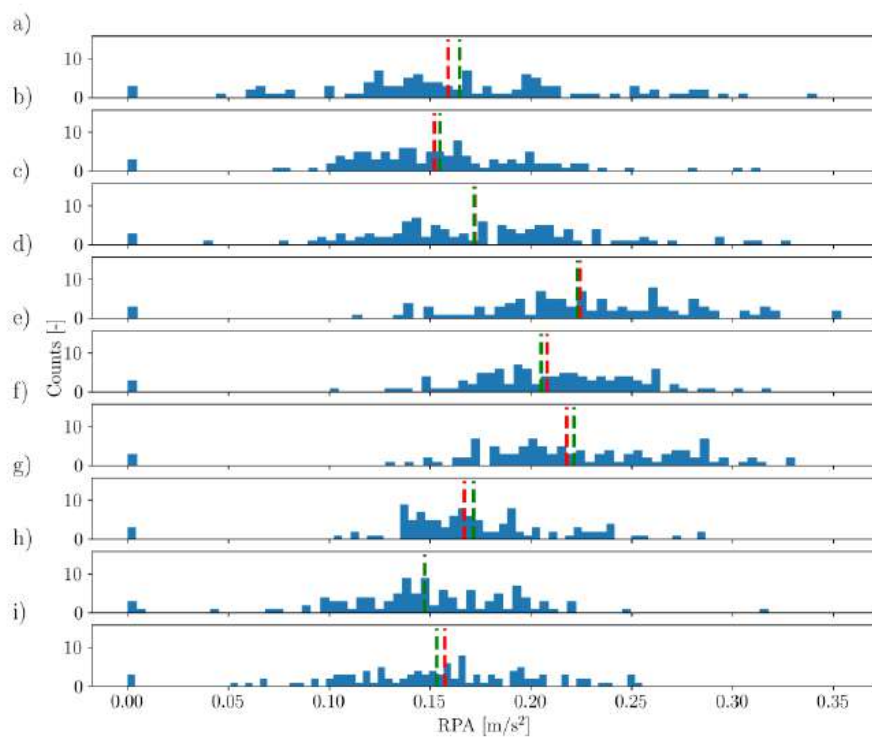
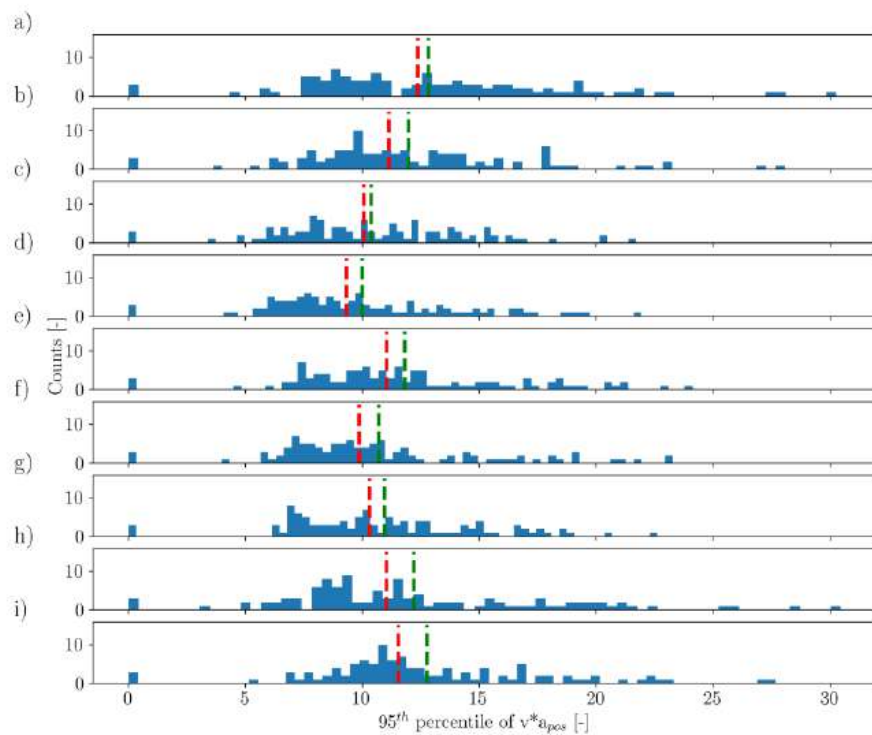


Figure 6: Distribution of RPA for each subsegment. The red dashed line is the median of the distribution. The green dashed line is the mean of the distribution.



*Figure 7: Distribution of v*a_{pos}[95] for each subsegment. The red dashed line is the median of the distribution. The green dashed line is the mean of the distribution.*

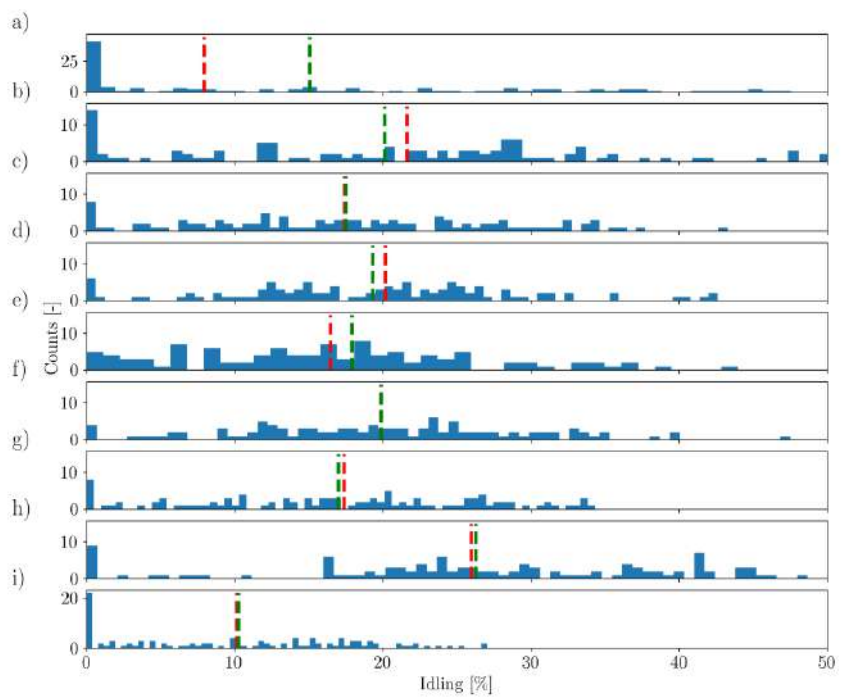


Figure 9: Distribution of the percentage of idling per subsegment. The red dashed line is the median of the distribution. The green dashed line is the mean of the distribution.

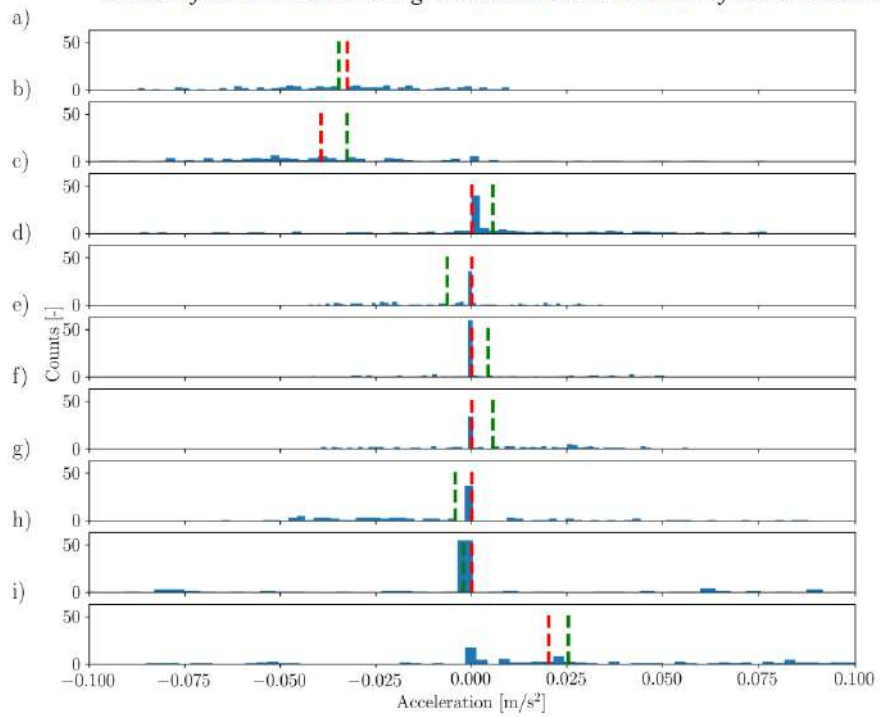


Figure 8: Distribution of the mean acceleration per subsegment. The red dashed line is the median of the distribution. The green dashed line is the mean of the distribution.

2.10.5 Ultrafine particle dispersion in the wake of a squareback vehicle model

R. Rodriguez¹, F. Murzyn^{1*}, A. Méhel² and F. Larrarte³

Affiliation of authors, include e-mail address for corresponding author (Arial 9). [style: Affiliation]

¹ Department of Mechanical Engineering, ESTACALAB, ESTACA West Campus, 53000, Laval, France,
frederic.murzyn@estaca.fr

² Department of Mechanical Engineering, ESTACALAB, ESTACA Paris Saclay Campus, 78066, Saint Quentin en Yvelines, France

³ Department GERS, IFSTTAR, 44340, Bouguenais, France

Introduction

Around 7 millions worldwide annual deaths are due to air pollution. This pollution has different origins such as manufactories, cars, planes, agriculture... Among all pollutants, Ultra Fine Particles (UFP), which correspond to particle having an aerodynamic diameter below 100nm, cause strong adverse health effects. Indeed, their concentrations (in mass and number) can reach very high levels (Morawska et al., 2004). One of the most important sources of UFP is transportation systems. Cars, trains, buses and motorbikes emit UFP from the tailpipe (due to engine combustion) as well as from brakes and tyres. Meanwhile, there is an exponential need of road transport as people travel more and more because they tend to live increasingly away from city centers. Factually, UFP exposure reaches its most significant levels in urban areas (Buseck and Adachi, 2008) in which road traffic is often heavy. This has led to an increasing exposure of car passengers, cyclists and pedestrians to air pollution making this problem a key issue for many scientists. Recent studies (Mehel et al., 2019) have shown that higher concentrations of UFP may be encountered in the car cabin compared to the outside level. This mainly occurs in tunnels or in the ring of big cities such as Paris (France). As we spend more and more time in transportation systems, reducing the exposure of commuters has become a major goal. Having that in mind, different strategies can be set up. Reducing the infiltration using filters (such High Efficiency Particulate Air), improving the ventilation settings and getting a better understanding of the pollutant dispersion in the wake of car are some options. In this paper, we particularly address the last one. Improving our knowledge on the physical processes involved in this dispersion could lead to an optimization of air entrances of cars as well as of tailpipe (in terms of shape, size and/or position...). Therefore, in the present paper, we aim at studying the links between the wake flow properties of a squareback simplified car model and UFP concentration fields downstream of the same car model. The originality of our experimental approach is based on the use of solid particles that are representative of those emitted by a real car. To date, studies dealing with the dispersion of pollutants (Kanda et al., 2006 ; Carpentieri et al., 2012) have used gaseous tracer. However, they do not have the same dynamics as solid particles and do not allow Particle Number Concentration (PNC) measurements.

In the next part, the experimental facilities and measurement techniques are described and our approach is explained. Then, the wake flow properties are presented in terms of mean and turbulent velocity fields. The topology of the flow is accurately depicted and compared to the literature to validate our experimental setup. Then, the PNC fields are characterized showing the strong influence of the recirculation region on the dispersion of these UFP. From our experimental data, we also propose a model that allow the determination of a diffusion coefficient with a high level of accuracy. It is believed that this result may be useful for the calibration of numerical models.

Experimental facilities and measurements techniques

As mentioned above, this paper is related to an experimental study. Measurements have been conducted in an open-circuit wind tunnel manufactured by DELTALAB (reference model EA103). The test section is 1m in length, 0.3m in both height and width. The maximum speed of the air flow is 40m/s. An important calibration campaign has been carefully achieved to characterize the incoming flow with an empty test section (Rodriguez, 2018). The main conclusions state that the

maximum streamwise turbulence intensity u'/U_0 was less than 1% (outside of the boundary layer) and that this boundary layer is turbulent with a maximum thickness of 12mm at the exit of the test section (that is partially-developed inflow conditions). The car model used in this study is a 0.19 scaled Ahmed body (Ahmed et al., 1984) with a rear slant angle of 0° ($\varphi=0^\circ$). It has a length $L=196\text{mm}$, a width $l=73\text{mm}$ and a height $H=54\text{mm}$. The model is fixed on the floor of the test section by a cylindrical rod (diameter 5mm) and four stilts are used which height and diameter are 15mm (defined as h_s) and 6mm respectively. Note that this height is larger than the maximum boundary layer thickness. The relative ground clearance is $H_s=h_s/H=0.28$. The blockage coefficient, defined as the ratio between the model frontal area and the test section area is below 5%. Then, no correction is needed for the blockage effect (Wang et al., 2013). Figure 1 is a sketch of this model. For experiments with particles, a tailpipe has been stuck on the bottom part of the car. Its diameter is 4mm. From a practical point of view, it is supposed to correspond to a real light commercial vehicle. On Figure 1, the red arrow indicates the flow direction. The coordinate system (x,y,z) associated with the model is indicated. (X,Y,Z) are the corresponding dimensionless distance, the height H of the car being the scaling length. (u,v,w) are the components of the velocity vector, (U,V,W) being the time averaged values, (u',v',w') the corresponding fluctuations according to the Reynolds decomposition.

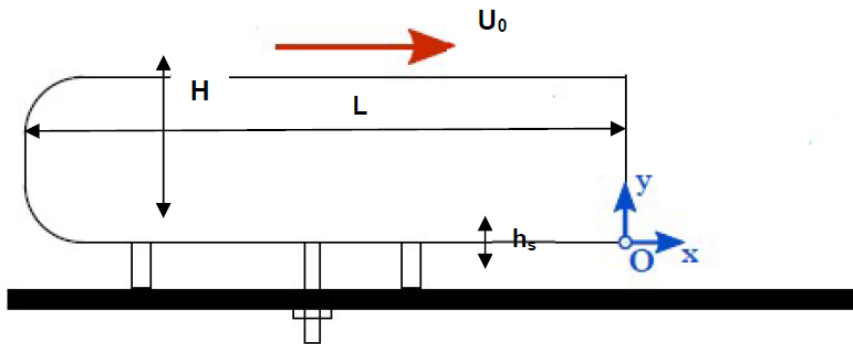


Figure 1: Sketch of the Ahmed body and axis ($\varphi=0^\circ$)

It is important to note that we decided to keep the ratio between velocities of the upstream flow (U_0) and the exhaust gas one (U_{eg}) similar for our experiments to that of a real car moving in an urban area at 13.9m/s. Then, considering our experimental facilities, a constant upstream velocity of $U_0=14.3\text{m/s}$ is considered in the present paper. The Reynolds number based on the model height ($Re = \frac{U_0 H}{\nu}$) is $Re=4.95 \cdot 10^4$ (where ν is the kinematic viscosity of air).

Velocity measurements were recorded with a 2D LDV system manufactured by DANTEC Dynamics (model 2D Flow Explorer). In terms of optical properties, the two pairs of LASER beams have wavelengths of 660nm and 785nm. The fringe spacings were $5.45\mu\text{m}$ and $6.40\mu\text{m}$ in the longitudinal and vertical directions, respectively. The diameter and length of the measuring volume (in the z direction) are $168\mu\text{m}$ and 2.81mm respectively for the first component and $200\mu\text{m}$ and 3.34mm for the second component. The focal length is 500mm and the Bragg cell frequency shifting is 80MHz . The LDV displacement in the plane (x,y) is controlled by a 2D traverse system. The LDV and traverse system are controlled by a computer and data are acquired using BSA Flow Software (v5.03.00). The fog fluid used in this study is the SAFEX Inside Nebelfluid Extra Clean provided by DANTEC (SAFEX, 2003). It is a mixture of diethylene glycol and water. The fog generator is the SAFEX S 195 G with an adjustable flow rate. Generated seeding particles have a mean diameter of $1.068\mu\text{m}$. Algieri et al. (2005) recommended this seeding system for LDV measurements in air flows. Velocity measurements have been done in the wake flow region (downstream of the car model) corresponding to $0.09 < X < 5.65$, $0 < Y < 1.3$. Four planes ($Z=0$, $Z=-0.23$, $Z=-0.45$ and $Z=-0.68$) have been considered (side of the tailpipe). Due to interference with the ground, only 1D measurements have been undertaken in the region given by $-0.28 < Y < 0.09$. When measurements have to be done close to the ground, the traverse system was inclined at 4.1° with respect to the horizontal direction. Since it is less than 5° , no correction on the velocity measurements is required (Tachie, 2000). For 2D measurements, data acquisition lasts 90s at each location in agreement with the calibration study. For 1D measurement and due to the finer

spatial mesh, acquisitions have been recorded of a period of 10s. Out of the boundary layer, measurements have been done at 780 positions. Data were analyzed according to a new and original method based on a filtering technique described by Rodriguez (2018) and Rodriguez et al. (2017, 2018a-b). For more details, one can refer to them. Note this innovative technique ensures accurate results whatever the seeding conditions are (homogeneous or non-homogeneous).

UFP have been generated using a PALAS, model DNP 2000 (PALAS, 2009). They are carbon particles with an aerodynamic diameter between 20 and 100nm. They are carried by a nitrogen flow with a flow rate of 8L/h. The mass flow rate of these UFP is 6.5mg/h. As mentioned above, for similitude reasons, the diameter of our tailpipe was 4mm. The exit of this tailpipe is at a dimensionless position given by (0, -0.04, -0.31). The exit velocity of UFP is 10.6m/s. Particles Number Concentration (PNC) have been recorded with an ELPI (Electrical Low Pressure Impactor). This device has been developed at the University of Tampere (Finland). More details about this device can be found in Rodriguez (2018) and Dekati (2010). Particles have been collected using a sampling probe with a suction flow rate of 10L/s. According to diameter of the sampling probe (4mm), the aspiration speed is 13.3m/s which is close to the upstream velocity (isokineticism). UFP have been collected at 642 positions downstream of the car model ranging from 0.57 to 7.06 (X), -0.04 to 1.07 (Y) and -1.85 to 1.85 (Z). Data acquisition lasts at least 80s for each point.

A sketch of the experimental arrangement is shown on Figure 2.

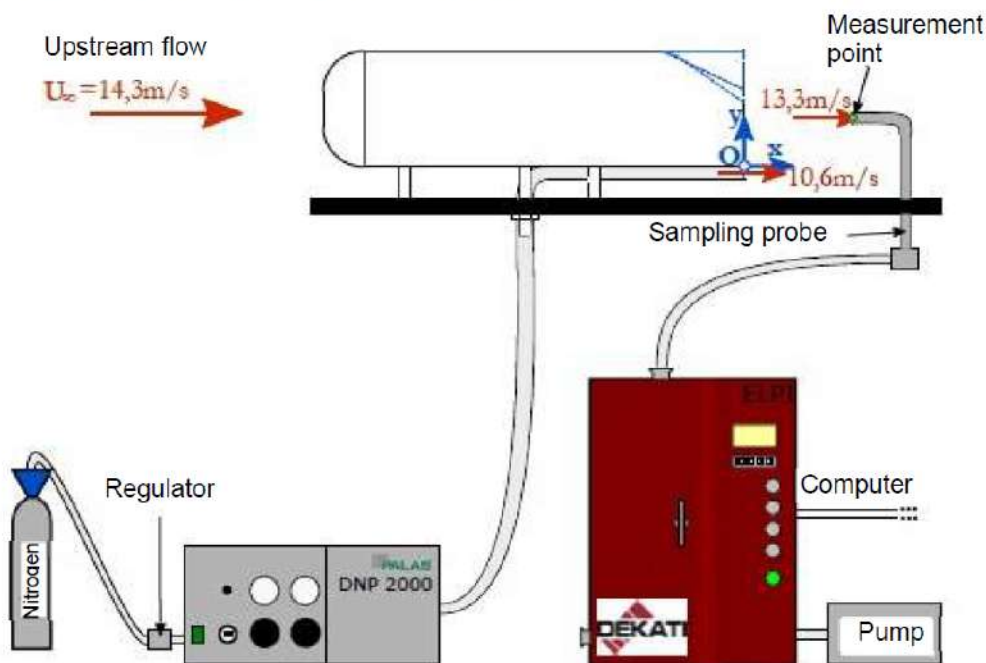


Figure 2: Sketch of the experimental arrangement

Results: Velocity fields

Figure 3 present the 2D maps of mean and turbulent properties of the wake flow at the centreline of the wind tunnel ($Z=0$). Figures 4a and 4b correspond to the dimensionless horizontal (U/U_0) and vertical (V/U_0) mean velocity, respectively. Figures 3c and 3d are dedicated to the dimensionless turbulent kinetic energy ($E_c^* = \frac{1}{2} \frac{(u'^2 + v'^2)}{U_0^2}$) and Reynolds stresses ($\tau^* = \frac{u'v'}{U_0^2}$), respectively. On these figures, $x/H=0$ corresponds to vertical rear face of the car model, its bottom being at $y/H=0$ and its top at $y/H=1$.

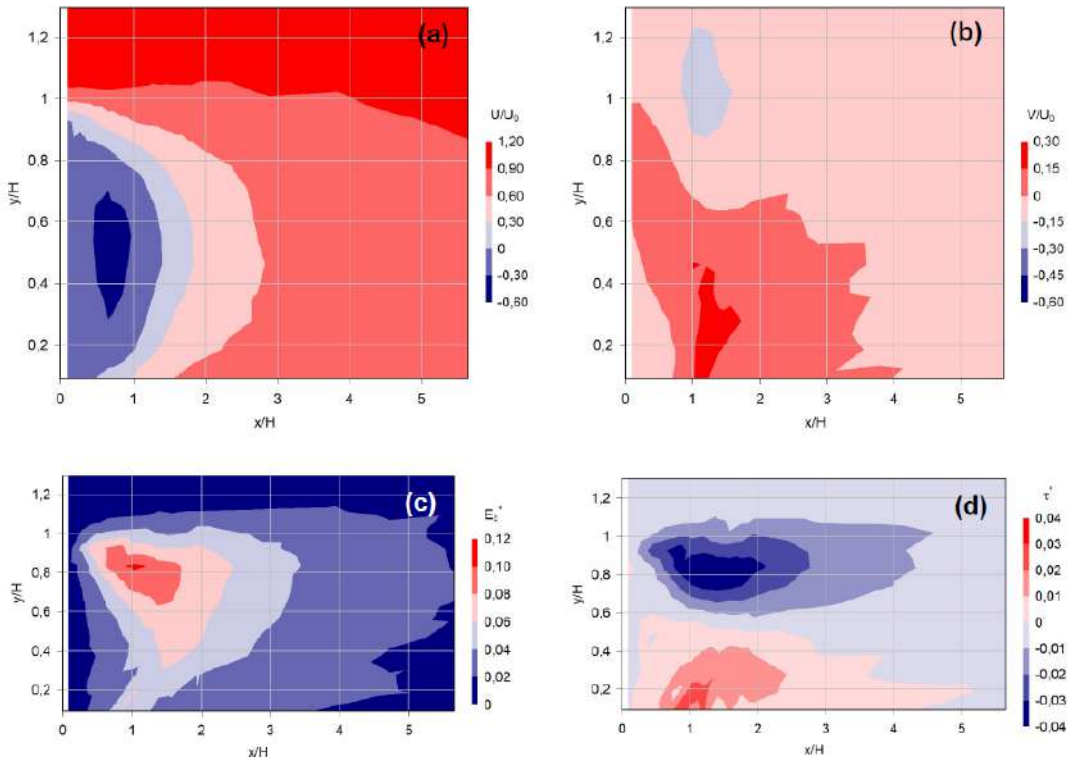


Figure 3: Dimensionless properties of the velocity field in the symmetry plane ($Z=0$). (a) Horizontal component, (b) Vertical component, (c) Turbulent kinetic energy and (d) shear stresses

Different flow characteristics can be put in evidence from these figures. First, a region with negative horizontal velocities develops in the close wake of the car (Figure 3a). For $X=x/H < 1.39$, negative values for U are found. This corresponds to a recirculation region which length is $L=1.39H$. We also observe a symmetry on Figure 3a with respect to $Y=y/H \sim 0.5$. This is in agreement with previous studies (Gosse, 2005 ; Eulalie, 2014 ; Lahaye, 2014 ; Barros, 2015). For the vertical component (Figure 3b), the field tends to be antisymmetric with respect to $Y=y/H=0.5$. By combining these two 2D maps (Figure 3a and Figure 3b), the flow topology is depicted. It indicates that two counter rotating vortex develop. The upper one ($Y>0.5$) is clockwise whereas the lower one ($Y<0.5$) is counterclockwise. Positions of the centres of these two vortex have been identified. The upper one is located at $(0.62, 0.84, 0)$ while the lower one is at $(0.70, 0.14, 0)$. This is also in agreement with previous results given by some experimental studies available in the literature (Eulalie, 2014 ; Lahaye, 2014). Overall, these preliminary results validate our experimental set-up, our flow topology being in line with the state of the art for similar experimental conditions.

Regarding the turbulent kinetic energy and the Reynolds shear stresses, our results are presented on Figure 3c and 3d, respectively ($Z=0$). On the one hand, they point out that the highest levels of turbulent kinetic energy are found in the upper shear layer, the maximum being reached at $(1, 0.8, 0)$. This upper shear layer tends to be more intense compared to the lower one. This is probably due to the ground clearance which is larger compared to the literature (Barros, 2015). On the other hand, the Reynolds shear stresses are almost symmetrical (in magnitude) with respect to $y/H=Y=0.5$.

Results: PNC

In this section, PNC in the wake of the squareback Ahmed body are presented. Mean data provided by the ELPI ($\overline{C_{f,t}}$) have been divided by the maximum concentration (C_{max}) measured at the exit of the tailpipe. C_{max} is about 7.10^7 part/cm³. Furthermore, the ambient level of the concentration ($\sim 10^2$ to $\sim 10^4$ part/cm³) has been subtracted to the data. So, $\overline{C_{f,t}}^* = \frac{\overline{C_{f,t}}}{c_{max}}$.

Figure 4 are 2D vertical maps corresponding to plans defined by $Z=-0.31$ (Figure 4a), $Z=0$ (Figure 4b) and $Z=+0.31$ (Figure 4c). Note that the boundary of the recirculation region is plotted with black dotted lines for information. Each measurement position is marked with a black spot.

Figure 4a shows that the highest PNC levels are found in the tailpipe axis. At a distance $X=\sim 0.60$, PNC levels are about one third of those measured at the emission point. Regions of high PNC are observed over roughly the total height of the car model. Farther downstream, we notice a downwards deviation trend. Overall, this behaviour is imposed by the flow topology and the two counter rotating vortex mentioned in the above section. In the close vicinity of the rear face of the car model, a large part of the UFP ejected from the tailpipe are entrapped by these turbulent structures and sucked upwards. Compared to Figure 4b and Figure 4c, it is obvious that the highest PNC are measured for $Z=-0.31$, that is in line with the tailpipe. In the symmetry plan (Figure 4b), PNC are 10 times lower than the maximum. For this PNC field, results indicate a certain homogeneity over the whole height of the car model. One more time, the topology of the flow explains this results as a toric structure has been observed in the close wake. In the opposite plan (Figure 4c), PNC levels are lower even if particles are still carried in the horizontal direction. We also note that results for $Z=0$ and $Z=0.31$ tend to be symmetric with respect to $Y=0.5$.

In order to get a better description of the horizontal mixing, Figure 5 correspond to 2D horizontal maps of the PNC in 3 horizontal planes: $Y=-0.04$ (tailpipe level, Figure 5a), $Y=0.33$ (within the recirculation region, Figure 5b) and $Y=0.70$ (within the recirculation region, Figure 5c).

At the tailpipe level (Figure 5a), highest levels of found for $Z=-0.31$ as expected. Up to $X\sim 1.5$, the PNC field is not symmetric as most of the UFP are located in the same half width of the tailpipe. At this relative height above the ground, the recirculation region is not yet effective. By moving in the upper section (Figure 5b), we penetrate into the recirculation region. Contrary to the previous situation, the horizontal mixing occurs and the symmetry in the PNC field is obvious. Even if the highest levels of PNC are still measured in the side of the tailpipe for $X<2$, the PNC field becomes symmetric farther. One more time, this is due to the flow topology as we reach the recirculation region at $Y=0.33$. The same behaviour is observed on Figure 5c ($Y=0.70$) as we are still in this recirculation region.

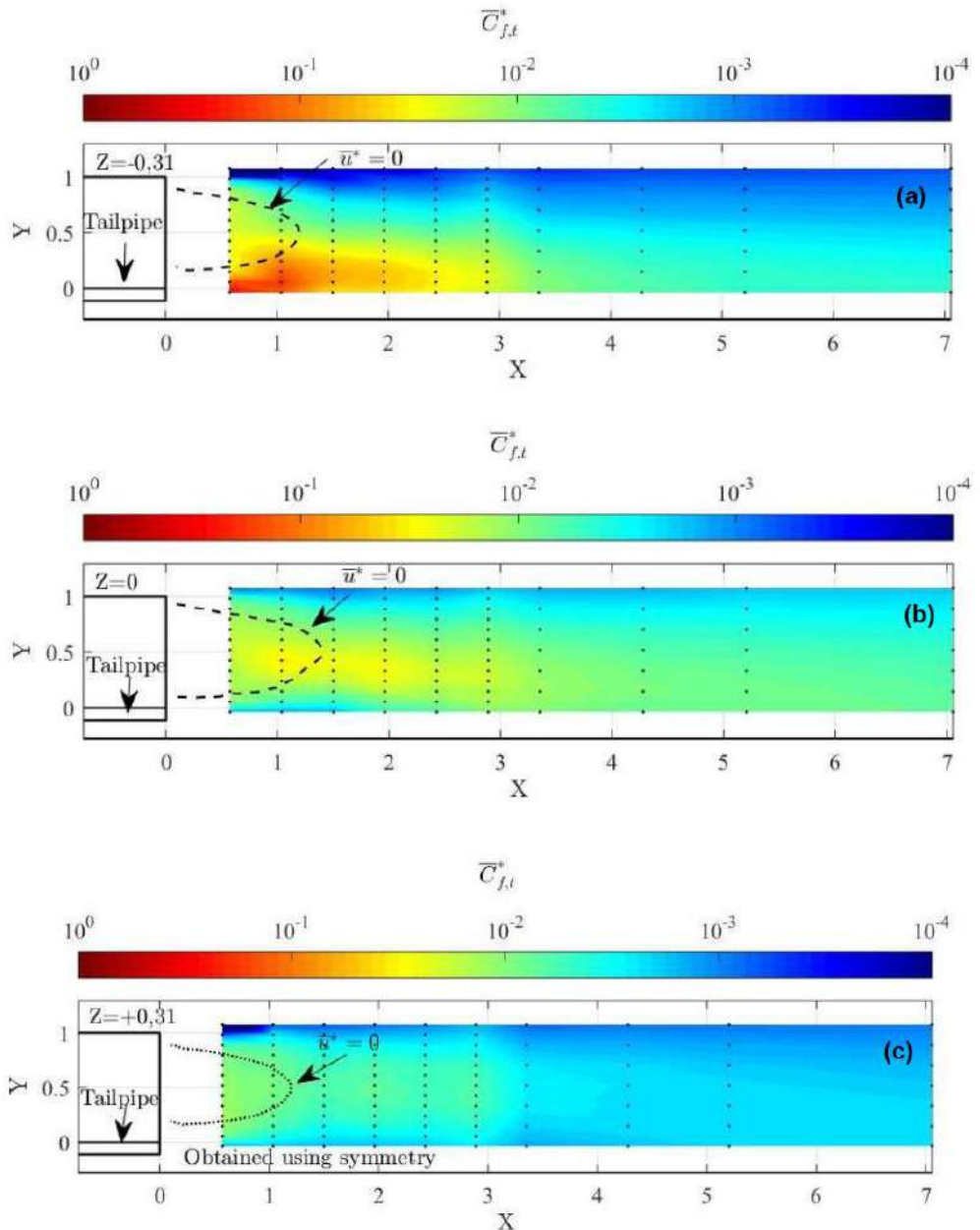


Figure 4: 2D vertical map of dimensionless PNC in different planes. (a) $Z=-0.31$ (tailpipe plan), (b) $Z=0$ (symmetry axis) and (c) $Z=+0.31$ (opposite side of the tailpipe)

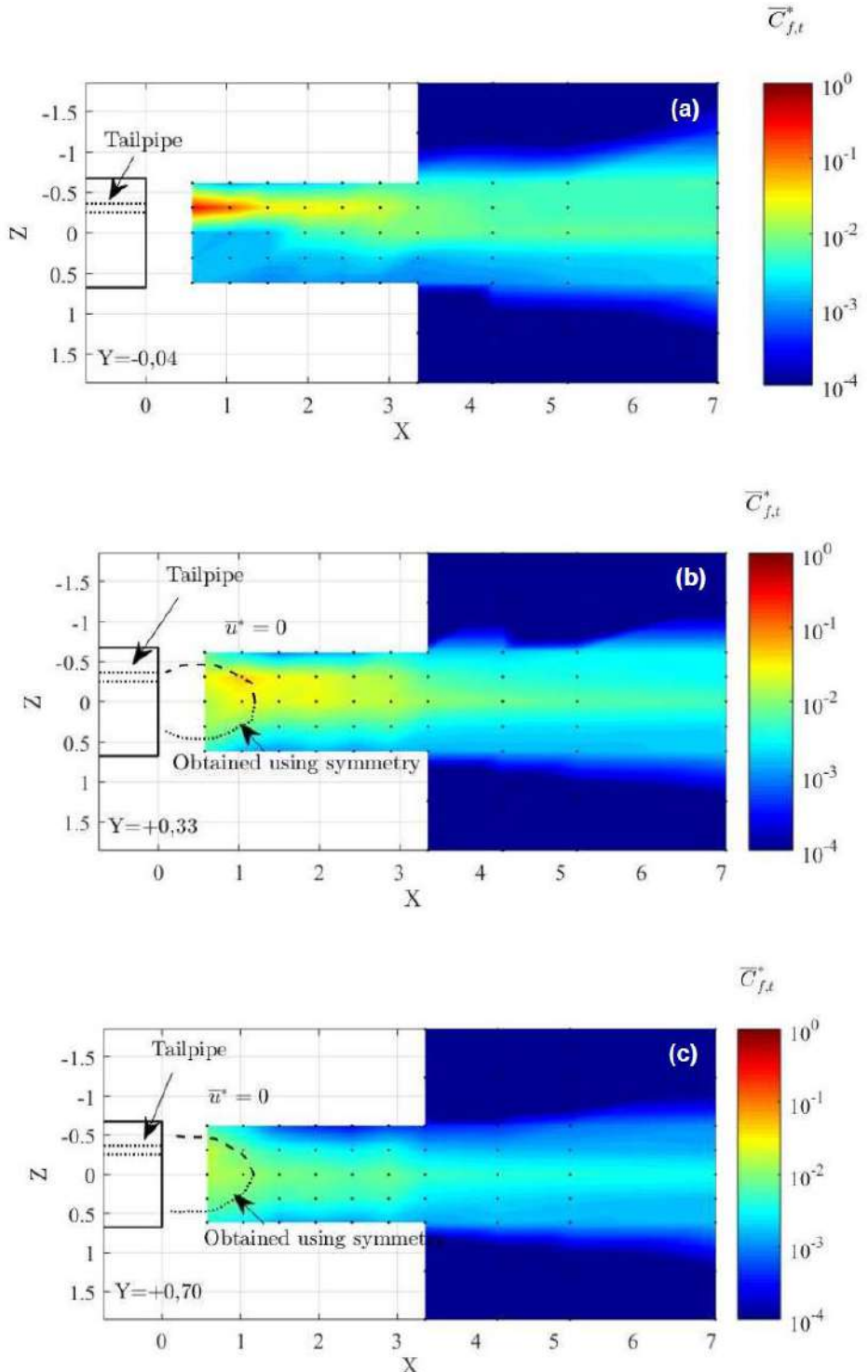


Figure 5: 2D horizontal of dimensionless PNC. (a) $Y=-0.04$ (tailpipe level), (b) $Y=0.33$ and (c) $Y=0.70$

To get a better overview of the whole results, Figure 6 presents a 3D map of the PNC in the wake of the squareback Ahmed body including all measurements. This figure summarizes the previous results.

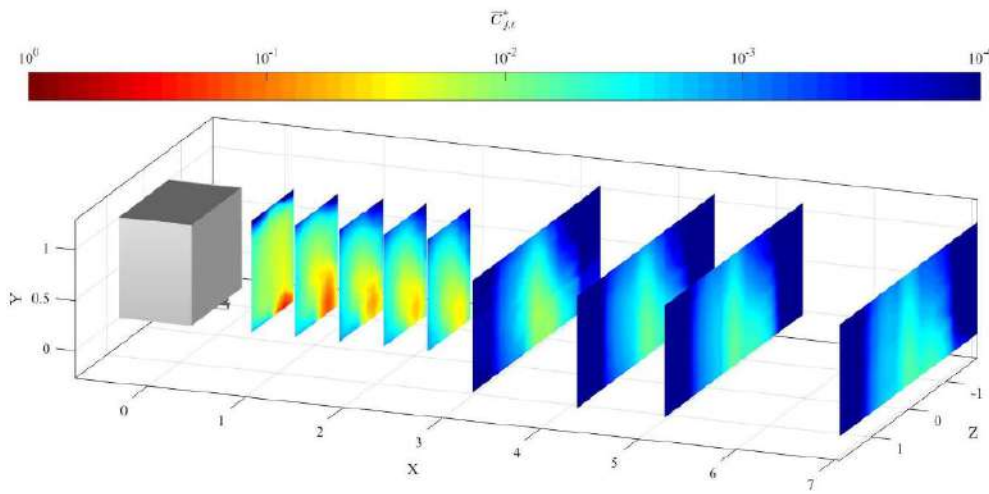


Figure 6: 3D map of dimensionless PNC considering all measurement positions

This figure proves that as we move farther downstream of the car model, the distribution of the UFP become more and more homogeneous and symmetric with respect to $Z=0$.

To go further ahead in the analysis, a diffusion coefficient (D_y) has been assessed in the vicinity of the car model in the vertical direction. Assuming a permanent and 2D flow, a constant velocity U_0 , $\frac{\partial C}{\partial x} \ll \frac{\partial C}{\partial y}$ and a constant diffusion coefficient, then the following diffusion equation governing the concentration should be satisfied:

$$\frac{\partial^2 C}{\partial y^2} = \frac{U_0}{D_y} \frac{\partial C}{\partial x}$$

According to the previous hypothesis, Chanson (1997) gave the following solution:

$$C(y) = C_{max} * \exp \left(-\frac{1}{4} \frac{U_0}{D_y} \frac{(y - y_{C_{max}})^2}{x} \right)$$

Based on our experimental data, C_{max} and $y_{C_{max}}$ are easily known. Then, using a linear regression, the diffusion coefficient D_y has been assessed with an excellent level of accuracy ($r^2 > 0.9$). For this configuration, that is the squareback model, D_y has been determined for each dimensionless positions X and for $Z=-0.31$, 0 and 0.31 . Our results show that D_y is roughly constant for $0.5 < X^* < 7$ and for $Z=-0.31$, 0 and 0.31 with an averaged value of $2.1 \times 10^{-2} \text{ m}^2/\text{s}$. This tends to indicate that this model is robust and able to provide an interesting information that can be used for numerical modelling. In the z -direction, it was more difficult to assess a diffusion coefficient D_z even if a comparable magnitude is suggested ($D_z \sim 1.67 \times 10^{-2} \text{ m}^2/\text{s}$). Nevertheless, the dispersion of the data is larger and this result must be considered carefully.

Conclusions and future works

In the present paper, our interest was focused on the UFP dispersion in the wake of a squareback Ahmed body. Experimental investigations have been conducted in an open wind tunnel. First, the flow topology was characterized using a 2D LDV system. We pointed out that a recirculation region develops which has a length of 1.39H. Two counter rotating vortex developing in the close wake of the car model have been identified as well as some turbulent properties of the turbulent flow field. The dispersion of UFP has been characterized using a PALAS (particle generator) combined with an ELPI (Particle counter) for PNC measurements. We have been able to provide 2D and 3D maps of PNC in the wake of the Ahmed body. Our results indicate that the particle concentrations are strongly related to the flow topology. Particularly, the recirculation is able to suck particles and disperse them in both vertical and transversal directions. Using a simplified 2D diffusion equation, a diffusion coefficient (D_y) was deduced which value is about $2.1 \times 10^{-2} \text{ m}^2/\text{s}$.

In the future, we aim at investigating the interaction between two car models with different rear slant angles. Influence of distances between vehicles, ground clearance as well as bed roughness on particle dispersion are also interesting topics that should be studied. These experimental investigations will also serve as a tool to calibrate numerical models and to corroborate/explain embedded measurements. Indeed, in the last couple of years, we have collected different sets of data from on-board measurements in the context of a research project funded by ADEME.

Acknowledgements

The financial supports of Regional Council of Pays de la Loire (France) and ESTACA are greatly acknowledged.

References

- Ahmed, S.R., Ramm, G. and Faltin, G. (1984). Some Salient features of the time-averaged ground vehicle wake, *SAE Technical Paper series*, DOI: 10.4271/840300, pp. 1-30.
- Algieri, A., Bova, S. and De Bartolo, C. (2005). Experimental and numerical investigation on the effects of the seeding properties on LDA measurements, *Journal of Fluids Engineering*, 127, 3, DOI: 10.1115/1.1899167, pp. 514-522.
- Barros, D. (2015). Wake and manipulation of a bluff body using fluidic forcing, PhD Thesis, ISAE-ENSMA, 82 pages.
- Buseck, P. and Adachi, K. (2008). Nanoparticles in the atmosphere, *Elements*, 4, DOI: 10.2113/gselements.4.6.389, pp. 389-394.
- Carpentieri, M., Kumar, P. and Robins, A.G. (2012) Wind tunnel measurements for dispersion modelling of vehicle wakes, *Atmospheric Environment*, 62, DOI:10.1016/j.atmosenv.2012.08.019, pp. 9-25.
- Chanson, H. (1997). *Air bubble entrainment in free-surface turbulent shear flows*, Academic Press, London (UK), ISBN: 0-12-168110-6, 401 pages.
- Dekati. (2010). *ELPI user manual*, v4.11, 148 pages.
- Eulalie, Y. (2014). Etude aérodynamique et contrôle de la traînée sur un corps de Ahmed à culot droit, PhD Thesis, University of Bordeaux, 198 pages.
- Gosse, K. (2005). Etude expérimentale de la dispersion d'un scalaire passif dans le proche sillage d'un corps d'Ahmed, PhD Thesis, University of Rouen, 178 pages.
- Kanda, I., Uehara, K., Yamao, Y., Yoshikawa, Y. and Morikawa, T. (2006). A wind tunnel study on exhaust-gas dispersion from road vehicles-part 2: effect of vehicle queues, *Journal of Wind Engineering and Industrial Applications*, 94, 9, DOI: 10.1016/j.jweia.2006.06.002, pp. 659-673.
- Lahaye, A. (2014). Caractérisation de l'écoulement autour d'un corps d'Ahmed à culot droit, PhD Thesis, University of Orléans, 159 pages.
- Mehel, A., Murzyn, F., Cuvelier, P., Deville Cavellin, L., Baudic, A., Joly, F., Patte Rouland, B., Varea, E. and Sioutas, C. (2019). CORTEA 2015 : Projet CAPTIHV, Final report, ADEME, 135 pages.

GETTING IN TOUCH WITH THE EU

In person

All over the European Union there are hundreds of Europe Direct information centres. You can find the address of the centre nearest you at: https://europa.eu/european-union/contact_en

On the phone or by email

Europe Direct is a service that answers your questions about the European Union. You can contact this service:

- by freephone: 00 800 6 7 8 9 10 11 (certain operators may charge for these calls),
- at the following standard number: +32 22999696, or
- by electronic mail via: https://europa.eu/european-union/contact_en

FINDING INFORMATION ABOUT THE EU

Online

Information about the European Union in all the official languages of the EU is available on the Europa website at: https://europa.eu/european-union/index_en

EU publications

You can download or order free and priced EU publications from EU Bookshop at: <https://publications.europa.eu/en/publications>. Multiple copies of free publications may be obtained by contacting Europe Direct or your local information centre (see https://europa.eu/european-union/contact_en).

The European Commission's
science and knowledge service
Joint Research Centre

JRC Mission

As the science and knowledge service of the European Commission, the Joint Research Centre's mission is to support EU policies with independent evidence throughout the whole policy cycle.



EU Science Hub
ec.europa.eu/jrc



@EU_ScienceHub



EU Science Hub - Joint Research Centre



Joint Research Centre



EU Science Hub



Publications Office
of the European Union

doi:10.2760/978944

ISBN 978-92-76-17329-8